Advanced Photon Counting Techniques for Long-Range Depth Imaging

Ximing Ren

Submitted for the Degree of Doctor of Philosophy

Heriot-Watt University

School of Engineering and Physical Sciences

October 2015

Abstract

The Time-Correlated Single-Photon Counting (TCSPC) technique has emerged as a candidate approach for Light Detection and Ranging (LiDAR) and active depth imaging applications. The work of this Thesis concentrates on the development and investigation of functional TCSPC-based long-range scanning time-of-flight (TOF) depth imaging systems. Although these systems have several different configurations and functions, all can facilitate depth profiling of remote targets at low light levels and with good surface-to-surface depth resolution. Firstly, a Superconducting Nanowire Single-Photon Detector (SNSPD) and an InGaAs/InP Single-Photon Avalanche Diode (SPAD) module were employed for developing kilometre-range TOF depth imaging systems at wavelengths of ~1550 nm. Secondly, a TOF depth imaging system at a wavelength of 817 nm that incorporated a Complementary Metal-Oxide-Semiconductor (CMOS) 32×32 Si-SPAD detector array was developed. This system was used with structured illumination to examine the potential for covert, eye-safe and high-speed depth imaging. In order to improve the light coupling efficiency onto the detectors, the arrayed CMOS Si-SPAD detector chips were integrated with microlens arrays using flip-chip bonding technology. This approach led to the improvement in the fill factor by up to a factor of 15. Thirdly, a multispectral TCSPC-based full-waveform LiDAR system was developed using a tunable broadband pulsed supercontinuum laser source which can provide simultaneous multispectral illumination, at wavelengths of 531, 570, 670 and ~780 nm. The investigated multispectral reflectance data on a tree was used to provide the determination of physiological parameters as a function of the tree depth profile relating to biomass and foliage photosynthetic efficiency. Fourthly, depth images were estimated using spatial correlation techniques in order to reduce the aggregate number of photon required for depth reconstruction with low error. A depth imaging system was characterised and re-configured to reduce the effects of scintillation due to atmospheric turbulence. In addition, depth images were analysed in terms of spatial and depth resolution.

Acknowledgements

First, I thank the Scottish Universities Physics Alliance (SUPA) very much for offering scholarship for my PhD. I was delighted to join the Single Photon Group and work with my supervisor Professor Gerald S. Buller and all my fellow colleagues (in particular for Dr. Aongus McCarthy, Dr. Nathan R. Gemmell, Dr. Robert J. Collins, Dr. Nils J. Krichel, Giuseppe Intermite, Dr. Ryan E. Warburton, Aurora Maccarone and Rachael Tobin). I whole-heartedly thank Gerald for his great support and mentorship during my research work. I am very fortunate to work with Aongus and really appreciate him for his great research assistance, hard work on all the experimental work, and for his patient guidance on how to be a meticulous researcher. In terms of constructive comments and advice for my English academic writing, I would like to thank Gerald, Aongus, Robert and Rachael for a great deal of their time and effort. I thank Nathan very much for every research discussion with him, which positively enlightened me and helped efficiently improve my research work.

I have really great memories in the Brewster roof lab which is the most unique physics lab at Heriot-Watt University. It was the first lab that I stepped in when I landed in Edinburgh on the 2nd June 2011. I remember all this as if it just happened yesterday. Hereby I would like to thank all the collaborators for their great contributions on a number of successful time-of-flight experiments in the Brewster roof lab: Dr. Michael G. Tanner and Prof. Robert H. Hadfield (University of Glasgow, UK); Adriano Della Frera and Dr. Alberto Tosi (Politecnico di Milano, Italy); Daniel Martinez-Ramirez and Prof. Andrew M. Wallace (Institute of Sensors, Signals and Systems, Heriot-Watt University, UK) and Simone Morak, Prof. Iain H. Woodhouse and Dr. Caroline J. Nichol (The University of Edinburgh); Dr. Federica Villa, Rudi Lussana and Prof. Franco Zappa (Politecnico di Milano, Italy); Dr. Yoann Altmann and Prof. Steve McLaughlin (Institute of Sensors, Signals and Systems, Heriot-Watt University, UK); and Dr. Kirmani Ahmed (MIT, USA).

Many thanks also go to Dr. Cristtel Ramirez, Dr. Rose Mary, Dr. Richard McCracken

and Dr. Frauke Izdebski for their kindly encouragement and help during my PhD research and study. In addition, I thank all my Chinese buddies in Edinburgh for the great fun that I have with them in my daily life (in particular for Jianyong Chen, Jun Gao, Fuyong Yue, Dandan Wen, Haoyu Li, Maoshuai Li, Dr. Lei Yang, Dr. Zhen Qiu, Dr. Wenxing Tang, Dr. Jia Ni, Dr. Xinghui Dong, Prof. Zhaowei Zhang, Dr. Yong Ma and Dr. Xianzhong Chen).

Finally, I thank all my family for their selfless and endless love and support. I respect and appreciate my grandfather for enlightening my soul due to his modesty and patience. I am hugely grateful for my parents, sister, and brother in law for the visiting me here in the UK and for all the great times we had together. Great thanks also go to my little niece for her every cute and sweet smile, which never fails to make me happy.

Thank all of you very much.

ACADEMIC REGISTRY
Research Thesis Submission

Name:			
School/PGI:			
Version: *(i.e. First, Resubmission, Final)*		Degree Sought (Award **and** Subject area)	

Declaration

In accordance with the appropriate regulations I hereby submit my thesis and I declare that:

1) the thesis embodies the results of my own work and has been composed by myself
2) where appropriate, I have made acknowledgement of the work of others and have made reference to work carried out in collaboration with other persons
3) the thesis is the correct version of the thesis for submission and is the same version as any electronic versions submitted*.
4) my thesis for the award referred to, deposited in the Heriot-Watt University Library, should be made available for loan or photocopying and be available via the Institutional Repository, subject to such conditions as the Librarian may require
5) I understand that as a student of the University I am required to abide by the Regulations of the University and to conform to its discipline.

* *Please note that it is the responsibility of the candidate to ensure that the correct version of the thesis is submitted.*

Signature of Candidate:		Date:	

Submission

Submitted By *(name in capitals):*	
Signature of Individual Submitting:	
Date Submitted:	

For Completion in the Student Service Centre (SSC)

Received in the SSC by *(name in capitals):*			
Method of Submission *(Handed in to SSC; posted through internal/external mail):*			
E-thesis Submitted (***mandatory for final theses)***			
Signature:		Date:	

Please note this form should bound into the submitted thesis.

Updated February 2008, November 2008, February 2009, January 2011

Contents

Glossary of Acronyms and Terms

ADC	Analogue-to-Digital Converter
AMP	Amplifier
AM	Amplitude Modulation
AOTF	Acousto-Optic Tunable Filter
APD	Avalanche Photodiode
AQ	Active Quenching
AQC	Active Quenching Circuit
ASC	Advanced Scientific Concepts
ASCII	American Standard Code for Information Interchange
BPF	Band-pass Filter
BS	Beam Splitter
CA	Clear Aperture
CAD	Computer Aided Design
CB	Conduction Band
CCD	Charge-Coupled Device
CDF	Cumulative Density Function
CEOI	Centre for Earth Observation Instrumentation

CFD	Constant Fraction Discriminator
CMOS	Complementary Metal-Oxide-Semiconductor
C_n^2	Refractive-index structure parameter
cps	counts per second
CS	Compressed Sensing
CW	Continuous-Waveform
DCR	Dark Count Rate
DLL	Delay-Locked Loop
DNL	Differential Nonlinearity
DOE	Diffractive Optical Element
DSM	Deep Submicron
dTOF	Direct Time Of Flight
EF	Effective Focal length
E_g	Material band gap energy
FAQ	Fast-Active Quenching
FC	Fibre Collimator
FC/APC	Ferrule Connector / Angled Physical Contact
FC/PC	Ferrule Connector / Physical Contact
FCS	Fluorescence Correlation Spectroscopy
FD	Fibre Delivery
FIFO	First-In-First-Out
FLIM	Fluorescence Lifetime Imaging Microscopy

FM	Frequency Modulation
FM-CW	Frequency Modulation Continuous-Waveform
FN	Facet Normal
FOV	Field of View
FPGA	Field Programmable Gate Array
FPA	Focal Plane Array
FRET	Fluorescence Resonance Energy Transfer
FWHM	Full Width at Half Maximum
Ge	Germanium
GM	Galvanometer scan mirror
GmAPD	Geiger mode Avalanche Diode
GN	Grating Normal
HV-CMOS	High-Voltage Complementary Metal-Oxide-Semiconductor
HWP	Half Wave Plate
IF	Improvement Factor
IFOV	Instantaneous Field of View
INL	Integral Nonlinearity
InGaAs	Indium Gallium Arsenide
InP	Indium Phosphide
IR	Infrared
IRF	Instrumental Response Function
ISL	French–German Research Institute of Saint-Louis

iTOF	Indirect Time Of Flight
kcps	10^3 counts per second
Ladar	Laser Radar
LiDAR	Light Detection And Ranging
LP	Linear Polariser
LPF	Long-pass Filter
LSB	Least-Significant Bit
MCMC	Markov Chain Monte Carlo
MCP	Microchannel Plate
MDF	Medium-Density Fibreboard
MISEC	Micro Systems Engineering Centre
MiSPIA	Microelectronic Single-Photon 3D Imaging Arrays for low-light high-speed Safety and Security Applications
MMF	Multi-Mode Fibre
MPD	Micro Photon Devices
MSE	Mean Squared Error
NA	Numerical Aperture
NASA	National Aeronautics and Space Administration
NbN	Niobium Nitride
NbTiN	Niobium Titanium Nitride
NDVI	Normalised Differential Vegetation Index
NEP	Noise-Equivalent Power

NIM	Nuclear Instrumentation Module
NPV	Non-Photosynthetic Vegetation
OCT	Optical Coherence Tomography
OL	Objective Lens
PBS	Polarising Beam Splitter
PC	Personal Computer
PCF	Photonic Crystal Fibre
PDF	Probability Density Function
PE	Power Efficiency
PLI	Princeton Lightwave, Inc.
PMF	Polarisation-Maintaining Fibre
PM-SMF	Polarisation-Maintaining Single-Mode Fibre
PMT	Photomultiplier Tube
PPG	Pulse Pattern Generator
PQ	Passive Quenching
PQC	Passive Quenching Circuit
PRI	Photochemical Reflectance Index
PV	Photosynthetic Vegetation
QE	Quantum Efficiency
RAM	Random-Access Memory
RE-SPAD	Red-Enhanced Single Photon Avalanche Diode
RJMCMC	Reversible-jump Markov Chain Monte Carlo

RL	Relay Lens
RMS	Root Mean Square
ROIC	Readout Integrated Circuit
Rx	Receive
SACM	Separate Absorption, Charge and Multiplication
SAGCM	Separate Absorption, Grading, Charge and Multiplication
SAM	Separate Absorption and Multiplication
SBR	Signal-to-Background Ratio
SER	Single Electron Response
SI	Scintillation Index
Si	Silicon
SIMPL	Slope Imaging Multi-polarisation Photon Counting LiDAR
SMF	Single-Mode Fibre
SNR	Signal-to-Noise Ratio
SNSPD	Superconducting Nanowire Single Photon Detector
SPAD	Single Photon Avalanche Diode
SPDE	Single Photon Detection Efficiency
SPF	Short-pass Filter
Std	Standard derivation
SWIR	Short-Wave Infrared
TAC	Time-to-Amplitude Converter
TEC	Thermoelectric Cooler

TCSPC	Time-Correlated Single-Photon Counting
TDC	Time-to-Digital Converter
TOF	Time Of Flight
TTL	Transistor-Transistor Logic
TTTR	Time-Tagged-Time-Resolved
Tx	Transmit
USB	Universal Serial Bus
USM	Ultrasonic Motor
UV	Ultraviolet
VB	Valence Band
V_{BD}	Breakdown voltage
V_{DC}	DC voltage
V_E	Excess bias voltage
VLQC	Variable Load Quenching Circuit
WSi	Tungsten Silicide
YBCO	Yttrium-Barium-Copper-Oxide
2D	Two Dimensional or Two Dimensions
3D	Three Dimensional or Three Dimensions
f	Focal length
λ	Wavelength
h	Planck's constant and
c	The speed of light

ν	The frequency of the photon
μ	Micro
ρ	Reflectance of the target surface
τ	Time

List of Publications

Journal Publications

- A. Maccarone, A. McCarthy, **X. Ren**, R. E. Warburton, A. M. Wallace, J. Moffat, Y. Petillot and G. S. Buller, "Underwater depth imaging using time-correlated single photon counting," submitted to Optics Express (October 2015)
- G. Intermite, A. McCarthy, R. E. Warburton, **X. Ren**, F. Villa, A. J. Waddie, M. R. Taghizadeh, A. Tosi, F. Zappa, and G. S. Buller, "Fill-factor improvement of Si CMOS single-photon avalanche diode detector arrays by the integration of diffractive microlens arrays," submitted to Optics Express (August 2015)
- Y. Altmann, **X. Ren**, A. McCarthy, G. S. Buller and S. McLaughlin, "Lidar waveform based analysis of depth images constructed using sparse single-photon data," submitted to IEEE Transactions on Image Processing (2015)
- D. Wen, F. Yue, S. Kumar, Y. Ma, M. Chen, **X. Ren**, P. E. Kremer, B. D. Gerardot, M. R. Taghizadeh, G. S. Buller, and X. Chen," Metasurface for characterization of the polarization state of light," Optics Express (23), 10272-10281 (2015).
- A. M. Wallace, A. McCarthy, C. J. Nichol, **X. Ren**, S. Morak, D. Martinez-Ramirez, I. H. Woodhouse, and G. S. Buller, "Design and Evaluation of Multispectral LiDAR for the Recovery of Arboreal Parameters," IEEE Transactions on Geoscience and Remote Sensing (52), 4942-4954 (2014).
- A. McCarthy, **X. Ren***, A. Della Frera, N. R. Gemmell, N. J. Krichel, C. Scarcella, A. Ruggeri, A. Tosi, and G. S. Buller, "Kilometer-range depth imaging at 1550 nm wavelength using an InGaAs/InP single-photon avalanche diode detector," Optics Express (21), 22098-22113 (2013). ***Corresponding author***
- A. McCarthy, N. J. Krichel, N. R. Gemmell, **X. Ren**, M. G. Tanner, S. N. Dorenbos, V. Zwiller, R. H. Hadfield, and G. S. Buller, "Kilometer-range, high resolution depth imaging via 1560 nm wavelength single-photon detection," Optics Express

(21), 8904-8915 (2013).

Conference Publications and Presentations

- G. S. Buller, A. McCarthy, **X. Ren**, A. Maccarone, N. R. Gemmell, A. M. Wallace, Y. Petillot, "Single–photon Depth Imaging in Free–space and Underwater", ***Invited Paper***, OSA Imaging and Applied Optics Congress, Arlington, Virginia, UA (June 2015)
- A. Maccarone, A. McCarthy, **X. Ren**, R. E. Warburton, A. M. Wallace, J. Moffat, Y. R. Petillot, and G. S. Buller, "Underwater Depth Imaging using Time–correlated Single Photon Counting", 4th EOS Topical Meeting on Blue Photonics–Optics in the Sea (Blue Photonics 4), Barcelona, Spain (May 2015)
- A. Maccarone, A. McCarthy, **X. Ren**, R. E. Warburton, A. M. Wallace, J. Moffat, Y. R. Petillot, and G. S. Buller, "Underwater depth imaging using time–correlated single photon counting", SPIE DSS Sensing Technology + Applications, Baltimore, Maryland, USA (April 2015)
- G. Intermite, R.E. Warburton, A. McCarthy, **X. Ren**, F. Villa, A. J. Waddie, M. R. Taghizadeh, F. Zappa and G. S. Buller, "Enhancing the fill–factor of CMOS SPAD arrays using microlens integration", ***Invited Paper***, SPIE Optics + Optoelectronics, Prague, Czech Republic (April 2015)
- **X. Ren**, A. McCarthy, A. M. Wallace, and G. S. Buller, "Multispectral single-photon detection in time–of–flight depth profiling", Photon14, London, UK (September 2014)
- R. H. Hadfield, N. R. Gemmell, R. Aspden, M.G. Tanner, A. McCarthy, **X. Ren**, G. S. Buller, and M. J. Padgett, "Single photon imaging with superconducting nanowire single photon detectors", Applied Superconductivity Conference (ASC) 2014, Charlotte, North Carolina, USA (August 2014)
- **X. Ren**, A. McCarthy, A. Della Frera, N. R. Gemmell, N. J. Krichel, C. Scarcella, A. Ruggeri, A. Tosi, and G. S. Buller, "Time–of–flight Depth Imaging at 1550 nm Wavelength at Kilometer–range Distances Using an InGaAs/InP Single–Photon Avalanche Diode Detector ", CLEO 2014, San Jose, USA (June 2014)
- G. S. Buller, A. McCarthy, **X. Ren**, N. R. Gemmell, A. Maccarone, Y.R. Petillot,

and A.M. Wallace, "Applications of depth imaging based on time–correlated single–photon counting", ***Invited Paper***, SPIE DSS 2104, Baltimore, Maryland, USA (May 2014)

- A. McCarthy, **X. Ren**, A. Della Frera, N. R. Gemmell, N. J. Krichel, C. Scarcella, A. Ruggeri, A. Tosi, and G. S. Buller, "Kilometer–Range Depth Imaging Using an InGaAs/InP Single–Photon Avalanche Diode Detector Operating at a Wavelength of 1550 nm", Single Photon Workshop 2013, Oak Ridge, USA (October 2013)
- A. McCarthy, N. J. Krichel, N. R. Gemmell, **X. Ren**, M. G. Tanner, S. D. Dorenbos, V. Zwiller, R. H. Hadfield, and G. S. Buller, "Kilometre–range, high resolution depth imaging using 1560 nm wavelength single–photon detection", CLEO/Europe-IQEC, Munich, Germany (May 2013)
- N. R. Gemmell, A. McCarthy, **X. Ren**, N. J. Krichel, M. G. Tanner, R. H. Hadfield, and G. S. Buller, "Kilometre Range Depth Imaging at 1550nm wavelength using a Superconducting Nanowire Single Photon Detector", SPIE Security + Defence - Electro–Optical Remote Sensing, Edinburgh, UK (September 2012)
- **X. Ren**, A. McCarthy, N. R. Gemmell, N. J. Krichel, M. G. Tanner, R. H. Hadfield, G. S. Buller, "Kilometre range single–photon depth imaging system at 1560 nm wavelength", Photon 12, Durham, UK (September 2012)
- G. S. Buller, A. McCarthy, N. R. Gemmell, **X. Ren**, N. J. Krichel, R. J. Collins, S. N. Dorenbos, V. Zwiller, M. G. Tanner and R. H. Hadfield, "Kilometer range single–photon depth imaging at wavelengths of 850nm and 1560nm", ***Invited Paper***, SPIE Optics and Photonics, San Diego, USA (August 2012)
- D. Martinez-Ramirez, G. S. Buller, A. McCarthy, **X. Ren**, A. M. Wallace, S. Morak, C. Nichol, and I. Woodhouse, "Developing Hyperspectral LiDAR for Structural and Biochemical Analysis of Forest Data," Advances in Geosciences, Proceedings of EARSEL Conference, Mykonos, Greece (May 2012)

Chapter 1
Introduction

Time-of-Flight (TOF) Light Detection and Ranging (LiDAR) systems are capable of non-contact, non-invasive depth measurements of remote objects by directly interpreting the time difference between the outbound and return signal pulses. The TOF based 3D imaging systems are well-established tools in the remote sensing applications such as aerial surveying, terrain mapping and bathymetry [1.1]. They have also been used in a wide range of application areas, e.g. security (such as environment monitoring [1.2], remote object recognition and vehicle safety [1.3] using 3D mapping) and computer vision (such as 3D robotic vision and gesture recognition [1.4]).

For conventional LiDAR-based TOF depth imaging systems, the detection Signal-to-Noise Ratio (SNR) and working distance (R) are often forced to compromise due to the collection light power limited by a roll-off factor of $1/R^2$. However, the TOF depth imaging systems based on the Time-Correlated Single Photon Counting (TCSPC) technique can improved this. These systems are of increasing interest as improved semiconductor-based single-photon detectors, more flexible and powerful pulsed laser sources and versatile, high-speed data acquisition modules become available. The TCSPC-based depth imaging can offer shot-noise-limit detection with excellent surface-to-surface depth resolution [1.5] even with the average output optical power constrained to an eye-safe level. Therefore, it allows the high resolution depth profiling of remote low-signature targets under photon-starved conditions [1.6].

The work carried out in this Thesis concentrates on the development and characterisation of functional TCSPC-based TOF LiDAR systems for a series of end-applications. This includes long distance imaging systems operating at 1550nm wavelength, using InGaAs/InP Single Photon Avalanche Diodes (SPADs), and a Superconducting Nanowire Single Photon Detectors (SNSPDs). A system using a 32×32 CMOS Si-SPAD detector array was constructed and analysed. A multispectral

depth imaging system was designed and investigated for geoscience applications. Finally, the characterisation of the scanning depth imaging systems was examined temporally and spatially in order to gain a better understanding of its performance and some latent factors during measurements. This included the use of image processing with spatial correlations and a study of the effect of atmospheric scintillation.

The work in this Thesis was carried out by Gerald S. Buller's Single Photon Group. Particularly, it includes the contributions by Aongus McCarthy, Nathan R. Gemmell, Nils J. Krichel and Robert J. Collins. The work was also made possible through collaborations with many other researchers at Heriot-Watt University (in particular for Andrew M. Wallace, Yoann Altmann, Steve McLaughlin, Neil Ross, Andrew J. Waddie and Mohammad R. Taghizadeh) as well as several other groups (including Robert H. Hadfield's Quantum Sensors Group at University of Glasgow, and Franco Zappa and Alberto Tosi's groups in Politecnico di Milano). A large amount of the work described in this Thesis builds on previous work conducted by the Single Photon Group.

1.1 Thesis structure

Chapter 2 reviews advanced photon counting techniques, the relatively mature single photon detectors and the previously realised TOF depth imaging systems. In particular, modern TCSPC systems with time-tagged-time-resolved modes will be highlighted. Detectors used in this Thesis will also be highlighted, for example Si and InGaAs/InP SPADs and SNSPDs.

Chapter 3 represents a common scanning imaging platform, which can be reconfigured and used to construct different systems for the experiments reported in the later chapters. It is composed of four key sub-systems: a pulsed laser source, a bespoke scanning monostatic transceiver system (firstly used for the work published in [1.7]), a single-photon detector module, and a data acquisition module. A mode-locked pulsed fibre laser and a broadband pulsed supercontinuum laser source will be briefly introduced, as this will be used in the depth imaging systems in later chapters. The structure and feature of other subsystems will also be discussed.

Chapter 4 describes two kilometre-range scanning depth imaging systems using at $\lambda \sim 1550$ nm. One system used a discrete free-running SNSPD and the other had an InGaAs/InP SPAD detector module operating in gated-mode [1.8-1.9]. These systems were developed for an increased eye-safety threshold, high atmospheric transmission and a reduction in solar background.

Chapter 5 describes a SPAD-array-based scanning depth imaging system at λ=817 nm using structured illumination based on a fanout diffractive optical element (DOE). This system was characterised in order to examine the potential for covert, eye-safe and high-speed TCSPC-based depth imaging. The integration of the microlens arrays and low fill-factor arrayed detectors is an effective way to achieve good fill-factor recovery. Thus, this can enhance the light coupling efficiency onto the photosensitive areas of the CMOS Si-SPAD arrays for improved-efficient single photon detection. The design of the diffractive and refractive microlens arrays will be briefly introduced. The new approach for integration of the arrayed detector chips and microlens arrays by the use of flip-chip bonding technology will be described. In addition, the characterisation of the bonded assemblies will be discussed [1.10].

Chapter 6 reports a full-waveform multispectral TCSPC-based scanning TOF depth imaging system at λ=531, 570, 670 and ~780 nm using a tunable pulsed supercontinuum laser source. In this system, a diffraction-grating-based wavelength-routing system was used for wavelength de-multiplexing in the receive channel. This system was developed for depth profiling on tree samples, which are examples of low signature distributed targets. The characterisation of the first-generation wavelength-routing system will be reported and its refined design will be discussed. In order to demonstrate the capabilities of the multispectral depth imager with regards to the recovery of structural and physiological parameters from tree samples, several field trial results carried out on a Nordmann fir tree as well as several example specimens will be reported [1.11].

Chapter 7 focuses on temporal and spatial characterisation of the scanning TOF single-photon depth imaging systems at λ ~ 840 nm. Depth images were fully analysed in terms of spatial and depth resolution and the depth imaging system was characterised and re-configured to reduce the effects of scintillation due to atmospheric turbulence. Depth images were estimated using spatial correlation techniques in order to reduce the aggregate number of photons required for depth reconstruction with low error [1.12].

Chapter 8 summarises the results of all the experimental chapters and presents the outlook of further work.

1.2 References

[1.1]. C. Glennie, W. Carter, R. Shrestha, and W. Dietrich, "Geodetic imaging with airborne LiDAR: the Earth's surface revealed," Rep. Prog. Phys. (76), 086801 (2013).

[1.2]. B. Schwarz, "LIDAR: Mapping the world in 3D," Nat. Photonics (4), 429-430 (2010).

[1.3]. S. Hsu, S. Acharya, A. Rafii, and R. New, "Performance of a time-of-flight range camera for intelligent vehicle safety applications," in *Advanced Microsystems for Automotive Applications 2006*(Springer, 2006), pp. 205-219.

[1.4]. S. Foix, G. Alenya, and C. Torras, "Lock-in time-of-flight (ToF) cameras: a survey," IEEE Sens. J. (11), 1917-1926 (2011).

[1.5]. J. S. Massa, G. S. Buller, A. C. Walker, G. Smith, S. Cova, M. Umasuthan, and A. M. Wallace, "Optical design and evaluation of a three-dimensional imaging and ranging system based on time-correlated single-photon counting," Appl. Opt. (41), 1063-1070 (2002).

[1.6]. G. S. Buller, and A. M. Wallace, "Ranging and three-dimensional imaging using time-correlated single-photon counting and point-by-point acquisition," IEEE J. Select. Topics Quantum Electron. (13), 1006-1015 (2007).

[1.7]. A. McCarthy, R. J. Collins, N. J. Krichel, V. Fernandez, A. M. Wallace, and G. S. Buller, "Long-range time-of-flight scanning sensor based on high-speed time-correlated single-photon counting," Appl. Opt. (48), 6241-6251 (2009).

[1.8]. A. McCarthy, N. J. Krichel, N. R. Gemmell, X. Ren, M. G. Tanner, S. N. Dorenbos, V. Zwiller, R. H. Hadfield, and G. S. Buller, "Kilometer-range, high resolution depth imaging via 1560 nm wavelength single-photon detection," Opt. Express (21), 8904-8915 (2013).

[1.9]. A. McCarthy, X. Ren, A. Della Frera, N. R. Gemmell, N. J. Krichel, C. Scarcella, A. Ruggeri, A. Tosi, and G. S. Buller, "Kilometer-range depth imaging at 1550 nm wavelength using an InGaAs/InP single-photon avalanche diode detector," Opt. Express (21), 22098-22113 (2013).

[1.10]. G. Intermite, R. Warburton, A. McCarthy, X. Ren, F. Villa, A. Waddie, M. Taghizadeh, Y. Zou, F. Zappa, and A. Tosi, "Enhancing the fill-factor of CMOS SPAD arrays using microlens integration," *SPIE Optics+ Optoelectronics*, International Society for Optics and Photonics, pp. 95040J-95040J-95012, (2015).

[1.11]. A. M. Wallace, A. McCarthy, C. J. Nichol, X. Ren, S. Morak, D. Martinez-Ramirez, I. H. Woodhouse, and G. S. Buller, "Design and Evaluation of Multispectral LiDAR for the Recovery of Arboreal Parameters," IEEE Trans. Geosci. Remote Sens.

(52), 4942-4954 (2014).

[1.12]. Y. Altmann, X. Ren, A. McCarthy, G. S. Buller, and S. McLaughlin, "Lidar waveform based analysis of depth images constructed using sparse single-photon data," arXiv preprint arXiv:1507.02511 (2015).

Chapter 2
Time-correlated single-photon counting and time-of-flight depth imaging

2.1 Introduction

At a fundamental level, a photon can be recognised as a quantised energy packet of electromagnetic radiation (refer to Page 3 of [2.1]). Single photon detection is a booming technological field, which is of great importance in high sensitivity detection. It has seen massive expansion in the last two decades as rapid data acquisition hardware and new detectors have brought the technique into widespread applications.

This Chapter will review the time-correlated single-photon counting (TCSPC) technique and relevant single-photon detectors. Depth imaging approaches using laser sources will also be reviewed, in particular single photon time-of-flight depth imaging.

2.2 Time-correlated single-photon counting

2.2.1 TCSPC principles

The TCSPC technique has been used in areas such as nuclear physics and astronomy to provide precise time measurements. It has been further driven by time-resolved applications of life sciences [2.2], such as fluorescence correlation spectroscopy (FCS), fluorescence lifetime imaging microscopy (FLIM), and fluorescence resonance energy transfer (FRET) microscopy. Typical fluorescence lifetimes are in the range from 100s ps to 10s ns. In addition, the fluorescence photon flux is typically weak in most cases, meaning that single-photon sensitivity is required. As the TCSPC technique has the advantages of significantly higher timing precision and no amplitude-jitter-induced noise, it is often used to detect optical transients excited by the repetitive pulsed radiation. Moreover, it is an excellent method to resolve the fluorescence intensity profile in the time domain. Note that in terms of TCSPC-based measurements, many

modern laser sources such as pulsed laser diodes, fibre lasers and supercontinuum lasers have been widely employed as illumination photon sources [2.3]. Their features include short pulse width, which offers high timing resolution for TCSPC measurements as well as moderate optical powers to provide sufficient light to interact with targets. In addition, some of these sources are capable of varying repetition rates to locate the pulse period to the targeted operation time window. As shown in Figure 2-1, the start trigger of a typical TCSPC measurement setup is synchronised to the pulsed laser source, while the single photon detector provides the stop trigger. Each independent detected photon event corresponds to an individual start-stop time difference, shown in Figure 2-2.

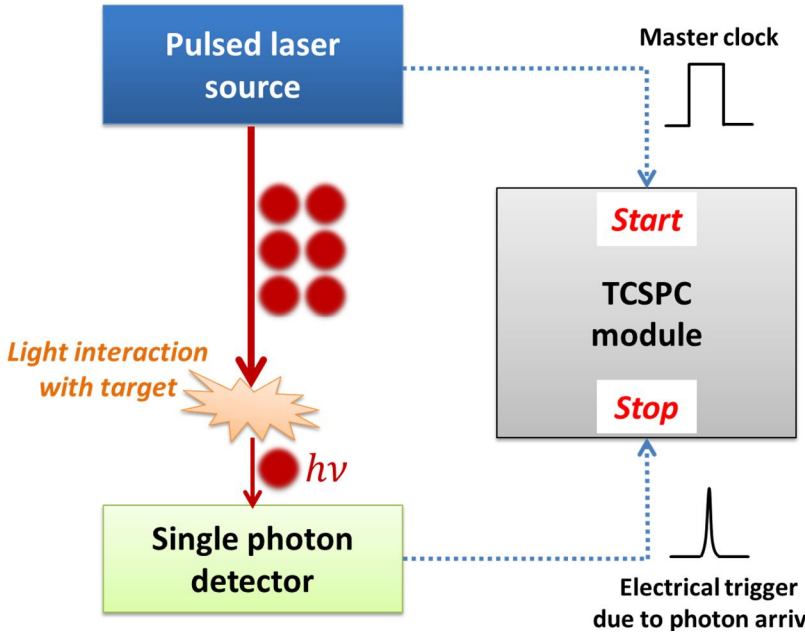

Figure 2-1 Time-correlated single-photon counting (TCSPC) measurement setup.

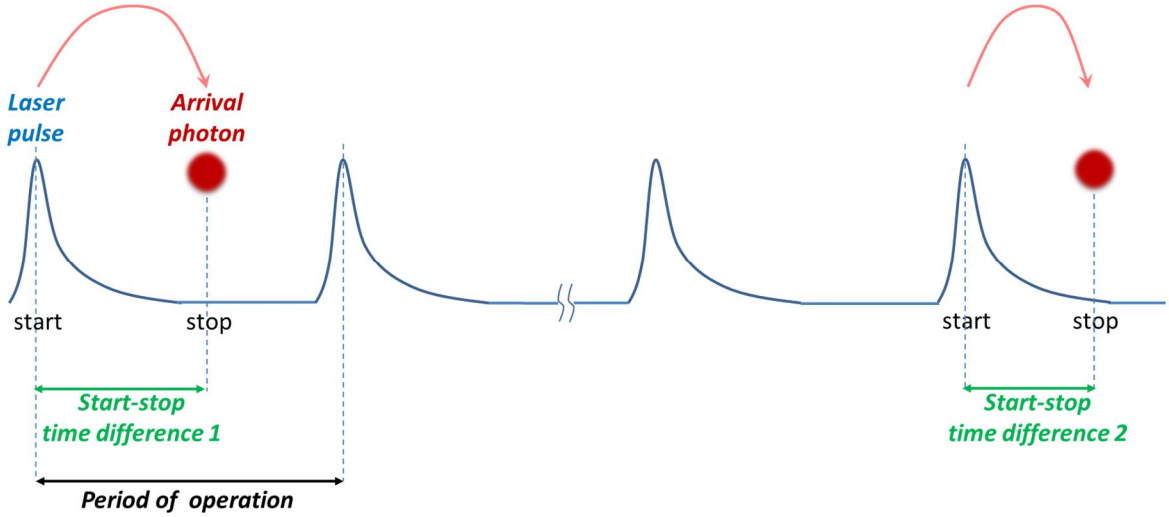

Figure 2-2 Start-stop time difference measurements associated with independent photon events.

If more than one photon incident occurs within one period of operation, as shown in Figure 2-3, then only one of these photons can be detected and the others cannot (this is likely to be the first photon, however this likelihood depends on the efficiency of the detector). If the average number of photons per period gets too large, then this can result in distortion of the signal waveform known as "pulse pile-up" as shown in Figure 2-4. As an example, shown in Figure 2-4, if the lifetime is an exponential decay then it will appear to be shorter than the real lifetime if pulse pile-up occurs. This is shown in Figure 2-4. The exponential lifetime can be estimated by the recorded intensity-weighted mean lifetime as a function of the number of photons per period of operation (P) which has small values (refer to Pages 334-336 [2.4]):

$$\tau_{mean,i} \approx \tau(1 - \frac{P}{4}) \qquad \text{Equation (2.1)}$$

where τ is the correct lifetime. The relevant relative intensity-weighted lifetime can be described as:

$$\tau_{relative} = \frac{\tau_{mean,i}}{\tau} \approx (1 - \frac{P}{4}) \qquad \text{Equation (2.2)}$$

Lower $\tau_{relative}$ represents a more significant influence of the pile-up effect on the recorded lifetime due to higher P (see Figure 2-5). For practical TCSPC measurements, keeping P as low as 0.01 to 0.1 can effectively mean a realistic measurement of a signal waveform with tolerable or minimised distortion due to the pile-up effect. In order to ensure that this condition can be met, the average incident power on the detector will have to be adjusted to ensure that the ratio of the detection count rate to the synchronisation clock rate is monitored. This creates a rule of thumb for the threshold at which a true signal waveform can be detected using the TCSPC technique.

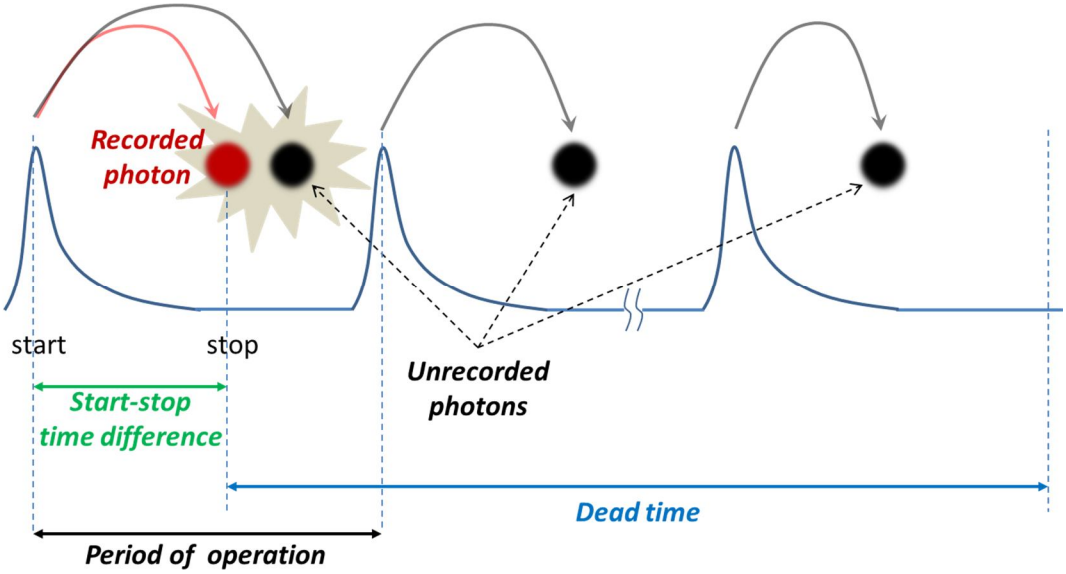

Figure 2-3 The pile-up effect occurs within one period of operation when more than one photon incident occurs. The dead time is initiated after one recorded photon event.

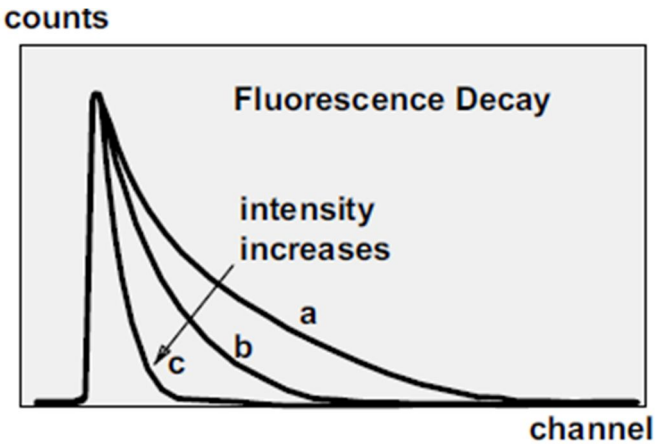

Figure 2-4 The fluorescence decay indicated by "a" represents the correct signal waveform. The decays indicated by "b" and "c" show how the signal is distorted by the pile-up effect as the input light intensity (or incident photons) increases. (Reproduced from Page 333 of [2.4]).

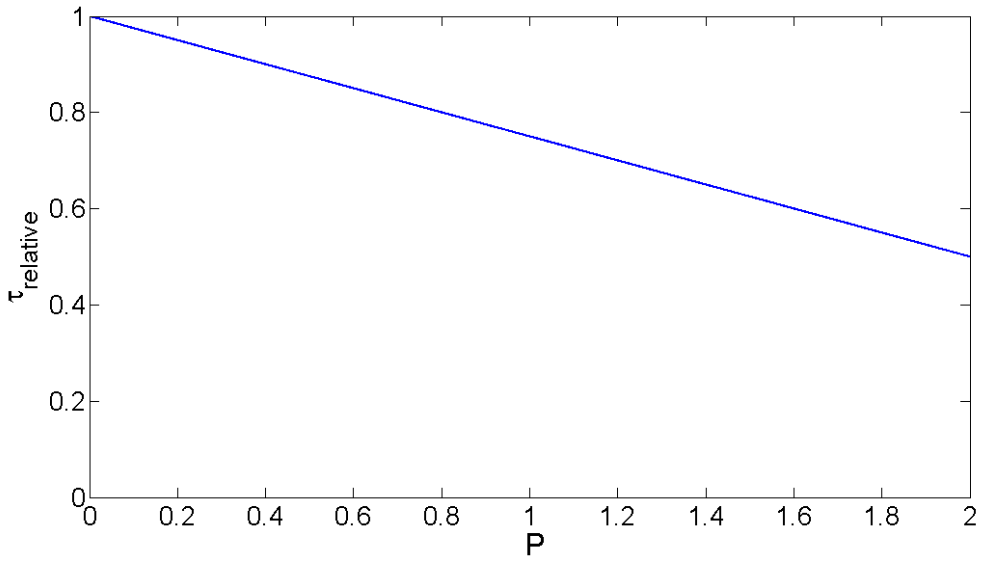

Figure 2-5 The plot of the relative intensity-weighted life time ($\tau_{relative}$) versus the number of photons per period of operation (P) that corresponds to the ratio of the detector count rate to the repetition rate of the pulsed laser source.

As shown in Figure 2-3, each recorded photon event can cause average system dead time (T_d), the time during which the system does not respond after registering the event. In other words, any photons which occur within T_d of the TCSPC system cannot be recorded (refer to Page 129 of [2.5]). Note that, in many cases, T_d is primarily due to the dead time of the time-to-amplitude converter (TAC) and analogue-to-digital converter (ADC) or the time-to-digital converter (TDC) used in the TCSPC system as these are typically longer than any detector reset times. T_d is typically about 100 ns to 125 ns for TCSPC devices from Becker & Hickl GmbH (refer to Page 19 of [2.5]). It is typically less than 90 ns and 80 ns for TCSPC modules of PicoHarp 300 and HydraHarp 400 (from PicoQuant GmbH, Germany), respectively. Given a pulsed laser source with a certain repetition rate, the maximum detected total count rate (C_{det}) is limited by the aforementioned rule of thumb outlined above, in order to minimise the pile-up effect. It is worth noting that the maximum count rate commonly listed in datasheets of TCSPC devices is equal to the reciprocal of the average system dead time (i.e. $1/T_d$). This corresponds to the "saturated count rate" when only the detected count rate is theoretically infinite. In fact, the maximum useful count rate (C_{max}) can be determined from the recorded count rate (C_{rec}) when C_{det} reaches the saturated count rate (refer to Page 131 of [2.5] and Page 338 of [2.4]):

$$C_{rec} = \frac{C_{det}}{1 + C_{det}T_d} \qquad \text{Equation (2.3)}$$

$$C_{max} = \frac{1}{2T_d} \qquad \text{Equation (2.4)}$$

When the detected average photon events per pulse are sparse compared to the excited laser pulses, as shown in Figure 2-6, the desired signal waveform can be reconstructed into a photon histogram associated with repetitive photon events from a large number of independent time measurements (i.e. TCSPC measurements) over all periods of operation.

The instrumental response function (IRF) of the entire TCSPC system is commonly used to characterise its timing resolution. The timing uncertainties of individual components in the system (such as the single photon detector, pulsed laser source and TCSPC electronics) all contribute to the system IRF. In a statistical sense and according to propagation of uncertainty, the timing jitter of the system IRF in the form of a Full Wide at Half Maximum (FWHM) can be estimated as [2.6]:

$$t_{IRF_{sys}} \approx \sqrt{t_{IRF_{det}}^2 + t_{IRF_{laser}}^2 + t_{IRF_{TCPSC}}^2 + \sum t_{IRF_{others}}^2} \qquad \text{Equation (2.5)}$$

where $t_{IRF_{det}}$, $t_{IRF_{laser}}$ $t_{IRF_{TCSPC}}$ and $t_{IRF_{others}}$ are the timing jitter FWHM of a single photon detector, pulsed laser source, TCSPC electronics and any other contributing components, respectively. $t_{IRF_{det}}$ corresponds to the timing uncertainty of the conversion from the arrival photon to a detectable electrical response by the detector. $t_{IRF_{laser}}$ indicates the laser pulse duration time. For example, $t_{IRF_{det}}$ is typically in the order of a few 10s ps to 100s ps for state-of-the-art single photon detectors, whereas $t_{IRF_{laser}}$ can be as low as in the order of fs for modern laser sources, while $t_{IRF_{TCSPC}}$ is $\approx$ 10 ps or less. Therefore, the timing jitter of the single photon detector makes significant contributions to the system IRF with typical 100s ps or less FWHM. In addition, the time-bin width (i.e. timing accuracy) of a modern TCSPC module, which can be 1 ps or less, is much shorter than the system IRF. In summary, the TCSPC timing resolution is significantly superior to analogue recording techniques, which are limited by the pulse width (typical order of ns FWHM) of the detector's single electron response (SER). Note that the SER is an electrical pulse which outputs from a photodetector for a single photoelectron (refer to Page 17 or Page 54 of [2.5]).

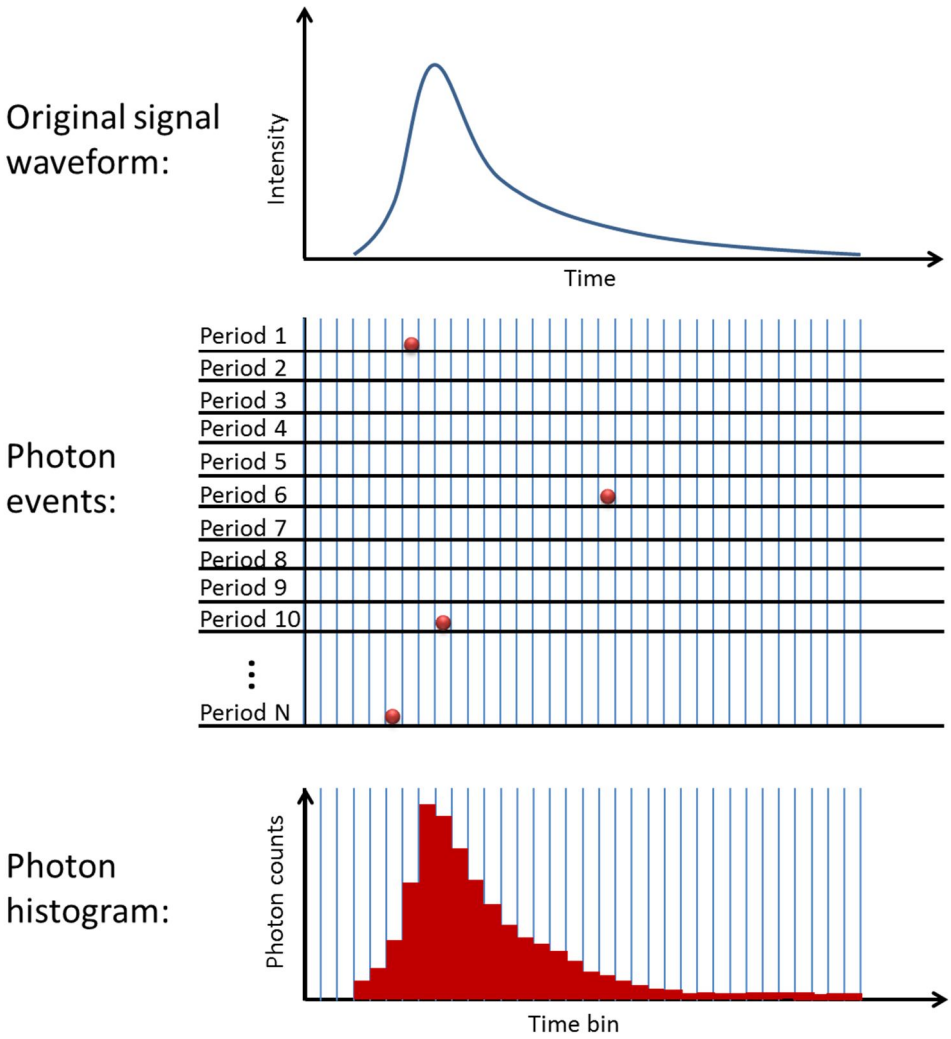

Figure 2-6 Sampling illustration of the principle of TCSPC operation, after Page 16 of [2.5]. The original waveform is for example only.

As the photon collection of each time bin follows a Poisson statistic process, the reconstructed photon histogram presents a distribution of photon probability over all time bins related to the original signal waveform. Given that a total number of recorded photon events (N_i) are accumulated in the ith time bin, then the Poissonian noise is equal to its standard deviation ($\sqrt{N_i}$). The signal-to-noise ratio (SNR) of a TCSPC measurement can be evaluated as [2.7]:

$$SNR = \frac{N_{PK}}{\sqrt{N_{PK} + N_B}} \qquad \text{Equation (2.6)}$$

where N_{PK} is the maximum number of photon counts within a time bin in the range measured and N_B is the average background counts per time bin. It should be noted that the average background counts consist of the dark counts of the detector (see section 2.3.3.2), potential contributions from the solar background and contributions from other

ambient light sources. Therefore, in order to maximise the SNR of a TCSPC measurement, it is desirable to increase N_{PK} and reduce N_B. In addition, the signal-to-background ratio (SBR) is worth assessing:

$$SBR = \frac{N_{PK}}{N_B} \qquad \text{Equation (2.7)}$$

As shown in Figure 2-7, the same signal was resolved by two examples of TCSPC measurements, under two different background conditions. This means that the SBR values are significantly different in each case. However, for both measurements the SNR is of the same order, with a slightly higher SNR under condition one due to its lower SBR compared to that under condition two. This indicates that it is imperative to keep the background noise as low as possible in order to be able to sufficiently reconstruct a signal from TCSPC measurements.

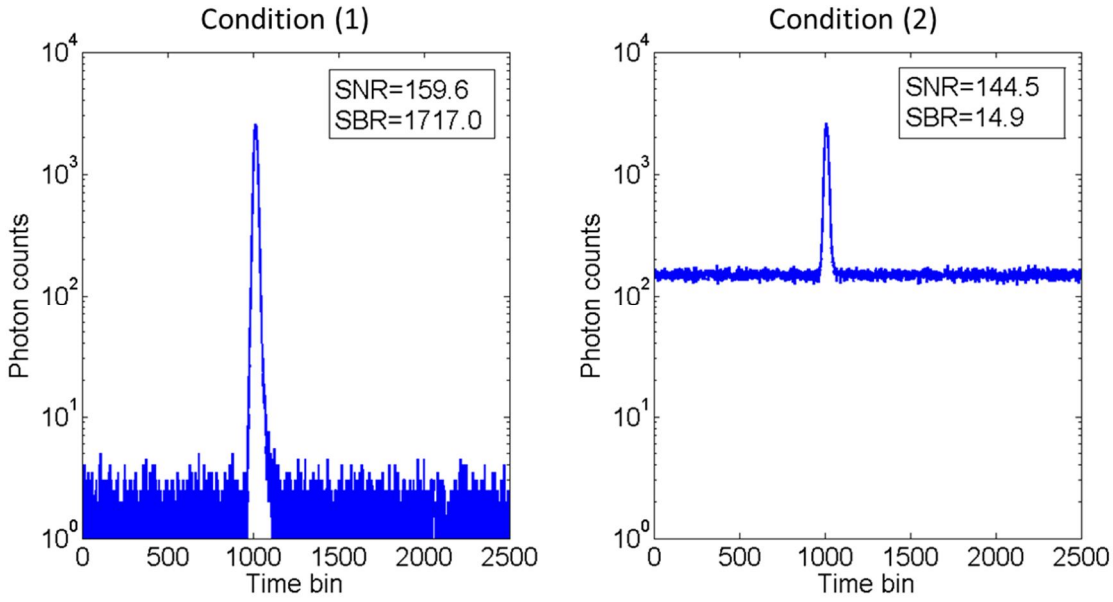

Figure 2-7 Signal-to-noise ratio (*SNR*) and signal-to-background ratio (*SBR*) comparisons of TCSPC measurements using a single photon detector [2.8] from Perkin Elmer Optoelectronics (now Excelitas Technologies Corp.) under different background conditions with the same total acquisition time of 60 s. Condition (1) corresponds to a measurement taken with an incandescent lamp source off, whereas condition (2) corresponds to a repeat measurement but this time with the source switched on. The average background count per time bin for condition (1) was 15 while in condition (2) the average background count per time bin was 1497. The maximum counts in each peak-count time bin of two conditions (i.e. ~25k counts for condition (1) versus ~22k counts for condition (2)) are very similar.

2.2.2 Conventional TCSPC system designs

As shown in Figure 2-8, TCSPC is described in a forward start-stop configuration with two channels (i.e. start and stop timing channels). Commonly the reference pulses for the start timing channel are derived from a synchronised light source such as pulsed laser source. These pulses can either be generated from a photodetector, by sensing part of the laser output power, or synchronised to an external clock, which is applied to drive the laser source. To guarantee a high-precision timing trigger, a constant fraction discriminator (CFD) is used to reshape the original input pulse, which is likely to contain timing jitter or shift induced by the instability of pulse amplitude. The difference among triggers, based on basic leading edge and constant fraction mechanisms, can be seen by comparing their relevant discrimination mechanism as shown in Figure 2-9. Given a constant trigger threshold, the leading-edge triggering has a significant dependence on the pulse amplitude. This is because the timing jitter induced by amplitude jitter is as high as the order of the pulse rising time. In contrast, the constant-fraction triggering corresponds to the baseline transition of a reshaped pulse with a zero point, which has an increased resistance to fluctuations in the pulse amplitude. Note that the formation of the reshaped pulse is the difference between the original input pulse and the related delayed pulse. As for the stop timing channel, it is necessary to also employ another CFD as the random jitters either from the amplification mechanism of detectors or other external sources induce considerable amplitude jitters among detection responses. The outputs of two CFDs are fed in a TAC. The TAC generates a pulse-amplitude that is proportional to the time difference between start and stop triggers (see Figure 2-10). The output analogue signal from a TAC is amplified by an amplifier (AMP) and then delivered to an ADC before being stored in digital format for later histogramming (refer to Page 20 of [2.5]).

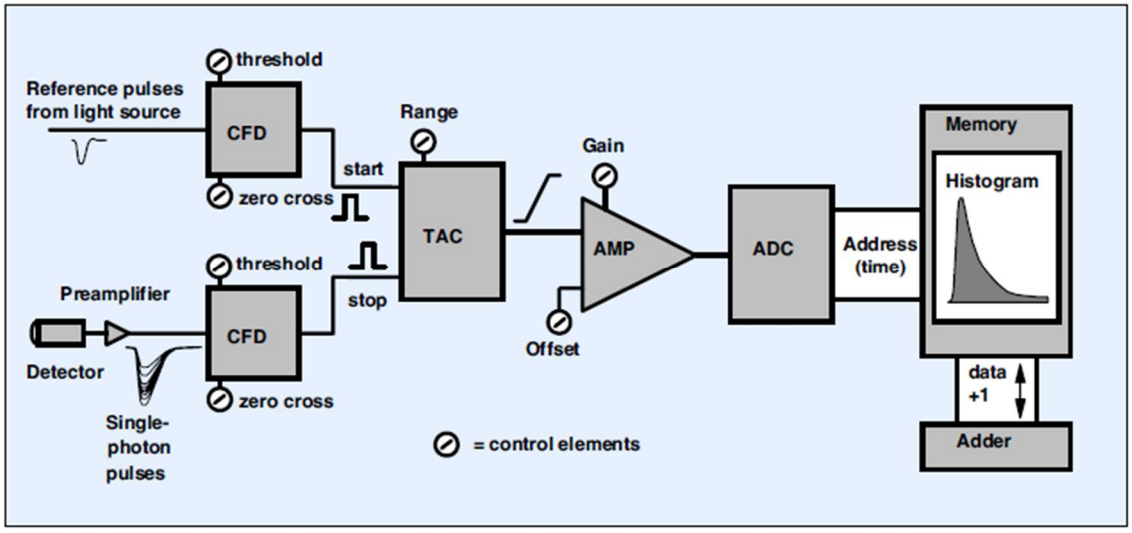

Figure 2-8 Block diagram of a forward start-stop TCSPC module. CFD: constant fraction discriminator; TAC: time-to-amplitude converter; AMP: amplifier; ADC: analogue-to-digital converter. (From Page 19 of [2.5]).

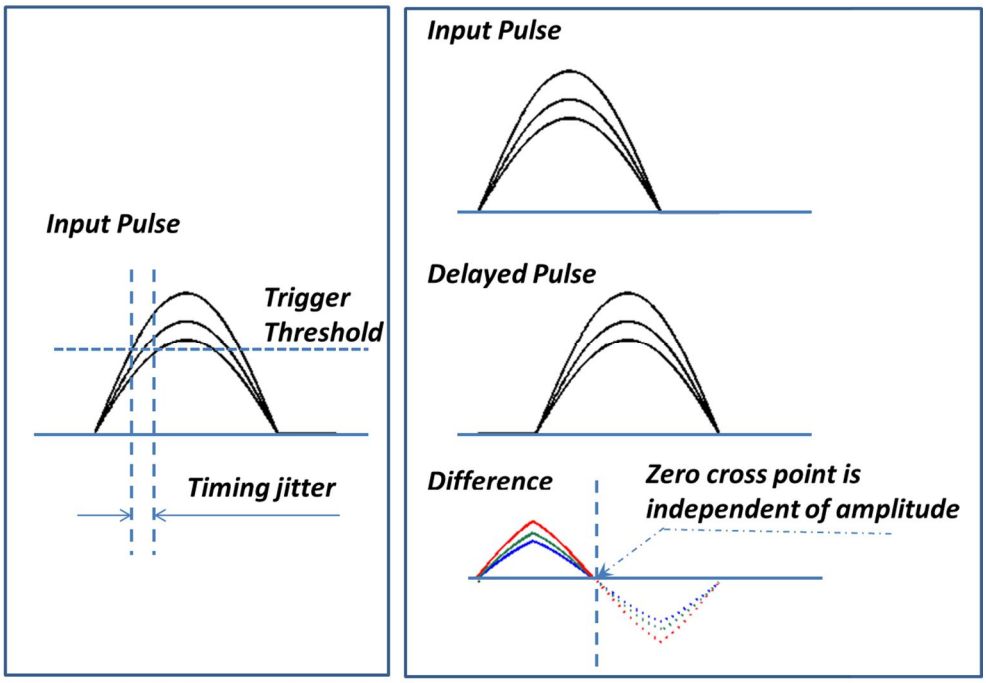

Figure 2-9 Left: Triggering based on the amplitude-dependent leading edge mechanism; Right: Triggering based on the constant fraction mechanism. (After Page 35 of [2.5]).

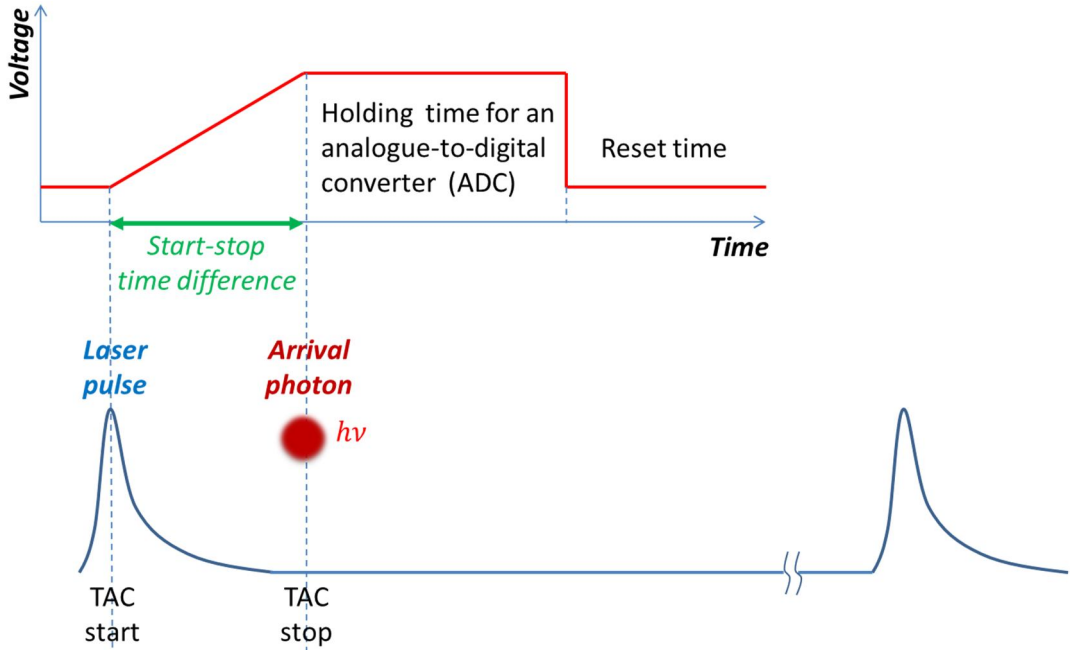

Figure 2-10 Illustration of an analogue time-to-amplitude converter (TAC) principle. Top: Operating voltage level versus time of a TAC; Bottom: The TAC start is triggered by a synchronisation reference pulse while the stop is generated from a photon. Similar to the timing mechanism of a stopwatch, the start-stop time difference can be measured repetitively.

Due to no prior knowledge of the arrival photons, the TAC of the classic forward start-stop TCSPC configuration must be started upon each synchronisation period. As many periods do not have any detected photons, it is necessary to have a dedicated circuit to reset the started TAC once the timing span is out of the pre-set range. The mechanism of first-start and subsequent-reset on the TAC works well for measurements with low repetition rates. However, it is not applicable for cases with high repetition rates (e.g. ≥50 MHz) unless further efforts are made. This is because the TAC must be reset for every synchronisation period (e.g. ≤20 ns) which is shorter than the dead time of a typical combination of TAC and ADC. An optimised alternative is to operate the TCSPC in a reversed start-stop configuration as shown in Figure 2-11. In this configuration, the start trigger is generated due to the photon arrival while the next synchronisation reference pulse from the laser source provides the stop trigger. This suggests that it is able to skip a large number of idler synchronisation periods and only retain the start-stop timings with respect to rare detected photon events (refer to Page 21 of [2.5]). However, for the reversed start-stop timing, the inevitable pulse-to-pulse jitter of the reference signal can impair the timing accuracy. Nevertheless, as shown in Figure 2-12, appropriately delaying the reference pulses that actually initiate the

detected photons can accomplish high-quality reversed start-stop time differences which are independent to the periods of reference pulses (refer to Page 92 of [2.5]).

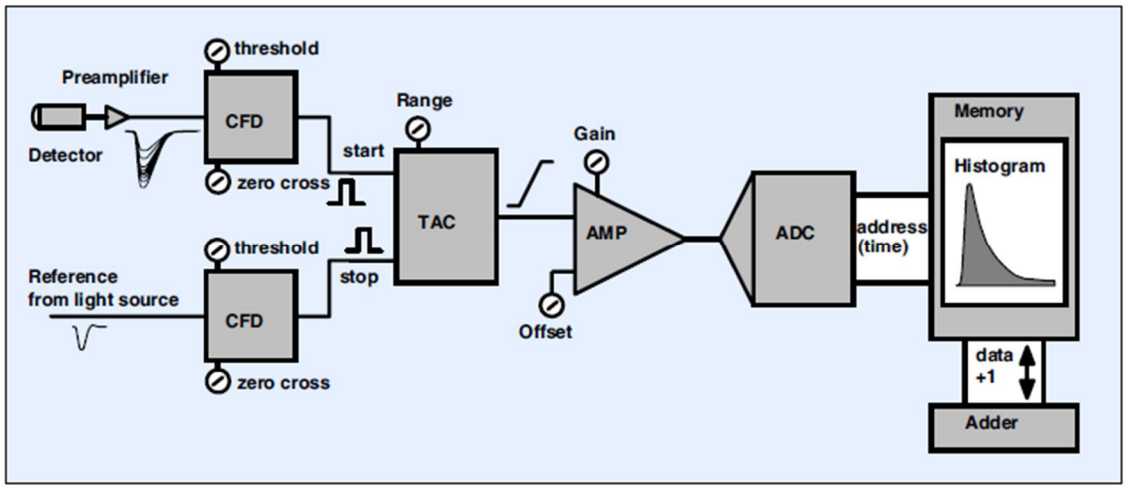

Figure 2-11 Block diagram of a reversed start-stop TCSPC module. CFD: constant fraction discriminator; TAC: time-to-amplitude converter; AMP: amplifier; ADC: analogue-to-digital converter. (From Page 21 of [2.5]).

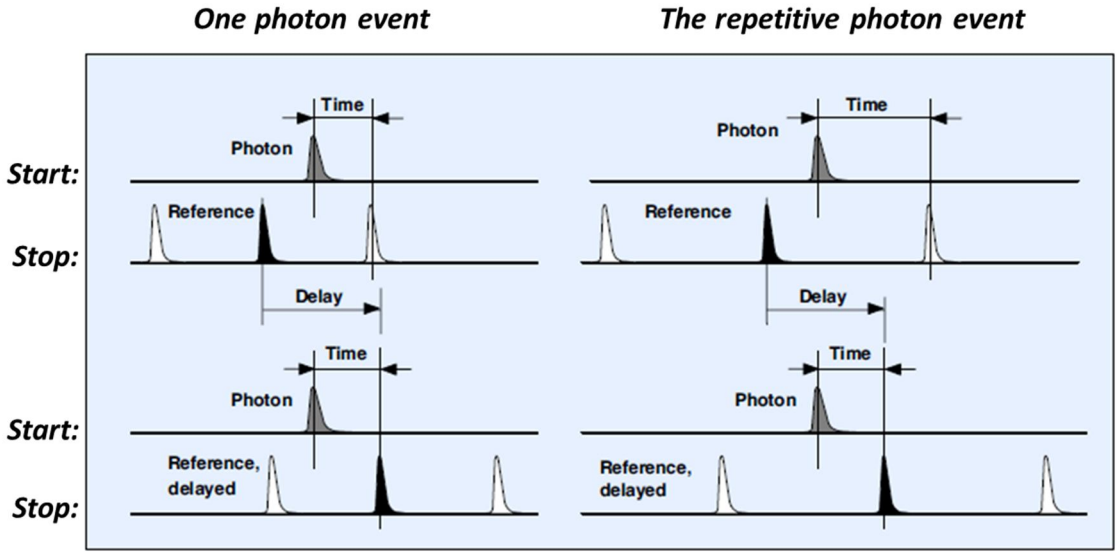

Figure 2-12 Illustration of no-delay and delay implementations with respect to reversed TCSPC start-stop mode. The time differences associated with one example photon event (left part) and its repetitive one (right part). Top part: reversed start-stop time differences with non-delayed reference pulses. Bottom part: reversed start-stop time differences with delayed reference pulses. The reference pulse shown in black is the one that actually contributed to the detected photon. (Reproduced from Page 92 of [2.5]).

2.2.3 Modern TCSPC system designs

One technical alternative to conventional TAC-and-ADC-based TCSPC systems is a TCSPC system with TDCs. The TDC is a modern, high-speed digital circuit for picosecond-resolution time measurements. It is a cost-efficient monolithic on-chip circuit system capable of direct and high-speed digital acquisition and processing. Compared to a combination of TAC and ADC, it has lower differential nonlinearity (DNL) in the voltage ramp and can offer longer time range (e.g. time range from 160 ns to 10 µs in [2.9]) along with shorter reset time [2.2]. A typical TDC is a crystal-clock-based digital counter implemented by high-speed semiconductor technologies. If the TDC solely operates with a semiconductor gate at an extremely high-speed (40 GHz) clock rate, it has the problem of high power consumption. To avoid this problem, an alternative based on a combination of coarse and fine counters has been designed. The coarse counter corresponds to a clock operating at a moderate rate while the fine counter is formed by means of tapped delay lines to subdivide the periods of the former. To make TDCs that can accommodate temperature fluctuations that occur during measurements, on-chip tunable delay lines combined with a delay-locked loop (DLL) can perform a robust calibration on the supply voltage and minimise the DNL in the voltage ramp. Wahl *et al.* [2.10] reported 25 ps timing bin width for their TDC. In 2014, Tamborini *et al.* [2.9] demonstrated a low power consumption TDC module with 20 ps timing bin width.

Features of contemporary-designs of TDC-based TCSPC systems (such as the PicoHarp 300 and HydraHarp 400 from PicoQuant GmbH, Germany) are embodied in the concepts of time tagging for independent timing channels and synchronisation frequency down-conversion. They are highly suitable for high-repetition rate applications. The block diagram of the typical modern TCSPC system can be seen in Figure 2-13. The two independent channels both have their own CFDs and TDCs. The functionality of the employed CFDs is the same as the one for the conventional TCSPC systems. It aims to be able to accommodate the input signal pulse with fluctuating amplitudes. The timing solution with a TDC is suitable for long-term timing acquisitions such as continuously obtaining multiple events across many repeated synchronising cycles. The time measurements of the two TDCs are perfectly synchronised and equally calibrated as long as the TDCs are both locked to the same high stability crystal clock. Ch 0 (see Figure 2-13) has a synchronisation divider, which can be employed to down-convert the input high repetition synchronisation pulse train,

or bypassed. It facilitates a forward start-stop TDC-based TCSPC configuration, which still works well for the synchronisation channel with high repetition rate input. Since two TDCs are armed for timing measurements, the time tagging for each channel can be recorded and the start-stop difference time between the time tags of the two channels can be arbitrarily long. A comparison of the time tagging (i.e. macro time) and start-stop difference time (i.e. micro time) with respect to photon detections is shown in Figure 2-14. By virtue of a field programmable gate array (FPGA) with a proper memory, the TCSPC system is capable of capturing the macro times with picosecond resolution and/or immediate on-line histogramming of the micro times. The recorded raw data is queued in a first-in-first-out (FIFO) buffer and continuously delivered to the host PC via a USB readout port, thereby making room for fresh incoming events [2.2].

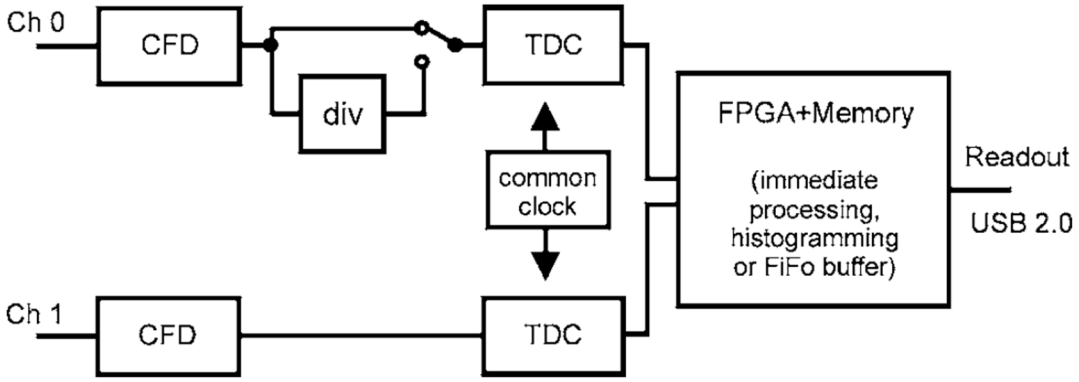

Figure 2-13 Typical block diagram of the advanced time-correlated single photon counting (TCSPC) instrument. CFD: constant fraction discriminator; TDC: time-to-digital converter; FIFO: first in first out; FPGA: field programmable gate array; Div: divider. (From[2.11]).

In terms of the outlook on TDC-based TCSPC systems, researchers and engineers are still striving to create devices of smaller size, lower power consumption and high data throughput, along with lower costs. This can be potentially achieved by employing modern, mature semiconductor technologies. There is the potential to implement real-time digital processing by means of powerful microprocessors and computers with multiple cores and threads. The concept and implementations of time-tagging photon data recordings provide sufficient information associated with the real-world time measurements [2.2].

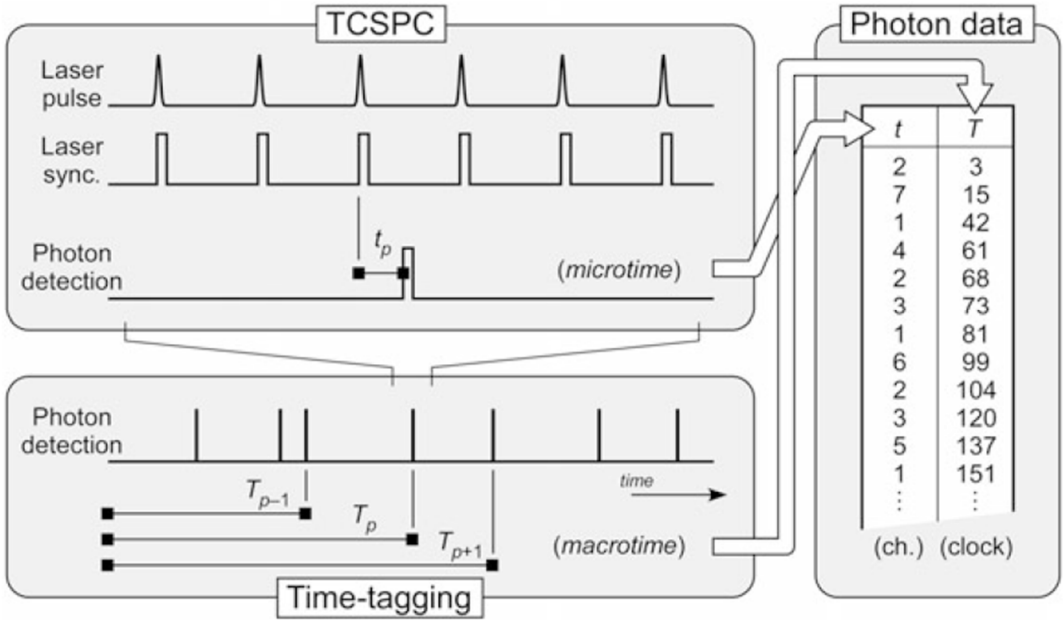

Figure 2-14 Comparison of micro time and macro time approaches. Micro time corresponds to the start-stop time difference of one effective photon detection event of a TCSPC measurement as shown in Figure 2-2. Macro time is the time since the start of the measurement. (From [2.12]).

2.2.4 Time-tagged-time-resolved mode

This subsection describes one of the time-tagged-time-resolved (TTTR) modes (i.e. T3 mode [2.2, 2.11]) of an advanced TCSPC module - HydraHarp 400 (by PicoQuant GmbH, Germany) for data recording upon a TCSPC-based laser scanning imaging system, as shown schematically in Figure 2-15. It is worth noting that the TTTR modes are not limited to the HydraHarp 400, and available for other TCSPC modules. For example, PicoHarp 300 (by PicoQuant GmbH, Germany) also has "T2 mode" and "T3 mode", but has slightly longer dead time (~90 ns). Other recent devices, such as those with a plug-in card for a high-speed serial computer expansion buses interface of computers, can offer shorter dead time (25 ns) for "T2 mode" and "T3 mode" [2.10].

"T3 mode" of the HydraHarp 400 is specifically designed to use periodic synchronisation signals and allows for operation at high synchronisation rates (up to 150 MHz). The periodic signal is fed to the dedicated synchronisation channel (e.g. "Sync in" in Figure 2-15). Events are triggered on "Sync in" by the internal clock of the pulsed photon source and closely correspond to the time at which a photon pulse is emitted. Photons reflected from the target are recorded by a single-photon triggered detector which generates an electrical pulse directed to an input channel (e.g. "Ch 1" in Figure 2-15). Operating in "T3 mode", the macro-time of both "Sync in" and "Ch 1"

can be obtained by simply counting the number of effective synchronisation pulses as the precise synchronisation period is known and the period-to-period jitter (within a few picoseconds) is tolerable. Meanwhile, the micro-time between the return photon event in "Ch 1" and the corresponding excitation event in "Sync in" is also recorded. Note that "T3 mode" is different from the other TTTR modes of the HydraHarp 400 (i.e. "T2 mode" [2.2, 2.11] which operates with two functionally identical input channels and records the macro-time independently for both channels). The "T2 mode" can use only photon detectors upon both input channels and has no need of any external synchronisation signal. Both "T2 mode" and "T3 mode" of the HydraHarp 400 have the same dead time (typically 80 ns). The main advantage of "T2 mode" operation is its lack of requirement of a synchronisation signal since the two input channels are identical. Thus, the "T2 mode" can be used for the cross-correlation measurements between these two channels. This has benefits in applications that use non-periodic "start" signals, such as those described in section 2.4.1.2. However, this results in time tags, which are recorded in a large data format, and that each event is recorded, even if the event is, for example, a repetitive synchronisation signal representing the "start" signal. In many measurement scenarios, this results in a significant amount of recorded data, which has no value. The rate at which data can be transferred from the HydraHarp 400 is limited to ~4 MHz by the transfer rate of the USB2.0 connection to the control computer. This means that a significant fraction of the data transfer can be taken up with repetitive "start" synchronisation signals in "T2 mode". By contrast, the "T3 mode" more efficiently records data without recording the unused start signals. However, the "T3 mode" can slightly increase the overall timing jitter of the TCSPC measurement due to a contribution from the synchronisation signal. For many measurements, the "T3 mode" offers the possibility to obtain long duration TCSPC measurements, such as those that would be required with only a moderate photon count rate, and still retain compact data storage requirements.

As shown in Figure 2-15, by virtue of the scanning galvo mirrors combined with the TCSPC measurement setup, we can obtain the spatial origin of time-tagged photon events using "T3 mode". Each time the mirrors are advanced to a new pixel, an external marker event is recorded on the HydraHarp 400 by transmitting an electrical signal from the galvo driving electronics to the "Marker" input. This input is one of the TTL input channels for markers on the HydraHarp 400. Finally, raw 32 bit data tags (consisting of 1 bit for the special indication, 6 bits for the channel number, 15 bits for the micro-time

and 10 bits for the counter of synchronisation periods) can be streamed by custom scanning control and data recording software from the HydraHarp 400 directly to storage without any processing.

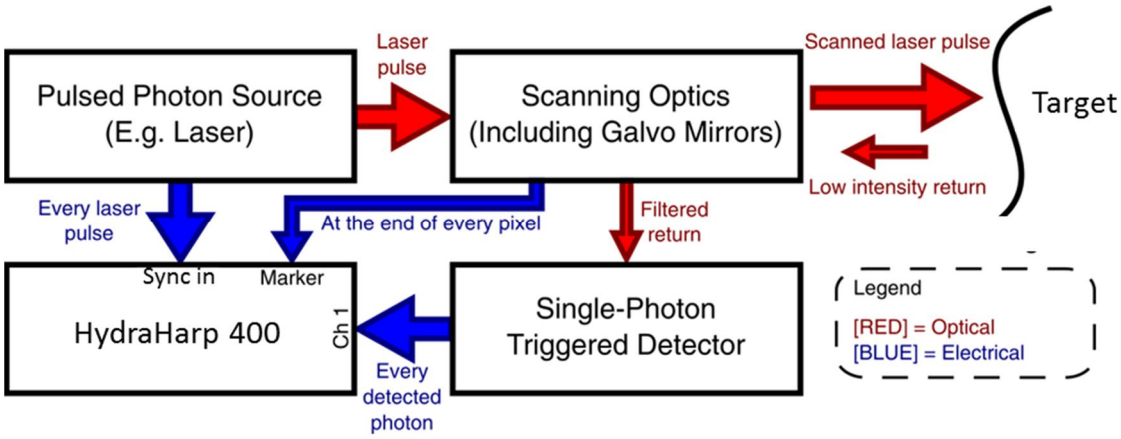

Figure 2-15 Schematic of a TCSPC-based laser scanning imaging system.

2.3 Single-photon detectors

2.3.1 Single photon detector characteristics

Single photon detectors can be grouped into two main types: photon-number resolving detectors and non-photon-number resolving (i.e. triggering) detectors. The photon-number resolving detectors can determine the number of photons in the receive pulse but are not essential in a great number of applications. To date, practical non-photon-number resolving detectors can be broadly divided by their operating principles into three major families: photomultipliers, semiconductors and superconductors. To evaluate the performance of single photon detectors, the following key figures of merit are commonly used:

(1) Single photon detection efficiency

The single photon detection efficiency (SPDE) of a triggering single photon detector is the probability that an incident photon will, either directly or indirectly, strike the photoactive area of the detector and subsequently generates a detectable electrical pulse. More specifically, as shown in Figure 2-16, it is common that the indirect and direct detections correspond to the fibre-coupled and free-space-coupled configurations, respectively. The SPDE of the fibre-coupled configuration can be described as (refer to Pages 53-55 of [2.1]):

$$\eta_{SPDE} = \eta_f \eta_c^{out} \eta_a \eta_{QE}^{i} \eta_{th} \quad \text{Equation (2.8)}$$

where η_f is the wavelength-dependent optical fibre transmission. η_c^{out} is the output coupling efficiency which is the fill factor of the output spot from the fibre combined with coupling optics (e.g. fibre collimation package) to the active area of the detector. η_a is the absorption efficiency which is photon absorption probability on the active area of the detector. η_{QE}^{i} is the internal quantum efficiency which is the ratio of the number of photoelectrons that contribute to the output electrical signal to the number of absorbed photons. η_{th} (typically close to 100%) is the threshold efficiency which quantifies the probability of generated output electrical signal detected by the external electronics (refer to Pages 53-55 of [2.1]). By contrast, the free-space-coupled configuration is without the fibre delivery system and its SPDE can be expressed as:

$$\eta_{SPDE} = \eta_a \eta_{QE}^{i} \eta_{th} \quad \text{Equation (2.9)}$$

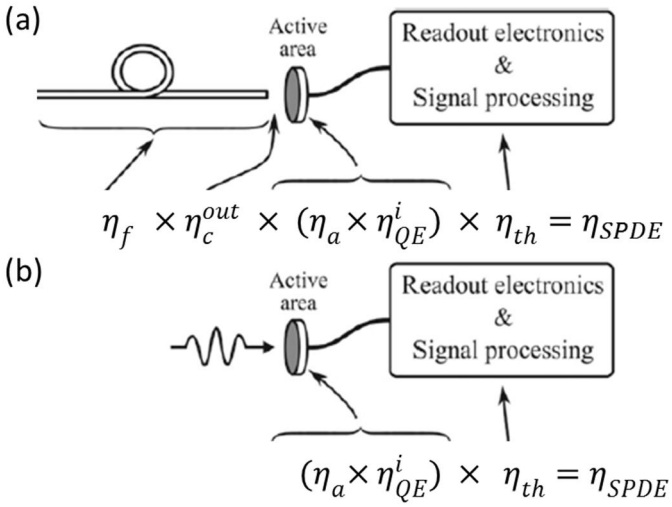

Figure 2-16 (a) Fibre-coupled and (b) free-space-coupled single photon detection systems. (Reproduced from Page 54 of [2.1]).

(2) Dark count rate

The dark count rate (DCR) is the average number of counts per second (cps) measured with no corresponding input photons. A higher DCR corresponds to a higher probability of false detection counts.

(3) Noise-equivalent power

The noise-equivalent power (NEP) is a figure of merit used to evaluate the minimum detectable optical power of the detector, thereby characterising its detecting ability. It

can be calculated as:

$$NEP = \frac{h\nu}{SPDE}\sqrt{2DCR} \qquad \text{Equation (2.10)}$$

where h is Planck's constant and ν is the frequency of incident photon. Smaller NEP represents a detector with better detecting ability [2.13].

(4) Timing jitter

The photon-induced electrical output pulse is discriminated by a given threshold. The definitions of the rise time (τ_{rise}) and latency time ($t_{latency}$) are depicted in Figure 2-17. Given that δ is the difference between the threshold and the maximum value of the pulse, τ_{rise} is defined by the time difference between time stamps with 10% and 90% δ in the leading edge above the threshold of the pulse. $t_{latency}$ can be characterised as the delay between an incident photon and the corresponding output electrical signal, and is measured from the registered time of the incident photon event to the time stamp within the ranges dominated by τ_{rise} of the output electrical signal (refer to Page 62 of [2.1]). The event-to-event variance in $t_{latency}$ is the timing jitter which is generally characterised by the instrumental response function (IRF) of a single photon detector as shown in Figure 2-18.

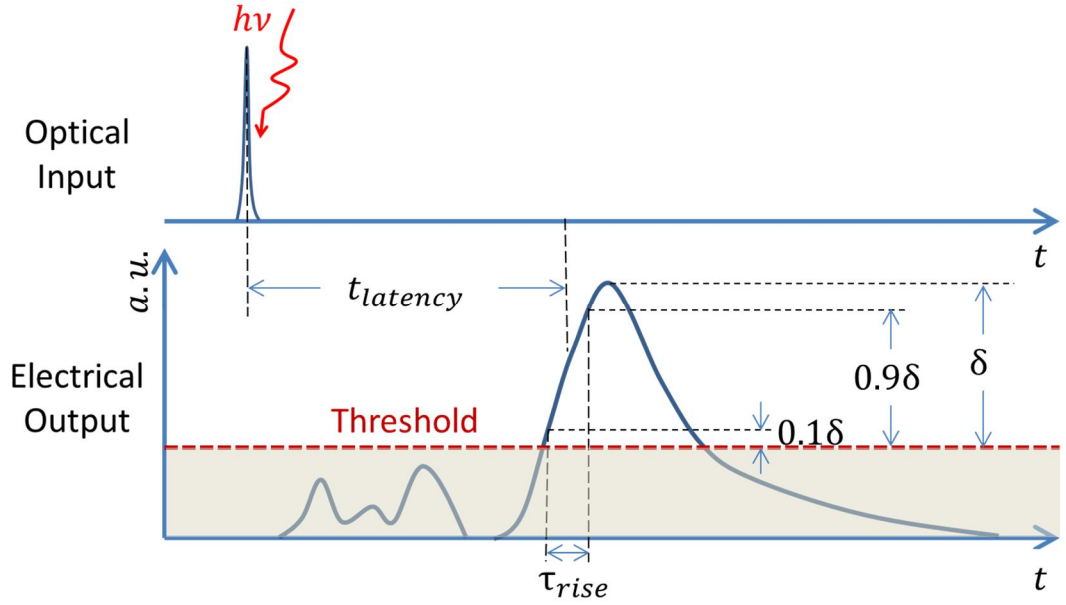

Figure 2-17 Diagram of the rise time (τ_{rise}) and latency time ($t_{latency}$), after Page 62 of [2.1]. The significant photon-induced electrical output pulse is discriminated by a pre-set threshold. Given δ is the difference between the threshold and the maximum value of the pulse, $\tau_{rise}$is defined by the time difference between time stamps with 10% and 90% δ in the leading edge of the pulse. $t_{latency}$ can be characterised as the elapsed time which is measured from the registered time of the incident photon event to the time stamp within the ranges dominated by τ_{rise}.

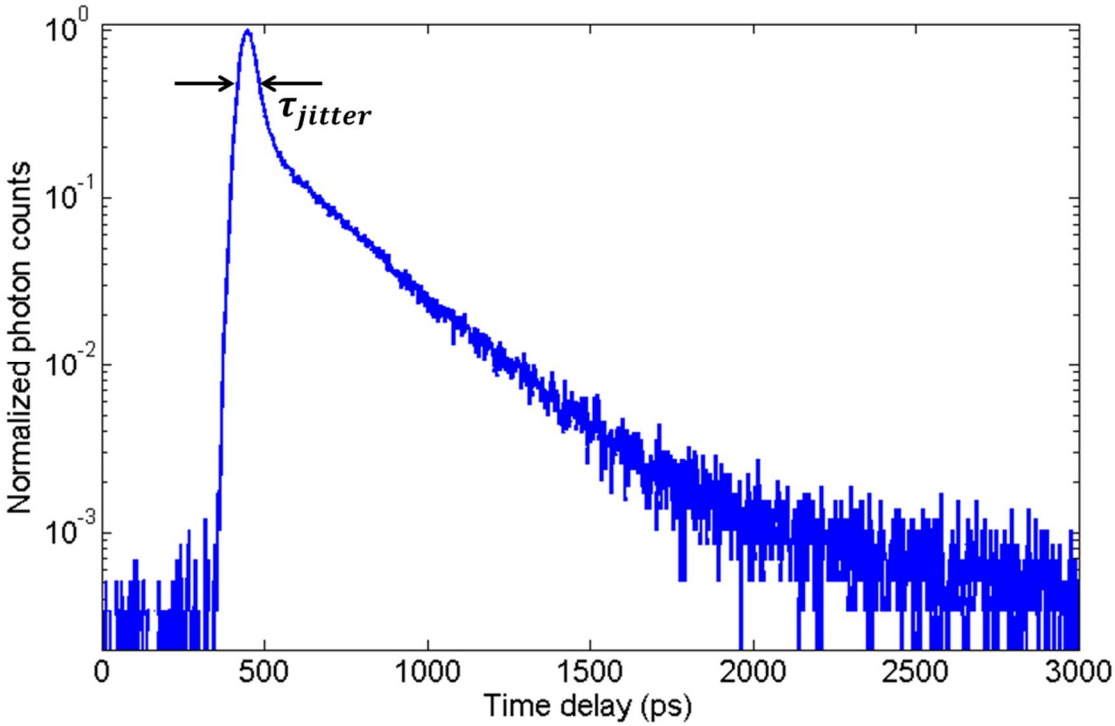

Figure 2-18 Example instrumental response function (IRF) of a single photon detector. The timing jitter (τ_{jitter}) of full width at half maximum (FWHM) is used to characterise $t_{latency}$. For the detector here, τ_{jitter} is ~60 ps.

(5) Dead time

Single-photon detectors are photodetectors with a specific armed and recovery mechanism where, upon accepting an incident photon, the whole detection system becomes effectively blind to the new incoming photons and requires recovery time to be capable of effective photon detection once again. The dead time (T_d^{det}) is the elapsed time after an initial photon detection during which no additional incident photons can be registered. In addition, the time for initialising the detector back to a steady photon detection state is called reset time (T_{res}^{det}). The overall time lag recovering from no photon detection state to steady photon detection state is defined as the recovery time (i.e. $T_{rec}^{det} = T_{res}^{det} + T_d^{det}$) of a detector. When $T_{res}^{det} \ll T_d^{det}$, $T_{rec}^{det} \cong T_d^{det}$ which means the dead time is considered to be equivalent to the recovery time (refer to Pages 64-65 of [2.1]). As a consequence, the maximum photon count rate (C_d^{det}) of the triggering detectors is limited theoretically by the recovery time and can be expressed as:

$$C_d^{det} = \frac{1}{T_d^{det}} \qquad \text{Equation (2.11)}$$

2.3.2 Photomultiplier tubes

A photomultiplier consists of a photoemissive compound, which emits electrons due to incident photons. These emitted electrons are then accelerated in a strong electric field to a positively charged dynode from which secondary electron emission occurs. These electrons are then accelerated to further dynode stages to create a large, multiplied electron current. This arrangement is formed within a vacuum tube as shown in Figure 2-19. Once the photons of an incident light beam pass the entrance window of a photomultiplier tube (PMT), the effective photon detection procedure can be briefly divided into three steps:

(1) Photoelectron emission. The operation of PMTs is based on the external photoelectric effect. This occurs when photons strike a metal or semiconductor, and electrons are subsequently emitted from the material's surface, resulting in photoelectrons. The photocathode in a PMT is a semiconductor with a finite band-gap capable of limited spectral-range photoelectron detection. When it is struck by a photon with a sufficiently high frequency, electrons in the valence band of the semiconductor absorb the photon energy. If the photon energy is equal to or exceeds the work function of the photoelectric material, the electrons can be excited, migrate to the photocathode

surface and finally are emitted from the surface into the vacuum to become photoelectrons (refer to Pages 14-15 of [2.14]).

(2) Secondary electron emission and amplification. By using a focusing electrode, the photoelectrons can be focused from the photocathode onto the first dynode surface, which is capable of secondary electron emission. Based on the acceleration of primary (incoming) electrons by an electric field between the dynodes, as well as the multiple secondary electron emissions through multi-stage dynodes (typically from 10 to 20), an amplification mechanism of the photoelectrons can be efficiently achieved. Thus, it can implement an overall high-gain electron multiplier (refer to Page 17 of [2.1]).

(3) Secondary electron collection and electrical current output. An optimum-designed anode is used to collect the secondary electrons from the final dynode. To obtain a large output electrical current pulse without any space charge effects, the potential difference between the last dynode and the anode needs to be set appropriately. Typically, a final current pulse of ~10^6 electrons can be generated at the node from a beginning primary electron. Finally, detection electronics are employed to detect the current pulse (refer to Pages 13-18 of [14]).

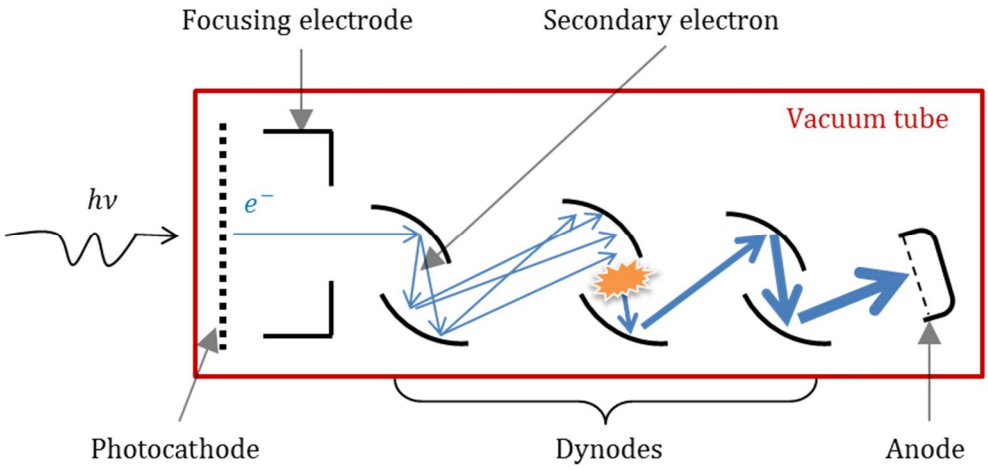

Figure 2-19 Schematic of a typical photomultiplier tube (PMT). Photoelectron emits from the photocathode. The focusing electrode is used to focus the released photoelectrons onto the first dynode surface to excite secondary electrons. Subsequently they are accelerated on the multiple-stage dynodes. The electrons are collected on the anode. (After Page 13 of [2.14]).

The important features of PMTs are large active areas (typically diameters of 3 mm to 8 mm [2.15]) which simplify the coupling optical system, and photon sensitivity of a wide spectral range from 115 to 1700 nm [2.16]. The dead time of PMTs is affected by the threshold of the discriminator for the detection of the output pulses and the width of

these pulses (refer to Page 81 of [2.1]). The variation of the photoelectron transit time in the tube from the photocathode to the anode primarily results in the timing jitter of PMTs (refer to Pages 48 of [2.14]). The photon response characteristics of a PMT can be evaluated by their quantum efficiency which is the ratio of the number of emitted photoelectron by the PMT to the number of incident photons (refer to Page 37 of [2.14]). The spectral quantum efficiencies of PMTs strongly depend on the characteristics of their applied photocathodes as shown in Figure 2-20. Visible-wavelength PMTs offer excellent performance in terms of quantum efficiency and detection speed. For photomultiplier tubes with GaAsP photocathodes (e.g. H7422-40 from Hamamatsu Photonics) at a wavelength of 500 nm, the maximum quantum efficiency is ~40% and the highest reported count rates are 10 MHz. In addition, the dark count rates are as low as 100 Hz and the typical timing jitter is ~300 ps at FWHM [2.17]. However, compared to PMTs operating at visible wavelengths, near-infrared PMTs have a lower performance in terms of both photon detection efficiency and DCR. Note that DCR in a PMT is primarily caused by thermionic emission from the photocathode or the dynodes (refer to Page 67 of [2.14]). For example, PMTs (e.g. R5509-73 from Hamamatsu Photonics) with an InP/InGaAs photocathode can operate at a wavelength of 1550 nm at 200 K. Its photon detection efficiency is as low as 2% and the DCR is up to 200 kHz [2.18]. In addition, in terms of reliability and scalability, non-solid-state PMTs are bulky and require vacuum tube technology as alongside high operating voltages, preventing their use in monolithic arrays [2.19].

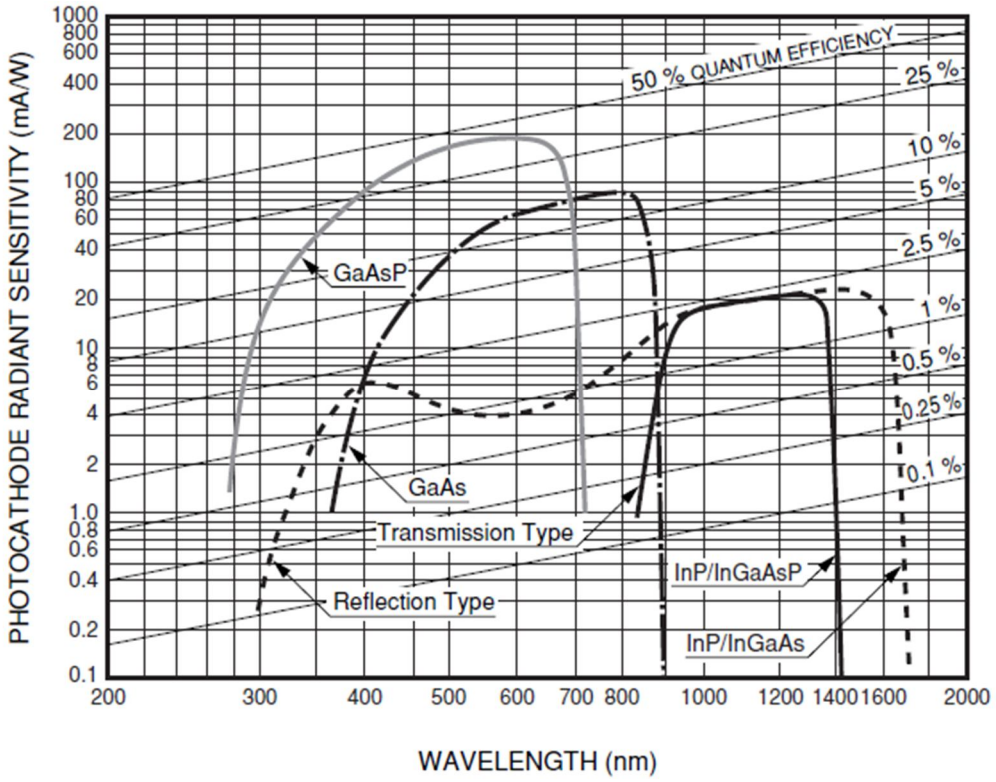

Figure 2-20 Typical spectral responses of various types of semiconductor photocathodes of PMTs. (From Page 33 of [2.14]).

2.3.3 Semiconductor-based single photon detectors

2.3.3.1 Linear and Geiger modes

In recent years, semiconductor-based single photon detectors have emerged as the main alternative to PMTs for single photon detection. The internal amplification mechanism of avalanche photodiodes (APDs) is achieved by impact ionisation of carriers in reverse-biased avalanche regions. The reverse bias level is either below or above the breakdown voltage of the APD, resulting in two different operational modes: linear and Geiger modes, which are related to the current-voltage characteristics of the APD as shown in Figure 2-21. Linear multiplication mode performance defines the behaviour of the APD below its breakdown voltage (V_{BD}). In linear multiplication mode, the avalanche region means that we can consider the device as a detector with an internal analogue amplifier. The photocurrent, due to the internal photoelectric effect below V_{BD}, is proportional to the input optical power, thereby achieving linear gain of the detector. By contrast, the dark current is the current, which is present in the avalanche region with no input optical power and consists of the current derived from thermally generated carriers and leakage currents, some of which are multiplied.

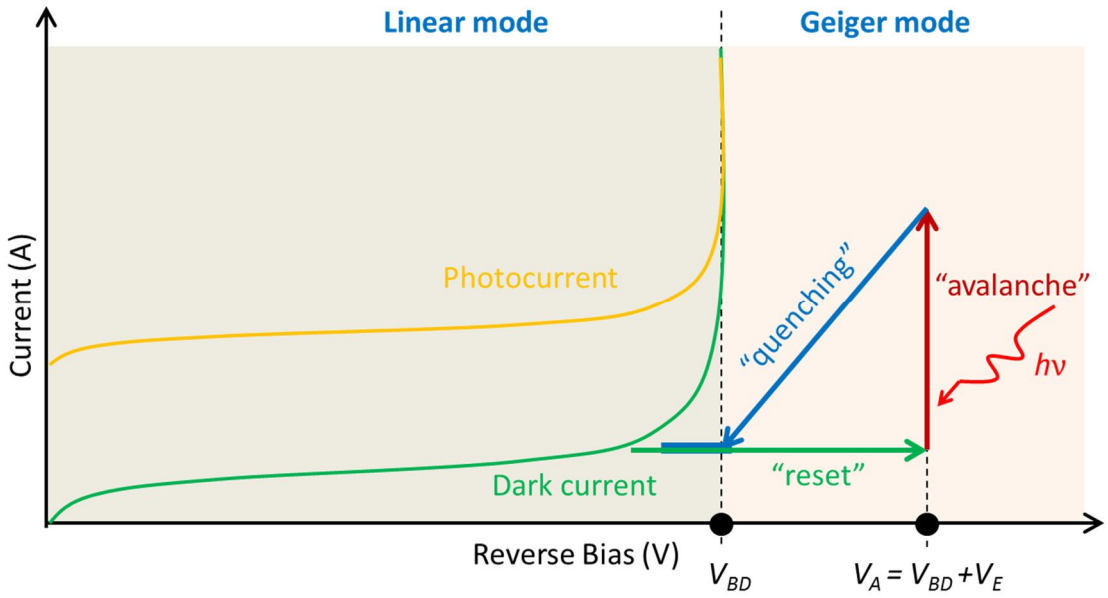

Figure 2-21 Illustration of avalanche photodiode (APD) voltage-current characteristics: Linear and Geiger modes. Linear mode performance defines the behaviour of the APD below its breakdown voltage (V_{BD}). The photocurrent below V_{BD} is proportional to input optical power, thereby linear gain of the detector. In linear mode, this avalanche region means that we consider this detector as having an internal analogue amplifier. Geiger-mode (when APD operates above its V_{BD}) APD is capable of self-sustaining avalanche of carriers once ignited by an incident photon. V_E is the excess bias voltage. In Geiger mode, a SPAD can be considered a detector with an internal digital flip-flop.

In Geiger mode (when the APD operates above its V_{BD}), an APD is capable of a self-sustaining avalanche of carriers once initiated by a carrier created by a single absorbed photon. Hence, the detector can be said to have single photon sensitivity. Note that the Geiger-mode APD is usually called a single photon avalanche diode (SPAD). In Geiger mode, the single-photon avalanche photodiode can be considered a detector with an internal digital flip-flop which has an operation loop of "avalanche-quenching-reset" as shown in Figure 2-21. The self-sustaining avalanche is driven by carriers from the impact ionisation process as shown in Figure 2-22. When the detector is biased at a voltage of V_A, which is above V_{BD} by an excess bias voltage (V_E), it is in the quiescent state. When there is no current flow through the avalanche region, the device is considered to be in the "OFF" state as no free carrier is present even in the presence of the high electric field in the multiplication region of the junction. In this triggering mode, even one injected single charge carrier can be accelerated significantly in the high electric field and induce impact ionisation to liberate a secondary carrier pair, starting the process to create a self-sustaining avalanche of carriers. This can result in

an exponential growth of the current, which can increase up to a constant level that is proportional to V_E but limited due to the space-charge effect. Thus, a constant macroscopic avalanche current flows through the avalanche region, thereby turning the detector into the "ON" state. As long as the detector operates in Geiger-mode the avalanche current is self-sustaining, thereby making the detector immune to any further incident photons. Therefore, quenching electronics are required to quench the avalanche. The quenching process is achieved by driving the operated voltage to (or below) V_{BD}. After quenching, the voltage level is reset above V_{BD}, which changes the detector back in to a photon detection steady state where it is ready for the next effective iteration (refer to Pages 85-86 of [2.1]).

It should be noted that the timing jitter in SPADs is affected by the different transit times of excited carriers due to different locations of photon absorption points and their subsequent carrier drift to the avalanche region. This results in excess-bias-dependent variations of avalanche build-up time (refer to Pages 117 of [2.1]) and jitter associated with the spread of the avalanche laterally across the avalanche region, leading to a jitter dependence on the device diameter. SPAD dead times depend on the recovery time of the quenching electronics for the devices (see section 2.3.3.3).

2.3.3.2 DCR and afterpulsing of SPADs

Dark counts in SPADs are caused by several different factors. Firstly, carriers generated thermally within the SPAD have a considerable contribution. At a certain temperature, the thermal-generated dark counts have Poissonian fluctuations. Also, higher DCRs occur at higher temperature and higher excess bias voltage V_E. This is derived from higher avalanche-triggering probability and stronger field enhancement of the carrier generation rate within the SPAD junction, which contributes to higher SPDE and increased DCR (refer to Pages 88-89 of [2.1]). Therefore, in order to reduce the DCR, the operating temperature and excess bias must be reduced. In addition, during the avalanche process some carriers are trapped in deep levels (e.g. the ones which are located at intermediate levels between mid-gap and band edge, refer to Pages 89-90 of [2.1]) of the multiplication material and later released [2.20]. This leads to the afterpulsing effect for semiconductor-based detectors due to band-to-band and trap-assisted tunnelling effects, and hence enhances the total DCR of the detectors. In comparison to the increased dark count rate at higher temperature, the afterpulsing rate can be reduced as the temperature is increased. Therefore, in terms of the minimisation

of the total DCR, there is a trade-off between DCR and afterpulsing evident in varying the operating temperature. Besides quenching the self-sustaining avalanche as fast as possible to further reduce the effects of afterpulsing, another way this can be achieved is to lower the probability of trap or defect formation and deformation, thus restricting the afterpulse probability as well as reducing the DCR. For example, the use of highly pure materials to fabricate the device can reduce the formation of trap or defect. In addition, using a long hold-off time after an event allows for more effective relaxation of traps (like the active quenching which will be described in the next section).

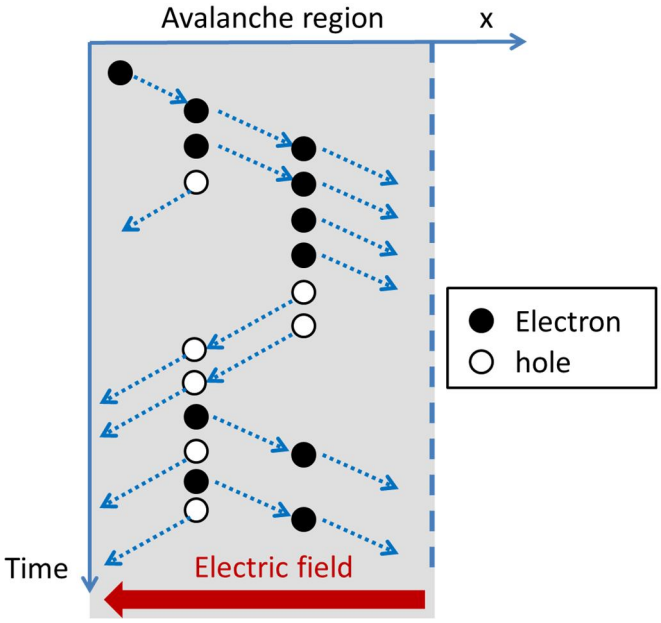

Figure 2-22 The process of impact ionisation in a single photon avalanche diode (SPAD). When an APD is biased into the Geiger mode, an absorbed photon (i.e. hv) excites a charge carrier pair (i.e. electron-hole pair). In this case, an electron from the excited electron-hole pair is injected into the avalanche region under a high electric field. This can trigger the impact ionisation process, with secondary carriers also undergoing impact ionisation, eventually leading to a self-sustaining avalanche.

2.3.3.3 Quenching mechanisms

There are three main types of quenching mechanisms for SPADs: passive, active and gated mode [2.21]. Their features are reviewed in the following sections.

(1) Passive quenching

The implementation of the passive quenching circuit (PQC) (see Figure 2-23(a)) can be considered as an effective combination of resistors and capacitances (see Figure 2-23(b)). A large ballast resistor R_L (typically sub-MΩ) is used to allocate appropriate

reversed bias for the SPAD while a small resistor R_s (typical 50Ω) is employed for sensing the signal pulse. The junction capacitance C_d of the diode and the stray capacitance C_s are combined to form the total capacitance C_T (typical a few pF) for the avalanche current discharges at the diode terminal. As soon as the constant macroscopic avalanche current flows through the diode, the voltage V_d across the diode with a resistance of R_d drops toward V_{BD} and thus the avalanche current is reduced until completely quenched. Note that the complete quenching happens when the current through the large ballast resistor is $(V_A - V_{BD})/R_L$.

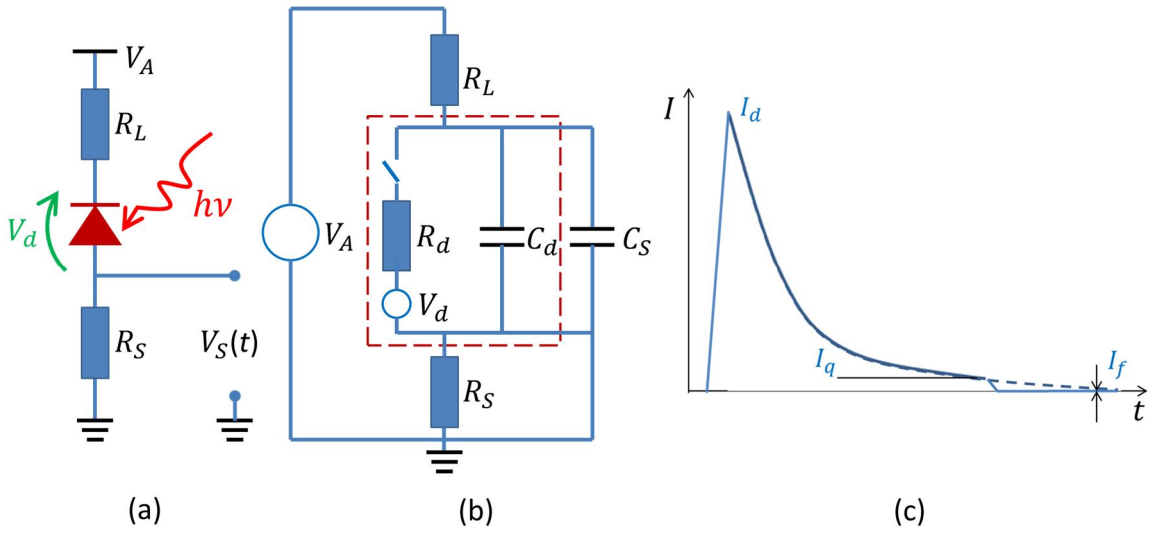

Figure 2-23 (a) Schematic diagram of a SPAD with a passive quenching circuit (PQC). (b) The equivalent circuit of the one shown in (a). The network within the dash red box corresponds to the diode. (c) The relation between the avalanche current and time. Note that as the avalanche current discharges the capacitances, I_d (i.e. diode current) exponentially drops to the asymptotic steady-state value of I_f (i.e. excess current). I_q denotes a latching current level. During discharge process, the avalanche is self-quenching below I_q. By contrast, it is self-sustaining above I_q. (After [2.22]).

As shown in Figure 2-23(c), as the avalanche current discharges the capacitances, I_d (i.e. diode current) exponentially drops to the asymptotic steady-state value of I_f (i.e. excess current). In addition, as the total charge Q in the avalanche pulse can be evaluated as: $I_f R_L C_T$, there is a trade-off between the excess current and the recovery time, which is determined by a potentially long time constant of $R_L C_T$. As shown in Figure 2-23(c), I_q denotes a latching current level. During discharge process, the avalanche can be self-sustaining (above I_q) or self-quenching (below I_q). Correspondingly, if $I_f \gg I_q$, there is no quenching for the avalanche and a steady

current flows in the diode [2.22]. However, if $I_f \ll I_q$ (i.e. large R_L is required), the PQC can neatly quench the avalanche after a distinct or stable time and thus it offers reasonably short timing jitter [2.22]. Due to the large R_L, the reset transition duration that corresponds to the recovery time is relatively long (typical a few μs) and results in a long dead time. However, this recovery time can be reduced by lowering C_s. For example, a reduced C_s with a value of far below 1 pF has been implemented in a monolithic integration of detector and ballast resistor with respect to silicon SPADs to achieve a reset transition time below 1 μs (refer to Page 95 of [2.1]).

(2) Active quenching

The mechanism of the active quenching circuit (AQC) of a SPAD operates in a controllable loop of avalanche-quenching-reset. As shown in the prototype AQC in Figure 2-24, a comparator is employed to effectively observe an avalanche pulse (i.e. $V_s(t)$). The bias voltage is switched down to V_{BD} or less when a voltage driver is triggered by the observing comparator. A short controlled duration (hold-off time) is used to achieve the fast quenching. In turn, the reset transition is implemented to set the bias voltage back to the level of V_A as fast and accurately as possible.

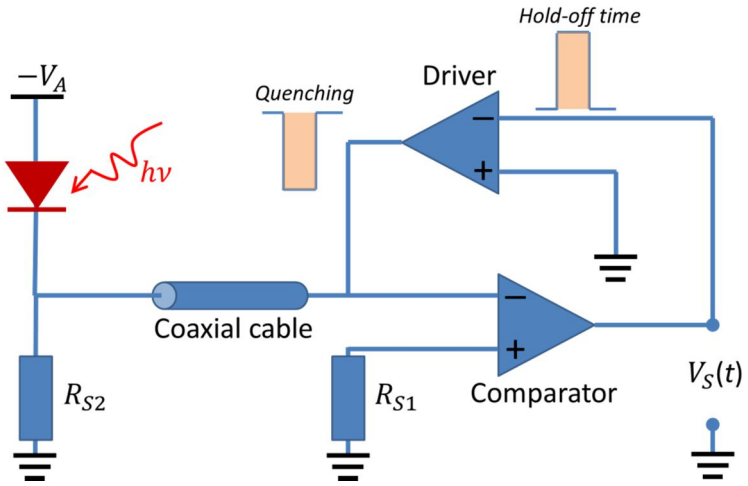

Figure 2-24 Simplified basic active quenching circuit (AQC) diagram in a "coincident quenching and sensing terminals" arrangement of the SPAD. The coaxial cable is employed to avoid spurious retriggering of the AQC at the end of the reset transition. (After [2.22] and Page 95 of [2.1]).

However, there is a trade-off for the adjustment of the hold-off time. In order to achieve high-speed effective quenching and attain the highest count rate of the detector, the hold-off time must be minimised. By contrast, the hold-off time is required to be long enough to release carriers trapped in deep levels, thereby reducing the afterpulsing effect (refer to [2.22] and Page 95 of [2.1]).

(3) Gated-mode quenching

The gated-mode quenching circuit integrates gating and avalanche discrimination systems to control the SPAD. As shown in Figure 2-25 for a gated-mode passive quenching circuit (G-PQC), the constant DC voltage (V_{DC}) is biased on the cathode of the SPAD and held at certain value below the breakdown voltage (V_{BD}) of the SPAD. The AC coupled gating signal (V_{gate}) is superimposed to the cathode of the SPAD, thereby taking the SPAD into Geiger mode. A threshold comparator can be used to distinguish the avalanches caused by single photon events from the gate transients and a level of the discrimination threshold voltage (V_{th}) that is higher than the rising gate transient. By contrast, when V_{gate} is off, it can quench the self-sustaining avalanche.

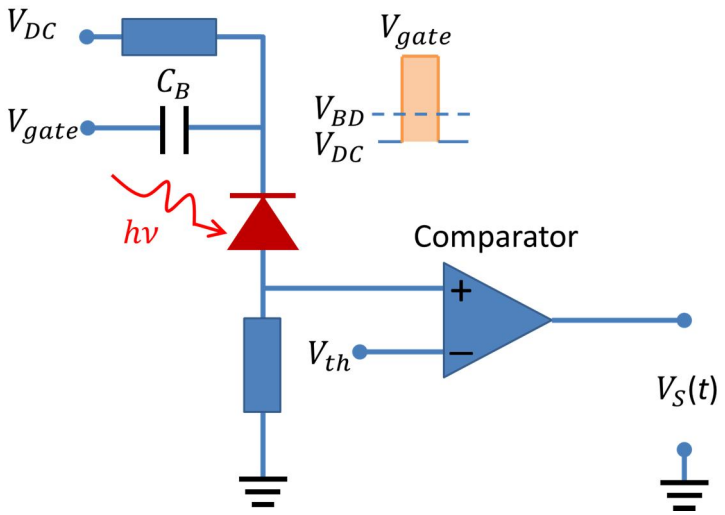

Figure 2-25 A simple gated-mode passive quenching circuit (G-PQC), after Page 122 of [2.1]. The constant DC voltage (V_{DC}) is biased on the cathode of the SPAD and held at certain value below the breakdown voltage (V_{BD}) of the SPAD. In addition, the AC coupled gating signal (V_{gate}) is superimposed to the cathode of the SPAD, thereby taking the SPAD into Geiger mode. A threshold comparator can be used to distinguish the avalanches due to single photon absorption from the gate transients and a level of the discrimination threshold voltage (V_{th}) that is higher than the rising gate transient. By contrast, when V_{gate} is off, it can quench the self-sustaining avalanche. (After Page 122 of [2.1]).

In the G-PQC, the quenching resistor at V_{DC} and the small capacitance of the SPAD (for recharging) can construct a low-pass filter. Due to this filtering effect, significant distortions occur for the electrical gate rising and falling edges resulting in distorted over-bias pulses, which are applied to gate the SPAD. Consequently, this results in a varying bias across the gate, potentially leading to dark counts at the onset of the high-

bias regions, and possibly more than one count per gate. Thus, it is difficult for the G-PQC to provide both clean stable over-bias pulses and effective quenching. However, this can be addressed by the use of a capacitive quenching circuit (CQC) (see Figure 2-26), which can be adapted for gated-mode SPADs. CQC can ensure only one count per gate as a capacitor (i.e. C_B shown in Figure 2-26), which is used to quench the avalanche current, needs to be charged up by the next over-bias pulse. In addition, in comparison to the G-PQC, as a lower total charge flows through the device, this will reduce the effects of afterpulsing on the device.

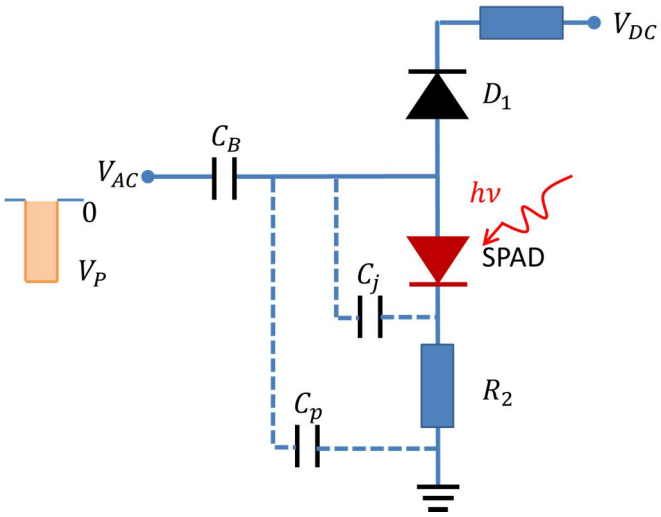

Figure 2-26 Diagram of a capacitive quenching circuit (CQC). The magnitude of the constant DC bias voltage (V_{DC}) is slightly lower than the breakdown voltage of the SPAD. Note that C_j is the SPAD capacitance and C_p is the parasitic capacitance. C_B is the biasing capacitor and D_1 denotes a diode. The AC coupled pulses with a high level of V_p are fed to the device via C_B. In order to ensure that a detectable avalanche pulse is met, it is imperative to choose R_2 with an appropriate resistance (e.g. 50 Ω used in [2.23]). (After [2.23]).

2.3.3.4 Silicon-based SPADs

Off-the-shelf silicon SPADs at operating temperatures typically close to room temperature are available for use in the wavelength range from 400 nm to 1000 nm. They are used for a variety of photon counting applications including biochemistry [2.24], astronomy [2.25], quantum optics [2.26], material science [2.27] and time-of-flight depth imaging [2.28-2.30]. Thin junction [2.31-2.34] and thick junction [2.35-2.39] silicon SPADs can be fabricated using custom process technology, i.e. the technology using bespoke manufacturing processes developed specifically for single-photon detectors. In addition, silicon SPAD devices have been fabricated in a

complementary metal-oxide-semiconductor (CMOS) technology, which allows far better integration of the detectors with the associated circuitry.

A thin junction SPAD [2.40] has a depletion layer with a thickness of only a few micrometres [2.8] (see right of Figure 2-27). Such a device structure is optimised for fast timing jitter, which can be as low as 30 ps FWHM biased at low excess bias levels. In these devices, the SPDE in the red and near infrared regions is low since the absorption lengths become long at these wavelengths. As shown in Figure 2-28, the SPDEs of a typical thin SPAD from Politecnico di Milano [2.40] at wavelengths from 800 nm to 1000 nm are lower than 15 %. The thin junction SPAD structure fabricated by using CMOS technology has an advantage over both integrating multiple detectors and associated circuitry. This enables implementation of monolithic integration of arrays [2.41]. Note that the time delay between the arrival time of each absorbed photon that generates charge carriers and the onset of the avalanche pulse is fluctuating, resulting in the timing jitter of SPADs. The timing jitters of SPADs are dependent on the device structure and the applied electric field. As shown in Figure 2-18, a narrow main peak and a slow tail in the IRF of a thin junction SPAD with timing jitter of ~60 ps FWHM are present. The formation of the primary narrow peak stems from an immediate acceleration of the photogenerated carriers by the electric field within the junction depletion layer. By contrast, within neutral regions near the depletion layer, the carriers migrate relatively slowly by diffusion, subsequently arriving on the edge of the depletion layer. These carriers are eventually accelerated by the electric field, thereby forming the slow tail. Relatively higher electric fields can lead to a narrower main peak, whereas a thicker neutral region can lengthen the diffusion tail.

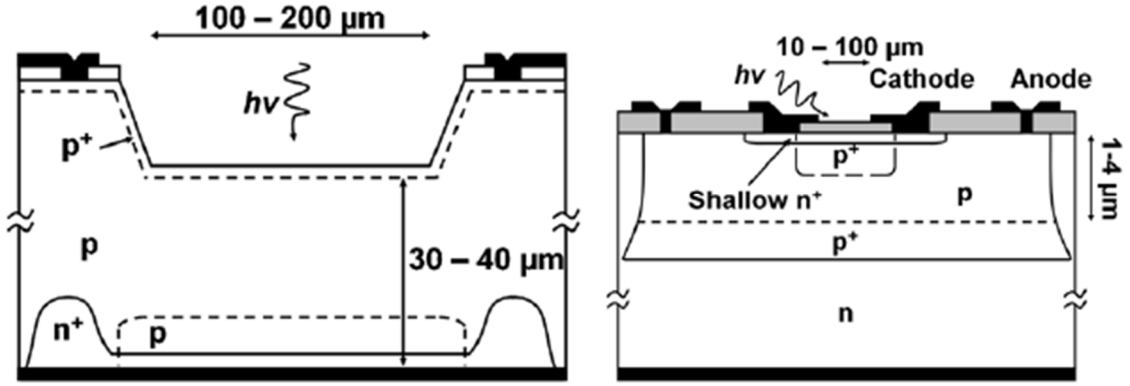

Figure 2-27 Left: a device structure of a thick junction silicon SPAD. Right: a device structure of a thin junction silicon SPAD. (From [2.42]).

As opposed to the thin junction SPADs, thick junction SPADs fabricated with a thick

absorption layer (typically 30 μm) (see left of Figure 2-27) offer a superior SPDE even at the longer wavelengths. As shown in Figure 2-28, the SPDE of a typical thick junction SPAD from Perkin Elmer Optoelectronics [2.8] (now Excelitas Technologies Corp.) at a wavelength of 800 nm is ~55% compared to only ~15% SPDE for a thin junction SPAD. However, the thick junction SPADs suffer from a longer timing jitter, which is typically as high as a few hundreds of picoseconds FWHM. For example, as seen in Figure 2-29, a typical thick junction SPAD and a selected thick SPAD both from Perkin Elmer Optoelectronics have timing jitters of ~480 ps and ~280 ps FWHM at a wavelength of 820 nm, respectively. The inherently complex fabrication technology makes the thick junction SPAD devices more delicate and degradable, along with lower compatibility with on-pixel electronics, results in huge challenges in their use in monolithic detector arrays.

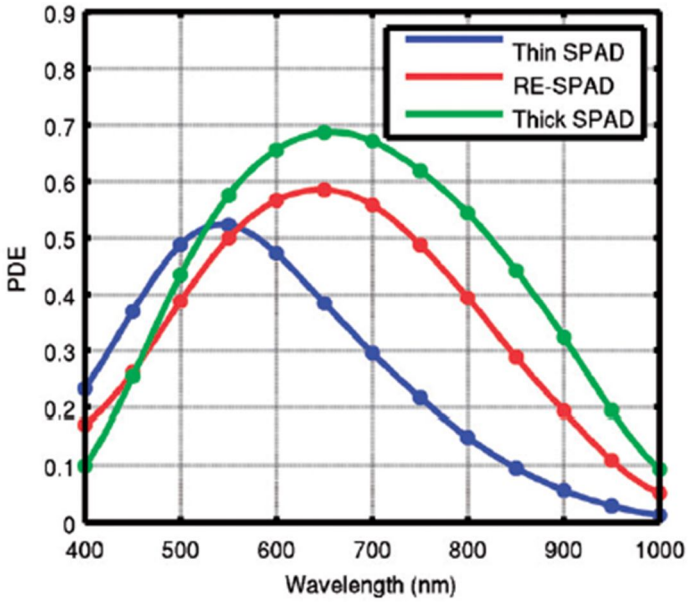

Figure 2-28 Spectral SPDEs of three different types of SPAD devices: a typical thin junction SPAD from Politecnico di Milano (blue), a red-enhanced SPAD (red) and a typical thick junction SPAD from Perkin Elmer Optoelectronics (green) (now Excelitas Technologies Corp.). (From [2.41]).

More recently, a new device structure called red-enhanced SPADs (RE-SPADs) has been developed. These devices have a separated thick (~10 μm) absorption region with low electric field and a thin multiplication region with a high peaked electric field profile (refer to Page 102 of [2.1]). They were designed to have relatively high SPDE at red and near infrared wavelengths and moderate timing jitter. The high SPDE, due to the enhancement of the avalanche-triggering probability, and the reduced timing jitter are achieved by a high maximum electric field profile in the thin multiplication.

Therefore, RE-SPADs act as a good compromise between the performance of thin and thick junction SPADs. At a wavelength of 800 nm, there is a SPDE of higher than 30% and a timing jitter of less than 100 ps FWHM. In addition, as the new devices are fabricated by using a planar technology they are suitable for implementation of established detector arrays [2.41].

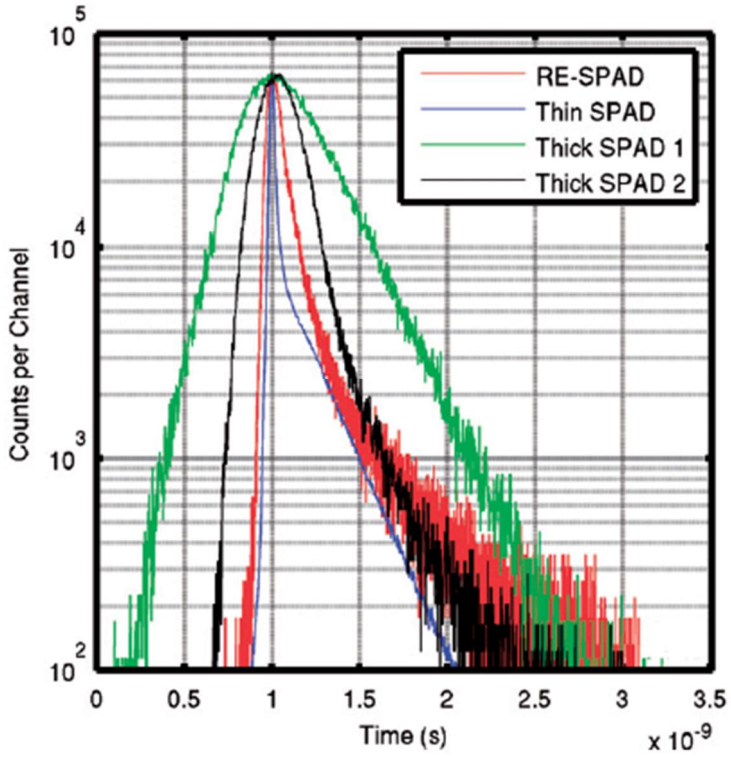

Figure 2-29 Temporal responses of different types of detectors: (1) a thin junction SPAD from Politecnico di Milano (blue) with timing jitter of ~60 ps FWHM; (2) a red-enhanced SPAD (red) with timing jitter of ~93 ps FWHM; (3) a typical thick junction SPAD (i.e. Thick SPAD 1) (green) with timing jitter of ~480 ps FWHM and a selected thick junction SPAD (i.e. Thick SPAD 2) (black) both from Perkin Elmer Optoelectronics (now Excelitas Technologies Corp.) with timing jitter of ~280 ps FWHM. Measurements were performed at λ=820 nm with unfocused light. (From [2.41]).

To date, high-voltage CMOS (HV-CMOS) and deep-submicron (DSM) resolution technologies can be utilised for the fabrication of CMOS-based SPADs. Both HV-CMOS in submicron resolution and DSM CMOS technologies offer a method for the fabrication of high pixel-density SPAD arrays. The characteristics of each pixel-wise detector of an arrayed SPAD device are relatively inferior to a discrete SPAD device fabricated in custom technology due to lower flexibility in high-performance structure designs. This presents even more of a challenge when reducing the size of the SPAD

device to a few micrometres (refer to Page 104-107 of [2.1]). However, arrayed SPADs are promising candidates for low-light-level 2D imaging capable of high-frame rate and direct and indirect time-of-flight 3D imaging. Over the last decade the performance of SPAD arrays have made rapid progress. A 32×32 pixel SPAD array fabricated with 0.8 μm HV-CMOS technology was first implemented by Niclass *et al.* [2.43]. However, it had two shortcomings: (1) off-chip CMOS time-to-digital converters (TDCs) were used to achieve the functionality of photon timing; (2) a sequential access with pixel-by-pixel processing across the entire array results in low frame rate. The same group reported in-column array designs. The corresponding processing capability was improved by sharing clusters of pixels. However, a drawback of the readout approach devised for these designs [2.44-2.45] is that simultaneous detection of photons in the same column is not allowed. To overcome the drawback, the latchless pipeline readout scheme [2.46] was proposed by preserving timing externally and indirectly. By virtue of state-of-the-art CMOS electronics, a combination of a high performance SPAD detector and a series of functional circuitry and modules can form a smart pixel. The level of in-pixel integration complexity depends on the pixel-wise performed functional electronics, such as circuitry for analogue sensing and avalanche quenching, photon timing and counting, and local storage (refer to Pages 108-110 of [2.1]). The simplest one is that pixel-wise counters make all pixels capable of photon counting simultaneously and independently [2.47-2.48]. Furthermore, in-pixel integration of a TDC can have a photon timing mode in a monolithic SPAD array [2.49-2.54]. Villa *et al.* [2.52] reported one TDC per pixel CMOS imager with 32×32 smart pixels fabricated in 0.35 μm HV-CMOS technology (see Figure 2-30). Each pixel (150 μm× 150 μm) has completely independent photon counting and photon-timing channels. Aside from a 30 μm diameter SPAD detector, the smart pixel has in-pixel integrated electronics including an analogue variable load quenching circuit (VLQC) capable of fast avalanche sensing and quenching [2.55], pulse shaping electronics, and a 10 bit TDC as well as a 10 bit memory latch. In addition, a frequency doubler and a global delay locked loop (DLL) are integrated on-chip to feed all in-pixel TDCs with common signals. The IRF of this type of smart pixel is ~100 ps FWHM. The peak SPDE of the SPAD detector is better than 50% at a wavelength of 410 nm, dropping to 5% at a wavelength of 800 nm with very low noise performance with a reported median DCR of ~120 cps at room temperature at an excess bias of 5 V. An almost negligible afterpulsing effect is due to using a high performance VLQC. The in-pixel 10 bit TDC can operate with 312 ps timing bin width and cover 320 ns full timing scale range

[2.52].

In addition, to fulfil the application requirement (in particular for life sciences) of the low-light-level 2D imaging at high frame rates, the development trend of CMOS-based SPAD arrays [2.56-2.58] has concentrated on larger pixel sizes with diameters between 50 and 100 µm, high SPDE and arrays with moderate pixel number (typical less than 100) (refer to Page 111 of [2.1]).

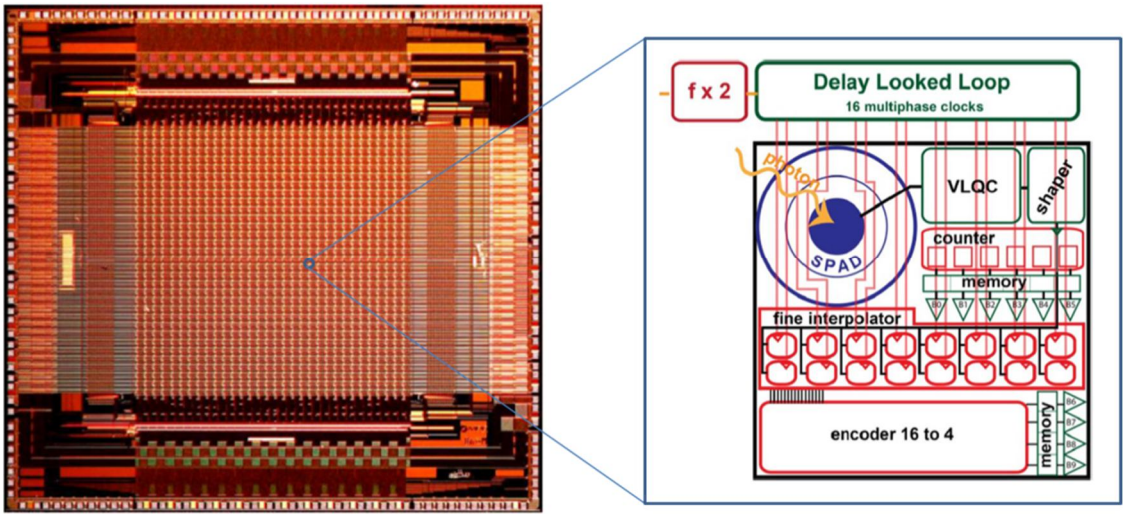

Figure 2-30 Left: Micrograph of a 32×32 pixel SPAD array chip fabricated in a 0.35 µm high-voltage CMOS technology. The total chip size is ~9 mm × 9 mm [2.52]. Right: The zoom in block diagram is a smart pixel (150 µm× 150 µm) with 30 µm diameter SPAD detector. The fill factor of the photoactive area is ~3.14%. Apart from a SPAD detector, there is a variable load quenching circuit (VLQC), pulse shaper, coarse counter, fine interpolator, 16-to-4 encoder, memory and 10 bit output buffer in the diagram. Also, the global on-chip frequency doubler and the delay locked loop (DLL) line are shown in the diagram. (From [2.59]).

Driven by user demand based on the detector performance, the future requirements for silicon SPADs will place emphasis on the enhancement of several different aspects of the system. These factors include detection efficiency, larger photosensitive area, faster photon timing capability with a shortened diffusion tail in the instrumental temporal response. Also desirable are arrayed configuration SPAD devices with larger formats ($> 10^6$ pixels), a higher fill factor as well as front-illuminated and back-illuminated detectors [2.38] integrated with a higher level of functionality (refer to Page 113 of [2.1]).

2.3.3.5 SPADs for short-wave infrared wavelengths

As silicon SPADs cannot operate efficiently beyond a wavelength of 1 μm due to the inherent low optical absorption of the material, SPADs designed for longer wavelengths rely on low bandgap semiconductor photosensitive materials, such as Ge and InGaAs.

Ge SPADs [2.60] were first implemented for short-wave infrared (SWIR) single photon detections. SPADs made from Ge grown on Si substrates show promise for integration with other Si-based electronics or optical circuitry. The structure of a Ge-on-Si SPAD is based on a heterostructure composed of a Ge layer as a narrow bandgap absorber and a low-noise single photon avalanche multiplication layer composed of the larger bandgap Si. In addition, since all-Si SPADs have much lower afterpulse probability compared to all-Ge SPADs, the Ge-on-Si material system is promising for low-noise single photon detection with relatively less afterpulsing effect due to the Si-based multiplication region where the afterpulsing is most likely to occur [2.61]. Recently, a NEP of 10^{-14} W/$\sqrt{\text{Hz}}$ at a temperature of 100 K for a Ge-on-Si SPAD at a wavelength of 1310 nm was reported by Warburton *et al.* [2.61].

Currently, InGaAs/InP SPADs [2.62] are the most widely used single photon detectors at telecommunications wavelengths of 1300 nm and 1550 nm. The separate absorption and multiplication (SAM) regions structure is used for InP-based avalanche photodiodes [2.63]. By tailoring the layers of absorption, grading, charge and multiplication for specific applications, these photodiodes can achieve high single-photon detection performance. The representative builds have a separate absorption, charge and multiplication structure (SACM structure [2.64]) and a separate absorption, grading, charge, and multiplication (SAGCM) heterostructure [2.65]. A SAGCM-structure-based InGaAs/InP SPAD is shown in Figure 2-31, where the electron-hole pair is photo-generated due to single photon absorption in the $In_{0.53}Ga_{0.47}As$ layer ($E_g \approx 0.75$ eV at 300 K). The structure is lattice-matched to the InP multiplication layer ($E_g \approx 1.35$ eV at 300 K), and is photosensitive in the spectral range of 950 nm to 1650 nm due to the narrow gap of the InGaAs layer. The structure is designed to have a high electric field in the multiplication region, and a relatively low, but non-zero electric field, in the InGaAs region. This is achieved by careful design of a charge layer located between the absorption and multiplication regions. The electric field must be kept low in the InGaAs layer to avoid the tunnelling effect, which would contribute to dark counts. After photon absorption occurs, the created electron-hole pair is separated by the

electric field. Subsequently, once the hole has drifted to the InP multiplication layer, a self-sustaining avalanche current develops. The holes drifting to the avalanche region are helped over the valence band discontinuity at the InGaAs-InP heterointerface [2.65] by an InGaAsP grading layer.

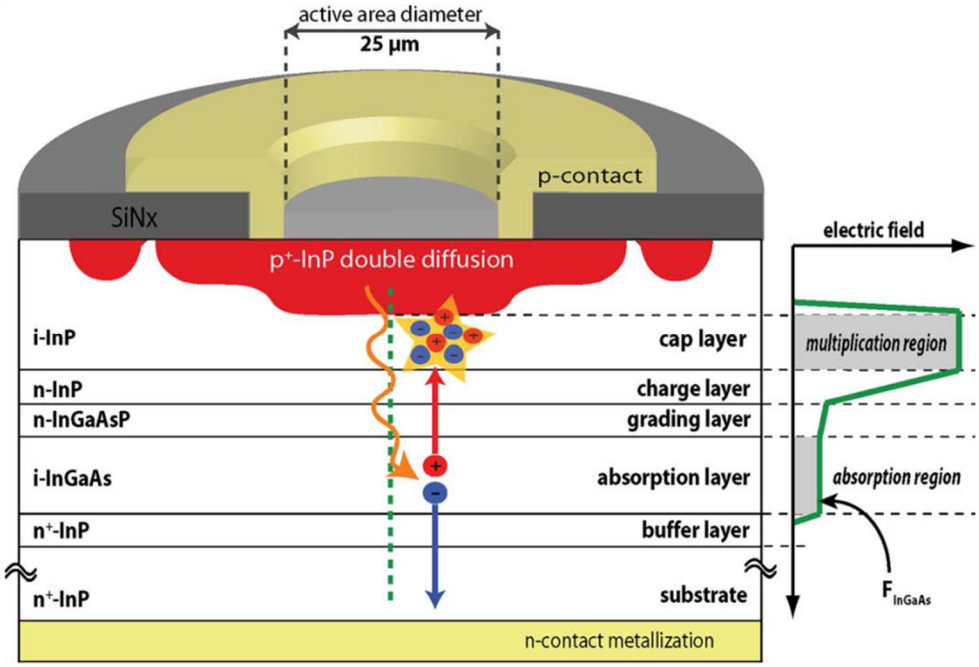

Figure 2-31 Schematic of a front-illuminated planar InGaAs/InP SPAD device with a separate absorption, grading, charge, and multiplication (SAGCM) heterostructure (at left) and associated internal electric field (at right) along the centre of the active area (green dash line). The electron-hole pair is photogenerated due to single photon absorption. Single photon, electron and hole are indicated in orange arrow, blue spot and red spot respectively (at left). (Reproduced from [2.65]).

The SPDE of an InGaAs/InP SPAD depends on mainly on three probabilities including (1) the probability of an incident single photon absorption in the InGaAs absorber; (2) the probability that the photogenerated hole reaches the avalanche region; and (3) the probability that the photogenerated hole succeeds in inducing a self-sustaining avalanche in the InP-based multiplication region. The avalanche triggering probability rises linearly, at the low voltage, with increasing excess bias until saturation at the high voltage [2.22, 2.66]. In terms of the DCR in the InGaAs/InP SPAD, the thermal carrier generation in the narrow bandgap absorber induces the primary DCR. The secondary DCR is due to the trap-assisted tunnelling in the multiplier. Both contribute to the overall dark count rate of a well-designed InGaAs/InP SPAD. Generally, the thermal generation is more significant while the tunnelling effect is less active under operating conditions at higher temperatures and lower bias voltages. As illustrated in Figure 2-32,

the DCR is below 10^3 cps at a SPDE of 20% and when the SPDE increases to 40% the DCR is still below 10^4 cps for an InGaAs/InP SPAD with 25 μm active area diameter operating at a temperature of 223 K and at a wavelength of 1550 nm (refer to Page 116 of [2.1]). As shown in Figure 2-33, in terms of a gated-mode $In_{0.53}Ga_{0.47}As/InP$ SPAD with 40 μm active area diameter (by Princeton Lightwave, Inc. (PLI) USA) [2.67] operating at a temperature of 200 K at λ=1550 nm, high excess bias voltage is desirable for high SPDE but leads to high DCR [2.20]. The progressive enhancement of the tunnelling effect gives rise to an almost exponential increase of DCR at a high level excess bias. According to the spectral SPDE curves shown in Figure 2-34, excess bias voltages of 3 V and 5 V are applied on an active area with 25 μm diameter of an InGaAs/InP SPAD in gated mode with a passive quenching circuit. The SPDEs for both biased cases are more than 10% in the wavelength range of 950 nm to 1600 nm at a temperature of 200 K. In particular, more than 25% SPDE at a wavelength of 1550 nm is provided by the SPAD at an excess bias of 5 V, whereas at a wavelength of 1000 nm the SPDE is up to 40% and at a wavelength of 1700 nm the SPDE is still ~2.5%. Excess-bias-dependent timing jitters of the same SPAD device are illustrated in Figure 2-35. It is evident to see that the timing jitter becomes better as the excess bias increases. The timing jitters are less than 100 ps FWHM when the excess biases are ≥ 5 V.

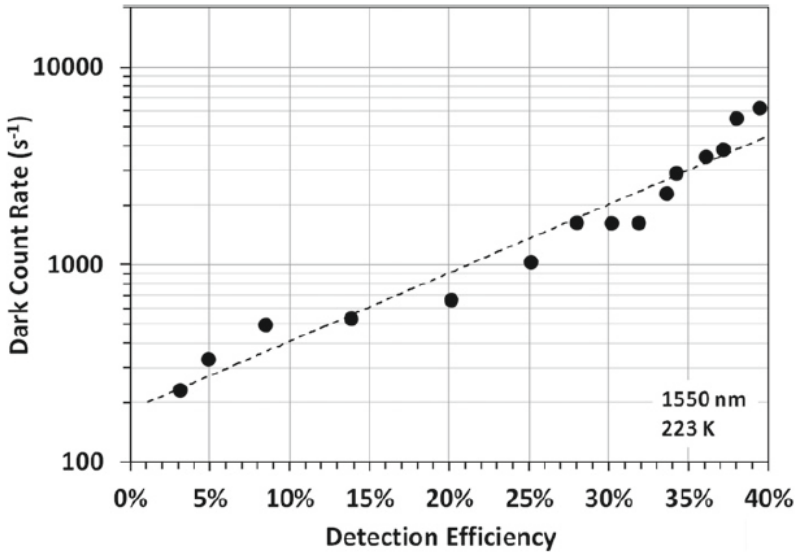

Figure 2-32 The plot of dark count rate versus detection efficiency of an InGaAs/InP SPAD with 25 μm active area diameter operating at a temperature of 223 K and at a wavelength of 1550 nm. The dashed line indicates the general trend in performance. (From Page 117 of [2.1]).

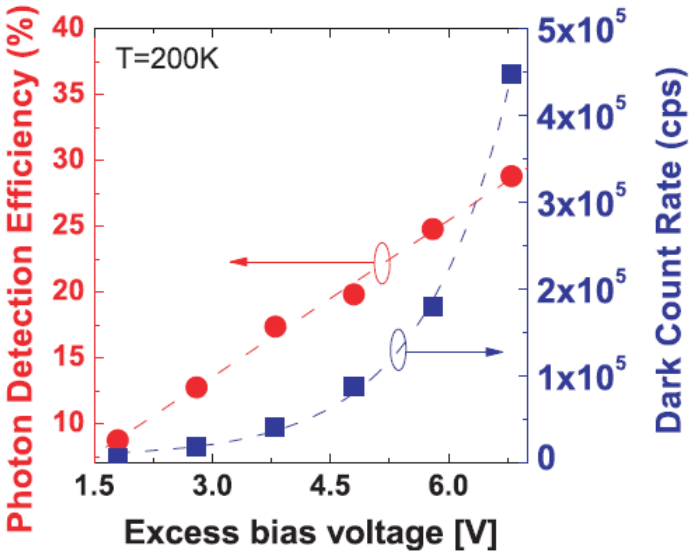

Figure 2-33 Excess-bias-dependent photon detection efficiency and dark count rate of a gated-mode $In_{0.53}Ga_{0.47}As/InP$ SPAD with 40 µm active area diameter (by Princeton Lightwave, Inc. USA) [2.67] operating at a temperature of 200 K and at a wavelength of 1550 nm.(From [2.20]).

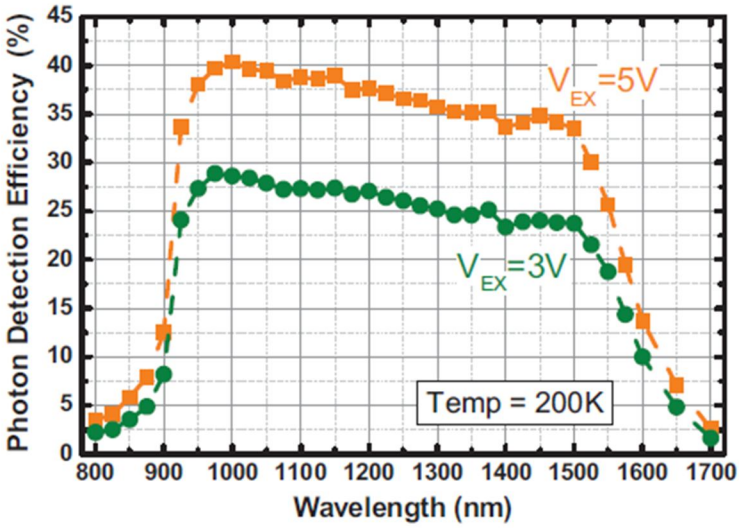

Figure 2-34 Excess-bias-dependent spectral photon detection efficiency of a 25 µm active area diameter InGaAs/InP SPADs in gated mode with a passive quenching circuit at temperature of 200 K. (From [2.68]).

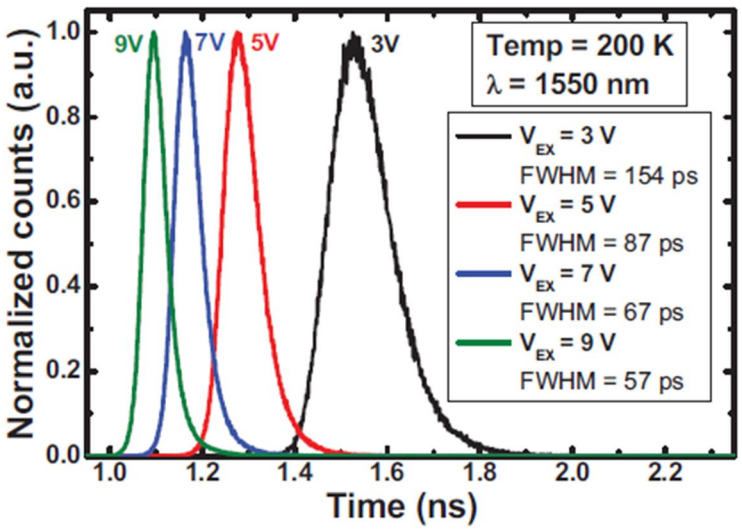

Figure 2-35 Excess-bias-dependent normalised temporal response distributions of the a 25 μm active area diameter InGaAs/InP SPADs in gated mode with a passive quenching circuit at a wavelength of 1550 nm and at a temperature of 200 K. (From [2.68]).

Afterpulsing due to the trap-assisted tunnelling effect is a significant noise problem for a free-running InGaAs/InP SPAD, thereby increasing its DCR and further reducing its SPDE. Therefore, in order to reduce the afterpulse possibility InGaAs/InP SPADs are commonly operated with gated detection systems. The idea of gating a SPAD is to shorten the gate duration and therefore perform as little multiplication as necessary to detect an individual photon event. Hence, it is preferable for the SPAD to be biased for a sufficiently long time in the linear-multiplication regime whereas only a short time for the self-sustaining avalanche process in order to perform a detectable signal. A variety of approaches of gating and avalanche discrimination systems have been employed as biasing schemes can limit the effects of afterpulsing in InGaAs/InP SPAD detection systems whilst still maintaining acceptable levels of efficiency and jitter. These techniques include a typical low-frequency (~100 MHz) gating scheme (e.g. robust cancellation scheme) and high-speed (GHz) periodically gated schemes such as: sine-wave gating, self-differencing and harmonic subtraction (refer to Pages 122-132 of [2.1]). However, in terms of the sine-wave gating scheme, the additional jitter derived from the effect of the dispersive filters reduces timing resolution significantly and leads to an increased likelihood of a lower average detection efficiency (refer to Pages 127-129 of [2.1]). The self-difference scheme inherently reduces the SNR of the avalanche output by 3 dB unless further efforts are made (refer to Pages 129-131 of [2.1]). In the harmonic subtraction scheme, it is very challenging to maintain precise control over the

amplitude and phase of the signal for the implementation of destructive interference in order to supress the gate transients (refer to Pages 131-132 of [2.1]). To date, commercial InGaAs/InP SPAD modules (e.g. the detection head ($IR-DH-025-C-F) in conjunction with the control unit ($IR-CU-PC) [2.69] by Micro Photon Devices, Italy) are based on the relatively mature low-frequency gating scheme. The cancellation mechanism of the gate transients [2.70] is illustrated in Figure 2-36 in more detail. An opposing pair of gate transients can be generated when both non-inverting and inverting reflections of a gating signal from the ends of matched transmission lines pass through the SPAD. The cancellation of the gate transients is finally implemented in a passive network. The avalanche signal can be revealed by the subtraction between the gate transients. To avoid excessively high dependence on the quality of the transmission lines, there is a range of alternative configurations available. For example, two individual balanced SPADs were applied for transient suppression. A gate frequency of 80 MHz can be biased and a SPDE as high as 43% at a wavelength of 1310 nm was reported [2.71-2.72]. Using a "dummy" component, such as a diode [2.73] or a capacitor [2.74], to substitute one of the SPADs can simplify implementation of the cancellation and still keep the comparative electrical response of a SPAD device reducing the avalanche discrimination threshold. A gate repetition frequency of 133 MHz was validated in a fully programmable module with a SPAD, whose timing jitter was less than 100 ps FWHM [2.75].

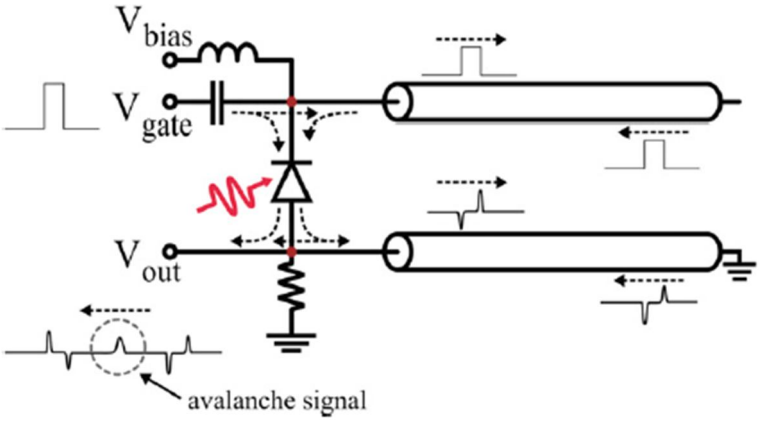

Figure 2-36 Block diagram of a gating system with cancellation of the gate transients. An opposing pair of gate transients can be generated when both noninverting and inverting reflections of a gating signal from the ends of matched transmission lines pass through the SPAD. The cancellation of the gate transients is finally implemented in a passive network. The avalanche signal can be revealed by the subtraction between the gate transients. (From Page 123 of [2.1]).

In summary, a variety of bias and control circuitry has been used to achieve high-performance detection with discrete InGaAs/InP SPAD devices. In addition, the InGaAs/InP SPAD arrays are valuable devices for parallel high-throughput measurements in the fields of low-light-level 2D and 3D imaging. A first-generation 32×32 array of InGaAs/InP SPADs with a 100 μm pitch was developed by Princeton Lightwave, Inc. USA [2.76]. Its DCR was <50 kcps for all pixels at a temperature of 253 K, the average pixel SPDE was ~22% at λ=1.5 μm and typically timing jitter was 350 ps. This timing jitter corresponds to the standard derivation (i.e. σ=350 ps) of the time distribution for the photon timing. The maximum frame rate of this sensor was 186 kHz [2.77]. The company later released a 32×32 InGaAsP/InP SPADs array sensor with a 100 μm pitch as shown in Figure 2-37 and 128×32 InGaAsP/InP SPADs array sensors with a 50 μm pitch which have spectral sensitivity between 0.9 and 1.06 μm. The 32×32 pixel and 128×32 pixel arrayed SPADs have average SPDEs of 35% and 30%, the average DCRs of 8.0 and 5.0 kcps, and the maximum frame rates of 186 kHz and 72 kHz, respectively at a wavelength of 1.06 μm operating at 20 ^{o}C. Their typically timing jitters are σ=350 ps and σ=300 ps respectively [2.77-2.78]. In general, it seems that there is a trend of developing high performance, good uniformity and large and dense format InP-based SPAD arrays [2.79-2.81].

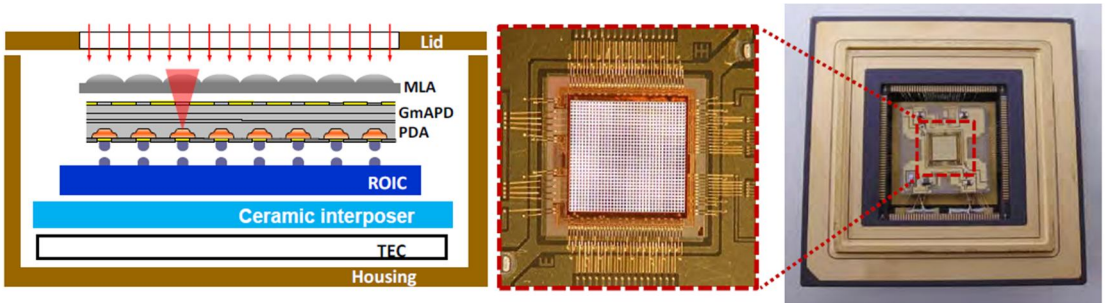

Figure 2-37 Left: schematic of an assembled focal plane array (FPA) module based on InGaAsP/InP Geiger-mode avalanche photodiodes (GmAPDs) operating at a wavelength of 1.06 μm. MLA: GaP microlens array; PDA: InGaAsP/InP photodiode array; ROIC: a custom CMOS readout integrated circuit; TEC: thermoelectric cooler. Centre: photograph of wire-bonded chip sit on a ceramic interposer. Right: photograph of a full packaged FPA sensor. (From [2.80]).

2.3.4 Superconducting nanowire single photon detectors

Superconducting nanowire single photon detectors (SNSPDs) were first demonstrated by Gol'tsman *et al.* [2.82]. Despite the reliance on potentially bulky and expensive refrigeration systems, they have a widespread reputation for broadband sensitivity, high

efficiency, fast recovery, and both low noise and jitter (refer to Pages 191-192 of [2.1]). To date, a majority of SNSPDs (e.g. the one with the meander-pattern wire shown in Figure 2-38) are triggering detectors. Their triggering implementation is derived from the occurrence of a phase transition of the superconducting material at a certain temperature (e.g. ~4 K for NbN and 120 mK for WSi) due to the current density beyond a critical level (J_C). In a qualitative sense, this can be outlined by the current-voltage relation of a superconducting wire shown in Figure 2-39. The sharp phase transition of the wire is facilitated by increasing the bias current to its critical value (I_C) due to photon absorption. This corresponds to a switch from an initial superconducting state to a resistive state, which is associated with a triggering process. The essence of the phase transition is the breaking of the energy gap shown in Figure 2-40(c). This energy gap, with the order of meV, is between the ground state where the Cooper pairs (i.e. bound pairs of charge carriers such as electrons formed in a superconductor) can be found and the low-lying electronic excited states where the formation of quasiparticles (i.e. broken Cooper pairs) can happen (refer to Page 186 of [2.1]).

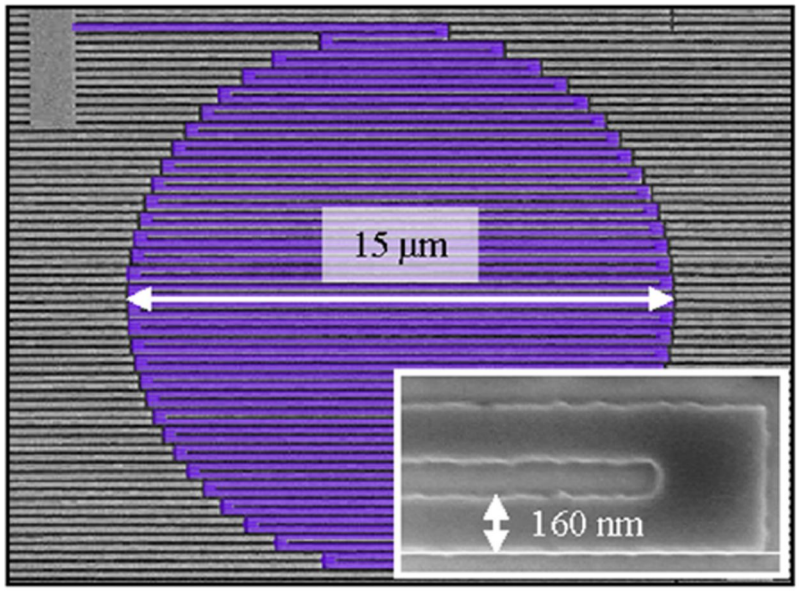

Figure 2-38 Scanning electron micrograph of the active area of a WSi superconducting nanowire single photon detector with the meander- pattern wire (see inset). (From [2.83]).

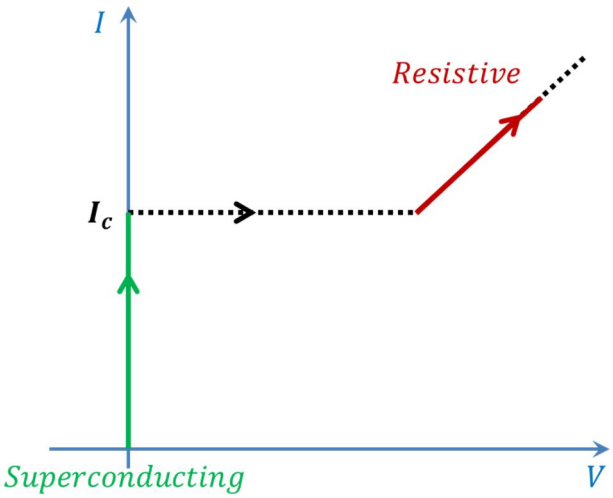

Figure 2-39 A current-voltage relation of an operating superconducting nanowire single photon detector (SNSPD) to illustrate a phase transition which one of superconducting material properties at a fixed temperature. The sharp phase transition of the nanowire is facilitated by increasing the bias current to its critical value (I_C) due to photon absorption. This corresponds to a switching from an initial superconducting state (in green) to a resistive state (in red), which is associated with a triggering process. (After Page 187 of [2.1]).

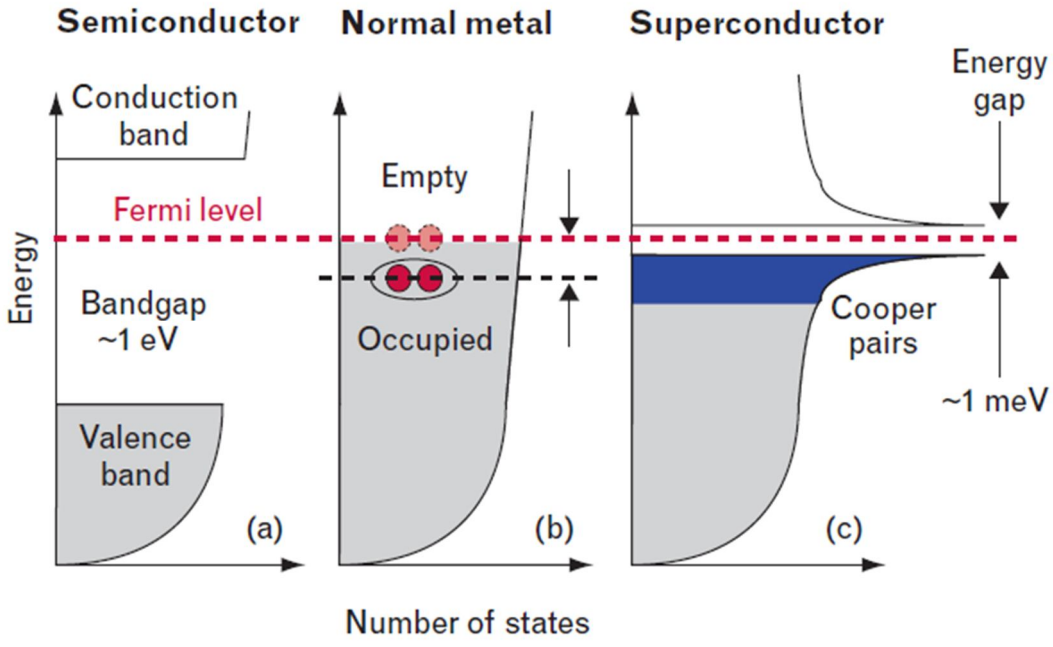

Figure 2-40 Schematic of band structures associated with specific particles for three different types of material systems. (a) represents the semiconductor material while (b) represents the conductor material such as a normal metal or a superconductor material operating well above its critical temperature (T_C). (c) shows the schematic of the band structure of a superconductor material operating below its T_C. The bound pairs of charge carriers such as electrons formed in a superconductor, so-called

Cooper pairs (in dark blue) are in the ground state. If they are excited out of the ground state, the formation of quasiparticles can occur on low-lying electronic excited states, resulting in dissociation of Cooper pairs. The breaking of the energy gap with order of meV between the ground state and the low-lying electronic excited states can lead to a phase transition. (From [2.84]).

As shown in Figure 2-40 (b), no energy bandgap exists in the conductor material such as a normal metal or a superconductor material operating well above its critical temperature (T_C). By contrast, there are energy bandgaps in the semiconductor material system (see Figure 2-40(a)) and the superconductor material system operating below its T_C (see Figure 2-40(c)). Particularly, it means that the critical temperature of the superconductor suggests the existence of an energy bandgap in the superconductor material system. However, the physics of superconductors' energy band formation is different from that of the semiconductors. As electrons cannot occupy the same energy level, due to the Pauli exclusion, in principle electrons in the semiconductors fill the available quantum states until the Fermi level (refer to Page 43 of [2.85]). By contrast, for superconductors, a bound pair of electrons (i.e. Cooper pair) has a very different behaviour compared to two individual electrons: each Cooper pair has lower energy in comparison to the binding energy of two individual electrons [2.84]. Thus, these Cooper pairs are not only forbidden from condensing to the same energy state, but also tend to condense together into this lower energy state [2.84]. This is a phenomenon known as Bose-Einstein condensation [2.84]. As shown in Figure 2-40(c), the energy gap ($2|\Delta|$) of superconductors can be expressed as in weak-coupling approximation (refer to Page 17 of [2.86]):

$$2|\Delta| = 2 \times 1.76 k_B T_C \qquad \text{Equation (2.12)}$$

where k_B is the Boltzmann constant. In comparison to a bandgap of about 1 eV for the semiconductor, as shown in Figure 2-40(a), a significantly narrower bandgap (about 1 meV) occurs near the Fermi level in the superconductor. This ultra-narrow bandgap is related to the single-particle excitation spectrum [2.84].

As illustrated in Figure 2-41, the SNSPD detection mechanism can be explained as follows: (1) A superconducting nanowire biased just below its critical bias current (I_C) is approaching its phase transition, which moves sharply from the superconducting state to the resistive state. (2) When a single photon at a visible or near-infrared wavelength strikes on the superconducting nanowire, it has sufficient energy to create order of 100s

or 1000s of the quasiparticles (i.e. excited electrons) which, in turn, produces a localised hotspot. Therefore, it can force the bias current above its critical density. (3) The localised hotspot contributes to form a resistive barrier, which spans the entire narrow cross section and a nanoscopic length in the axis of the nanowire resulting in the formation of a localised resistor. (4) The Joule heating of the hotspot promotes the resistive region with a length of hundreds of nanometres along the nanowire and the current is diverted to a detectable voltage pulse such as the one shown in Figure 2-42(a). (5) As the current along the wire is readout by the external electronics, Joule heating is removed. The wire is cooled quickly as the extremely thin and narrow film offers very low thermal resistance between the nanowire and the substrate. Eventually, the nanowire is completely recovered to the superconducting state.

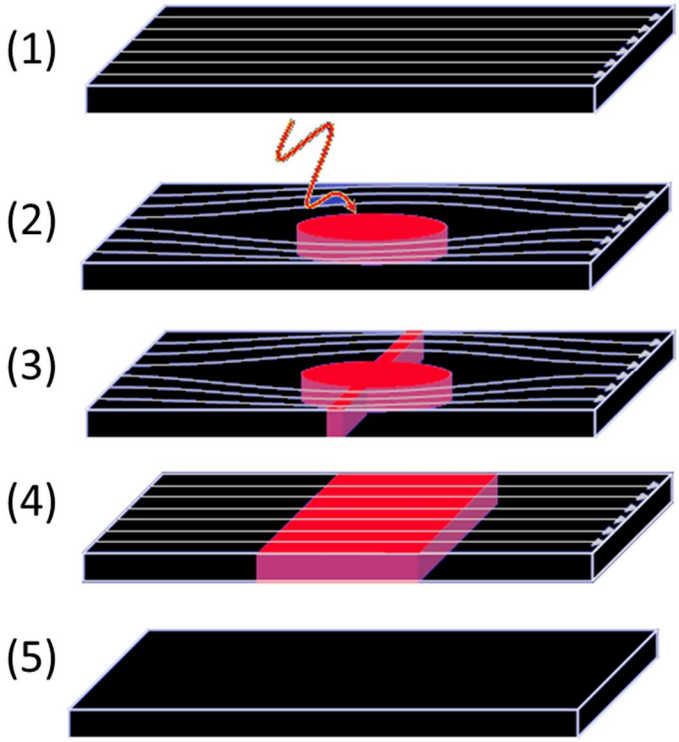

Figure 2-41 Diagram of the SNSPD detection mechanism. (1) The device is biased close to its critical current; (2) An incident photon is absorbed; (3) A localised resistor is formed; (4) The current in the resistive region is diverted to a detectable voltage pulse; (5) The device is restored to the superconducting state.

From the perspective of electrical equivalent circuits, the processes of a SNSPD detection system can be described as shown in Figure 2-42(b). The kinetic inductance of the superconducting nanowire is characterised by an inductor L_K and a time-dependent hotspot resistance which is described as resistor $R_n(t)$. Correspondingly, a time-dependent voltage pulse $V(t)$ can be produced by the parallel load impedance

R_{load} across the detector with feed-in current. The circuit models are in labels along the time-varying readout pulse as shown in Figure 2-42(a): (1) Given a certain bias current I_{bias}, the detector is biased to be ready for photon absorption. (2) A self-sustaining thermal avalanche due to single photon absorption induces the formation of resistance in the nanowire. (3) The restoration of superconductivity starts when the effective voltage pulse reaches its maximum level. The restoration time (typical 10 ns) is subject to a LR-circuit-imposed time constant dominated by L_K and R_{load}. The value of L_K is dependent on the total length of the wire. For example, the kinetic inductances of 47.1 nH and 109 nH correspond to the total nanowire lengths of 60 µm (corresponding to a 3 µm×4 µm active area) and 120 µm (corresponding to a 4 µm×6 µm active area). SNSPDs with 60-µm-long and 120-µm-long wires require ~3.5 ns and ~8 ns respectively to restore the relative detection efficiency (i.e. instantaneous detection efficiency normalised by the highest efficiency) of 90% as shown in Figure 2-43. Therefore, there is a trade-off when implementing high-performance SNSPDs in terms of coupling efficiency and recovery time. It is desirable to have a large active area (long nanowire) to couple photons with high probability. However, long nanowire corresponds long recovery time which limits the detection bandwidth of the devices [2.84].

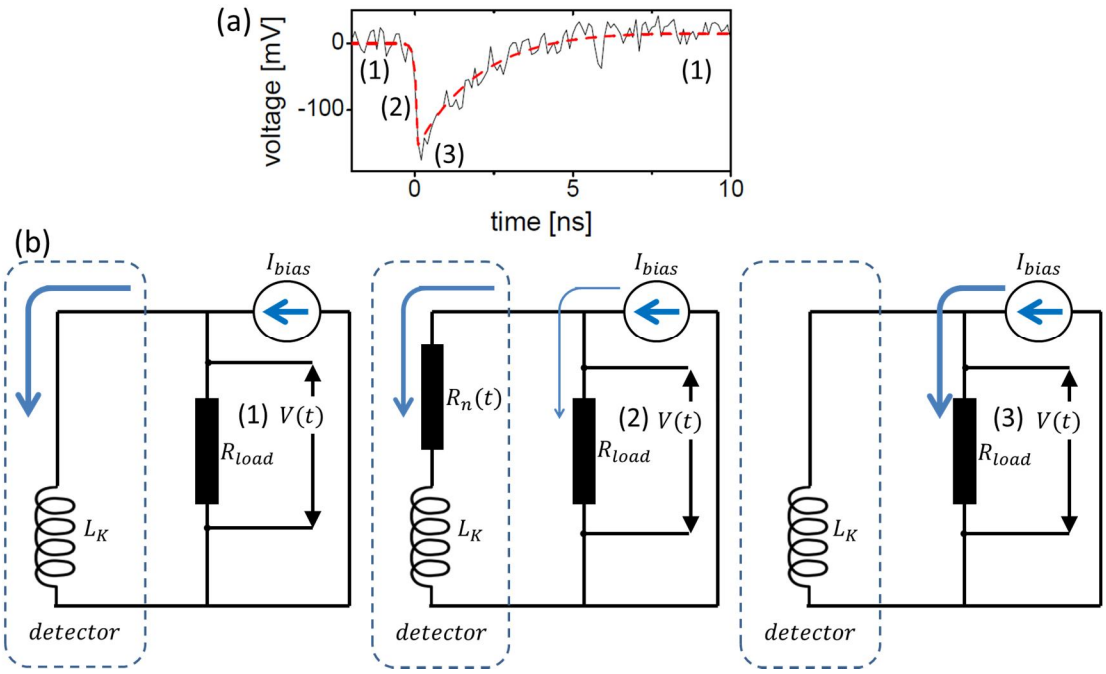

Figure 2-42 (a) Example readout negative voltage pulse detected by a SNSPD system. (Reproduced from [2.87]). (b) Electrical equivalent circuits, after Page 189 of [2.1] for a SNSPD detection system can outline the switching of resistance and pulse readout mechanism.

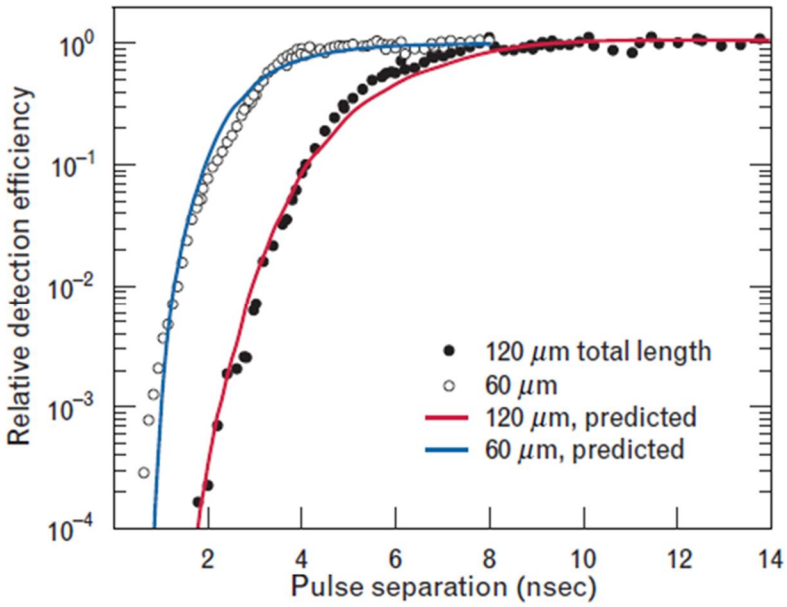

Figure 2-43 The plots of relative detection efficiency (i.e. instantaneous detection efficiency normalised by the highest efficiency) versus pulse separation time. Note that the pulse separation time here can be used to characterise the restoration time for single photon detection of SNSPDs with two different total lengths of nanowires. The open and solid circles represent the experimental results while the solid curves illustrate the predictions. For the SNSPD with the 60µm-long (120µm-long) wire, it requires ~3.5 ns (~8 ns) to restore the relative detection efficiency of 90%. (From [2.84]).

Higher critical currents in the SNSPDs with highly uniform nanowires offer better timing jitter [2.88-2.89]. Yamashita et al. [2.90] demonstrated that the dominant origin of the dark count in the SNSPDs is the current-assisted unbinding of vortex-antivortex pairs. However, the origin of the exponential rise of dark count rate with increased bias current, which approaches the critical current, for the SNSPDs is not fully explained in the literature [2.89-2.90]. To the best of my knowledge, there is still open and active research on the microscopic physics of the SNSPD photoresponse mechanism (refer to Page 192 in [2.1]). However, better understanding of this mechanism could offer greater scope for the engineering improvement on the performance of the SNSPDs, in particular for their timing jitter and dark count rates (refer to Page 192 [2.1]).

NbN, NbTiN and WSi are excellent materials with which SNSPD devices with wideband (from UV to mid-IR) sensitivity can be fabricated. They have lower critical temperature and stronger disorder in comparison to high temperature superconducting materials (e.g. Yttrium-Barium-Copper-Oxide (YBCO) and its T_C is ~90 K which is above the boiling point of liquid nitrogen) [2.91-2.92]. Experimentally, the disordered

lower-T_C superconducting materials are able to form the resistive state with higher probability due to the fact that when absorbing an incident photon more quasiparticles can be generated due to narrower superconducting gap. Also, larger normal-state resistivity (for faster Joule heating) and lower effective Cooper-pair density (for lower thermal energy disruption so that faster restoration of the superconducting state can be achieved) can be produced due to stronger disorder (refer to Page 190 of [2.1]). Nitride-based materials (the most commonly used materials) SNSPDs with meander-pattern nanowires are typically ≤200 nm in width and ≤10 nm in thickness [2.89, 2.93-2.97] and they commonly operate at temperatures of ~4K. Early devices had the highest detection efficiency with ~12% at a wavelength of 1550 nm being reported [2.89]. By contrast, devices with a narrower nanowire or those using a lower energy gap (low-T_C) superconducting material have the advantage of higher detection efficiency. For example, a NbN device with 20-50 nm width wire [2.98] and an $a-W_XSi_{1-X}$ SNSPD [2.99] both have the detection efficiency as high as ~20% at λ=1550 nm. Note that T_C of WSi is 3.7 K whereas T_C is 7.3 K for NbN or NbTiN. In 2013, WSi SNSPDs operating at T =120 mK with >90% detection efficiency at λ=1550 nm was demonstrated by Marsili *et al.* [2.100] with ~1 cps DCR, ~150 ps FWHM timing jitter and 40 ns reset time. In 2014, commercial detection systems (ID280 by ID Quantique SA, Switzerland [2.101]) with NbN or NbTiN SNSPDs have a detection efficiency of >50% at an operating temperature of 2.3 K with a typical DCR of 100 cps, timing jitter of 70 ps FWHM and recovery time of 70 ns. Along with the meander pattern nanowire (≤200 nm in width) to absorb incoming photons efficiently, it is also critical to guarantee the uniformity in width along the length of the nanowire with no imperfections or sharp corners. Furthermore, micro-fabricated optical coupling structures such as an optical cavity or stack can enhance the light coupling on the nanowire film [2.84, 2.97, 2.100, 2.102]. SNSPDs with optical nano-antennae [2.103-2.104] and integrated with waveguides have been demonstrated at telecommunications wavelengths. A SNSPD on a GaAs ridge waveguide was firstly reported by Sprengers *et al.* [2.105]. Light coupling capability of nearly no loss was achieved (Pernice *et al.* [2.106]) by burying the hairpin-pattern nanowire in a silicon waveguide. In addition, the detection efficiency of SNSPDs is polarisation sensitive. Its polarisation dependence varies due to the applied materials and nanowire arrangements on the devices [2.83, 2.107-2.108]. A recent patented design is shown in Figure 2-44 with two stacked meander WSi SNSPDs which are vertically insulated by a SiO_2 layer but electrically joint in parallel, and the orientations in the axis of two meander-patterned

wires are mutually orthogonal. This design can reduce the polarisation dependence of the high detection efficiency (87.7%) to less than 2% at λ=1560 nm [2.83, 2.109-2.110].

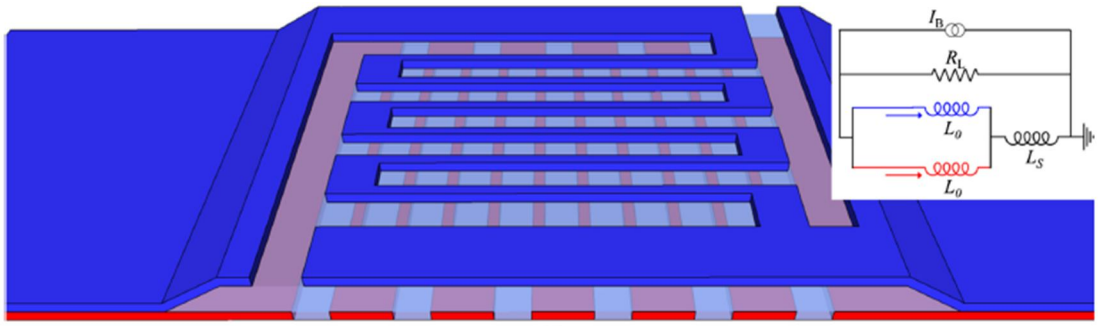

Figure 2-44 Schematic of a low-polarisation-dependence SNSPD design: two stacked meander WSi SNSPDs (i.e. the top one in blue and the bottom one in red) are insulated by a SiO_2 layer in vertical but electrically joint in parallel and the orientations in the axis of two meander-patterned wires are mutually orthogonal. The block diagram of the electrical equivalent circuit corresponding to the detectors is shown in right top inset. I_B is the bias current source; R_L is the load resistor; L_o in blue (red) is the inductance of the top (bottom) detector; L_S is the on-chip inductor fabricated in the top layer but not shown in the schematic. (From [2.83]).

To meet the requirements of a variety of applications, different light coupling options have been developed for SNSPD detection systems. They include free space coupling [2.111] and fibre coupling using both optical single-mode fibres (SMFs) [2.100, 2.102] and multi-mode fibres (MMFs) [2.112-2.113]. Detection systems with multi-element or arrayed SNSPDs have also been demonstrated. A 4×4 SNSPD array was used for lunar communication by NASA [2.114-2.115]. Free-space single photon imaging using a 8×8 SNSPD array at a short distance was demonstrated [2.111, 2.116]. They all require high performance readout electronics [2.83]. Recently, a scalable approach was developed to achieve integration between SNSPDs and photonics-integrated circuits by the use of flip-chip technology [2.117]. The development of SNSPD detection systems seems to concentrate on the performance improvements of discrete or arrayed detectors by means of optical and electronic on-chip designs and packages [2.83], and the extension of their photon sensitivity to longer wavelengths (up to 5 μm) [2.118].

2.4 Review of depth imaging systems

2.4.1 Overview of light detection and ranging systems

As an optical analogue of radar, light detection and ranging (LiDAR) systems have been developed using laser sources since the 1960s [2.119]. LiDAR systems that are active

and non-contact sensing tools have a high dynamic range of working distance from mm to 100s km ranges. In addition, they have good depth resolution that can be at a micrometre level for short distance (<5 m) measurements [2.120-2.122]. They are capable of resolving complex information (e.g. temporal and spatial dimensions, and spectral and polarisation properties) of the observed objects. In addition, they have strong environmental adaptation (e.g. the systems are non-cooperative with targets and independent to the diurnal cycle). This allows them to deploy in a variety of platforms for ranging and imaging applications [2.123], such as in the space-borne [2.124], air-borne [2.125] and underwater [2.126-2.127].

In general, LiDAR systems have bistatic (i.e. the transmit and receive channels are separated) and monostatic (i.e. the transmit and receive channels are partly joint) configurations as shown in Figure 2-45. Commonly the majority of LiDAR systems operate in a homodyne detection that is a direct detection mechanism. They resolve the return signal based on the amplitude-associated information directly rather than the coherent nature of the laser source whereas the heterodyne (or mixing) detection systems can resolve the coherent information between the local reference signal and the return signal.

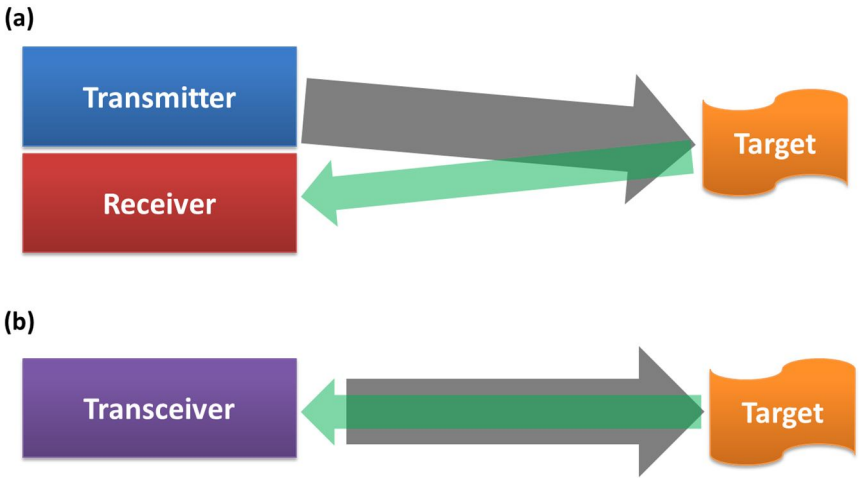

Figure 2-45 Schematic of light detection and ranging systems with (a) bistatic and (b) monostatic configurations.

2.4.1.1 LiDAR equation

Assuming that the footprint of the laser beam of the LiDAR system is smaller than the target surface, the relevant LiDAR equation (after Page 14 of [2.119]) can be expressed as:

$$P_r = P_t \rho \frac{1}{\Omega_s R^2} \frac{\pi D^2}{4} \eta_{sys} \eta_{atm} \qquad \text{Equation (2.13)}$$

where P_t is the transmit output optical power. P_r is the return optical power from the target. ρ is the reflectance of the target surface. Ω_s is the scattering steradian solid angle along the incident point on the target. R is the travel distance of the laser beam within the line-of-sight of the system. D is the effective aperture diameter of the receiver. η_{sys} is the transmission efficiency of the transmitting and receiving optics and η_{atm} is the atmospheric attenuation which is spectral-dependent as shown in Figure 2-47. If the targets of interest have Lambertian (or diffused) surfaces, Ω_s is approximately π. In addition, when the LiDAR system use a pulsed laser source with a repetition rate of f and the output photon number per pulse is N_t, the number of scattered return photons (N_r) acquired by a photon detector within an acquisition time of T_{Acq} can be described as:

$$N_r = N_t f \rho \frac{D^2}{4R^2} \eta_{sys} \eta_{atm} T_{Acq} \qquad \text{Equation (2.14)}$$

2.4.1.2 Direct and indirect time-of-flight range findings

LiDAR systems based on time of flight can employ pulsed or continuous-waveform (CW) laser sources. By using periodic pulsed illumination with a repetition rate of f_{rep}, pulsed time-of-flight LiDAR can directly achieve ranging by the interpretation of the time difference (τ_{ToF}) (i.e. round-trip time) between outbound and return pulsed signal (see Figure 2-48):

$$R = \frac{c\tau_{ToF}}{2} = \frac{c}{2f_{rep}} \qquad \text{Equation (2.15)}$$

where c is the speed of light. However, if multiple indistinguishable illumination pulses are in transit (to and/or from the target) at any given time then there can be ambiguity in the absolute range measurement. If the pulsed illumination has a repetition rate of 50 MHz (as, for example, in the case of one of the imaging systems described in Chapter 4), the unambiguous absolute range possible is limited to only 3 metres. If the illumination pulses are indistinguishable then it is no longer possible to assign a return signal to a unique illumination pulse. Due to the range ambiguity effects of high frequency, periodic illumination causing multiple indistinguishable illumination pulses

in transit at any given time, the high periodic repetition rate (e.g. 10's MHz) of the laser used in many of these experiments means that absolute depth measurements cannot be made unambiguously. However, depth profiling measurements can still be made if the depth-of-field is less than the pulse-to-pulse distance. The use of pulsed illumination at high repetition rates, however, can offer high average output power and consequently lead to a reduction of the data acquisition time.

In order to overcome this range ambiguity issue, pseudorandom pulse trains at high laser repetition rates have previously been used for long-range ranging [2.128] and imaging [2.129]. In [2.129], the unambiguous range is determined using a pseudo-random pattern matching technique and a cyclic cross-correlation technique for coded range resolution. Note that the cross-correlation technique is described in section 2.4.2. Figure 2-46 (a) shows a pseudo-random non-periodic pulse train at a base clock rate of f_{Base}, which is generated by a pulse pattern generator. It is used to trigger a pulsed laser diode with the same non-periodic output pulse pattern, as shown in Figure 2-46(b). Using prior knowledge of the system temporal response and the pseudo-random pattern, a reference signal is generated for the cross-correlation processing, as shown in Figure 2-46(c). Figure 2-46(d) shows the return signal reflected from the target surfaces. It can be seen that the cyclic recorded histogram of Figure 2-46(d) has been shifted by the round-trip time of $2d/c$ relative to the outgoing optical pulses of Figure 2-46(b). Note that in certain cases (indicated by dashed returns in Figure 2-46(d)), the laser pulses are scattered away from the target and do not result in any registered photon events. A maximum at $2d/c$ (see Figure 2-46(e)) can be identified by the use of the cross-correlation function of the reference and the target response and this allows the absolute range to be resolved. However, the research scope of this Thesis concentrates on the depth profiling for remote targets rather than the interpretation of their absolute ranges and, consequently, a repetitive periodically pulsed signal was used for all of the research presented in this Thesis.

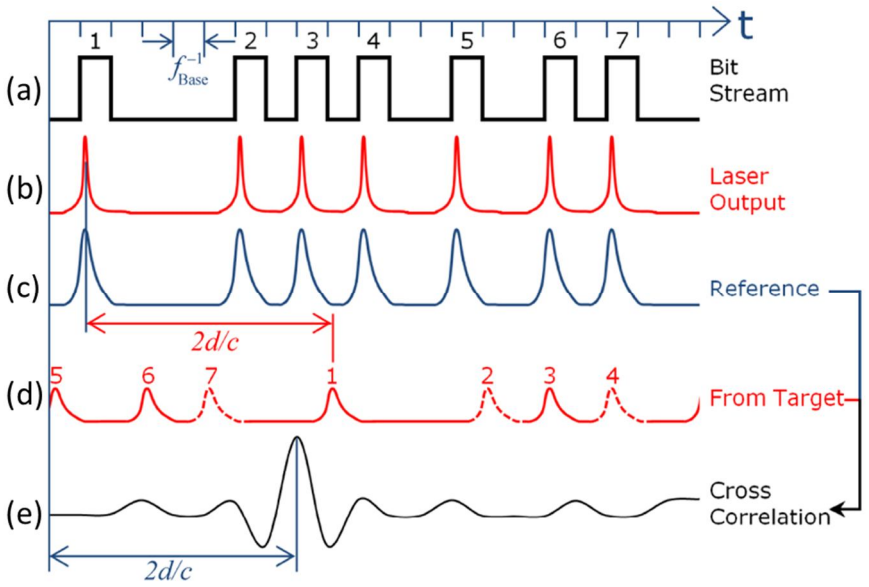

Figure 2-46 Unambiguous range determined using a pseudo-random pattern matching technique and a cyclic cross-correlation technique for coded range resolution. (From [2.129]).

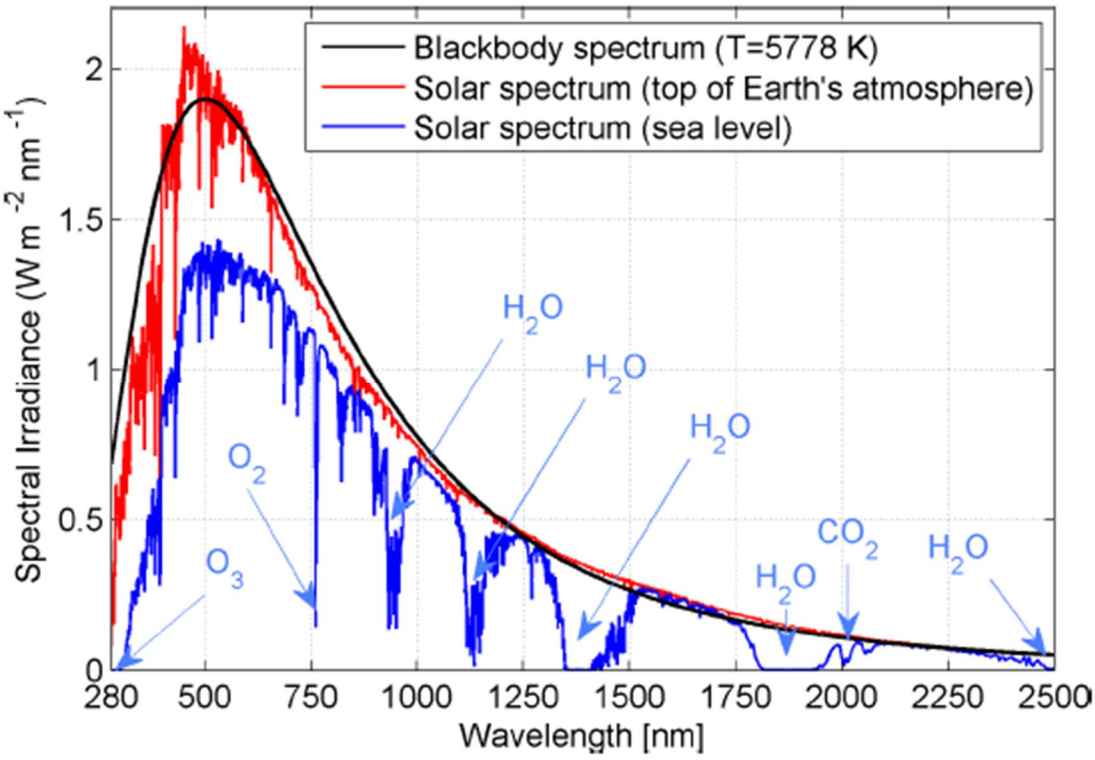

Figure 2-47 The spectral emission characteristic of a blackbody radiation at the Sun's approximate surface (in black) and solar spectral irradiance on the top of Earth (in red) and near the sea level (in blue). Note that, the absorption wavelength windows and their causing atmospheric constituents near the sea level are illustrated in blue. (From Page 15 of [2.130]).

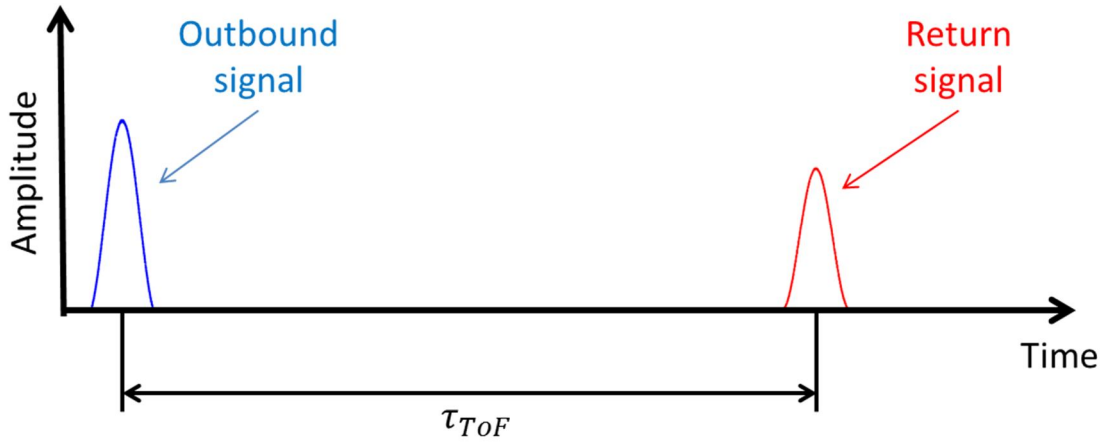

Figure 2-48 Direct pulsed time-of-flight LiDAR mechanism. τ_{ToF} is the time difference between outbound and return signal.

CW-based LiDAR systems are mainly classified as amplitude modulation (AM) and frequency modulation (FM) systems. They can achieve time-of-flight ranging indirectly. If the intensity of the laser source is modulated with a certain frequency of f which corresponds to a period of T in the time domain, there is a phase shift ($\Delta\Phi$) between the modulated outbound signal and return signal from the remote target of interest (see Figure 2-49). The relevant round-trip delay time (Δt) and R can be worked out as:

$$\Delta t = \frac{\Delta\Phi T}{2\pi} \qquad \text{Equation (2.16)}$$

$$R = \frac{c\Delta\Phi T}{4\pi} = \frac{c\Delta\Phi}{4\pi f} \qquad \text{Equation (2.17)}$$

Note that in order to avoid any range ambiguous maximised modulation frequency f is limited by following $\Delta\Phi < 2\pi$.

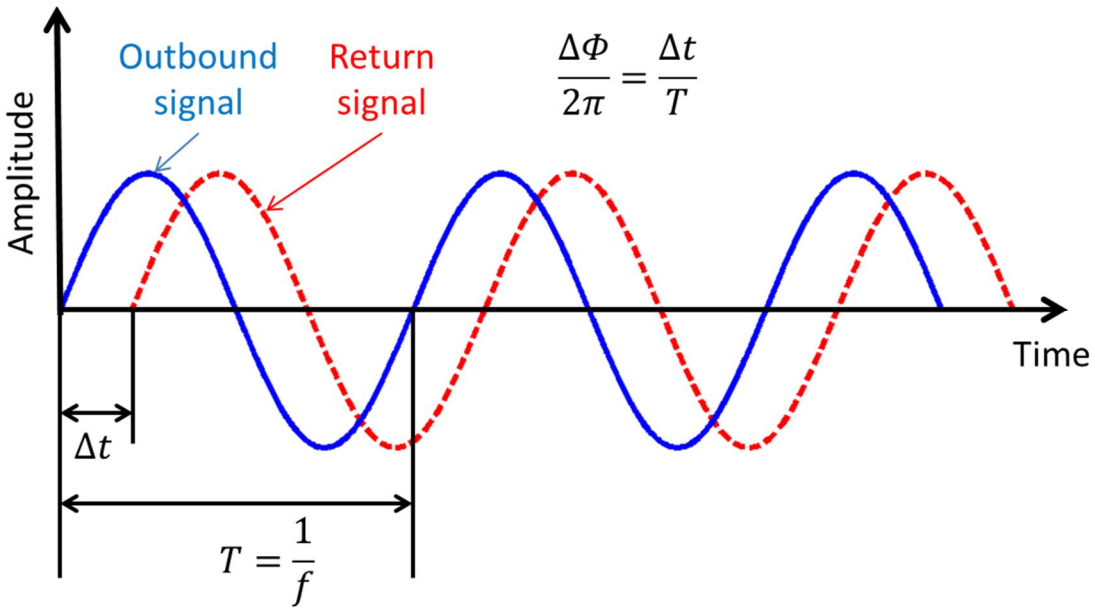

Figure 2-49 Typical amplitude modulation time-of-flight LiDAR mechanism. f is the modulation frequency. $\Delta\Phi$ is the phase shift between the modulated outbound signal and return signal from the remote target of interest and Δt is the related round-trip delay time.

As for the typical frequency modulation LiDAR as shown in Figure 2-50, a saw-tooth bias current with a given period of t_m generated by a ramp generator is used to modulate the tunable laser source with the instantaneous frequencies (f_{if}) chirped periodically by a total frequency shift of Δf (see Figure 2-51). The relation between Δf and the round-trip delay time (τ) here as well as the range difference between the reference mirror and the object (R) can be calculated as:

$$\tau = \frac{t_m f_{if}}{\Delta f} \qquad \text{Equation (2.18)}$$

$$R = \frac{c t_m f_{if}}{2\Delta f} \qquad \text{Equation (2.19)}$$

Note that by using a FM-CW LiDAR, the coherence length of the laser source (e.g. typically 10s metres for laser diodes) can limit the maximal range-finding distance [2.131].

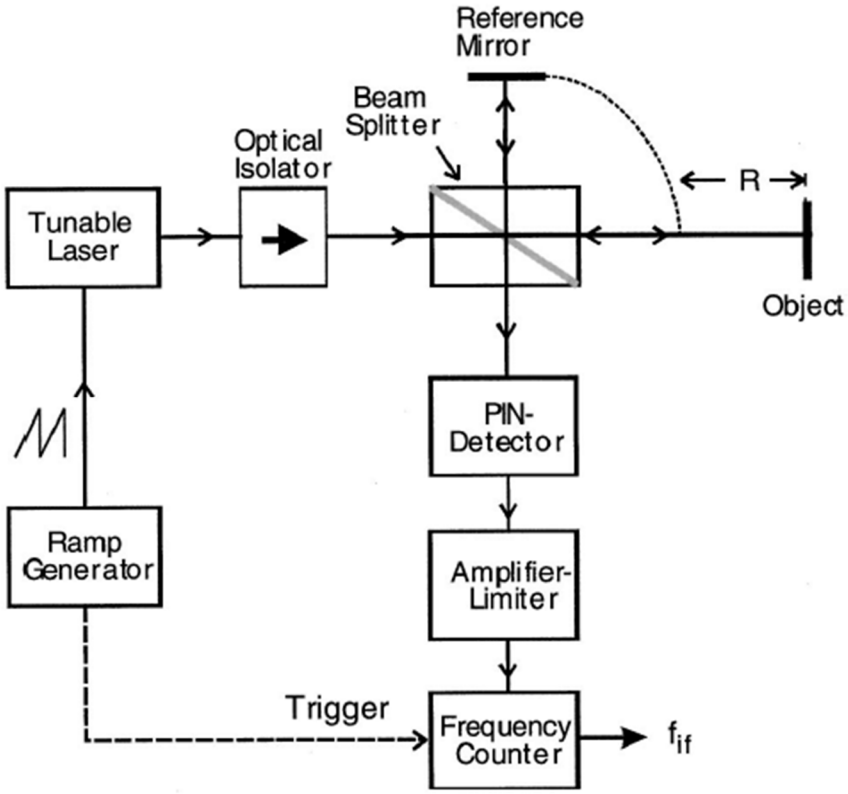

Figure 2-50 Schematic of a typical frequency modulation time-of-flight LiDAR setup with frequency mixing. Saw-tooth bias current with a given period of t_m generated by a ramp generator is used to modulate the tunable laser source with the instantaneous frequencies (f_{if}) chirped periodically by a total frequency shift of Δf. f_{if} of the reflected signals is obtained eventually using a frequency counter. (From [2.131]).

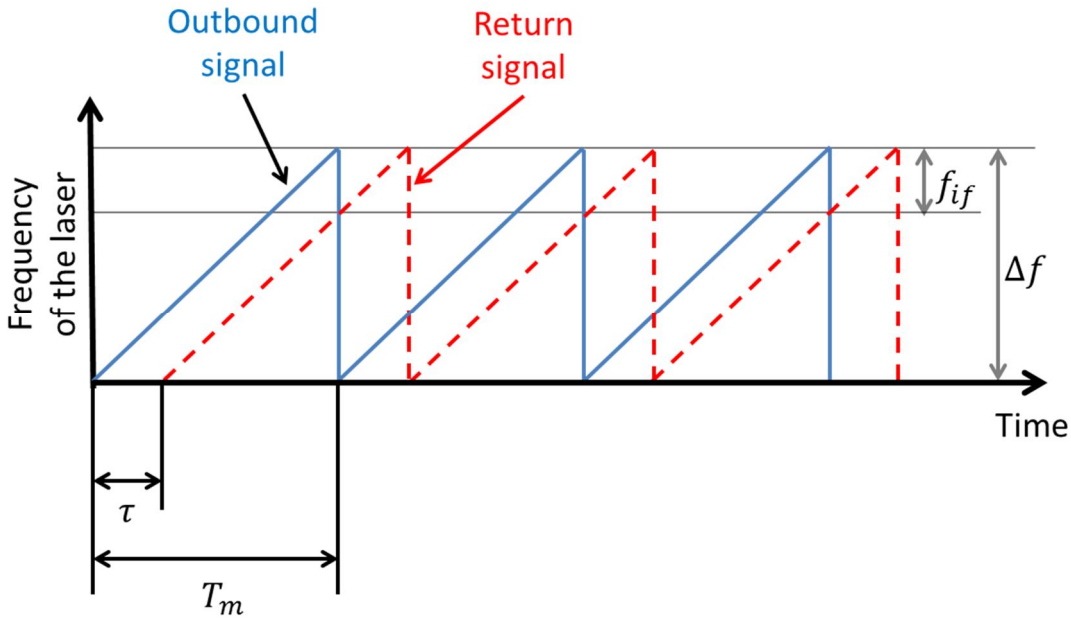

Figure 2-51 A schematic of a typical frequency modulation approach in the time-of-flight LiDAR. This approach is related to the system setup shown in Figure 2-50.

2.4.1.3 Full-waveform LiDAR

In order to obtain the depth profile of a distributed target, it is better to use a full waveform LiDAR system. A full waveform LiDAR system can capture and accumulate the huge amount of returned signal among a series of recording time intervals (e.g. the formation of amplitudes or photon counts as a function of time). This full waveform signal can be used to retrieve as much detail as possible within the line-of-sight of the sensor. This is preferable to a discrete return LiDAR system that only records relatively sparse returns (e.g. first or/and last returns, or another few returns) [2.132]. As shown in Figure 2-52, when detecting the tree canopy, the discrete return LiDAR can only record several depths of the target, whose signal peaks are higher than a pre-determined threshold. However, the full waveform LiDAR has the capability to collect almost all scattered return energy from the target within the line-of-sight. For example, when an airborne full waveform LiDAR is employed to detect forest canopies, multiple reflections within the laser footprint of single measurement are acquired. They correspond to complex layers of the forest canopies, i.e. vertical structure of forest canopies. This can yield important information, which can be used in canopy surface classification and interpretation. Thus, analysis based on a full waveform topographic LiDAR is significant in both detection of forest canopies and also monitoring environmental changes [2.133-2.134]. Full waveform LiDARs can also work with both small and large laser footprints [2.135], shown in Figure 2-53. Figure 2-53(a) illustrates a received waveform of a small-laser-footprint LiDAR. The waveform shape is formed within a small-sized footprint but it has a high probability to miss the peaks from the ground as the branches or leaves can block the laser beam; Figure 2-53(b) shows a received waveform of a large-laser-footprint LiDAR. The large laser beam spot covers several targets. Each return peak integrates the information in the same depth or layer. Thus, within the timing resolution of the detection system, distinct peaks corresponding to various layers of forest structure can be acquired from the ground to forest canopy.

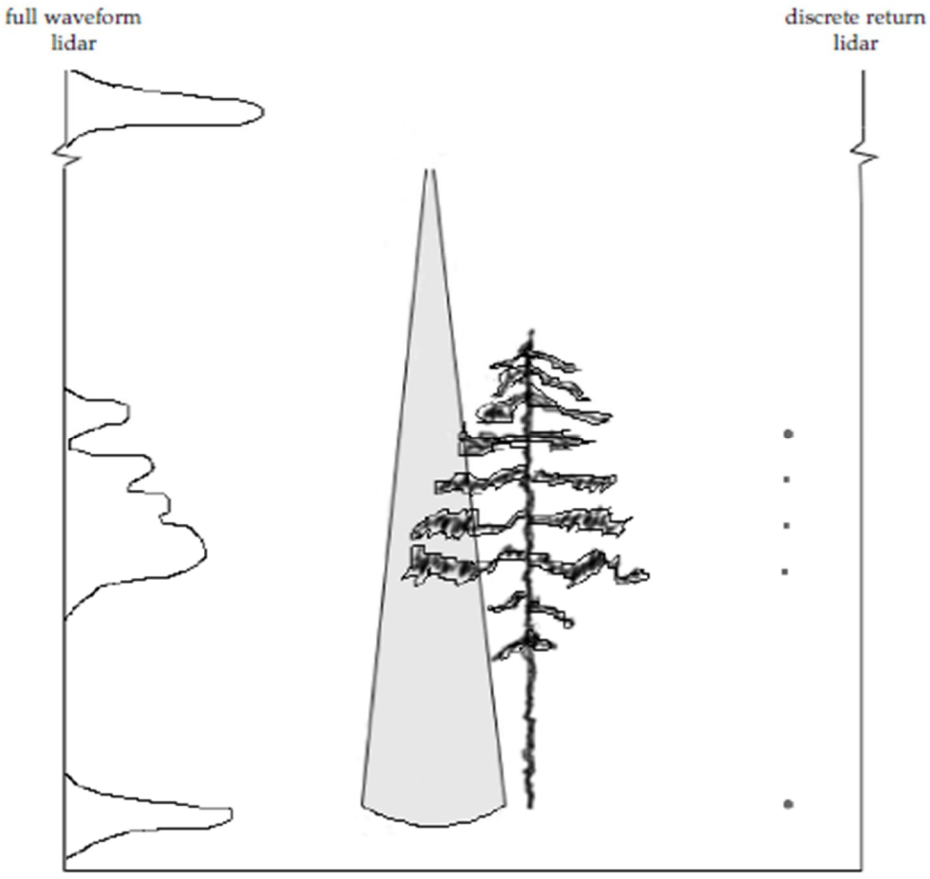

Figure 2-52 Different received signal patterns between a full waveform (left) and a discrete return (right) LiDAR. (From [2.132]).

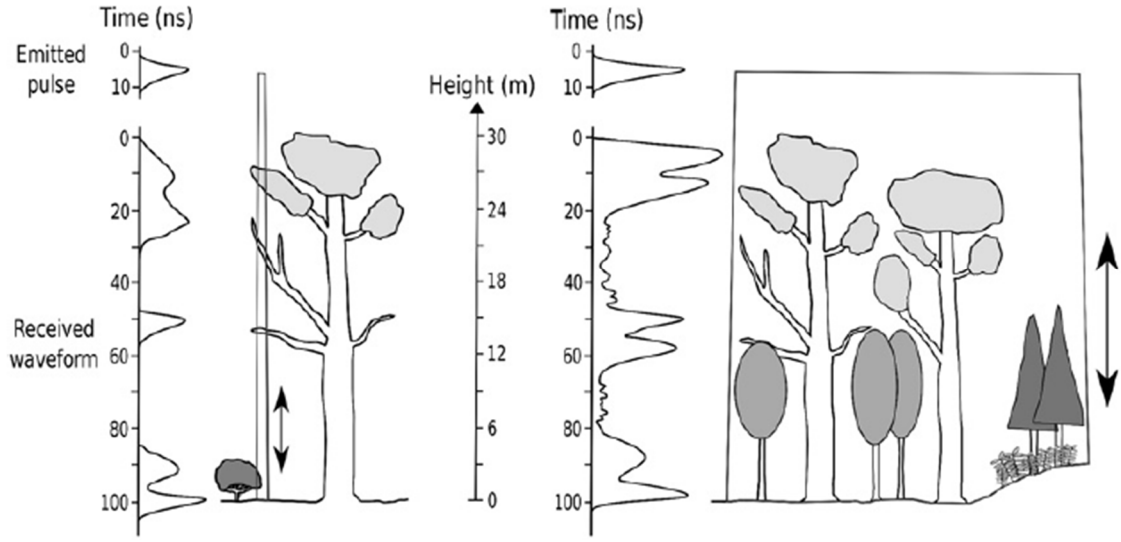

Figure 2-53 Top-to-down demonstration of the full waveform LiDAR return of a forest structure. (From [2.135]). Left: Received waveform of a small-laser-footprint LiDAR. Right: Received waveform of a large-laser-footprint LiDAR.

2.4.2 Time-of-flight photon count data processing techniques

Histograms of photon counts versus time obtained by the TCSPC-based time-of-flight

depth imaging systems can be used to estimate the depth profiles of remote targets. In the experimental systems reported in this Thesis, the starting time (or "zero time") for the histogram is taken as each repetitive synchronisation ("start") electrical signal and the duration of the histogram time axis is equal to the period of the synchronisation signal. The minimum binning size is determined by hardware limitations and is equal to 1 ps for the HydraHarp 400. For example, Figure 2-54(a) shows the pixel-wise histogram of the scan on the plywood board at a stand-off distance of 4400 m using one of the depth imaging systems described in Chapter 4. The duration of the histogram axis corresponds to the period the synchronisation signal. The frequency of this signal is down-divided by a factor of 16 from the repetition rate of 40 MHz for the pulsed laser source. Thus, there are 16 repetitive pulse periods within the histogram. One of the period-wise histograms.is highlighted in Figure 2-54(b). Apart from positions (or depths) of the scattered returns from the remote target surfaces, their amplitudes (or photon counts) and/or number of returns/peaks can also be characterised depending on different time-of-flight data processing methods [2.136].

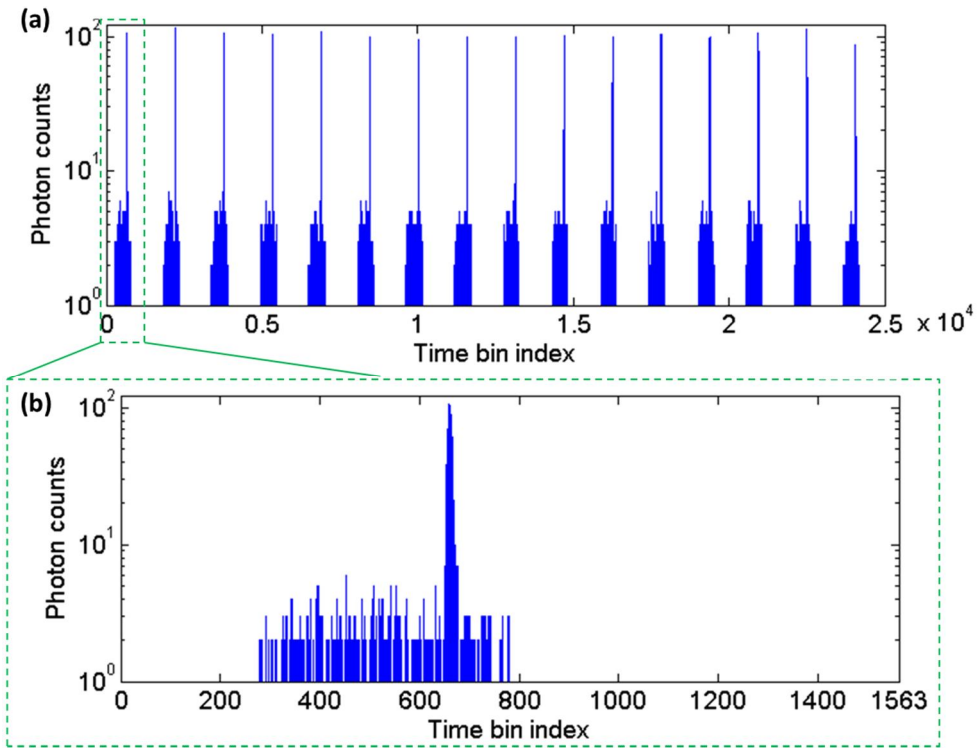

Figure 2-54 (a) shows the pixel-wise histogram of the scan on the plywood board at a stand-off distance of 4400 m using one of the depth imaging systems described in Chapter 4. The frequency of the synchronisation signal is down-divided by a factor of 16 from the repetition rate of 40 MHz for the pulsed laser source. A timing bin size of 16 ps was used to record the histogram. One of the 16 pulse periods in the histogram, as shown in (a), is highlighted in (b).

Given a pre-determined photon count threshold, locating the time/depth associated with a local maximum/peak in the photon histogram can be achieved using a peak-finder algorithm. However, as shown in Figure 2-55, a photon count histogram with reasonably high SNR is necessarily required to achieve a single return discrimination from the background noise. In addition, in order to effectively distinguish the signal, this method often strongly requires user to determine the photon count threshold.

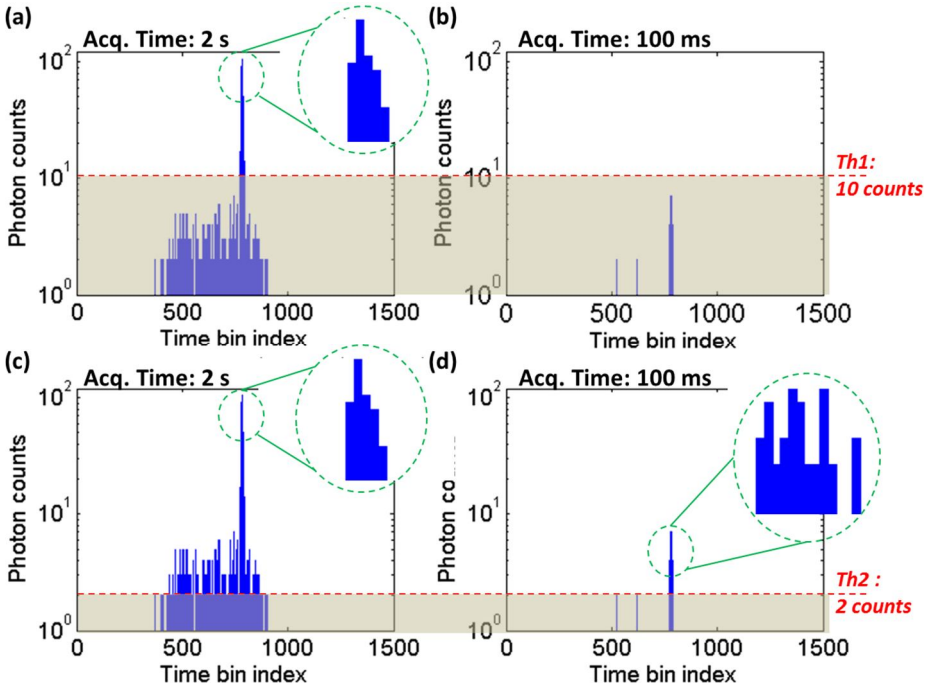

Figure 2-55 The photon count histogram with 2 s acquisition time, 16 ps timing bin and SNR of ~10.2 is shown in (a) or (c). The photon count histogram with 100 ms acquisition time, 16 ps timing bin and SNR of ~2.6 is shown in (b) or (d). The insets in (a), (c) and (d) show the zoom-in potential peaks. Note that they are portion of Pixel 50 histograms of the scans on the plywood board at a stand-off distance of 4400 m using one of the depth imaging systems described in Chapter 4. The photon count threshold of 10 counts (i.e. Th1=10 counts) or 2 counts (i.e. Th2=2 counts) is chosen for the peak finding. Locating the time associated with a local maximum/peak in the photon histogram can be achieved well in (a) and (c). By contrast, the maximum counts in the histogram with the 100 ms acquisition time is less than Th1 so that no effective signal can be distinguished in (b). Even if Th2=2, two local maximum peaks are found, as shown in (d), so that it still cannot ensure that the time of flight associated with the depth of the target is located in the histogram.

By contrast, the cross-correlation method, which measures the degree of similarity between the photon count histogram and the reference instrumental response function (IRF) of the system, can be used to determine the depth profile in photon data with a

reduced SNR [2.137]. The essence of the cross-correlation method is similar to a convolution between two functions. It aims to estimate the similarity between the return signal (see Figure 2-56 (a)) and the time-shifted reference (see Figure 2-56(b)), and in turn to locate the position of the maximum cross correlation (see Figure 2-56(c)), which corresponds to the most likely location of the signal matching the reference. This can be expressed as:

$$C_k = \sum_{n=1}^{r} H_{n+k} R_n \qquad \text{Equation (2.20)}$$

where k varies in $[-r, h]$ and C_k is the time-bin-wise cross-correlation, which is performed between the acquired photon count histogram H with h time bins and the reference instrumental response function response R with r time bins. The highest cross-correlation can reveal the time bin associated with the target return. Therefore, the cross-correlation approach can be used effectively to estimate the time/depth of the return.

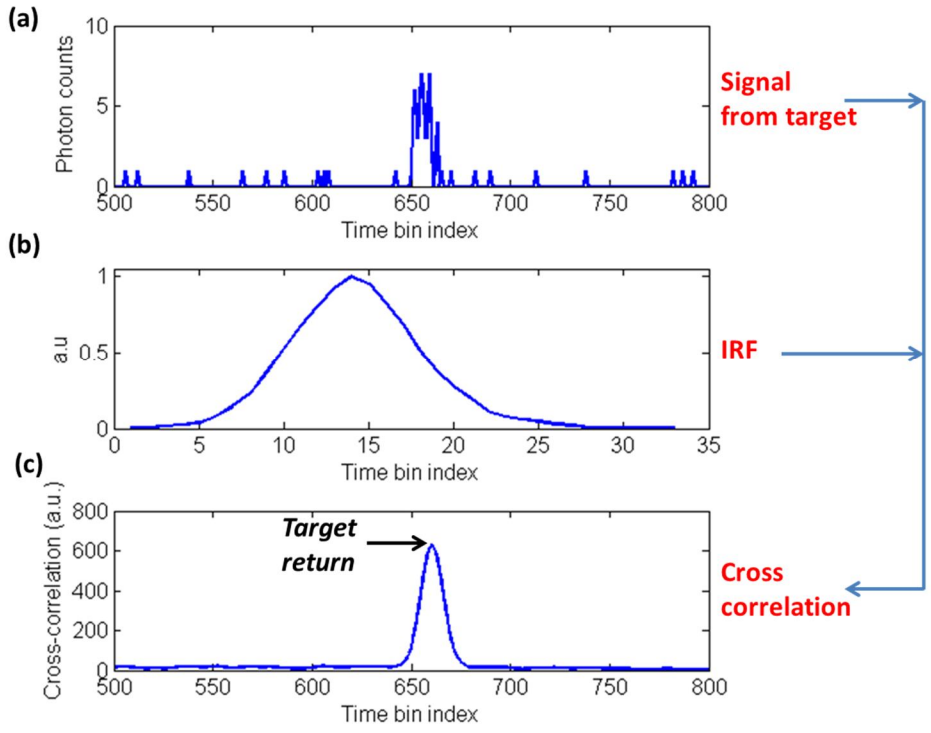

Figure 2-56 The cross-correlation technique aims to estimate the similarity between the return signal (a), which is the same to the signal with a SNR of ~2.6 shown in Figure 2-55(b) or (d), and the time-shifted reference (b), and in turn to locate the position of the maximum cross correlation, as shown in (c), which corresponds to the most likely location of the signal matching the reference. IRF: the reference instrumental response function of the system.

The cross-correlation method is a standard estimation method, which only covers the estimation procedure of the processing strategy, as shown in Figure 2-57. It offers a highly efficient approach to data processing and is not specific to the analysis of photon data. However, particularly, Poisson noise that typically occurs in photon counting techniques is not considered in the cross-correlation method. It can generally degrade the time/depth estimation performance due to the increased variance of the estimation and/or the introduction of a bias. In addition, the cross-correlation method does not take into account the background counts either. This can further degrade the time/depth estimation. If there is poor estimation of the depth position, then this will affect the estimation of the number of photon counts in the peak, if required. In addition, the cross-correlation method is not suitable to resolve multiple returns/peaks in a photon count histogram without some a-priori knowledge of the number or distribution of those returns/peaks.

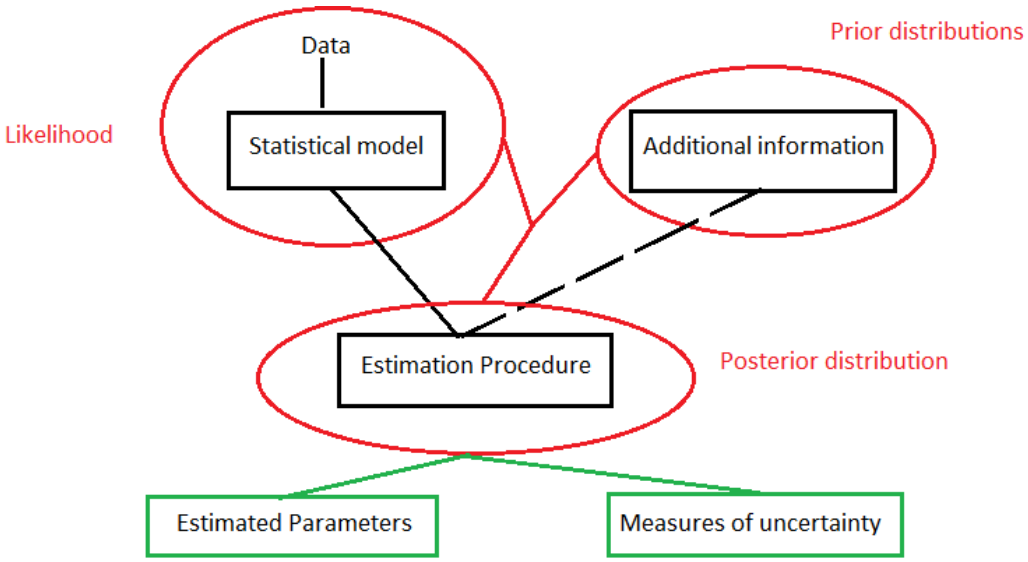

Figure 2-57 Graphical model of a systematic strategy for (but not limited to) photon count data processing,

An alternative to the cross-correlation method is the family of Bayesian methods, which can be used to process single-photon data with reduced SNR while incorporating additional useful information (see Figure 2-57). Given that the observed data and the prior information are available, this is possible to derive a posterior distribution, which models more knowledge about the unknowns. This means that multiple parameters (e.g. number, positions, and amplitudes of returns/peaks) can be simultaneously estimated. A statistical model is involved to evaluate the likelihood for the data, for example the assumption of Poisson noise realisations in the data. Such methods can incorporate additional information through prior distributions, such as positive

amplitudes, smooth depth variation, background counts with low variation, distribution of the return/peak number and observation conditions. In order to obtain not only estimated parameters but also measures of the relevant uncertainty, Markov chain Monte Carlo (MCMC) techniques seem particularly appropriate methods. MCMC methods generally consist of generating a Markov chain of random variables that converges toward a distribution of interest (the posterior distribution shown in Figure 2-57) [2.136]. Standard MCMC methods are, however, not well adapted for problem where the number of unknowns (e.g. number of peaks) is undetermined [2.136]. In such cases, reversible jump MCMC (RJMCMC) methods can be used, which allow moves between different parameter spaces if the parameters correspond to individual state spaces [2.138].

Both cross-correlation-based and Bayesian-based data processing techniques are widely used to estimate depth images using individual pixel-wise photon count histograms in isolation (see for example [2.139-2.145]). This allows the 3D surface reconstruction of the remote target based on pixel-wise processing using these algorithms. Note that both pixel-wise cross-correlation methods and the RJMCMC algorithm are used to process the TCSPC-based photon data presented in the later Chapters of this Thesis. Particularly, the photon data from a distributed target (e.g. tree) is processed by the RJMCMC algorithm, which is an adaptive approach (see Chapter 6). In addition, processing neighbouring pixels simultaneously using spatial-correlation approaches, which incorporated MCMC algorithms (see Chapter 7) [2.146] or convex optimisations (with knowledge of photon macro times [2.29]), has been proposed for efficient depth/intensity estimation from the photon data or even sparse photon data. By considering the relationships between adjacent pixels these approaches can optimise the analysis conducted by peak-finder algorithms to more efficiently generate depth/intensity profiles. For example, if a cluster of adjacent pixel from an approximate flat plane at a particular distance, it is unlikely that one further adjacent single pixel is likely to be at a distance that is widely separated from the plane.

2.4.3 Conventional LiDAR-based depth imaging systems

Compared to AM-CW and FM-CW LiDAR systems, direct time-of-flight ranging based on a pulsed laser is more straightforward, simplifying the configuration of LiDAR systems. In addition, direct time-of-flight LiDAR systems with discrete detectors combined with spatial scanning mechanisms (e.g. mirror-based raster scanning and

refractive-optics-based Risley prism scanning) or using focal panel arrayed (FPA) detectors are capable of depth imaging. To implement 2D mapping of targets, imaging using a discrete detector observes a series of spatial origin of instantaneous field of views (IFOVs) sequentially to cover the entire FOV of interest. In contrast, the FPA-based imaging is able to stare the entire FOV formed by pixel-wise IFOVs. LiDAR-based depth imaging systems can map the world in three dimensions which corresponds to an assembly of spatial-point-wise depths [2.123, 2.147]. As opposed to passive optical imaging techniques with stringent dependence on light conditions related to the diurnal cycle, LiDAR-based depth imaging systems that are active optical imaging systems have dedicated illumination sources to initiate photons and can retrieve information from the detected photons. This makes them powerful sensors for laser-based remote sensing [2.124, 2.148-2.149] and more recently computer vision communities [2.150].

Conventional hundred-metre-range LiDAR-based depth imaging systems employ laser sources with a pulse width in the order of a nanosecond FWHM and photon detectors with linear amplified gain. They can resolve depth resolutions of typically higher than a centimetre. For example, commercial scanning LiDAR sensors (e.g. HDL-64E S2 by Velodyne CA, USA [2.151]) can obtain high-definition 3D mapping of a target scene. The high resolution 3D image of urban scenes as shown in Figure 2-58 depicts some hard targets (e.g. buildings and street curbs) and distributed targets (e.g. trees and overhead wires) clearly. The image was acquired using a high definition LiDAR sensor from Velodyne CA, USA. The wide-field-of-view LiDAR sensor using 64 lasers with 5 ns pulse duration time operating at λ=905 nm has range accuracy of 1.5 cm at a working distance of ~100 m. In addition, it can generate ~1.3 million data points per second.

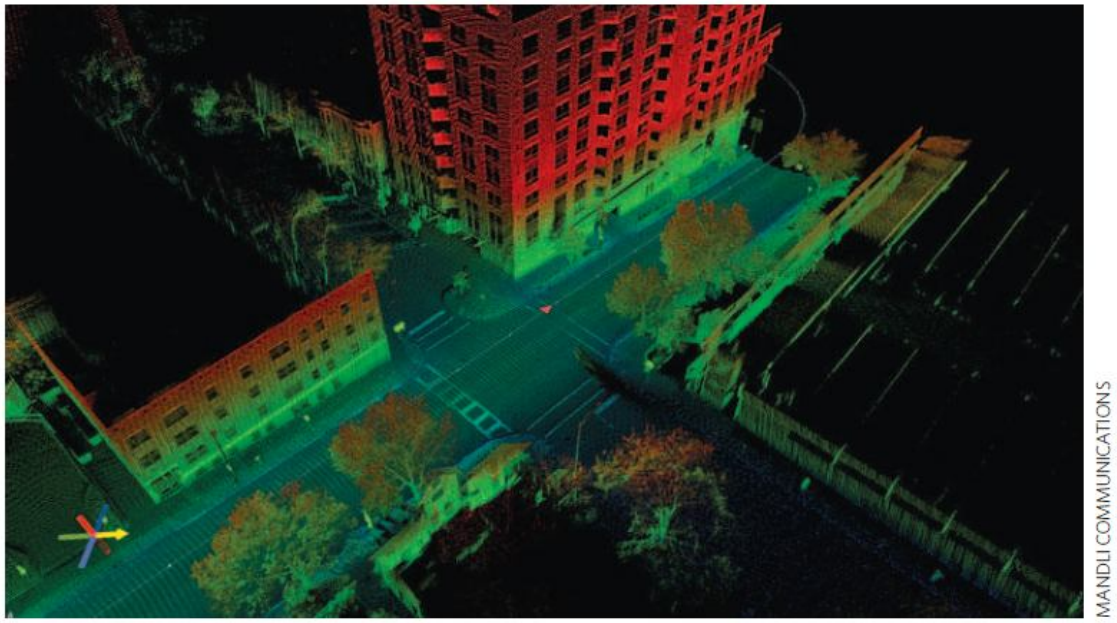

Figure 2-58 High resolution 3D point-cloud mapping of urban scenes including hard targets (e.g. buildings and street curbs) and distributed targets (e.g. trees and overhead wires). Colours represent the depth information. The image was acquired using a high definition LiDAR sensor from Velodyne Inc., USA. The wide-field-of-view LiDAR sensor integrated with 5-ns-pulse-duration 64 lasers operating at λ=905 nm has range accuracy of 1.5 cm at a working distance of ~100 m and is capable of generation of ~1.3 million data points per second. (From [2.147]).

An example of an airborne LiDAR-based depth imaging system configuration using a detector array is shown in Figure 2-59. As for LiDAR-based 3D imaging systems using detector arrays and flood illumination, Advanced Scientific Concepts (ASC), Inc., USA produces 3D imaging cameras using FPA detectors (e.g. linear-mode InGaAs APD arrays with 128×128 pixels), which can be called staring 3D imagers. Some field trial results (for example, the one shown in Figure 2-60) at hundred metre distances using this type of depth imager with 128×128 FPA devices were reported using pulsed laser sources at 1540 nm and 1570 nm wavelengths with a few ns pulse duration and 10s mJ pulse energy [2.152-2.153].

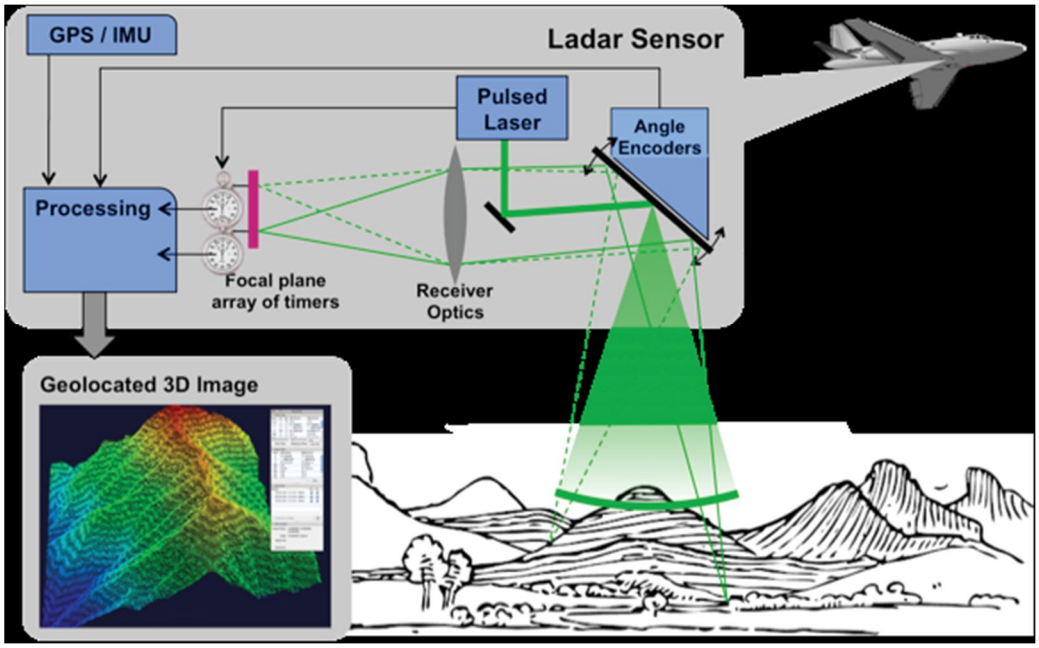

Figure 2-59 Block diagram of an airborne LiDAR depth imaging system using arrayed detectors (i.e. focal plane array in the diagram). Ladar: laser radar; GPS/IMU: global positioning system/inertial measurement unit. (From [2.154]).

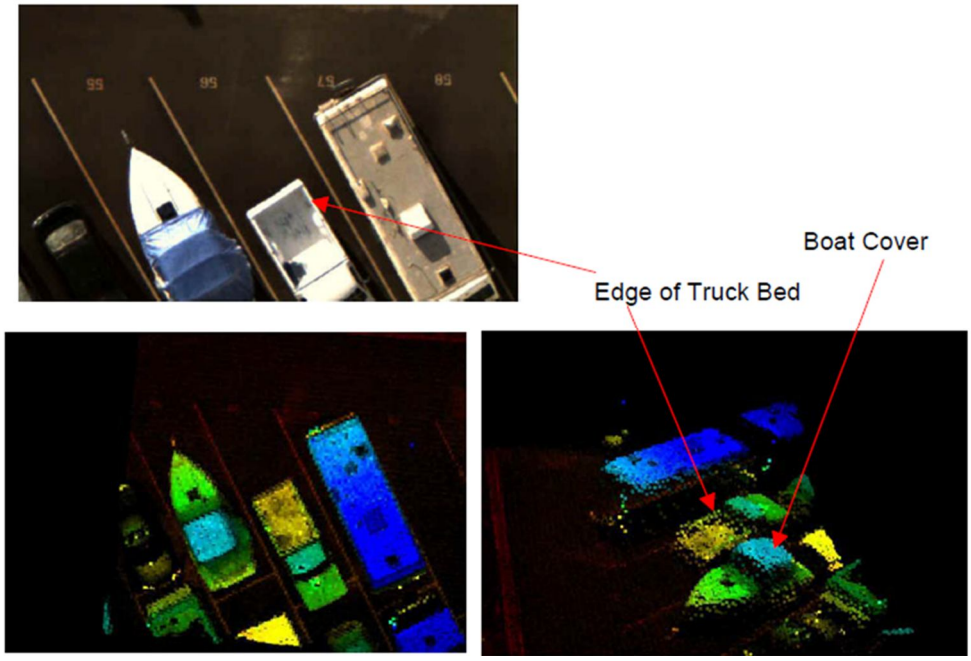

Figure 2-60 Top: A photograph of a parking lot at a stand-off distance of ~300 metres. Colours represent the depth information. Bottom: 3D images in two views of a parking lot at ~300 metres acquired by a 128×128 3D imaging camera (by Advanced Scientific Concepts, Inc., USA) which was put in an airplane platform. (From [2.153]).

In addition, another type of staring depth imager which uses burst illumination can be built based on a range-gated mechanism. This type of system requires prior knowledge

of the working distance in order to control the delayed gates appropriately. As shown in Figure 2-61 the system retrieves depth profiling of the target by integrating a series of gated-viewing intensity images, which were acquired by a CCD-based sensor with a precise gate control module. For example, French–German Research Institute of Saint-Louis (ISL) demonstrated a gated viewing active imaging system working up to a distance of 1500 m at λ=808 nm [2.155].

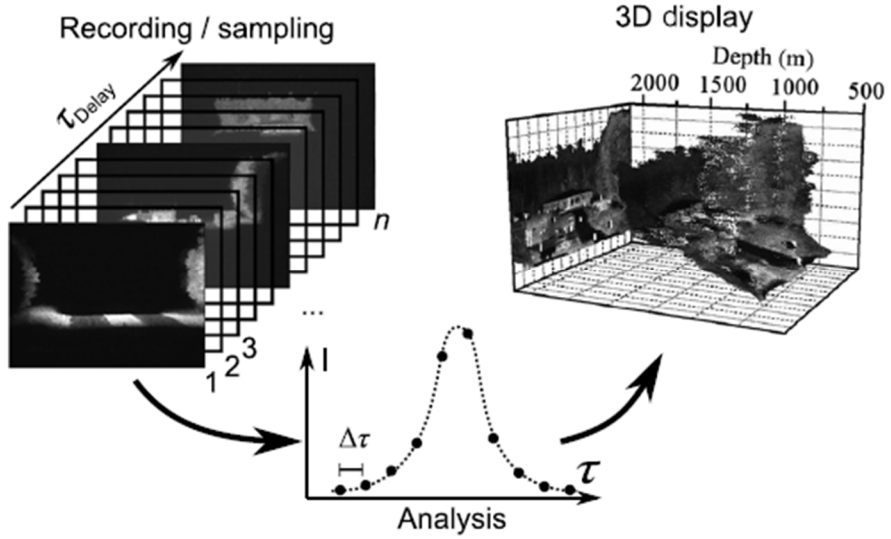

Figure 2-61 Depth imaging based on the range-gated mechanism. Left: Time-delayed slices of intensity images of target scene acquired by a CCD-based sensor with a precise gate control module. Middle: Post-processing of the time-related intensity information associated with the time-delayed slices; Right: The reconstructed depth profile of the target scene consists of a building and trees. The depth value presents the reflective intensity data. (From [2.156]).

This type of system is usually also called a burst-illumination LiDAR system. Due to its range-gating operation, this imaging technique is known to overcome strong backscattering from obscurants such as camouflage, fog or water. It can achieve time-delayed slices to represent the depth profiles of targets. For example, by configuring the CCD-based or other FPA-based devices, gated viewing depth imagers operating in kilometre-range free space at λ=1550 nm [2.157] or short-distance underwater at λ=532 nm [2.158] have been developed. In addition, Figure 2-62 shows 2D burst-illumination LiDAR image and a simultaneous range image of a vehicle and building at a stand-off distance of >10s metres. They were obtained by a burst-illumination LiDAR system based on a 320×256 HgCdTe APD array with 24 μm pitch. A laser source with 20 ns pulse duration.at a wavelength of 1550 nm was used to provide illuminating light [2.159]. Parameters of the mentioned state-of-the-art conventional LiDAR-based depth

imaging systems are summarised in Table 2-1.

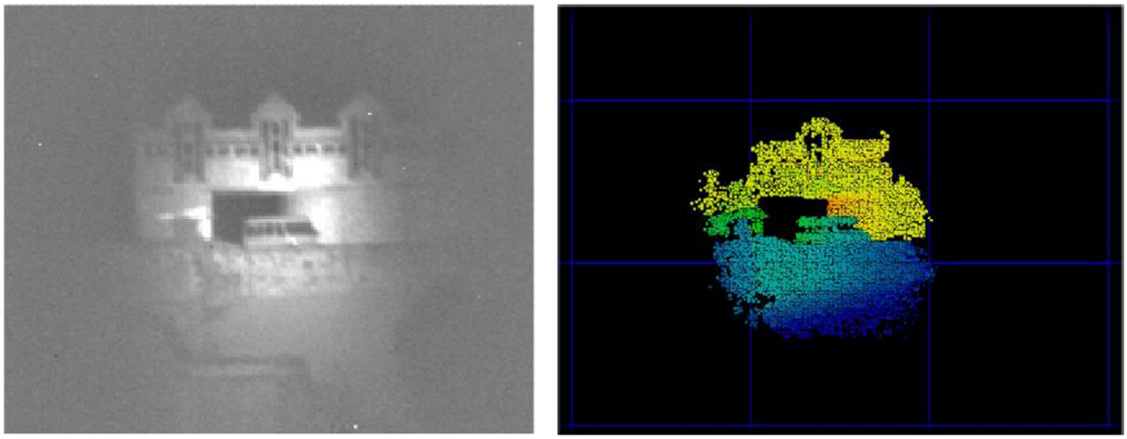

Figure 2-62 2D burst-illumination LiDAR image (left) and a simultaneous range image (right) of a vehicle and building at a stand-off distance of >10s metres obtained by a burst-illumination LiDAR system based on a 320×256 HgCdTe APD array with 24 μm pitch at a wavelength of 1550 nm. The range image is encoded in colour. Along the line-of-sight of the sensor, blue presents the nearest distance to the sensor whereas red corresponds to the furthest away range. (From [2.159])

	[2.151] by Velodyne	[2.153] by ASC	[2.155] by ISL	[2.159] by Selex
Mechanism	Scanning	FPA	FPA	FPA
Laser wavelength	λ=905 nm	λ ~ 1550 nm	λ=808 nm	λ=1550 nm
FWHM pulse width	5 ns	2 ns	>200 ns	20 ns
Output power/energy	Class one	Pulse energy of 45 mJ	Peak power of 1 kW	-
Detector		Linear-mode 128×128 InGaAs APD array	1392×1040 CCD + GEN II intensifier	320×256 HgCdTe APD array with 24 μm pitch*
Range	120 m	~300 m	~1500 m	>10s m
Depth accuracy	1.5 cm	15 cm	<30 m	<0.7 m
Comments	64 laser-detector pairs		Gated viewing	Gated viewing; *Based on the Selex SiGMA electronics module

Table 2-1 Comparison of performance to some state-of-the-art conventional LiDAR-based depth imaging systems.

However, as the working distance is extended to kilometre range or longer, the limited pulse energy of the laser sources significantly impairs the detection performance of LiDAR-based depth imaging systems. In particular, the FPA-based systems are affected due to considerable atmospheric attenuation and turbulent effect. (refer to [2.123,

2.135, 2.160] and Appendix A of [2.161]).

2.4.4 Single-photon time-of-flight depth imaging systems

The last two decades have seen a rise in interest in sensitive, fast optical detection performing at the quantum limit - the measurement of single or small numbers of photons. LiDAR systems using photon counting detection are emerging for high photon-efficient remote sensing. These systems have high sensitivity (i.e. shot-noise limited sensitivity). In addition, by virtue of high timing resolution devices (e.g. TCSPC modules), they can exact excellent surface-to-surface depth resolution at low light levels. This section will review several functional time-of-flight depth imaging LiDAR systems using single photon detection that have been tested by field trials and also several relevant proof-of-concept systems.

In 2002, NASA Goddard Space Flight Centre reported a PMT-based photon counting LiDAR system capable of airborne and space borne rapid topographic measurements with high power efficiency [2.162]. The system was tested at an altitude of 300 km with 5 m horizontal resolution and decimetre depth accuracy. A 2×2 element PMT device with GaAsP photocathodes, metal channel dynodes and segmented anodes (Hamamatsu Model R5900U) was employed in the imaging receiver. This commercial and space-qualified detector has a detection efficiency of ~40% and a typical dead time of ~10 ns at a wavelength of 532 nm. Although a TDC with a timing bin width of 50 ps (7.5 mm in depth) was used, the depth resolution was limited to about 5 cm root mean square (RMS) by the laser pulse-width and detector timing jitter [2.162]. To implement higher fidelity 3D imaging with higher speed, Sigma Space Corporation developed a system recently using a high energy efficiency diffractive optical element (DOE) which generates a 10×10 array of quasi-uniform intensity spots in the transmitter channel and also a 10×10 segmented anode microchannel plate photomultiplier (MCP/PMT) by Hamamatsu Photonics in the imaging receiver channel [2.163]. One example result of a large-scale biomass measurement obtained by this system [2.164] can be seen in Figure 2-63. According to the highlight image, depth profiles of the tree canopy, fire tower, and chain link fence were well-resolved by this system.

NASA has also developed a dual-wavelength photon counting airborne system called slope imaging multi-polarisation photon counting LiDAR (SIMPL) to measure spectral variation from ice sheets and forest canopies and has acquired data over the ice-covered Lake Erie in February 2009 to evaluate the performance and capabilities of SIMPL

[2.165]. Its transmitter was capable of two wavelength (532 nm and 1064 nm) outputs, which were split into four push-broom beams. In addition, its receiver employed single photon counting modules (i.e. Si-SPADs manufactured by Perkin Elmer Optoelectronics, now Excelitas Technologies Corp.) with ~65% and ~2% detection efficiency at 532 nm and 1064 nm, respectively. This system can be used for polarimetric ranging at dual wavelengths. Not only can it acquire sampling of topographic structures, e.g. surface elevation and slope with a system temporal response of ~1 ns (15 cm in depth), but also geomorphic features, e.g. surface roughness and depolarising scattering properties. The ice, cloud and land elevation satellite (ICESat-2) program [2.124] of NASA scheduled for launch in 2016 will employ several technologies advanced by SIMPL, in particular for the single photon ranging at 532 nm. Thus, it is a quite clear deployment route of photon counting space borne LiDAR systems due to their advantage of high power efficiency and moderate depth resolution at long range for geosciences application in NASA.

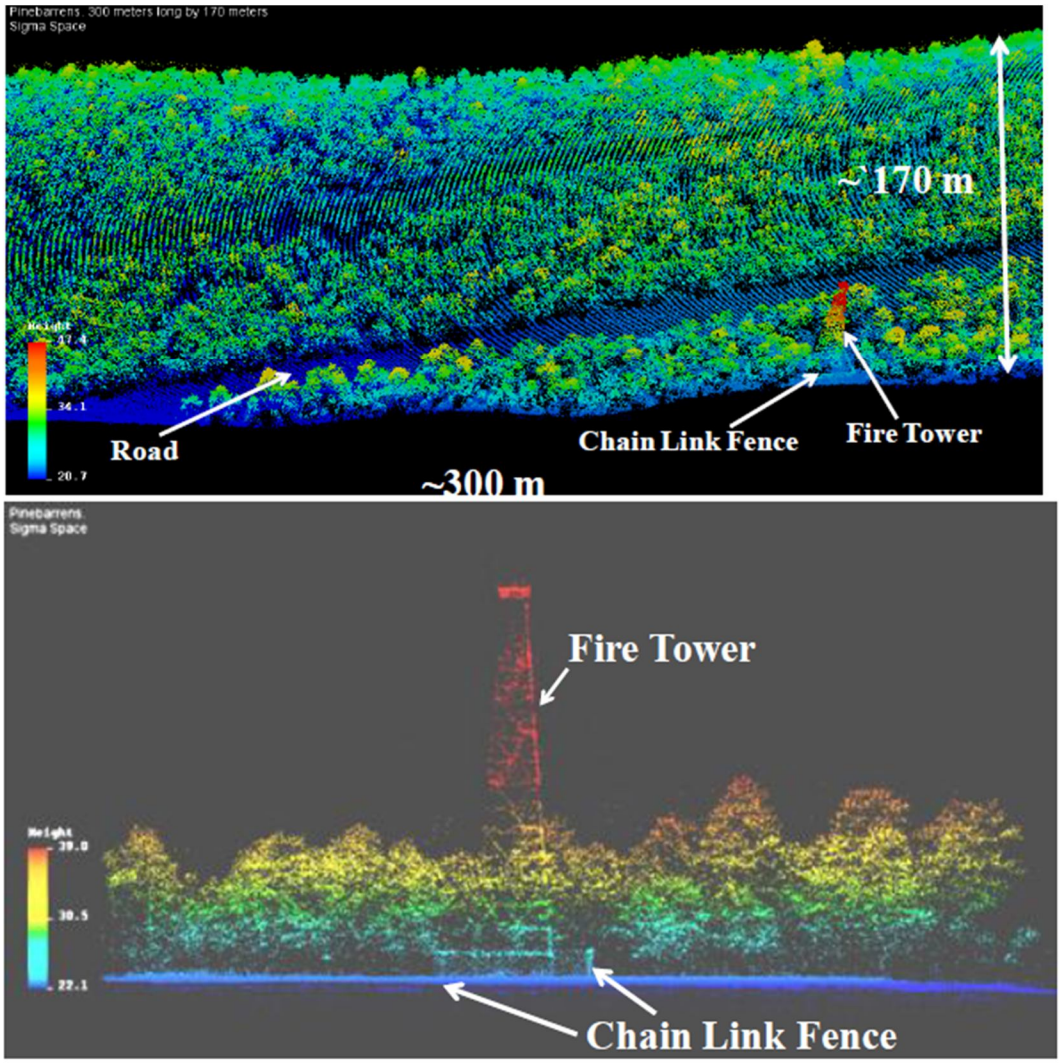

Figure 2-63 Top: High altitude view of the 3D imaging result covering the scene over New Jersey Pine Barrens with ~300m × ~170 m. Some hard targets such as a road and a fire tower near a chain link fence were highlighted. Bottom: The detailed point-cloud image in the side view shows the depth profiles of the tree canopy, fire tower, and chain link fence. Colours represent the depth information. (From [2.164]).

Massachusetts Institute of Technology Lincoln Laboratory (MIT-LL) did early work on Geiger-mode Si-APD arrays integrated with CMOS readout circuits to construct compact FPA detectors. In 2002, a 3D laser radar system by using a 4×4 Geiger-mode Si-APD array with an appropriate scanning scheme was developed by this lab. It was reported to achieve high-speed 128×128 pixel 3D imaging with few-centimetre range resolution at λ=532 nm [2.125, 2.166]. In 2005, they demonstrated another 3D photon counting imager with an upgraded 32×32 Geiger-mode Si-APD array with average detection efficiency of 20% at λ=532 nm along with a Risley scanner. Several field trial measurements using the imager in a helicopter flight-test platform were done at hundred-metre range and 40 cm range resolution was reported in [2.167].

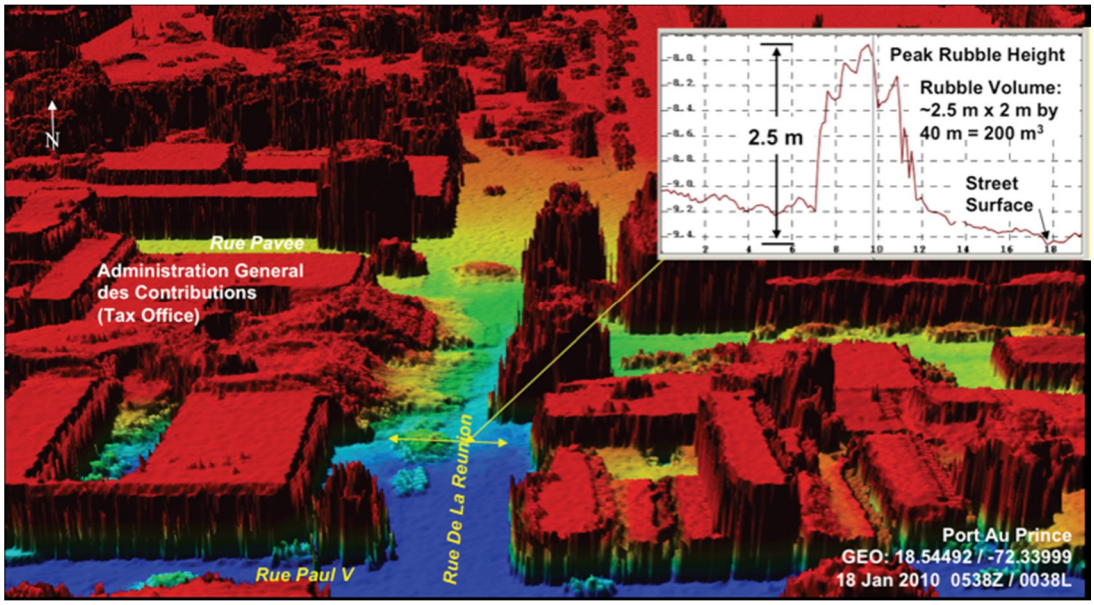

Figure 2-64 A 3D point-cloud image obtained by the airborne laser radar (Ladar) imaging research testbed (ALIRT) during one single flight over a city of Port Au Prince in Haiti after the earthquake in 2010. Colours represent the depth information. Inset: The depth profile across a specific location (i.e. the Rue de la Reunion) reveals the peak rubble height of 2 m above the street surface. This can provide information for assessing the trafficability of the road and bridge. In addition, the precise location (i.e. the geographic latitude and longitude information) and orientation can be provided in the image. This thanks to the global positioning system/inertial measurement unit (GPS/IMU) integrated in the testbed. (From [2.154]).

Recently, an airborne high-speed and wide-area laser radar (Ladar) imaging system (see Figure 2-59) - airborne laser radar (Ladar) imaging research testbed (ALIRT). It has been tested and can provide decimetre depth accuracy from altitudes of 3 km and also 3D high-resolution maps of terrain from altitudes up to 9 km which is almost four times that of other available imaging LiDAR systems. In addition, the ALIRT features high data-collection rates, which are about ten times larger than any other available imaging LiDAR systems. Due to its capability of precise object identification based on the 3D imagery, it was employed to obtain data for assessment of the street trafficability (see Figure 2-64) after the 2010 Haiti earthquake [2.154].

The operating wavelengths of laser-based LiDAR systems are strongly correlated with the feasibility and practicability of illumination sources and photon detectors. Compared to the visible wavelengths (e.g. 532 nm), the reduced solar background as well as atmosphere attenuation at longer wavelengths such as short-wave near infrared wavelengths – 850 nm and 1550 nm can be seen in Figure 2-47. In 2005, the research group at Heriot-Watt University, Edinburgh, demonstrated a multispectral TCSPC-based ranging system. This system had potential for geoscience applications using TCSPC and used six separate laser diodes that provided illumination at λ=630, 686, 780, 841, 911 and 975 nm [2.168-2.169]. Previously, the group worked in TCSPC-based ranging [2.7, 2.170-2.172] and depth imaging [2.122, 2.173-2.175]. In 2009, the research group demonstrated a time-of-flight scanning depth imaging system based on TCSPC technique using a 90 ps FWHM pulse-width laser diode at 842 nm [2.139]. A discrete thick-junction Si-SPAD was employed in the system. The depth profiles (e.g. one of the results can be seen in Figure 2-65) with ~20 mm depth uncertainty on a non-cooperative target were achieved at a stand-off distance of 325 m. By using a similar imager in 2010, multilayer depth profiling was demonstrated and reported [2.143]. In 2013, sub-centimetre depth resolution, kilometre-range time-of-flight scanning depth imagers with advanced discrete SNSPD and InGaAs/InP SPAD devices by using ~4 pJ per laser pulse at ~1550 nm wavelengths have been demonstrated and tested in daylight conditions by the research group. The details about the systems will be discussed in the later chapters.

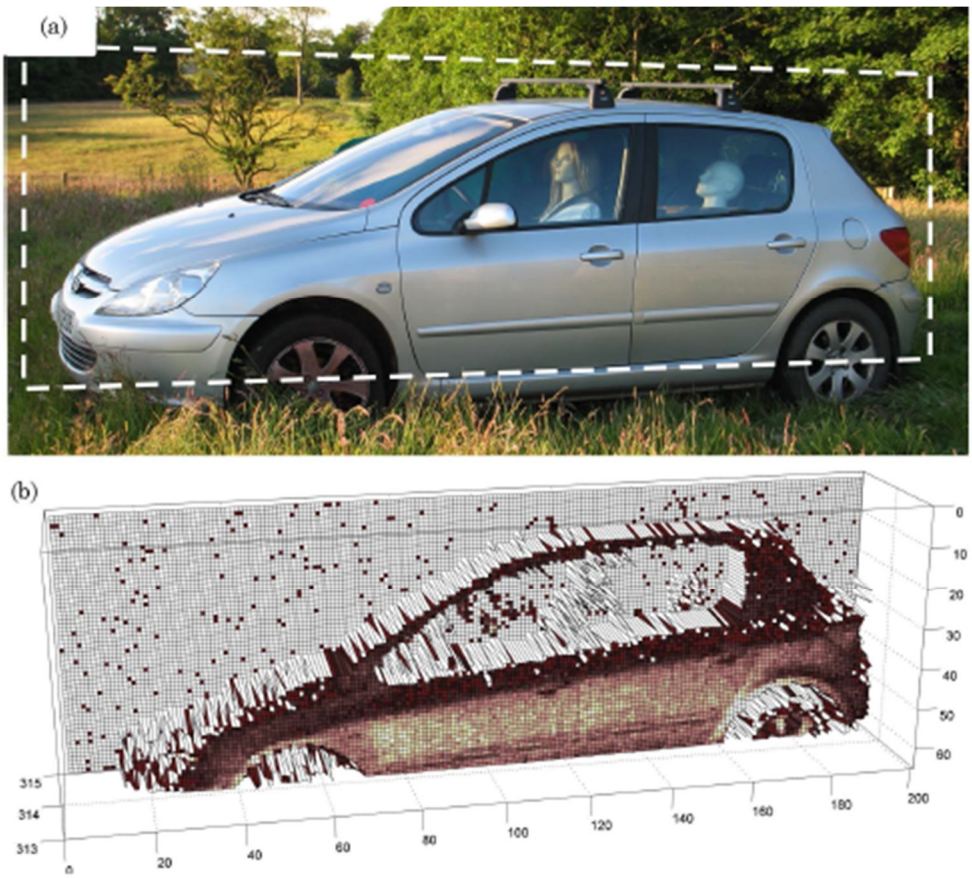

Figure 2-65 The close-up photograph of a car shown in (a). The car was scanned pixel-by-pixel by a single-photon time-of-flight depth imager based on TCSPC at λ=842 nm. (b) shows the reconstructed 200×60 pixel depth profile of the car obtained at a stand-off distance of 330 metres. (From [2.28]).

Recently Selex ES Edinburgh have extended time-of-flight single photon depth imagers by using a discrete InGaAs/InP SPAD and a 32×32 pixel InGaAs/InP SPAD camera (by Princeton Lightwave, Inc. USA) at λ=1550 nm to capture 3D profiles (e.g. some of their results can be seen in Figure 2-67 and Figure 2-66) of non-cooperative targets up to ~9 km. However, the order of a few μJ per laser pulse was sent out for sensing and the reported depth resolution was a few centimetres [2.176-2.178]. Parameters of some of single photon time-of-flight depth imaging systems tested by field trials are summarised in Table 2-2.

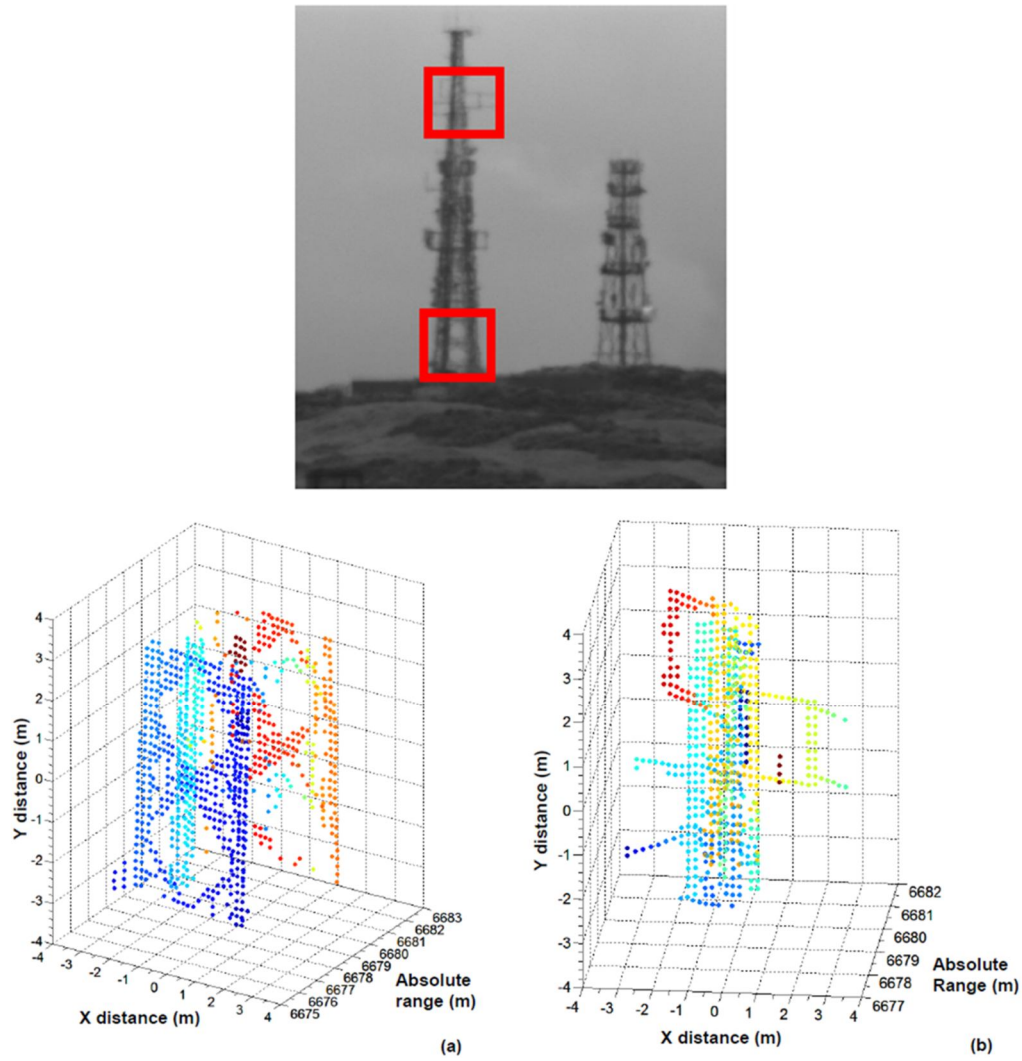

Figure 2-66 Depth profiling a hard target at a stand-off distance of ~7 km by the depth imager (by Selex ES, Edinburgh, UK) using a 32×32 pixel InGaAs SPAD array camera (by Princeton Lightwave, Inc. USA). Top: A photograph of the mast of a communication base station at a stand-off distance of ~7 km acquired by a CCD camera in the line-of-sight of the imager. Boxes in red indicate two field-of-regard regions corresponding to depth profiles (a) the base section and (b) the top section of the mast. (From [2.176]).

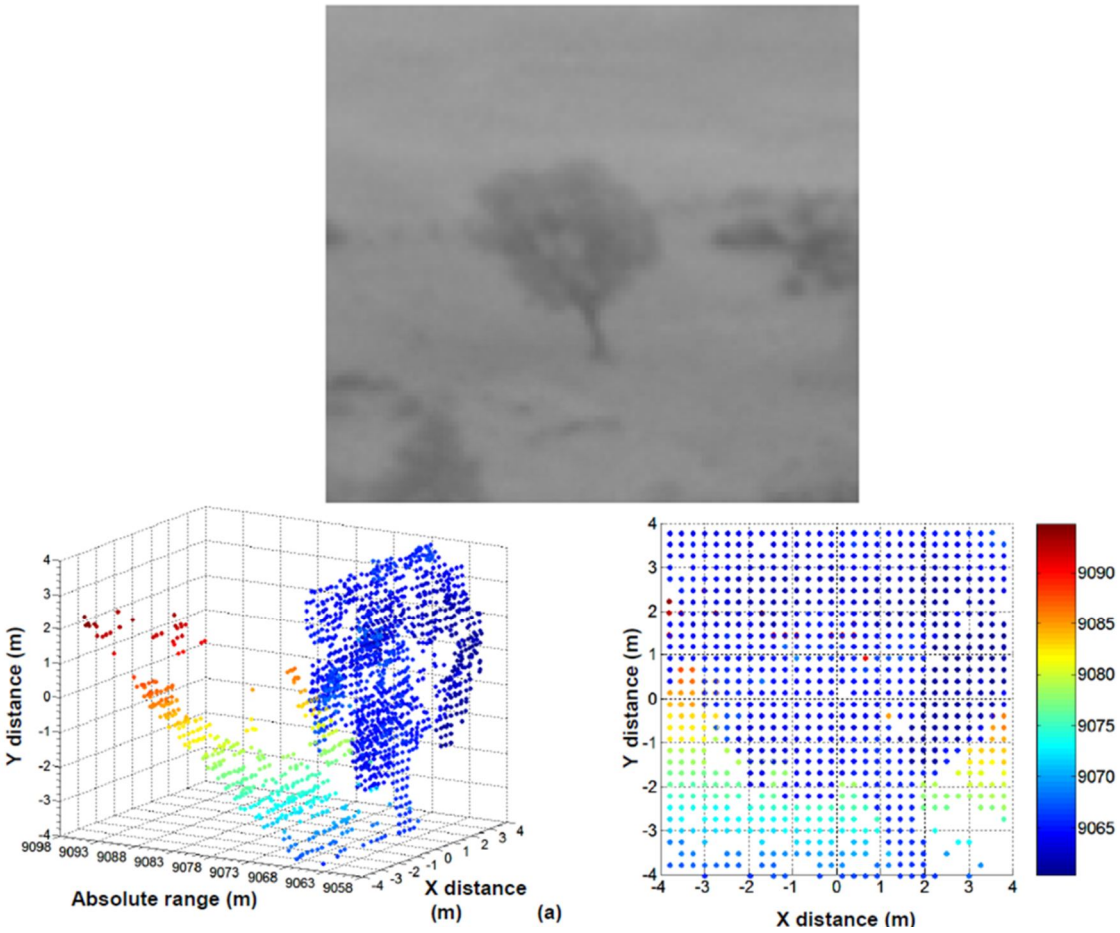

Figure 2-67 Depth profiling of a distributed target at a stand-off distance of ~9 km by the depth imager (by Selex ES, Edinburgh, UK) using a 32×32 pixel InGaAs SPAD array camera (by Princeton Lightwave, Inc. USA). Top: The photograph of a tree at a stand-off distance of ~9 km acquired by a CCD camera in the line-of-sight of the imager. Bottom: The resolved depth profiles of the tree in two views at ~9 km. (From [2.176]).

	[2.165] by NASA	[2.167] by MIT-LL	[2.177] by Selex ES
Mechanism	Scanning	FPA	FPA
Laser wavelength	λ=532 nm and 1064 nm	λ=532 nm	λ=1550 nm
Pulse rate	11 kHz	16 kHz	100 kHz
FWHM pulse width	1 ns	~300 ps	~800ps
Pulse energy	~8 mJ	~5 μJ	~4 μJ
Detector	16 discrete Si-SPADs, from PerkinElmer	32×32 Si-SPAD array	32×32 InGaAs/InP-SPAD array, from PLI
Range	13 km	150 m	9 km

Table 2-2 Comparison of performance to some single-photon time-of-flight depth imaging systems tested by field trials

In addition, several proof-of-principle photon counting LiDAR systems have been proposed recently. Discarding point-by-point scanning schemes, Howland *et al*. [2.179] proposed a time-of-flight photon counting depth imager (see Figure 2-68) using a discrete single photon detector based on compressed sensing (CS) technique. This is based on the principle that with fewer samplings upon a signal than required by the Shannon-Nyquist sampling theorem, the signal can still be estimated through optimisation by virtue of its sparsity [2.180]. Based on the CS theory frame, this technique aimed to effectively compress the signal of interest during measurements given the representation of the signal is sparse in a prior basis. The concept of the imager is to form a series of gated-viewing CS-reconstructed 2D intensity slices to a depth profile. More recently, using a similar depth imaging system to obtain data, they demonstrated an approach to exact the target depth profile by the CS-reconstructed depth-intensity-mixing map over the CS-reconstructed 2D intensity map [2.181]. Ease of reconfiguration of the single pixel detectors is an advantage in regards to great compatibility for uses in different spectral applications. However, depth resolutions were within the decimetre range for the bench-top imagers. Nevertheless, this gives rise to the fact that the field of photonics and optics cooperating with computational imaging communities may improve visual performance and may lead to a better understanding of the nature of the imagery. The photon-efficient single photon depth images reported by Kirmani *et al.* [2.29] and the depth images constructed using sparse photon data by Altmann *et al.* [2.146] are two such examples of recent developments.

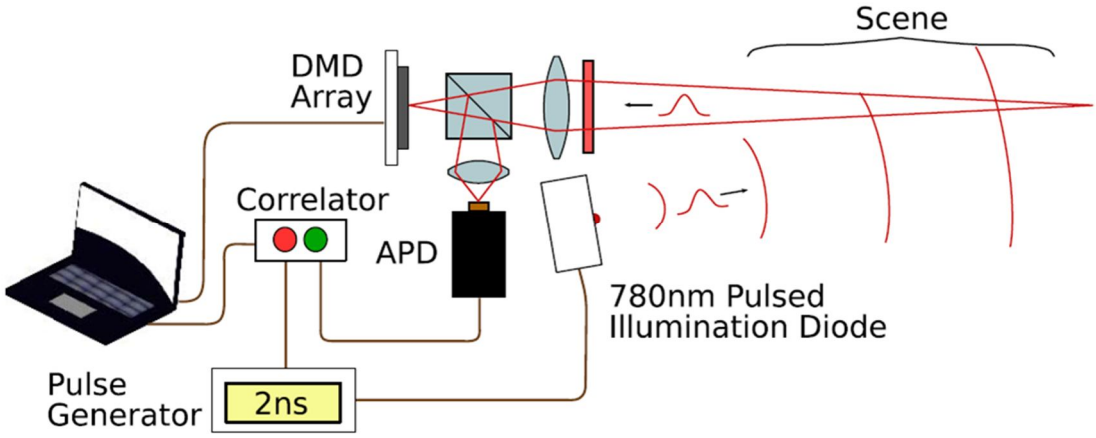

Figure 2-68 Experimental setup of a proof-of-concept single-photon time-of-flight depth imager based on compressed sensing. The correlator used here is a TCSPC module. DMD array: digital micro-mirror device array. (From [2.179]).

2.5 References

[2.1]. A. Migdall, S. V. Polyakov, J. Fan, and J. C. Bienfang. eds., *Single-Photon Generation and Detection: Physics and Applications* (Elsevier, 2013).

[2.2]. M. Wahl, "Modern TCSPC electronics: principles and acquisition modes," Springer Series on Fluorescence (2014).

[2.3]. T. Schönau, S. Riecke, A. Bülter, and K. Lauritsen, "Modern Pulsed Diode Laser Sources for Time-Correlated Photon Counting," Springer Series on Fluorescence (2014).

[2.4]. W. Becker, *Advanced Time-Correlated Single Photon Counting Techniques* (Springer, Berlin, 2005).

[2.5]. W. Becker, *The bh TCSPC Handbook, 2nd Edition* (Becker&Hickl GmbH 2006).

[2.6]. "PicoHarp 300 User's Manual and Technical Data," PicoQuant GmbH, Ver (2.3).

[2.7]. S. Pellegrini, G. S. Buller, J. M. Smith, A. M. Wallace, and S. Cova, "Laser-based distance measurement using picosecond resolution time-correlated single-photon counting," Meas. Sci. Technol. (11), 712-716 (2000).

[2.8]. M. Ghioni, A. Gulinatti, I. Rech, F. Zappa, and S. Cova, "Progress in silicon single-photon avalanche diodes," IEEE J. Select. Topics Quantum Electron. (13), 852-862 (2007).

[2.9]. D. Tamborini, D. Portaluppi, F. Villa, S. Tisa, and A. Tosi, "Multichannel low power time-to-digital converter card with 21 ps precision and full scale range up to 10 μs," Rev. Sci. Instrum. (85), 114703 (2014).

[2.10]. M. Wahl, T. Röhlicke, H.-J. Rahn, R. Erdmann, G. Kell, A. Ahlrichs, M. Kernbach, A. W. Schell, and O. Benson, "Integrated multichannel photon timing instrument with very short dead time and high throughput," Rev. Sci. Instrum. (84), 043102 (2013).

[2.11]. M. Wahl, H.-J. Rahn, I. Gregor, R. Erdmann, and J. Enderlein, "Dead-time optimized time-correlated photon counting instrument with synchronized, independent timing channels," Rev. Sci. Instrum. (78), 033106 (2007).

[2.12]. K. Ishii, T. Otosu, and T. Tahara, "Lifetime-Weighted FCS and 2D FLCS: Advanced Application of Time-Tagged TCSPC," Springer Series on Fluorescence

(2014).

[2.13]. R. C. Jones, "Phenomenological description of the response and detecting ability of radiation detectors," Proc. IRE (47), 1495-1502 (1959).

[2.14]. Hamamatsu Photonics K. K. , "Photomultiplier tubes: Basics and applications," Edition 3a (2007).

[2.15]. A. Bülter, "Single-photon counting detectors for the visible range between 300 and 1,000 nm," Springer Series on Fluorescence (2014).

[2.16]. R. H. Hadfield, "Single-photon detectors for optical quantum information applications," Nat. Photonics (3), 696-705 (2009).

[2.17]. Hamamatsu, "Metal Package PMT with Cooler-Photosensor Modules H7422 Series, Datasheet. online (https://www.hamamatsu.com/resources/pdf/etd/m-h7422e.pdf) last accessed 09-01-2015."

[2.18]. Hamamatsu, "NIR-Photomultiplier Tubes and Their Applications, Datasheet. online (http://www.hamamatsu.com/resources/pdf/etd/NIR-PMT_APPLI_TPMO1040E.pdf) last accessed 09-01-2015."

[2.19]. M. D. Eisaman, J. Fan, A. Migdall, and S. V. Polyakov, "Invited Review Article: Single-photon sources and detectors," Rev. Sci. Instrum. (82), 071101 (2011).

[2.20]. A. Tosi, A. D. Mora, F. Zappa, and S. Cova, "Single-photon avalanche diodes for the near-infrared range: detector and circuit issues," J. Mod. Opt. (56), 299-308 (2009).

[2.21]. A. Gallivanoni, I. Rech, and M. Ghioni, "Progress in quenching circuits for single photon avalanche diodes," IEEE Trans. Nucl. Sci. (57), 3815-3826 (2010).

[2.22]. S. Cova, M. Ghioni, A. Lacaita, C. Samori, and F. Zappa, "Avalanche photodiodes and quenching circuits for single-photon detection," Appl. Opt. (35), 1956-1976 (1996).

[2.23]. S. Dimler, J. Ng, R. Tozer, G. Rees, and J. David, "Capacitive quenching measurement circuit for Geiger-mode avalanche photodiodes," IEEE J. Select. Topics Quantum Electron. (13), 919-925 (2007).

[2.24]. H. Yang, G. Luo, P. Karnchanaphanurach, T.-M. Louie, I. Rech, S. Cova, L. Xun, and X. S. Xie, "Protein conformational dynamics probed by single-molecule electron transfer," Science (302), 262-266 (2003).

[2.25]. S. Billotta, M. Belluso, G. Bonanno, S. d. Mauro, M. C. Timpanaro, G.

Condorelli, P. G. Fallica, M. Mazzillo, D. Sanfilippo, and G. Valvo, "Characterization of detectors for the Italian Astronomical Quantum Photometer Project," J. Mod. Opt. (56), 273-283 (2009).

[2.26]. P. J. Clarke, R. J. Collins, V. Dunjko, E. Andersson, J. Jeffers, and G. S. Buller, "Experimental demonstration of quantum digital signatures using phase-encoded coherent states of light," Nat. Commun. (3), 1174 (2012).

[2.27]. J. Blokland, V. Claessen, F. Wijnen, E. Groeneveld, C. de Mello Donegá, D. Vanmaekelbergh, A. Meijerink, J. Maan, and P. Christianen, "Exciton lifetimes of CdTe nanocrystal quantum dots in high magnetic fields," Phys. Rev. B (83), 035304 (2011).

[2.28]. A. McCarthy, R. J. Collins, N. J. Krichel, V. Fernández, A. M. Wallace, and G. S. Buller, "Long-range time-of-flight scanning sensor based on high-speed time-correlated single-photon counting," Appl. Opt. (48), 6241-6251 (2009).

[2.29]. A. Kirmani, D. Venkatraman, D. Shin, A. Colaço, F. N. Wong, J. H. Shapiro, and V. K. Goyal, "First-Photon Imaging," Science (343), 58-61 (2014).

[2.30]. G. S. Buller, and A. M. Wallace, "Ranging and three-dimensional imaging using time-correlated single-photon counting and point-by-point acquisition," IEEE J. Select. Topics Quantum Electron. (13), 1006-1015 (2007).

[2.31]. A. Lacaita, M. Ghioni, and S. Cova, "Double epitaxy improves single-photon avalanche diode performance," Electron. Lett. (25), 841-843 (1989).

[2.32]. M. Ghioni, S. Cova, A. Lacaita, and G. Ripamonti, "New silicon epitaxial avalanche diode for single-photon timing at room temperature," Electron. Lett. (24), 1476-1477 (1988).

[2.33]. W. Kindt, and H. Van Zeijl, "Modelling and fabrication of Geiger mode avalanche photodiodes," IEEE Trans. Nucl. Sci. (45), 715-719 (1998).

[2.34]. E. Sciacca, A. C. Giudice, D. Sanfilippo, F. Zappa, S. Lombardo, R. Consentino, C. Di Franco, M. Ghioni, G. Fallica, and G. Bonanno, "Silicon planar technology for single-photon optical detectors," IEEE Trans. Electron Devices (50), 918-925 (2003).

[2.35]. H. Dautet, P. Deschamps, B. Dion, A. D. MacGregor, D. MacSween, R. J. McIntyre, C. Trottier, and P. P. Webb, "Photon counting techniques with silicon avalanche photodiodes," Appl. Opt. (32), 3894-3900 (1993).

[2.36]. R. J. McIntyre, "Silicon avalanche photodiode with low multiplication noise," (U.S. Patent 4972242 A, Nov 20, 1990).

[2.37]. R. J. McIntyre, and P. P. Webb, "Low-noise, reach-through, avalanche photodiodes," (U.S. Patent 5583352 A, Dec 10, 1996).

[2.38]. Laser Components Inc USA, " SAP500-Series. Datasheet. online (http://www.lasercomponents.com/fileadmin/user_upload/home/Datasheets/lcd/sap-series.pdf) last accessed 20-02-2015."

[2.39]. M. Stipčević, H. Skenderović, and D. Gracin, "Characterization of a novel avalanche photodiode for single photon detection in VIS-NIR range," Opt. Express (18), 17448-17459 (2010).

[2.40]. Micro Photon Devices Italy, "MPD PDM series. Datasheet. online (http://www.micro-photon-devices.com/Docs/Datasheet/PDM.pdf) last accessed 20-02-2015."

[2.41]. A. Gulinatti, I. Rech, F. Panzeri, C. Cammi, P. Maccagnani, M. Ghioni, and S. Cova, "New silicon SPAD technology for enhanced red-sensitivity, high-resolution timing and system integration," J. Mod. Opt. (59), 1489-1499 (2012).

[2.42]. G. S. Buller, and R. J. Collins, "Single-photon generation and detection," Meas. Sci. Technol. (21) (2010).

[2.43]. C. Niclass, A. Rochas, P.-A. Besse, and E. Charbon, "Design and characterization of a CMOS 3-D image sensor based on single photon avalanche diodes," IEEE J. Solid-State Circuits (40), 1847-1854 (2005).

[2.44]. C. Niclass, M. Sergio, and E. Charbon, "A single photon avalanche diode array fabricated in deep-submicron CMOS technology," *Design, Automation and Test in Europe, 2006. DATE'06. Proceedings*, IEEE, pp. 1-6, (2006).

[2.45]. C. Niclass, C. Favi, T. Kluter, M. Gersbach, and E. Charbon, "A 128 128 single-photon image sensor with column-level 10-bit time-to-digital converter array," IEEE J. Solid-State Circuits (43), 2977-2989 (2008).

[2.46]. M. Sergio, C. Niclass, and E. Charbon, "A 128× 2 CMOS Single-Photon Streak Camera with Timing-Preserving Latchless Pipeline Readout," *Solid-State Circuits Conference, 2007. ISSCC 2007. Digest of Technical Papers. IEEE International*, IEEE, pp. 394-610, (2007).

[2.47]. C. Niclass, C. Favi, T. Kluter, F. Monnier, and E. Charbon, "Single-photon synchronous detection," IEEE J. Solid-State Circuits (44), 1977-1989 (2009).

[2.48]. F. Guerrieri, S. Tisa, A. Tosi, and F. Zappa, "Two-dimensional SPAD imaging

camera for photon counting," IEEE Photonics J. (2), 759-774 (2010).

[2.49]. B. Markovic, S. Tisa, A. Tosi, and F. Zappa, "Monolithic single-photon detectors and time-to-digital converters for picoseconds time-of-flight ranging," *IS&T/SPIE Electronic Imaging*, International Society for Optics and Photonics, pp. 78750P-78750P-78756, (2011).

[2.50]. M. Gersbach, Y. Maruyama, E. Labonne, J. Richardson, R. Walker, L. Grant, R. Henderson, F. Borghetti, D. Stoppa, and E. Charbon, "A parallel 32× 32 time-to-digital converter array fabricated in a 130 nm imaging CMOS technology," *ESSCIRC, 2009. ESSCIRC'09. Proceedings of*, IEEE, pp. 196-199, (2009).

[2.51]. J. Richardson, R. Walker, L. Grant, D. Stoppa, F. Borghetti, E. Charbon, M. Gersbach, and R. K. Henderson, "A 32× 32 50ps resolution 10 bit time to digital converter array in 130nm CMOS for time correlated imaging," *Custom Integrated Circuits Conference, 2009. CICC'09. IEEE*, IEEE, pp. 77-80, (2009).

[2.52]. F. Villa, R. Lussana, D. Bronzi, S. Tisa, A. Tosi, F. Zappa, A. Dalla Mora, D. Contini, D. Durini, and S. Weyers, "CMOS imager with 1024 SPADs and TDCs for single-photon timing and 3D time-of-flight," IEEE J. Select. Topics Quantum Electron. (2014).

[2.53]. M. Gersbach, Y. Maruyama, R. Trimananda, M. W. Fishburn, D. Stoppa, J. A. Richardson, R. Walker, R. Henderson, and E. Charbon, "A time-resolved, low-noise single-photon image sensor fabricated in deep-submicron CMOS technology," IEEE J. Solid-State Circuits (47), 1394-1407 (2012).

[2.54]. J. A. Richardson, L. A. Grant, and R. K. Henderson, "Low dark count single-photon avalanche diode structure compatible with standard nanometer scale CMOS technology," IEEE Photonics Technol. Lett. (21), 1020-1022 (2009).

[2.55]. S. Tisa, F. Guerrieri, and F. Zappa, "Variable-load quenching circuit for single-photon avalanche diodes," Opt. Express (16), 2232-2244 (2008).

[2.56]. A. Restelli, I. Rech, P. Maccagnani, M. Ghioni, and S. Cova, "Monolithic silicon matrix detector with 50 μm photon counting pixels," J. Mod. Opt. (54), 213-223 (2007).

[2.57]. S. Marangoni, I. Rech, M. Ghioni, P. Maccagnani, M. Chiari, M. Cretich, F. Damin, G. Di Carlo, and S. Cova, "A 6× 8 photon-counting array detector system for fast and sensitive analysis of protein microarrays," Sensors and Actuators B: Chemical (149), 420-426 (2010).

[2.58]. X. Michalet, R. Colyer, G. Scalia, A. Ingargiola, R. Lin, J. Millaud, S. Weiss, O. H. Siegmund, A. S. Tremsin, and J. V. Vallerga, "Development of new photon-counting detectors for single-molecule fluorescence microscopy," Philos. Trans. R. Soc. London, Ser. B (368), 20120035 (2013).

[2.59]. F. Villa, B. Markovic, S. Bellisai, D. Bronzi, A. Tosi, F. Zappa, S. Tisa, D. Durini, S. Weyers, and U. Paschen, "SPAD smart pixel for time-of-flight and time-correlated single-photon counting measurements," IEEE Photonics J. (4), 795-804 (2012).

[2.60]. B. Levine, and C. Bethea, "Single photon detection at 1.3 μm using a gated avalanche photodiode," Appl. Phys. Lett. (44), 553-555 (1984).

[2.61]. R. E. Warburton, G. Intermite, M. Myronov, P. Allred, D. R. Leadley, K. Gallacher, D. J. Paul, N. J. Pilgrim, L. J. Lever, Z. Ikonic, R. W. Kelsall, E. Huante-Cerón, A. P. Knights, and G. S. Buller, "Ge-on-Si Single-Photon Avalanche Diode Detectors: Design, Modeling, Fabrication, and Characterization at Wavelengths 1310 and 1550 nm," IEEE Trans. Electron Devices (60), 3807-3813 (2013).

[2.62]. B. Levine, C. Bethea, and J. Campbell, "Near room temperature 1.3 μm single photon counting with a InGaAs avalanche photodiode," Electron. Lett. (20), 596-598 (1984).

[2.63]. K. Nishida, K. Taguchi, and Y. Matsumoto, "InGaAsP heterostructure avalanche photodiodes with high avalanche gain," Appl. Phys. Lett. (35), 251-253 (1979).

[2.64]. J. Campbell, A. Dentai, W. Holden, and B. Kasper, "High-performance avalanche photodiode with separate absorption ‘Grading’and multiplication regions," Electron. Lett. (19), 818-820 (1983).

[2.65]. F. Acerbi, M. Anti, A. Tosi, and F. Zappa, "Design Criteria for InGaAs/InP Single-Photon Avalanche Diode," IEEE Photonics J. (5), 6800209-6800209 (2013).

[2.66]. W. G. Oldham, R. R. Samuelson, and P. Antognetti, "Triggering phenomena in avalanche diodes," IEEE Trans. Electron Devices (19), 1056-1060 (1972).

[2.67]. M. A. Itzler, R. Ben-Michael, C.-F. Hsu, K. Slomkowski, A. Tosi, S. Cova, F. Zappa, and R. Ispasoiu, "Single photon avalanche diodes (SPADs) for 1.5 μ m photon counting applications," J. Mod. Opt. (54), 283-304 (2007).

[2.68]. A. Tosi, F. Acerbi, M. Anti, and F. Zappa, "InGaAs/InP Single-Photon Avalanche Diode With Reduced Afterpulsing and Sharp Timing Response With 30 ps Tail," IEEE

J. Quantum Electron. (48), 1227-1232 (2012).

[2.69]. Micro Photon Devices Italy, "InGaAs Single-Photon Counter.Datasheet. online (http://www.micro-photon-devices.com/Docs/Datasheet/InGaAs_Datasheet.pdf) last accessed 19-02-2015."

[2.70]. D. S. Bethune, and W. P. Risk, "An autocompensating fiber-optic quantum cryptography system based on polarization splitting of light," Quantum Electronics, IEEE Journal of (36), 340-347 (2000).

[2.71]. Z. Lu, W. Sun, J. C. Campbell, X. Jiang, and M. A. Itzler, "Corrections to "Common-Mode Cancellation in Sinusoidal Gating With Balanced InGaAs/InP Single Photon Avalanche Diodes"[Dec 12 1505-1511]," Quantum Electronics, IEEE Journal of (49), 59-59 (2013).

[2.72]. J. C. Campbell, W. Sun, Z. Lu, M. A. Itzler, and X. Jiang, "Common-mode cancellation in sinusoidal gating with balanced InGaAs/InP single photon avalanche diodes," Quantum Electronics, IEEE Journal of (48), 1505-1511 (2012).

[2.73]. G. Wu, C. Zhou, X. Chen, and H. Zeng, "High performance of gated-mode single-photon detector at 1.55 μm," Opt. Commun. (265), 126-131 (2006).

[2.74]. A. Dalla Mora, A. Tosi, F. Zappa, S. Cova, D. Contini, A. Pifferi, L. Spinelli, A. Torricelli, and R. Cubeddu, "Fast-gated single-photon avalanche diode for wide dynamic range near infrared spectroscopy," IEEE J. Select. Topics Quantum Electron. (16), 1023-1030 (2010).

[2.75]. A. Tosi, A. Della Frera, A. B. Shehata, and C. Scarcella, "Fully programmable single-photon detection module for InGaAs/InP single-photon avalanche diodes with clean and sub-nanosecond gating transitions," Rev. Sci. Instrum. (83) (2012).

[2.76]. M. A. Itzler, M. Entwistle, M. Owens, K. Patel, X. Jiang, K. Slomkowski, S. Rangwala, P. F. Zalud, T. Senko, and J. Tower, "Geiger-mode avalanche photodiode focal plane arrays for three-dimensional imaging LADAR," *SPIE Optical Engineering+ Applications*, International Society for Optics and Photonics, pp. 78080C-78080C-78014, (2010).

[2.77]. Princeton Lightwave Inc, "CAM32X32A-GMA-0 and CAM32X32B-GMA-0. 32 x 32 Geiger-mode Avalanche Photodiode (GmAPD) Cameras. PRODUCT SUMMARY. online (http://www.princetonlightwave.com/images/pli_content/PLI%2032x32%20GmAPD%2

0Camera%20-%20ProdSum%20Rev%202.2.0.pdf), last accessed 25-04-2015."

[2.78]. Princeton Lightwave Inc, "CAM128X32A-GMA-0. 128 x 32 Geiger-mode Avalanche Photodiode (GmAPD) Camera. PRODUCT SPECIFICATION. online (http://www.princetonlightwave.com/images/pli_content/PLI%20128x32%20GmAPD%20Camera%20-%20ProdSum%20Rev%202.0.pdf), last accessed 25-04-2015."

[2.79]. M. A. Itzler, M. Entwistle, U. Krishnamachari, M. Owens, X. Jiang, K. Slomkowski, and S. Rangwala, "SWIR Geiger-mode APD detectors and cameras for 3D imaging," *SPIE Sensing Technology+ Applications*, International Society for Optics and Photonics, pp. 91140F-91140F-91112, (2014).

[2.80]. M. A. Itzler, M. Entwistle, X. Jiang, M. Owens, K. Slomkowski, and S. Rangwala, "Geiger-mode APD single-photon cameras for 3D laser radar imaging," *Aerospace Conference, 2014 IEEE*, IEEE, pp. 1-12, (2014).

[2.81]. X. Jiang, M. A. Itzler, K. O'Donnell, M. Entwistle, M. Owens, K. Slomkowski, and S. Rangwala, "InP-based Single Photon Detectors and Geiger mode APD Arrays for Quantum Communications Applications," IEEE J. Select. Topics Quantum Electron. (2015).

[2.82]. G. Gol'Tsman, A. Semenov, Y. P. Gousev, M. Zorin, I. Godidze, E. Gershenzon, P. Lang, W. Knott, and K. Renk, "Sensitive picosecond NbN detector for radiation from millimetre wavelengths to visible light," Supercon. Sci. Technol. (4), 453 (1991).

[2.83]. E. A. Dauler, M. E. Grein, A. J. Kerman, F. Marsili, S. Miki, S. W. Nam, M. D. Shaw, H. Terai, V. B. Verma, and T. Yamashita, "Review of superconducting nanowire single-photon detector system design options and demonstrated performance," Opt. Eng (53), 081907 (2014).

[2.84]. A. J. Kerman, E. A. Dauler, B. S. Robinson, R. Barron, D. O. Caplan, M. L. Stevens, J. J. Carney, S. A. Hamilton, W. E. Keicher, and J. K. Yang, "Superconducting nanowire photon-counting detectors for optical communications," Lincoln Laboratory Journal (16), 217 (2006).

[2.85]. J. Wilson, and J. F. Hawkes, *Optoelectronics-an introduction* (1989).

[2.86]. M. Tinkham, *Introduction to superconductivity* (McGraw-Hill College, 1996).

[2.87]. A. J. Kerman, E. A. Dauler, W. E. Keicher, J. K. Yang, K. K. Berggren, G. Gol'Tsman, and B. Voronov, "Kinetic-inductance-limited reset time of superconducting nanowire photon counters," Appl. Phys. Lett. (88), 111116 (2006).

[2.88]. S. Miki, H. Terai, T. Yamashita, K. Makise, M. Fujiwara, M. Sasaki, and Z. Wang, "Superconducting single photon detectors integrated with single flux quantum readout circuits in a cryocooler," Appl. Phys. Lett. (99), 111108 (2011).

[2.89]. C. Natarajan, M. Tanner, and R. Hadfield, "Superconducting nanowire single-photon detectors: physics and applications," Supercon. Sci. Technol. (25) (2012).

[2.90]. T. Yamashita, S. Miki, K. Makise, W. Qiu, H. Terai, M. Fujiwara, M. Sasaki, and Z. Wang, "Origin of intrinsic dark count in superconducting nanowire single-photon detectors," Appl. Phys. Lett. (99), 161105 (2011).

[2.91]. K. Xu, and J. R. Heath, "Long, highly-ordered high-temperature superconductor nanowire arrays," Nano Lett. (8), 3845-3849 (2008).

[2.92]. R. Arpaia, M. Ejrnaes, L. Parlato, F. Tafuri, R. Cristiano, D. Golubev, R. Sobolewski, T. Bauch, F. Lombardi, and G. Pepe, "High-temperature superconducting nanowires for photon detection," Physica C (509), 16-21 (2015).

[2.93]. A. Verevkin, J. Zhang, R. Sobolewski, A. Lipatov, O. Okunev, G. Chulkova, A. Korneev, K. Smirnov, G. Gol'tsman, and A. Semenov, "Detection efficiency of large-active-area NbN single-photon superconducting detectors in the ultraviolet to near-infrared range," Appl. Phys. Lett. (80), 4687-4689 (2002).

[2.94]. S. Miki, M. Fujiwara, M. Sasaki, B. Baek, A. J. Miller, R. H. Hadfield, S. W. Nam, and Z. Wang, "Large sensitive-area NbN nanowire superconducting single-photon detectors fabricated on single-crystal MgO substrates," Appl. Phys. Lett. (92), 061116-061116-061113 (2008).

[2.95]. M. G. Tanner, C. Natarajan, V. Pottapenjara, J. O'Connor, R. Warburton, R. Hadfield, B. Baek, S. Nam, S. Dorenbos, and E. B. Ureña, "Enhanced telecom wavelength single-photon detection with NbTiN superconducting nanowires on oxidized silicon," Appl. Phys. Lett. (96), 221109 (2010).

[2.96]. J. K. Yang, E. Dauler, A. Ferri, A. Pearlman, A. Verevkin, G. Gol'tsman, B. Voronov, R. Sobolewski, W. E. Keicher, and K. K. Berggren, "Fabrication development for nanowire GHz-counting-rate single-photon detectors," IEEE Trans. Appl. Supercond. (15), 626-630 (2005).

[2.97]. K. M. Rosfjord, J. K. Yang, E. A. Dauler, A. J. Kerman, V. Anant, B. M. Voronov, G. N. Gol'Tsman, and K. K. Berggren, "Nanowire single-photon detector with an integrated optical cavity and anti-reflection coating," Opt. Express (14), 527-534

(2006).

[2.98]. F. Marsili, F. Najafi, E. Dauler, F. Bellei, X. Hu, M. Csete, R. J. Molnar, and K. K. Berggren, "Single-photon detectors based on ultranarrow superconducting nanowires," Nano Lett. (11), 2048-2053 (2011).

[2.99]. B. Baek, A. E. Lita, V. Verma, and S. W. Nam, "Superconducting a-WxSi1− x nanowire single-photon detector with saturated internal quantum efficiency from visible to 1850 nm," Appl. Phys. Lett. (98), 251105 (2011).

[2.100]. F. Marsili, V. Verma, J. Stern, S. Harrington, A. Lita, T. Gerrits, I. Vayshenker, B. Baek, M. Shaw, and R. Mirin, "Detecting single infrared photons with 93% system efficiency," Nat. Photonics (7), 210-214 (2013).

[2.101]. ID Quantique SA, "ID280 SUPERCONDUCTING NANOWIRE SINGLE-PHOTON DETECTOR. Datasheet. online (http://www.idquantique.com/wordpress/wp-content/uploads/ID280-Datasheet.pdf) last accessed 13-01-2015."

[2.102]. M. G. Tanner, C. M. Natarajan, V. K. Pottapenjara, J. A. O'Connor, R. J. Warburton, R. H. Hadfield, B. Baek, S. Nam, S. N. Dorenbos, E. Urena, T. Zijlstra, T. Klapwijk, and V. Zwiller, "Enhanced telecom wavelength single-photon detection with NbTiN superconducting nanowires on oxidized silicon," Appl. Phys. Lett. (96) (2010).

[2.103]. X. Hu, E. A. Dauler, R. J. Molnar, and K. K. Berggren, "Superconducting nanowire single-photon detectors integrated with optical nano-antennae," Opt. Express (19), 17-31 (2011).

[2.104]. R. M. Heath, M. G. Tanner, T. D. Drysdale, S. Miki, V. Giannini, S. A. Maier, and R. H. Hadfield, "Nanoantenna Enhancement for Telecom-Wavelength Superconducting Single Photon Detectors," Nano Lett. (2015).

[2.105]. J. Sprengers, A. Gaggero, D. Sahin, S. Jahanmirinejad, G. Frucci, F. Mattioli, R. Leoni, J. Beetz, M. Lermer, and M. Kamp, "Waveguide superconducting single-photon detectors for integrated quantum photonic circuits," Appl. Phys. Lett. (99), 181110 (2011).

[2.106]. W. Pernice, C. Schuck, O. Minaeva, M. Li, G. Goltsman, A. Sergienko, and H. Tang, "High-speed and high-efficiency travelling wave single-photon detectors embedded in nanophotonic circuits," Nat. Commun. (3), 1325 (2012).

[2.107]. V. Anant, A. J. Kerman, E. A. Dauler, J. K. Yang, K. M. Rosfjord, and K.

K. Berggren, "Optical properties of superconducting nanowire single-photon detectors," Opt. Express (16), 10750-10761 (2008).

[2.108]. E. Driessen, F. Braakman, E. Reiger, S. Dorenbos, V. Zwiller, and M. De Dood, "Impedance model for the polarization-dependent optical absorption of superconducting single-photon detectors," Eur. Phys. J. Appl. Phys. (47), 10701 (2009).

[2.109]. S. W. Nam, and B. Baek, "Efficient Polarization Independent Single Photon Detector," (U.S. Patent 20140087952 A1, Mar 27, 2014).

[2.110]. V. Verma, F. Marsili, S. Harrington, A. E. Lita, R. P. Mirin, and S. W. Nam, "A three-dimensional, polarization-insensitive superconducting nanowire avalanche photodetector," Appl. Phys. Lett. (101), 251114 (2012).

[2.111]. M. Allman, V. B. Verma, R. Horansky, F. Marsili, J. A. Stern, M. D. Shaw, A. D. Beyer, R. P. Mirin, and S. W. Nam, "Progress Towards a Near IR Single-Photon Superconducting Nanowire Camera for Free-Space Imaging of Light," *CLEO: Applications and Technology*, Optical Society of America, p. AW3P. 3, (2014).

[2.112]. M. E. Grein, A. J. Kerman, E. A. Dauler, O. Shatrovoy, R. J. Molnar, D. Rosenberg, J. Yoon, C. DeVoe, D. Murphy, and B. Robinson, "Design of a ground-based optical receiver for the lunar laser communications demonstration," *Space Optical Systems and Applications (ICSOS), 2011 International Conference on*, IEEE, pp. 78-82, (2011).

[2.113]. D. M. Boroson, and B. S. Robinson, "The lunar laser communication demonstration: NASA's first step toward very high data rate support of science and exploration missions," Space Sci. Rev., 1-14 (2014).

[2.114]. D. M. Boroson, B. S. Robinson, D. A. Burianek, D. V. Murphy, A. Biswas, and H. Hemmati, "Overview and Status of the Lunar Laser Communications Demonstration," Free-Space Laser Communication Technologies Xxiv (8246), 82460C (2012).

[2.115]. M. E. Grein, M. Willis, A. Kerman, E. Dauler, B. Romkey, D. Rosenberg, J. Yoon, R. Molnar, B. S. Robinson, and D. Murphy, "A fiber-coupled photon-counting optical receiver based on NbN superconducting nanowires for the Lunar Laser Communication Demonstration," *CLEO: Science and Innovations*, Optical Society of America, p. SM4J. 5, (2014).

[2.116]. M. Allman, V. Verma, M. Stevens, T. Gerrits, R. Horansky, A. Lita, F.

Marsili, A. Beyer, M. Shaw, and D. Kumor, "A Near-Infrared 64-pixel Superconducting Nanowire Single Photon Detector Array with Integrated Multiplexed Readout," arXiv preprint arXiv:1504.02812 (2015).

[2.117]. F. Najafi, J. Mower, N. C. Harris, F. Bellei, A. Dane, C. Lee, X. Hu, P. Kharel, F. Marsili, and S. Assefa, "On-chip detection of non-classical light by scalable integration of single-photon detectors," Nat. Commun. (6) (2015).

[2.118]. F. Marsili, F. Bellei, F. Najafi, A. E. Dane, E. A. Dauler, R. J. Molnar, and K. K. Berggren, "Efficient single photon detection from 500 nm to 5 μm wavelength," Nano Lett. (12), 4799-4804 (2012).

[2.119]. R. D. Richmond, and S. C. Cain, *Direct-detection LADAR systems* (SPIE Press Bellingham, 2010).

[2.120]. E. Baumann, F. R. Giorgetta, J.-D. Deschênes, I. Coddington, L. C. Sinclair, W. C. Swann, and N. R. Newbury, "Micrometer-precision 3D Imaging At 4-Meter Standoff Distance," *Applications of Lasers for Sensing and Free Space Communications*, Optical Society of America, p. LW3A. 5, (2013).

[2.121]. F. Aflatouni, B. Abiri, A. Rekhi, and A. Hajimiri, "Nanophotonic coherent imager," Opt. Express (23), 5117-5125 (2015).

[2.122]. J. S. Massa, G. S. Buller, A. C. Walker, G. Smith, S. Cova, M. Umasuthan, and A. M. Wallace, "Optical design and evaluation of a three-dimensional imaging and ranging system based on time-correlated single-photon counting," Appl. Opt. (41), 1063-1070 (2002).

[2.123]. P. F. McManamon, "Review of ladar: a historic, yet emerging, sensor technology with rich phenomenology," Opt. Eng. (51), 060901-060901-060901-060913 (2012).

[2.124]. W. Abdalati, H. J. Zwally, R. Bindschadler, B. Csatho, S. L. Farrell, H. A. Fricker, D. Harding, R. Kwok, M. Lefsky, and T. Markus, "The ICESat-2 laser altimetry mission," Proc. IEEE (98), 735-751 (2010).

[2.125]. M. A. Albota, R. M. Heinrichs, D. G. Kocher, D. G. Fouche, B. E. Player, M. E. O'Brien, B. F. Aull, J. J. Zayhowski, J. Mooney, B. C. Willard, and R. R. Carlson, "Three-dimensional imaging laser radar with a photon-counting avalanche photodiode array and microchip laser," Appl. Opt. (41), 7671-7678 (2002).

[2.126]. A. D. Gleckler, "Multiple-slit streak tube imaging lidar (MS-STIL)

applications," *AeroSense 2000*, International Society for Optics and Photonics, pp. 266-278, (2000).

[2.127]. J. S. Jaffe, "Underwater Optical Imaging: The Past, the Present, and the Prospects."

[2.128]. P. A. Hiskett, C. S. Parry, A. McCarthy, and G. S. Buller, "A photon-counting time-of-flight ranging technique developed for the avoidance of range ambiguity at gigahertz clock rates," Opt. Express (16), 13685-13698 (2008).

[2.129]. N. J. Krichel, A. McCarthy, and G. S. Buller, "Resolving range ambiguity in a photon counting depth imager operating at kilometer distances," Opt. Express (18), 9192-9206 (2010).

[2.130]. N. J. Krichel, "Long-range depth profiling based on time-correlated single-photon counting," PhD Thesis, Heriot-Watt University (2011).

[2.131]. M. Amann, T. Bosch, M. Lescure, R. Myllyla, and M. Rioux, "Laser ranging: a critical review of usual techniques for distance measurement," Opt. Eng. (40), 10-19 (2001).

[2.132]. K. Lim, P. Treitz, M. Wulder, B. St-Onge, and M. Flood, "LiDAR remote sensing of forest structure," Prog. Phys. Geog. (27), 88-106 (2003).

[2.133]. C. Vega, and B. St-Onge, "Height growth reconstruction of a boreal forest canopy over a period of 58 years using a combination of photogrammetric and lidar models," Remote Sens. Environ. (112), 1784-1794 (2008).

[2.134]. F. Hosoi, and K. Omasa, "Estimating vertical plant area density profile and growth parameters of a wheat canopy at different growth stages using three-dimensional portable lidar imaging," ISPRS J. Photogramm. Remote Sens. (64), 151-158 (2009).

[2.135]. C. Mallet, and F. Bretar, "Full-waveform topographic lidar: State-of-the-art," ISPRS J. Photogramm. Remote Sens. (64), 1-16 (2009).

[2.136]. S. Hernandez-Marin, A. M. Wallace, and G. J. Gibson, "Bayesian analysis of Lidar signals with multiple returns," IEEE Trans. Pattern Anal. Machine Intell. (29), 2170-2180 (2007).

[2.137]. G. P. Penney, J. Weese, J. Little, P. Desmedt, D. L. Hill, and D. J. Hawkes, "A comparison of similarity measures for use in 2-D-3-D medical image registration," IEEE Trans. Med. Imaging (17), 586-595 (1998).

[2.138]. P. J. Green, "Reversible jump Markov chain Monte Carlo computation and Bayesian model determination," Biometrika (82), 711-732 (1995).

[2.139]. A. McCarthy, R. J. Collins, N. J. Krichel, V. Fernandez, A. M. Wallace, and G. S. Buller, "Long-range time-of-flight scanning sensor based on high-speed time-correlated single-photon counting," Appl. Opt. (48), 6241-6251 (2009).

[2.140]. N. J. Krichel, A. McCarthy, I. Rech, M. Ghioni, A. Gulinatti, and G. S. Buller, "Cumulative data acquisition in comparative photon-counting three-dimensional imaging," J. Mod. Opt. (58), 244-256 (2011).

[2.141]. A. McCarthy, N. J. Krichel, N. R. Gemmell, X. Ren, M. G. Tanner, S. N. Dorenbos, V. Zwiller, R. H. Hadfield, and G. S. Buller, "Kilometer-range, high resolution depth imaging via 1560 nm wavelength single-photon detection," Opt. Express (21), 8904-8915 (2013).

[2.142]. A. McCarthy, X. Ren, A. Della Frera, N. R. Gemmell, N. J. Krichel, C. Scarcella, A. Ruggeri, A. Tosi, and G. S. Buller, "Kilometer-range depth imaging at 1550 nm wavelength using an InGaAs/InP single-photon avalanche diode detector," Opt. Express (21), 22098-22113 (2013).

[2.143]. A. M. Wallace, J. Ye, N. J. Krichel, A. McCarthy, R. J. Collins, and G. S. Buller, "Full Waveform Analysis for Long-Range 3D Imaging Laser Radar," Eurasip Journal on Advances in Signal Processing (2010).

[2.144]. A. M. Wallace, C. Nichol, and I. Woodhouse, "Recovery of Forest Canopy Parameters by Inversion of Multispectral LiDAR Data," Remote Sens. (4), 509-531 (2012).

[2.145]. A. M. Wallace, A. McCarthy, C. J. Nichol, X. Ren, S. Morak, D. Martinez-Ramirez, I. H. Woodhouse, and G. S. Buller, "Design and Evaluation of Multispectral LiDAR for the Recovery of Arboreal Parameters," IEEE Trans. Geosci. Remote Sens. (52), 4942-4954 (2014).

[2.146]. Y. Altmann, X. Ren, A. McCarthy, G. S. Buller, and S. McLaughlin, "Lidar waveform based analysis of depth images constructed using sparse single-photon data," arXiv preprint arXiv:1507.02511 (2015).

[2.147]. B. Schwarz, "LIDAR: Mapping the world in 3D," Nat. Photonics (4), 429-430 (2010).

[2.148]. C. Glennie, W. Carter, R. Shrestha, and W. Dietrich, "Geodetic imaging

with airborne LiDAR: the Earth's surface revealed," Rep. Prog. Phys. (76), 086801 (2013).

[2.149]. M. Pfennigbauer, and A. Ullrich, "Multi-wavelength airborne laser scanning," *Proceedings of the International Lidar Mapping Forum, ILMF, New Orleans*, (2011).

[2.150]. S. Foix, G. Alenya, and C. Torras, "Lock-in time-of-flight (ToF) cameras: a survey," IEEE Sens. J. (11), 1917-1926 (2011).

[2.151]. Velodyne Acoustics USA, "HDL-64E S2. Datasheet. online (http://velodynelidar.com/lidar/products/brochure/HDL-64E%20S2%20datasheet_2010_lowres.pdf) last accessed 16-02-2015."

[2.152]. R. Stettner, H. Bailey, and R. D. Richmond, "Eye-safe laser radar 3D imaging," *Defense and Security*, International Society for Optics and Photonics, pp. 111-116, (2004).

[2.153]. R. Stettner, H. Bailey, and S. Silverman, "Large format time-of-flight focal plane detector development," *Defense and Security*, International Society for Optics and Photonics, pp. 288-292, (2005).

[2.154]. R. Knowlton, "Airborne Ladar Imaging Research Testbed," (The Defense Technical Information Center Document, 2011).

[2.155]. M. Laurenzis, F. Christnacher, and D. Monnin, "Long-range three-dimensional active imaging with superresolution depth mapping," Opt. Lett. (32), 3146-3148 (2007).

[2.156]. M. Laurenzis, and A. Woiselle, "Laser gated-viewing advanced range imaging methods using compressed sensing and coding of range-gates," Opt. Eng. (53), 053106-053106 (2014).

[2.157]. O. Steinvall, P. Andersson, M. Elmqvist, and M. Tulldahl, "Overview of range gated imaging at FOI," *Defense and Security Symposium*, International Society for Optics and Photonics, pp. 654216-654216-654213, (2007).

[2.158]. J. Busck, "Underwater 3-D optical imaging with a gated viewing laser radar," Opt. Eng. (44), 116001-116001-116007 (2005).

[2.159]. I. Baker, D. Owton, K. Trundle, P. Thorne, K. Storie, P. Oakley, and J. Copley, "Advanced infrared detectors for multimode active and passive imaging applications," *SPIE Defense and Security Symposium*, International Society for Optics

and Photonics, pp. 69402L-69402L-69411, (2008).

[2.160]. O. Steinvall, M. Elmqvist, T. Chevalier, and O. Gustafsson, "Active and passive short-wave infrared and near-infrared imaging for horizontal and slant paths close to ground," Appl. Opt. (52), 4763-4778 (2013).

[2.161]. W. C. Stone, M. Juberts, N. Dagalakis, J. Stone, and J. Gorman, "Performance Analysis of Next-Generation LADAR for Manufacturing, Construction, and Mobility," (NISTIR, 2004).

[2.162]. J. J. Degnan, "Photon-counting multikilohertz microlaser altimeters for airborne and spaceborne topographic measurements," J. Geodyn. (34), 503-549 (2002).

[2.163]. J. J. Degnan, and D. N. Wells, "Scanner/optical system for three-dimensional lidar imaging and polarimetry," (U.S. Patent 8493445 B2, Jul 23, 2013).

[2.164]. J. J. Degnan, R. Machan, E. Leventhal, G. Jodor, C. Field, and J. M. Sirota, "Cryosphere and Biomass Measurements using a Photon-Counting 3D Imaging Lidar," *CLEO: Applications and Technology*, Optical Society of America, p. ATuA3, (2011).

[2.165]. P. Dabney, D. Harding, J. Abshire, T. Huss, G. Jodor, R. Machan, J. Marzouk, K. Rush, A. Seas, C. Shuman, X. Sun, S. Valett, A. Vasilyev, A. Yu, and Y. Zheng, "The Slope Imaging Multi-polarization Photon-counting Lidar: Development and performance results," 2010 IEEE International Geoscience and Remote Sensing Symposium, 653-656 (2010).

[2.166]. M. A. Albota, B. F. Aull, D. G. Fouche, R. M. Heinrichs, D. G. Kocher, R. M. Marino, J. G. Mooney, N. R. Newbury, M. E. O'Brien, B. E. Player, B. C. Willard, and J. J. Zayhowski, "Three-Dimensional Imaging Laser Radars with Geiger-Mode Avalanche Photodiode Arrays," Lincoln Lab. J (13), 351-370 (2002).

[2.167]. R. M. Marino, and J. W. R. Davis, "Jigsaw: A Foliage-Penetrating 3D Imaging Laser Radar System," Lincoln Lab. J. (15), 23-26 (2005).

[2.168]. A. Wallace, G. Buller, R. Sung, R. Harkins, A. McCarthy, S. Hernandez-Marin, G. Gibson, and R. Lamb, "Multi-spectral laser detection and ranging for range profiling and surface characterization," J. Opt. A: Pure Appl. Opt. (7), S438 (2005).

[2.169]. G. S. Buller, R. D. Harkins, A. McCarthy, P. A. Hiskett, G. R. MacKinnon, G. R. Smith, R. Sung, A. M. Wallace, R. A. Lamb, and K. D. Ridley, "Multiple wavelength time-of-flight sensor based on time-correlated single-photon

counting," Rev. Sci. Instrum. (76), 083112 (2005).

[2.170]. J. S. Massa, A. M. Wallace, G. S. Buller, S. Fancey, and A. C. Walker, "Laser depth measurement based on time-correlated single-photon counting," Opt. Lett. (22), 543-545 (1997).

[2.171]. J. S. Massa, G. S. Buller, A. C. Walker, S. Cova, M. Umasuthan, and A. M. Wallace, "Time-of-flight optical ranging system based on time-correlated single-photon counting," Appl. Opt. (37), 7298-7304 (1998).

[2.172]. R. E. Warburton, A. McCarthy, A. M. Wallace, S. Hernandez-Marin, R. H. Hadfield, S. W. Nam, and G. S. Buller, "Subcentimeter depth resolution using a single-photon counting time-of-flight laser ranging system at 1550 nm wavelength," Opt. Lett. (32), 2266-2268 (2007).

[2.173]. M. Umasuthan, A. M. Wallace, J. S. Massa, G. S. Buller, and A. C. Walker, "Processing time-correlated single photon counting data to acquire range images," IEE Proceedings-Vision Image and Signal Processing (145), 237-243 (1998).

[2.174]. A. Wallace, G. Buller, and A. Walker, "3D imaging and ranging by time-correlated single photon counting," Computing & Control Engineering Journal (12), 157-168 (2001).

[2.175]. G. Buller, and A. Wallace, "Ranging and three-dimensional imaging using time-correlated single-photon counting and point-by-point acquisition," IEEE J. Select. Topics Quantum Electron. (13), 1006-1015 (2007).

[2.176]. P. A. Hiskett, K. J. Gordon, J. W. Copley, and R. A. Lamb, "Long range 3D imaging with a 32x32 Geiger mode InGaAs/InP camera," *SPIE Sensing Technology+ Applications*, International Society for Optics and Photonics, pp. 91140I-91140I-91113, (2014).

[2.177]. K. J. Gordon, P. A. Hiskett, R. Pilkington, J. Copley, A. Pawlikowska, and R. A. Lamb, "New Trends in Integrated Imaging Lidar," *Applications of Lasers for Sensing and Free Space Communications*, Optical Society of America, p. LW3A. 1, (2013).

[2.178]. A. M. Pawlikowska, R. M. Pilkington, K. J. Gordon, P. A. Hiskett, G. S. Buller, and R. A. Lamb, "Long-range 3D single-photon imaging lidar system," *SPIE Security+ Defence*, International Society for Optics and Photonics, pp. 925007-925007-925010, (2014).

[2.179]. G. A. Howland, P. B. Dixon, and J. C. Howell, "Photon-counting compressive sensing laser radar for 3D imaging," Appl. Opt. (50), 5917-5920 (2011).

[2.180]. M. F. Duarte, M. A. Davenport, D. Takhar, J. N. Laska, T. Sun, K. E. Kelly, and R. G. Baraniuk, "Single-pixel imaging via compressive sampling," IEEE Signal Process Mag. (25), 83 (2008).

[2.181]. G. A. Howland, D. J. Lum, M. R. Ware, and J. C. Howell, "Photon counting compressive depth mapping," Opt. Express (21), 23822-23837 (2013).

Chapter 3
Configuration of scanning time-of-flight single-photon depth imaging systems

3.1 Introduction

Time-of-flight (TOF) single-photon depth imagers are designed to acquire depth profiles under photon-starved conditions. By using shot-noise limited detection approaches, the single-photon approach offers the potential for longer distance ranges, or smaller aperture optics than more conventional rangefinders. Imagers using high-density single-photon detector arrays (e.g. 32×32 pixels) can capture full-field information in parallel, but such arrays generally suffer from relatively low fill factor in the photon sensitive area compared with the pixel area, leading to inefficiencies in optical return. Single-photon depth imagers combined with scanning approaches can implement pixel-wise depth profiling using high-detection-performance discrete or low pixel-density array (e.g. 4×4 pixels [3.1] and 10×10 pixels [3.2]) detectors. This can cover the desired field of view (FOV) of the target scene. Scanning TOF depth imagers, using the time-correlated single photon counting (TCSPC) technique, are composed of four key elements: a pulsed laser source, a scanning transceiver system, a single-photon detector module and a data acquisition module as shown in Figure 3-1. This type of imager can offer flexibility of spatial and temporal samplings e.g. extension of pixel density as well as user-determined acquisition time per pixel.

This Chapter will cover details of the scanning TOF systems used for the measurements reported in this Thesis. The transceiver was adapted for depth imaging at $\lambda \sim 1550$ nm, multiple wavelengths (i.e. 531, 570, 670 and ~780 nm), $\lambda \sim 817$ nm, and $\lambda \sim 842$ nm. For these different transceiver configurations, the relevant optical & optomechanical layout, alignment techniques and optical filtering approaches are discussed in this Chapter.

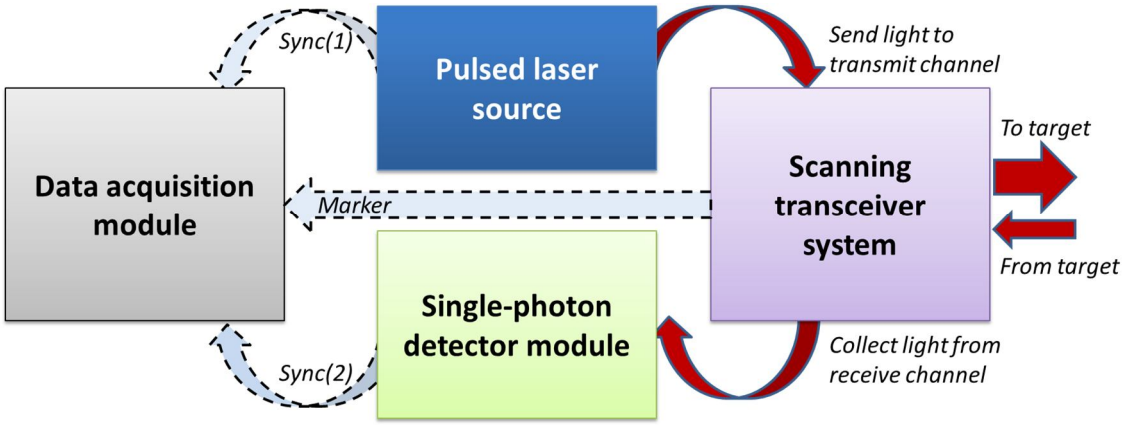

Figure 3-1 Illustration of a scanning time-of-flight (TOF) depth imager using the time-correlated single photon counting (TCSPC) technique. The data acquisition module is a TCSPC system to record time-tag data stream. The time-tag data stream is related to "Sync(1)" and "Sync(2)" clocks which are linked to the pulsed laser source and single-photon detector module respectively, as shown in the figure. Using the time-tag data, the relevant TOF information can be extracted from the time difference between electrical "Sync(1)" and "Sync(2)" signals. The electrical "Marker" (shown in the figure) stream carrying synchronisation information derived from the scanning system can be used to distinguish spatial origin of the detected photons [3.3].

3.2 Transceiver scanning system

3.2.1 Technical background

TOF light detection and ranging (LiDAR) systems can be categorised as either bistatic or monostatic systems. Bistatic TOF LiDAR systems have spatially separated transmit and receive channels. By contrast, in a monostatic LiDAR transceiver system the transmit and receive channels have a common aperture with coaxial alignment of both channels. Hence, realignment is not required for the monostatic system when the target stand-off distance is changed. The transceiver described in this Thesis was in monostatic configuration and used for measurements at stand-off distances of 40, 325, 910 and 4500 metres.

When the LiDAR system incorporates a beam steering mechanism that is capable of directing the single laser beam in both dimensions across the scene of interest, in principle a full 3D image can be measured. One such beam steering mechanism is based on moving the entire sensor. For example, for an airborne system, the forward flight of the aircraft can provide one scanning dimension. The other dimension can be

measured by a one-dimensional beam scanner which moves perpendicular to the direction of flight [3.4]. Another example of a moving-sensor-based scanning mechanism is one which relies on moving a pan/tilt or pan-and-tilt head for scanning [3.5-3.6]. Alternatively, there are a variety of types of beam scanning mechanisms, such as polygonal mirrors, galvanometric mirrors, acousto-optic single beam scanners, a rotating Risley prism beam steering arrangement and scanning micro mirror beam arrays including microelectromechanical systems (MEMS) [3.7]. However, for high angular resolution (e.g. <1 μrad) and high speed (e.g. ~1 μs response time) beam steering, mechanical mechanism scanners have limitations due to mechanical inertia. An alternative device is based on optical phased array technology [3.8] which may overcome the angular resolution and speed limitations mentioned above. For example, the two dimensional chip-scale nanophotonic phased array recently reported by Sun *et al.* [3.9] and Yaacobi *et al.* [3.10] opens up possibilities for high-speed scanning LiDAR applications, although this work is at a relatively early stage for implementation in long-range depth scanning systems. In addition, there are disadvantages caused by the limitations of the small effective apertures available (typically <1 mm for MEMS) for the beam array scanners to use in scanning LiDAR systems. In this Thesis, moving-magnet galvanometer scan mirrors [3.11] were employed in the depth imaging systems described in this Thesis as they are reliable, commercial off-the-shelf components, and have large effective aperture (10 mm), moderate deflection angular resolution (~10 μrad) as well as having suitable rapid response times for the intended applications (~500 μs step response).

3.2.2 Optical configuration

The previous TOF depth imaging system operating at $\lambda \sim 850$ nm using a bespoke scanning transceiver unit was developed by members of the Heriot-Watt group [3.12]. The transceiver unit was designed to be modular and reconfigurable for different photon sources, detectors and operating wavelengths. The optical arrangement of the transceiver unit is in a monostatic configuration, i.e. with coaxial transmit and receive channels. Therefore, a number of optical components are common to both channels as can be seen in Figure 3-2. Those components are two galvanometer scan mirrors (SM1, SM2) in X and Y, three relay lenses (RL1, RL2 and RL3) and an objective lens. As shown in Figure 3-2, a polarising beam splitter (PBS) is used to separate the transmit and receive light beams. Typically, the laser source will be linearly polarised, allowing low-loss reflection from the PBS. The scattered return can be regarded as unpolarised,

thus incurring a 50% loss at this component. In the transmit channel, a fibre collimator (i.e. FCT shown in Figure 3-2) is used to couple the fibre-to-free-space light in the launching front end. The receive channel is free-space-to-fibre coupling using another fibre collimator (i.e. FCR shown in Figure 3-2) and subsequently delivered to a detector. The standard fibre terminations in both the transmit and receive channels of the transceiver unit were compatible with laser sources with fibre-delivery outputs (such as a supercontinuum laser source) and fibre-coupling detectors. Nevertheless, the free-space coupling options can still be used in the transceiver unit when an arrayed detector is used in the receive channel (see Chapter 5).

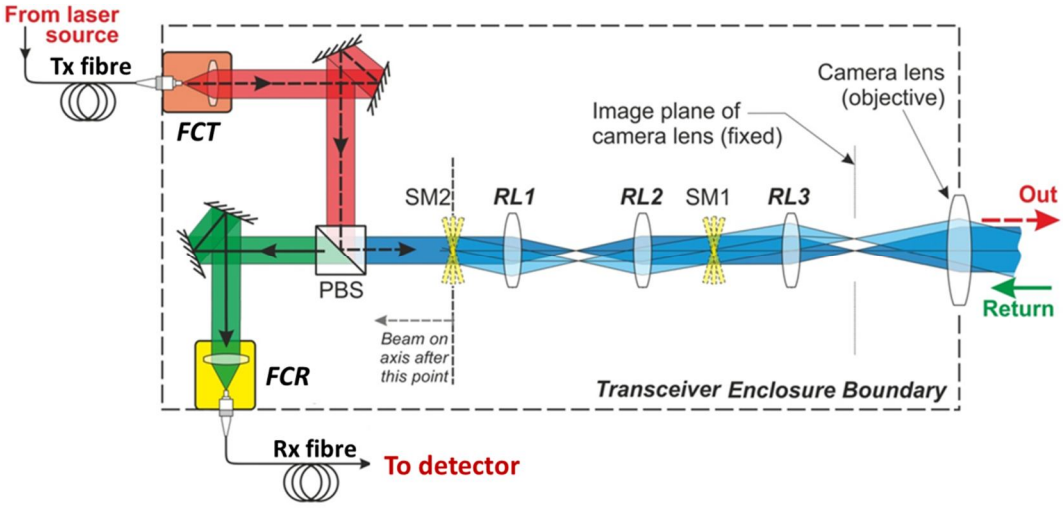

Figure 3-2 Schematic of the layout of the transceiver unit. Its key optical components include fibre collimators (FCT, FCR) in the transmit and receive channels, a polarising beam splitter (PBS), galvanometer scan mirrors (SM1, SM2) in X and Y, relay lenses (RL1, RL2, RL3) and an objective lens.

3.2.3 Raster scanning by two galvanometer scan mirrors

In order to implement target profiling, commonly two galvanometer mirrors in XY were employed to steer the laser beam in a raster pattern over the field of view of interest with a move-stare-move mode. X and Y galvanometer scan mirrors can be arranged as in the configurations shown in Figure 3-3. One configuration shown in top of Figure 3-3 is intuitive as the rotation axis of the Y scan mirror is about the X axis and the rotation of X scan mirror is about the Z axis. The optical axis of the incident beam is along the Z axis while the optical axis of the output beam is along the X axis. $\delta\theta_r$ denotes the angle disparity between the reflection beams before and after the scan mirror (X or Y scan mirror) deflects. Once the deflection angle is θ_d, $\delta\theta_r = 2\,\theta_d$ for both the X and Y scan mirrors in this configuration. Hence, both offer the same efficiency of beam

directing.

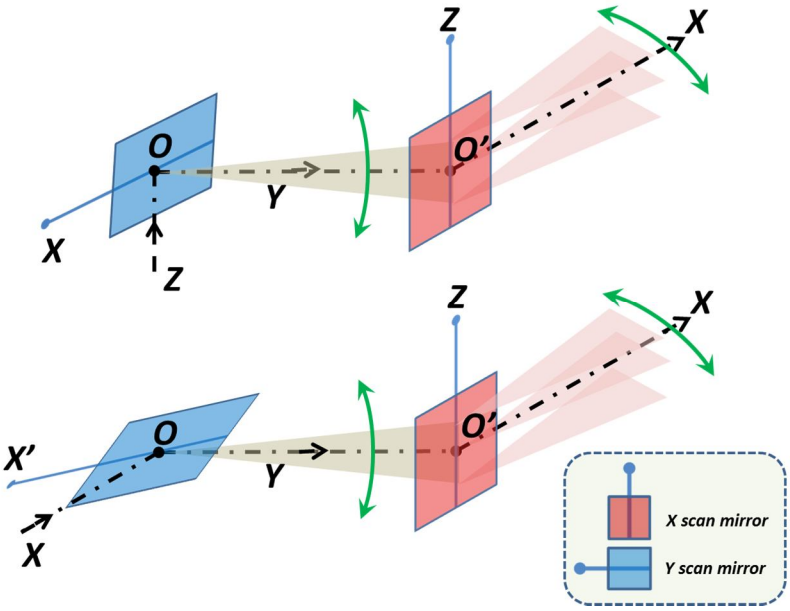

Figure 3-3 Configurations of the X and Y galvanometer scan mirrors. Top: The rotation axis of the Y scan mirror is about the X axis and the rotation of the X scan mirror is about the Z axis. The optical axis of incident beam is along the Z axis while the optical axis of output beam is along the X axis. Bottom: The rotation axis of the Y scan mirror is about OX' which is not parallel to the X axis but still in the OXY plane. The optical axes of incident beam and output beam are both parallel to the X axis. Two galvanometer scan mirrors of the scanning transceiver unit are implemented in this configuration. It allows the optical axes of optical components within the transceiver unit to be in the same plane, which is convenient for optical alignments.

In the other configuration, the rotation axis of one of the two scan mirrors is not about, or parallel to, the X, Y or Z axes. For example, the rotation axis of the Y scan mirror in bottom of Figure 3-3 is about OX' which is not parallel to the X axis but still in the OXY plane. The optical axes of the incident beam and output beam are both parallel to the X axis. By virtue of this configuration, it allows the optical axes of all the employed optical components to be in the same plane and thus is convenient for optical alignments. Figure 3-4 shows that the reflection angle disparity, $\delta\theta_r$, (i.e. effective deflection or steering angle) of the beam in a certain plane (e.g. OYZ plane for the Y scan mirror and the OXY plane for the X scan mirror). $\delta\theta_r$ varies along with the deflection angle for the X or Y scan mirror with the configuration shown in bottom of Figure 3-3. This configuration was employed for the X and Y scan mirrors in the transceiver system reported in this Thesis.

The angle disparity between the reflection beams before and after the X scan mirror deflects can described as:

$$\delta\theta_r^X = 2\,\theta_d \qquad \text{Equation (3.1)}$$

Given that the angle between OX' and OX within the OXY plane is 45° for the Y scan mirror, the relationship between its $\delta\theta_r$ and θ_d can be expressed as:

$$\cos\delta\theta_r^Y = 1/\sqrt{1+2\,(\tan\theta_d)^2} \qquad \text{Equation (3.2)}$$

As shown in Figure 3-4, compared to the Y scan mirror, the X scan mirror provides more efficient beam directing and its angle disparity is proportional to the deflection angle of the scan mirror.

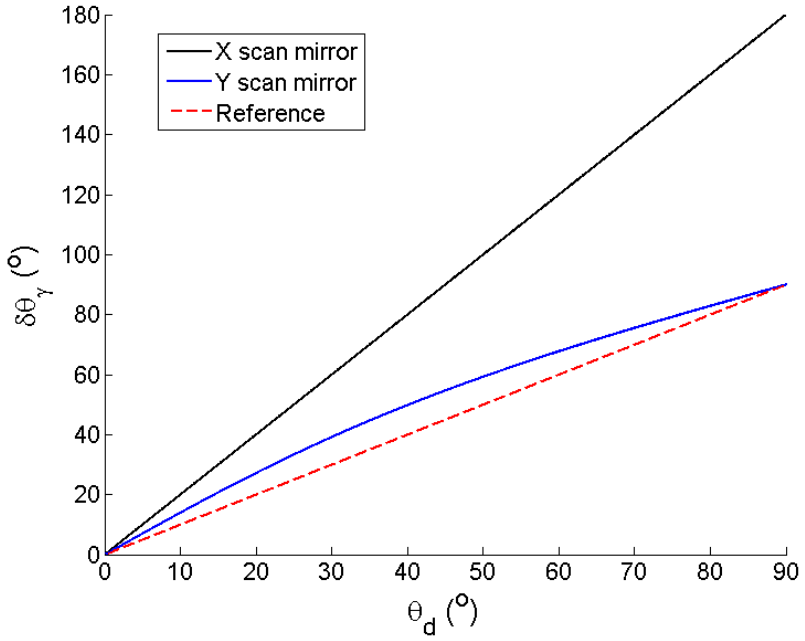

Figure 3-4 The reflection angle disparity (i.e. effective deflection or steering angle) of the beam in a certain plane (e.g. OYZ plane for the Y scan mirror and OXY plane for the X scan mirror) varies along with the deflection angle for the X or Y scan mirrors with the configuration shown in bottom of Figure 3-3. θ_d denotes the deflection angle and the angle disparity $\delta\theta_r$ between the reflection beams before and after the scan mirror deflects.

3.2.4 System implementation

Figure 3-5 shows the computer aided design (CAD) drawing and a photograph of the transceiver unit. The slotted baseplate and the enclosure of the unit were made from black anodised aluminium to minimise stray reflections. The free-space optical

components are arranged on the top of the baseplate while the control electronic modules for the scanning optics are mounted on the back surface of the baseplate. A lid that also made from anodised aluminium is usually placed over the assembly, to reduce background light during measurements.

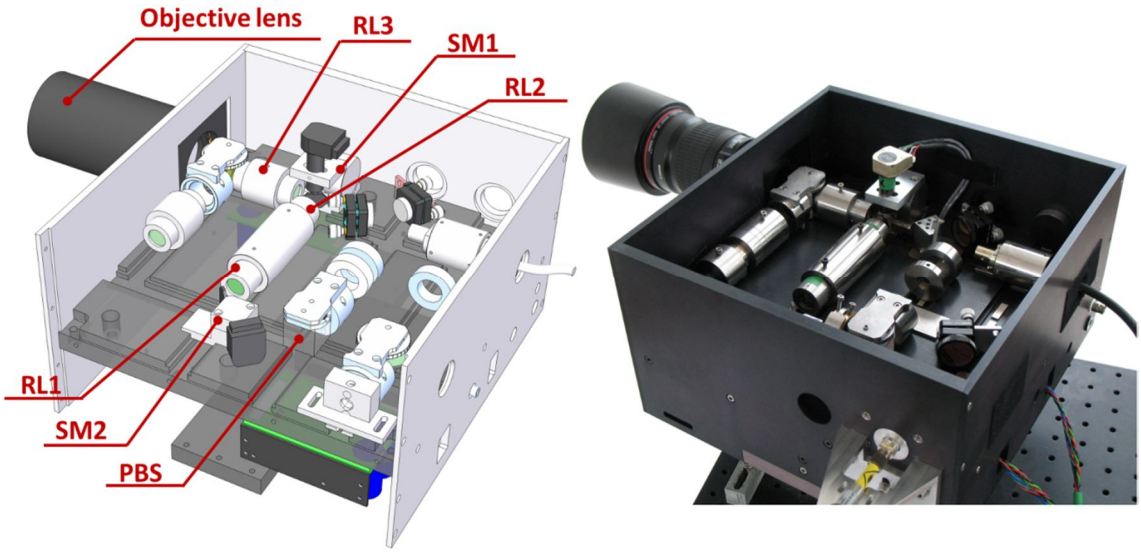

Figure 3-5 A computer aided design (CAD) drawing and photograph of the transceiver unit. PBS: polarising beam splitter; SM1 and SM2: galvanometer scan mirrors in X and Y; RL1, RL2, and RL3: relay lenses.

In the transceiver unit, two independent mirror configurations can be achieved, either with or without the use of intermediate optics. Without a relay optical system between the two flat scan mirrors on perpendicular axes, the two mirrors must be positioned as close as possible and share a telecentric plane located at the mid-point between them. If two mirrors are close-coupled without intervening relay optics, it can only implement an approximate telecentric configuration. By contrast, for the case with longer spacing between two flat scan mirrors on perpendicular axes, a relay optical system containing three telecentric lenses (RL1, RL2 and RL3) shown in Figure 3-2 (not limited to this arrangement) is required to optimise the performance of the scanning optics. As this approach can meet the telecentric requirement perfectly it is used in the transceiver (see Figure 3-5) for all the measurements in this Thesis. More specifically, an image of the Y scan mirror (SM2) can be formed on the rotation axis of the X scan mirror (SM1) by using an achromatic pair of RL1 and RL2. Consequently, the X scan mirror is also within a conjugate telecentric plane when the Y scan mirror is placed in a telecentric plane [3.13]. In addition, once RL3 is employed, an image of scan mirrors in X and Y can be formed in the fixed primary image plane of the system's objective lens. In fact, RL3 plays the role of a scan lens and hence this limits the effective acceptance angle of

the scanning transceiver by the effective numerical aperture of RL3 in the image space. In the current system described in this Thesis, this numerical aperture corresponds to a minimum f-number of f/4. In this case, even if the system objective lens had a low f-number (e.g. Canon EF 200 mm f/2.8L II USM), the f-number of the transceiver system for imaging is constrained to f/4.

To optimise the transceiver for imaging at different wavelengths and stand-off working distances, the free-space optical components in the transceiver were carefully selected and aligned. As our transceiver is based on the monostatic configuration, it is inevitable to have optical back-reflections from the component surfaces along the common transmit and receive optical path. These optical back-reflections have the potential to form "ghost signals", which can confuse the signal of interest. In addition, in a time-correlated single-photon counting set-up, these back-reflections have the potential to cause pulse pile-up or cause a saturation of the detector acquisition chain, rendering the entire system ineffective. However, there are several ways to reduce the optical back-reflection effect, such as using optical components with high performance anti-reflective coating. In addition, the performance of components PBS, RL1, RL2 and RL3 is wavelength-dependent. For imaging at specific wavelengths, components PBS, RL1, RL2 and RL3 each with an appropriate coating at the wavelengths of operation were chosen. On the other hand, the employed components RL1, RL2 and RL3 were all achromatic lenses. The spacing between SM2, RL1, RL2, SM1 and RL3 was optimised to form a good-quality scanning beam. In contrast, for broadband imaging, the components with good performance at a weighted wavelength for the broad wavelength range were selected. It is worth noting that as the effective aperture of both two galvanometer scan mirrors (i.e. SM1 and SM2) with silver coating is 10 mm, they have broadband operation with high reflection for transmit and receive light beams [3.11]. More details about the software and hardware approaches to remove these unwanted back-reflections are discussed in the Chapter 4 - 7.

In terms of the alignment of the scanning optics, the spacing between the SM1 and SM2 was set to $4f$, based on the pair of relay lenses (i.e. RL1 and RL2 shown in Figure 3-2). The off-the-shelf achromatic lenses were required to have suitable AR-coatings, clear apertures and focal lengths to optimise the relay optics between two scan mirrors. The separation of f_{RL1}+f_{RL2} associated with different pairs of relay lenses was simulated in Zemax. This can ensure that the combination of the relay lens pair with optimum parameters has a good match to the spacing between the SM1 and SM2. The relevant

commercial lenses can then be appropriately chosen.

In order to complete the high performance relay and scanning optics for the scanners, the selected optical components were required to appropriately align in the transceiver unit. Once the placement of SM1 and SM2 is fixed, it is necessary to align the relay optical system to the scan mirrors. As shown in Figure 3-6(a), a temporary lens with a proper focal length is placed between two scan mirrors and it is employed to focus the collimation laser beam on the moving SM1. Adjusting the spacing between RL3 and SM1 until the point source (P1) on the moving SM1 has a relatively stationary image in sharp focus on the CCD camera, ensures that RL3 is a distance equal to a focal length, f_{RL3}, from SM1. The next step is to align a pair of achromatic lenses, RL1 and RL2, to SM2. Note that the achromatic lenses, RL1 and RL2, are pre-aligned to be separated by f_{RL1}+f_{RL2} at the operating wavelengths. As shown in Figure 3-6(b), the other temporary lens with a proper focal length is used to focus the collimation laser beam on the moving SM2. By adjusting the spacing between the achromatic pair and SM2 until the point source (P2) on the moving SM2 has a relatively stationary image in sharp focus on the CCD camera, this can ensure that RL1 is a distance equal to a focal length, f_{RL1}, from SM2.

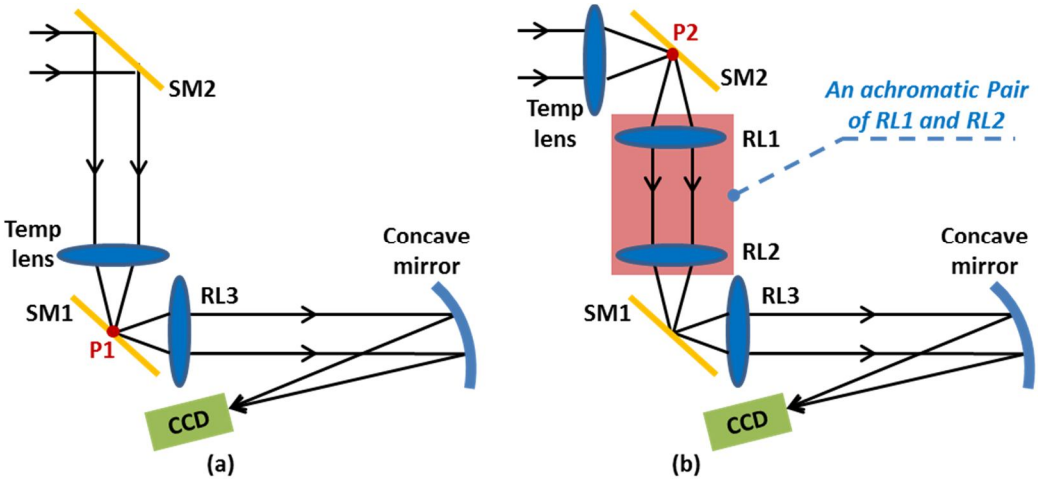

Figure 3-6 Alignment between the relay lenses (RL1, RL2, &RL3) and the scan mirrors (SM1 and SM2) within the transceiver unit. (a) shows the schematic of positioning RL3 with a distance equal to a focal length, f_{RL3}, from SM1. The focussed spot on SM1 is considered as a point source (P1) for the image in the CCD camera. (b) shows the schematic of positioning an achromatic pair of RL1 and RL2 and ensures that RL1 a distance equal to a focal length, f_{RL1}, from SM2. The focussed spot on SM2 is considered as a point source (P2) for the image in the CCD camera.

The optical path of the transmit and receive channels within the transceiver unit for alignment is highlighted in Figure 3-7. The figure also shows the pair of mirrors included in the transmit channel, and the pair in the receive channel, that are adjusted to align each channel to ensure that both channels are coaxial. It is imperative that the coaxial alignment of the system is correct for use in long range imaging applications.

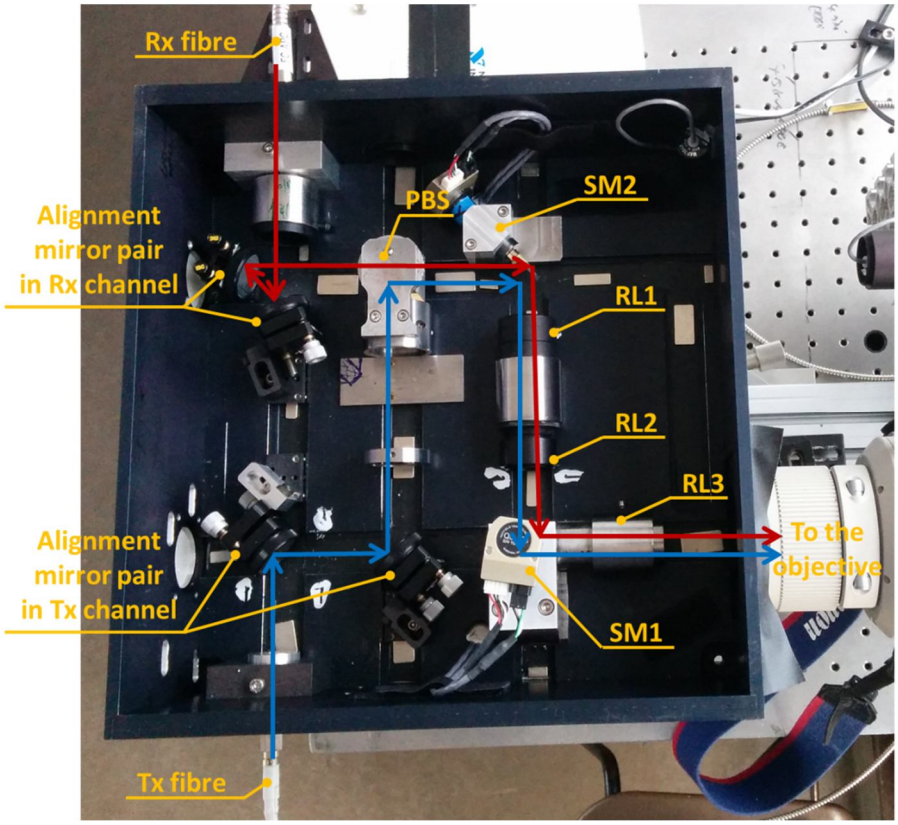

Figure 3-7 The optical path within the transceiver unit of the coaxial optical alignment scheme shown in Figure 3-8 between the transmit (Tx) and receive (Rx) channels.

Figure 3-8 illustrates a coaxial optical alignment scheme to optimise the coaxial overlapping between the transmission and collection aperture of the monostatic transceiver and thus offer high performance detection. Figure 3-8(a) shows the schematic of a coaxial optical alignment setup for the transmit and receive channels of the transceiver unit using a concave mirror with a focal length of 505 mm and a CCD camera. Given that there are fibre collimators in both the transmit channel front-end and receive channel back-end, laser beams can be delivered from a fibre and collimated in free space for both the transmit and receive channels. The fibre-to-free-space coupled laser beams pass through the transceiver unit and are focused into the CCD camera by the concave mirror. As illustrated in Figure 3-8(b), the centroid overlapping of the focussed fibre core images does not guarantee that the transmit and receive

channels are perfectly coaxial. This is because there is the potential for orientation difference with respect to the optical axis between the two focussed beams from the transmit and receive channels. To achieve coaxial alignment of the transmit and receive channels, the centroid overlapping between the images of the in-focus and out-of-focus fibre cores needs to be inspected. This was done by shifting the CCD camera forward and backward along the optical axis. Inspection of the images of the fibre cores can provide alignment hints and visual tracing in order to perform coarse adjustments for coaxial optimisation between the transmit and receive channels. By combining a microscope objective lens with a CCD camera, the magnified images of the fibre core can be used to implement fine adjustments for further coaxial optimisation.

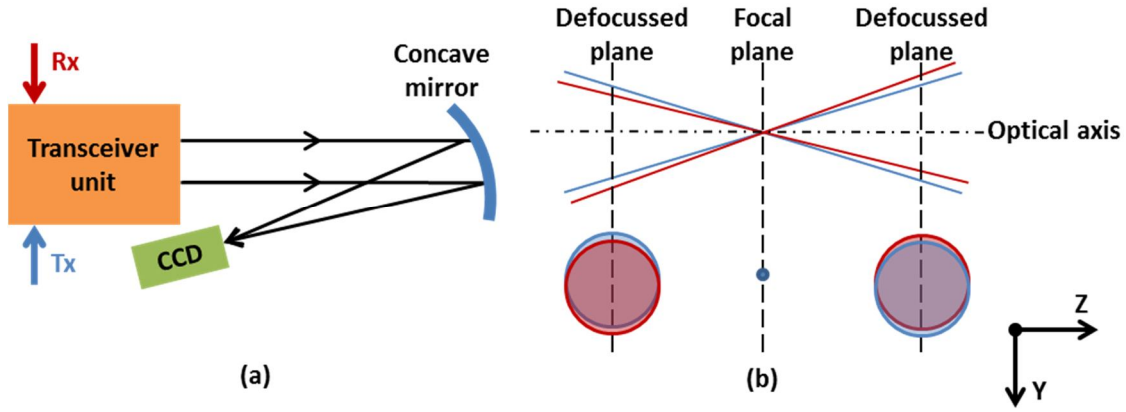

Figure 3-8 The coaxial optical alignment scheme between the transmit and receive channels. (a) The schematic of an optical alignment setup that is used to align the transmit and receive channels of the transceiver unit using a concave mirror and a CCD camera. (b) Top: Illustrations of the focusing beam ray traces on the CCD camera in the Y – Z plane of the transmit and receive channels. Bottom: Illustrations of the images of the fibre cores in focus (centre) and out of focus (left and right) associated with the transmit and receive channels. The light beam and the images of the fibre cores in the transmit receive channel are shown in blue while the ones shown in red are for the receive channel.

An electrical driver system was used to simultaneously control the two galvanometer scan mirrors and thus achieve a raster scan. The schematic of the driver system for the XY scanning galvo mirrors with support devices can be seen in Figure 3-9. Note that the implemented driver system operates in a non-closed-loop. A digital-to-analogue converter (DAC) generates control voltages to drive the X-axis and Y-axis galvo motors. Note that the control voltages are preset values assembled in XY from a control computer in order to achieve a certain scan pattern for the X-axis and Y-axis servo controllers. In the meantime, a trigger signal associated with the generation of control

voltages can be generated from the DAC module to an external system, for example to be as a marker for the TCSPC module. By contrast, this trigger signal can also be provided from the external system to trigger the DAC module. For example, the silicon single photon avalanche diode (SPAD) array camera described in Chapter 5 generates a trigger as a marker to control the DAC module. In addition, a power supply unit can power on two servo controllers simultaneously.

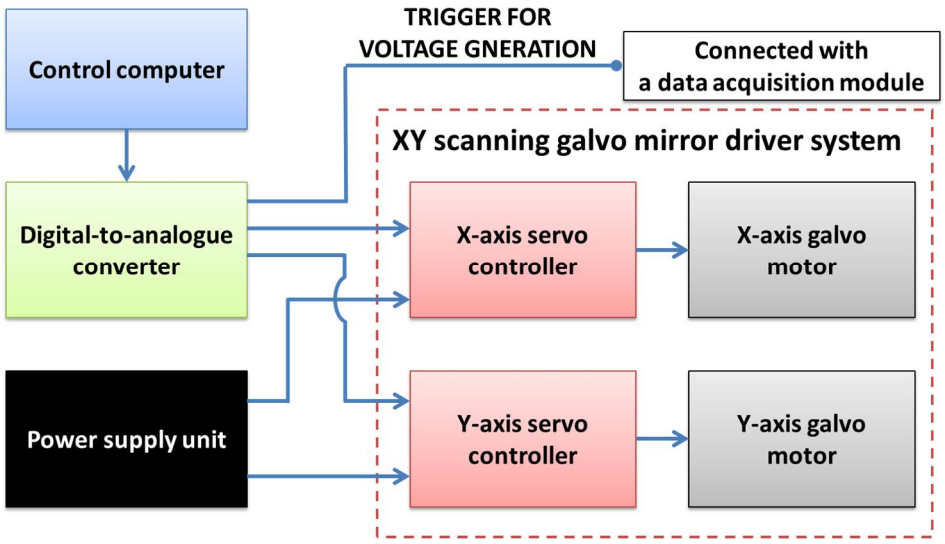

Figure 3-9 Schematic of a driver system for XY scanning galvo mirrors. A digital-to-analogue converter generates control voltages which are preset values sent to the X and Y-axis servo controllers to achieve a certain scan pattern for the X-axis and Y-axis galvo motors. In the meantime, a trigger signal associated with the generation of control voltages is provided to/from the data acquisition module. In addition, a power supply unit can power the two servo controllers simultaneously.

3.3 Pulsed laser sources

For the measurements reported in this Thesis, a pulsed mode-locked fibre laser and spectrally tunable pulsed supercontinuum laser source were used and they were fibre-coupled to the transmit channel of the transceiver system.

3.3.1 Pulsed mode-locked fibre laser source

A 1560 nm pulsed mode-locked fibre laser based on a CNT-1560 laser engine by Kphotonics, USA was used as an illumination source in a developed single-photon depth imager using a superconducting nanowire single photon detector [3.14] (See Chapter 4). The mode-locked fibre laser engine [3.15], which is a mode-locked laser oscillator operating around λ=1550 nm, uses a saturable absorber based on a fibre taper

with single-walled carbon nanotube. The mode can be locked by pumping a λ=980 nm laser into the engine to provide sub-ps duration laser pulses with ~1 mw average output power [3.16]. The laser output optical power spectrum of this pulsed mode-locked fibre laser can be seen in Figure 3-10. The spectrum was measured using an optical spectrum analyser (Anritsu MS96A). The drawback of this fibre laser is that it can output a mode-locked pulse train along with continuous wave (CW) light in the background at similar wavelengths if the saturable absorber is ageing or the pre-adjusted polarisation controller within the fibre ring is not well maintained. This leaking CW light can lead to an increased background level during time-resolved measurements, in particular for sensitive detections e.g. using the single photon TOF imagers with a monostatic configuration.

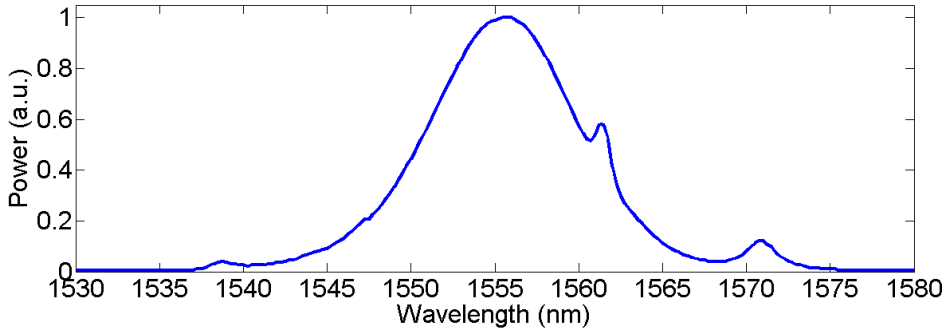

Figure 3-10 Optical power spectrum of a pulsed mode-locked fibre laser based on a CNT-1560 laser engine by Kphotonics (Tucson, AZ, US). The spectrum was measured using an optical spectrum analyser (Anritsu MS96A) in our laboratory.

3.3.2 Pulsed supercontinuum laser source

Supercontinuum laser sources have the capability of producing collimated, coherent and broadband light beams with the brightness of monochromatic laser light. Many commercial supercontinuum light sources are generated by photonic crystal fibre (PCF) with a wide wavelength range typically from around 400 nm to more than 2000 nm [3.17]. They can be used in a wide range of applications, e.g. fluorescence lifetime imaging microscopy (FLIM), optical coherence tomography (OCT), metrology and sorting systems, LiDAR and material processing [3.17-3.19]. Most of the research work reported in this Thesis was conducted using pulsed supercontinuum laser sources as they provide powerful and versatile illumination. Two supercontinuum lasers were used in this work. They consisted of two PCF-based supercontinuum sources (SuperK Extreme EXW-6 and EXW-12, NKT Photonics, Denmark), two acousto-optic tunable filter (AOTF) units (SuperK SELECT, NKT Photonics), and fibre delivery systems.

The wavelength ranges of the EXW-6 and EXW-12 sources covered 500 nm-2400 nm and 485 nm-2400 nm respectively. They both can be controlled using the easy-to-use software (SuperKontrol developed by NKT Photonics). These supercontinuum laser sources are generated by launching a pulsed seed laser source, typically with repetition rates in MHz range, into a PCF. Lower repetition rates can be achieved by the use of a pulse picker. The EXW-6 source includes a pulse picker option for selecting repetition rates as low as ~300 kHz and are equal to the down-divided frequencies which are worked out by the frequency of the seed laser of ~80 MHz divided by a number of discrete ratios. The pulse duration of the PCF-based supercontinuum laser source has a strong dependence on the pulse width of the seed laser source. For example, a gain-switched seed source at λ=1064 nm has a pulse width of ~5 ps. In addition, the length of the PCF and its dispersion properties allow temporal and spectral broadening at both sides of the seed wavelength [3.20]. The full width at half maximum (FWHM) pulse duration of the supercontinuum laser source is wavelength-dependent (see Figure 3-11) and varies between ~30 ps and 100 ps at wavelengths from ~450 nm to 800 nm. Note that these pulse durations were measured using a streak camera by NKT Photonics, Denmark.

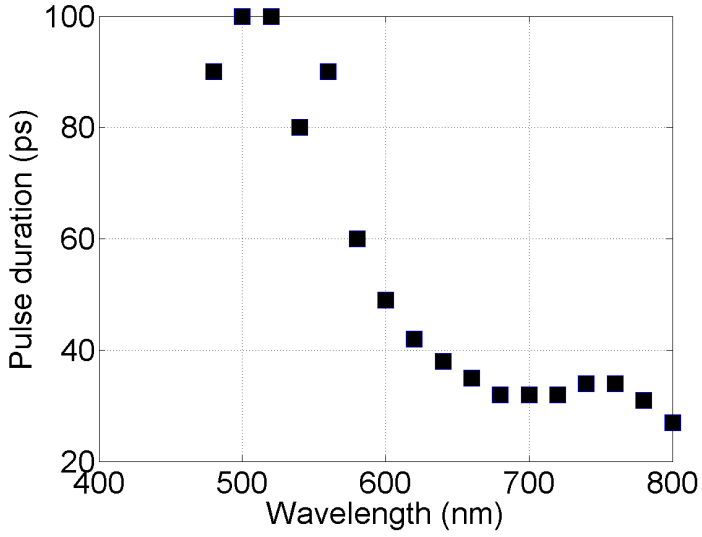

Figure 3-11 Variation of full width at half maximum (FWHM) pulse durations along with wavelengths (from ~450 nm to 800 nm) of a supercontinuum laser source (SuperK EXTREME EXW-6, NKT Photonics, Denmark).

A proper combination of dielectric optical filters (e.g. long-pass, band-pass and short-pass optical filters) can effectively filter out the wavelength range of interest from the supercontinuum source. For multichannel filtering, the AOTF unit can be connected to the output of the supercontinuum source. This set up is capable of providing a light

beam containing maximum 8 tunable wavelengths simultaneously with free-space or fibre delivery output. Figure 3-12 shows the plot of the power ratio versus bandwidth. The power ratio is equal to the total output power over the output power of only a single wavelength channel (with central wavelength at 800 nm) with 2 nm (black dots), 5 nm (blue diamonds) and 10 nm (black squares) bandwidth spans among wavelength channels. The power ratios for 2 to 8 wavelength channels (from bottom-left to top-right) are illustrated for each bandwidth span case.

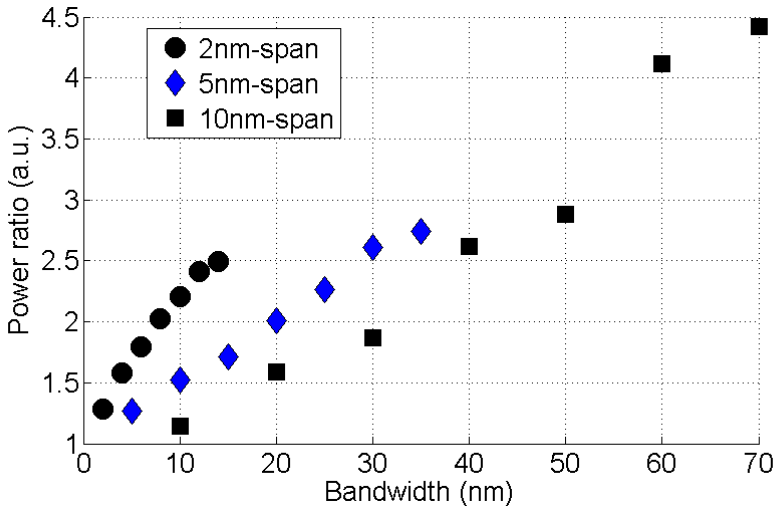

Figure 3-12 Simultaneous multiple wavelength channels (from 2 to 8 channels) output from a supercontinuum laser source (SuperK EXTREME, EXW-12, NKT Photonics, Denmark) with an AOTF. The plots illustrate the relevant power ratios. The power ratio is equal to the total output power over the output power of only single wavelength channel (with a central wavelength at 800 nm) with 2 nm (black dots), 5 nm (blue diamonds) and 10 nm (black squares) bandwidth spans among wavelength channels. The power ratios for 2 to 8 wavelength channels are illustrated from bottom-left to top-right for each bandwidth span case shown in Figure 3-13, Figure 3-14 and Figure 3-15.

According to the optical power spectrum of the 2 nm, 5 nm and 10 nm wavelength span cases shown in Figure 3-13, Figure 3-14 and Figure 3-15, more output wavelength channels can provide higher power but have wider output bandwidth.

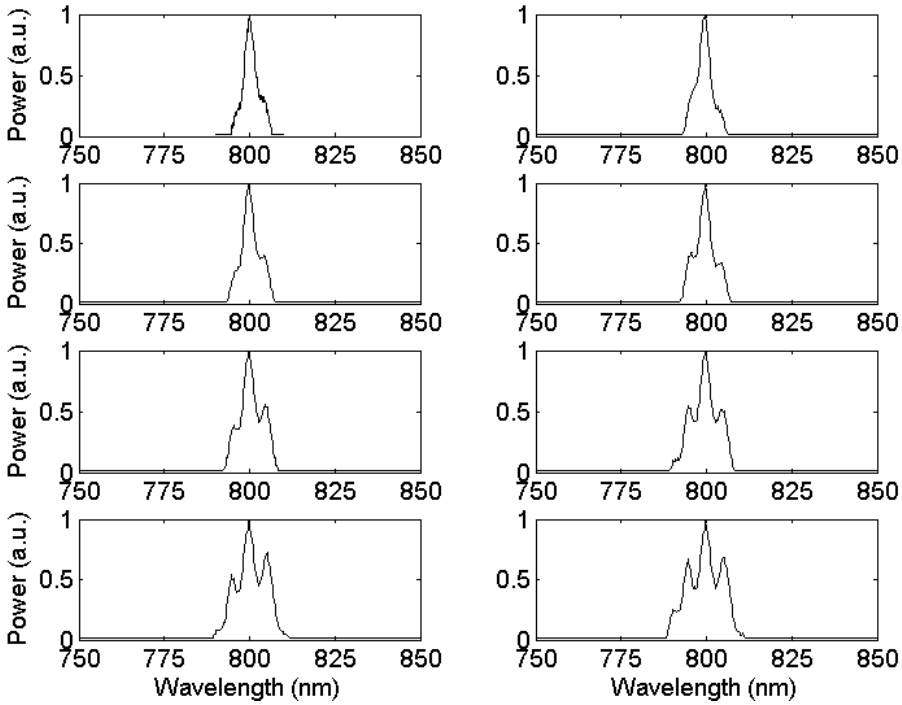

Figure 3-13 The optical power spectrum for 1 to 8 wavelength channels (from left to right and top to bottom) with 2 nm wavelength span.

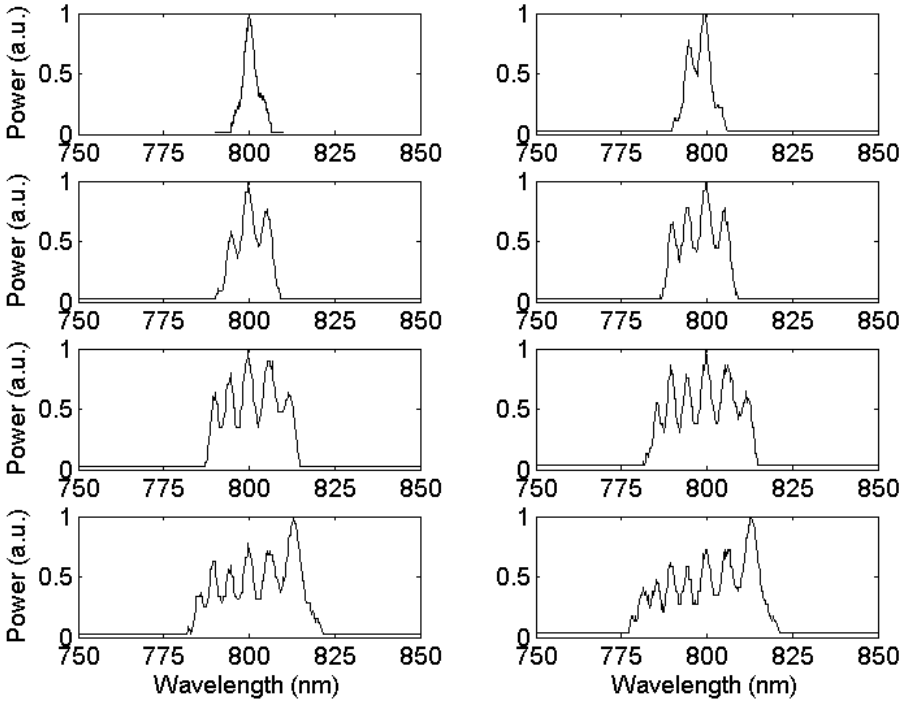

Figure 3-14 The optical power spectrum for 1 to 8 wavelength channels (from left to right and top to bottom) with 5 nm wavelength span.

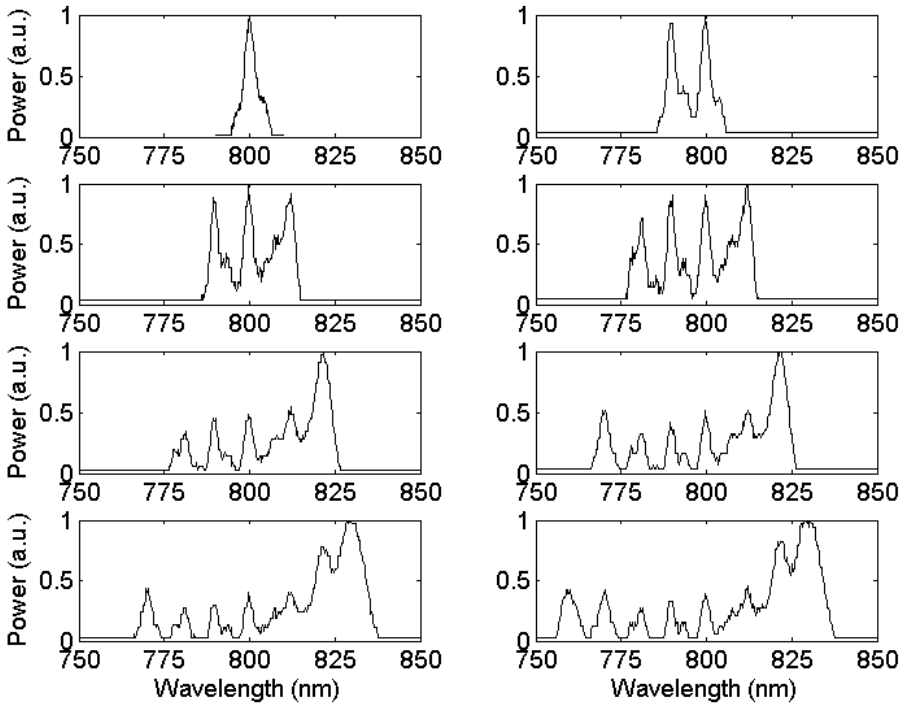

Figure 3-15 The optical power spectrum for 1 to 8 wavelength channels (from left to right and top to bottom) with 10 nm wavelength span.

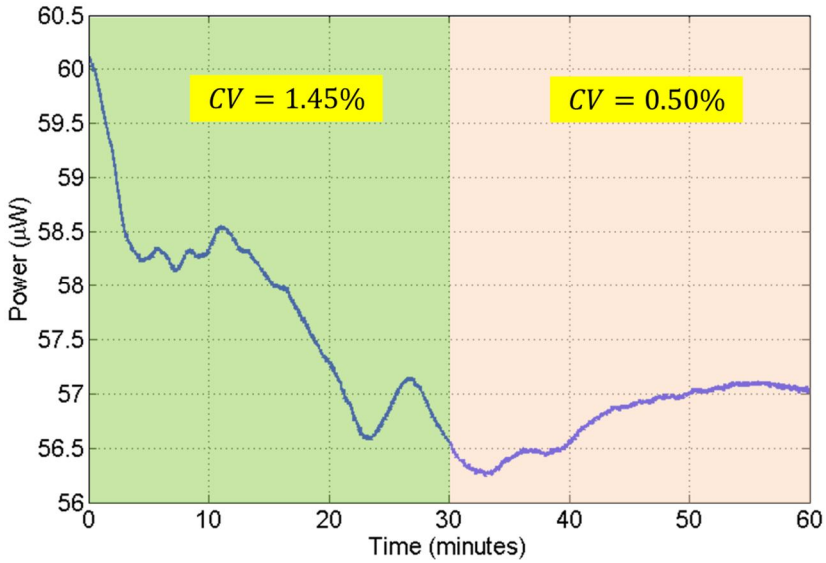

Figure 3-16 One example of power monitoring along with time (sampling per second) at a wavelength of 842 nm of a supercontinuum laser source (i.e. SuperK EXTREME EXW12, NKT Photonics, Denmark) operating at a repetition rate of 19.5 MHz. The power data was acquired using the Thorlabs PM100D power meter. The coefficient of variation (CV) is the ratio of the standard deviation (μ) to the mean (σ) of the power value measured per second.

In terms of the output optical power stability of the supercontinuum source in conjunction with the AOTF unit, one example of power monitoring as a function of time

at λ=842 nm can be seen in Figure 3-16. The output power fluctuation can be evaluated by considering the coefficient of variation (CV). The CV is the ratio of the standard deviation (μ) to the mean (σ) of the power value measured per second. It shows the power fluctuation over the hour since the source was turn on in our laboratory. It is evident to see that the emitting laser power changed significantly in the first half an hour (with the CV value of 1.45%) but tended to be much more stable in the second half (with the CV value of 0.5%). This strongly suggests that it is necessary to warm up the supercontinuum laser source before it can provide steady output power for measurements, in order to reduce additional fluctuations of photon counts in the TCSPC measurements.

3.4 Single-photon detectors used in the scanning depth imaging system

Both discrete and arrayed single-photon detectors were used with the scanning depth imaging system. Fibre-coupled discrete silicon SPAD, InGaAs/InP SPAD and NbTiN superconducting nanowire single photon detectors (SNSPDs) have been successfully used for the majority of scanning TOF depth imaging systems [3.12, 3.14, 3.21-3.22] reported in this Thesis. The advantages of the fibre-coupled single-photon detectors over free-space-coupled detectors include the reduced background noise and compatibility with standard connections in the receive channel. In terms of fibre connectors for the detectors, there are fibre pigtail assigned and fibre receptacle pre-aligned to the detectors. The fibre pigtail option is implemented with pre-optimised optical coupling to the detectors, but prohibits the usage of different fibre types which the receptacle pre-aligned option is designed to be compatible with. In terms of fibre types for the detectors, there are single-mode fibres (SMFs) and multimode fibres (MMFs). The SMFs can propagate single spatial mode well but have limited mode field diameter or numerical aperture, thereby restricting light-gathering capacity. MMFs chosen with appropriate core sizes and delivery lengths can balance the trade-off between the light-gathering capacity, collection of unwanted background and reduced spatial resolution. In addition, the scanning TOF depth imaging systems was used in conjunction with a free-space-coupled detector array – the work carried out using a 32×32 Si-SPAD array produced by the European-Commission-funded project, MiSPIA (Microelectronic Single-Photon 3D Imaging Arrays for low-light high-speed Safety and Security Applications) is described in detail in Chapter 5.

3.5 Data acquisition module in scan mode

For all the measurements reported in this Thesis, the TCSPC-based data acquisition modules were PicoHarp 300 and HydraHarp 400 by PicoQuant GmbH, Germany or the on-chip module for the 32×32 Si-SPAD arrays produced by the MiSPIA project. These devices, in conjunction with an external scanning system (see Figure 3-1), can record spatial origin of micro-time or macro-time photon events to construct a 2D array of waveform blocks and perform depth imaging. Each waveform block corresponds to a pixel of the image. There is a single waveform for single detection channel or multiple waveforms for multiplexing detection channels within a waveform block.

As shown in Figure 3-17, when the TCSPC measurements are synchronised to the scan clock pulses from the counters of the combined scanners in X and Y performing a raster scan, the data acquisition module is in a "scan sync in" mode (refer to Page 40 of [3.23]). Note that a pixel-clock pulse from the counter of the scanner in X sets the waveform block marker to the next pixel within a line. A line-clock pulse from the counter of the scanner in Y performs the beginning marker of the next line. On the other hand, a frame-clock pulse from the combined scanners in X and Y is employed as individual frame marker. The pixel-wise acquisition time is determined by the clock period of the scanner in X. Given the total scanning pixel numbers in X and Y, the collection time of a frame is known and thus scans of multiple frames can be accumulated (refer to Page 41 of [3.23]). The functionalities of scan mirror control and data acquisition are all integrated in the original custom software described in Page 72-75 of [3.24].

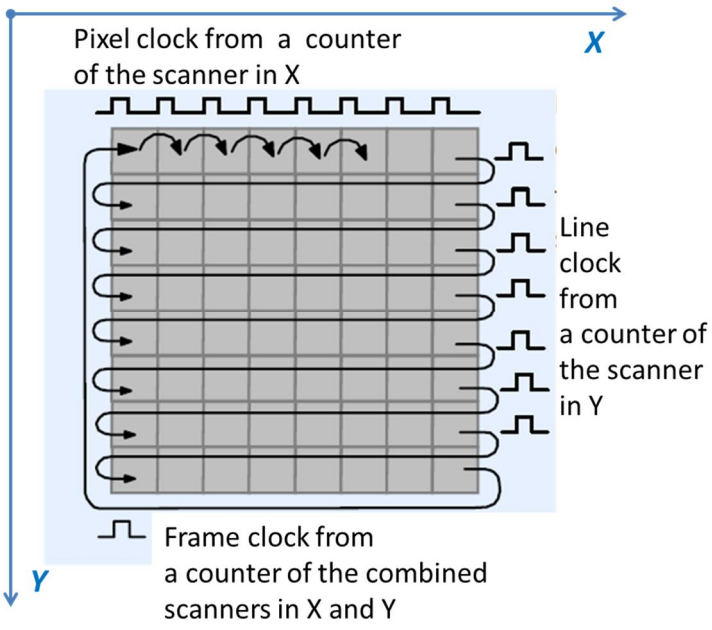

Figure 3-17 The operation of a "scan sync in" mode data acquisition. A raster scan recording is synchronised to the scan clock pulses from the counters of the external combined scanners in X and Y. (Reproduced from Page 40 of [3.23]).

3.6 Discussion

3.6.1 Overview of the scanning depth imaging systems

The generic optical path and control pipeline for the depth imaging systems reported in this Thesis can be seen in Figure 3-18. The digital-to-analogue converter was the National Instruments USB-6221 multifunction data acquisition device [3.25]. The USB-6221 was connected via a USB 2.0 port to a control computer. As seen in Figure 3-9, it generated the analogue control signal to the driver system of the scanning mirrors mounted in the transceiver unit. In addition, it provided a control voltage generation trigger as a marker for a pixel-wise TCSPC measurement. The TCSPC module was connected via a USB 2.0 port for data delivery to the control computer. The pipeline for the USB-6211 and TCSPC module was managed by the custom control and data acquisition software (Pages 72-75 of [3.24]) which was first developed by Dr. Nils J. Krichel, and further developed by Dr. Robert J. Collins, Dr. Nathan R. Gemmell and the author later on. In terms of the control pipeline, the schematic shown in Figure 3-18 details the Sync(1) and Sync(2) illustrated in Figure 3-1 as START and STOP respectively. Note that the TCSPC module illustrated in Figure 3-9 is in the forward start-stop configuration only for clear demonstration. The TCSPC module can be a discrete device or on-chip module integrated with the detectors. The START signal for the TCSPC module was from the synchronisation clock provided by the pulsed laser source directly, or generated using an external detector to sense part of the output laser light. The single photon detector module operated in free-running or gated mode. It is interesting to note that there was a bottleneck of acquisition time per pixel for the TCSPC measurements. It is derived from the inherent limited response time (~500 μs) of the specific galvanometer scan mirrors that were employed in our scanning imagers. In contrast, the data acquisition time of the TCSPC module can be much shorter than the response time of the scan mirrors. It is clear there is scope for increasing the scan response time by using faster galvo-mirrors.

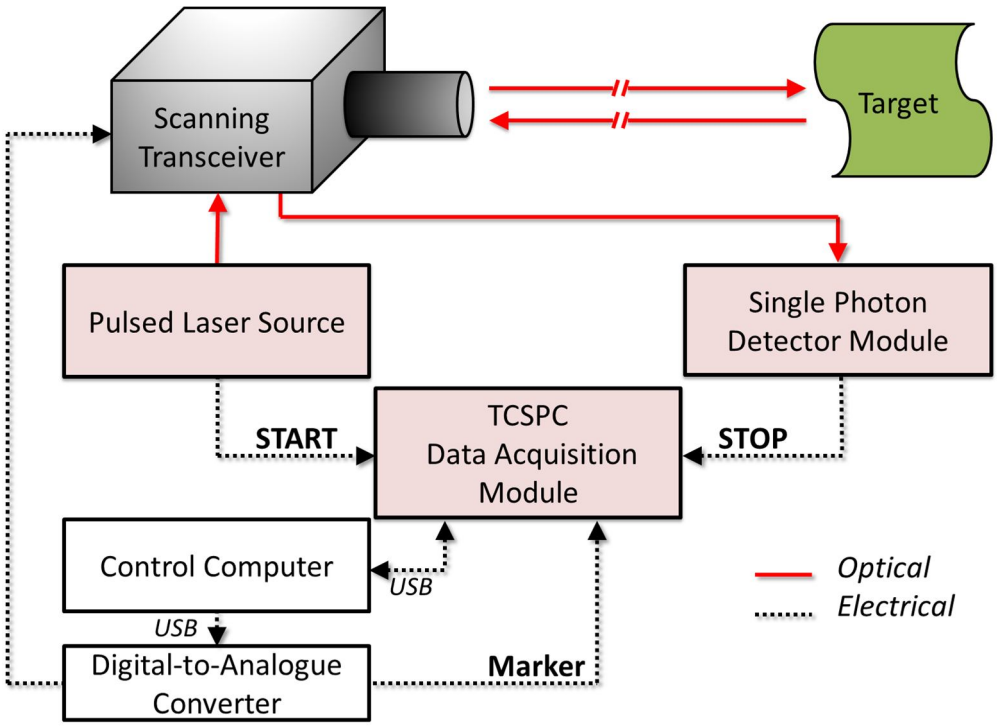

Figure 3-18 Generic optical path and control pipeline of the scanning depth imaging system. Note that the digital-to-analogue converter was the National Instruments USB-6221 multifunction data acquisition device [3.25]

3.6.2 Measurement setup

The typical configuration of the measurement setup for the depth imaging systems was implemented within the rooftop lab of David Brewster Building at Heriot-Watt University as shown in Figure 3-19. The rooftop lab offers a wide field of view for observation of targets located in several accessible field locations at stand-off distances of 40, 325, 910 and 4500 metres. The scanning transceiver system was put on the top of a rotation stage on a small optical bench. This allows horizontal adjustment of the system. There was a lifting jack underneath the optical bench, which is not only used to support the bench but also capable of tilting the system vertically. Other devices were arranged near the transceiver unit. This ensures that the minimum length possible of connection cables and delivery fibres could be employed between other devices and the transceiver system.

Figure 3-20 shows that an alignment CCD camera and lens mounted alongside the objective lens of the transceiver system are also on the rotation stage. The alignment camera in conjunction with an alignment monitor allows for visual location of the sensor's field of view for the operator.

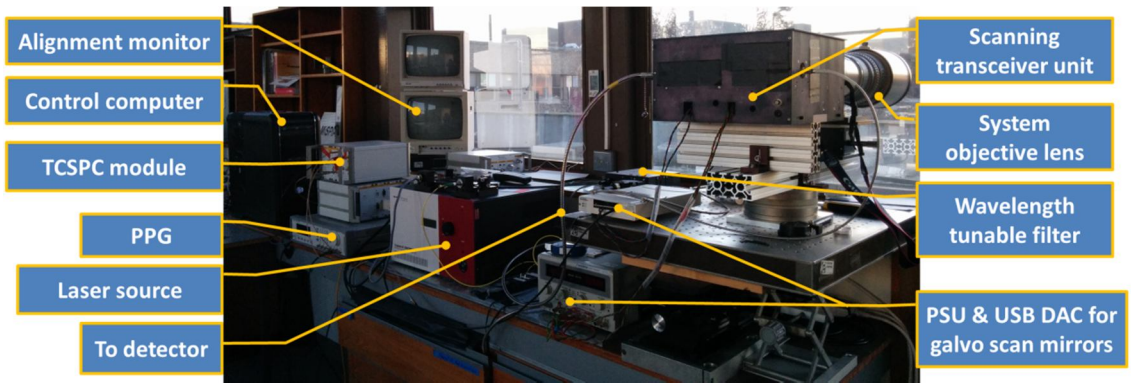

Figure 3-19 A typical configuration of the measurement setup for the depth imager in the rooftop lab of David Brewster Building at Heriot-Watt University. PSU: power supply unit; DAC: digital-to-analogue converter (i.e. National Instruments USB-6221); PPG: pulse pattern generator; TCSPC: time-correlated single photon counting.

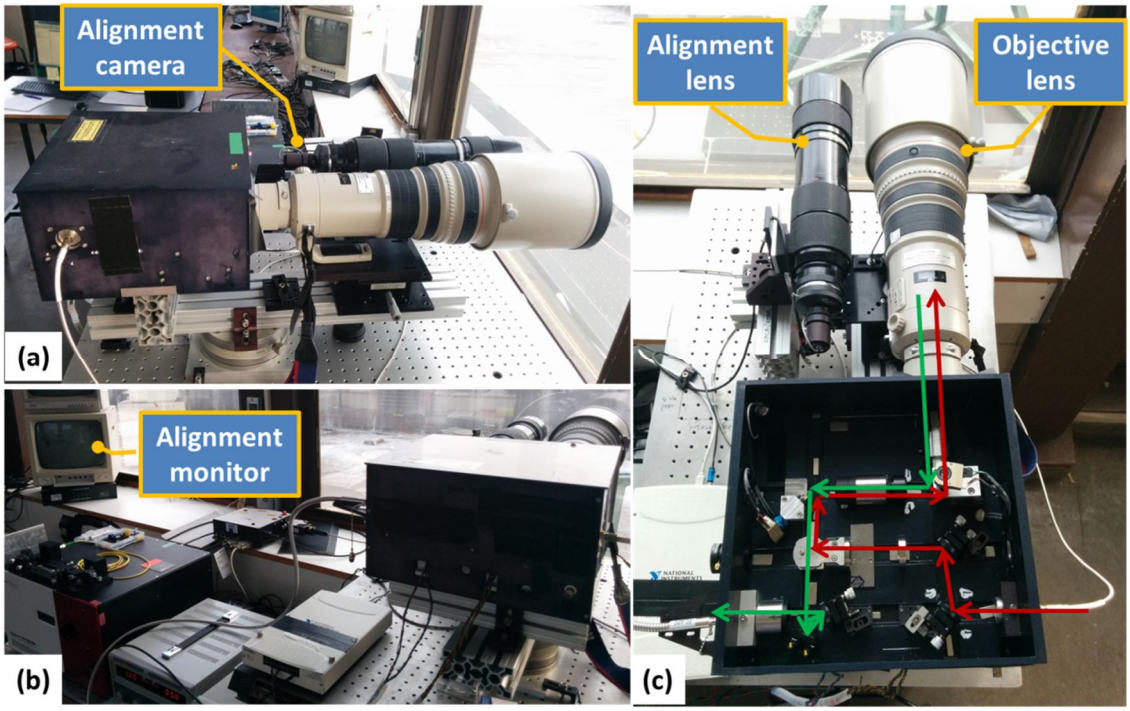

Figure 3-20 Different views of the transceiver system on the optical bench. (a) A side view of the system. An alignment camera with a lens alongside the system objective lens is mounted on the rotation stage. (b) The view approximately along the line-of-sight of the system of the target in the field. The alignment camera in conjunction with an alignment monitor can help to establish the field of view of the senor on the scene. (c) Top-view of the transceiver system. Note that the path in red indicates the transmitting light while the one in green illustrates the receiving light path.

3.6.3 Optical filtering at the receiver

The inherent time-gated filtering mechanism can distinguish the time-resolved signal

from the background noise with a constant power spectral density using TCSPC measurements. In order to perform detection with high signal-to-noise ratio, spectral and spatial filtering approaches can be also used in the receive channel to restrict the background noise originating predominantly from the solar background. The spectral filtering approach can be based on the dielectric optical filters or diffraction gratings. When a single, fixed operating wavelength is used, dielectric optical filters were chosen, which offered a combination of out-of-band rejection and high in-band transmittance. Once the objective lens, relay lenses, and the fibre collimators are fixed within the transceiver unit, the size of the received beam spot is determined at a specific target stand-off distance. In this case, the core of the fibre that is employed in the receive channel plays a role of a spatial filter. The core diameter of the receive fibre corresponds to an effective received aperture of ϕ_r on the target under test. As shown in Figure 3-21, three different sizes of ϕ_r against the same effective illumination aperture of ϕ_t on the target under test are illustrated.

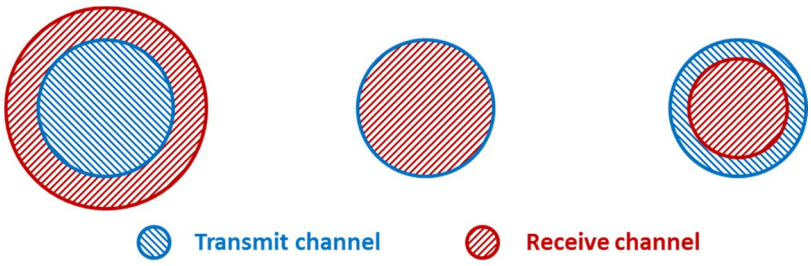

Figure 3-21 Effective illumination aperture (ϕ_t) for the transmit channel versus effective collection aperture (ϕ_r) for the receive channel. Left: $\phi_t < \phi_r$; Centre: $\phi_t = \phi_r$; Right: $\phi_t > \phi_r$.

The collection area of scattered return photons in the line-of-sight of the transceiver is located within the active illumination region (i.e. $\phi_t \leq \phi_r$), offering highly efficient collection of the scattered return photons. It can restrict background noise when $\phi_t = \phi_r$. By contrast, when $\phi_t < \phi_r$ there is a non-overlapping area. This area corresponds to the passive illumination region where the background noise is dominated. Thus, in this case, higher background noise is coupled by the transceiver. However, the advantage in this scenario is the higher tolerance for the beam wander effect, which commonly occurs in free space systems due to atmospheric turbulence. Note that the beam wander effect can be described as the real-time tracing of the centroid of the instantaneous beam spot. Each instantaneous beam spot is with a pattern of random wandering in the plane of a receiver aperture (refer to Pages 29-30 of [3.26]). The beam wander effect contributes to photon counts scintillation at the receiver (see Chapter 7).

In terms of $\phi_t > \phi_r$, the scattered photon collection efficiency is lower, but it can offer higher coaxial tolerance for background noise reduction and also better spatial resolution for 2D scan mapping. Thus, this was implemented in most of the imaging systems described in this Thesis. The scintillation, signal-to-background ratio and spatial resolution of the scanning system were characterised in Chapter 7 using a number of combinations of objective lenses with different focal lengths and receive fibres with different core diameters.

3.7 Conclusions

The scanning system developed has proved a very useful test-bed for long-distance depth imaging under a variety of operating wavelengths, and even in multiple wavelength use, as discussed later in the Thesis. The scanning system has also been used in conjunction with SPAD detector arrays with structured illumination. The alignment techniques described in section 3.2.4 for the transceiver assembly ensured that the scanning system was stable and worked over a very large dynamic range. Note that field trials carried out using the scanning system at stand-off working distances of 40 , 325 , 910 , and 4500 metres are reported later in the Thesis. In additon, the optical components and optomechanics of the transceiver assembly of the scanning system have shown good long-term mechanical stability with the assembly maintaining its optical alignment over the course of month-long field trials. Typically, these trials were conducted from our roof laboratory facility where the temperature can vary by about 10 °C over the course of a day.

The author, with assistance from Dr. Aongus McCarthy, devised the alignment techniques (described in section 3.2.4) for the relay and scan optics in the transceiver system. The author solely characterised the optical power spectra of the laser sources and carried out the power monitoring measurement of the supercontinuum laser source (described in section 3.3). The author made key contributions to the determination of appropriate optical components (by assessing their specifications and modelling in Zemax) and the developments of the transceiver systems with several different configurations and functions, which are more fully described in Chapter4 – 7.

3.8 References

[3.1]. M. A. Albota, R. M. Heinrichs, D. G. Kocher, D. G. Fouche, B. E. Player, M. E. O'Brien, B. F. Aull, J. J. Zayhowski, J. Mooney, B. C. Willard, and R. R. Carlson,

"Three-dimensional imaging laser radar with a photon-counting avalanche photodiode array and microchip laser," Appl. Opt. (41), 7671-7678 (2002).

[3.2]. J. J. Degnan, and D. N. Wells, "Scanner/optical system for three-dimensional lidar imaging and polarimetry," (U.S. Patent 8493445 B2, Jul 23, 2013).

[3.3]. "PicoHarp 300 User's Manual and Technical Data," PicoQuant GmbH, Ver (2.3).

[3.4]. C. Glennie, W. Carter, R. Shrestha, and W. Dietrich, "Geodetic imaging with airborne LiDAR: the Earth's surface revealed," Rep. Prog. Phys. (76), 086801 (2013).

[3.5]. G. Atanacio-Jiménez, J.-J. González-Barbosa, J. B. Hurtado-Ramos, F. J. Ornelas-Rodríguez, H. Jiménez-Hernández, T. García-Ramirez, and R. González-Barbosa, "Lidar velodyne hdl-64e calibration using pattern planes," International Journal of Advanced Robotic Systems (8), 70-82 (2011).

[3.6]. G. S. Buller, and A. M. Wallace, "Ranging and three-dimensional imaging using time-correlated single-photon counting and point-by-point acquisition," IEEE J. Select. Topics Quantum Electron. (13), 1006-1015 (2007).

[3.7]. National Institute of Standards and Technology USA, "Performance Analysis of Next-Generation LADAR for Manufacturing, Construction, and Mobility. Internal Report. Online (http://www.nist.gov/customcf/get_pdf.cfm?pub_id=822493) last accessed 12-07-2015," (2004).

[3.8]. P. F. McManamon, T. A. Dorschner, D. L. Corkum, L. J. Friedman, D. S. Hobbs, M. Holz, S. Liberman, H. Q. Nguyen, D. P. Resler, and R. C. Sharp, "Optical phased array technology," Proc. IEEE (84), 268-298 (1996).

[3.9]. J. Sun, E. Timurdogan, A. Yaacobi, E. S. Hosseini, and M. R. Watts, "Large-scale nanophotonic phased array," Nature (493), 195-199 (2013).

[3.10]. A. Yaacobi, J. Sun, M. Moresco, G. Leake, D. Coolbaugh, and M. R. Watts, "Integrated phased array for wide-angle beam steering," Opt. Lett. (39), 4575-4578 (2014).

[3.11]. Nutfield Technology, "QuantumScan seraies -Moving Magnet Galvanometer scanners. Datasheet. online (http://nutfieldtech.com/wp-content/uploads/2015/02/Nutfield-Techs-OPD-Galvo-Scanners-Data-Sheet.pdf) last accessed 13-04-2015."

[3.12]. A. McCarthy, R. J. Collins, N. J. Krichel, V. Fernandez, A. M. Wallace, and G. S. Buller, "Long-range time-of-flight scanning sensor based on high-speed time-

correlated single-photon counting," Appl. Opt. (48), 6241-6251 (2009).

[3.13]. N. S. Claxton, T. J. Fellers, and M. W. Davidson, "Laser scanning confocal microscopy," online (http://www.olympusconfocal.com/theory/LSCMIntro.pdf) last accessed 13-04-2015 (2006).

[3.14]. A. McCarthy, N. J. Krichel, N. R. Gemmell, X. Ren, M. G. Tanner, S. N. Dorenbos, V. Zwiller, R. H. Hadfield, and G. S. Buller, "Kilometer-range, high resolution depth imaging via 1560 nm wavelength single-photon detection," Opt. Express (21), 8904-8915 (2013).

[3.15]. Kphotonics, "Compact femtosecond mode-locked fiber laser engine CNT-1550 series. Datasheet. online

(http://nebula.wsimg.com/a7ca674e4c6e7d52de360320a3845e20?AccessKeyId=7586B3C14CE1F121F573&disposition=0&alloworigin=1) last accessed 13-04-2015."

[3.16]. K. Kieu, and M. Mansuripur, "Femtosecond laser pulse generation with a fiber taper embedded in carbon nanotube/polymer composite," Opt. Lett. (32), 2242-2244 (2007).

[3.17]. N. Savage, "Supercontinuum sources," Nat. Photonics (3), 114-115 (2009).

[3.18]. "Supercontinuum Generation in Photonics Crystal Fibers," (NKT Photonics, 2009).

[3.19]. J. M. Dudley, G. Genty, and S. Coen, "Supercontinuum generation in photonic crystal fiber," Rev. Mod. Phys. (78), 1135-1184 (2006).

[3.20]. T. Schönau, S. Riecke, A. Bülter, and K. Lauritsen, "Modern Pulsed Diode Laser Sources for Time-Correlated Photon Counting," Springer Series on Fluorescence (2014).

[3.21]. A. McCarthy, X. Ren, A. Della Frera, N. R. Gemmell, N. J. Krichel, C. Scarcella, A. Ruggeri, A. Tosi, and G. S. Buller, "Kilometer-range depth imaging at 1550 nm wavelength using an InGaAs/InP single-photon avalanche diode detector," Opt. Express (21), 22098-22113 (2013).

[3.22]. A. M. Wallace, A. McCarthy, C. J. Nichol, X. Ren, S. Morak, D. Martinez-Ramirez, I. H. Woodhouse, and G. S. Buller, "Design and Evaluation of Multispectral LiDAR for the Recovery of Arboreal Parameters," IEEE Trans. Geosci. Remote Sens. (52), 4942-4954 (2014).

[3.23]. W. Becker, *The bh TCSPC Handbook, 2nd Edition* (Becker&Hickl GmbH 2006).

[3.24]. N. J. Krichel, "Long-range depth profiling based on time-correlated single-photon counting," PhD Thesis, Heriot-Watt University (2011).

[3.25]. National Instruments, "M Series Multifunction DAQ for USB - 16-bit, 250 kS/s, up to 80 Analog Inputs. Datasheet. online (http://www.ni.com/datasheet/pdf/en/ds-10) last accessed 11-06-2015."

[3.26]. L. C. Andrews, R. L. Phillips, and C. Y. Hopen, *Laser beam scintillation with applications* (SPIE press, 2001).

Chapter 4
Kilometre-range depth imaging using single-pixel single-photon detectors at λ ~ 1550nm

4.1 Motivation for depth imaging at λ ~ 1550nm

Time-of-flight (TOF) light detection and ranging (LiDAR) systems have been used for a variety of remote sensing applications including terrain mapping, environmental monitoring, and security [4.1-4.3]. A new class of LiDAR system based on time-correlated single-photon counting (TCSPC) techniques [4.4-4.5] has emerged in recent years. As reviewed in Chapter 2, in comparison with conventional TOF LiDAR systems [4.6], TOF ranging and imaging can be extended to the shot noise limit using detectors with single-photon sensitivity [4.3] which offers excellent surface-to-surface resolution and an inherent flexibility in the trade-off between acquisition time and depth resolution [4.4, 4.5]. There are a number of detector choices for single-photon LiDAR systems operating at wavelengths shorter than 1000 nm, for example: micro-channel plate (MCP) detectors [4.7], photomultiplier tubes (PMTs) [4.8] or silicon-based single-photon avalanche diodes (SPADs) [4.9-4.12]. Highly optimised individual SPADs have been used in a number of single-photon counting systems but significant progress has also been made on the development of CMOS Si-SPAD arrays and their use in TOF depth imaging systems [4.13-4.15].

Compared to the single-photon imagers operating at visible wavelengths, systems working in the short-wavelength infrared (SWIR) range (1400 to 3000 nm) have the advantages of being less affected by solar background noise and less attenuated by the atmosphere (see Figure 4-1). Moreover, they remain eye-safe at significantly higher power levels than wavelengths in the retinal hazard region of the spectrum which extends from 400 to 1400 nm [4.16]. Innovations in both single-photon detectors [4.17-4.18] and data acquisition technology [4.4] in recent years have transformed TCSPC into an advantageous and practical approach to next generation TOF range-finding and

depth imaging systems in particular. In this wavelength band, existing optical telecommunications component technology can be used in these depth imagers if operated at 1310 nm and 1550 nm wavelengths.

Recently, superconducting nanowire single photon detectors (SNSPDs) have demonstrated promising results for infrared single-photon detection with low noise and excellent timing jitter performance [4.19-4.20], and have been successfully used for ranging [4.21] and depth imaging at long distances [4.22]. SNSPDs require cooling to temperatures typically less than 4 K [4.20, 4.23], but miniaturised closed-cycle cooling has made this considerably more practical in recent years. High-performance SNSPD devices can play a crucial role in certain applications, and hence its relatively large dimensions and high power consumption cannot be regarded as prohibitive factors in many cases.

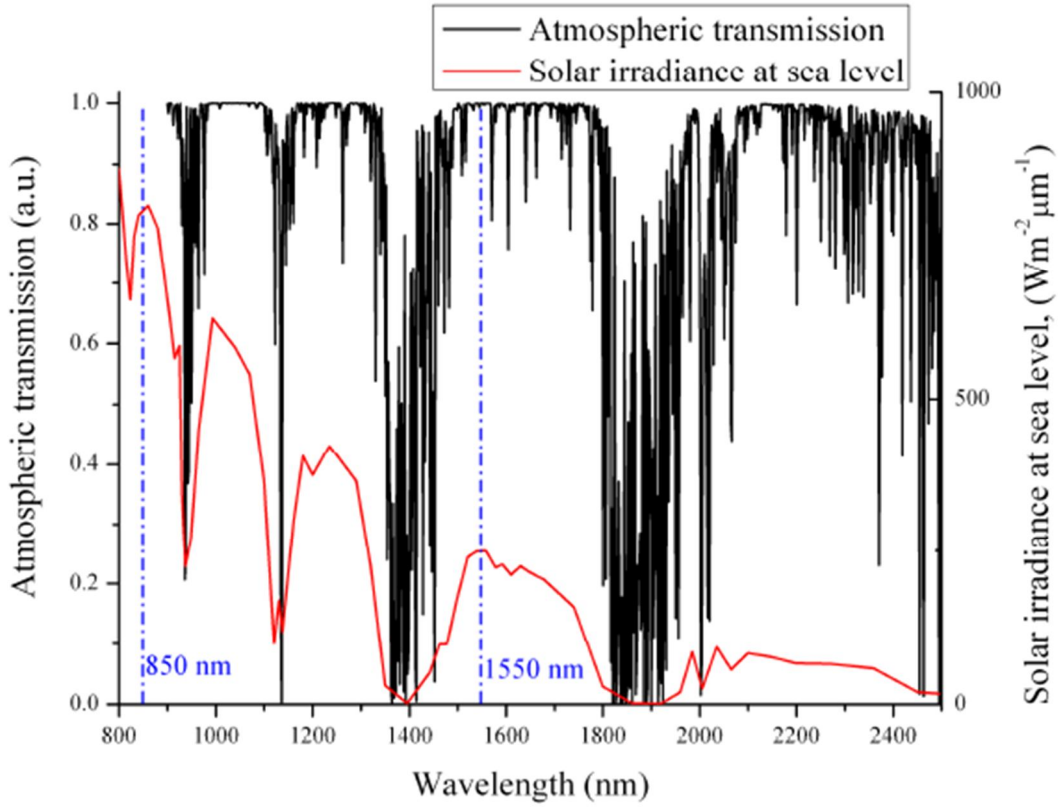

Figure 4-1 Spectral atmospheric transmission (in black) and solar irradiance at sea level (in red) at a wavelength range from 800 to 2500 nm. (From Page 213 of [4.24]).

Semiconductor-based single-photon detectors operating at SWIR region generally have had issues with significantly increased dark count rates [4.19] compared to SNSPD devices. However, there have been reports of measurements made using SPAD arrays fabricated from InGaAsP/InP and InGaAs/InP operating at 1064 nm [4.25] and 1550 nm

wavelength [4.26] respectively, as well as with arrays of Sb-containing devices [4.27] although kilometre-range depth imaging with such devices has not been reported in the literature. From the standpoint of compact LiDAR system designs, which are compatible to a variety of application platforms, miniaturised modules with solid-state InGaAs/InP SPADs are the outstanding candidates.

Prior to the author joining the Single Photon group led by Professor Gerald S. Buller at Heriot-Watt University in June 2011, TOF depth imaging had been carried out using wavelengths around 850 nm. Part of the research work in this Thesis concentrated on the development of two eye-safe kilometre-range depth imaging systems using a discrete SNSPD device at λ=1560 nm and an InGaAs/InP SPAD module at λ=1550 nm. Dr. Aongus McCarthy, Dr. Nils J. Krichel, Dr. Nathan R. Gemmell and the author developed the depth imaging system with the SNSPD provided from Professor Robert H. Hadfield's Quantum Sensor group. The measurements were carried out using this system in November 2011. One year later, in November 2012, Dr. Aongus McCarthy, Dr. Nathan R. Gemmell and the author developed a new imager with the prototype InGaAs/InP SPAD module provided from Dr. Alberto Tosi's group. We used the system to carry out several field trial measurements with the assistance of Adriano Della Frera. Dr. Aongus McCarthy, Dr. Robert J. Collins and Dr. Nils J. Krichel contributed to the original design of the scanning transceiver unit, system control and scan data acquisition software and also the data analysis Matlab scripts for both depth imaging systems. Dr. Aongus McCarthy, Dr. Nathan R. Gemmell and the author processed the data related to all results present in this Chapter. It should be noted that it was the successful trial of the system with the SNSPD that directly led to the attempt at field trials with the InGaAs/InP SPAD module.

4.2 Overview of the employed SNSPD and InGaAs/InP SPAD device configurations

4.2.1 The SNSPD device

The SNSPD device structure used on the field trials is shown in Figure 4-2 (a). The device consisted of a structured NbTiN film on a Si substrate whose top is covered with a 225-nm-thick SiO_2 to achieve improved detection efficiency at telecom wavelengths. This is because the constructive interference from the SiO_2/Si interface contributes to enhanced reflection for the incident light at telecom wavelengths and ensures a maximum in the electric field at the thin superconducting layer, resulting in increased

optical absorption within the NbTiN film. The device chip consisted of a 10 µm×10 µm detector with a meander 6-nm-thick, 100-nm-wide and 200-nm-pitch wire. It was mounted inside a Gifford-McMahon refrigerator system and cooled down to a temperature of 2.8 K. Incident photons were coupled into the chip by a single-mode optical fibre (as seen in Figure 4-3, the detector had a single mode fibre coupling configuration). A white-light interferometer was used to align the chip-to-fibre spacing (i.e. d shown in Figure 4-2 (a)) and it was less than 10 µm at a temperature of 2.8 K. For the structure shown in Figure 4-2(a), the wavelength-dependent absorption of the NbTiN layer was designed using transfer matrix simulations of multilayer reflectivity. The thickness of the SiO_2 layer designed for an optimum wavelength of 1300 nm was equal to $\lambda_{eff}/4$. Note that the effective wavelength of the device is denoted as $\lambda_{eff} = \lambda/n$, where n is the refractive index of SiO_2. Although the optimum operating wavelength was 1310 nm, the device was enhanced in efficiency over the wavelength range from 830 to 1700 nm, as shown in Figure 4-2(b). The input light was coupled to the detector by the standard telecommunication single-mode optical fibre and portion of the fibre was placed inside the refrigerator. This coupling approach helps in filtering out a large proportion of room temperature black body radiation [4.20].

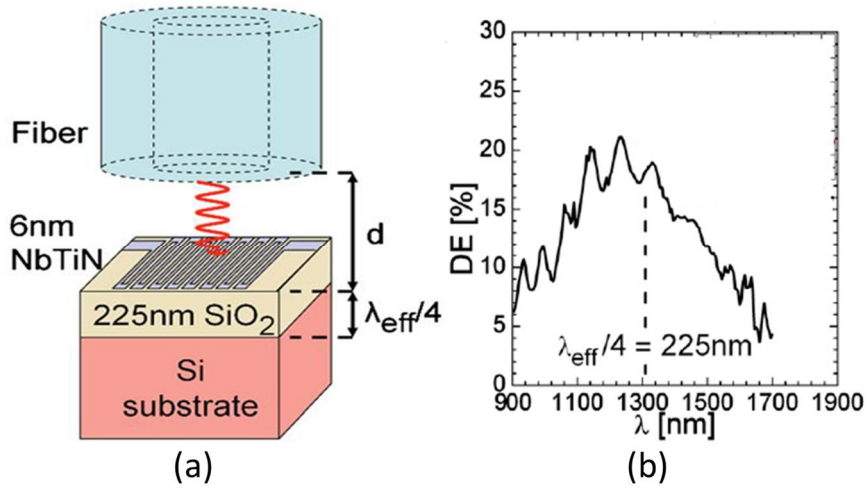

Figure 4-2 (a) Schematic of a front-side fibre-coupled NbTiN SNSPD device with a structure designed for enhancement of photon absorption at the short infrared wavelength. (b) Single-photon detection efficiency spectrum at a dark count rate of 1.7 kHz. This plot represents the polarisation-independent average detection efficiencies produced by a series of proper measurements. (Reproduced from [4.20]).

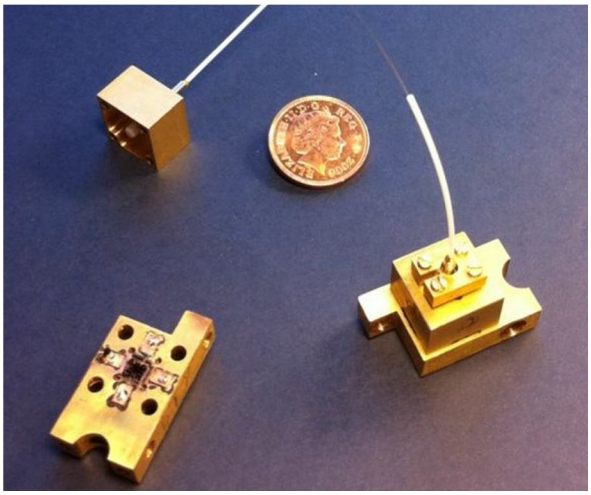

Figure 4-3 Close-up photograph of a single mode fibre coupled SNSPD. (From [4.28]).

4.2.2 The InGaAs/InP SPAD detector module

A fully programmable detection module with a fibre-pigtailed InGaAs/InP SPAD detector, as shown in Figure 4-4, was employed for the field trials. The InGaAs/InP SPAD detector manufactured by Princeton Lightwave Inc., USA is a back-illuminated photodetector with an active area diameter of 25 μm and it was cooled down to ~230 K by means of a three-stage in-package thermo-electric cooler controlled by a temperature controller. The detector was sensitive to wavelengths up to λ ~ 1700 nm. The module was combined with custom control software for set-up and re-configurability. It offered adjustable photon detection efficiency and hold-off time, while its gate width could be varied from 1 ns to 500 ns. The module could be triggered at frequencies of up to 133 MHz by an internal or external clock.

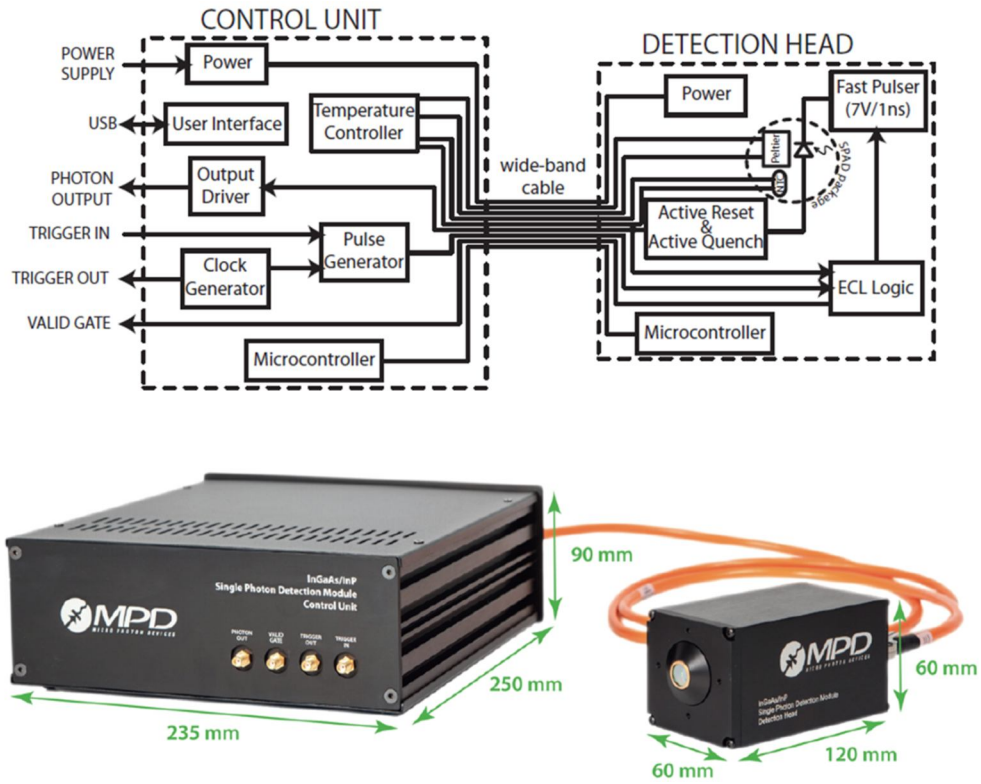

Figure 4-4 Top: Block diagram of an InGaAs/InP-SPAD-based single-photon detection module which consists of a control unit (left) and a detection head (right); Bottom: Close-up photograph of the detection module with dimensions, which is joint by a wide-band cable between the control unit (left) and the detection head (right) shown with free-space coupling option. (From [4.29]).

In order to minimise the strong afterpulsing which leads to increased dark counts and impairs the detection efficiency of the InGaAs/InP SPAD, it is desirable to operate the device in gated mode. Low-frequency (typically at ~100 MHz) gating and discrimination electronics are employed as shown in Figure 4-5. As a combined mechanism of passive (PQ), active (AQ), and fast-active (FAQ) quenching enables both at the anode and at the cathode of the SPAD a fast quenching time is implemented (as short as < 1 ns to significantly mitigate afterpulsing). The gate transient suppression is achieved by using a cancellation mechanism of the gate transients. The circuitry implementation is to add a "dummy" capacitive path which has only spurious capacitive spikes whereas the SPAD path has both avalanche signal pulse and spurious capacitive spikes. Eventually, the avalanche signal can be revealed from the difference between the two paths which is sensed by a comparator [4.29]. In terms of its compensation approach on the gate transients, the cost-efficient designed electronics in the module have the advantage of controllability on gate-off time over other methods [4.30-4.31].

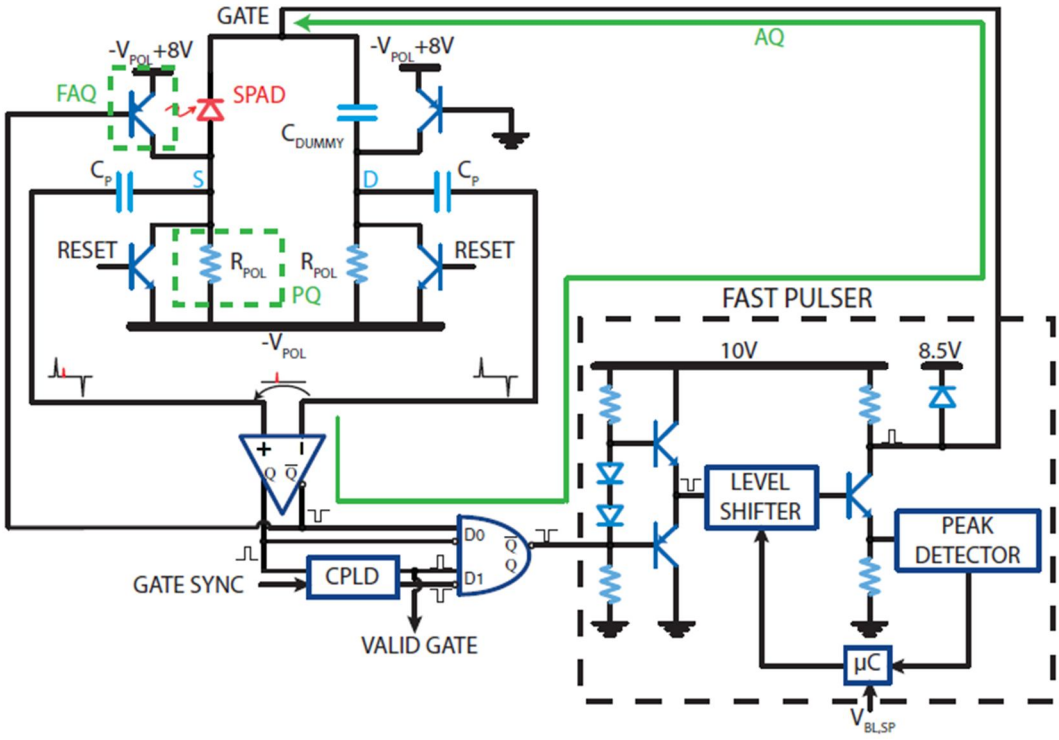

Figure 4-5 Front-end quenching and discrimination electronics, and circuit of fast pulser. A combined mechanism of passive (PQ), active (AQ), and fast-active (FAQ) quenching enables both at the anode and at the cathode of the SPAD. Thus, a fast quenching time is as short as <1 ns to significantly mitigate afterpulsing. The gate-transient suppression is achieved by using a cancellation mechanism of the gate transients. The circuitry implementation is to add a "dummy" capacitive path, which has only spurious capacitive spikes whereas the SPAD path has both avalanche signal pulse and spurious capacitive spikes. Eventually, the avalanche signal can be revealed from the difference between the two paths, which is sensed by a comparator. (From [4.29]).

4.3 Experiments and results

4.3.1 Scanning depth imager using a SNSPD

4.3.1.1 System description

A schematic of a scanning depth imaging system using a SNSPD is shown in Figure 4-6(a) and the whole imaging system in the lab is shown in Figure 4-6(b). The scanning transceiver (see Chapter 3) was adapted from previous work at 842 nm wavelength and reconfigured for use at λ=1560 nm. A mode-locked fibre laser was provided from Prof. Robert H. Hadfield's group in 2011. This fibre laser with a central wavelength of 1560 nm, a pulse repetition rate of 50 MHz, a pulse width of <1 ps, and a typical

maximum average output power of 2 mW was employed as the illumination source. Due to the range ambiguity effects of high frequency, periodic illumination caused by multiple indistinguishable illumination pulses in transit at any given point, the 50 MHz periodic repetition rate of the laser meant that we were limited to making depth profiling measurements rather than absolute depth measurements. In theory, it is obvious that increasing the repetition rate results in a reduction in the maximum depth-of-field for the depth profiling. The repetition rate of the employed fibre laser was fixed at 50 MHz, but it allowed the depth profiling with a maximum depth-of-field of 3 metres, which was suitable to cover all the scanned remote targets in this Chapter. Future work will implement the use of pseudorandom pulse trains in order to overcome this range ambiguity issue found at high laser repetition rates [4.12]. The output light from the 90% channel of a fibre splitter was coupled into the transmit channel of the scanning transceiver. The 10% output channel from the fibre splitter was directed to a trigger detector (i.e. a fibre-coupled, high-speed InGaAs APD, DET10C/M from Thorlabs), whose output was used as the start signal for the TCSPC [4.4] hardware module. This start trigger signal, with a frequency of 50 MHz, was electrically down-divided to a frequency of 1.57 MHz in order to match the working range of the TCSPC module. This module had 20 ps Full Width at Half Maximum (FWHM) jitter and was configured with a 16 ps time bin width.

A pair of galvanometer mirrors in the transceiver enabled the laser beam to be raster scanned across the target scene through computer control. The transmit and receive channels of the custom scanning transceiver were coaxial and the two galvanometer mirrors were common to both channels. These channels were separated via a polarising beam splitter only after the return signal had reflected from both galvanometer mirrors. The objective lens was a cemented, achromatic doublet with a focal length of 500 mm and an 80 mm diameter aperture. The scattered target return collected by the transceiver was spectrally filtered. The collected photon flux from the receiver channel of the scanning transceiver was delivered to a superconducting nanowire single-photon detector (SNSPD) system [4.23] via a 2 metre long armoured single mode optical fibre. This generated a stop trigger pulse for the TCSPC module.

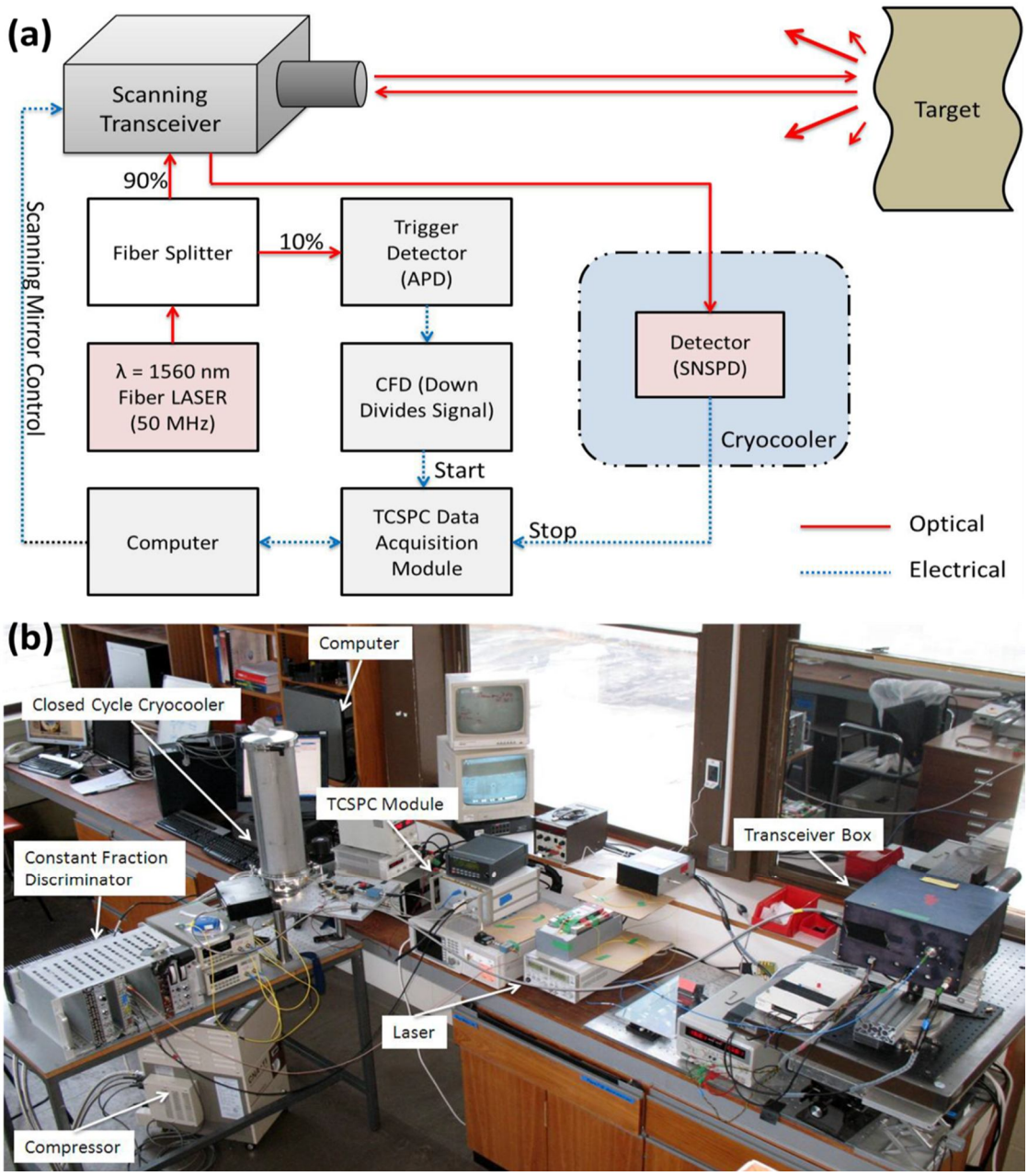

Figure 4-6 (a) Schematic of the photon counting depth imaging system based on sub-picosecond 1560 nm wavelength illumination and a superconducting nanowire single-photon detector (SNSPD). CFD, constant fraction discriminator; APD, avalanche photodiode; TCSPC module, time correlated single-photon module. (From [4.22]). (b) Photograph of the depth imaging system in the lab, and the closed cycle cryocooler along with the compressor are shown.

In all the measurements reported here, the average emitted optical power was less than 250 μW. As shown in Figure 4-7, the detector was maintained at an operating temperature of ~3 K. When biased at a level consistent with a 1 kHz dark count rate, the SNSPD had a practical single-photon detection efficiency of 18% at 1560 nm wavelength. Output voltage pulses from the SNSPD were amplified (580 MHz, 3dB

roll off) outside the cryostat at room temperature and routed to the TCSPC module. Spatial and spectral filtering of the return signal within the transceiver unit ensured that even under bright daylight conditions, the solar background level was limited to a maximum of approximately 8 kHz. The overall system instrumental timing response of the system was <100 ps FWHM (see the inset in Figure 4-8) which, owing to the increased complexity of this transceiver setup, was marginally greater than the timing jitter achieved in our first 1550 nm wavelength single photon depth ranging tests with SNSPDs [4.21].

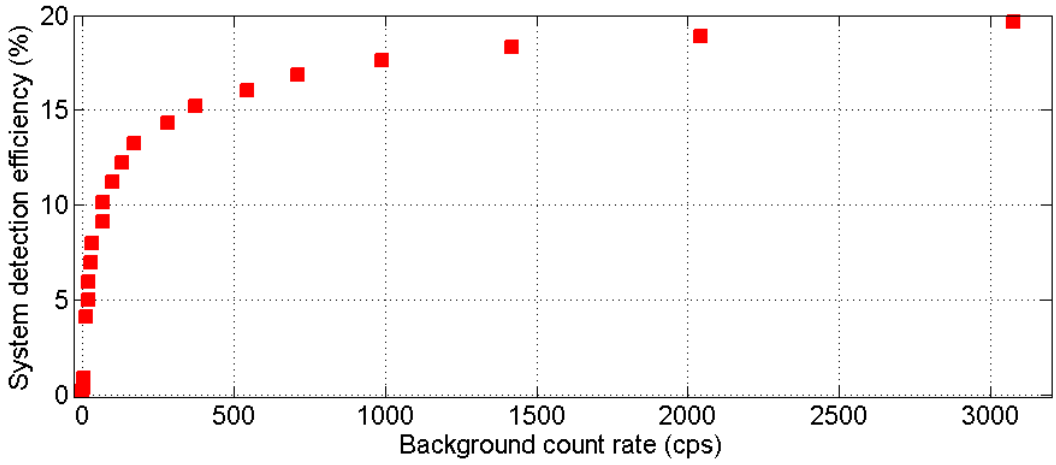

Figure 4-7 System detection efficiency versus background count rate of the employed NbTiN SNSPD device at an operating temperature of ~3 K. Note that a system detection efficiency of ~18% at a background count rate of ~1 kcps for the SNSPD were configured during the measurements.

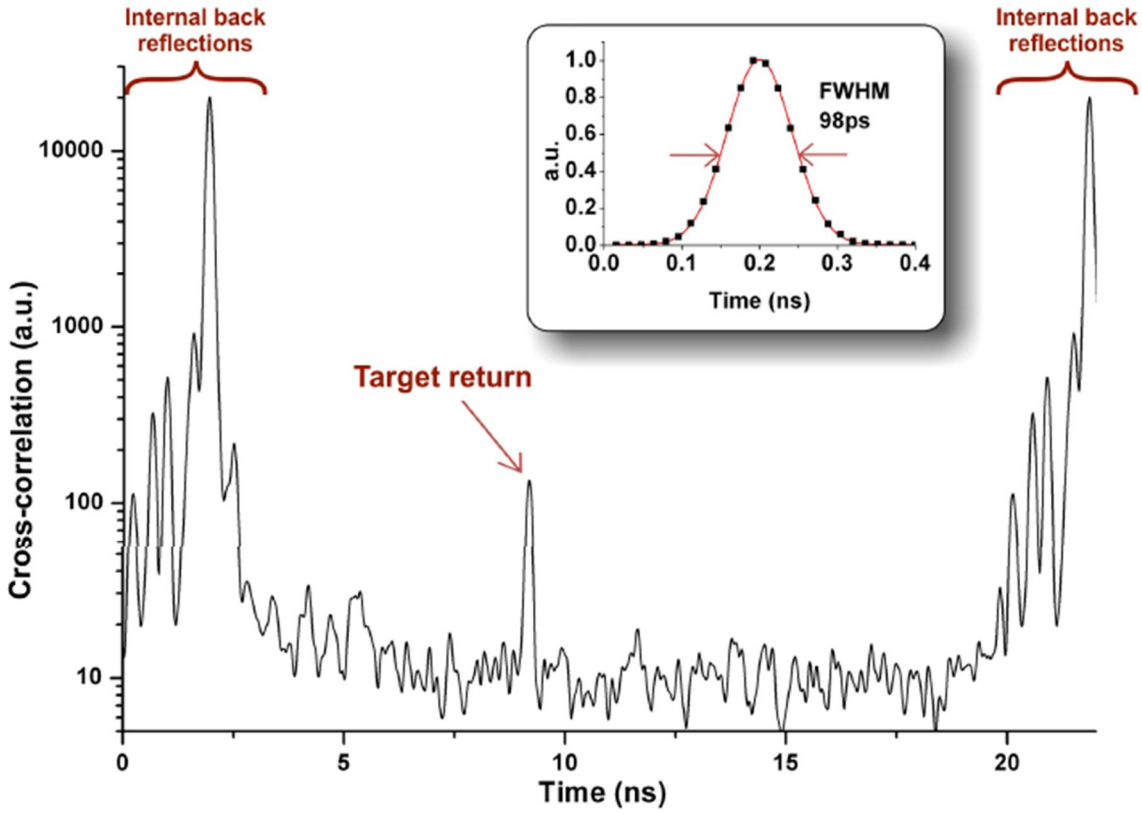

Figure 4-8 Processed histogram by cross-correlation method. Example of the cross-correlation function C of a processed pixel shows the return peak (at approximately 9 ns) standing clearly above the background. Also present are the internal back reflections from the scanning system. The inset shows a normalised instrumental response of the system with 98 ps Full Width at Half Maximum (FWHM) timing jitter. (From [4.22]).

The detected photon events were time-tagged by the TCSPC module and streamed to the control computer. Software reconciled this photon return timing with field position in order to calculate depths at individual target positions, producing a depth image of the scanned optical field. An instrumental reference response was constructed by taking a histogram from retro-reflective material over a long integration time (using the same 16 ps bin width as in the scan measurements). A peak from this measurement was then isolated and normalised in height, shown in the inset of Figure 4-8. A cross-correlation algorithm written in house (based on that presented in [4.32]) analyses the histogram for each pixel in a scan. It begins by preparing a periodic reference response (R), of equal length to the histogram (H), containing multiple versions of the instrumental reference peak spaced equally at the period of the fibre laser's output. A cross correlation (C) can then be calculated via: $C = F^{-1}[F(H).\times F^{*}(R)]$, where F denotes fast Fourier transform, and $.\times$ denotes element-wise multiplication. An example of C is shown in

Figure 4-8. The calculation of $F^*(R)$ is performed only once per scan to speed up processing. This cross correlation discriminates against random noise peaks, amplifying the probability of finding a target return signal amongst noise. The algorithm checks for a peak within the cross correlation by looking for the highest signal within the time window which does not contain any back reflections (determined by the user), and outputs the position of its maximum. This position can then be converted from bin number (time) into a distance. A 4500 pixel depth image, such as those in Figure 4-9, was processed in under two minutes on a standard desktop computer.

4.3.1.2 Depth profiling results

The measurements were made by using the imager at stand-off distances of 325 metres, 910 metres and 4500 metres. These distances correspond to suitable locations (see Figure 4-10) to which we had both access and a clear line-of-sight from our roof laboratory facility. We used a clothed, life-size mannequin as a target object for initial field trials. Figure 4-9 shows scans of the same scene acquired at a stand-off distance of 325 m in daylight conditions, using different per-pixel dwell times. The depicted surface plots clearly demonstrate reliable target resolution at dwell times as short as 1 ms per pixel; even at the shortest per-pixel dwell time of 0.5 ms, the majority of the depth pixels were resolved correctly. At long dwell times, the uncertainty on the per-pixel target return intensity is low enough to convey another layer of information. In addition, as the acquisition time changes, it results in different per-pixel detected photon numbers, which are also material-dependent as shown in Figure 4-11. The surface plot's colour mapping can be set to correspond to the calculated number of detected return photons in the histogram peak for each individual pixel. This is shown in the 10 ms per pixel intensity images in Figure 4-12(c) and Figure 4-12(f). Clear intensity differences are evident, based on the material type and the angle of the surface relative to the incident beam. It is apparent from the depth image shown in Figure 4-12(e) that the returns from human skin were very low in comparison to the other materials. This results in the majority of the facial pixels having insufficient detected return photons to provide depth information for this acquisition duration when illuminated with 1560 nm wavelength. This is consistent with the findings of Bashkatov *et al.* who reported reduced scattering from human skin and subcutaneous tissue at wavelengths in the vicinity of λ = 1550 nm when compared to λ = 850 nm [4.33].

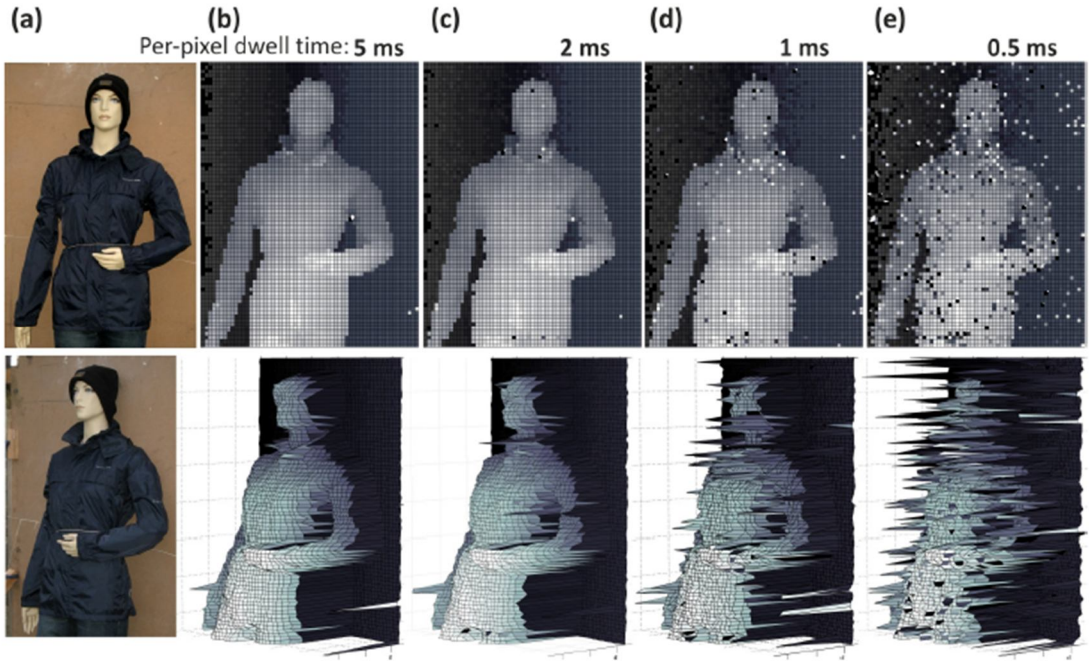

Figure 4-9 Depth profile measurements made in daylight on a life-size mannequin from a stand-off distance of 325 metres. The images shown in column (a) are close-up photographs showing different viewpoints of the scene which consisted of the mannequin against a 6 mm thick median-density fibreboard (MDF) sheet. This MDF sheet acted as a backplane. The depth scans were acquired in daylight and each scan covered an area of approximately 800×1000 mm using 60×75 pixels, resulting in a pixel-to-pixel spacing of approximately 13 mm in X and Y. Plots of the depth data obtained for per-pixel acquisition times of 5, 2, 1, and 0.5 ms are shown in columns (b) through (e) – each of these columns show two different viewpoints of the surface plot constructed from the data obtained using the specified per-pixel dwell time. A per-pixel dwell time of 1 ms equated to a total scan time of 4.5 s for this scene. The face-on view shown in the top row gives an indication of the spatial resolution of the system, and the centimetre-scale depth resolution can be gauged from the oblique view in the bottom row. The colour shading in the plots is used to map depth, and the images are surface plots of the raw depth data for all pixels i.e. no curve fitting or extrapolation has been applied to enhance the data returned by the system. (From [4.22]).

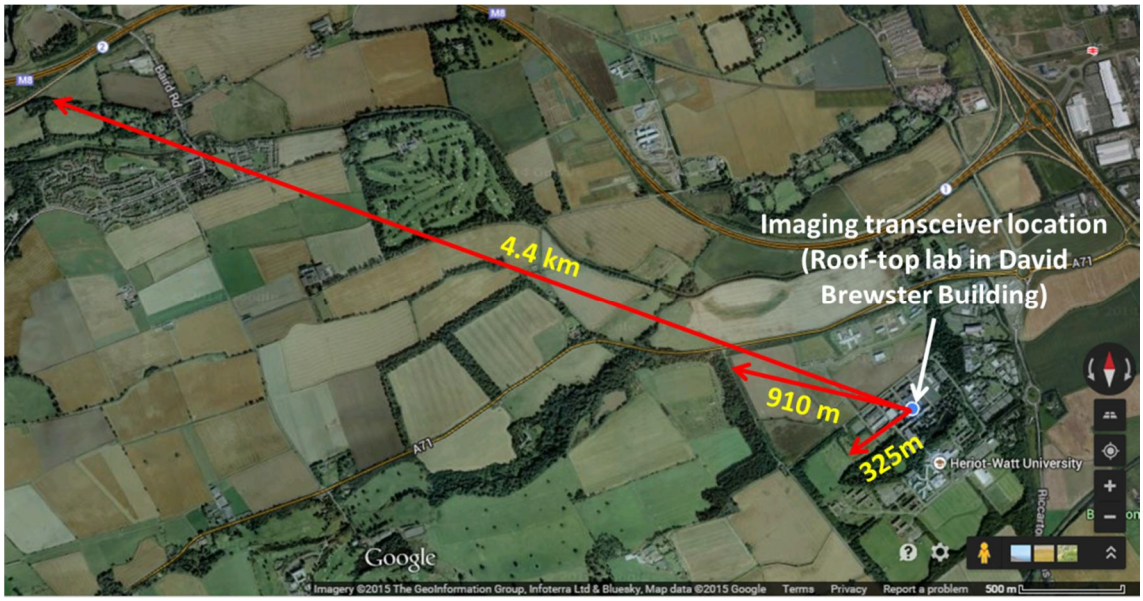

Figure 4-10 Satellite photograph of the accessed target ranges which are approximate laser beam paths. (Reproduced from Google Earth).

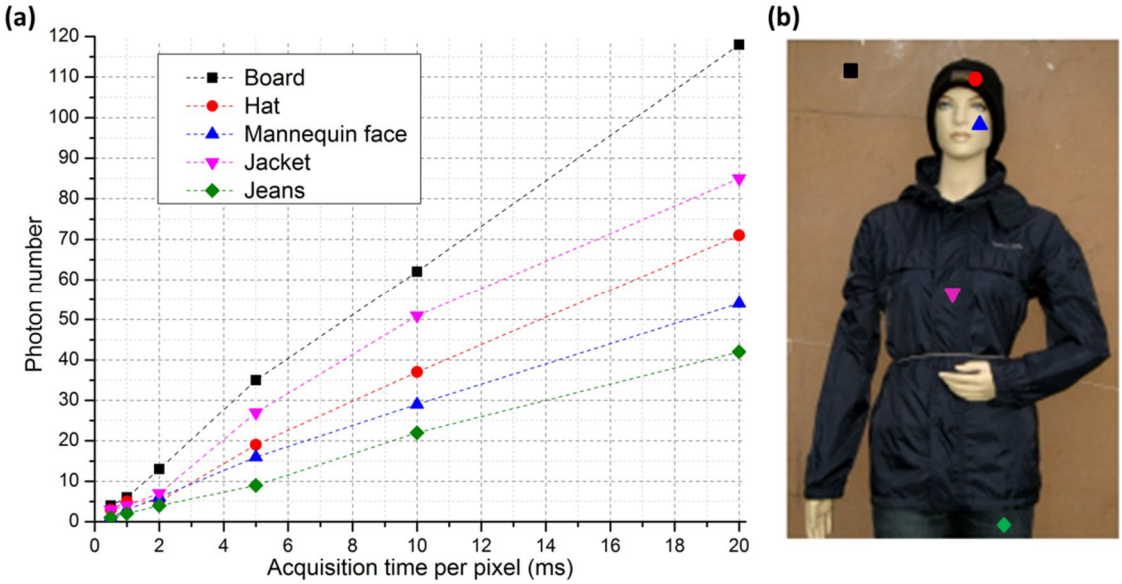

Figure 4-11 Material-dependent integrated photon number versus acquisition time per-pixel. The data for the graph shown in (a) was extracted from depth profile scans acquired in daylight of a life-sized mannequin at a stand-off distance of 325 m. Acquisition times of 0.5, 1, 2, 5, 10, and 20 ms per-pixel were used. Note that the integrated photon number is a nine-pixel-based average using a single pixel and eight neighbours. The dashed lines in the graph, linking the set of data points for each material, are included as a guide for the reader. The pixel locations corresponding to the plotted data are indicated in the photograph shown in (b).

Apart from scanning the non-cooperative hard target, measurements on a distributed target such as a tree were made using the depth imager. As shown in Figure 4-13(a), a tree was mounted horizontally for measurements. The top of the tree was closest to the roof lab. Several plywood sheets, standing perpendicular to the trunk and resting against the top of the plant pot, acted as a backplane. The distance from the backplane plywood board to the top of the tree was ~2.5 m, which corresponds to a time-of-flight round-trip time of ~16 ns. The truck of the tree is ~0.8 m above the ground. This setup was used in order to simulate an aerial measurement. A 10×10 pixel scan using a per pixel acquisition time of 10 s was done on the area annotated in Figure 4-13(b). The accumulated 100-pixel photon count histogram (see Figure 4-13(c)) (by chopping off the internal back reflections) can be used to reveal different layers of the tree and the back plywood board. In order to confirm this, several single-pixel measurements were carried out with a per pixel acquisition time of 20 s on a number of specific location points (see Figure 4-13(d)) of the tree and the back plywood board. As shown in Figure 4-13(e), the overlaid histogram plots of returns obtained from four points (three on the tree canopy and one on the board) can be evident to present the locations of interest within the scene.

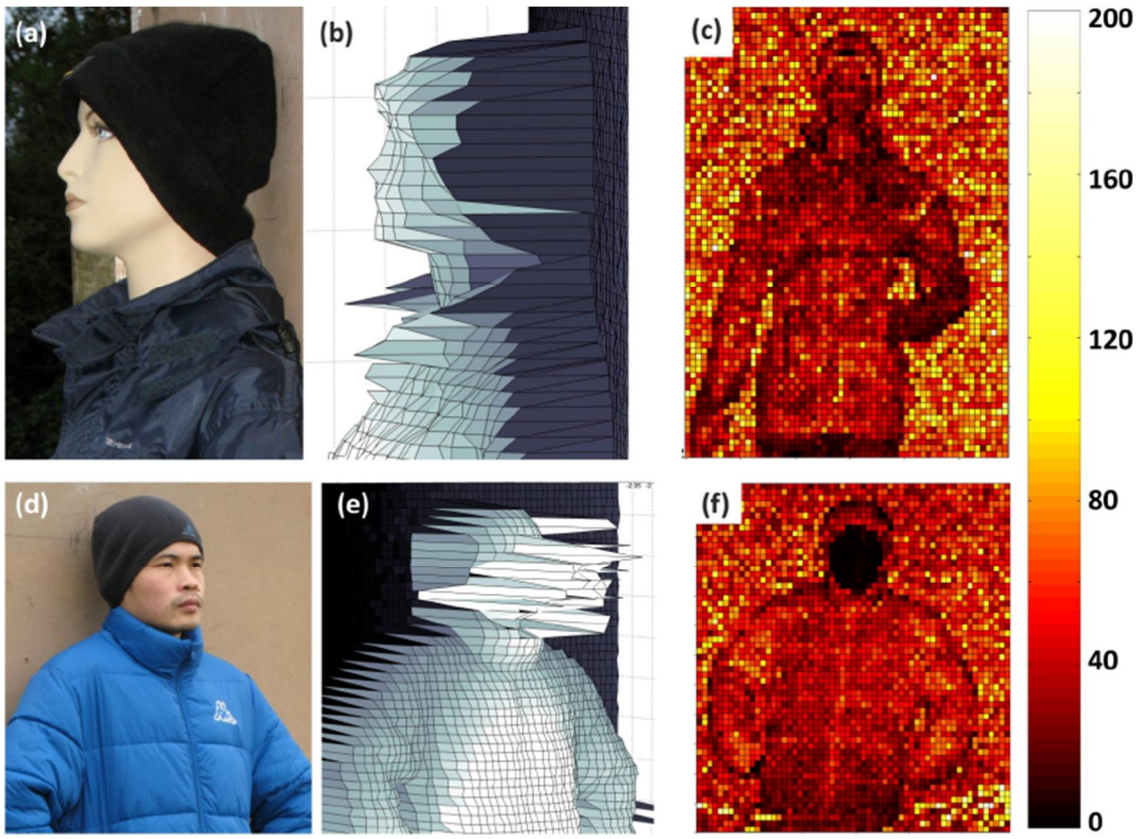

Figure 4-12 Comparison between the results obtained from scans of a mannequin and a human at a range of 325 metres using a per-pixel dwell time of 10 ms. A close-up photo of the mannequin's head is shown in (a), and the surface plot of depth data acquired at a range of 325 metres with a 10 ms per-pixel dwell time is shown in (b) from a similar viewpoint. The plot shown in (c) uses colour to map the calculated number of detected return photons in the histogram peak for each individual pixel. At per-pixel dwell times of 10 ms and greater, almost all of the pixels in this scene had sufficient detected photons to provide a true depth reading at this range as is evident from the centimetre-scale features evident in (b). However, the detected photon returns from human skin were significantly lower at this wavelength. The scene shown in (d) of myself was scanned with a 10 ms per-pixel dwell time and the surface plot in (e) was obtained – in this case, most of the facial pixels had insufficient detected photons for the determination of a depth. The low number of detected return photons from the facial skin is obvious on the corresponding colour map shown in (f). The plots in (c) and (f) also confirm that there are lower returns from the areas of the scene that the illuminating beam strikes at glancing angles e.g. edges. (From [4.22]).

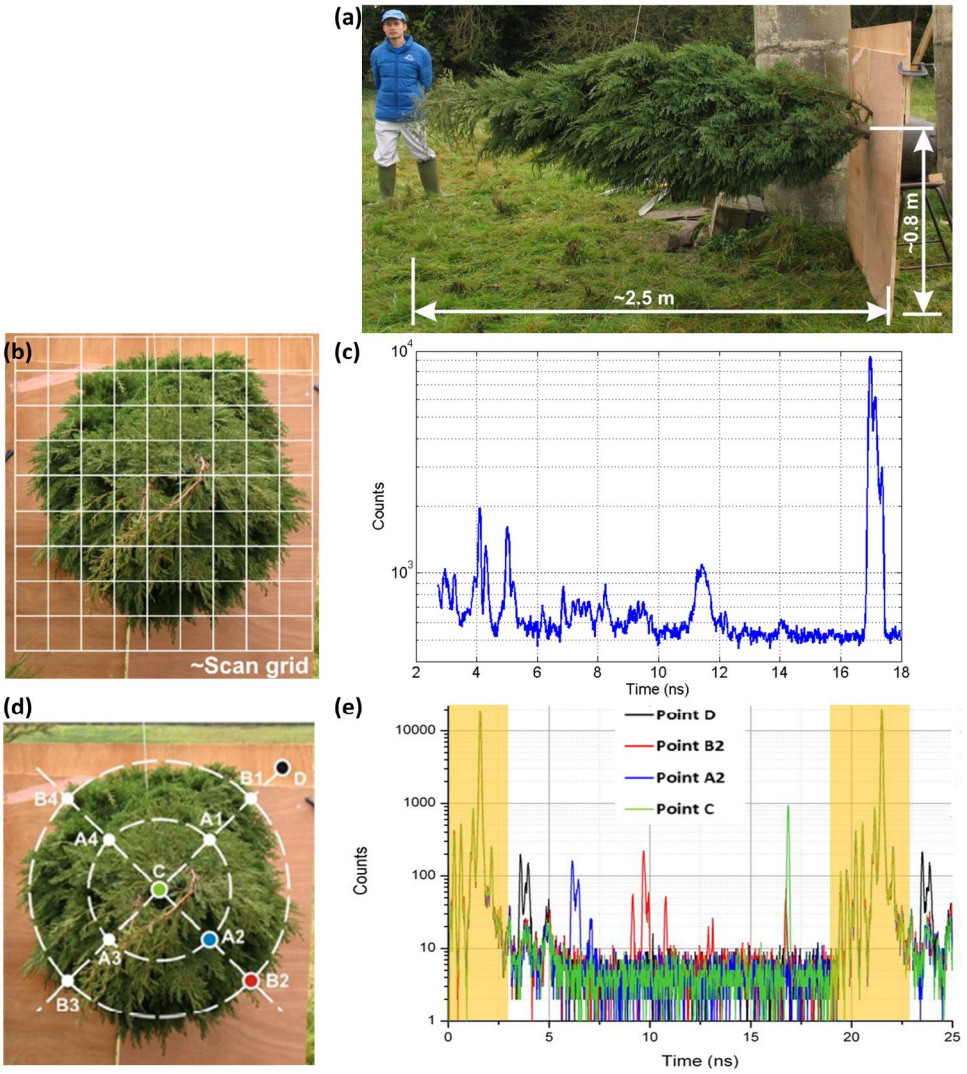

Figure 4-13 (a) Setup of a tree mounted horizontally for measurements. The top of the tree was closest to the roof lab. Several plywood sheets, standing perpendicular to the trunk and resting against the top of the plant pot, acted as a backplane. The distance from the backplane plywood board to the top of the tree was ~2.5 m, which corresponds to a time-of-flight round-trip time of ~16 ns. The truck of the tree is ~0.8 m above the ground. (b) Annotated photograph indicating the approximate size of ~1 m×1 m scan area and location of the 10×10 pixel scan grid. (c) Portion of the accumulated 100-pixel photon count histogram, in which the internal back reflection is not shown, with a per pixel acquisition time of 10 s. This processed histogram can be used to reveal different layers of the tree and the back plywood board. (d) Nine selected positions of the tree (C, A1, A2, A3, A4, B1, B2, B3, B4) and one position of the plywood board (D); ~1 m×1 m scan area at the scene. (e) Overlaid histogram plots of returns obtained from four points in the scene based on single pixel measurements using an acquisition time of 20 s. From the top of the tree to the board: C (green curve), A2 (blue curve), B2 (red curve) and D (black curve). Two yellow regions cover the internal back reflections peaks.

In order to assess the performance of our system over kilometre-scale distances we carried out measurements using an available 910 metre range, with the mannequin, Dr. Aongus McCarthy, and the author posing as targets. Figure 4-14 shows three different viewpoints of the depth data obtained of the mannequin at different per-pixel dwell times. The frontal perspective of the depth images, shown in the top row, gives a visual indication of the XY centimetre-scale spatial resolution that was achieved at this range. This illustrates that different shapes and forms can be easily identified even at per-pixel acquisition times as low as 2 ms. Figure 4-15 shows the author and another member of our research group posing for depth profile scans at the stand-off distance of 910 metres at per-pixel acquisition times of 50 ms and 10 ms. Depth features on the centimetre scale, such as folds in the clothing, are evident in all of the depth images shown in Figure 4-14 and Figure 4-15. However, as was already mentioned regarding the results shown in Figure 4-12(e) and Figure 4-12(f), it is evident from the depth images shown in Figure 4-15(b) and Figure 4-15(d) that the returns from human skin were relatively low.

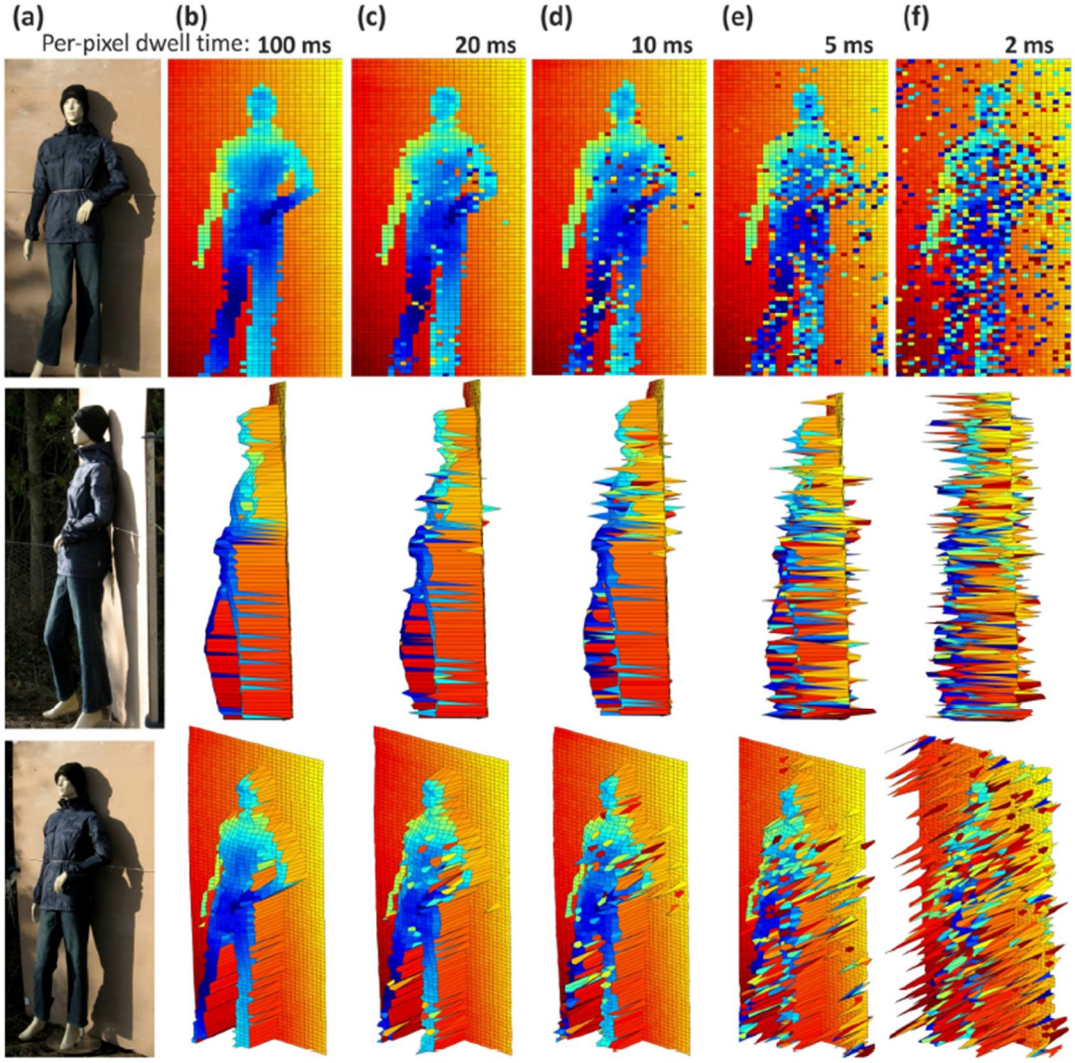

Figure 4-14 Depth profile measurements made in daylight of a life-size mannequin from a stand-off distance of 910 metres. The close-up photographs in column (a) are different viewpoints of the scanned scene, which was comprised of the mannequin against a MDF sheet. This MDF sheet acted as a backplane. The depth scans were acquired in daylight and each scan covered an area of approximately 800×2000 mm using 30×80 pixels, resulting in a pixel-to-pixel spacing of approximately 25 mm in X and Y. Surface plots of the raw depth data obtained for per-pixel acquisition times of 100, 20, 10, 5, and 2 ms are shown in columns (b) to (f) - each of these columns show three different views of the data obtained with the specified per-pixel dwell time. A per-pixel dwell time of 10 ms equated to a total scan time 24 s for this scene. The colour is used to map depth. The face-on view shown in the top row gives an indication of the spatial resolution of the system at a kilometre, and the centimetre scale depth resolution can be gauged from the oblique and side-on views in the bottom two rows. (From [4.22]).

Figure 4-15 Depth profile measurements of humans, acquired in daylight at a stand-off distance of 910 metres. The close-up photographs in columns (a) and (c) are different viewpoints of the scanned scenes – the author and Dr. Aongus McCarthy, respectively posed in front of a MDF sheet. The depth scans were acquired in bright daylight and each scan covered an area of approximately 800×2000 mm using 40×80 pixels, corresponding to a maximum field of view of 2 mrad. Surface plots of the raw depth data obtained are shown in columns (b) and (d) - these columns show two different views of the data obtained with the specified per-pixel dwell time. It took 32 seconds to acquire the data shown in (d). The colour shading in the surface plots is used to map depth. (From [4.22]).

We also performed daylight measurements at a stand-off distance of 4400 metres. A 20×12 pixel scan was carried out on an area measuring approximately 2000×1200 mm, as shown from different viewpoints in Figure 4-16. Sub-centimetre depth resolution was achieved, using a per-pixel dwell time of 2 seconds, for the parts of the scene containing cooperative targets e.g. retro-reflective material similar to that used for car

license plates. At this range, the spatial resolution was judged to be approximately 250 mm. Evidently, these relatively long acquisition times would be reduced with higher laser power, which was not available in these initial trials.

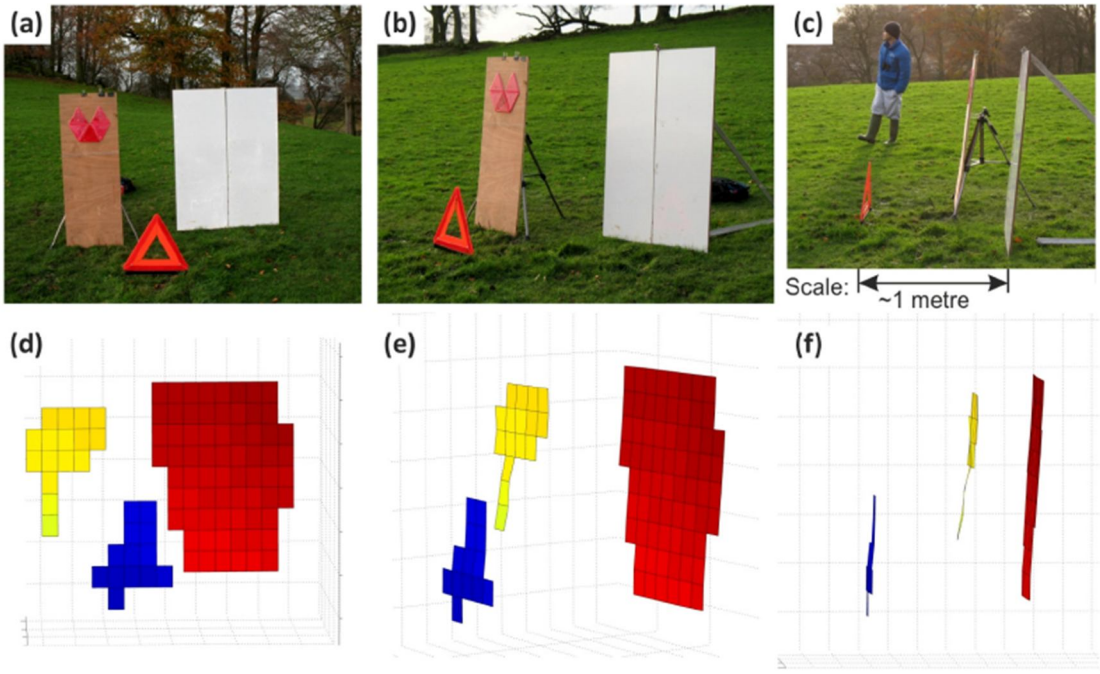

Figure 4-16 Depth profile measurement made on a scene from a stand-off distance of 4400 metres in broad daylight. The photographs (a), (b) and (c) are different viewpoints of the scanned scene with (a) being the view as seen from the approximate direction of the transceiver. The scene consisted of 1.2 metre tall boards with retro-reflective material (one plywood panel with a set of five red retro-reflecting triangles, and two adjoining panels covered in white retro-reflecting material), and a 400 mm tall red retro-reflective roadside warning triangle. The distance between the base of the white panels and the base of the red retro-reflective warning triangle was approximately 1 metre, as indicated in (c). The per-pixel acquisition time was 2 seconds. The surface plot of the 20×12 pixel depth data is shown from three different viewpoints in (d), (e) and (f), nominally corresponding to the viewpoints of the photographs. (From [4.22]).

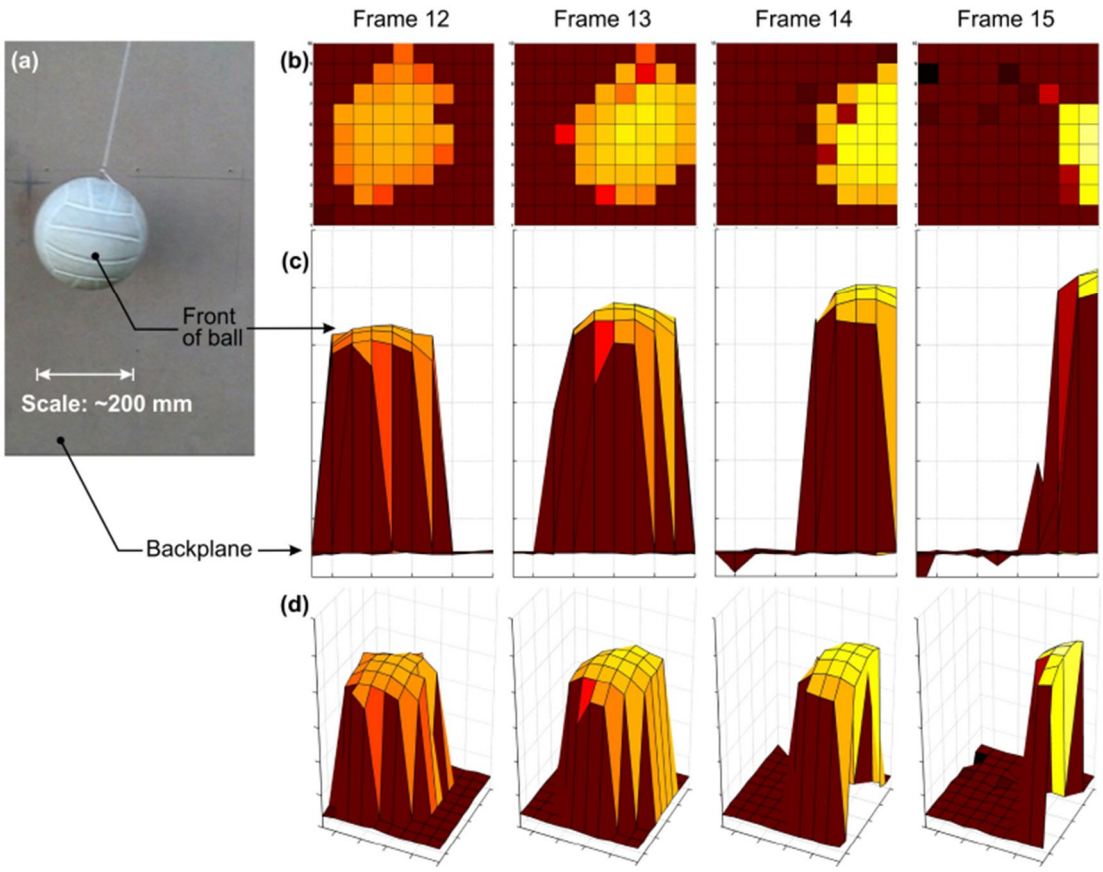

Figure 4-17 Time-of-flight depth profile movie, recorded in daylight, of a scene from a stand-off distance of 325 metres. The image shown in (a) is a close-up photograph of the scene which consisted of a ~200 mm diameter soccer ball suspended in front of a MDF backplane. The "ball pendulum" was set in motion with the plane of the oscillation at an angle to the backplane. A four-second movie was recorded in daylight at 10 frames per second - each frame had 10×10 pixels, and consequently a per-pixel dwell time of 1 ms. The data acquired for four consecutive frames (numbers 12 to 15) is shown. The columns labelled Frame 12 to Frame 15 show three different views of the plotted raw depth data for each frame - row (b) is a front view, row (c) is a top-down view, and row (d) is an oblique view. Colour is used to map depth and is consistent across all of the plots. The curvature of the front surface of the ball is evident in the depth profile views shown in rows (c) and (d), as is the increasing separation between the ball and the backplane when moving from frame 12 to frame 15. (From [4.22]).

The achievable pixel-to-pixel depth uncertainty at stand-off distances of 325, 910, and 4400 m was investigated by scanning a planar target surface covered in retro-reflective material. Mathematical planes were fitted to the surface pixels of the acquired data, and the standard deviation of the pixel residuals served as an indicator of the system depth resolution. A per-pixel dwell time of 1 ms resulted in a pixel-to-pixel depth uncertainty

of 0.8 mm for the 325 m range. Using a per-pixel dwell time of 10 ms for the 910 metre range, and 2 seconds for the 4400 metre range yielded depth residuals of 1.1 mm and 1.5 mm respectively. These rapid acquisition times enabled us to record a 1 mrad field-of-view depth profile movie of a moving object at a stand-off distance of 325 m using a pixel dwell time of 1 ms. This four-second movie, whose example frames can be seen in Figure 4-17, has centimetre resolution in XYZ and was captured in daylight at 10 frames per second with, each frame having 10×10 pixels.

4.3.2 Scanning depth imager using a gated InGaAs/InP SPAD module

4.3.2.1 System description

A schematic of the scanning depth imager using a gated InGaAs/InP SPAD is shown in Figure 4-18. The 1550 nm wavelength pulsed laser illumination was provided by a supercontinuum laser source (SuperK EXTREME EXW-6, NKT Photonics, Denmark). Although the supercontinuum laser source has relatively larger size in comparison to the mode-locked fibre laser, it offers spectral tunability and variable repetition rates, as described in section 3.3.2 of Chapter 3, making it suitable to use for the development of research systems. For future prototype field instruments, less expensive and more compact sources will be used, at the expense of laser functionality. For the measurements reported here, the repetition frequency of the laser was set to 40 MHz and the illumination beam had an average optical power of less than 600 μW upon exiting the transceiver unit, corresponding to approximately 15 pJ per pulse. The pulse width of the laser was less than 50 ps. The supercontinuum laser system provided flexibility for exploring the performance parameters of the depth imaging system but the timing jitter of the system and the optical power levels used for the measurements presented here are fully consistent with using, for example, a relatively inexpensive gain-switched picosecond diode laser as the source. In these experiments, the wavelength selection from the broadband laser output was achieved by using a series of optical filters: a 30 nm wide band-pass filter (BPF1) with a central wavelength of 1550 nm, a long-pass filter (LPF1) with a cut-on wavelength of 1500 nm, and a short-pass filter (SPF) with a cut-off wavelength of 1845 nm. This spectrally selected output was delivered to the transceiver unit through a polarisation-maintaining fibre (PMF). A linear polariser (LP) and a half-wave plate (HWP) were used to orientate the polarisation in order to optimise coupling into the fibre, and transmission through the transceiver.

The custom-built scanning transceiver system, as can be seen in Figure 4-18, is akin to the one used in the depth imager at λ ~ 850 nm [4.11]. With the exception of the spectral filters, the near infrared optical components and the 500 mm focal length objective lens (OL) were the same as those previously used for depth imaging with an SNSPD system at 1560 nm [4.22]. The optical receive channel of the transceiver included a long-pass filter (LPF2) with a cut-on wavelength of 1500 nm whose spectral transmission can be seen in Figure 4-19, and a band-pass filter (BPF2) with a central wavelength of 1550 nm and a bandwidth of 30 nm FWHM whose spectral transmission can be seen in Figure 4-20, in order to reduce the amount of solar background in the collected scattered return signal. An armoured, 10 µm diameter core, single mode fibre (SMF) was used to deliver the spectrally filtered return signal, to the fibre-coupled detection head of the InGaAs/InP SPAD detector.

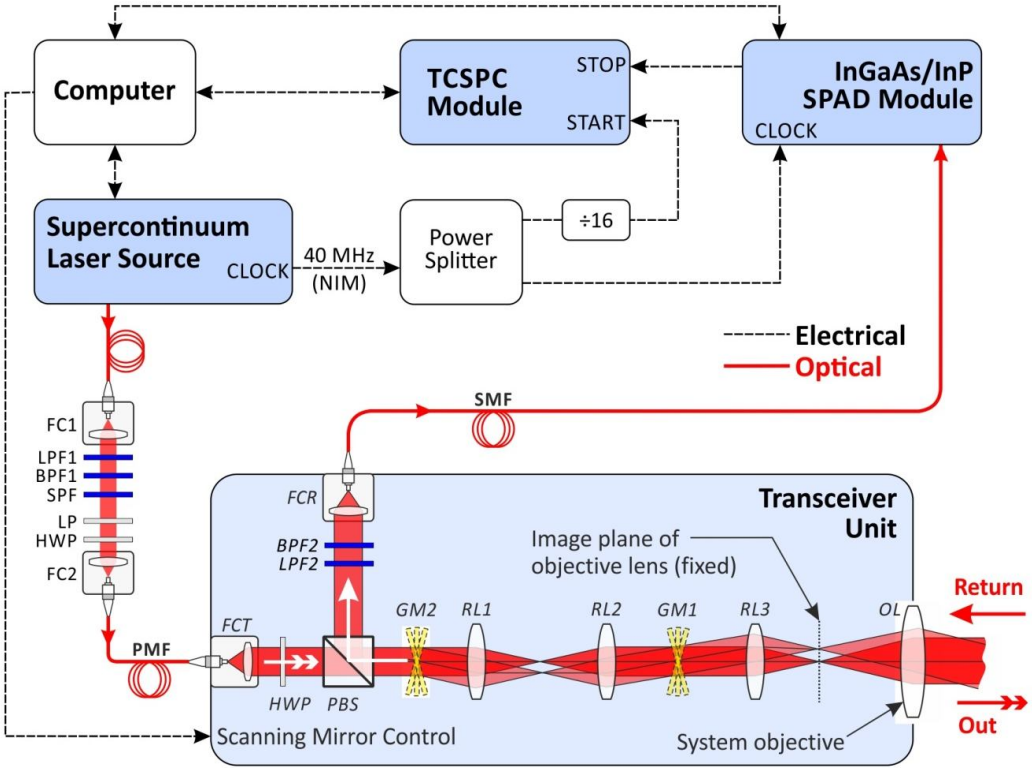

Figure 4-18 Schematic of the layout of the 1550 nm single-photon depth imaging system, which comprises a supercontinuum laser source, an InGaAs/InP SPAD detector, a TCSPC module, and a custom transceiver. Optical components include: fibre collimation packages (FC1, FC2, FCT, FCR); polarising beam splitter (PBS); galvanometer scan mirrors (GM1, GM2); relay lenses (RL1, RL2, RL3); objective lens (OL); long-pass filters (LPF1, LPF2); band-pass filters (BPF1, BPF2); short-pass filter (SPF); linear polariser (LP); half wave plate (HWP); polarisation-maintaining fibre (PMF); single mode fibre (SMF). Other abbreviations used: nuclear

instrumentation module (NIM); single-photon avalanche diode (SPAD); time correlated single-photon counting (TCSPC). (From [4.34]).

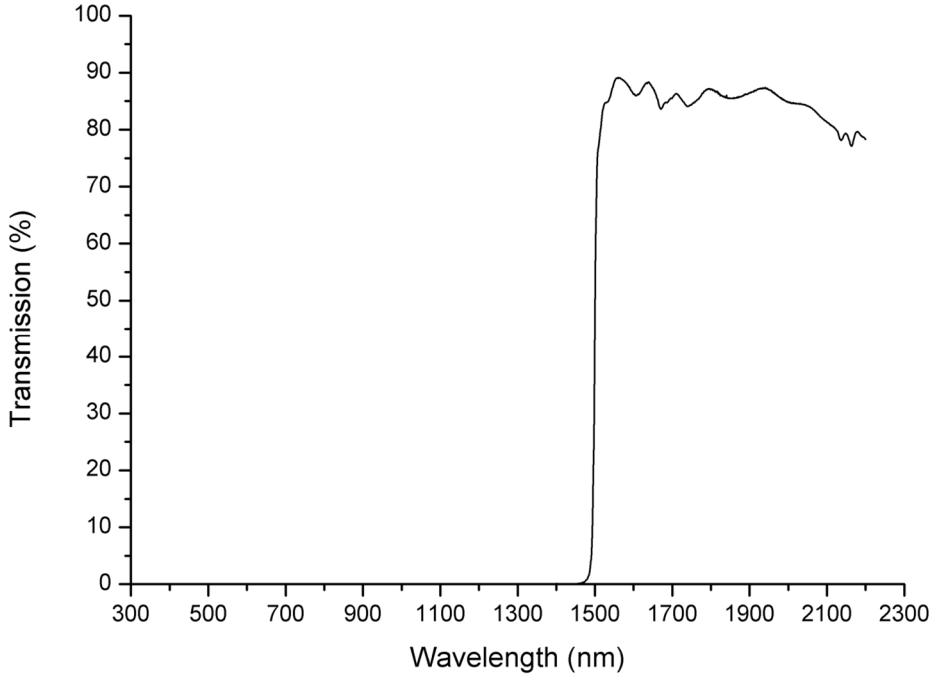

Figure 4-19 Spectral transmission plot of a long-pass filter with a cut-on wavelength of 1500 nm (FEL1500, Thorlabs, USA).

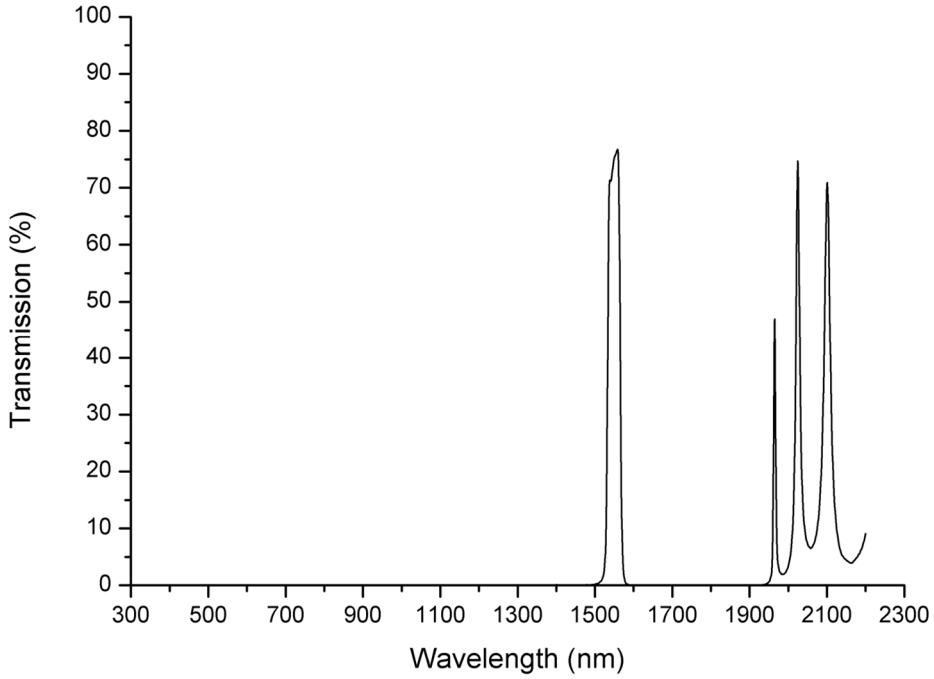

Figure 4-20 Spectral transmission plot of a band-pass filter with a central wavelength of 1550 nm and a bandwidth of 30 nm FWHM (62824, Edmund Optics, UK).

A synchronous electrical trigger mechanism between the laser source, the detector, and the acquisition module was needed for accurate time correlation. This was provided by

the laser source as a nuclear instrumentation module (NIM) pulse signal with a frequency of 40 MHz for all our measurements using this system. This signal was split in two by a power splitter – one part was used to trigger the control unit of the InGaAs/InP SPAD detector, and the other was down-divided to 2.5 MHz to accommodate the maximum count rate limit of the start trigger input of the TCSPC module (PicoHarp 300, PicoQuant GmbH, Germany). This therefore provided 16 optical pulses per histogram width, and all returned photons were efficiently recorded within this time window subject to the usual statistical rules governing TCSPC, as described below and reference [4.4]. The output of the InGaAs/InP SPAD detector provided the stop trigger of the TCSPC module. The TCSPC module, the scanning galvanometer mirrors (GM1 and GM2), and the InGaAs/InP SPAD detector, were controlled via custom-designed software. Overall, the system design reduces background noise counts via a combination of spectral, spatial, and time-gated filtering approaches. The spectral filtering is achieved by the two optical filters used in the receive channel of the system (see Figure 4-18), the spatial filtering is performed by the 10 µm diameter core of the fibre connected to the detector, and the time-gating is inherent to the TCSPC technique.

The InGaAs/InP SPAD detector was cooled to a temperature of 230 K during our measurements and used an electrical gating approach to switch the detector to above avalanche breakdown, into the Geiger mode, at pre-programmed time intervals for a gate-on time of 7 ns, as shown in Figure 4-21. The excess bias was set to 5 V and the resulting photon detection efficiency was about 26 %, with a dark count rate of 16 kcps as shown in Figure 4-22. InGaAs/InP SPAD detectors suffer from afterpulsing, an effect where charge carriers are trapped during the avalanche process, and are subsequently released causing further avalanche events, which increase the background counts. In order to reduce the contribution of afterpulsing, the detector was biased below avalanche breakdown for a pre-programmed hold-off time to allow for trap states to empty prior to the detector being re-activated, thus lowering the afterpulsing probability to negligible levels. Typically, this hold-off time was greater than 10 µs, which was well in excess of the gating period, meaning that a number of detection gates were skipped after each event. As is usual in the time-correlated single-photon counting technique, it is important that the probability of a detection event is low compared to the excitation rate (typically below 5 %) to avoid the effects of "pulse pile-up" [4.4], and this probability must include the effect of skipped detection gates.

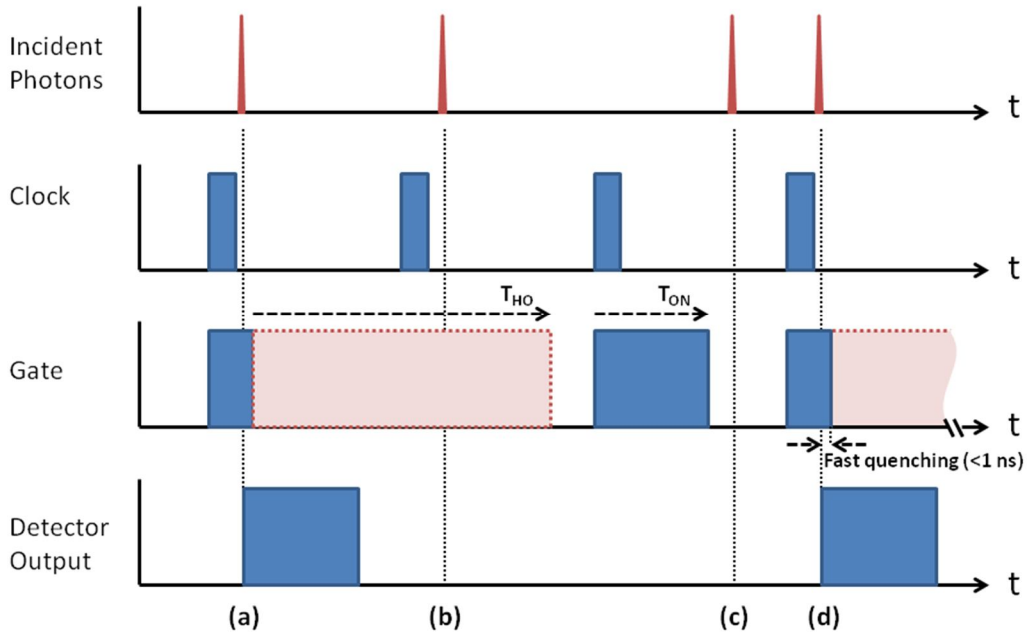

Figure 4-21 Timing diagram for the gated mode operation used with the SPAD detector. A 40 MHz synchronous clock signal was supplied to the detector module. Using this clock as a trigger, the detector was gated on for a pre-determined period, T_{ON}, then switched off until the next clock trigger. If an avalanche event is triggered within the detector (e.g. by an incident photon) during the gate then an output pulse will be registered, as shown at time (a) in the figure. The detector will be rapidly quenched and remain off for a set hold-off time, T_{HO}, to reduce the probability of afterpulsing. Any clock triggers (and thus incident photons) will be ignored during this period, e.g. at time (b). Once the hold-off duration is complete, the gate is once again ready to be triggered by the clock. Any photons arriving outside the gate window will be ignored (c), but any photons arriving within the gate window, for example (d), will be detected. (From [4.34]).

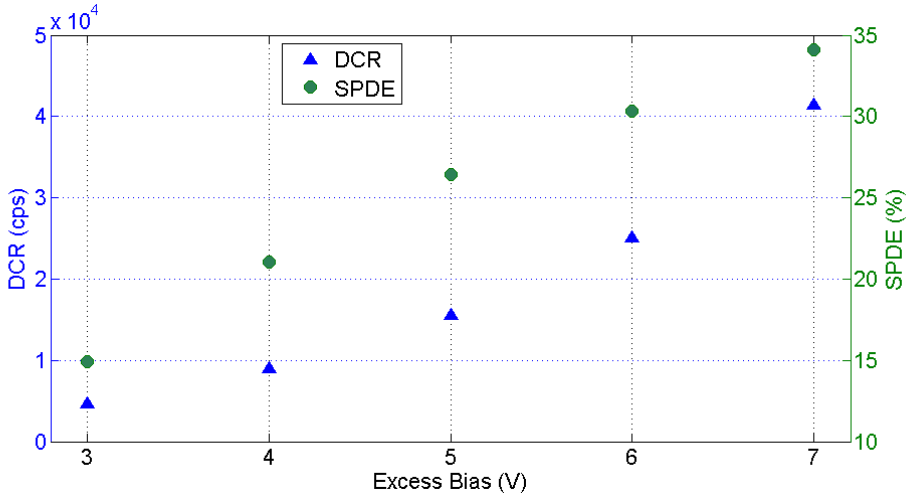

Figure 4-22 Excess-bias-dependent dark count rate (DCR) and single photon detection efficiency (SPDE) of the employed gated-mode InGaAs/InP SPAD.

The dedicated gated detection scheme guarantees a flat and linear temporal response of the detection system to photon events. This allows for low timing jitter to be achieved – approximately 140 ps FWHM in the measurements shown below - which permits centimetre resolution depth profiling. The use of a programmable electrical gate means that profiling of surfaces with a depth extent corresponding to half the gate width can be achieved, and this gate duration can be adjusted as necessary for a specific target type. Another major consideration in a monostatic optical system is that the use of a gated detector can eliminate potentially serious issues with back-reflections from optical components. Of course, the electrical gate must be located in the vicinity of the target for most efficient detection. This can be achieved by an initial time-scan of the start-stop time difference (over only 25 ns at the 40 MHz laser repetition rate used in these measurements) as in the burst illumination depth imaging approach [4.35], or by the use of the pseudo-random pulse trains to ascertain unambiguous range prior to depth profiling previously used in single-photon depth imaging [4.12]. A short detector gate gives the least afterpulsing for a given target scenario, and hence a better signal-to-noise (SNR) can be achieved. However, longer gate durations can be used to locate a target. When using a longer duration gate it is possible to increase the hold-off time to mitigate the effects of increased afterpulsing. Hence, a combination of longer gate and longer hold-off times does mean that SNR can be preserved at the expense of a longer acquisition time. Another detector gating approach reported is the use of sine-wave gating of an InGaAs/InP SPAD [4.36] used in free-running mode in order to avoid the need for establishment of range before profiling [4.37], however the resulting additional jitter will reduce depth resolution significantly as well as an increased likelihood of a lower average detection efficiency.

As was mentioned above, optical back reflections can be a significant issue in a monostatic transceiver arrangement. This was made apparent previously when using the free-running SNSPD system [4.22], where we found that the return histogram included the internal back reflections caused by the laser illumination as it left the transceiver. The contribution of the back reflections can be seen in an example of a processed histogram shown in Figure 4-23(a). The sections of the histogram containing the peaks caused by the back reflections were easily removed during the software analysis. However, during data acquisition these back-reflections add to the overall count rate of the detector, increasing the likelihood of pulse-pile-up effects appearing in the histograms. The use of a gated detector meant that such back-reflections could

easily be avoided in the return histogram as demonstrated in Figure 4-23(b).

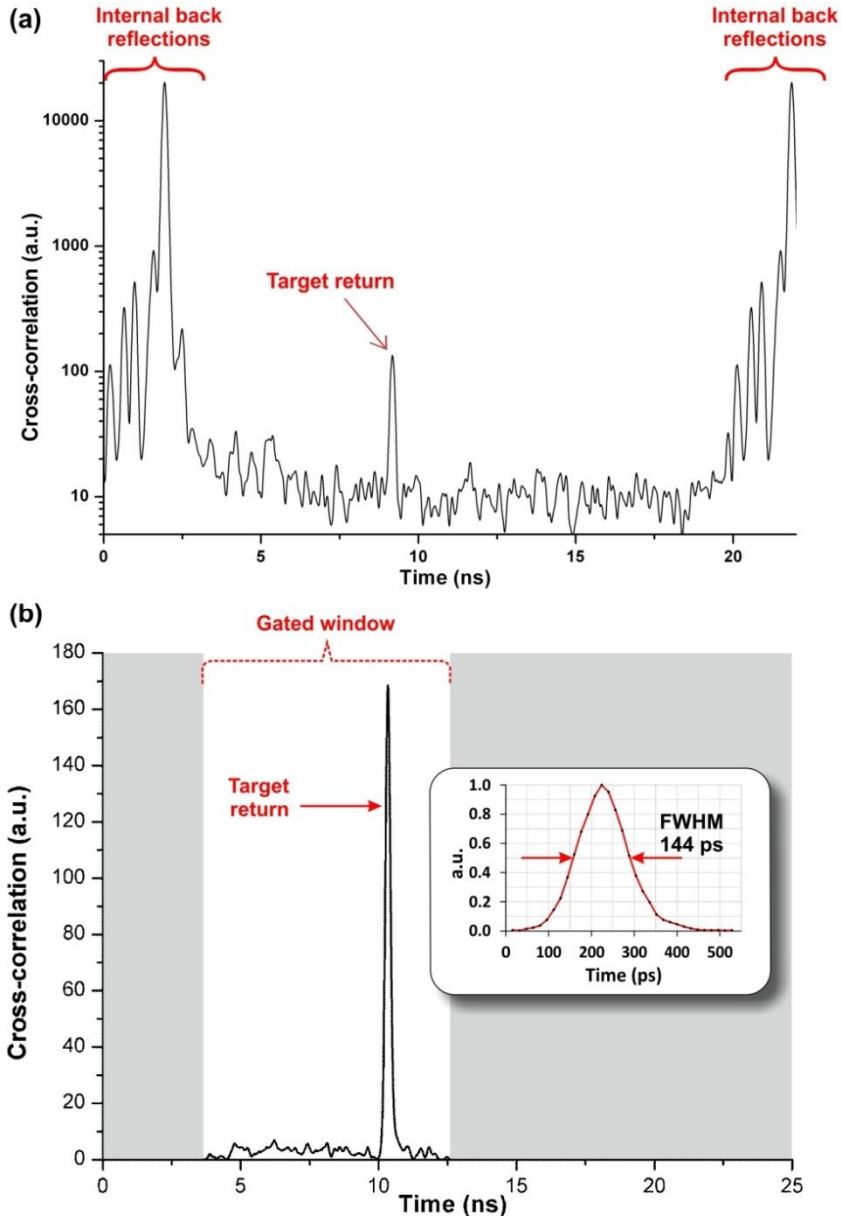

Figure 4-23 The plot in (a), after Figure 4-8, shows an example of a processed histogram for a single pixel obtained from the measurements made using a free-running SNSPD – peaks corresponding to the optical back reflections from the transceiver components are present. The plot in (b) is from a pixel measurement using the gated InGaAs/InP detector module and shows the result of a cross-correlation between the normalised instrumental timing response (see inset) and the original timing histogram of return photon counts within one period of the laser pulse train. The inset shows the instrumental response function, which had a 144 ps full width at half maximum timing jitter. Most of the non-zero cross-correlation is within a gated window of only 7 ns width, and the cross-correlation peak corresponds to the time position of the return signal peak (i.e. 10.34 ns in the example). (From [4.34]).

4.3.2.2 Depth profiling results

A series of field trials in bright daylight were performed in order to investigate the acquisition of depth images from scenes containing a variety of typical non-cooperative materials (e.g. wood, woven fabrics, leather, and plastic). The measurements were also made in three appropriate locations at stand-off distances of 325 metres, 910 metres and 4500 metres as shown in Figure 4-10. A 6 mm thick median-density fibreboard (MDF) sheet was used as a backplane for the measurements made at 325 m and 910 m. This acted as a convenient and defined "backstop" meaning that the acquired data was clearly discernible and not obscured by data from other less clearly defined background objects It also enabled the XY extents of the scans to be easily measured. Variations in the weather conditions, and the angle of the Sun relative to the optic axis of the transceiver's objective lens both affected the measurements to some extent. The calculated normalised background noise count rate, measured at different times over the course of the field trials, varied between approximately 30 kcps and 100 kcps.

At a range of 325 metres, we scanned two scenes consisting of a human model as shown in Figure 4-24(a) and Figure 4-24(d). The data was acquired with a normalised background noise count rate of around 90 kcps, and the depth images obtained for per-pixel acquisition times of 5, 2, 1, and 0.5 ms are shown in Figure 4-24. Two different viewpoints of the raw plotted depth data are shown for each acquisition time in order to convey the XY spatial resolution of the system and the level of depth detail that was realised. Note that the depth profiles present here are all retrieved by the aforementioned pixel-wise cross-correlation method. It is evident from the depth images that some of the pixels coinciding with the areas of exposed skin on both human models did not give sufficient returns, at these per-pixel acquisition times, to obtain reliable depth measurements at these per-pixel acquisition times. Aside from on skin, results at an illumination wavelength of 1550 nm show that accurate sub-centimetre depth measurements can be made for the other materials in the scene using per-pixel acquisition times in the region of 2 to 5 ms. The results obtained for per-pixel acquisition times as short as 1 and 0.5 ms contain depth measurements for the vast majority of the pixels enabling the overall target outline and depth profile to be easily discerned.

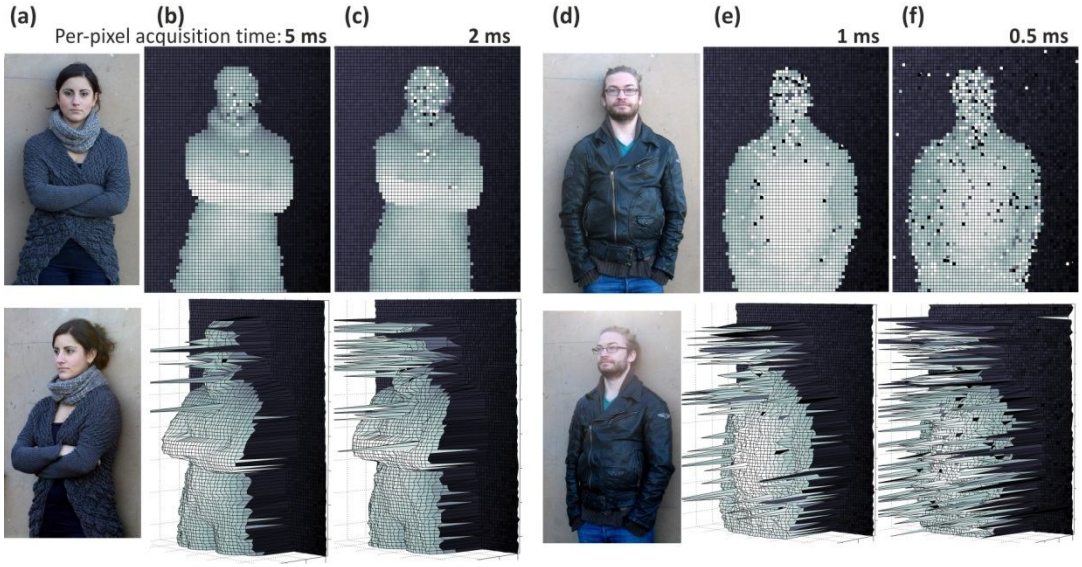

Figure 4-24 Depth profile measurements acquired in bright daylight of human models at a stand-off distance of 325 metres. The images in columns (a) and (d) are close-up photographs of the two scanned scenes. Both are shown from two different viewpoints and consist of a human standing in front of a MDF backplane with a maximum front-to-back surface separation of approximately 400 mm. The depth scans covered an area of approximately 800×1000 mm using 60×75 pixels, resulting in a pixel-to-pixel spacing of approximately 13 mm in both X and Y. Plots of the depth data obtained for per-pixel acquisition times of 5, 2, 1, and 0.5 ms are shown in columns (b), (c), (e) and (f) – each of these columns show two different viewpoints of the surface plot constructed from the data obtained using the specified per-pixel acquisition time, and the colour shading is used to map depth. A per-pixel acquisition time of 1 ms equated to a total scan time of 4.5 s for these scenes. The normalised background noise count rate was calculated to be approximately 93 kcps and 91 kcps for scenes (a) and (d) respectively. (From [4.34]).

The data acquired from three different scenes in daylight at a stand-off distance of 325 m and using an acquisition time of 5 ms per pixel is compared in Figure 4-25. The scenes consisted of a life-sized mannequin and the two human models shown in Figure 4-24. In the bottom row of Figure 4-25, two different viewpoints are shown of the greyscale colour-mapped surface plot of the depth data for each of the three scenes. The top row of Figure 4-25 includes a face-on view of the surface plot for each scene where the colour is used to map the number of detected return photons. For each individual pixel, the photon counts are mapped corresponding to the colour bar on the right hand side of the figure. It is immediately evident that the photon return from human skin is much less than the exposed surfaces of the mannequin and indeed all of the other materials in the scenes. The integrated number of photons is evidently also dependent

on the nature of the target. The scatter signature and the angle of incidence of the illuminating beam, for the different parts of the scene, contribute to the varying integrated photon returns. For the results shown in Figure 4-25, which were all obtained under similar weather conditions within the space of two hours, depth measurements were reliably made at integrated photon numbers greater than approximately 15 per pixel. The integrated photon returns for discrete points of the mannequin scene, shown in Figure 4-25(a1), are plotted in Figure 4-26 as a function of the acquisition time so as to provide an approximate indication of the variation between the different material types and indeed the variation between two different locations on the same material i.e. the mannequin's jacket. Material-dependent photon counts shown in Figure 4-26 have different trends in comparison to the one shown in Figure 4-11. That is because it has the likelihood that the illuminated regions occur at different incident angles, resulting in variation in the return. The results in Figure 4-11 or Figure 4-26 can only be regarded as examples to illustrate the effect of different materials, as the precise illumination conditions will also be a factor in the photon returns expected.

The results shown in Figure 4-24 and Figure 4-25, acquired with an illumination wavelength of approximately 1550 nm and an average output power of less than 600 μW, show sub-centimetre resolution depth images using per-pixel acquisition times. This is comparable with the results obtained previously using a free-running SNSPD system with 1560 nm wavelength illumination [4.22]. However, the acquisition times are significantly lower than those achieved in our earlier work at an illumination wavelength of ~ 850 nm [4.11, 4.32]. That work was carried out under similar daylight conditions and at the same stand-off distance of 325 m, albeit using a much lower average output illumination power of 50 μW. Nevertheless, on comparing the measurements carried out at the wavelengths of 850 nm and 1550 nm, the results indicate that the difference between the integrated number of photon returns for a pixel on human skin and a pixel on other materials, such as textiles and concrete, is not as pronounced at an illumination wavelength of ~ 850 nm compared to when using λ ~ 1550 nm. This is consistent with the findings of previous work [4.33] which investigated optical properties of human skin and subcutaneous tissue at these wavelengths.

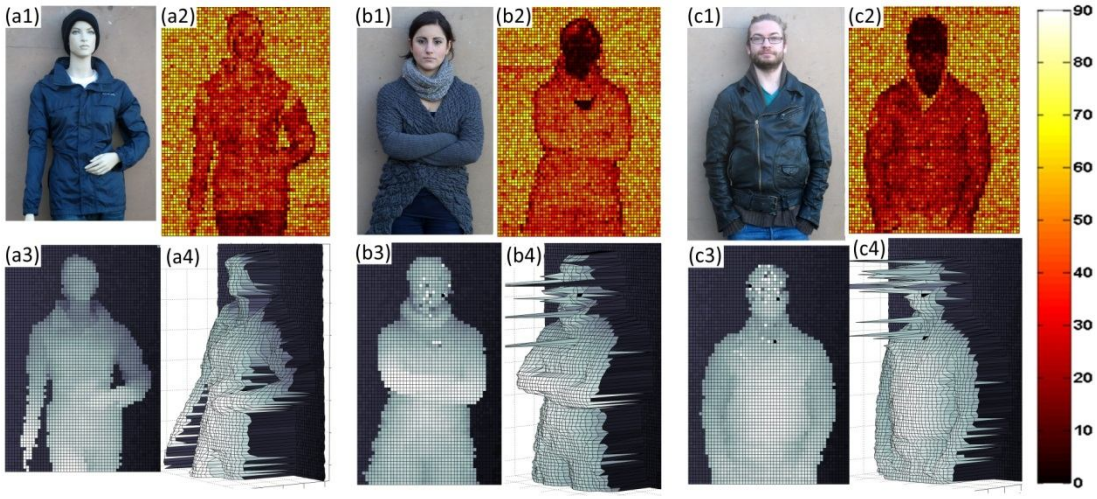

Figure 4-25 Comparison between the results obtained from depth profile scans of a life-sized mannequin and two different human models, at a range of 325 m using a per-pixel acquisition time of 5 ms. The photographs in (a1), (b1), and (c1) are close-up images of the three different scenes that were scanned in similar daylight conditions. The bottom row shows two viewpoints of the plotted depth data that was acquired for each of the three scenes, with the white to black colour shading being used to map depth. The plots shown in (a2), (b2), and (c2) use colour to map the calculated number of detected return photons in the histogram peak, for each individual pixel, according to the colour bar on the right. A distinct variation in the number of detected return photons from the different types of clothing materials can be seen from these intensity images e.g. the knitted cardigan on the female in (b2) has a slightly higher return in comparison to the mannequin's rain jacket in (a2). Both of these materials appear to have a significantly higher return than the leather jacket worn by the male in (c2). The plots of the human models in (b2) and (c2) highlight the relatively low returns from skin. (From [4.34]).

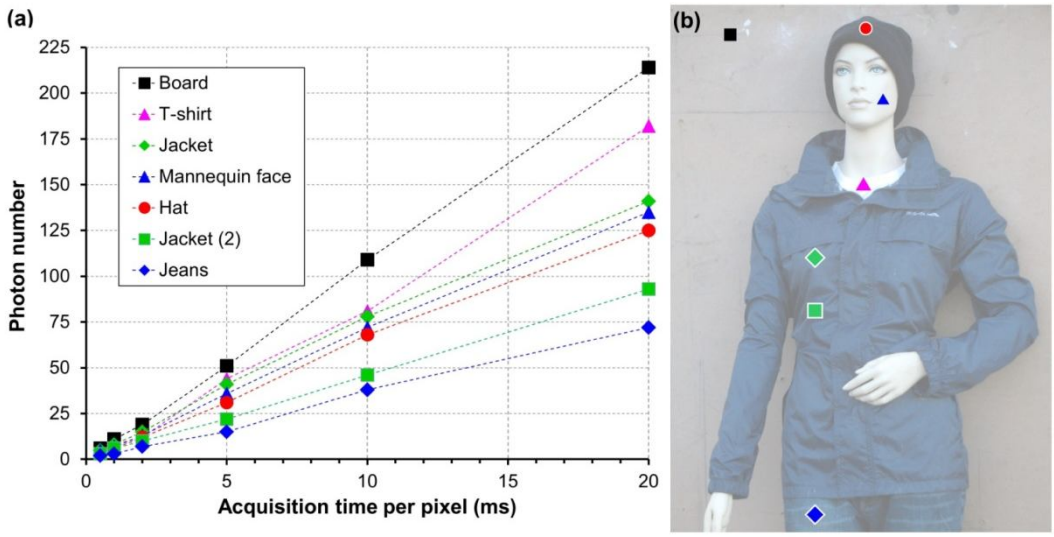

Figure 4-26 Material-dependent integrated photon number versus acquisition time per-pixel. The data for the graph shown in (a) was extracted from depth profile scans acquired in daylight of a life-sized mannequin at a stand-off distance of 325 m and using acquisition times of 0.5, 1, 2, 5, 10, and 20 ms per-pixel. Note that the integrated photon number is a nine-pixel-based average using a single pixel and its eight neighbours. The dashed lines in the graph, linking the set of data points for each material, are included as a guide for the reader. The pixel locations corresponding to the plotted data are indicated in the photograph shown in (b). Sets of data points for two different locations on the jacket material are included in the graph. These illustrate how the more pronounced creasing of the material at the lower location results in a significantly lower photon number due to the illuminating beam striking the material at glancing angles. This is similar to what happens at edges, e.g. points on the mannequin outline (see the integrated photon return plots in Figure 4-25). (From [4.34]).

Having achieved good quality depth images at 325 metres using per-pixel acquisition times of 1.0 ms, we proceeded to scan a moving target – a ~200 mm diameter soccer ball, suspended by a ~1.2 m long string, which was set swinging with a conical pendulum motion in front of a MDF backplane i.e. the ball swung in a horizontal circle. A depth movie of four seconds duration was acquired using a 1 ms per-pixel dwell time. The movie was recorded in daylight at 10 frames per second, with 10×10 pixels per frame. Ten consecutive frames of the depth movie are shown in Figure 4-27 where two different views of the data acquired for each frame are shown. In frames 24 to 28 we can see the ball moving from left to right as well as the distance from the backplane to the front surface of the ball increasing by approximately 100 mm. No significant left-right motion of the ball is visible between frames 28 to 30 as it "turns the corner" but

the distance from the backplane to the front surface of the ball continues to increase by approximately 60 mm. In frames 31 to 33, we can see the ball moving from right to left with the distance from the backplane still increasing to the point that it is approximately 200 mm further away from the backplane in frame 33 than in frame 24. In contrast to a 2D movie, the variation in depth of the swinging motion is obvious and quantifiable from this TOF depth data.

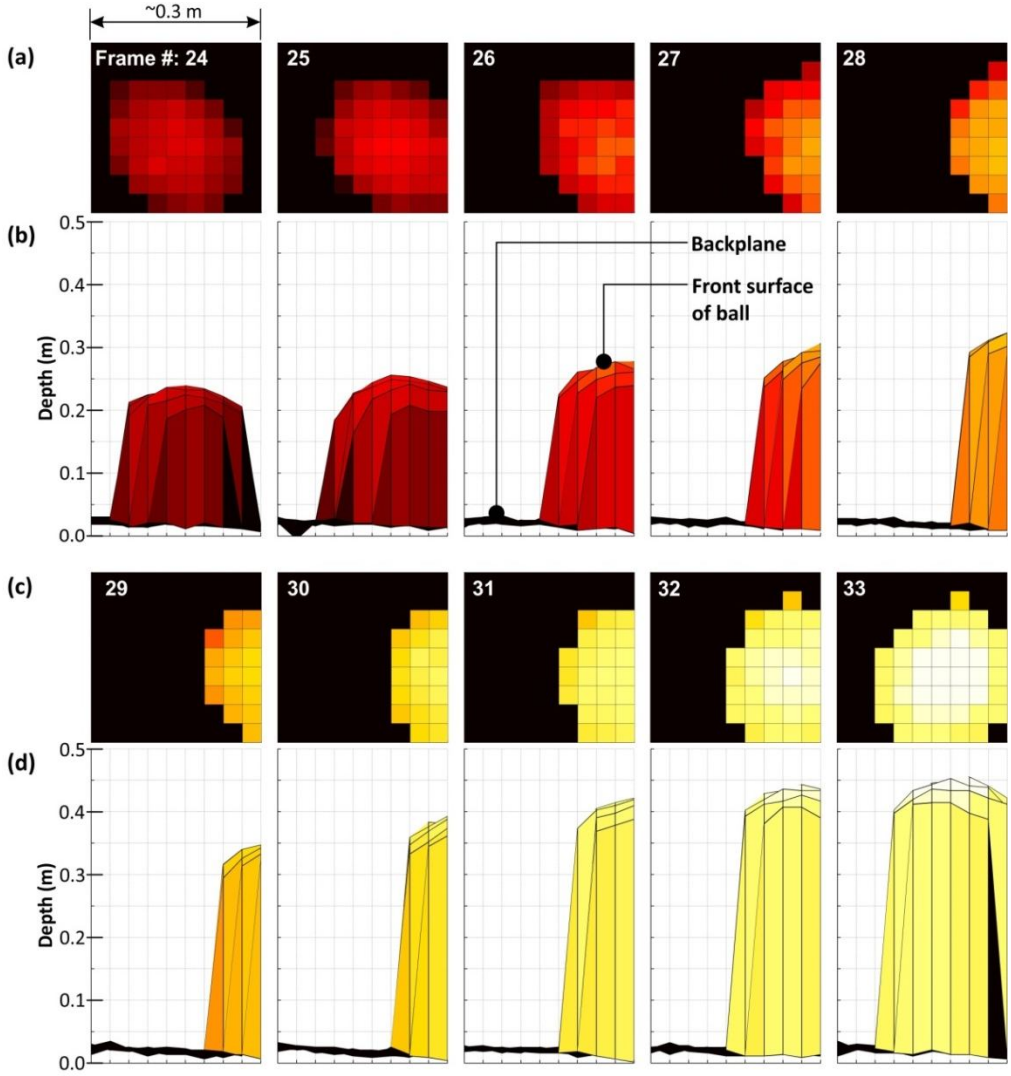

Figure 4-27 Time-of-flight depth profile movie of a swinging soccer ball, ~200 mm diameter, recorded in daylight from a stand-off distance of 325 metres. The movie recorded the ball swinging in a conical pendulum motion. The four-second, 10×10 pixel movie with 10 frames per second was acquired using an acquisition time of 1 ms per pixel. Two different views of the data from ten consecutive frames (numbers 24 to 33) are shown. The images shown in rows (a) and (c) are face-on views as seen from the direction of the transceiver, and the corresponding top-down depth view of the data for each of the frames is shown in rows (b) and (d). The same colour scheme is used to map depth in all of the plots. (From [4.34]).

Depth profiling at a longer stand-off distance of 910 m was performed in daylight with a corresponding normalised background noise count rate of approximately 32 kHz. Scanned depth images of the life-sized mannequin with per-pixel acquisition times of 20, 10, 5, and 2 ms are shown in Figure 4-28. As a result of the increase in stand-off distance, while still maintaining the same system parameters, longer per-pixel acquisition times were required at this distance in order to obtain images with a corresponding level of depth detail to those acquired at 325 m. Even so, for scans with per-pixel acquisition times as low as 5 ms, it is possible to clearly discern the outline of the mannequin, and the vast majority of the depth profile. The clear advantage of depth imaging compared with low-photon number imaging is evident in the photon-starved regime represented by the low per-pixel acquisition times. A number of the pixels that had achieved a reliable depth value in the image acquired with a 2 ms per-pixel dwell time, as shown in Figure 4-28(e), were analysed. The data from these pixels indicated that a maximum of 6 return photons had been detected for individual pixels on the MDF backplane, and a maximum of 4 return photons from individual pixels on the mannequin.

We also performed depth-profiling measurements of a scene at a stand-off distance of 4.5 kilometres. At this stand-off distance we expected much lower returns, in comparison to those obtained for the 325 m and 910 m measurements when using the same system parameters. Due to this, cooperative targets were used, i.e. retro-reflective material attached to flat boards. These measurements were carried out in bright daylight which corresponded to a normalised background noise count rate of approximately 78 kcps. Figure 4-29 shows the depth images of these cooperative targets measured using three different per-pixel acquisition times: 2 s, 500 ms, and 100 ms. Even at the relatively short pixel acquisition time of 100 ms, clear depth imaging profiles can be seen. The flat panels and the separation between the targets can be clearly seen. In these measurements, the separation between adjacent planes was approximately 270 mm and the spot size at this distance was approximately 300 mm diameter.

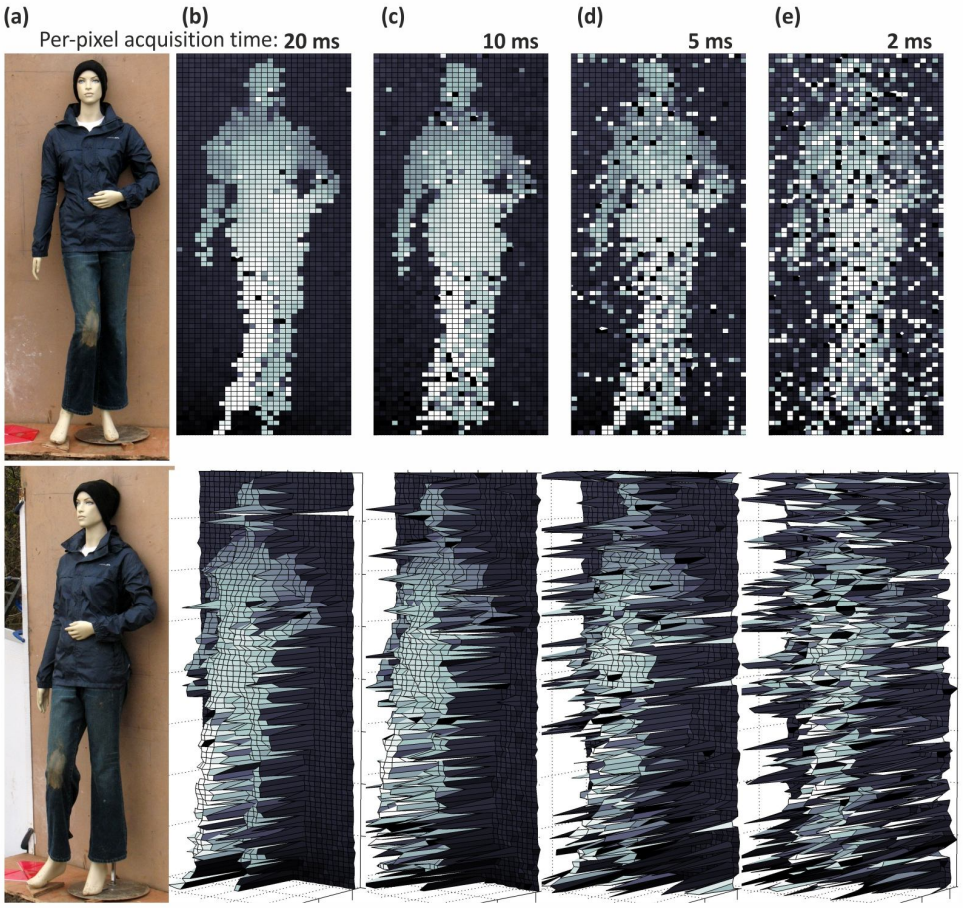

Figure 4-28 Depth profile measurements made in daylight of a life-size mannequin from a stand-off distance of 910 metres. The close-up photographs in column (a) are different viewpoints of the scene that was scanned which consisted of the mannequin against a MDF backplane. Each depth scan covered an area of approximately 800×2000 mm using 30×80 pixels, resulting in a pixel-to-pixel spacing of approximately 25 mm in X and Y. Surface plots of the raw depth data obtained for per-pixel acquisition times of 20, 10, 5, and 2 ms are shown in columns (b) to (e) - each of these columns show two different views of the same data obtained with the specified per-pixel acquisition time, and a white to black colour shading is used to map depth. A per-pixel acquisition time of 10 ms equated to a total scan time of 24 s for this scene. (From [4.34]).

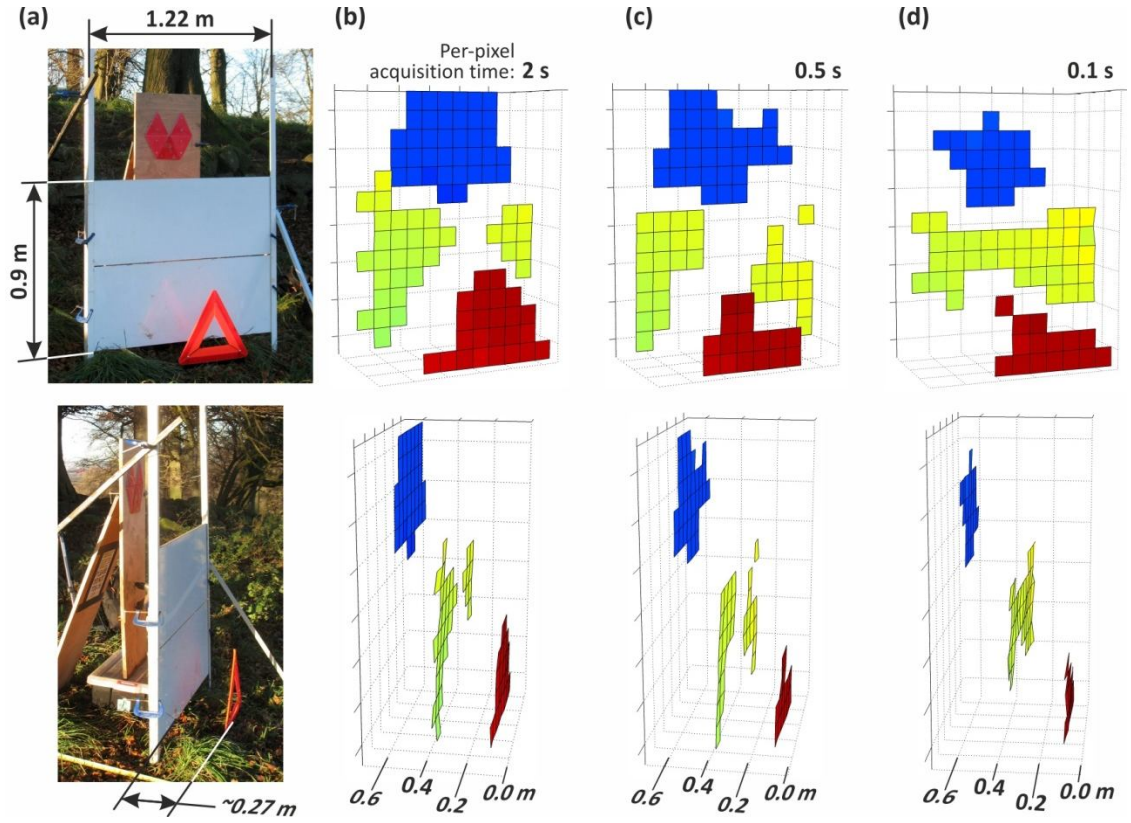

Figure 4-29 Depth images acquired in daylight at a stand-off distance of 4500 metres of a scene containing cooperative targets. The photographs in column (a) show two different viewpoints of the scene that was scanned. The scene consisted of two stacked 12.5 mm thick plywood panels (resulting in an area measuring 900 mm tall and 1220 mm wide) covered in white retro-reflecting material. Approximately 275 mm in front of this, on the ground, was a 400 mm tall red retro-reflective roadside warning triangle. A 400 mm wide plywood panel, with a set of five red retro-reflecting triangles, was placed centrally about 300 mm behind the white boards. Each depth scan covered an area of approximately 1500 mm tall by 1220 mm wide using 15×12 pixels, resulting in a pixel-to-pixel spacing of approximately 100 mm in X and Y. Surface plots of the depth data obtained for per-pixel acquisition times of 2, 0.5, and 0.1 s are shown in columns (b), (c) and (d) respectively - each of these columns show two different views of the same data obtained with the specified per-pixel acquisition time, and the colour shading is used to map depth. (From [4.34]).

4.3.3 Comparison of the scanning depth imagers using SNSPD and InGaAs/InP SPAD

Although the parameters for two scanning depth imagers using SNSPD and InGaAs/InP SPAD described above have been mentioned individually in last few sections, their main parameters are summarised in Table 4-1 so that the two individual systems can be

identified more readily. Note that the timing jitter of 98 ps FWHM for the SNSPD system is lower in comparison to 144 ps FWHM timing jitter for the InGaAs/InP SPAD system. Both systems have reduced jitter than that of the λ=850 nm system reported in [4.11] in 2009, but slower compared to the jitter of ~60 ps FWHM for the more recently upgraded system described in Chapter 7, which incorporates a thin-junction SPAD [4.38] (by Micro Photon Devices, Italy) operating in gate mode.

It is important that the aforementioned field trials used two individual systems (based on the SNSPD and InGaAs/InP SPAD) under different background levels and weather conditions. Hence, it is challenging to make a direct comparison between the performance of two independent systems. Two figures of merit of depth uncertainty and signal to noise ratio (SNR) will be discussed to make a performance comparison between two depth imagers.

In order to quantitatively evaluate the depth uncertainty at the three stand-off distances of 325 m, 910 m and 4500 m, we scanned a 12.5-mm-thick 900 mm×1220 mm flat plywood panel at near normal incidence. One side of this plywood panel was covered in white retro-reflective material (T6500 HIP by Avery Dennison) while the other side was uncovered. The plain plywood surface of the panel was scanned at the stand-off distances of 325 m and 910 m, and the retro-reflective side was scanned at 910 m and 4500 m. In each case, we measured a 2D array of pixels and fitted these depth measurements to a flat plane. The depth residual, expressed as one standard deviation, was recorded for the three stand-off distances and various per-pixel acquisition times in order to produce the results shown in Figure 4-30. As is shown in this plot, a per-pixel acquisition time of 20 ms yielded depth uncertainties of approximately 1.2 mm and 7 mm for the scans of the plywood surface of the panel at stand-off distances of 325 m and 910 m respectively. Scans of the retro-reflective surface of the panel at stand-off distances of 910 m and 4500 m at the same per-pixel acquisition time of 20 ms achieved depth residuals of approximately 2 mm and 4 mm respectively. These calculations are based on approximately 3600 pixels for the 325 m range, and approximately 300 pixels for the 910 m and 4500 m ranges. In terms of the data in shown in Figure 4-30, the SNSPD system exhibits slightly better performance even though employing lower photon detection efficiency and less average output power. This is likely to be a result of the improved time jitter of the SNSPD system (100 ps FWHM) compared to that of the InGaAs/InP SPAD system (140 ps FWHM), since the background will be dominated by solar background.

Detector	NbTiN SNSPD	InGaAs/InP SPAD
Laser source	Mode locked fibre laser	Supercontinuum laser
Wavelength	1560 nm (~10 nm FWHM)	1550 nm (~30 nm FWHM)
Pulse duration	<1 ps	<50 ps
Repetition rate	50 MHz	40 MHz
Average optical power	<250 μW	<600 μW
Optical energy per pulse	<5 pJ	<15 pJ
Detector collection fibre	~9 μm core diameter	
Objective lens	500 mm focal length, 80 mm diameter	
X-Y spatial resolution	~50 μrad	
Range	Scans performed at 325, 910 and 4400 metres	
Data acquisition module	PicoHarp 300, PicoQuant GmbH, Germany	
Photon detection efficiency	18%	26%
System temporal response (FWHM)	98 ps	144 ps
Dark count rate	1 kcps	16 kcps
Detector operating temperature	3 K	230 K

Table 4-1 Performance comparison of two depth imagers in terms of their main parameters

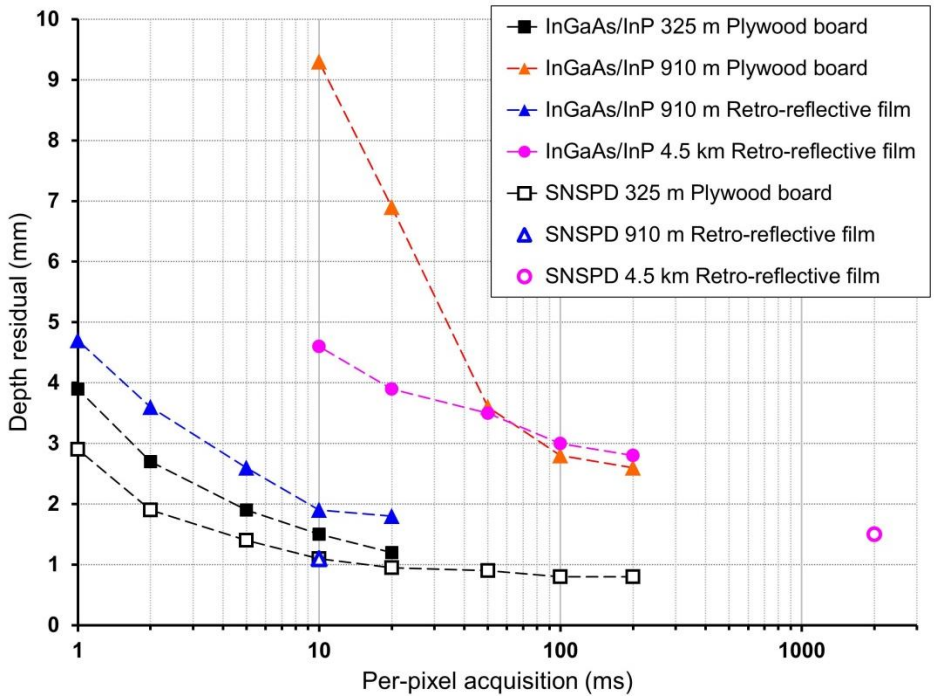

Figure 4-30 Depth uncertainty measurements made using the gated-mode InGaAs/InP SPAD detector (the filled marker points) and measurements made previously using a free-running SNSPD (unfilled marker points). The measurements were acquired by scanning a 900×1220×12.5 mm thick, flat plywood panel at stand-off distances of 325 metres, 910 metres, and 4500 metres. The panel was scanned at near normal incidence – one side of the plywood panel was covered in white retro-reflective material, and the other side was uncovered. The graph shows the depth residuals, expressed as one standard deviation from the mean, for scans made using various per-pixel acquisition times on the plywood surface (325 m and 910 m) and the retro-reflective surface (910 m and 4500 m). The residuals were calculated using approximately 3600 pixels for the scans at 325 m, and approximately 300 pixels for the scans at both 910 m and 4500 m. (From [4.34]).

In addition, it is necessary to use the measured photon count data to characterise the detection SNRs using Equation (2.6) of both systems. The same 6 mm thick MDF sheet was used as a reference backplane for all the mentioned field trials for both systems. In addition, the surface normal of the backplane was approximately parallel to the line-of-sight of the transceiver. The backplane is relatively flat and thus should provide returns that are more consistent in comparison to the mannequin, which presents a much greater variation in the surface normal and high reflectivity variations. It should also provide a quantifiable and repeatable basis for characterisation of the detection SNRs. Therefore, the SNRs of both systems were investigated by the use of the pixel-wise photon counts on this MDF backplane. By analysing approximately 400-pixel raw photon count data

on the MDF sheet at stand-off distances of 325 m and 910 m, the acquisition-time-dependent SNR data of two depth imagers can be seen in Figure 4-31. In comparison to the SNSPD system, higher SNR values at a stand-off distance of 325 m for the InGaAs system suggest that collected signal returns likely dominate the detection performance due to the higher illumination power used. When the working distance was extended to 910 m, given a fixed acquisition time, the collected photons for both systems dropped dramatically, as expected with the increase in stand-off distance. However, the decline rate of the SNR values of the InGaAs system is larger compared to that of the SNSPD system. It is likely due to lower timing jitter and DCR for the SNSPD. However, it is very difficult to make exact comparisons between them due to variations in the solar background between measurements.

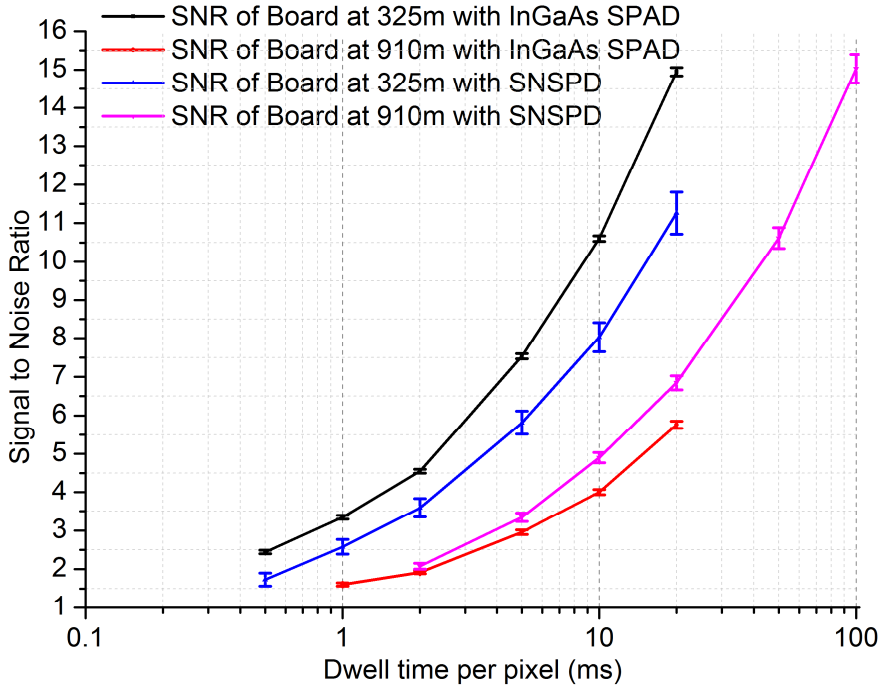

Figure 4-31 Characterisation of the signal-to-noise ratios (SNRs) of the imagers using InGaAs/InP SPAD and SNSPD by analysing the raw photon count data on the same 6 mm thick MDF sheet acting as a backplane for all the mentioned depth profiling measurements in this Chapter at stand-off distances of 325 m and 910 m. The photon data of ~400 pixels on this MDF sheet was evaluated and the error bars characterise the standard deviation of photon counts among the pixels of interest.

The relation between the depth resolution and SNR can be investigated by taking into account of both Figure 4-30 and Figure 4-31 and assuming similar reflectivity of both plywood and MDF boards. It seems that at least SNRs of 1 and 10 are required for depth profiling with depth resolutions of <5 mm and ~1 mm respectively on the targets

at a stand-off distance of 325 metres for both systems. It is expected that photon data with higher SNR offers better depth resolution. This implies that higher signal photon counts allow the reduction of susceptibility to background noise for high-quality single-photon depth images.

4.4 Conclusions

We have demonstrated two TOF scanning depth imaging systems operating at $\lambda \sim 1550$ nm using two advanced single-pixel single photon detector. Use of telecommunications wavelengths takes advantages of the reduced atmospheric attenuation and lower solar background when compared to operation at shorter wavelengths. In addition, in terms of eye safety, these wavelength bands are outside the retinal hazard region and therefore permits the use of a higher average optical power illumination beam in comparison to the previous output power used in measurements by our team made at 842 nm. By using an average laser power of less than 1 mW, excellent frame rates of movies have been achieved demonstrating that higher power sources can be utilised in future for higher frame rates or improved depth resolution whilst still maintaining entirely eye-safe operating conditions.

To the best of my knowledge, the scanning depth imager using a superconducting nanowire single photon detector with low noise and timing jitter was the first single-photon imaging system capable of depth profiling on low-signature, non-cooperative targets under bright daylight conditions at stand-off distances up to kilometre range using eye safe low average power illumination before 2013. The other imager was constructed by using a compact packaged, thermo-electrically-cooled, gated-mode InGaAs/InP SPAD detector with comparable performance of the SNSPD. The field trial results based on this system point the way towards the practical implementation of an eye-safe, 1550 nm wavelength depth imaging system with realistic potential of compact construction and low-power operation (optical and electrical). This system would therefore be compatible with a number of remote 3D imaging applications, including those using mobile platforms

In 2014, Selex ES developed single-photon depth imaging systems at $\lambda \sim 1550$ nm using both single-pixel and 32×32-pixel arrayed InGaAs/InP SPAD detectors with working distances up to ~10 km [4.39-4.41]. However, their employed transmit energy was up to a few μJ per laser pulse which was at least three orders higher than the one used in our systems. In addition, their reported depth resolution was a few centimetres.

Both our scanning depth imagers have facilitated the acquisition of depth profile images with millimetre-scale depth resolution – far beyond the capabilities of other current single-photon approaches at such ranges. These results demonstrate the flexibility of the TCSPC technique in negotiating the trade-offs between depth resolution, acquisition times of photon data, and optical power.

The author worked with Dr. Aongus McCarthy (AMcC), Dr. Nathan R. Gemmell (NRG) and Dr. Nils J. Krichel (NJK) to build the experimental setups and carry out the experiments and data analysis related to the work presented in this Chapter. The majority of the efficiency measurements (the result was described in section 4.3.2.1) on the InGaAs/InP SPAD detector were carried out by Dr. Ryan E. Warburton and Giuseppe Intermite with only a minor contribution from the author. NJK, AMcC and Dr. Robert J. Collins contributed to the original design of the scanning transceiver system, scan control and data acquisition software and also the Matlab data analysis scripts, which were updated by the author and NRG later. Prof. Robert H. Hadfield, Dr. Mike G. Tanner and Dr. Chandra Natarajan provided the SNSPD system and also the relevant maintenance. Dr. Alberto Tosi's group, particularly Adriano Della Frera, loaned the prototype InGaAs/InP SPAD detection module and provided for expertise in its use. All of the work presented in this Chapter was supervised by Prof. Gerald S. Buller.

4.5 References

[4.1]. B. Schwarz, "LIDAR: Mapping the world in 3D," Nat. Photonics (4), 429-430 (2010).

[4.2]. M. C. Amann, T. Bosch, M. Lescure, R. Myllyla, and M. Rioux, "Laser ranging: a critical review of usual techniques for distance measurement," Opt. Eng. (40), 10-19 (2001).

[4.3]. C. Mallet, and F. Bretar, "Full-waveform topographic lidar: State-of-the-art," ISPRS J. Photogramm. Remote Sens. (64), 1-16 (2009).

[4.4]. W. Becker, *Advanced Time-Correlated Single Photon Counting Techniques* (Springer, 2005).

[4.5]. G. S. Buller, and A. M. Wallace, "Ranging and three-dimensional imaging using time-correlated single-photon counting and point-by-point acquisition," IEEE J. Select. Topics Quantum Electron. (13), 1006-1015 (2007).

[4.6]. F. Blais, "Review of 20 years of range sensor development," J. Electron. Imaging (13), 231-243 (2004).

[4.7]. C. Ho, K. L. Albright, A. W. Bird, J. Bradley, D. E. Casperson, M. Hindman, W. C. Priedhorsky, W. R. Scarlett, R. C. Smith, J. Theiler, and S. K. Wilson, "Demonstration of literal three-dimensional imaging," Appl. Opt. (38), 1833-1840 (1999).

[4.8]. J. J. Degnan, "Photon-counting multikilohertz microlaser altimeters for airborne and spaceborne topographic measurements," J. Geodyn. (34), 503-549 (2002).

[4.9]. M. A. Albota, B. F. Aull, D. G. Fouche, R. M. Heinrichs, D. G. Kocher, R. M. Marino, J. G. Mooney, N. R. Newbury, M. E. O'Brien, B. E. Player, B. C. Willard, and J. J. Zayhowski, "Three-Dimensional Imaging Laser Radars with Geiger-Mode Avalanche Photodiode Arrays," Lincoln Lab. J (13), 351-370 (2002).

[4.10]. B. F. Aull, A. H. Loomis, D. J. Young, R. M. Heinrichs, B. J. Felton, P. J. Daniels, and D. J. Landers, "Geiger mode avalanche photodiodes for three-dimensional imaging," Lincoln Lab. J. (13), 335–350 (2002).

[4.11]. A. McCarthy, R. J. Collins, N. J. Krichel, V. Fernandez, A. M. Wallace, and G. S. Buller, "Long-range time-of-flight scanning sensor based on high-speed time-correlated single-photon counting," Appl. Opt. (48), 6241-6251 (2009).

[4.12]. P. A. Hiskett, C. S. Parry, A. McCarthy, and G. S. Buller, "A photon-counting time-of-flight ranging technique developed for the avoidance of range ambiguity at gigahertz clock rates," Opt. Express (16), 13685-13698 (2008).

[4.13]. C. Niclass, A. Rochas, P. A. Besse, and E. Charbon, "Design and characterization of a CMOS 3-D image sensor based on single photon avalanche diodes," IEEE J. Solid-State Circuits (40), 1847-1854 (2005).

[4.14]. D. Stoppa, L. Pancheri, M. Scandiuzzo, L. Gonzo, G. F. Dalla Betta, and A. Simoni, "A CMOS 3-D imager based on single photon avalanche diode," IEEE Trans. Circuits Syst. Regul. Pap. (54), 4-12 (2007).

[4.15]. C. Niclass, M. Soga, H. Matsubara, S. Kato, and M. Kagami, "A 100-m Range 10-Frame/s 340 x 96-Pixel Time-of-Flight Depth Sensor in 0.18-mu m CMOS," IEEE J. Solid-State Circuits (48), 559-572 (2013).

[4.16]. R. Henderson, and K. Schulmeister, *Laser Safety* (Institute of Physics Publishing, 2004).

[4.17]. G. S. Buller, and R. J. Collins, "Single-photon generation and detection," Meas. Sci. Technol. (21), 012002 (2010).

[4.18]. R. H. Hadfield, "Single-photon detectors for optical quantum information applications," Nat. Photonics (3), 696-705 (2009).

[4.19]. G. S. Buller, and R. J. Collins, "Single-photon generation and detection," Meas. Sci. Technol. (21), 012002 (2010).

[4.20]. M. G. Tanner, C. M. Natarajan, V. K. Pottapenjara, J. A. O'Connor, R. J. Warburton, R. H. Hadfield, B. Baek, S. Nam, S. N. Dorenbos, E. B. Urena, T. Zijlstra, T. M. Klapwijk, and V. Zwiller, "Enhanced telecom wavelength single-photon detection with NbTiN superconducting nanowires on oxidized silicon," Applied Physics Letters (96), 221109 (2010).

[4.21]. R. E. Warburton, A. McCarthy, A. M. Wallace, S. Hernandez-Marin, R. H. Hadfield, S. W. Nam, and G. S. Buller, "Subcentimeter depth resolution using a single-photon counting time-of-flight laser ranging system at 1550 nm wavelength," Opt. Lett. (32), 2266-2268 (2007).

[4.22]. A. McCarthy, N. J. Krichel, N. R. Gemmell, X. Ren, M. G. Tanner, S. N. Dorenbos, V. Zwiller, R. H. Hadfield, and G. S. Buller, "Kilometer-range, high resolution depth imaging via 1560 nm wavelength single-photon detection," Opt. Express (21), 8904-8915 (2013).

[4.23]. C. M. Natarajan, M. G. Tanner, and R. H. Hadfield, "Superconducting nanowire single-photon detectors: physics and applications," Supercond. Sci. Technol. (25), 063001 (2012).

[4.24]. N. R. Gemmell, "Infrared single photon sensing," PhD Thesis, Heriot-Watt University (2015).

[4.25]. P. Yuan, R. Sudharsanan, X. G. Bai, P. McDonald, E. Labios, B. Morris, J. P. Nicholson, G. M. Stuart, H. Danny, S. Van Duyne, G. Pauls, S. Gaalema, M. D. Turner, and G. W. Kamerman, "Three-dimensional imaging with 1.06 μm Geiger-mode LADAR camera," Laser Radar Technology and Applications XVII (8379), 837902 (2012).

[4.26]. M. Entwistle, M. A. Itzler, J. Chen, M. Owens, K. Patel, X. D. Jiang, K. Slomkowski, S. Rangwala, and J. C. Campbell, "Geiger-mode APD Camera System for Single Photon 3-D LADAR Imaging," Advanced Photon Counting Techniques VI

(8375) (2012).

[4.27]. M. A. Diagne, M. Greszik, E. K. Duerr, J. J. Zayhowski, M. J. Manfra, R. J. Bailey, J. P. Donnelly, and G. W. Turner, "Integrated array of 2-μm antimonide-based single-photon counting devices," Opt. Express (19), 4210-4216 (2011).

[4.28]. C. M. Natarajan, "Superconducting nanowire single-photon detectors for advanced photon-counting applications," PhD Thesis, Heriot-Watt University (2011).

[4.29]. A. Tosi, A. Della Frera, A. B. Shehata, and C. Scarcella, "Fully programmable single-photon detection module for InGaAs/InP single-photon avalanche diodes with clean and sub-nanosecond gating transitions," Rev. Sci. Instrum. (83) (2012).

[4.30]. D. S. Bethune, W. P. Risk, and G. W. Pabst, "A high-performance integrated single-photon detector for telecom wavelengths," J. Mod. Opt. (51), 1359-1368 (2004).

[4.31]. A. Tomita, and K. Nakamura, "Balanced, gated-mode photon detector for quantum-bit discrimination at 1550 nm," Opt. Lett. (27), 1827-1829 (2002).

[4.32]. N. J. Krichel, A. McCarthy, I. Rech, M. Ghioni, A. Gulinatti, and G. S. Buller, "Cumulative data acquisition in comparative photon-counting three-dimensional imaging," J. Mod. Opt. (58), 244-256 (2011).

[4.33]. A. Bashkatov, E. Genina, V. Kochubey, and V. Tuchin, "Optical properties of human skin, subcutaneous and mucous tissues in the wavelength range from 400 to 2000 nm," J. Phys. D: Appl. Phys. (38), 2543 (2005).

[4.34]. A. McCarthy, X. Ren, A. Della Frera, N. R. Gemmell, N. J. Krichel, C. Scarcella, A. Ruggeri, A. Tosi, and G. S. Buller, "Kilometer-range depth imaging at 1550 nm wavelength using an InGaAs/InP single-photon avalanche diode detector," Opt. Express (21), 22098-22113 (2013).

[4.35]. A. Nayak, E. Trucco, A. Ahmad, and A. M. Wallace, "SimBIL: appearance-based simulation of burst-illumination laser sequences," IET Image Proc. (2), 165-174 (2008).

[4.36]. N. Namekata, S. Adachi, and S. Inoue, "1.5 GHz single-photon detection at telecommunication wavelengths using sinusoidally gated InGaAs/InP avalanche photodiode," Opt. Express (17), 6275-6282 (2009).

[4.37]. M. Ren, X. R. Gu, Y. Liang, W. B. Kong, E. Wu, G. Wu, and H. P. Zeng, "Laser ranging at 1550 nm with 1-GHz sine-wave gated InGaAs/InP APD single-photon detector," Opt. Express (19), 13497-13502 (2011).

[4.38]. Micro Photon Devices Italy, "MPD PDM series. Datasheet. online (http://www.micro-photon-devices.com/Docs/Datasheet/PDM.pdf) last accessed 20-02-2015."

[4.39]. P. A. Hiskett, K. J. Gordon, J. W. Copley, and R. A. Lamb, "Long range 3D imaging with a 32x32 Geiger mode InGaAs/InP camera," *SPIE Sensing Technology+ Applications*, International Society for Optics and Photonics, pp. 91140I-91140I-91113, (2014).

[4.40]. K. J. Gordon, P. A. Hiskett, R. Pilkington, J. Copley, A. Pawlikowska, and R. A. Lamb, "New Trends in Integrated Imaging Lidar," *Applications of Lasers for Sensing and Free Space Communications*, Optical Society of America, p. LW3A. 1, (2013).

[4.41]. A. M. Pawlikowska, R. M. Pilkington, K. J. Gordon, P. A. Hiskett, G. S. Buller, and R. A. Lamb, "Long-range 3D single-photon imaging lidar system," *SPIE Security+ Defence*, International Society for Optics and Photonics, pp. 925007-925007-925010, (2014).

Chapter 5
Time-of-flight depth imaging with CMOS Si-SPAD array detectors

5.1 Introduction

To date, Complementary Metal-Oxide-Semiconductor (CMOS) silicon Single Photon Avalanche Diode (SPAD) array detectors are the most versatile solid-state single photon arrayed sensors working at wavelengths of less than 1000 nm. Typically, these arrays consist of smart pixels, with each pixel containing a photosensitive SPAD detector and electronics for photon timing, processing and short-term storage. A significant issue with these SPAD detector arrays is that they suffer from having a low fill factor i.e. the detector photosensitive area is small compared to the full area of each pixel. One way of increasing the fill factor is to integrate a microlens array with the SPAD array so that more of the incident light is directed onto the detector active area of each smart pixel.

MiSPIA (Microelectronic Single-Photon 3D Imaging Arrays for low-light high-speed Safety and Security Applications), was a European-Commission-funded project (FP7, grant agreement number: 257646) which ran from 2010 to 2014. The aim of the project was to explore, develop and test microelectronic technologies for cost-effective manufacturing of very fast, high sensitivity, 3D SPAD cameras. The collaborators included, amongst others, the Politecnico di Milano in Italy, the Fraunhofer Institute for Microelectronic Circuits and Systems in Duisburg, Germany and Heriot-Watt University. Professor Franco Zappa's group at the Politecnico di Milano designed the CMOS Si-SPAD array chips, which were then fabricated by the Fraunhofer Institute using high-voltage 0.35 μm CMOS technology. At Heriot-Watt University (HWU), microlens arrays were designed, fabricated, and integrated with the SPAD array chips. The performance of the integrated SPAD array / microlens assembly was then fully characterised at different operational wavelengths and illuminations at different f-numbers. In addition, long-range time-of-flight depth profiling experiments were

carried out at HWU using a SPAD array.

This Chapter describes the work that was carried out at HWU on the MiSPIA project. The nature and scale of the project meant that a number of people were involved in the work. The author's contributions will be made clear at appropriate points in the Chapter. In order to set the scene, section 5.2 provides some background information on the fabricated SPAD array chips and the key parameters related to the integration of the microlens array with the SPAD array. The factors, which influenced the choice and design of the microlenses, are covered in section 5.3. The following section deals with the processes used for bonding the microlens array to the SPAD array chip. Section 5.5 details the characterisation of the assembly and the performance gains. The use of a SPAD array (without microlenses) for time-of-flight ranging measurements over distances of 45 and 325 metres is detailed in sections 5.6 and 5.7.

5.2 CMOS Si-SPAD array detectors

By virtue of the extensive progress of CMOS integrated circuit technology over last 30 years, the CMOS-based monolithic fabrication of SPAD devices can benefit from the availability of mature, robust and cost-effective technology and further possibility of developing compact on-chip systems with a high level of complexity. The fabrication technologies of silicon SPAD array detectors reported to date can be classified into two streams (refer to Page 104 of [5.1]):

(1) SPADs fabricated in high-voltage (HV) CMOS technology. Differing from ordinary CMOS circuits, HV-CMOS circuits have more stringent features as they must operate under much higher voltages. Typically, the applied electric field intensity of the HV-CMOS-based SPAD devices is sufficiently high ($> 3 \times 10^5$ V/cm). Small-active-area (e.g. diameter is less than 20 μm) SPADs were implemented with reasonably low dark count rates using 0.8 μm HV-CMOS technology [5.2-5.4]. By using more advanced technology, such as 0.35 μm HV-CMOS technology, SPADs with moderate dark count rates of about 103 cps at an active area diameter of ~20 μm and peak single-photon detection efficiency (SPDE) of ~50% were obtained [5.5-5.6].

(2) SPADs fabricated in standard deep-submicron (DSM) CMOS technology. DSM-CMOS technologies are ideal for the fabrication of high pixel-density SPAD arrays integrated with smart in-pixel electronics. However, their inherent specifications are not necessarily consistent with the performance of a discrete SPAD detector. When

using DSM-CMOS technologies to fabricate SPADs, it is very challenging to precisely choose a suitable breakdown region in order to avoid band-to-band and trap-assisted tunnelling and thus reduce dark count rates. In addition, it is difficult to design a proper guard ring for SPADs with a few micrometres diameter active area to prevent premature edge breakdown (refer to Page 107 of [5.1]). High dark count rates (e.g. 105 cps) at ~10 μm diameter photoactive area and peak SPDE of ~30% were reported for SPADs fabricated using 130 nm and 180 nm CMOS technology with specific designs on guard rings [5.7-5.8].

Unlike charge-coupled devices (CCDs) and CMOS active pixel sensors, CMOS-based SPAD arrays are excellent for low-light-level high-speed 2D imaging and time-of-flight 3D imaging. This is because they have the advantage of ultra-low readout and excess noise, ultra-high photon sensitivity. In addition, by means of time-to-amplitude converters (TAC) or in particular time-to-digital converters (TDC), SPAD arrays can have an accurate time-revolved functionality. This can be obtained in pixel-level, column-level or array-level conversion [5.9-5.10]. Compared to the other two designs, the pixel-level-based implementation offers faster photon event detection as it has an individual processing channel dedicated to each detector. High complexity TDC circuits for high pixel-density SPAD arrays are employed along with in-pixel memory and dedicated high-speed readout circuits to properly buffer out the data stream. There is a trade-off in the performance of smart-pixel TDC electronics between timing bin width, time range, and timing linearity evaluated by integral (INL) and differential (DNL) nonlinearities in least-significant bit (LSB). For example, a brief summary of recent TDC devices is as follows: a TDC with 55 ps timing bin, 55 ns time range, 30% DNL and 250% INL was reported by Henderson's group [5.11]; a TDC with 119 ps timing bin, 120 ns time range, 50% DNL and120% INL was reported by Charbon's group [5.12]. However, within an individual pixel, the on-chip electronics cover a large area and hence the photosensitive area is small, resulting in low fill factor which is the ratio of photosensitive area to overall focal plane array area. For example, a fill factor of 5% was reported for the SPAD arrays fabricated using 0.35 μm CMOS technology in [5.13] compared to 1% [5.11] and 2.3% [5.12] fill factors for the devices fabricated using 130 nm CMOS technology.

In summary, as shown in Table 5-1, the reported SPAD arrays fabricated with HV-CMOS technologies tend to be better than those fabricated with DSM-CMOS technologies. This is taking into account the performance of devices with regards to

dark counts, detection efficiency, timing linearity, and pixel-wise fill factor of CMOS SPAD arrays with on-chip functional electronics. For example, silicon SPAD array detectors successfully implemented with the 0.35 μm high-voltage CMOS technology by the MiSPIA project are capable of both photon timing (i.e. measuring the photon arrival time) and photon counting (i.e. counting incident photons within a certain acquisition time). Their overall pixel pitch size is 150 μm×150 μm with an active detection area diameter of 30 μm resulting in a fill factor of 3.14% (see Figure 5-1), a TDC of 312 ps timing bin width, 320 ns time range, 2% DNL, and a 10% INL. The characteristics of their excess-bias-dependent photon detection efficiency and dark count rate can be seen in Figure 5-2 and Figure 5-3. The peak SPDE was ~50% at λ=410 nm while still 5% at the near-infrared wavelengths. The median dark count rate of less than 120 cps was achieved at around room temperature [5.14].

Si-SPAD array	**130 nm CMOS**[5.11]	**0.35 μm HV-CMOS** [5.12]
Peak SPDE	30%	50%
Dark counts at 20°	~10^5 cps for 10 μm diameter active area	~10^3 cps for 20 μm diameter active area
DNL (LSB)	30%	50%
INL (LSB)	250%	120%
Timing bin width	55 ps	119 ps
Time range	55 ns	120 ns
Fill factor	1%	2.3%

Table 5-1 Performance comparison of Si-SPAD arrays fabricated using 130 nm CMOS and 0.35 μm CMOS technologies respectively.

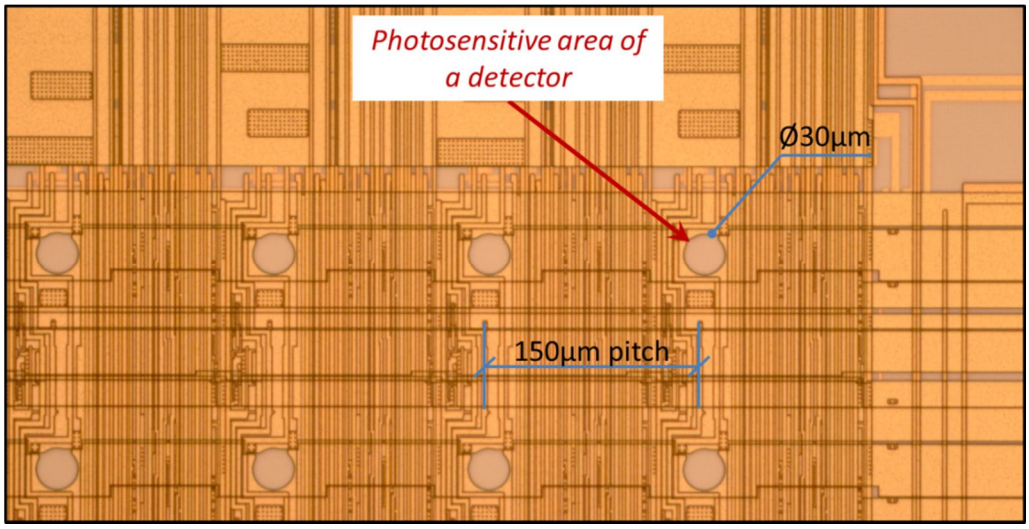

Figure 5-1 Microscope image obtained using a ×20 objective of a portion of a 32×32 SPAD array detector chip produced by the MiSPIA project. The diameter of the photosensitive area of a pixel detector is 30 µm and the pitch of the pixel detector is 150 µm, thus the fill factor of the photosensitive area to the entire area of each pixel detector is ~3.14 %.

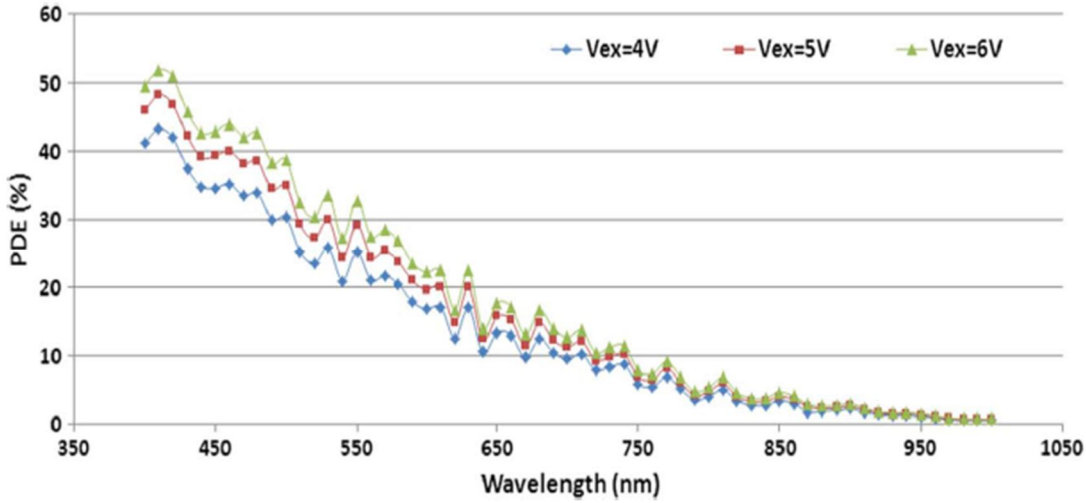

Figure 5-2 Spectral photon detection efficiency of MiSPIA 32×32 pixel CMOS Si-SPAD arrays. (From [5.14]).

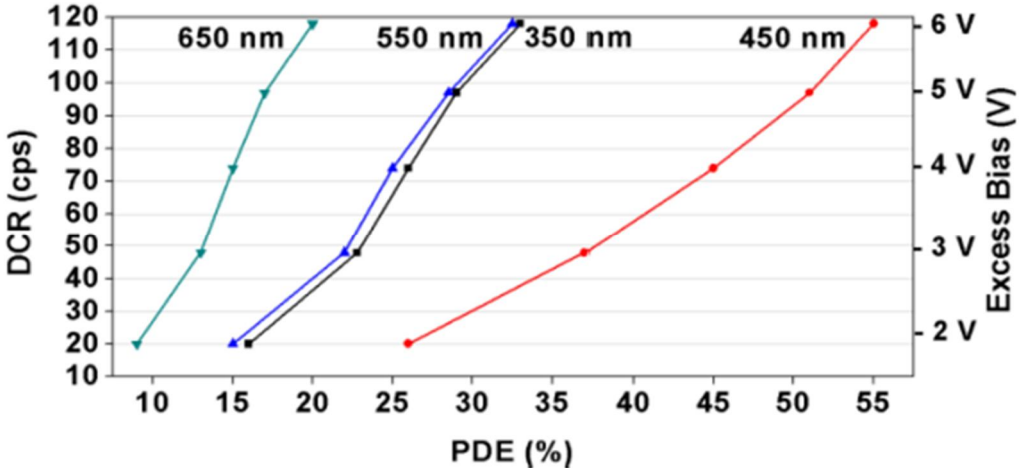

Figure 5-3 Plots of excess-bias-dependent median dark count rate versus photon detection efficiency at wavelengths of 350, 450, 550, 650 nm of MiSPIA 32×32 pixel CMOS Si-SPAD arrays. (From [5.15]).

5.3 Microlens arrays

Microlens arrays have been widely used as light concentrators to achieve enhancement of irradiance and fill-factor recovery for CCD and CMOS sensors [5.16]. Akin to the optical focusing functionality, it is also useful to integrate or package microlens arrays with SPAD arrays to enhance their fill factor. This is particularly important for the detectors typically combined with parallel electronics on the same wafer (i.e. front-illuminated SPAD arrays). These have lower fill factor compared to the ones implemented with wafer-to-wafer bonding 3D structure (i.e. back-illuminated InGaAs/InP SPAD arrays [5.17]).

5.3.1 Integration with detector array

Bonding between arrayed detector chip and microlens array can be implemented by using a thin layer of UV curable optical adhesive to attach the microlens array substrate directly onto the chip surface (see Figure 5-4). This bonding configuration is robust for handling and processing the bonded chip-lens array and seals the detector active area surface from dust and moisture. The dimensions in X and Y of the microlens substrate have to be significantly smaller than the detector chip in order to allow access to, and sufficient room for the bond pads around the perimeter of the chip for the wire bonding process. Furthermore, a precise volume of the optical adhesive is required to allocate for appropriate lens-to-chip bonding in order to avoid blocking periphery wire-bonding pads of the chip by the diffused adhesive. The actual bonded assemblies of the arrayed

detector chip and microlens array can be seen in Figure 5-5. As shown in Figure 5-5(a), a 32×32 microlens array (~5 mm×5 mm) was integrated with a 32×32 arrayed detector chip (~10 mm×10 mm). In addition, as shown in Figure 5-5(b), a 64×32 microlens array (~10 mm×5 mm) was integrated with a 64×32 arrayed detector chip (~20 mm×10 mm).

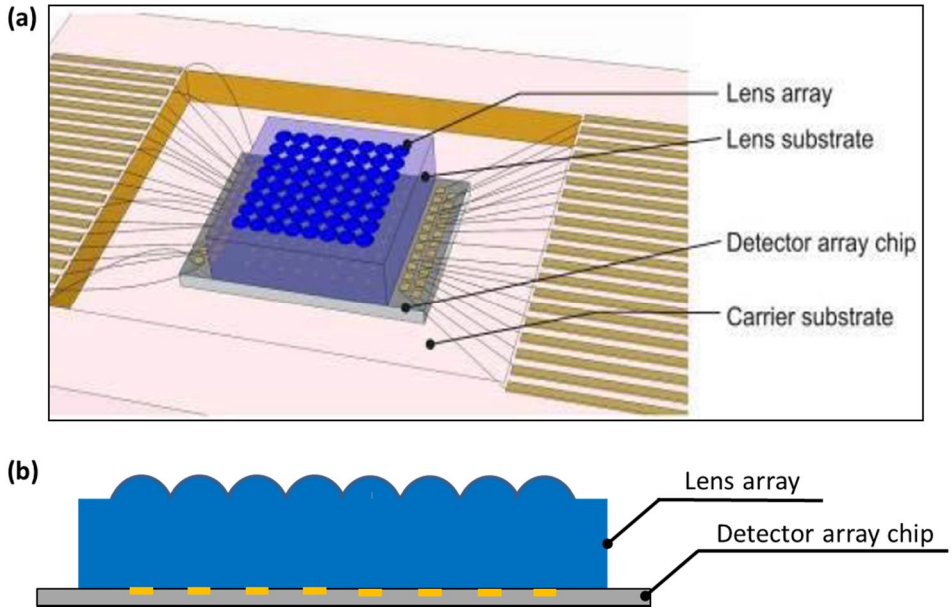

Figure 5-4 (a) Schematic diagram shows the direct lens-to-chip bonding configuration - 8×8 arrays of microlenses and detectors are shown here for clarity. Wire-bonding between the chip and external circuit is also illustrated. (b) shows a cross-sectioned view of the assembled lens and chip.

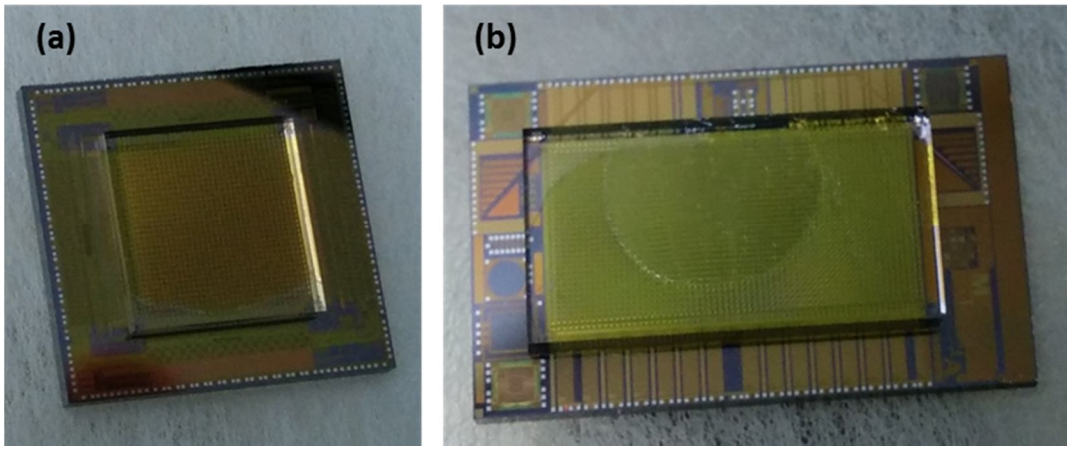

Figure 5-5 Bonded assemblies of (a) 32×32 and (b) 64×32 arrayed detector chip and microlens array. (a) A 32×32 microlens array (~5 mm×5 mm) was integrated with a 32×32 arrayed detector chip (~10 mm×10 mm). (b) A 64×32 microlens array (~10 mm×5 mm) was integrated with a 64×32 arrayed detector chip (~20 mm×10 mm).

5.3.2 Infinite and finite configurations

The microlens arrays integrated with the detector chips reported in this Chapter are all used to achieve optical focusing functionality. These focusing microlens arrays, fabricated on different glass substrate thicknesses, can function in infinite and finite imaging configurations when they are integrated with the detector arrays. The microlenses are classified into two groups: (1) an infinite conjugate lens (see Figure 5-6(a)) is compatible with an imaging configuration with an object or illumination source at infinity. (2) a finite conjugate lens (see Figure 5-6(b)), which is used to image an object, or illumination source placed at a finite distance from the microlens. It can produce an appropriate magnification, which enables its use in conjunction with a macro lens similar to a camera system.

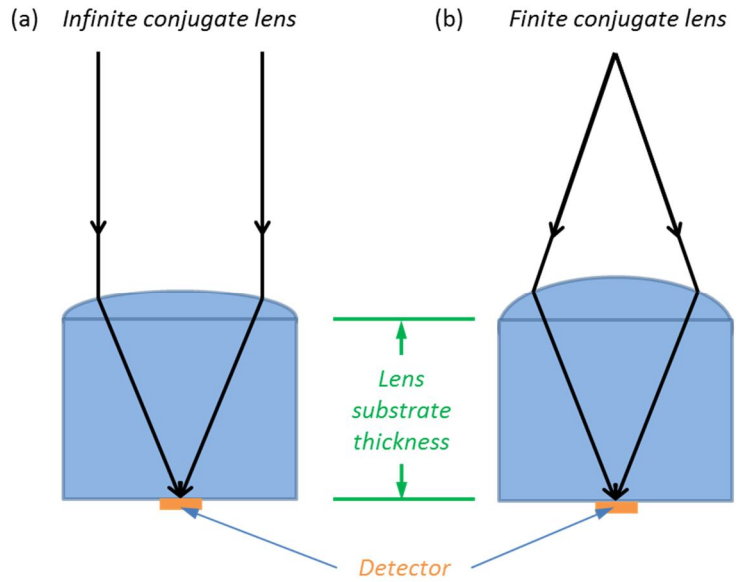

Figure 5-6 Infinite conjugate lens and finite conjugate lens imaging configurations (refer to Pages 9-10 and Pages 251-252 of [5.18]). (a) An object or illumination source at infinity is imaged into a detector by a focusing lens fabricated on the top of a glass substrate. For this infinite conjugate configuration, the image plane coincides with the focal plane. (b) An object or illumination source placed at a finite distance from the lens (fabricated on the top surface of the glass substrate) is imaged into a detector by a focusing lens fabricated on the top of a glass substrate. The image plane for this finite conjugate setup is located at a distance greater than the focal length.

Different types of microlens array can be fabricated on the glass substrate with a fixed thickness. However, the optimisation of focal length design of both microlens arrays is required to implement for the infinite and finite conjugate configurations. The design optimisation aims to form the conjugate imaging plane as close as possible to the back

surface of the substrate. Hence, the beam spot is focussed to be as small as possible on the detector photosensitive area. More specifically, the effective focal length of the microlenses in the glass substrate needs to be as close as possible to the thickness of the substrate for the infinite conjugate configuration. As for the finite conjugate imaging configuration, it is necessary to approximate a magnification of 0.2. This is inferred by shrinking the aperture of 150 µm that is equal to the detector pitch, down to the detector photosensitive area with a diameter of 30 µm as shown in Figure 5-7.

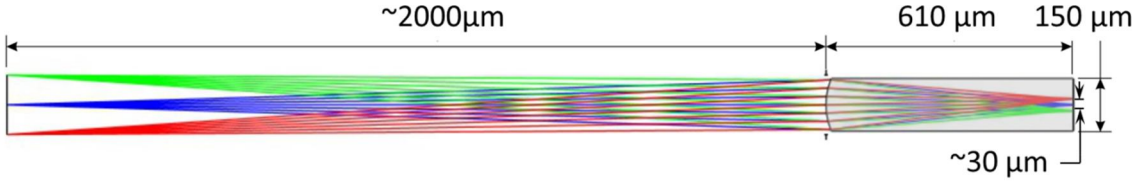

Figure 5-7 Ray-traced layout (from Zemax) shows a 150 µm diameter microlens, on a 610 µm thick substrate, used in a finite conjugate imaging configuration to form an image spot with ~30 µm diameter. In other words, it aims to achieve a magnification of 0.2 approximately in this finite conjugate imaging configuration.

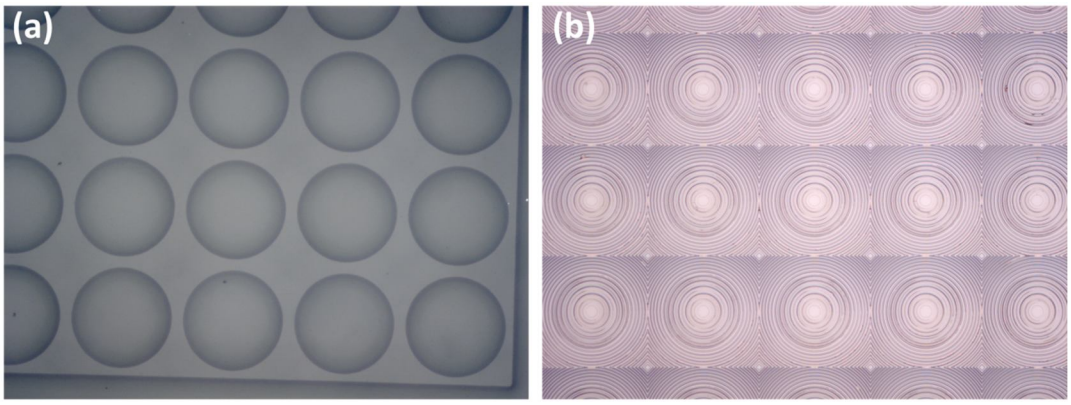

Figure 5-8 Left: Optical microscope images obtained using (a) ×20 objective in the top-down view of a portion of a 32×32 rectangular packed array of refractive fused silica microlenses. The microlens array has a pitch of 150 µm and the aperture diameter of the refractive microlens is ~135 µm; Right: Optical microscope images obtained using (b) ×20 objectives in the top-down view of part of a 32×32 rectangular packed array of diffractive fused silica microlenses. The microlens array has a pitch of 150 µm and the size of the square aperture of the diffractive microlens is 150 µm×150 µm in XY.

5.3.3 Types of microlenses

Microlens arrays are made in two main configurations: refractive and diffractive. In this project, both types were investigated, and photographs of examples of each are shown

in Figure 5-8. A refractive microlens has a continuous curved (spherical or aspheric) surface [5.19]. Its operating characteristics are determined by the conic factor of the surface, lens sag and dispersion of glass. As shown in Figure 5-9(a), a refractive microlens with an aperture radius of r is fabricated on a glass substrate with a thickness of T. The relationship between its radius of curvature (R) for the spherical lens profile, sag height (h) and effective focal length in air and in glass can be described as (Ref [5.19]):

$$R = \frac{h}{2} + \frac{r^2}{2h} \qquad \text{Equation (5.1)}$$

$$f_{r,air} = \frac{R}{n(\lambda) - 1} = \frac{h + \frac{r^2}{h}}{2(n(\lambda) - 1)} \qquad \text{Equation (5.2)}$$

$$f_{r,glass} = \frac{R}{n(\lambda) - 1} n(\lambda) = \frac{h + \frac{r^2}{h}}{2(n(\lambda) - 1)} n(\lambda) \qquad \text{Equation (5.3)}$$

where $n(\lambda)$ is the refractive index at a wavelength of λ. However, even operating at relatively wide range of wavelengths (e.g. from 600 nm to 850 nm), the effective focal length in glass of the refractive microlens is still quite tolerant to the changes in refractive index. Figure 5-10 shows the schematic of refractive microlens array fabrication using the photoresist reflow process and reactive-ion etching (RIE) technology (refer to Page 386 of [5.20]). After spinning the photoresist on the top of the substrate, a custom photomask and UV exposure were used to create cylindrical pedestals of photoresist (see Figure 5-10(a)). The resist reflow relies on the surface tension, which was used to form the dome-like microlens profile. This profile was then etched down to the substrate by the proportional RIE etching. For example, when the refractive microlenses are formed by resist reflow, disks of photoresist are deposited on a suitable substrate (or glass) and then melted. The surface tension forms the melted disc into a spherical surface and by careful manipulation of the etching process, thus the focal length and f-number of the microlens can be controlled. The microlenses have broadband operation and a low f-number can be achieved. However, it is challenging to fabricate full fill-factor lenses on the substrate as typically only a maximum ~80% fill factor for rectangular packed arrays of circular microlenses can be fabricated by resist reflow[5.19]. Note that as shown in Figure 5-9(b), the fill factor for rectangular packed arrays of circular refractive microlenses can be described as:

$$\eta_r = \frac{\pi r^2}{P_x P_y} \qquad \text{Equation (5.4)}$$

where P_x and P_y are the microlens pitches in X and Y respectively (Typically $P_x = P_y$). The overall light focusing efficiency of the refractive microlens can be estimated by Equation (5.4) (e.g. ~60 % for the ones shown in Figure 5-8(a)).

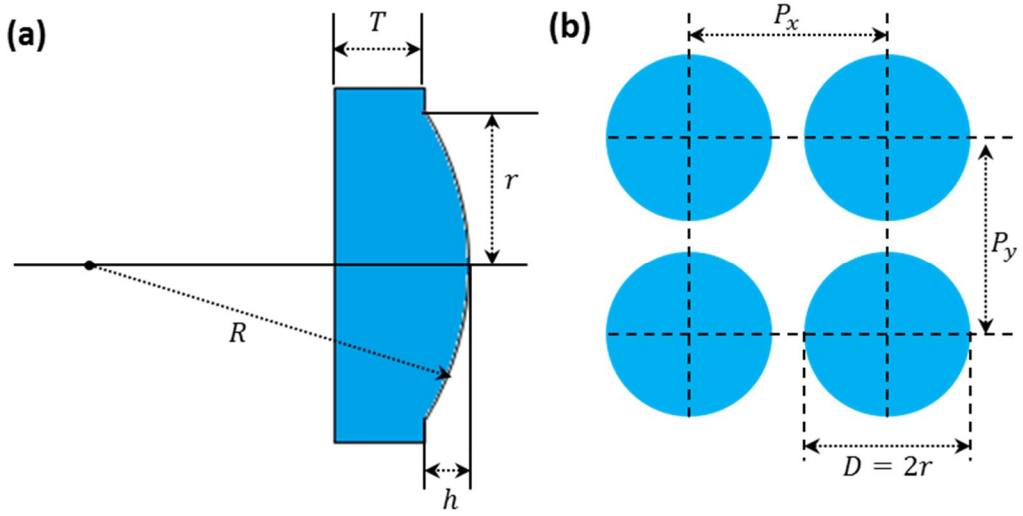

Figure 5-9 (a) Physical and optical properties of the plano-convex refractive microlens; (b) Rectangular packed microlens array. (After [5.19]).

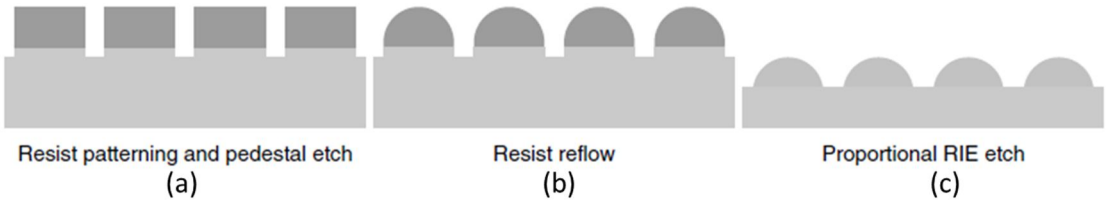

Figure 5-10 Schematic of refractive microlens array fabrication using the photoresist reflow process and reactive-ion etching (RIE) technology. (From Page 386 of [5.20])

By contrast, a diffractive microlens is based on the Fresnel zone plate (see Figure 5-11(a)) [5.20]. Its operating characteristics are primarily determined by the positions of the zone transition points (see Figure 5-11(b)), phase profile of the zones and dispersion of the glass. With integer numbers of waves departing from the expected focal spot as shown in Figure 5-11(b), the positions of the successive zones of the Fresnel lens can be described as:

$$r_N^2 = (f_0 + N\lambda_0)^2 - {f_0}^2 = 2Nf_0\lambda_0 + N^2\lambda_0^2 \qquad \text{Equation (5.5)}$$

where N is the number of zones and r_N is the radius of N^{th} zone, f_0 is the expected

design focal length. As $2Nf_0\lambda_0 \gg N^2\lambda_0^2$, with Equation (5.5) the relationship between the design focal length and wavelength can be estimated as:

$$f_0\lambda_0 \approx \frac{r_N^2}{2N} \qquad \text{Equation (5.6)}$$

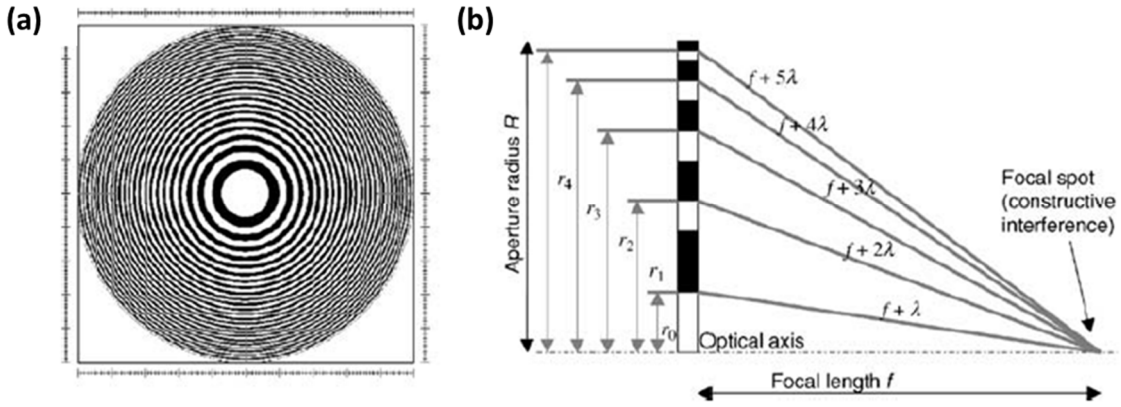

Figure 5-11 (a) The pattern of a Fresnel lens or Fresnel zone plate (FZP) consists of a series of concentric rings. This binary lens is highlighted by transparent (white) and opaque (black) zones. (b) The length between individual concentric ring of the Fresnel lens and the expected focal spot is longer than an expected focal length. Their length difference is a specific integer number of wave. Hence, the ring positions of the successive zones of the Fresnel lens can be worked out. (From Page 92 of [5.20]).

Given a fixed aperture diameter of the diffractive lens, $f_0\lambda_0$ is a constant and thus,

$$f_d(\lambda) = \frac{f_0\lambda_0}{\lambda} \qquad \text{Equation (5.7)}$$

It is evident to find that the focal lengths are linearly changed as the wavelengths vary. It means that the focal lengths of diffractive microlenses have a high dependence on the operational wavelength and thus they are typically designed for monochromatic operation.

In addition, in order to approximate the continuous surface-relief Fresnel lenses which have potentially high diffraction efficiency, the diffractive microlens can be encoded over phase levels of L (e.g. the 16-level diffraction lens shown in Figure 5-12). Its diffractive efficiency can be estimated using diffraction grating efficiency at the first diffraction order [5.21]:

$$\eta_d = sinc^2(1/L) \qquad \text{Equation (5.8)}$$

According to Equation (5.8), the diffractive microlens with higher phase levels is desirable to have higher diffractive efficiency which can represent its overall light focusing efficiency (e.g. ~80 % for the lenses at the design wavelength of 808 nm shown in Figure 5-8(b)). However, referring to Page 93 of [5.20], the diffractive efficiency increases slowly when $L \geq 8$. η_d approaches to 95% when $L = 8$ and to 99% when $L = 16$. In order to obtain high diffractive efficiency of the diffractive microlenses fabricated using traditional multilevel lithographic techniques, it is appropriate to choose between 8 or 16 phase levels. This is because it has higher potential to increase fabrication errors after 8 or 16 phase levels when using the multilevel lithographic techniques (e.g. UV lithography using multilevel masks), as shown in Figure 5-13, rather than direct e-beam or UV lithographic writing techniques (Page 93-94 of [5.20]).

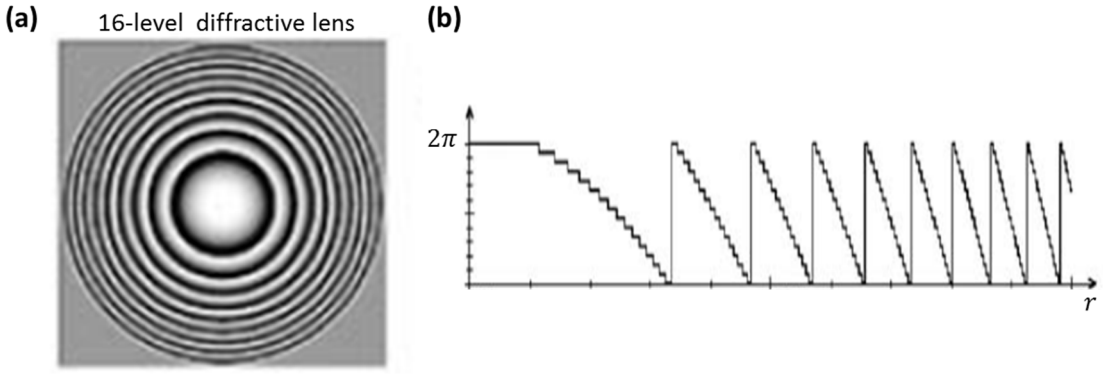

Figure 5-12 (a) shows the diffractive lens encoded over 16 phase levels; (b) The phase profile of multiple zones for the diffractive lens with 16 phase levels per zone. (Reproduced from Page 93 of [5.20]).

The relationship of the smallest feature (δ) and f-number of the diffractive lens can be described as (refer to Page 95 of [5.20]):

$$\delta = \frac{\Lambda_{min}}{L} \approx \frac{2\lambda}{L} f/\# \qquad \text{Equation (5.9)}$$

$$f/\# \approx \frac{\Lambda_{min}}{2\lambda} \qquad \text{Equation (5.10)}$$

where Λ_{min} is the minimum local grating period. In the conventional multi-level lithographic fabrication process, as shown in Figure 5-13, there is a constraint on the minimum feature size (~1.5 μm) primarily due to the attainable aspect ratio (< ~1.0), which is equal to the ratio of the height to width of the features of the micro-fabrication.

Λ_{min} is limited to this feature size, thus the monochromatic diffractive microlenses have limited f-number implementation.

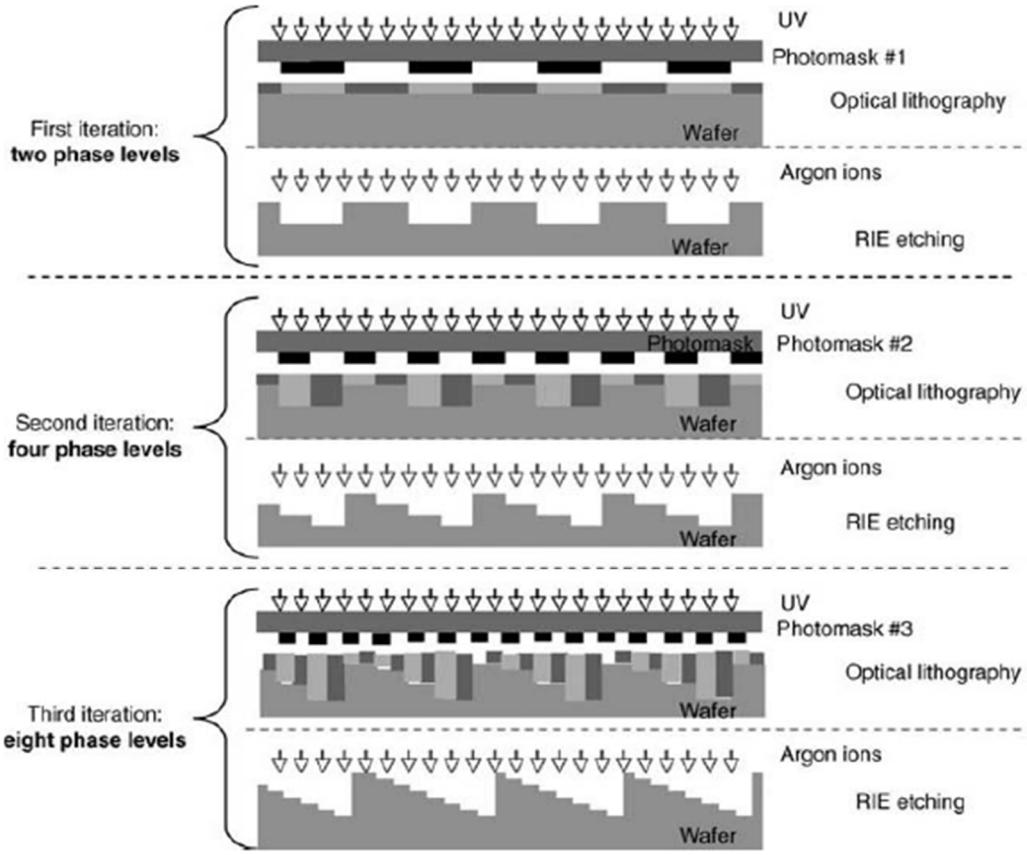

Figure 5-13 Steps of multiple phase level diffractive optic element fabricated using the optical lithographic technology. (From Page 352 of [5.20])

It should be noted that the maximum zone number for the design of diffraction microlens array in this Chapter are constrained to be 32 (see Figure 5-14) due to the typical fabrication error of ~1.5 μm for the multilevel lithographic techniques. By using Equation (5.5), the zone radius can be calculated and in turn the zone thicknesses are equal to the radius differences of adjacent zones. By taking into account the fabrication error of ~1.5 μm for each zone, the relevant zone-wise encoded phase level can be approximately obtained. In terms of the square aperture diffractive microlens with 150 μm×150 μm in XY, its zone thicknesses and encoded phase levels per zone are summarised in Table 5-2. According to Figure 5-14, there are only 5 zones (i.e. associated with a zero radius of 75 μm) that can be arranged along the central line of the aperture of the lens. In contrast, 10 zones (i.e. associated with a zone radius of ~106 μm) are arranged along its diagonal line. We can find Λ_{min}=7.9 μm in the fifth zone along the central line of the aperture. In order to have good support and robust mechanical handing of the microlens arrays, the 1 mm thick fused silica substrate was used for the

infinite conjugate diffractive microlens arrays with the design focal length of 690 μm at λ=808 nm. Finally, the microlenses with f/4.6 focusing capability were implemented on the 1 mm thick substrate.

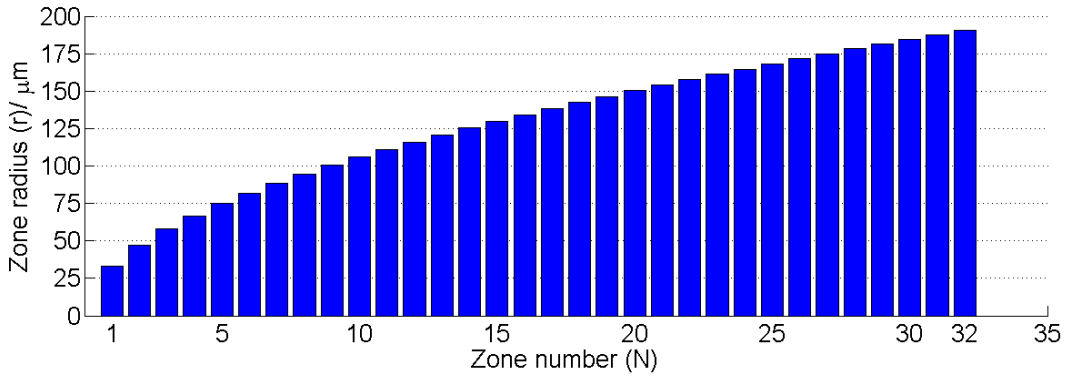

Figure 5-14 Plot of zone number (N) versus zone radius (r) for the design parameters of for the square aperture infinite conjugate diffractive lens with 150 μm×150 μm in XY shown in Figure 5-8(b).

	Along the diagonal line of the aperture									
	Along the central line of the aperture									
Zone number	1	2	3	4	5	6	7	8	9	10
Zone thickness (μm)	33.4	13.8	10.6	9.0	7.9	7.2	6.6	6.1	5.8	5.5
Phase levels	16	8	4	4	4	4	4	4	4	2

Table 5-2 Zone thicknesses and encoded phase levels per zone for the square aperture infinite conjugate diffractive lens with 150 μm×150 μm in XY shown in Figure 5-8(b).

To date, the few reports on microlenses used for fill-factor recovery with SPAD arrays are based on refractive microlens arrays. Recently, Charbon's group have demonstrated sol-gel polymer refractive microlens arrays imprinted on the top of the Si-SPAD arrays by the replica molding technique [5.22]. However, a maximum gain of ~10 at very high f-number (i.e. f/22) for the fill-factor recovery of the SPAD array was reported in Ref.[5.22]. In addition, to enhance fill factor for back-illuminated 128×32 InP/InGaAs(P) SPAD arrays, an antireflective-coated GaP refractive microlens array formed by resist reflow was aligned and attached to the detector chip by the use of the optical epoxy. Note that the 128×32 InP/InGaAs(P) SPAD arrays had a photosensitive area with 18 μm diameter in a pixel pitch of 50 μm and hence the resultant fill factor was ~10 %. When the InP/InGaAs(P) SPAD arrays integrated with the microlens arrays, an enhanced fill factor of 75% was reported by Itzler *et al.* [5.23] and thus the improvement factor of the fill factor was only ~7.5. For the mentioned work in [5.23] and [5.22], they did not describe their measurement setups to obtain improvement

factors of the fill factor of the SPAD arrays. This Chapter describes both diffractive and refractive microlens arrays integrated with Si-SPAD arrays. In particular, the diffractive microlenses have advantages over the refractive microlenses due to the higher fill factor on the microlens arrays as well as light focusing efficiency and tolerance angle for the incident beam. The characterisation of CMOS Si-SPAD array integrated with diffractive microlens array by a custom measurement setup will be discussed in the later section of this Chapter.

The key specifications of refractive and diffractive microlens arrays that have been designed and employed in this Chapter are summarised in Table 5-3.

Types of microlens	Refractive, Plano-Convex		Diffractive	
Array packing	Rectangular			
Microlens aperture pattern	Circular		Square	
Microlens aperture size	~134 μm diameter		150 μm×150 μm in XY	
Microlens pitch size	150 μm		150 μm	
Microlens fill factor	~62.6 %		100 %*	
Microlens array format	32×32	64×32	32×32	64×32
Entire array size	5 mm×5 mm	10 mm×5 mm	5 mm×5 mm	10 mm×5 mm
Substrate	Fused silica, n=1.45318 at λ=808 nm with: • a thickness of ~1 mm for infinite conjugate microlenses; • a thickness of ~0.610 mm for finite conjugate microlenses. Note that the choice of substrate thickness was constrained by availability of substrates.			
Comments	Sag height of the microlens is limited by fabrication process		* a fill factor of 100% for the infinite conjugate microlens array whereas ~95% fill factor for the finite conjugate ones	

Table 5-3 The key specifications of both refractive and diffractive microlens arrays fabricated on the top of a substrate

5.3.4 Microlens array inspection

The focussing characterisation of the microlens array was assessed directly prior to their integration. As the microlens array is used to focus incident light onto the detector photosensitive area, a CCD camera was used to inspect the focal plane, as shown in Figure 5-15. An incident laser beam is provided by a supercontinuum laser source with an acousto-optic tuneable filter (AOTF) unit. This provides flexibility to select the wavelength of interest (e.g. the design wavelength of the diffractive microlenses) in order to inspect the microlenses. Pinholes in the beam path are not only used for the

optical alignment but also for checking the back reflection from the microlenses surface through their central holes to ensure the collimated laser beam is at normal incident to the microlens array.

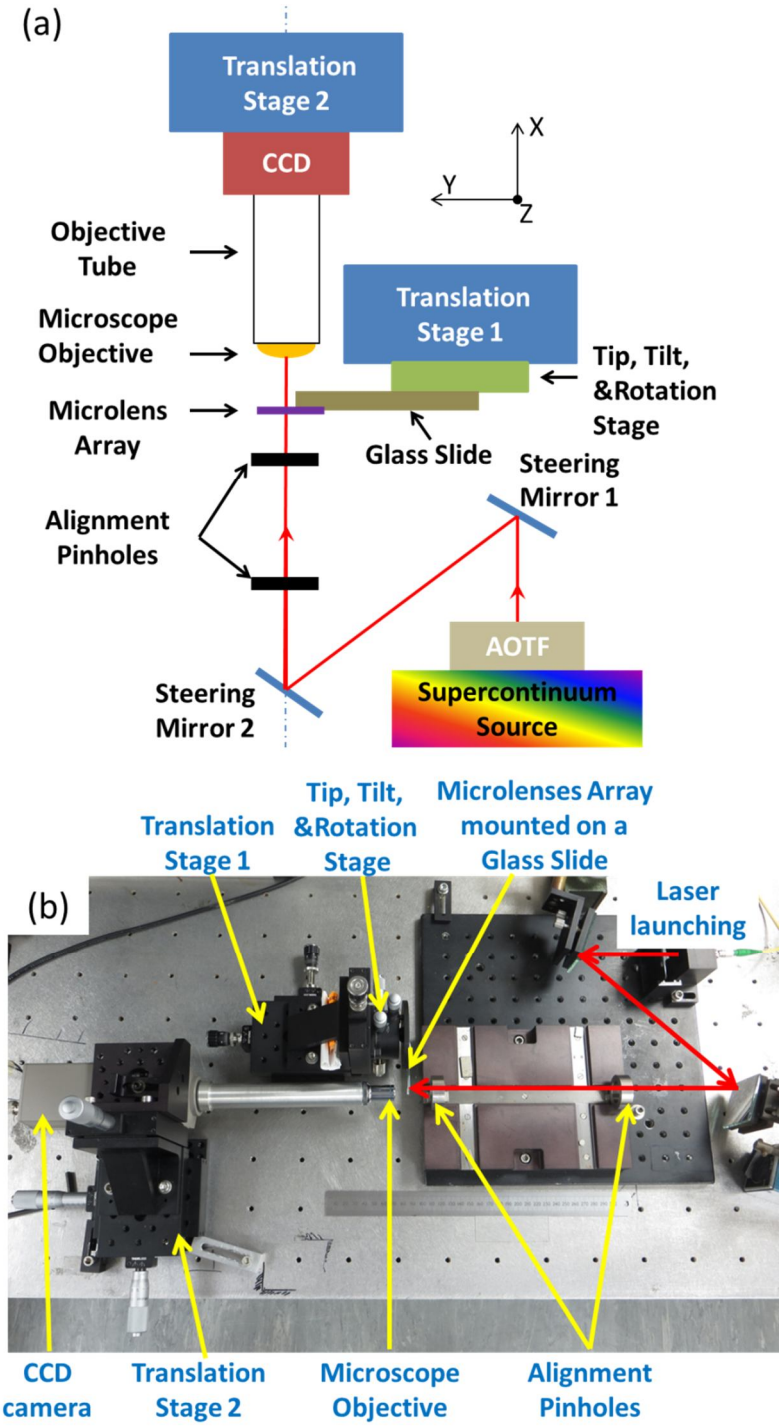

Figure 5-15 Custom characterisation setup for focal spots inspection of the microlens arrays. (a) Schematic of the setup. The inset coordinate system indicates the degrees of freedom of two three-axis micro-positioning translation stages. (b) Close-up photograph of the experimental setup on the bench. The laser beam path is shown in red. AOTF: acousto-optic tuneable filter.

Figure 5-16 shows the spatial profile of the beam after focussing by an infinite conjugate 64×32 diffractive microlens array fabricated on a 1 mm thick fused silica substrate. This microlens array with f/6.9 focusing capability is designed for operating at a wavelength of 808 nm. Since this microlens array is designed for infinite conjugate imaging, it is appropriate to use collimated incident illumination to investigate them. Based on the prior known pitch size of 150 µm, the diameter of an unsaturated-intensity focussed spot within the substrate can be estimated to be ~8 µm at full width $1/e^2$ maximum (see Figure 5-16(a)). The defocussed spots are on the back surface of the microlens substrate and the diameter of defocussed square pattern can be estimated to be ~55 µm at full width $1/e^2$ maximum (see Figure 5-16(b)). This suggests that even though this diffractive microlens array is integrated perfectly with an arrayed detector chip, the defocussed beam spots at the back surface will cover more than the 30 µm diameter active area of the SPAD, thus reducing the overall efficiency.

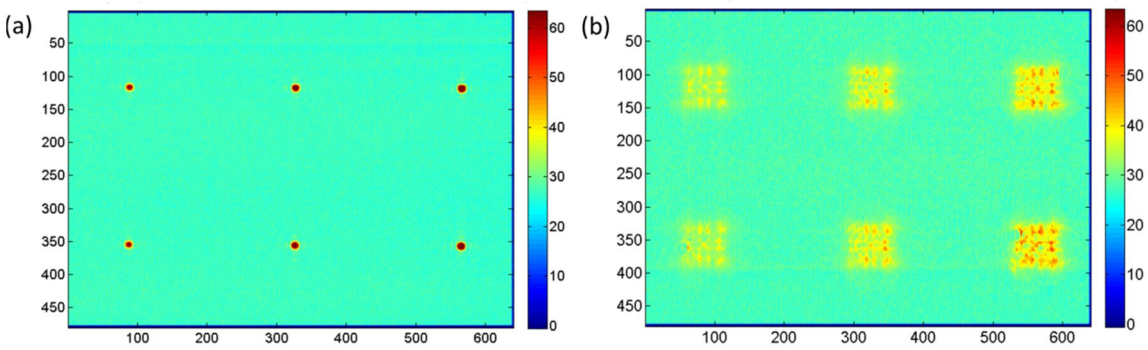

Figure 5-16 Optical images obtained using a ×20 microscope objective of (a) focussed and (b) defocussed of an infinite conjugate 64×32 diffractive microlens array (with f/6.9 focusing capability) with a pitch of 150 µm on a 1 mm thick substrate using an infinite imaging setup at λ= 808 nm. Note that the focussed spots are outside the back surface of the substrate (i.e. in air) in (a) and the defocussed spots on the back surface of the substrate in (b).

A finite conjugate 32×32 refractive microlens array fabricated on a 0.610 mm thick fused silica substrate (design wavelength of 808 nm) was also inspected using the custom characterisation setup. The results are shown in Figure 5-17(a) and (b) using an infinite conjugate imaging setup. The image of the defocussed spots shown in Figure 5-17(a) is on the back surface of the substrate. By contrast, the image in Figure 5-17(b) shows the sharply focussed spots, which were taken approximately 100 µm outside the back surface of the substrate as indicated in Figure 5-17(c). This measured value was included in our Zemax model of the microlens substrate. As shown in Figure 5-17(d),

based on the Zemax model, the sag surface with ~9.5 µm height of the microlens in Figure 5-17(c) is found given that the aperture diameter is ~133 µm at λ=808 nm.

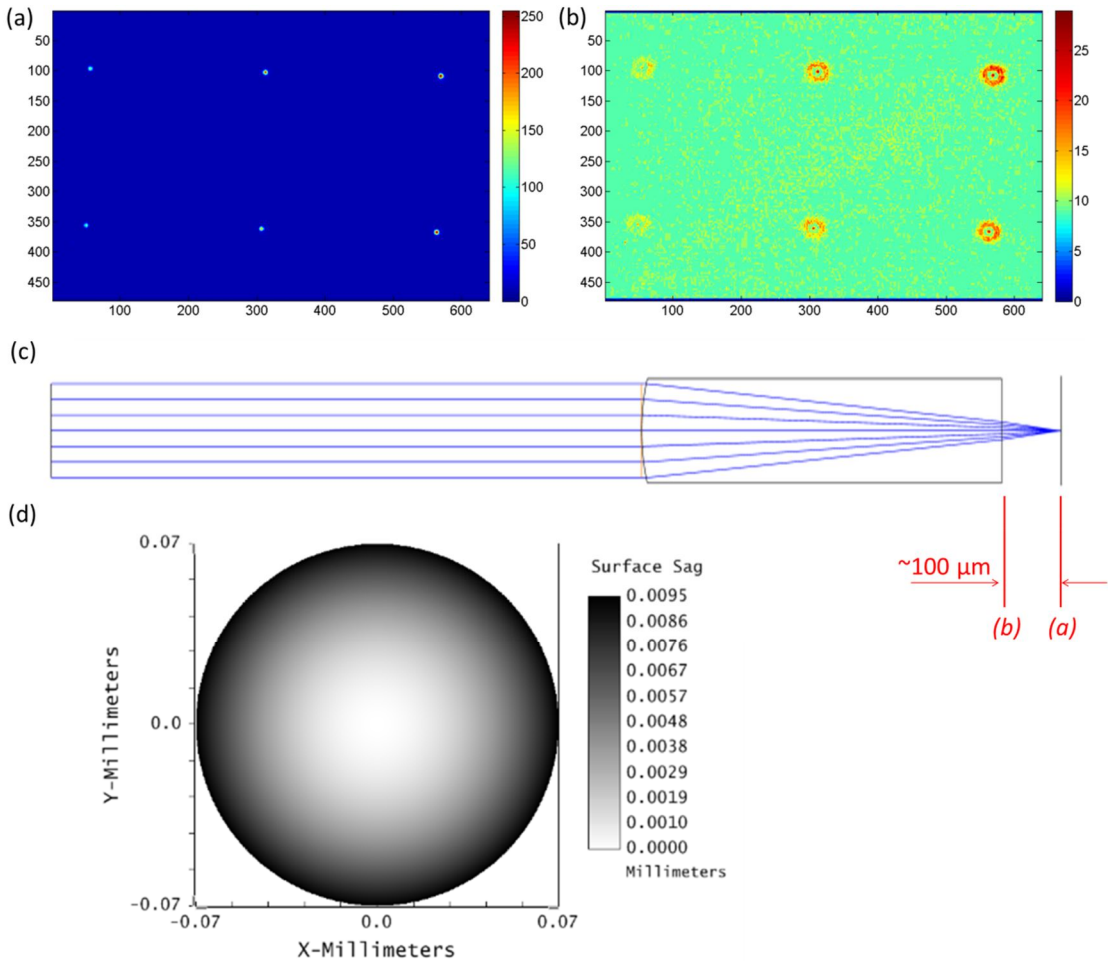

Figure 5-17 Optical images obtained using a ×20 microscope objective of (a) focussed and (b) defocussed spots of a finite conjugate 32×32 refractive microlens array on a 0.610 mm thick substrate using an infinite conjugate imaging setup at λ=808 nm. By using the collimated incident beam at λ=808 nm, (b) shows the defocussed spots on the back surface of the substrate. By contrast, (a) shows the focussed spots on the focal plane in air, which is ~100 µm away from the substrate back surface. (d) our Zemax model shows the height of surface sag of the microlens in (c) is ~9.5 µm at λ=808 nm given that the aperture diameter is ~133 µm.

In addition, the interferometric testing on the refractive microlens was carried out using a non-contact 3D scanning white light interferometer (NewView 600s by Zygo Corporation) with a ×50 objective. This interferometer allows the measurement of the surface height map of the microlens as shown in Figure 5-18(a), showing that it has low surface roughness. On the other hand, Figure 5-18(b) shows the height profile, which crosses the vertex of microlens. The measured maximum height of ~9.4 µm with respect to the top of the substrate corresponds to the height of the sag surface of the

microlens; the measured cross distance of ~136 µm in this height profile represents the aperture diameter of the microlens. Hence, the interferometric testing results are reasonably consistent with those simulated values by the Zemax model.

It should be noted that if this refractive microlens array is investigated using a finite conjugate setup, the image focal plane will be even farther than ~100 µm away from the substrate back surface. To refine the design of this refractive microlens array for higher fill-factor recovery upon the arrayed detectors, microlenses with shorter focal lengths are required to fabricate on the substrate with the same thickness. This corresponds that higher lens sag is required to achieve within an aperture with ~133 µm diameter.

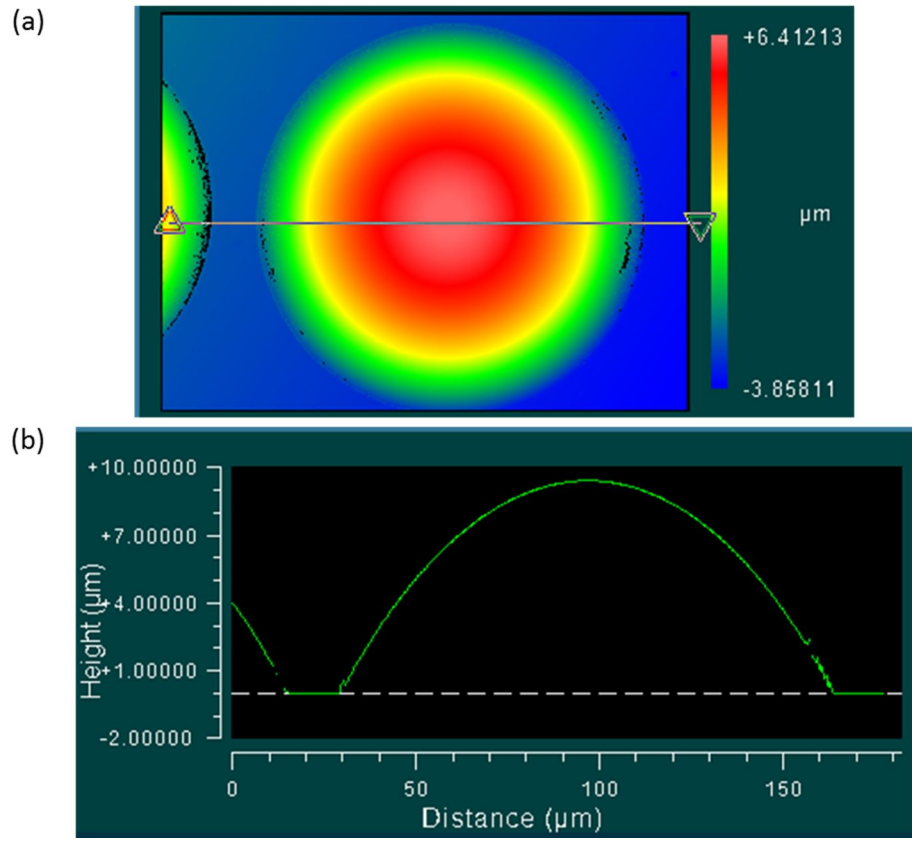

Figure 5-18 Interferometric testing for a finite conjugate refractive microlens array on a 0.610 mm thick substrate. (a) Surface height map of one of 32×32 microlenses acquired using a non-contact 3D scanning white light interferometer (NewView 600s by Zygo Corporation) with a ×50 objective. (b) shows the height profile of surface sag of the microlens along the line shown in (a). Note that the line in (a) approximately crosses the vertex of the microlens. The maximum height in (b) with respect to the flat base line is ~9.4 µm and the cross distance of the height profile in (b) is ~136 µm.

5.4 Integration of microlens and detector arrays

The integration between the microlens array and SPAD array described in this section is implemented using a bonding machine. The bonding machine is a Suss FC6 flip-chip bonder (by Karl Suss, France) which is located in the Micro Systems Engineering Centre (MISEC) cleanroom at Heriot-Watt University.

5.4.1 Overview of the flip-chip bonder

The Karl Suss FC6 flip-chip bonder has a user control panel as well as an interface, and two joysticks and a calibration video display. Details of the user control panel and interface can be seen in [5.24]. As shown in Figure 5-19(a), the user interface is displayed in the right monitor while the left one displays two superimposed reflected images in red and blue corresponding to the surfaces of the chip and substrate, respectively.

The bonder enables the precise alignment (better than 5 μm) and chip-to-substrate bonding under appropriate conditions of heat, pressure and time. As shown in Figure 5-19, the chip and substrate are mounted on the upper bonding arm (see Figure 5-19(b)) and lower stage (see Figure 5-19(c)) respectively, and held in place with vacuum chucks (see Figure 5-19(b)). The chip-to-substrate alignment is achieved using the alignment optics module (i.e. the microscope of the bonder).

The arrangement of the upper bonding arm, lower stage and alignment optics module can be seen in Figure 5-20. The upper arm which allows Z axis adjustment with 1 μm resolution is for holding the chip to be flipped. The lower stage is for holding the substrate and it can be adjusted in X, Y, and Z with 1 μm resolution and also can be rotated in θ. Note that in order to achieve the top-down chip-to-substrate bonding, the microlens array and SPAD array (held in place with vacuum chucks) are mounted in the upper arm and lower stage respectively. The layout of the alignment optics module is shown in Figure 5-20 and it has XYZ adjustment with 1 μm resolution. In order to implement very accurate (better than 5μm) real device bonding, an appropriate alignment calibration (the calibration detail can be seen in the bonder manual [5.24]) upon the upper arm, lower stage and alignment optics module of the bonder must be carried out. The alignment calibration can minimise any systematic errors of the bonder. Typically, this needs to be done every time the bonder is turned on.

In order to appropriately calibrate the systematic errors, bonding trials were performed

using test patterned square reticles prior to the actual lens-to-chip bonding. Figure 5-21 shows an example bonding trial result of four bonded small-size reticles arranged in the four corners of the larger reticle. The chip-to-substrate offset in XY between each small-size reticle and the larger reticle can be measured by examining their alignment fiducials under a microscope. For example, the corner-wise alignment fiducials of chip and substrate can be simultaneously observed in the individual microscope image shown in Figure 5-21 (a1), (a2), (a3) and (a4). Their vernier feature has fingers of width 5 µm. Their chip-to-substrate offsets in XY of approximately (+7 µm,- 7 µm), (+7 µm,-8 µm), (+6 µm,-7 µm) and (+5 µm,-5 µm) respectively were estimated through visual inspection. Thus, the average estimated offsets of approximately (+6 µm,-7 µm) can be characterised to be the systematic errors, which can be accounted for in the actual chip-to-lens bonding process.

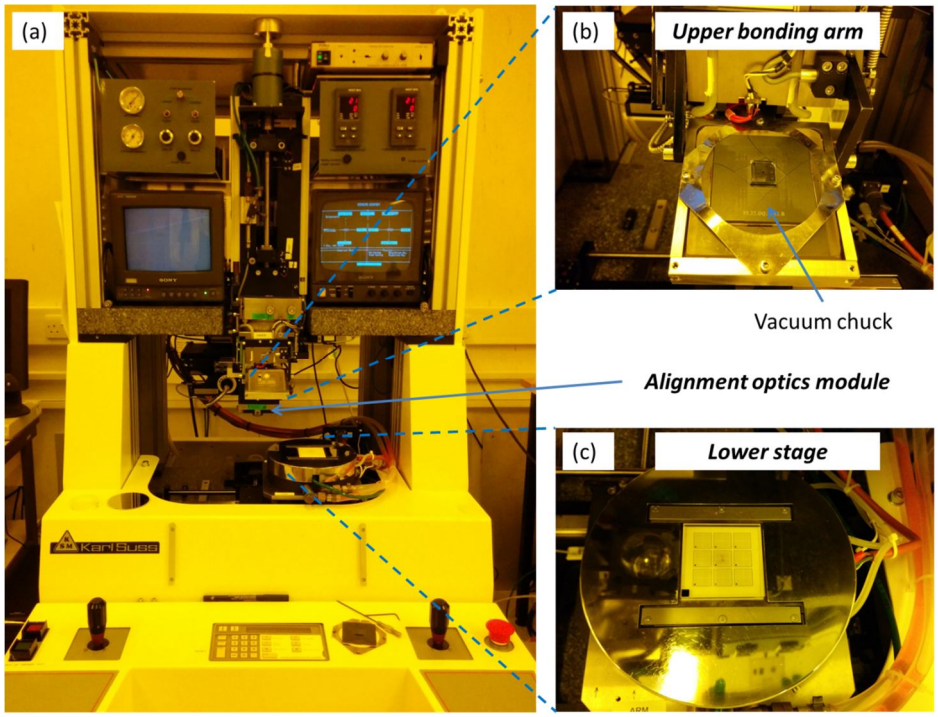

Figure 5-19 (a) Overview photograph of the Karl Suss FC6 flip-chip bonder in the cleanroom; (b) Close-up photograph of upper bonding arm and lower stage with translation stages for chip and substrate mounting respectively, and also the alignment optics module.

Within the alignment optics module, a CCD camera in conjunction with a white light illumination is employed for the optical inspections of both the upper arm and lower stage. It is necessary to carry out the calibration alignment consisting of parallelism and objective adjustments. In terms of a real device bonding process, the alignment of

SPAD array to microlens array is implemented using their fiducial markers designed by Dr. Aongus McCarthy (see Figure 5-22) as accurate references. Four fiducial markers are precisely arranged in four corners of the detector array and at least three are used for the microlens array. After an alignment sequence of the substrate to chip, a bonding cycle can be started. The cycle is enabled with previously programmed parameters that can be viewed in the user interface displayed in the right monitor of the bonder and modified by the operator. In addition, while the cycle is in progress, it can be interrupted by the operator if necessary.

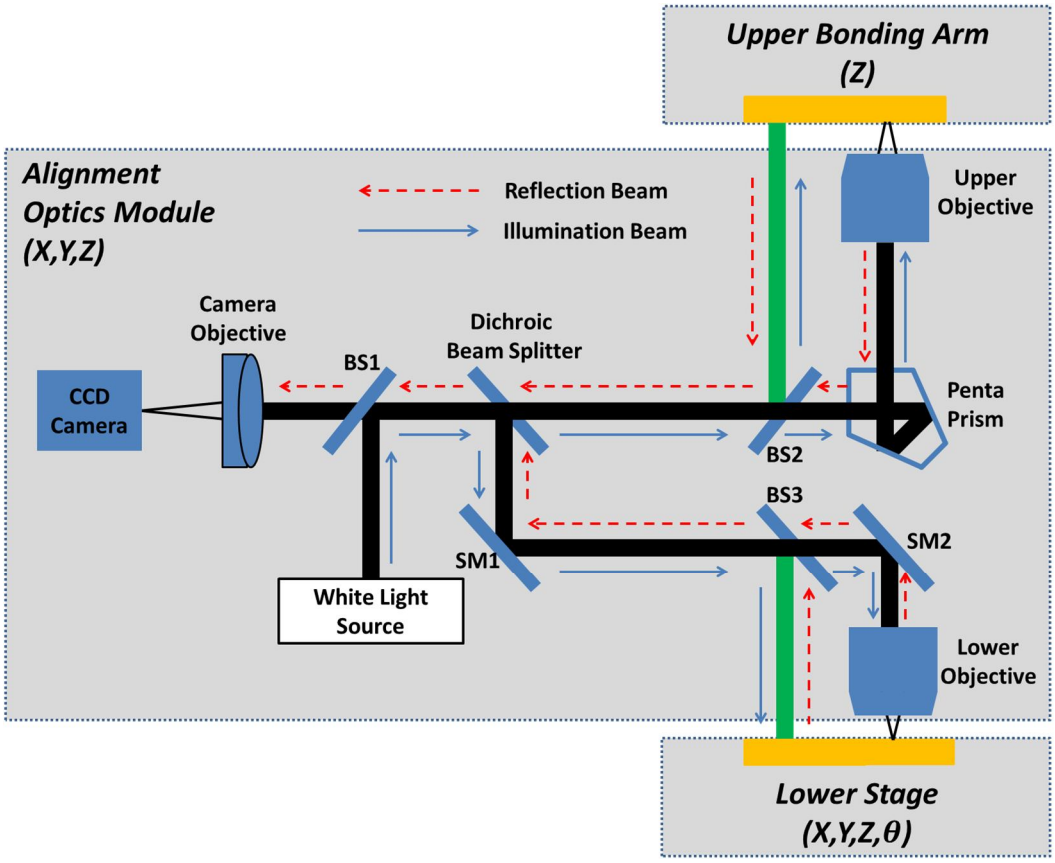

Figure 5-20 The arrangement of the upper bonding arm, lower stage and alignment optics module of the FC6 flip-chip bonder. In particular, the layout of the alignment optics module (or the microscope of the bonder) is illustrated. Beam splitters: BS1, BS2 and BS3; Steer mirrors: SM1 and SM2. BS2 and BS3 are used to reflect the collimation beam (in green) for the upper and lower optical observations of the autocollimator respectively.

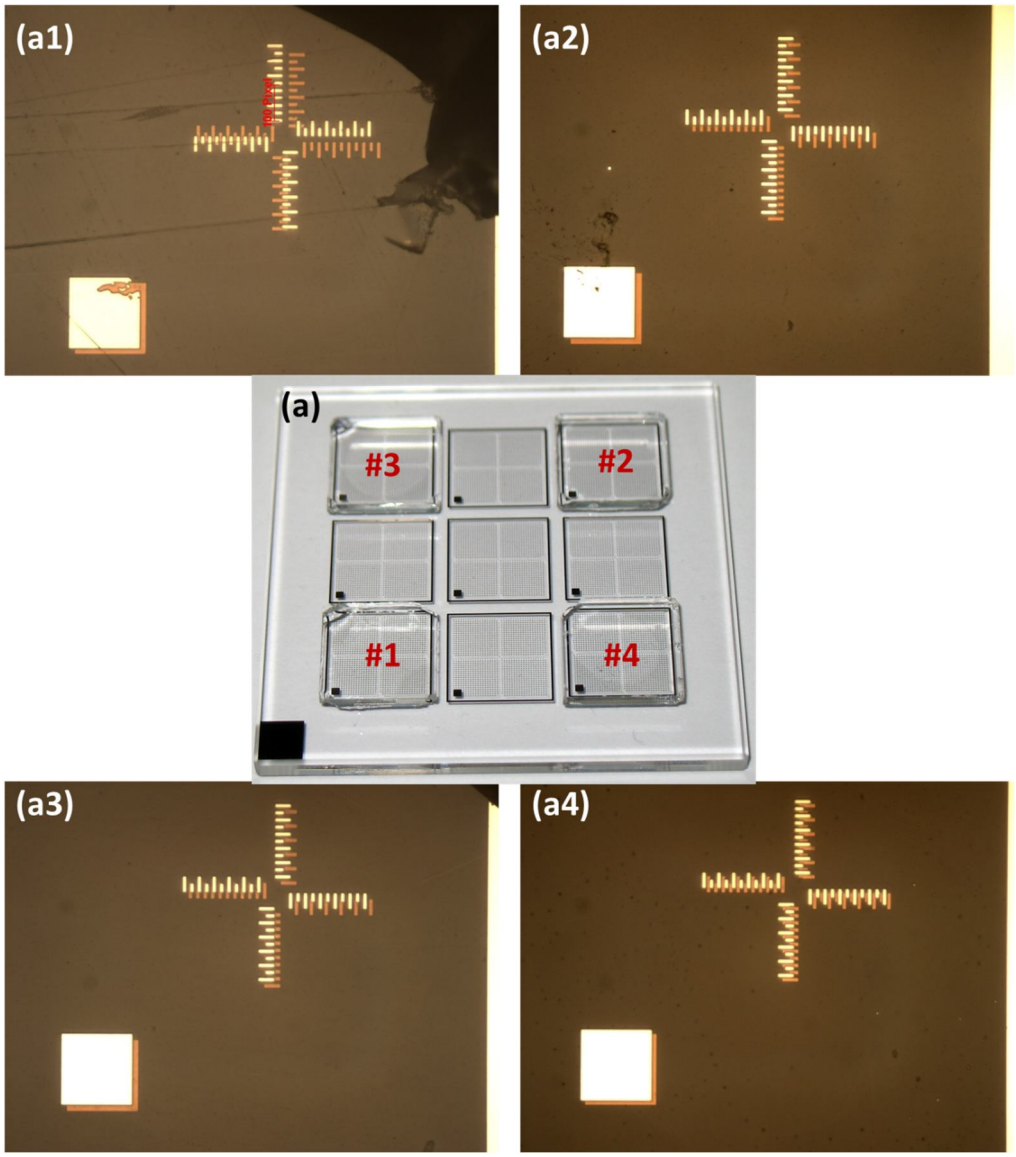

Figure 5-21 (a) four 10×10 mm patterned square reticles attached on the top of a 50×50 mm patterned square reticle associated with a bonding trial. These four small-size reticles (i.e. #1,#2, #3, & #4) were arranged in four different corners of the larger reticle respectively. Microscope images (a1), (a2), (a3) and (a4) with ×20 microscope objective show the offset in XY between the top (in white) and bottom (in copper) fiducials in the bottom left corner of #3, #2, #1, & #4 small-size reticles respectively.

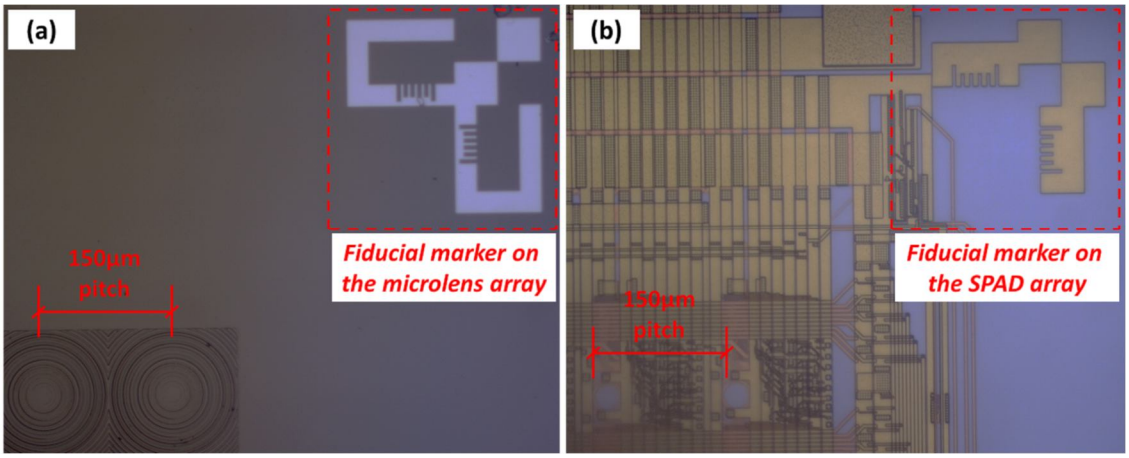

Figure 5-22 Metal-covered fiducial markers on the microlens array (a) and SPAD array (b) used for bonding alignment.

5.4.2 Lens-to-chip bonding

In order to hold the SPAD array chip and microlens array more firmly in place on the vacuum chucks (e.g. the one shown in Figure 5-19(b)) of the bonder for the lens-to-chip integration, two larger size glass substrates are attached to the chip and microlenses using a wax adhesive (Aremco Crystalbond). Correspondingly, the preparation of the SPAD array chip and microlens array assemblies consisted of three main steps (see Figure 5-23): (1) a hot plate was heated up to 121 ^{o}C, which is the melting point of the wax adhesive. (2) the SPAD array chip and the microlens array were put on the top of wax on the glass substrate. (3) the device was moved out of the heater and cooled for 2 minutes to make the SPAD array chip or microlenses array adhere to the glass substrate.

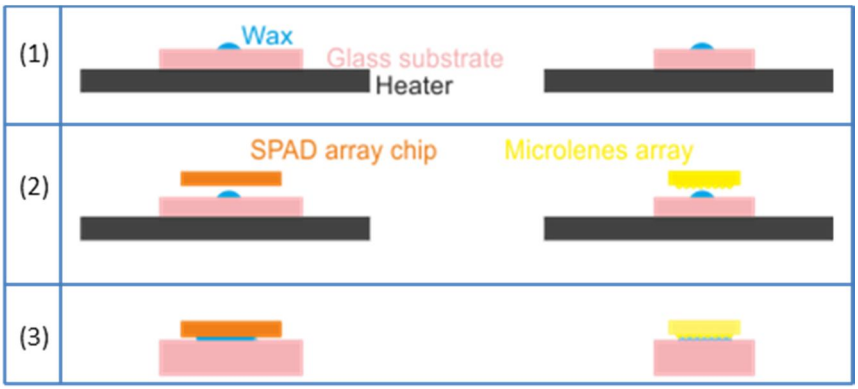

Figure 5-23 In order to achieve a more robust mounting of the components on the vacuum holders of the upper arm and lower stage of the bonder, the SPAD array chip and the microlens array substrate were attached to larger "carrier" glass substrates using wax adhesive.

As shown in Figure 5-24, the two main steps are for the bonding of devices: (1) the prepared microlens array and SPAD array chip assemblies were loaded and mounted on the upper arm and lower stage respectively first. (2) prior to the lens-to-chip bonding, and in order to facilitate the alignment of the lens substrate and chip, the microscope module of the FC-6 provided a superimposed image of the active surfaces of the microlens substrate (in blue tint) and chip (in red tint), on a monitor once both have been brought into focus. The images shown in Figure 5-25 are an example of the superimposed image obtained by the alignment optics module of the FC-6 bonder when an array of diffractive microlenses with chrome fiducials was being poorly aligned (Figure 5-25(a)) or aligned (Figure 5-25(b)) with the corresponding fiducial on the detector chip. This lens-to-chip alignment can be achieved by frequently checking the superimposed image of the lens and chip fiducial markers in different corners, in particular for the diagonal corners. After the alignment of SPAD array to the microlens array using fiducial markers and setting the average offset obtained from the calibration alignment check of the upper arm to the lower stage, the lens-to-chip bonding was carried out using UV adhesive under UV exposure.

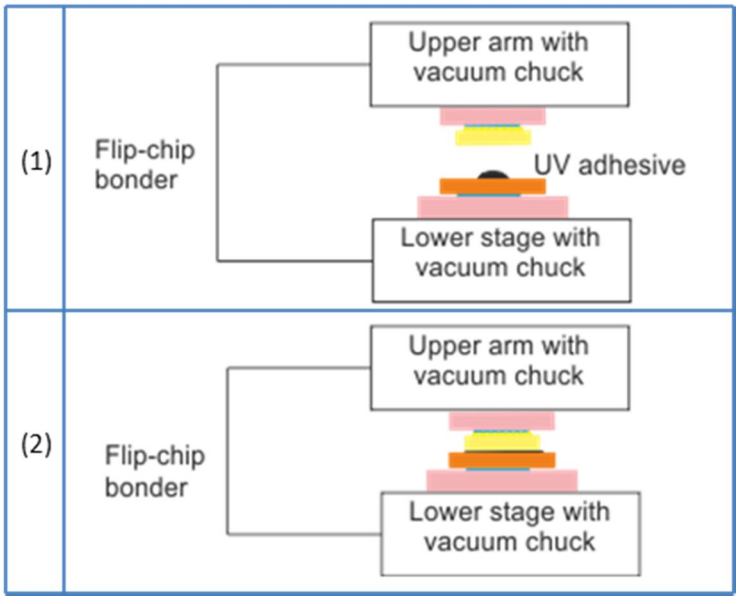

Figure 5-24 Steps for bonding of the devices: Step (1): loading and mounting the prepared assemblies of the microlens array and SPAD array chip in the upper arm and lower stage of the bonder respectively. Step (2): After the alignment is completed, the bonding cycle is initiated.

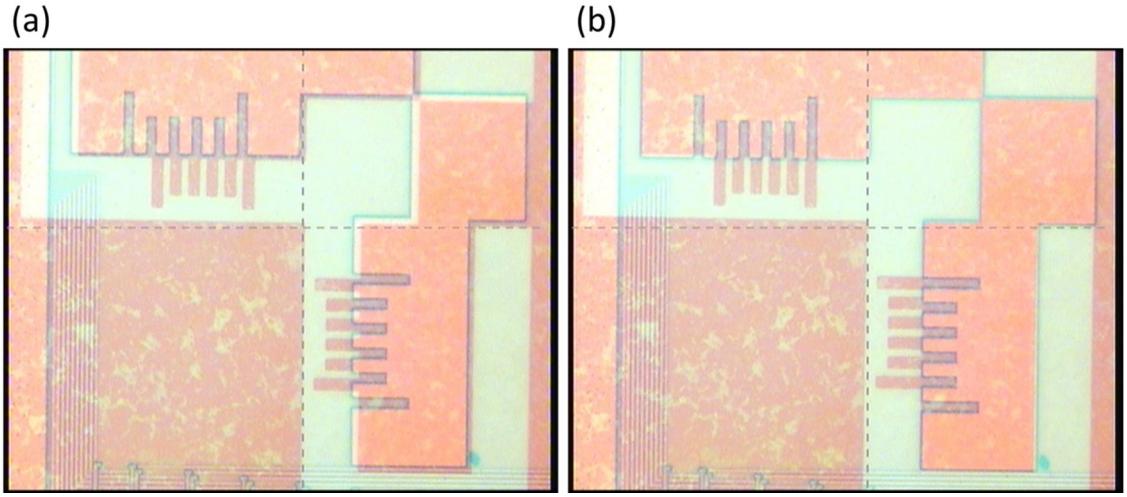

Figure 5-25 Images in focus of the metal-covered fiducial markers (whose dimension can be seen in Figure 5-26) of the microlens array (in blue tint) on the upper arm and the SPAD array chip (in red tint) on the lower stage for the alignment. (a) Poorly aligned fiducial markers: The comparison of two different fiducial markers indicates that the offset in XY is approximately (4 μm, 4 μm); (b) Aligned fiducial markers.

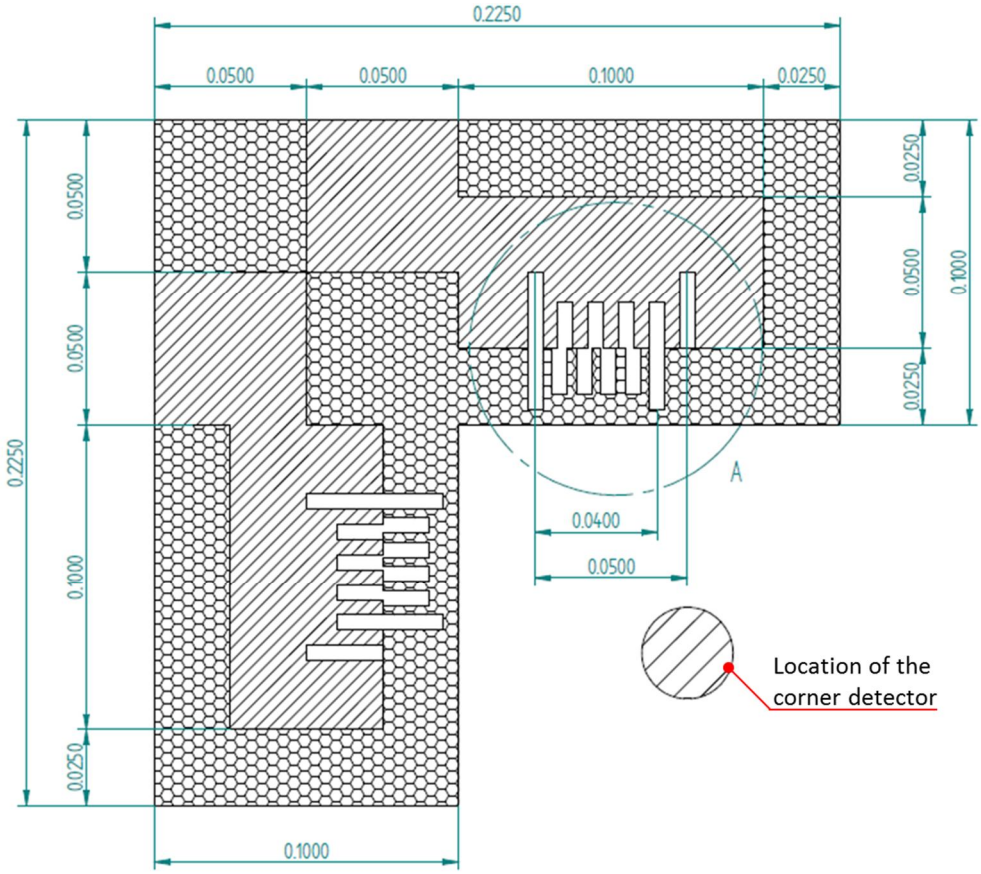

Figure 5-26 Sketch of combined chip (shaded lines) and lens (open hexagons) substrate fiducials for alignment of the SPAD detector array and microlens array substrate. The vernier feature labelled A has fingers of width 5 μm.

The empirical forces as a function of the processing time for the actual bonding can be found through a series of bonding trials using the patterned square reticles, as shown in Figure 5-21. The bonding cycle of empirical forces versus time is shown in Figure 5-27(a) along with the corresponding bonding illustration shown in Figure 5-27(b).

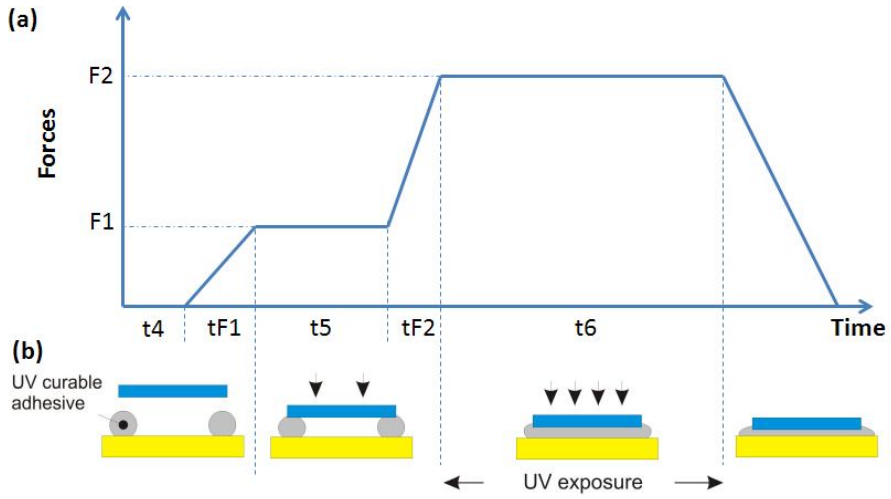

Figure 5-27 Example bonding cycle in terms of (a) forces versus time along with (b) illustration of lens-to-chip bonding with UV curable adhesive. The parameters were used for the actual bonding: F1=60 grams; F2=120 grams; t4=3 s; tF1=3 s; t5=6 s; tF2=5 s; and t6=60 s.

In addition, an optical adhesive (NOA81 by Norland Products, USA) was used to attach the microlenses and detector chip. Approximately 0.36 μL adhesive for 32×32 microlens arrays was typically used for the bonding with a force of 120 grams, as shown in Figure 5-27. This can result in approximately 10 μm thick adhesive on the bonded device. It offers excellent adhesion between glass and metal substrates. Its cure time is fast, typically less than 10 seconds for thin films when illuminating with a UV light source (LQ UV 1000 by LINOS). This UV light source with brightness control emits a spectrum of 250 to 450 nm. It has a flexible light guide output and a collimation lens attachment (refer to Page 696 of [5.25]). The HBO lamp with a power of 100 W is used in this source (H for Hg or mercury; B is the symbol for luminance; O for unforced cooling). Figure 5-28 shows the spectral transmission plot of the adhesive. Its transmission at λ=400-1000 nm is >95%, which is a good match to the spectral sensitivity window of the CMOS SPAD array.

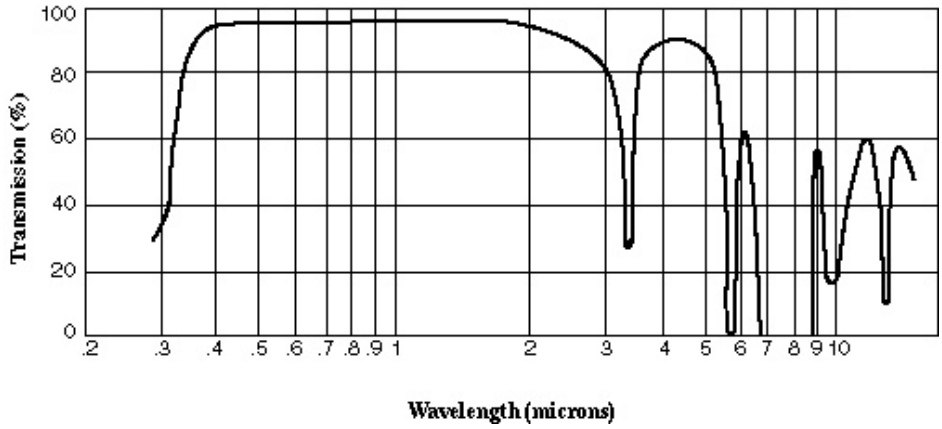

Figure 5-28 Spectral transmission characteristic of applied optical adhesive -NOA81 by Norland Products, USA. (From [5.26]).

The steps of unloading and cleaning of the bonded assembly can be seen in Figure 5-29: (1) the bonded device is put on the heater. The microlens side of the bonded device was reheated up to 121 ^{o}C for about 2 minutes to separate the glass substrate from the bonded device. (2) after turning around the bonded device, the detector chip side was also reheated and hence the glass substrate was taken away from the bonded device. (3) the bonded device without glass substrates was then placed in an acetone bath for about 5 minutes to clear the residual wax. (4) in order to remove any remaining wax (particularly on the microlens surface), the bonded device was put in ultrasonic bath with a mild detergent (Decon90 by Decon Laboratories Limited, UK) for about 5 minutes. After these cleaning processes, it is usually evident, under a microscope, to observe that the surfaces of microlenses on the bonded devices clean (see Figure 5-30).

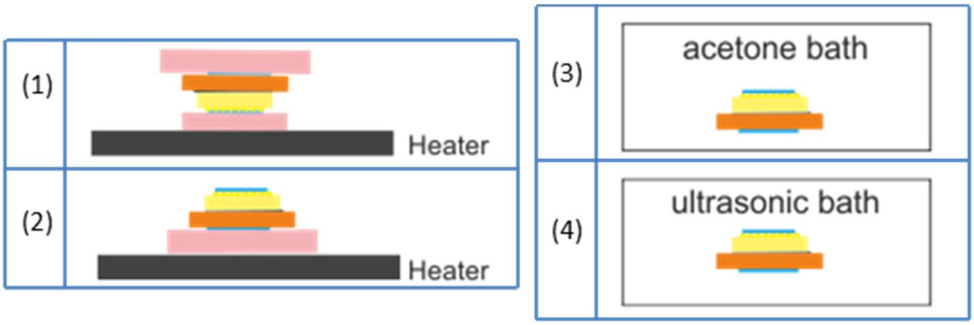

Figure 5-29 Step (1) & (2) are for unloading the bonded assembly from the glass substrates on a heater; Step (3) & (4) are for cleaning the bonded assembly in an acetone bath as well as ultrasonic bath.

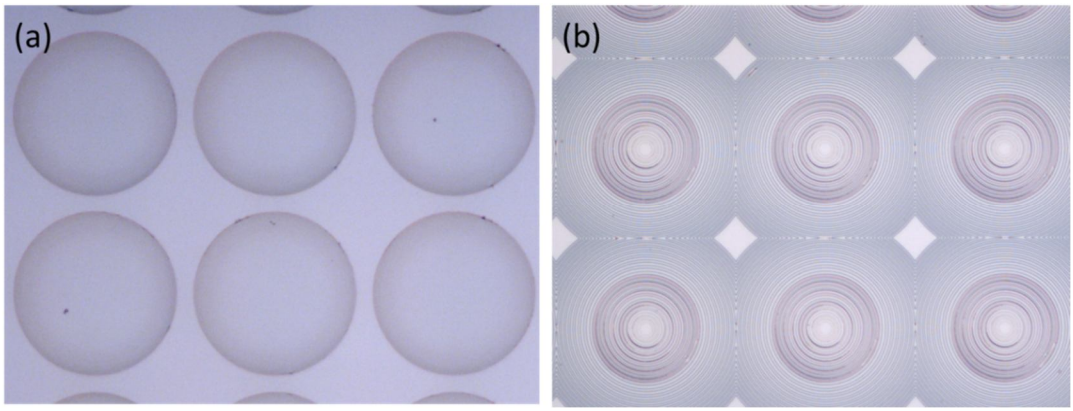

Figure 5-30 After the cleaning of the bonded assemblies, inspected microscope images obtained using ×20 objective of the finite conjugate 32×32 (a) refractive and (b) diffractive microlens arrays with a 0.63 mm thick substrate with design wavelength of 808 nm which were bonded with the 32×32 pixel SPAD array chips.

5.5 Characterisation of detector array with bonded microlenses

5.5.1 Post-bonding inspection using the flip-chip bonder microscope

Before unloading the bonded device from the bonder, the lens-to chip placement error can be inspected by the microscope of the bonder, whose optical layout can be seen in Figure 5-20. As the bonder has been calibrated to take into account of the parallelism between the lower objective and lower stage before bonding, the position offset between the images in focus of the fiducials of the microlens array and the SPAD array chip can be used to estimate the lens-to-chip placement error to some extent. For example, the placement errors of two example bonded devices, which were less than 5 μm in X and Y, can be seen in Table 5-4. Note that the images in focus of the fiducials of the microlens array and the SPAD array chip can be obtained by moving the lower stage up and down in Z direction.

Bonded date	Bonded devices	Placement errors in (X,Y)
13/01/2014	1-mm-thick-substrate f/6.9 infinite conjugate diffractive microlenses with a design wavelength of 633 nm integrated with 64×32 SPAD array chip (Defocussed spots on the back surface of the substrate)	(1 μm, 4 μm)
10/07/2014	0.55-mm-thick-substrate finite conjugate refractive microlenses with a design wavelength of 808 nm integrated with 32×32 SPAD array chip	(2 μm, 2 μm)

Table 5-4 Lens-to-chip placement errors of two example bonded devices were inspected by the microscope of the FC6 bonder.

5.5.2 Post-bonding inspection by custom characterisation setup

A schematic, and a photograph, of the post-bonding experimental inspection setup are shown in Figure 5-31. The bonded device is mounted on a tip, tilt and rotation stage along with a translation stage, which offers a six-axis micro-positioning adjustment. When the incident laser beam illuminates the top surface of the microlens array, adjusting the tip, tilt and rotation stage to achieve good overlap between the reflective beam spot and the centre of the pinhole guarantees the laser beam normal incident on the microlenses. The white light source combined with a long-pass filter with a cut-on wavelength at 750 nm provides relatively uniform illumination with a large field of view on the surface of the microlens array or the SPAD array detector chip. A CCD camera combined with a microscope objective was used to inspect the microlenses and the detector chip from one side in an appropriate angle.

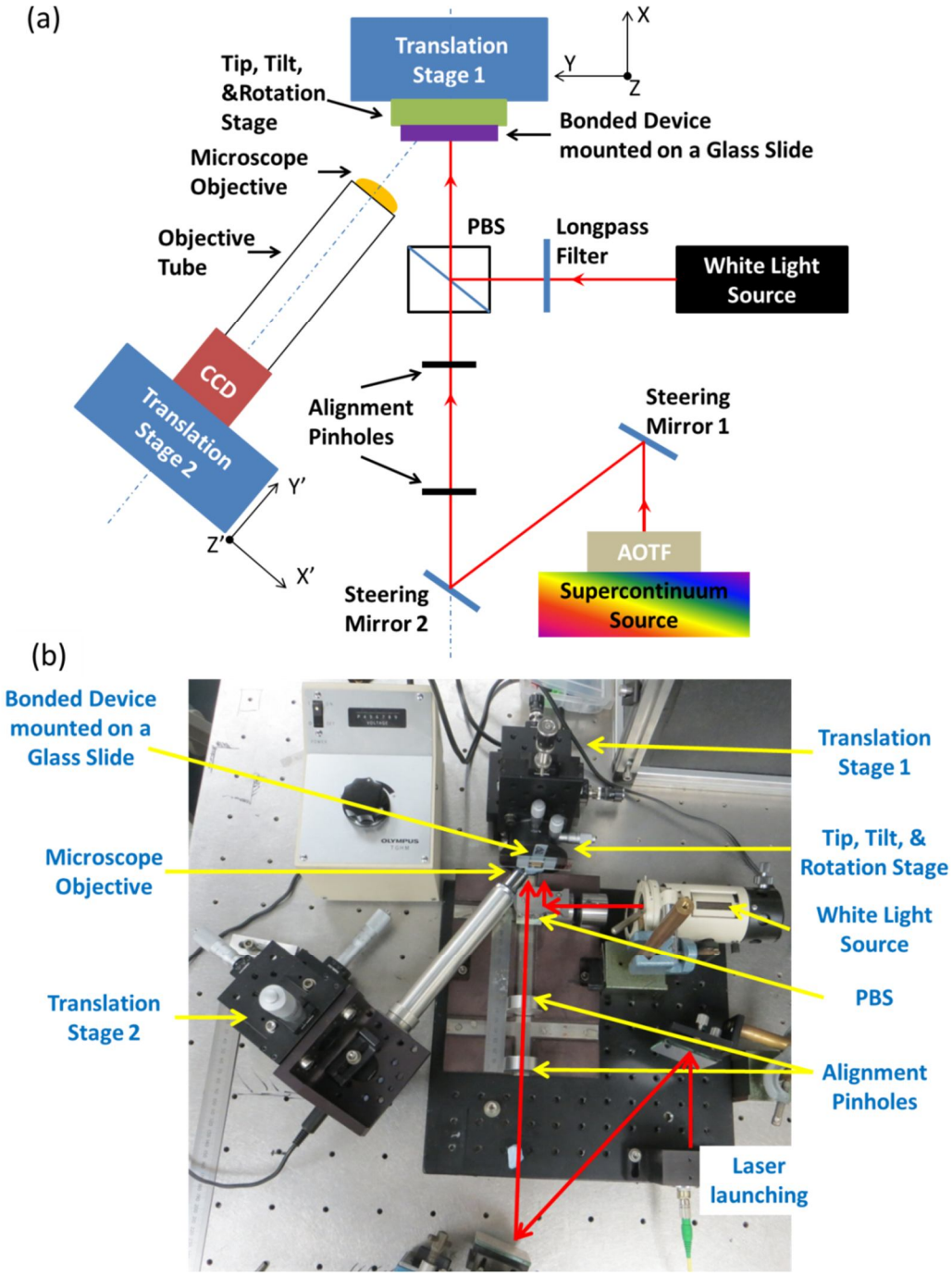

Figure 5-31 Post-bonding characterisation setup for the bonded devices. (a) shows the schematic of the setup. Two inset coordinate systems indicate the degrees of freedom of two three-axis micro-positioning translation stages respectively. (b) shows the close-up photograph of the experimental setup on the bench. Note that the arrows in red highlight the beam paths including the laser beam path and the white light beam path. PBS: polarising beam splitter; AOTF: acousto-optic tuneable filter.

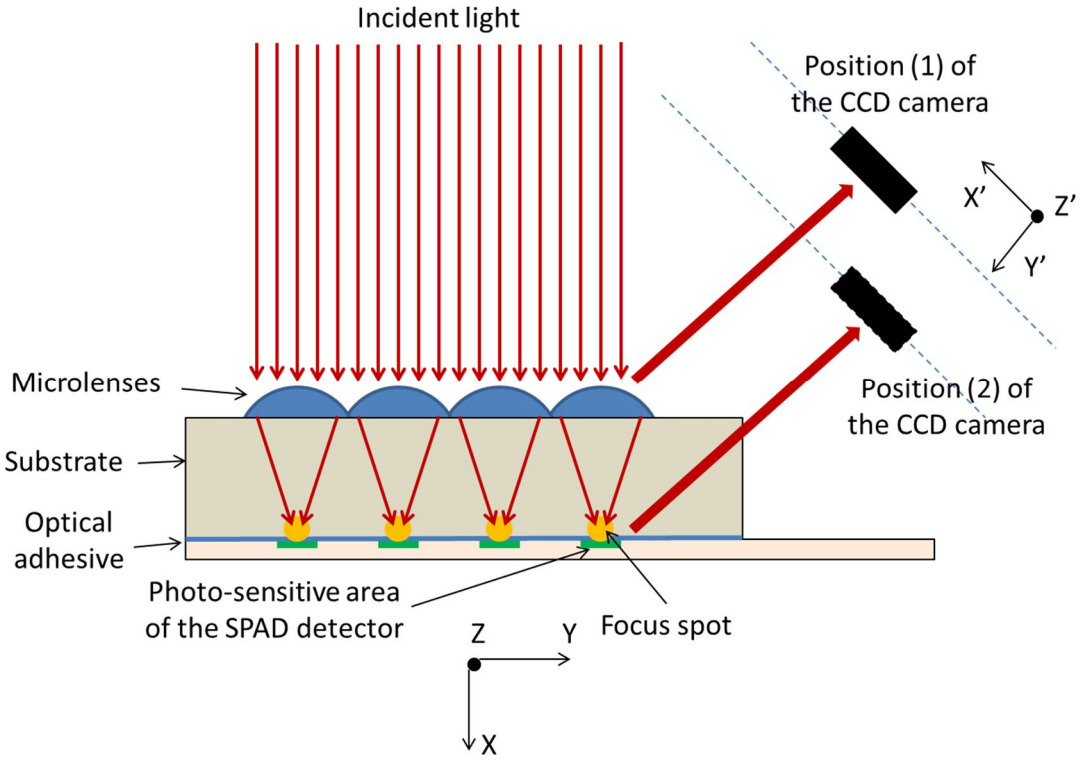

Figure 5-32 Illustration of the inspection process of the focussed spot (in yellow) and the photosensitive area (in green) of the SPAD detector near the edge of the chip using the post-bonding inspection setup shown in Figure 5-31. Note that two inset coordinate systems here match the ones illustrated in Figure 5-31.

As shown Figure 5-32, Position (1) of the CCD camera was associated with the case when the focus is on the top surface of the microlenses. The resultant image can be seen in Figure 5-33(a). By adjusting translation stage 2 in X' and Y' to move the CCD camera to Position (2), image in focus was aimed at the detectors associated with the observed microlenses. Note that this image is constructed when the reflective light from the detector area passes through the extremely thin optical adhesive layer and the fused silica substrate (or glass) directly rather than the non-flat surface of the microlenses. For example, it was able to inspect the outermost detectors of the bonded assembly as shown in Figure 5-33 directly. However, when using the white light illumination, strong light scattering happens on the metal surface of the detector chip. The inside of the substrate along with the photosensitive area, which absorbs most of the incident light, also scatter a large amount of the light. This leads to the obtained reflective images (e.g. Figure 5-33(b)&(b1) or (c)&(c1)) with strong background light present, making it difficult to recognise the photosensitive area of the detectors. Nevertheless, as shown in Figure 5-33(b2) and Figure 5-33(c2), the focussed spots for the diffractive microlenses with f/6.9 focusing capability form larger and brighter

shadows around the detector's photosensitive area (i.e. red box shown in Figure 5-33(c2)) compared to the ones for the diffractive microlenses with f/4.6 focusing capability. This suggests that the latter example is the case where light is concentrated effectively onto the photosensitive area. For both cases, it has the likelihood that the focussed spots are slightly mismatched to the photosensitive area as their shadows are not symmetric along the centre lines (i.e. dash yellow lines shown in Figure 5-33).

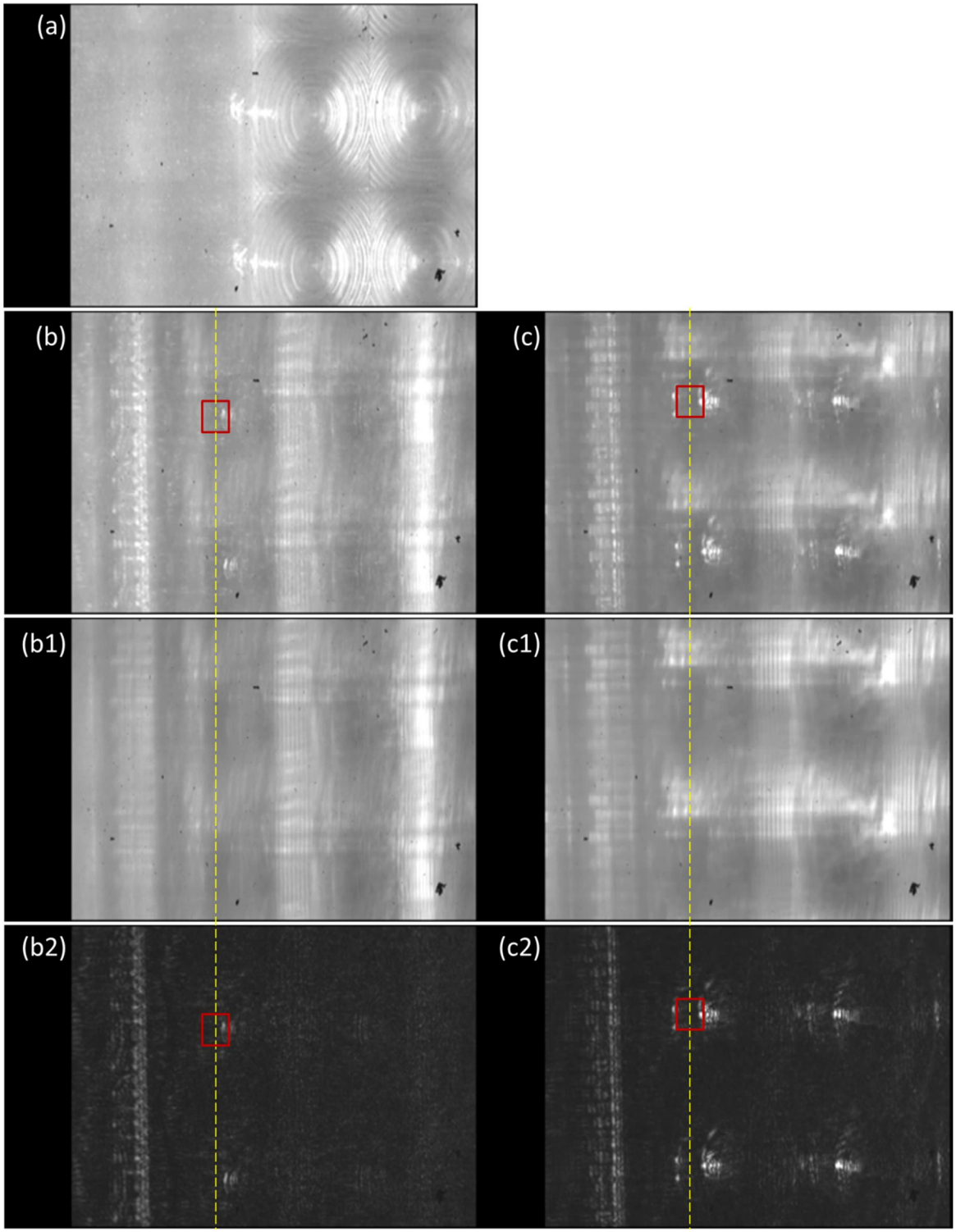

Figure 5-33 Post-bonding inspection images were acquired with a ×20 objective by the use of the setup shown in Figure 5-31. Left column: The image in focus, (a), of the top surface of the microlens array was acquired when using white light illumination. Images in focus , (b)-(b2), of the top surface of the 32×64 indirect time-of-flight (iTOF) SPAD array integrated with a microlens array. It is a 32×64 diffractive microlens array (with f/4.6 focusing capability) with 1 mm thick substrate designed for operating at λ=850 nm. Right column: Images in focus, (c)-(c2), of the top surface of the 32×64 iTOF SPAD array detector integrated with a microlens array. It is a 32×64 diffractive microlens array (with f/6.9 focusing capability) with 1 mm thick substrate designed for operating at λ=850 nm. Note that the images shown in (b) and (c) was acquired using both white light and λ=850 nm laser light illuminations. In contrast, the images shown in (b1) and (c1) were obtained using white light while only the laser light was used for the image shown in (b2) and (c2). The red boxes in (b)&(b2) and (c)&(c2) approximately cover the photosensitive area of the outermost SPAD detectors of the chip for both cases. The dash yellow lines approximately cross the centre of the photosensitive area.

5.5.3 Detection characterisation

The 32×32 Si-SPAD arrays integrated with diffractive microlens arrays were wire bonded by Professor Franco Zappa's group in Politecnico di Milano, Italy. Operating in photon counting mode, the detection performance of these detector arrays bonded with infinite or finite conjugate diffractive microlenses were investigated. Two figures of merit were used to characterise the detection performance of the SPAD arrays with microlenses: improvement factor and spatial uniformity of the photon detection.

The concept of improvement factor (IF) proposed in Ref [5.27] is used:

$$IF = \frac{E_O}{E_i} \qquad \text{Equation (5.11)}$$

where E_i is the input irradiance (optical power per unit area) at the microlens surface, and E_O is the output irradiance or the irradiance at the photosensitive area of the pixel.

In order to characterise the CMOS Si-SPAD arrays, the setup shown in Figure 5-34 was used. The IF and spatial uniformity of photon detection of the CMOS Si-SPAD arrays integrated with microlens arrays were investigated by illuminations with the spectral range between 500-900 nm. These illuminations were provided by a tunable supercontinuum laser source (SuperK EXTREME EXW-6 by NKT Photonics,

Denmark). A single-mode fibre with a core diameter of 5 µm was used to deliver light from the tunable supercontinuum laser source. The exiting light beam from the fibre end had a huge divergent angle. This divergent beam propagated along the optical bench over a length of ~500 mm to form a light beam with quasi-plane wavefront, which then illuminated a diffuser. This diffuser was employed to ensure that the incident light was diffused uniformly throughout a large cone angle of ~50º. Along with the diffuser, a ground glass plate with 220 grit was used as an object for the characterisation measurements. It was imaged onto the SPAD array camera using a double telecentric imaging system. This system was composed of two identical converging lenses with an aperture stop placed at the common focussed point. By changing the diameter of the aperture stop, different f-numbers (e.g. usually between f/2 and f/22) could be used for illumination. The SPAD array was mounted on a six-axis micro-positioning translation stage, and it was placed at a distance of slightly longer than f away from the rear lens of the telecentric system (note that f is the focal length of the rear lens). This allowed the system setup to have sufficient spacing to be compatible at different working distances at different f-numbers. All the reported measurements were implemented at room temperature and in completely dark conditions. Furthermore, all SPAD arrays under test (with and without microlenses) operated in photon counting mode using an excess bias voltage of 3 V.

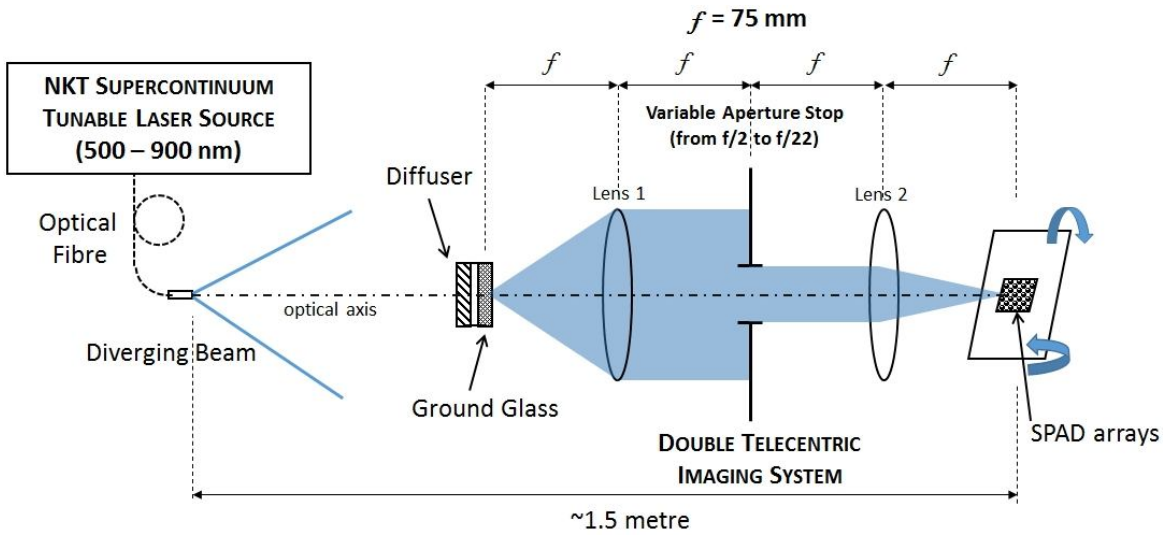

Figure 5-34 A characterisation setup used to evaluate the improvement factor (IF) resulting from microlens integration at varying f-numbers. This setup was also used to evaluate the uniformity of SPAD arrays.

The IF is the ratio of the detected photon event profile on the SPAD array with integrated microlenses to the detected photon event profile on the SPAD array without

integrated microlenses, under the same illumination conditions. Each detected photon event profile is equal to the difference between the signal counts (which is obtained when the sensor is illuminated by light) and the background counts (which is acquired by the sensor in complete darkness). The *IF* of a given f-number is associated with the results of two measurements, which were performed for each SPAD detector array, one measurement with integrated microlenses and the other measurement without microlenses. It is necessary to remove the hot pixels before the average *IF* is calculated using the pixel-wise *IF* values based on a median filter method. Note that a pixel with a DCR higher than 2.5 times the average DCR was considered as a hot pixel for all measurements reported in this Chapter. The proportion of hot pixels of SPAD arrays under test was less than 5% over the 32×32 pixels [5.28].

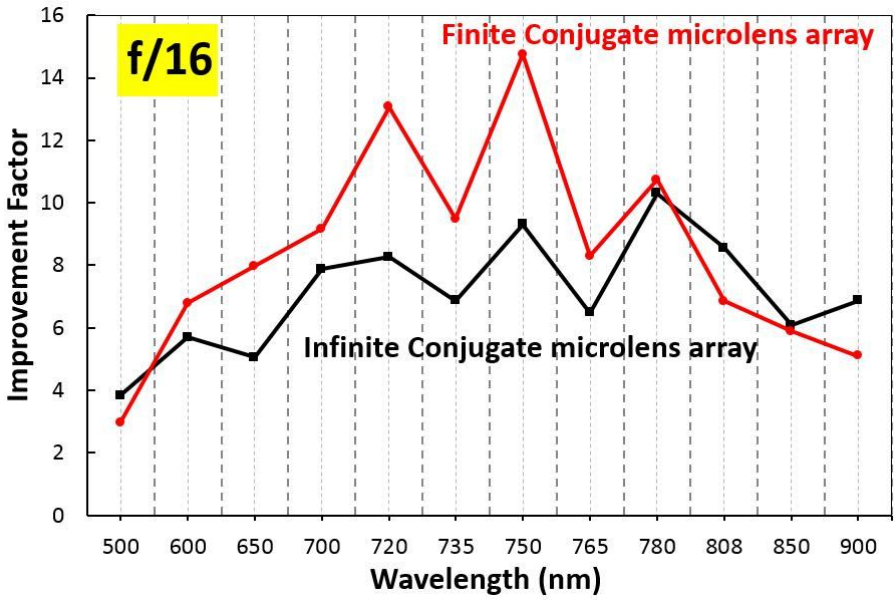

Figure 5-35 Comparison of the average *IF* calculated experimentally for the 32×32 array in the spectral range of interest (from λ=500 to 900 nm) for both infinite (black line and square) and finite (red line and circle) conjugate diffractive microlenses. In these measurements, the aperture was kept fixed to f/16.

Figure 5-35 shows a comparison for the average wavelength-dependent *IF* at f/16 between two chips integrated with infinite and finite conjugate diffractive microlenses respectively. Note that the infinite conjugate diffractive microlenses with f/4.6 focusing capability were fabricated on the 1 mm thick fused silica substrate. In addition, the finite conjugate diffractive microlenses were fabricated on the 0.64 mm thick fused silica substrate. Although both diffractive microlenses were designed with optimum operation at λ=808 nm, the *IF* measured for the infinite conjugate microlens array

exhibited a maximum value of ~10 at λ=780 nm and as for the finite conjugate microlenses, the maximum value of ~15 was obtained at λ=750 nm (see Figure 5-35). It is evident that the actual peak wavelength was not at 808 nm and shifted to slightly shorter wavelengths (i.e. 780 nm and 750 nm) for the infinite and finite conjugate diffractive microlenses respectively, likely due to fabrication tolerance errors. The *IF* values were measured at the design wavelength (i.e. λ=808 nm) as a function of the f-number ranging from f/2 to f/22 with one-stop increment and three assessment conclusions can be drawn from Figure 5-36:

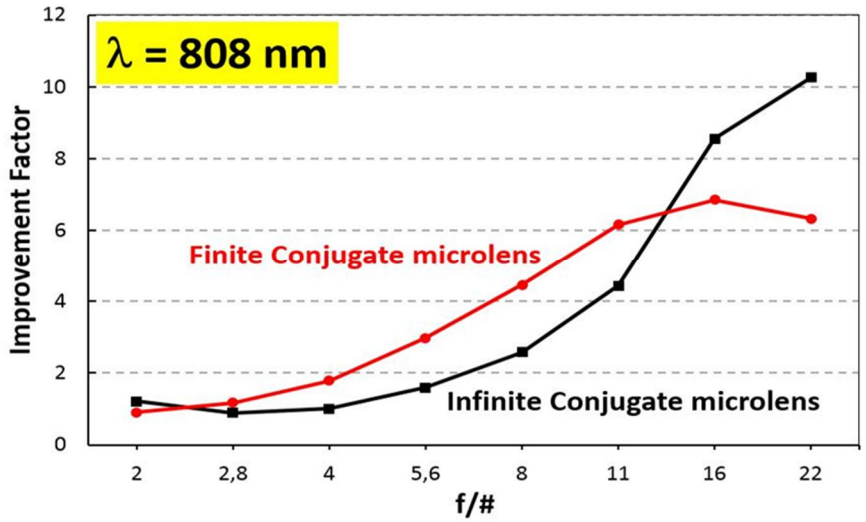

Figure 5-36 Comparison of the average *IF* at λ=808 nm measured at various f-numbers from f/2 to f/22 with a one-stop increment for both sets of microlenses, infinite (black) and finite (red) conjugate, respectively integrated with SPAD arrays.

(1) For both sets of microlens arrays, it is evident to find higher *IF* values at higher f-numbers and this can be explained in Figure 5-37. Low f-numbers between f/2 and f/5.6 (solid line) correspond to light with a larger cone angle (e.g. ~28.1° at f/2) exiting the telecentric imaging system. In contrast, the cone angle is ~2.6° at f/22. This suggests that at high f-number the cone angle of the illumination light beam is a good match to the numerical aperture of the microlenses, but it is not the case at lower f-numbers. Consequently, the efficiency of focusing light onto the photosensitive area of the SPAD array detectors of the microlenses at low f-numbers is lower in comparison to the cases at high f-numbers.

(2) The *IF* values of the bonded device with the finite conjugate microlens array are higher compared to the one with the infinite conjugate microlens array at low f-numbers, from f/2.8 to f/11. This is expected as all the measurements were carried out

using a finite conjugate imaging configuration. This configuration is suitable for the finite conjugate microlens array to form a focal spot on the detector photosensitive area. On the other hand, the spots on the back surface of the substrate of the infinite conjugate microlenses are defocussed. Hence, this can explain that the performance of the infinite conjugate microlenses is relatively degraded at low f-numbers.

(3) The infinite conjugate microlens case continues to increase over the measured range of f-numbers up to the highest f-number (f/22). This behaviour is expected as the higher f-number approaches the case for collimated light, or an object at infinity. These results also suggest that the *IF* of the infinite conjugate microlenses is likely to further increase at higher f-numbers than f/22. However, this could not be easily demonstrated, due to measurement inaccuracies at the low powers available in these experiments at the small aperture settings.

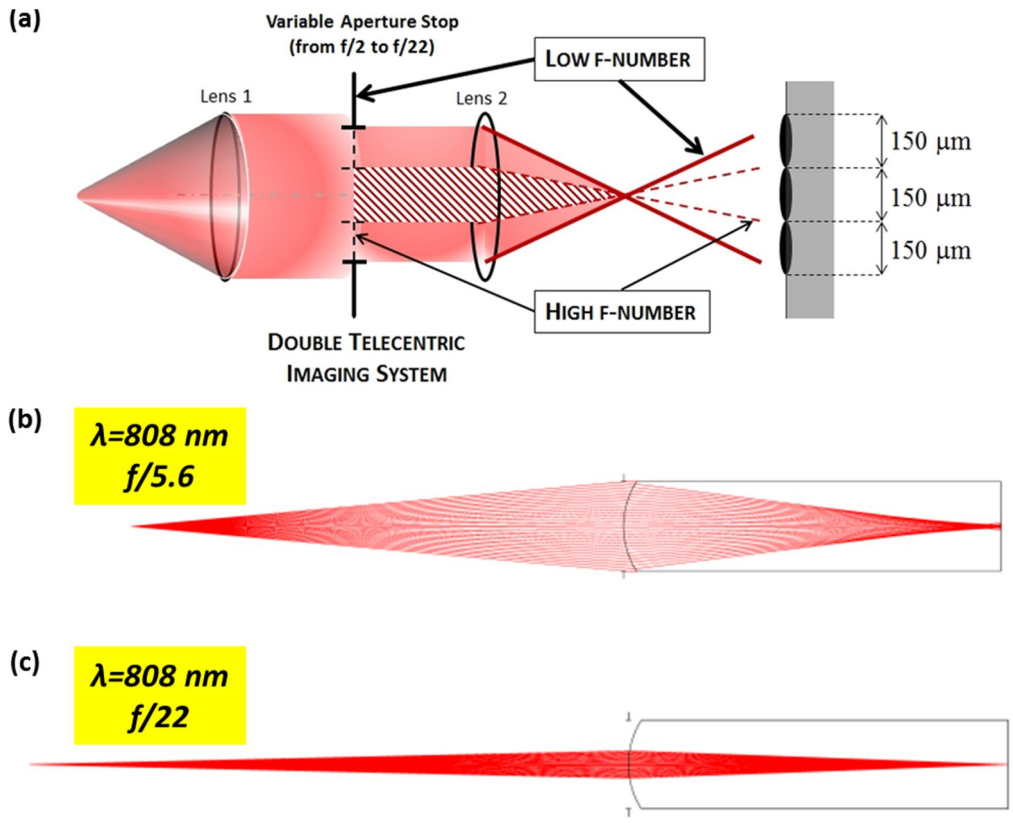

Figure 5-37 Ray-tracing model of the characterisation setup at different f-numbers. For clarity, the dimension of the microlens array has been exaggerated in comparison to the double telecentric imaging system. Low f-number (solid line) corresponds to light with a larger cone angle exiting the telecentric imaging system. For example, the ray-traced layout of a microlens (modelled in Zemax) at f/5.6 with large illuminating light cone is shown in (b). In contrast, the ray-traced layout of a microlens (also modelled in Zemax) at higher f-number (i.e. f/22) with smaller illuminating light cone is shown in (c).

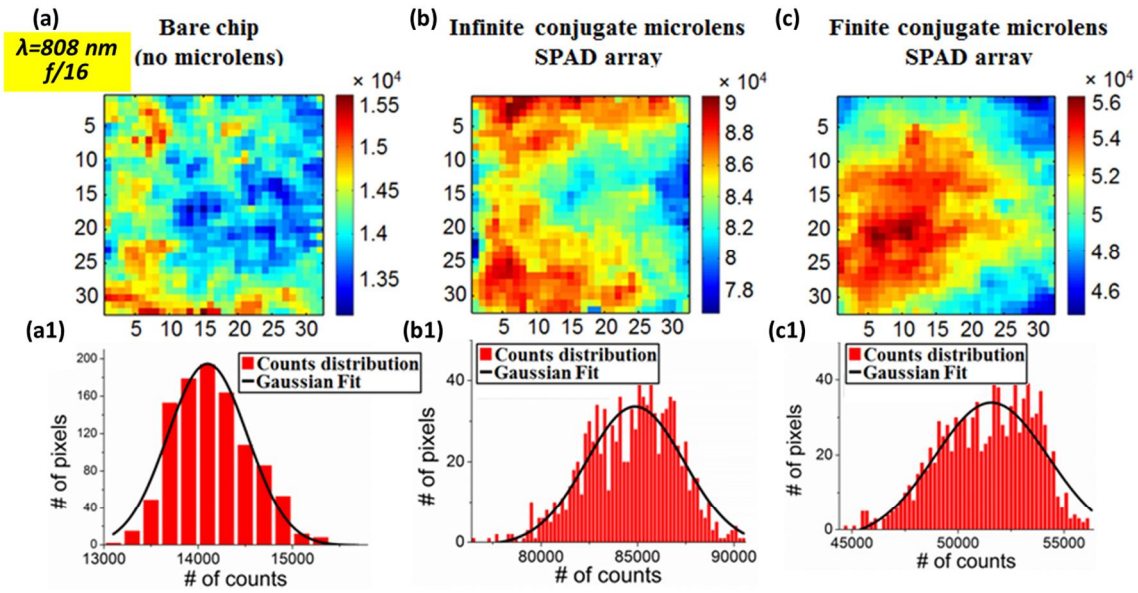

$\mu = 1.41 \times 10^4$	$\mu = 8.46 \times 10^4$	$\mu = 5.13 \times 10^4$
$\sigma = 403.7$	$\sigma = 2.32 \times 10^3$	$\sigma = 2.2 \times 10^3$
CV (%) = 2.8	CV (%) = 2.7	CV (%) = 4.2

Figure 5-38 Photon counts (which are the difference between signal and background counts) images (a), (b) and (c) obtained for each of the three SPAD arrays (i.e. one bare chip and another two chips with infinite and finite conjugate diffractive microlens respectively) under the same illumination conditions. These illumination conditions were at λ=808 nm and aperture stop associated with f/16 and correspondingly their improvement factor (*IF*) distributions are shown in (a1), (b1) and (c1) respectively. The values of mean (μ) and standard deviation (σ) of the measured photon counts were also reported for all images. Photon-counts-associated CV values of 2.8%, 2.7%, and 4.2% were obtained for the bare chip, and another two chips with infinite and finite conjugate diffractive microlenses, respectively.

The other important parameter for the detection characterisation of a SPAD array is the spatial uniformity of photon detection. The integration quality between the microlens and SPAD arrays can be estimated by this uniformity, which was evaluated by considering the coefficient of variation (CV that is expressed in percentage). The CV is the ratio of the standard deviation (σ) to the mean (μ) of the measured photon counts across the whole sensor. By investigating the CV values, the spatial uniformity of photon detection across the whole sensor can be characterised. As shown in Figure 5-38, it is evident to see the increased photon counts for the SPAD arrays integrated with microlenses due to their fill-factor recovery. For each array, the values of mean and standard deviation are also reported in Figure 5-38. Hence, CV values of 2.8%, 2.7%,

and 4.2% were obtained for the bare chip, and another two chips with infinite and finite conjugate diffractive microlenses, respectively under the same illumination conditions, at λ=808 nm and aperture stop associated with f/16. Both microlens and detector arrays contributed to the non-uniformity of photon detection across the whole sensor integrated with microlens arrays.

As shown in Figure 5-39, a uniformity of the photon detection of less than 6% at λ=808 nm was reported for both SPAD arrays with microlens arrays at all f-numbers under investigation. As a whole, the CV was reasonably constant across the whole f-number range (between f/2 and f/22) demonstrating a good integration process of the microlens array on top of the SPAD array as well as the robustness of the custom characterisation setup.

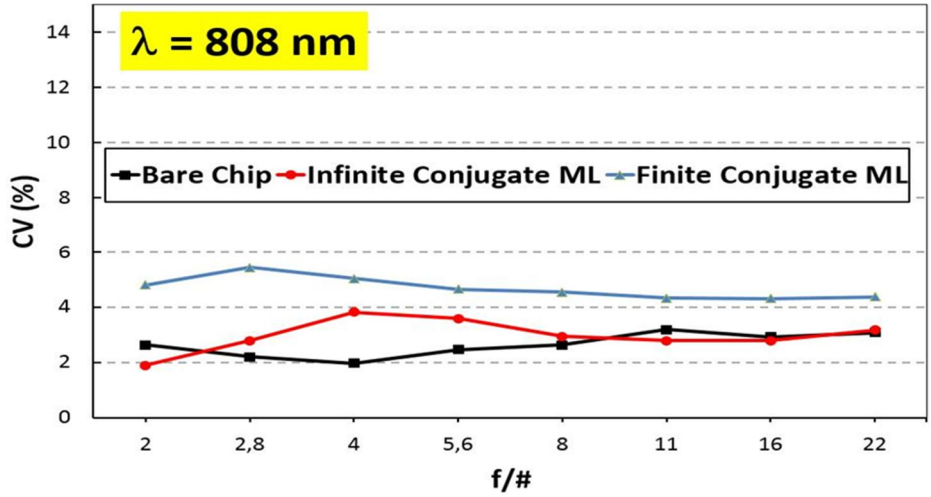

Figure 5-39 Spatial uniformity of photon-counts-associated CV values as a function of the f-number (from f/2 to f/22 with one-stop increment) at λ=808 nm for the bare chip (black), the infinite (red) and finite (light blue) conjugate diffractive microlens arrays.

5.6 SPAD-array-based depth imaging system

The 32×32 direct time-of-flight (dTOF) front-illuminated CMOS Si-SPAD arrays produced by the MiSPIA project are capable of not only counting single photons (i.e. operating in photon counting mode), but also accurately measuring their arrival times (i.e. operating in photon timing mode). A scanning depth imaging system incorporated the SPAD array camera in photon timing mode was developed by Dr. Aongus McCarthy and the author in 2014. The SPAD-array-based depth imaging system consisted of three key subsystems: an illumination source, a scanning transceiver unit and a SPAD array

camera. In order to optimise the usage of the illumination power for long-range imaging, structured illumination was used to match the return onto the individual SPAD active areas of the 32×32 detector array. Hence, an array of 32×32 illumination spots was projected onto the remote target and they were scattered back and imaged onto the 32×32 SPAD detector array. In addition, a reconfigured scanning monostatic transceiver (which is akin to the one described in Chapter 3) was employed in the system. This transceiver unit was adapted in a number of ways for this work. In particular, in the receiver channel, the received beam was free-space coupled to the arrayed sensor rather than by means of the fibre-coupled configurations previously used (see Chapter 4). In order to achieve imaging associated with larger FOV and higher resolution, raster scans on the remote target can also be implemented using our scanning depth imager.

5.6.1 Structured illumination

A key part of the optical setup in the transmit channel of the SPAD-array-based depth imaging system described in this Chapter, was the use of a diffractive optical element (DOE) to provide an array of illuminated spots matched to the pixels of the 32×32 detector array. An appropriate magnification needed to be achieved in order to illuminate the target using arrayed beams with the correct spot spacing and spot size at the detection windows of the 32×32 SPAD array when projected back along the receive channel of the optical system.

The employed DOE was designed by Dr. Andrew J. Waddie using the closed-form optimisation technique [5.29-5.30], which is for computer-generated holography. It is a binary transmissive structure, which was fabricated in fused silica at Heriot-Watt University using a conventional lithographic fabrication technique (refer to Page 350 of [5.20]) performed by Neil Ross. The binary phase pattern of the DOE is shown in Figure 5-40. It is a far-field, even-order-missing, phase-grating kinoform-type array generator which has periodic structure and is capable of generating a diffraction pattern with discrete spots. In comparison to DOEs with multi-level or continuous phase structure, the DOEs with binary phase pattern are easier to fabricate. In addition, this can ensure that they have lower error as well as higher uniformity (>98%) and moderate diffraction efficiency (~70-80%) [5.30].

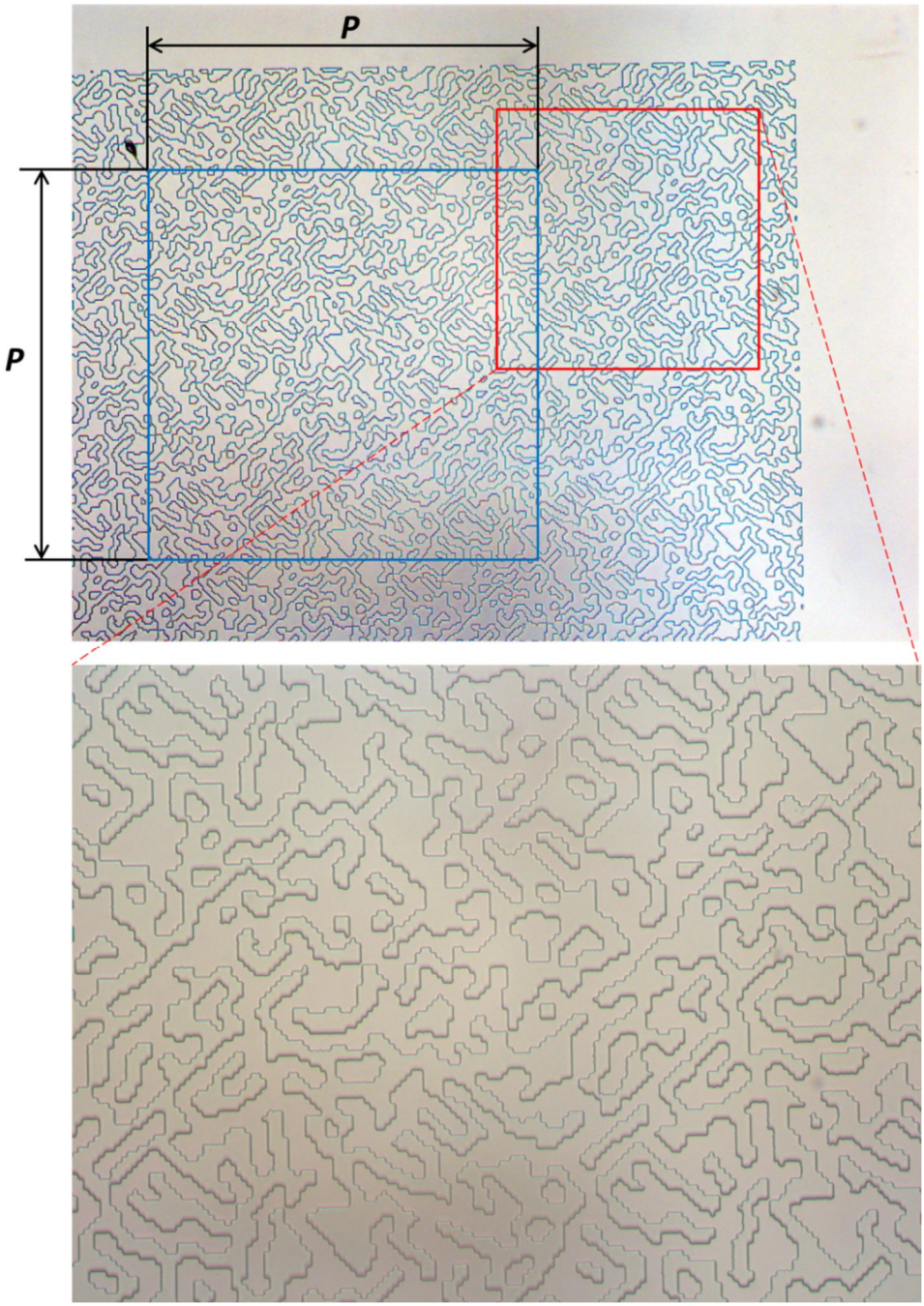

Figure 5-40 Optical microscope images obtained using ×20 objective (Top) and ×50 objective (Bottom, which corresponds to the structure within the red box shown in the top image) of a DOE with the binary phase structure used to create this 32×32 fanout spot array. Note that in the top image the blue box indicates an entire period of the grating-type DOE. The period (P) of the DOE is 323.20 μm.

As shown in Figure 5-41, a combination of a grating-type DOE [5.31] (with a period of P) and a transform lens (with a focal length of f) can generate an array of spots in the far field. Given an illumination source at a wavelength of λ, the spot spacing (S) between the 0 and +1 (or -1) orders in one dimension (e.g. in X) of a general grating-

type DOE in the far field can be shown to be [5.32]:

$$S = \frac{f\lambda}{P} \qquad \text{Equation (5.12)}$$

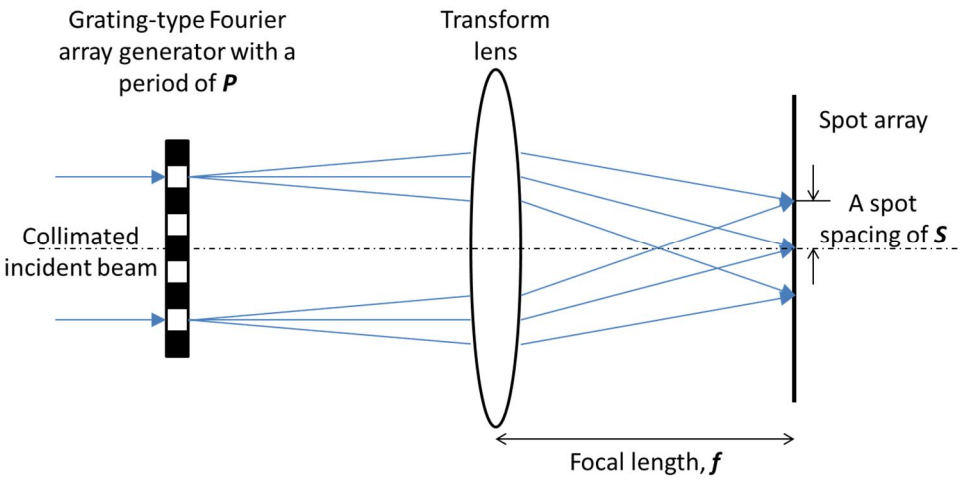

Figure 5-41 Fourier-transform-based spot array generation. Given a collimated incident beam a grating-type DOE combined with a transform lens is used to generate a spot array in the far field (only shown in one dimension for clarity). (After [5.32]).

However, in terms of the even-order-missing grating-type DOE, its S (corresponding to the spacing between the +1 and -1 orders) in the far field is:

$$S = \frac{2f\lambda}{P} \qquad \text{Equation (5.13)}$$

Inherently, the DOE is wavelength-dependent and hence the spectral operating range of the system is restricted. The employed fanout DOE in the imager has the design wavelength of 808 nm. It incorporated a lens with a focal length of 30 mm to form the spot spacing of 150 μm, which has a good match to the detector pixel pitch. Thus, a period of 323.20 μm for the DOE can be calculated using Equation (5.13). The actual output of the DOE was investigated experimentally using the input illuminations at λ=808 nm (see left of Figure 5-42) and λ=817 nm (see right of Figure 5-42). As the shadow of the illumination beamlet spots (in particular for the central spot) corresponds to the image of the core of a "Panda" style polarisation-maintaining fibre, it represents that the inspected images are both in focus. Given a reasonably close input laser power for both cases, the spots associated with λ=817 nm have smaller size but higher intensity than the ones associated with λ=808 nm. Apart from the spot comparison between these two wavelengths, spot arrays associated with illuminations at several

nearby wavelengths were also inspected and compared. The optimum operating wavelength of the employed DOE was eventually found to be 817 nm.

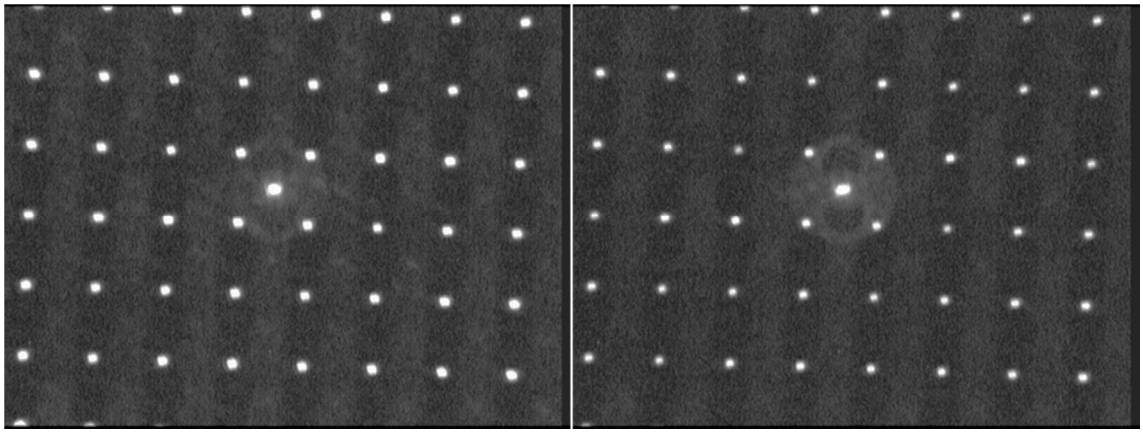

Figure 5-42 DOE illumination patterns inspected using a CCD camera on the image plane. Left: intensity spots associated with the input illumination at λ=808 nm. Right: intensity spots associated with the input illumination at λ=817 nm. The shadow of the illumination beamlet spots (in particular for the central spot) corresponds to the image of the core of a "Panda" style polarisation maintaining fibre.

5.6.2 Optical design of the scanning transceiver unit

The incoming light beam of the transceiver was provided by a pulsed supercontinuum laser source with an integrated AOTF. It was then delivered, via a polarisation-maintaining single-mode fibre (PM-SMF) with 10 μm diameter core and 0.12 numerical aperture (NA), to the lens TxLC, as shown in Figure 5-43. The lens with f=15 mm was used to collimate the launching beam to an appropriate size (i.e. ~4 mm diameter) for the custom fanout DOE with a period of 323.20 μm. The focal lengths of lens TxLC and lens TxLD were required to appropriately determine such that the magnified fibre core is suitable for use with the 30 μm diameter photosensitive area of the detectors. In addition, the lens TxLD was custom designed at Heriot-Watt University. It can be corrected for $f \sin\Theta$ distortion and its design was reported previously in [5.33]. The DOE, combined with the lens TxLD with f=30 mm (corresponding to the transform lens in Figure 5-41), formed an intermediate image of 32×32 diffraction-limited beamlet spots with a pitch of ~150 μm. This image was magnified and then projected onto the target surface using a combination of the lens TxLR with f=100 mm (in the transmit channel alone) and the final objective lens (in the transmit and receive channels).

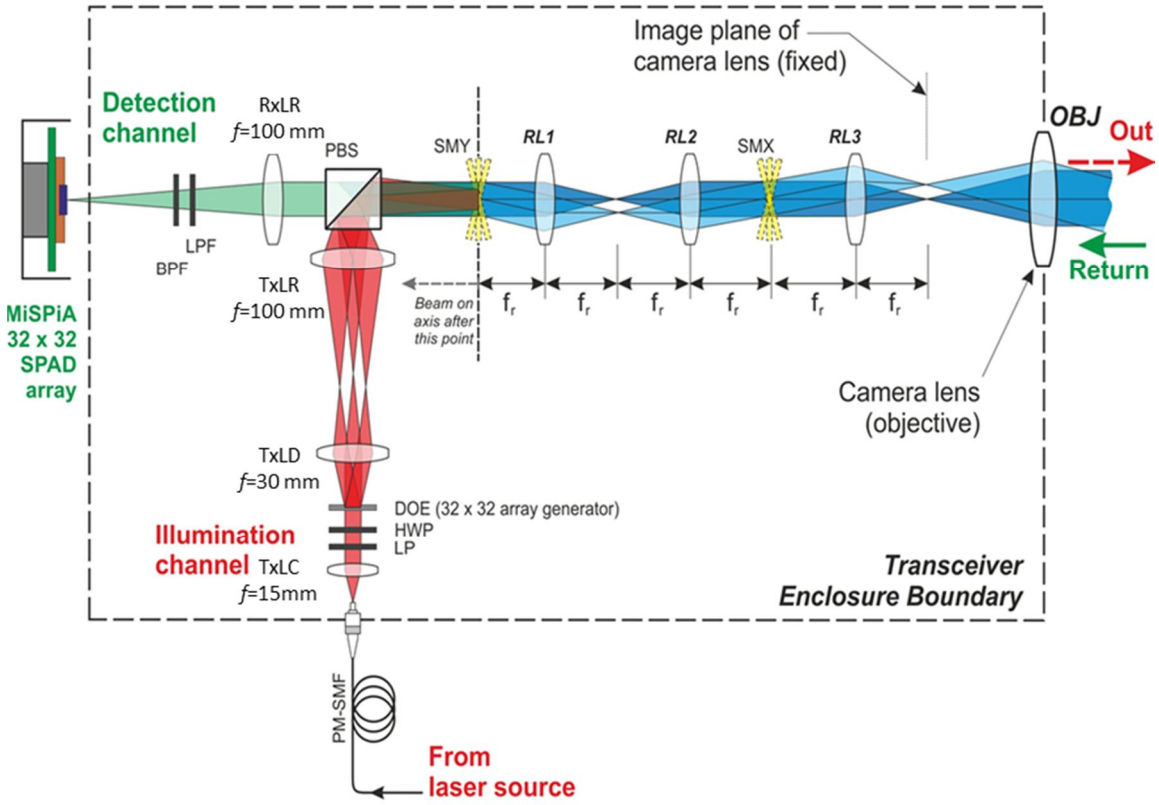

Figure 5-43 Schematic of the layout of the transceiver unit employed in the SPAD-array-based depth imaging system. LPF: a long-pass filter with a cut-on wavelength of 750 nm; BPF: a band-pass filter with a central wavelength of 810 nm and a bandwidth of 10 nm FWHM; TxLC: a lens for beam collimation in the transmit channel; LP: a linear polariser; HWP: a half-wave plate; DOE: a diffractive optical element; TxLD: a lens combined with the DOE for the generation of diffraction-limited beamlets in the transmit channel; TxLR and RxLR: two relay lenses with a suitable focal length to achieve the appropriate magnification to match the illumination and receive beamlets' patterns; PBS: a polarising beam splitter; SMX and SMY: galvanometer scanning mirrors in X and Y; RL1,RL2 and RL3: three relay lenses; OBJ: an objective lens. PM-SMF: a polarisation-maintaining single mode fibre.

Note that focal lengths of 30 mm, 35 mm and 30 mm for the lenses RL1, RL2 and RL3 were chosen respectively. The 32×32 illumination array of ~150 µm×~150 µm spot pitch was generated by the DOE incorporated the lens TxLD and had a full diagonal field of ~6.78 mm to match the entire detector array. The actual field in the fixed image plane of the custom lens RL3 [5.33] (which is similar to TxLD) was calculated to be ~1.74 mm full diagonal. It was less than the maximum field (i.e. 11 mm full diagonal) of the lens RL3. This corresponded to an effective FOV of ~3.5 mrad for the transceiver system using a f=500 mm objective lens. This means that when the system

was used for depth profiling on the target at a stand-off distance of 45 or 325 metres, the optical path difference (~0.1 or ~0.5 mm respectively) introduced by different pixels on the array was negligible.

In order to achieve high efficient imaging, the1024 beamlets are required to be precisely imaged onto the 1024 pixel array of the CMOS Si-SPADs with a pitch size of 150 µm and a 30 µm diameter photosensitive area. That was implemented by carefully choosing the magnification of the transmit and receive optical systems. As shown in Figure 5-43, a combination of the lenses TxLD, TxLR and the objective lens was used in the transmit optical system. In addition, a combination of the objective lens and the lens RxLR (that is the same as TxLR with f=100 mm) was used in the receive optical system. The choice of the same focal length of 100 mm for lenses TxLD, TxLR gives a suitable pixel spacing at long stand-off distances (e.g. 325 metres). In addition, this can ensure the transmit/receive beam diameter is less than the clear aperture (i.e. 10 mm) of the galvo mirrors. Referring to [5.34-5.36], a similar beamlet-to-pixel optical mapping approach was demonstrated as arrayed illuminations for 3D light detection and ranging (LiDAR) imaging systems. Overall, the use of the appropriate combination of diffractive and bulk optics in the transmit and receive optical systems can offer a highly efficient optical delivery process. That is due to the power-efficient structured illumination in comparison to the flood illumination and the optimised beamlet-to-pixel optical collection. In addition, the use of the galvo-scanners in the transceiver system, as shown in Figure 5-43, allows a larger FOV and higher resolution imaging.

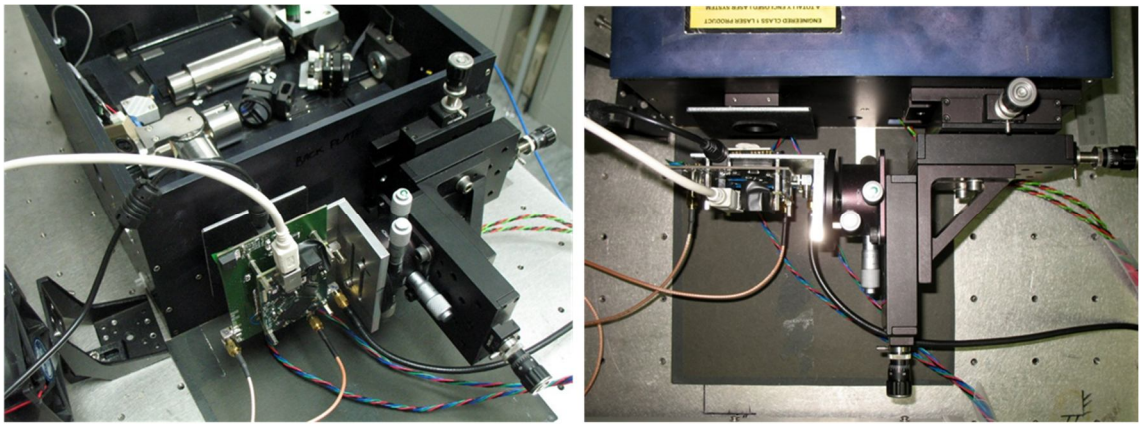

Figure 5-44 Pictures show two views of the mounting of the SPAD array camera onto the scanning transceiver. An optomechanical assembly containing micro-positioning in six axes: X, Y, Z and tilt, roll and rotation is also shown.

5.6.3 SPAD array camera

The optomechanical setup of the existing transceiver configuration (i.e. that used with fibre-coupled detectors, as seen in Chapter 4) required a number of significant adaptations so that the structured illumination and SPAD detector array could be incorporated. An optomechanical assembly containing micro-positioning in six axes (i.e. X, Y, Z and tilt, roll and rotation) for the SPAD array sensor was attached to the transceiver frame (see Figure 5-44). This mechanical positioner was necessary in order to align the collected return photons from the transmitted 1024 beamlets onto the 1024 pixel SPAD array. The advantage of this optical approach setup is that it removes the requirement for microlens arrays combined with the arrayed detectors, since only the SPAD detector windows are illuminated. A camera can be used to help during the alignment procedure to guide the adjustments in order to find optimum focus and rotation positions. A CCD image of the full illuminated 32×32 detector plane is shown in Figure 5-45 when 32×32 beamlets, with the illumination at λ=817 nm, were incident on target and back-reflected.

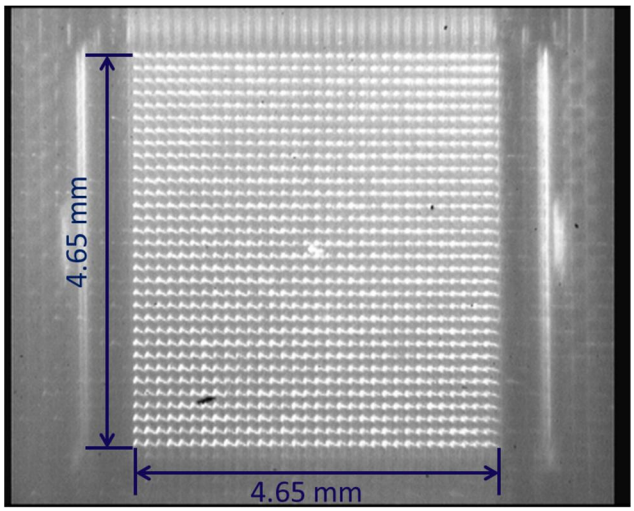

Figure 5-45 A CCD image of the full illuminated 32×32 detector plane when 32×32 beamlets, with the illumination at λ=817 nm, are incident on target and back-reflected.

The SPAD detector array module was directly interfaced to an integration module (XEM3010-1000, Opal Kelly Inc. Poland) based on a Spartan-6 field programmable gate array (FPGA) through an analogue board (see Figure 5-46). This integration module can also send a trigger signal to control a scanner. A 128 MB dynamic random access memory (RAM) was employed to store the data collected from the array sensor,

and the data was transferred to the computer via a USB 2.0 interface with 16384 frames per RAM block for the measurements described in this Chapter.

The SPAD array detection system has both photon counting and photon timing modes. When operating in the photon counting mode, the detection system can only resolve 2D maps based on pixel-wise photon counts. By contrast, pixel-wise time-correlated single photon counting (TCSPC) measurements can be implemented to acquire time and counts information simultaneously for depth profiling in photon timing mode. The TCSPC measurements operated in a reversed start-stop configuration. As shown in Figure 5-46, the stop signal fed in the SPAD array was a rectified signal via an analogue board, which is synchronised to a nuclear instrument module (NIM) pulse train provided by a pulsed laser source. Single, rather than multiple, gate-on acquisition window per frame was used for the photon timing measurements in this Chapter. The total number of frames (N) multiplied by the duration of the gate-on acquisition window per frame (T_{g-on}) (i.e. N=16384 frames and T_{g-on}=410 ns for all the measurements described in this Chapter) can work out the total gate-on acquisition time T_{Acq} (i.e. $T_{Acq} = NT_{g-on}$). Note that the acquired data needs to transfer from the memory of the digital processing board to the computer storage via USB 2.0 interface. However, the data transfer time per frame was typically 10s μs due to the limitations of the data readout on the board and the USB link. Hence, the data transfer time per frame was much longer than the gate-on time of the acquisition window per frame. In this Chapter, this large amount of data transfer time for this early-stage prototype device was ignored. Only the actual exposure time (i.e. gate-on data acquisition time) of the device was considered for the photon timing measurements discussed later. In addition, multiple RAM blocks (i.e. M RAM blocks) of data can be acquired on the board when not using the dynamic RAM operation. Correspondingly, the total gate-on time T_{Acq}^{M} associated with the data acquisition of M RAM blocks was MNT_{g-on}.

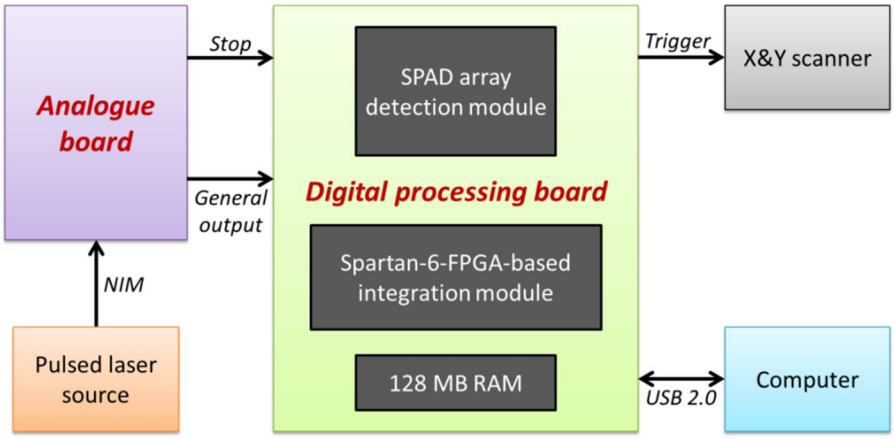

Figure 5-46 Block diagram of the SPAD array sensor and data acquisition system. Note that the Si-SPAD array detection module operated in the reversed start-stop TCSPC mode. The NIM signal from the pulsed laser source was fed into an analogue board for signal rectification. After this board, a stop signal was delivered to the Si-SPAD array detection module that is integrated in a digital processing board. NIM signal: nuclear instrument module signal.

In order to link the photon counting or photon timing measurements with the scanning steps when the imager operates in a scanning mode, the trigger signal for controlling the X&Y scanner (i.e. scanning step markers) was synchronised to the frame clock with a period equal to the acquisition window (see Figure 5-47). The time between adjacent markers consists of the total acquisition time of each desired measurement and a delay time of 500 µs from when the trigger signal for the scanner starts. This delay time was allocated to guarantee the servos of the galvo-mirrors had sufficient time to respond and the mirrors were steadied after their movements cease. Hence, the imager can stare at a certain FOV during each desired measurement within its entire acquisition time.

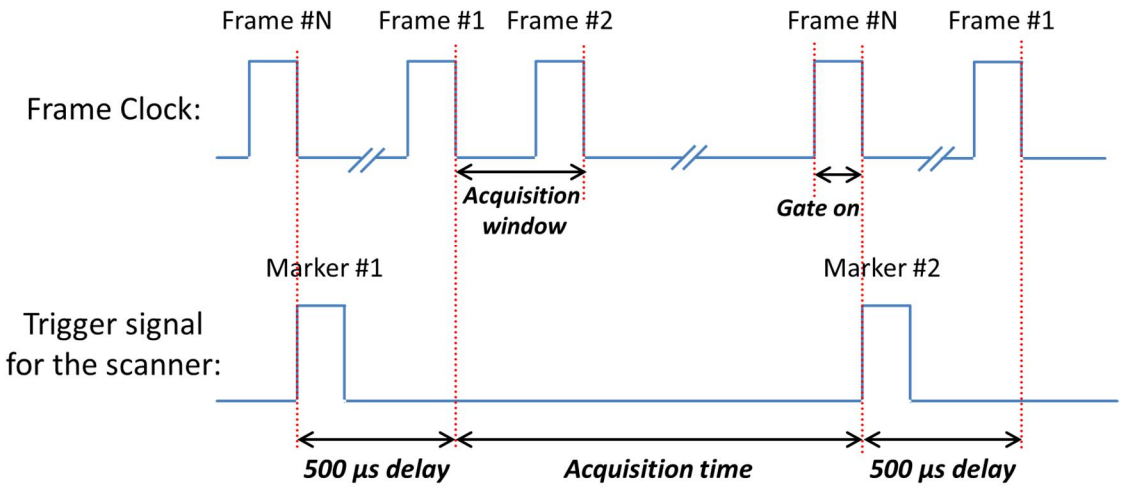

Figure 5-47 Time relation of the frame clock and the trigger signal for the scanner. Note that frames of one RAM block are acquired here for clarity.

In order to enable the XY galvanometer mirrors to scan the SPAD array camera for the depth imaging measurements (described in the next section), scan control software was developed with the Intel C++ Compiler. This scan control software operated in conjunction with the camera control and data acquisition software developed by Dr. Federica Villa and Rudi Lussana in Prof. Franco Zappa's group. Figure 5-48 shows the execution flowchart of the developed software for the SPAD array camera. The control voltages were pre-calculated based on the number of desired scan steps. The stepped voltage pattern for both scan mirrors were created and then loaded into the cache of the National Instruments USB-6221 multifunction data acquisition device (NI-DAQ). The software waited for a user start input for a step-by-step scanning. Each time the NI-DAQ received an effective step-wise trigger (a new marker) with 500 µs delay from the SPAD array camera, XY scan mirrors were advanced to a new movement step associated with an updated pair of XY voltages. Correspondingly, in the case of a marker event, the camera data acquisition software obtained the data of the measurement with user-determined exposure time first and then activated the next measurement. Once the last updated pair of XY voltages were used to position the XY scan mirrors, the scanning was stopped, although the camera is still active for measurements.

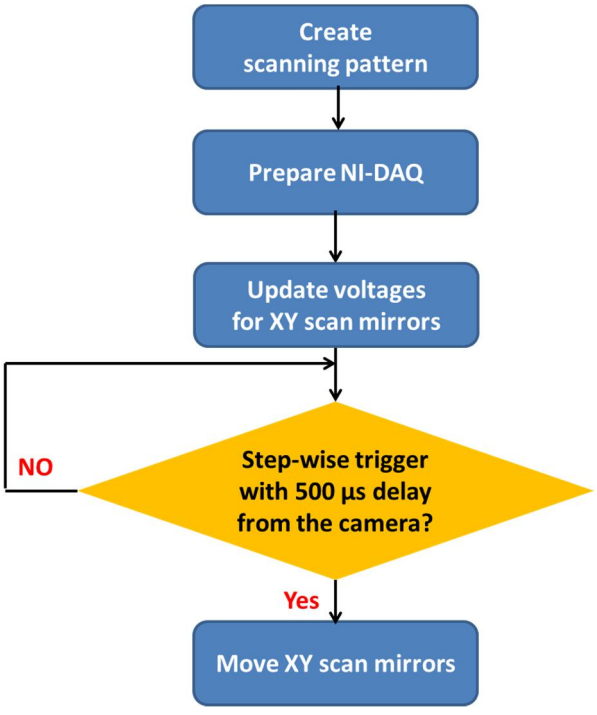

Figure 5-48 Execution flowchart of the scan control software for the SPAD array camera. NI-DAQ: National Instruments USB-6221 multifunction data acquisition device.

The main parameters of the SPAD-array-based depth imaging system are summarised in Table 5-5.

System Parameter	**Comment**
Transmit/Receive Alignment	Monostatic: Coaxial transmit and receive channels
Laser	Pulsed supercontinuum laser (SuperK EXTREME, EXW12, NKT Photonics, Denmark)
Laser Repetition Rate	39.01 MHz
Illumination Wavelength	817 nm
Laser Pulse Width	<50 ps
Objective Lens	Canon EF 500 mm f/4 IS USM
Illumination Array Generator	• Grating-type DOE with a period of 323.20 µm is combined with a transform lens with f=30 mm to generate a fanout 32×32 spot array; • Pitch of the illumination spots (~90 µrad): ~4 mm at 45 metres and ~30 mm at 325 metres • Diameter of the illumination spots (~45 µrad): ~2 mm at 45 metres and ~15 mm at 325 metres
Average Output Power	<50 µW exiting the system
Output energy per pulse	<1.3 pJ
Range	Scans performed at 45 and 325 metres
Beam Scanning Mechanism	Galvanometer controlled mirrors (X&Y) common to transmit and receive channels
Spectral Filters in Detection Channel	• Long-pass: 750 nm cut-on (FELH0750, Thorlabs, USA); • Band-pass: 10 nm FWHM, a central wavelength of 810 nm (FBH810-10, Thorlabs, USA)
Detector	• Free-space-coupled 32×32 direct time-of-flight (dTOF) front-illuminated CMOS Si-SPAD array sensor with a pitch size of 150 µm and 30 µm diameter photosensitive area produced by the MiSPIA project (chip size ~10 mm×10 mm). • Photon detection efficiency of ~5% and median dark count rate of ~100 cps at λ=817 nm operating at room temperature and excess bias voltage of 5 V.
Data Acquisition Module	• A timing bin width of 400.641 ps and a timing range of 410 ns for a 10-bit TDC. Note that the timing bin width is governed by the hardware internal clock rate of 156 MHz with 16× multiplication in half-coarse mode [5.37] • SPAD array combined with a Spartan-6-FPGA-based integration module (XEM3010-1000, Opal Kelly Inc. Poland) with 128 MB dynamic RAM using a USB 2.0 interface to deliver 16384 frames per RAM block to the computer.
System Temporal Response (jitter)	~800 ps FWHM
Depth accuracy	Centimetre-scale

Table 5-5 Summary of the Main System Parameters

The implementation of depth imaging system, in particular for the reconfigured transceiver system, can be seen in Figure 5-49.

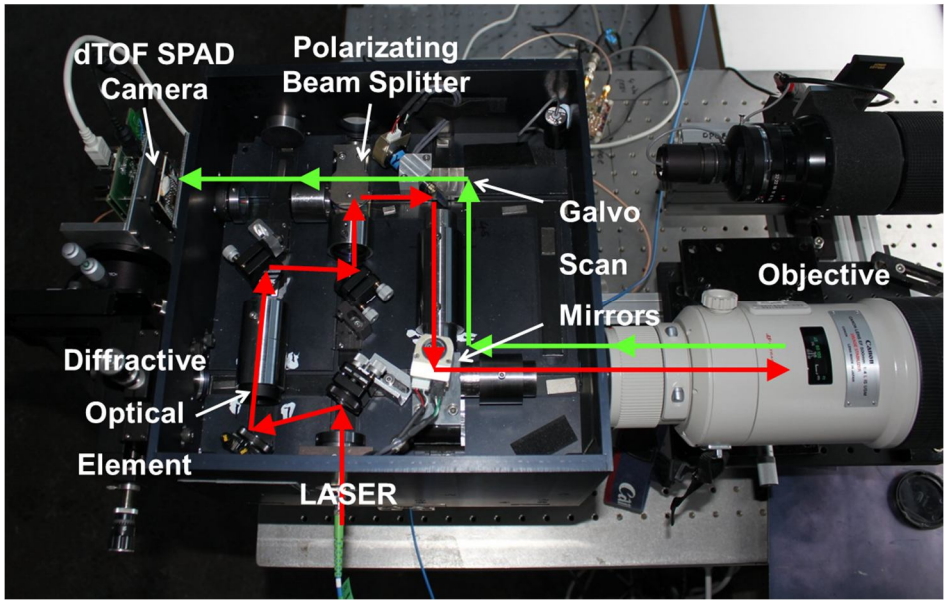

Figure 5-49 Close-up photograph of the used transceiver system shown in Figure 5-43. The paths in red and green indicate the transmit and receive channels respectively. The dTOF SPAD camera: 32×32 direct time-of-flight front-illuminated CMOS Si-SPAD array sensor was produced by the MiSPIA project.

Figure 5-50 Illustration of macro scan steps of the illumination array (Only an 8×8 array is shown here for clarity). For instance, two macro scan steps in X are shown: (a) the first step and (b) the later step. Dark spots indicate on-line scan pixels while light spots correspond to off-line scan pixels.

5.7 Depth imaging results

Our SPAD-array-based depth imager is capable of macro-scan-based and micro-scan-based depth profiling: (1) The macro-scan-based depth profiling, as illustrated in Figure 5-50 is implemented using galvo scan mirrors in XY to steer the entire illumination beam spot array and cover multiple target locations using inter-pixel samplings. It

allows the formation of a composite image, which corresponds to a large FOV. (2) The micro-scan-based depth profiling is achieved by selecting points between detection pixels to form virtual intra-pixels (or sub-pixels) and construct a composite image with higher resolution within a relatively smaller FOV. For example, scan pattern can be implemented in the formation as illustrated in Figure 5-51(a).

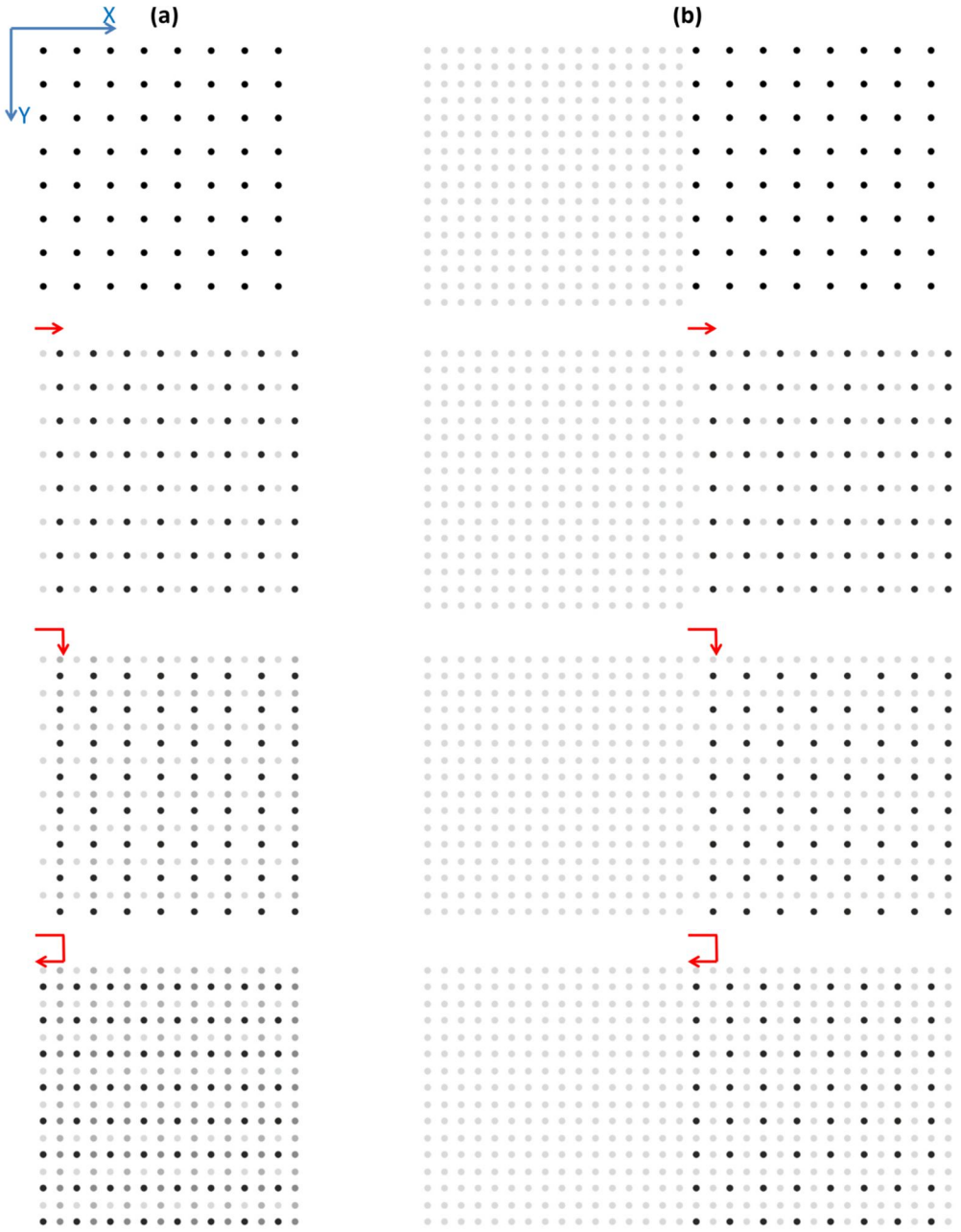

Figure 5-51 Illustration of 2×2 micro scan steps combined with two macro scans of the illumination array (Only an 8×8 array is shown here for clarity). For instance here, two macro scan steps in X while 2×2 micro scan steps within each macro scan are shown in (a) and (b) respectively. Note that 2×2 micro scan steps in XY are shown from top to bottom. Dark spots indicate on-line scan pixels while light spots correspond to off-line scan pixels.

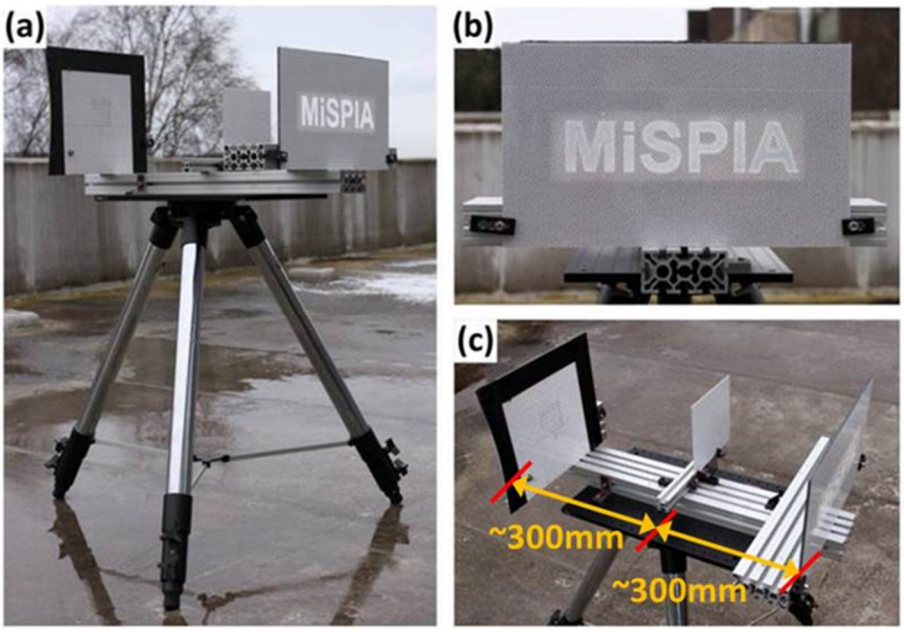

Figure 5-52 Target setup for the depth profiling at a stand-off distance of 45 m. (a), (b) and (c) represent three different perspectives of the target setup with three plane panels covered with white retro-reflective material (high intensity prismatic grade, Avery Dennison T6500 HIP) used for outdoor measurements. The word "MiSPIA" is shown against two different depths of backing, to illustrate three distinct depth planes at 0mm, 300 mm and 600 mm.

The depth imager used an objective lens with a focal length of 500 mm and f/4, and several field trials for depth profiling were carried out at stand-off distances of 45 and 325 metres. The sensor emitted a total average optical power of ~50 µW at a pulse repetition rate of ~40 MHz at an operational wavelength of 817 nm. This corresponded to less than 50 nW per beamlet – far lower than in almost all previous measurements. At this power level, the system was completely eye-safe. The detection system used a timing bin width of 400.641 ps of a 10-bit TDC and a gate-on acquisition window of 410 ns.

A depth image of the panels covered with white retro-reflective material (high intensity prismatic grade, Avery Dennison T6500 HIP) was acquired at a stand-off distance of 45 m with ~3 mrad FOV of the array (i.e. ~120×120 mm at 45 m). The arrangement of the retro-material panels can be seen in Figure 5-52 (a)-(c): one panel (~120×200 mm) with a hollowed-out word pattern of "MiSPIA", and another two panels backing placed at a distance of 300 mm and 600 mm from the wording on two different parts of the word. That is one group letters: "M", "i" and "S" and the other: "P", "I" and "A" are projected on the 600 mm and 300 mm away panels, respectively.

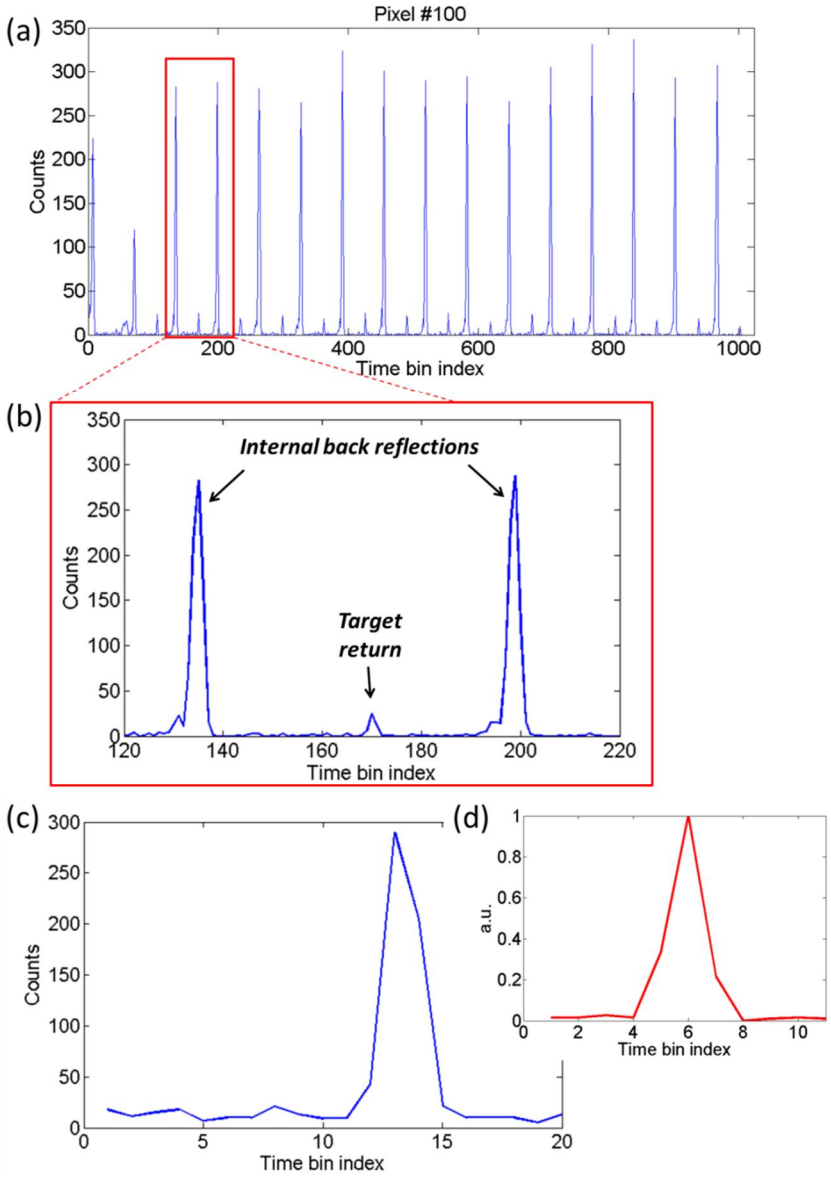

Figure 5-53 (a) Example photon timing result: a histogram of counts versus time with 16 pulses in terms of the 100th pixel of the SPAD array. (b) Portion of the histogram details the internal back reflections from the transceiver unit and the target return peak standing clearly above the background. In this case, a software gate allowed the removal of the section containing the back reflections, in order that we concentrated on the return peak within a pulse period. (c) An accumulated target return signal among the 16 pulse periods. (d) The prior-recorded normalised instrumental response function (IRF) on a Spectralon panel is used for a cross-correlation method.

One of the recorded pixel-wise histograms of counts versus time can be seen in Figure 5-53(a). There are 16 pulses in this histogram as the repetition rate of the actual stop signal for TCSPC measurements of the SPAD array was 2.44 MHz, which was from a synchronisation clock of 39.01 MHz, down-divided by a factor of 16. In addition, Figure 5-53 (b) details the unwanted internal back reflections from the transceiver unit

and the target return peak standing above the background. In terms of the depth estimation, using a software gate to chop off the back reflections can only concentrate on the return peak within a pulse period. Furthermore, the sum of return peaks among 16 pulses can result in an accumulated signal as shown in Figure 5-53 (c). The depth position, in terms of the pixel under test, can be estimated by locating the time bin index corresponding to the maximum cross-correlation between the pixel-wise accumulated signal, and instrumental response function previously recorded on a Spectralon panel (see Figure 5-53 (d)). It should be noted that the pixel-wise cross-correlation method is only one of the histogramming-based depth estimation approaches. For example, another method by locating the time bin associated with the maximum signal peak was used in Ref [5.15] to resolve the depth information from the data acquired by a bistatic depth imaging setup based on the same CMOS Si-SPAD array for the lab-range depth imaging.

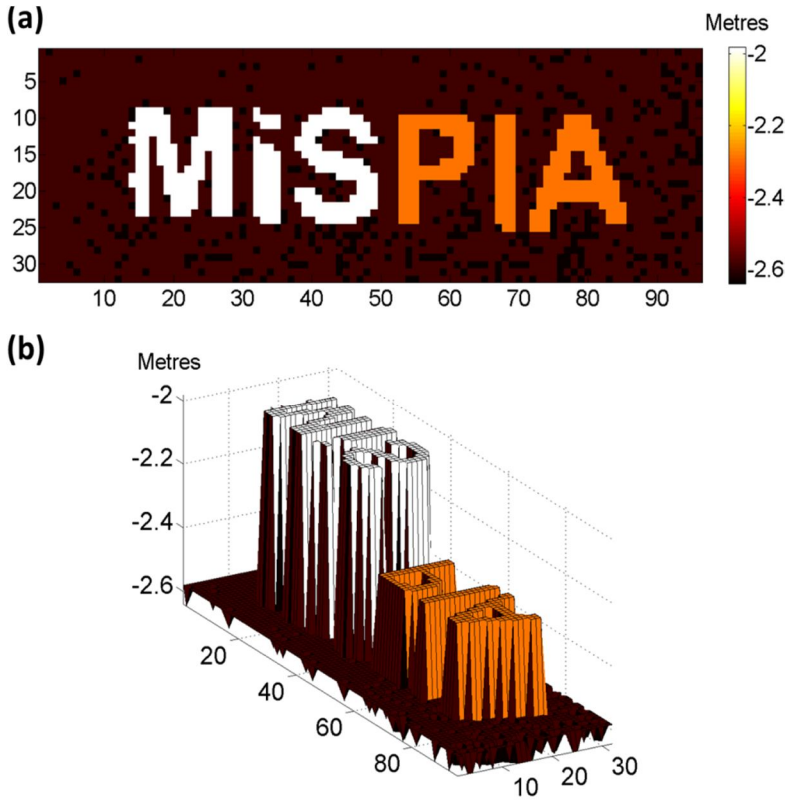

Figure 5-54 Two representations (a) and (b) of the 96×32 pixel depth image (estimated using the pixel-wise cross-correlation method) of the target shown Figure 5-52 with three depth planes are clearly displayed. This was implemented by moving three macro scan steps in X with an exposure time of 134 ms per entire 32×32 array. This corresponds to the gate-on (410 ns) acquisition time associated with 16384 frames per RAM block and 20 RAM blocks. Thus, a total exposure time was 402 ms.

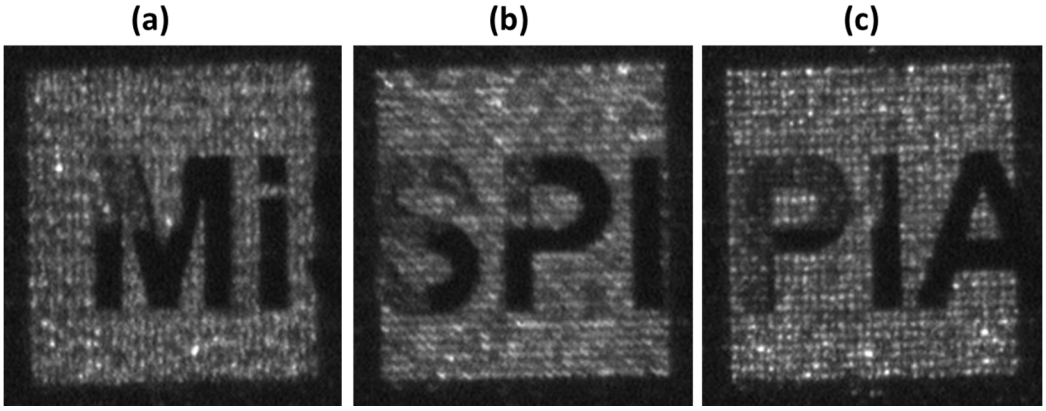

Figure 5-55 The whole DOE illumination pattern of the input illumination at λ=817 nm on the target enclosed with retro-material at a stand-off distance of 45 metres was imaged by a CCD camera in rooftop lab. The illuminated array size is 120 mm × 120 mm with a beam pitch of ~ 4 mm and a spot size of ~2 mm for (a), (b) and (c).

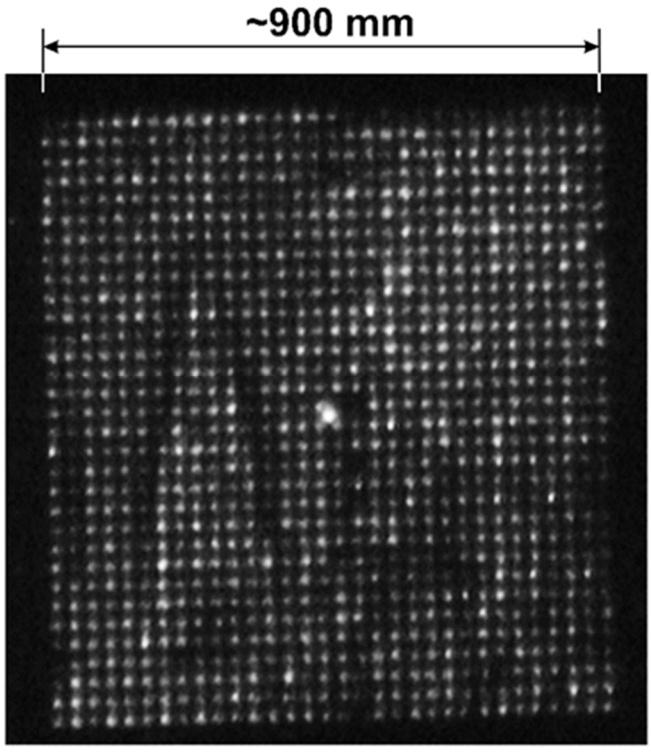

Figure 5-56 The whole DOE illumination pattern of the input illumination at λ=817 nm on the target enclosed with retro-material at a stand-off distance of 325 metres was imaged by a CCD camera in rooftop lab. The illuminated array size is 900 mm × 900 mm with a beam pitch of ~ 30 mm and a spot size of ~15 mm.

By moving three macro scan steps in X with an exposure time of 134 ms for the entire 32×32 array, the entire measurement with 96×32 pixels was implemented with a total exposure time of 402 ms. The 96×32 depth image was estimated by the pixel-wise

cross-correlation method. As shown in Figure 5-54, it is clear to see the image with millimetre-scale spatial resolution and centimetre-scale depth resolution. The illuminated patterns, at a stand-off distance of 45 m and 325 m for the field trial measurements, can be seen in Figure 5-55 and Figure 5-56 respectively. At a stand-off distance of 45 m, the illumination array size was 120 mm×120 mm with a beam pitch of ~ 4 mm and a spot size of ~2 mm. It extended to 900 mm×900 mm with a beam pitch of ~30 mm and a spot size of ~15 mm at a stand-off distance of 325 m. For field trial measurements at a stand-off distance of 325 m, a target setup, as shown in Figure 5-57, with the size of 900 mm×1800 mm was scanned. The 128×64 depth map (see Figure 5-58) that was formed by two macro and four micro scans on the target setup has centimetre-scale spatial and depth resolution. As shown in Figure 5-59, two images with different pixel density were reconstructed using the data of two raster-scan measurements. The scans covered the same entire FOV of the target scene with an exposure time of 269 ms per entire 32×32 array. As expected, it is clear to see that the 128×64 depth map implemented with a total exposure time of 2152 ms has better spatial resolution than the 64×32 depth map. Note that the 64×32 depth map was only achieved by two macro scans with a total exposure time of 538 ms. However, both have comparable centimetre-scale depth resolution. In addition, by using an exposure time of 67 ms rather than 269 ms for the image shown in the bottom of Figure 5-59, a large number of pixels of this depth map can still be locked on the target (see Figure 5-60).

Obviously, the advantage of the SPAD-array-based scanning time-of-flight imager over the imaging systems using discrete SPAD detectors is the potential of 3D profiling of remote targets with reduced exposure times. These experiments also reveal the issues with required structured illumination as well as the expected low power per beamlet. However, for a higher power, larger illumination area source, and improved fill-factor SPAD arrays, this approach has considerable potential for more rapid depth imaging of remote targets, avoiding the need for rapid galvo-scanning.

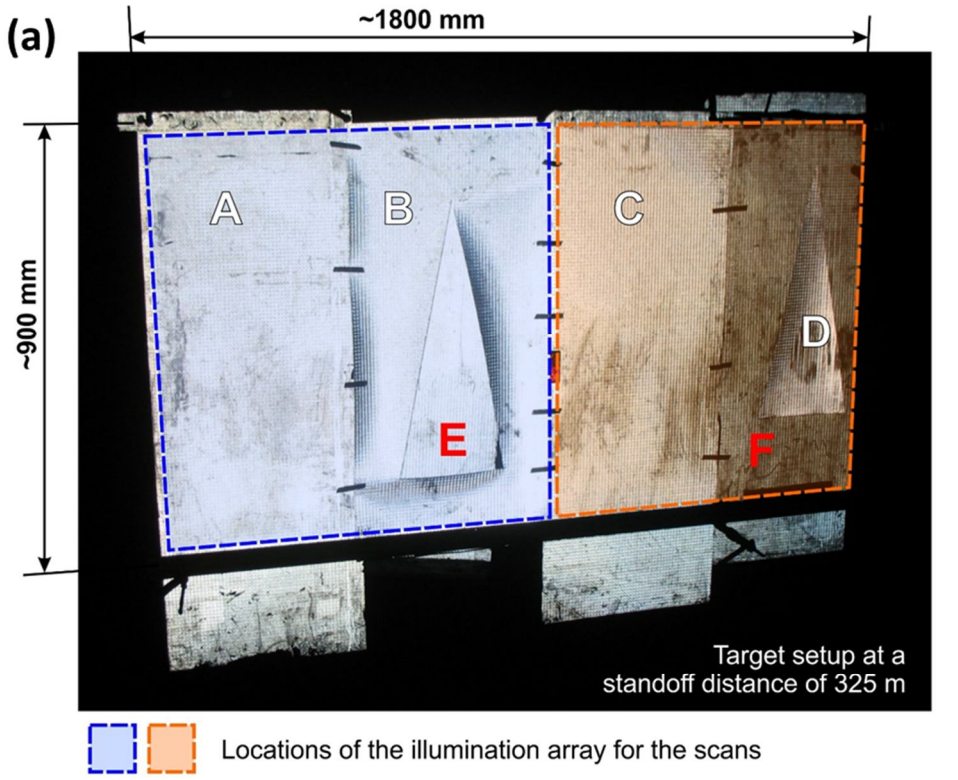

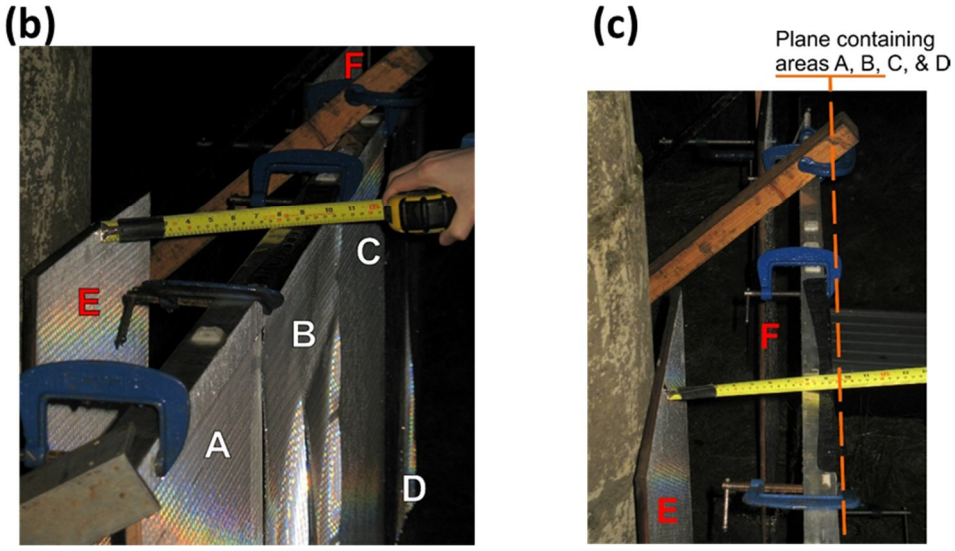

Figure 5-57 The target setup was used for outdoor measurements at a stand-off distance of 325 metres. (a), (b) and (c) represent three different perspectives of the target setup with three plane panels covered with white retro-reflective material (high intensity prismatic grade, Avery Dennison T6500 HIP). Note that, the areas, indicated by these letters: **A, B, C, & D**, are nominally in the same plane, i.e. they are the same distance from the scanner. E: This panel is ~220 mm behind the plane containing A, B, C, & D. F: This panel is ~120 mm behind the plane containing A, B, C, & D.

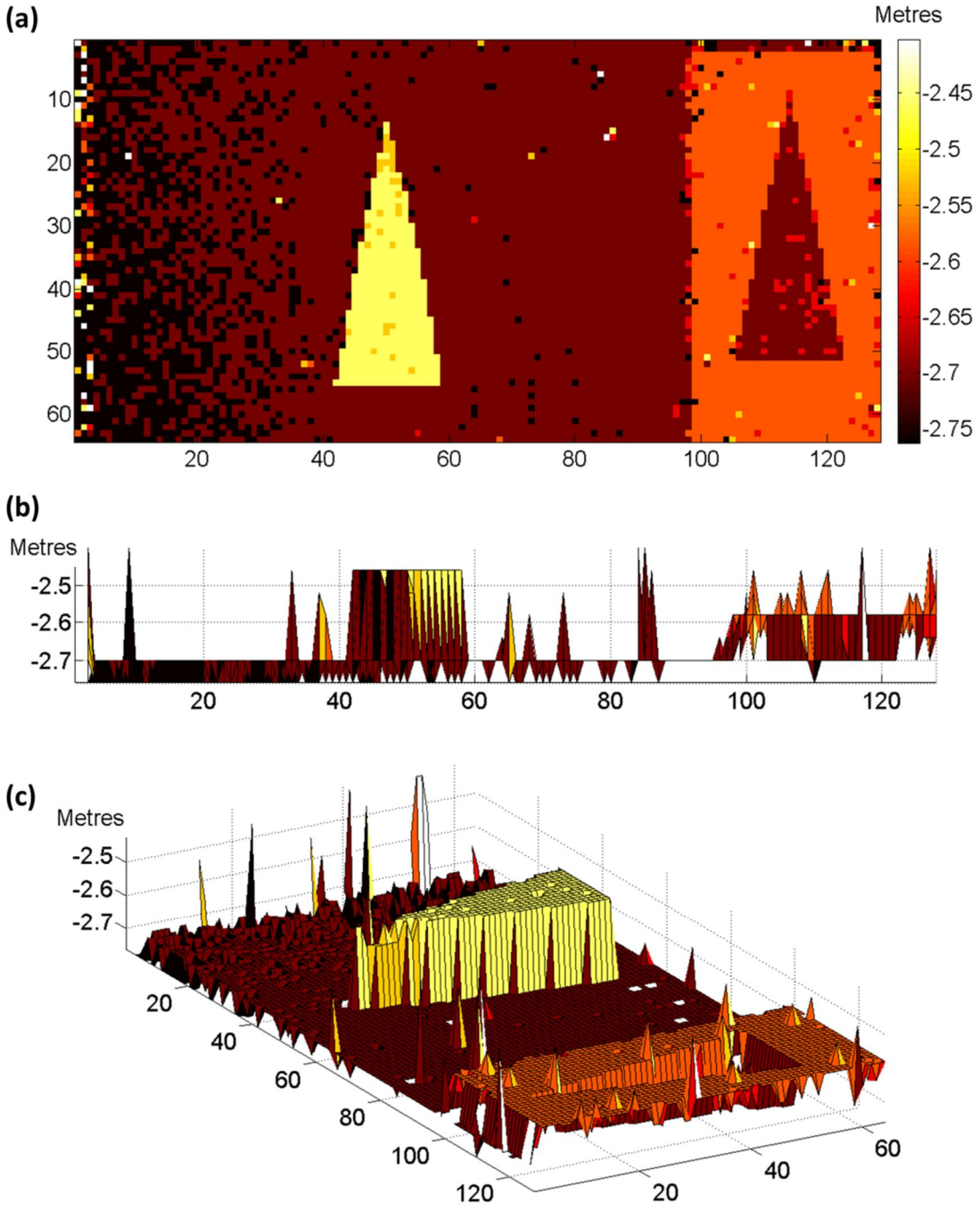

Figure 5-58 Three representations of the 128×64 depth image (estimated using the pixel-wise cross-correlation method) of the target setup at a stand-off distance of 325 m shown in Figure 5-57 constructed by two macro scans and 2×2 micro scans with 269 ms exposure time per entire 32×32 array pixel. This corresponds to the gate-on (410 ns) acquisition time associated with 16384 frames per RAM block and 40 RAM blocks. The depth map with a total exposure time of 2152 ms is shown in (a). Three depth planes can be clearly identified in (b) and (c), which are depth plots in two perspectives.

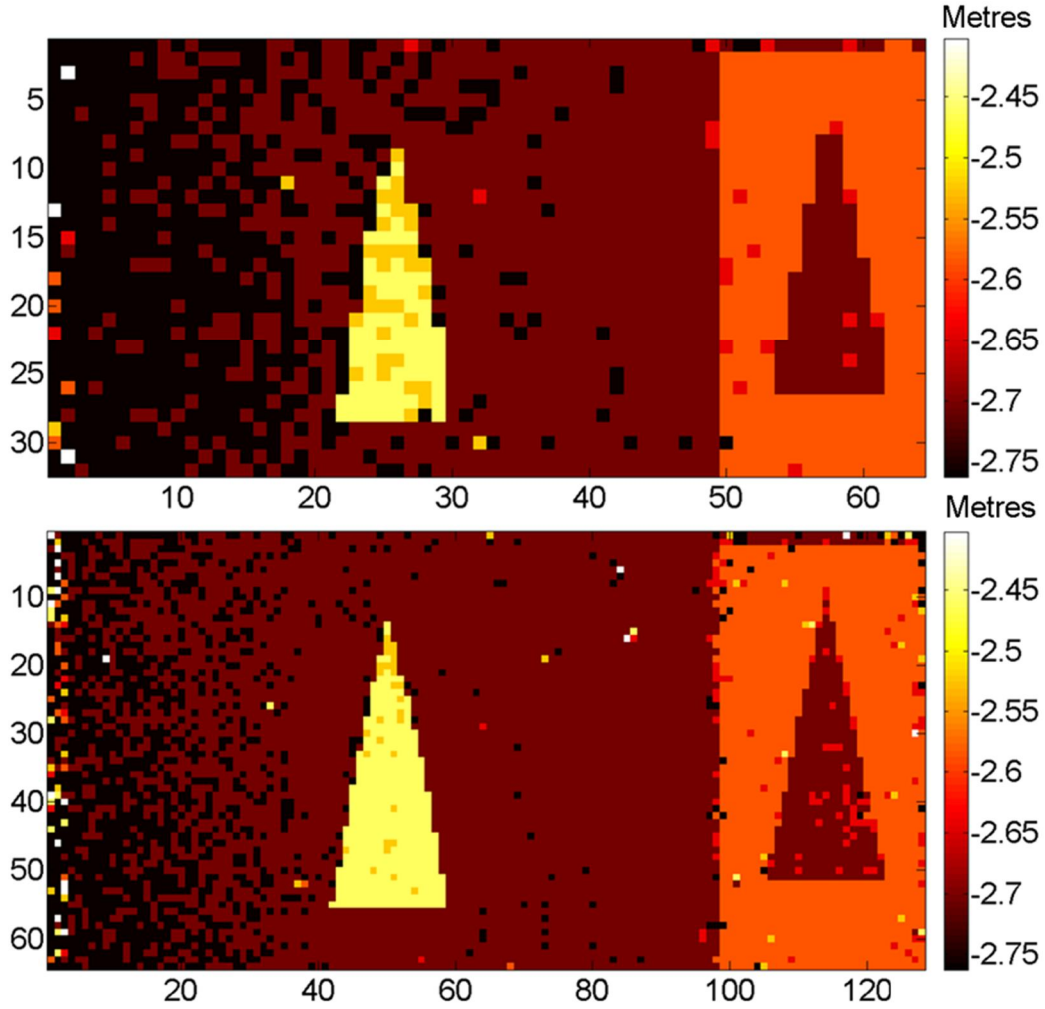

Figure 5-59 Depth maps (estimated using the pixel-wise cross-correlation method) at a stand-off distance of 325 m with 269 ms exposure time per entire 32×32 array. This corresponds to the gate-on (410 ns) acquisition time associated with 16384 frames per RAM block and 40 RAM blocks. Top: A 64×32 pixel depth map of the target setup shown in Figure 5-57 was formed by two macro scans with 32×32 pixel per scan and a total exposure time of 538 ms. Bottom: A 128×64 pixel depth map of the same target setup constructed by two macro scans and 2×2 micro scans with 32×32 pixel per scan and thus a total exposure time of 2152 ms.

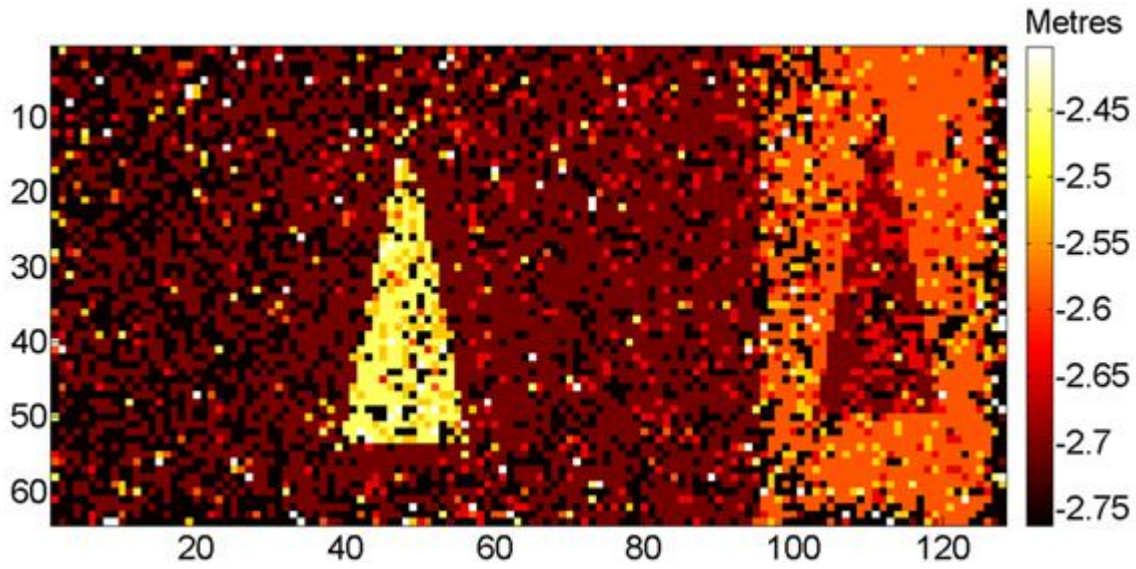

Figure 5-60 Depth map (estimated using the pixel-wise cross-correlation method) at a stand-off distance of 325 m with 128×64 pixels of the target setup shown in Figure 5-57 constructed by two macro scans and 2×2 micro scans using 67 ms exposure time per entire 32×32 array. This corresponds to the gate-on (410 ns) acquisition time associated with 16384 frames per RAM block and 10 RAM blocks. Thus, a total exposure time was 536 ms.

5.8 Conclusions

By virtue of the flip-chip bonding technique with micron-scale lens-to-chip placement error, microlens arrays have been successfully integrated with low fill factor front-illuminated CMOS Si-SPAD arrays giving the largest improvement factors of the fill factor in an array format reported to date. In terms of the SPAD-array-based scanning depth imager using DOE illumination array with eye-safe power level, to the best of my knowledge, SPAD arrays of this pixel number (>1000) have not been galvo-scanned in this manner and evaluated for long-range depth profiling before. Clearly, a number of challenges have to be overcome. For example, there is a major issue in terms of unwanted back-reflections, and refinements in the design of bulk and micro-optics components. It is also useful to evaluate the fill-factor-enhanced SPAD array sensor integrated with microlenses in the detection channel of the imager. This might simplify the illumination channel (e.g. based on flood illumination) in the imager, but induce low-usage of the illumination power.

In section 5.3, the author modelled the optical parameters of the microlenses, using Zemax, and made key contributions to the specification of the required microlens arrays (i.e. finite or infinite configuration, substrate thickness/focal length and the

corresponding sag). The author was solely responsible for the inspection work described in section 5.3.4.

In section 5.4, the author, with assistance from Dr. Aongus McCarthy (AMcC), devised the process for the bonding of the microlens array onto the SPAD array, and carried out the preparation, bonding, and cleaning of the assemblies that were taken forward for characterisation. The photomasks of the microlens arrays were designed by Dr. Andrew J. Waddie (AJW) in Prof. Mohammad R. Taghizadeh group. The microlens arrays were fabricated by Neil Ross (NR).

In section 5.5, the author was solely responsible for all of the post-bonding inspection work reported in sections 5.5.1 and 5.5.2. The majority of the characterisation work of the integrated microlens and SPAD assembly described in section 5.5.3 was carried out by Giuseppe Intermite, AMcC and Dr. Ryan Warburton with minor contributions from the author.

In section 5.6, the author contributed to the specification and redesign of the optical layout of the transceiver so that the DOE-based structured illumination and SPAD detector array could be incorporated (sections 5.6.1 and 5.6.2). Note that the DOE was designed by AJW and fabricated by NR. The design work for the optomechanical modifications to the transceiver system, in order to mount the SPAD array, was done by AMcC. The author, along with AMcC, carried out the assembly, alignment and optimisation of the modified system in preparation for the field trials. The author developed the scan control software described in section 5.6.3. Dr. Federica Villa (FV) provided expertise in the use of the SPAD array camera.

In section 5.7, the field trials were carried out in February 2014 by the author along with AMcC and FV. AMcC and the author constructed the targets. The author configured the system (electrically and optically) for the measurements and acquired the data with FV. The analysis of the data presented here was done by the author. All of the work in this Chapter was supervised by Prof. Gerald S. Buller.

5.9 References

[5.1]. A. Migdall, S. V. Polyakov, J. Fan, and J. C. Bienfang. eds., *Single-Photon Generation and Detection: Physics and Applications* (Elsevier, 2013).

[5.2]. A. Rochas, M. Gosch, A. Serov, P. Besse, R. Popovic, T. Lasser, and R. Rigler, "First fully integrated 2-D array of single-photon detectors in standard CMOS

technology," IEEE Photonics Technol. Lett. (15), 963-965 (2003).

[5.3]. F. Zappa, S. Tisa, A. Gulinatti, A. Gallivanoni, and S. Cova, "Complete single-photon counting and timing module in a microchip," Opt. Lett. (30), 1327-1329 (2005).

[5.4]. L. Pancheri, and D. Stoppa, "Low-noise CMOS single-photon avalanche diodes with 32 ns dead time," *Proceedings of the 37th European Solid-State Device Research Conference*, IEEE, pp. 362-365, (2007).

[5.5]. S. Tisa, F. Guerrieri, and F. Zappa, "Variable-load quenching circuit for single-photon avalanche diodes," Opt. Express (16), 2232-2244 (2008).

[5.6]. C. Niclass, M. Sergio, and E. Charbon, "A single photon avalanche diode array fabricated in 0.35-µm CMOS and based on an event-driven readout for TCSPC experiments," *Proc. SPIE 6372, Advanced Photon Counting Techniques*, pp. 63720S-63720S-63712, (2006).

[5.7]. N. Faramarzpour, M. J. Deen, S. Shirani, and Q. Fang, "Fully integrated single photon avalanche diode detector in standard CMOS 0.18-µm technology," IEEE Trans. Electron Devices (55), 760-767 (2008).

[5.8]. C. Niclass, M. Gersbach, R. Henderson, L. Grant, and E. Charbon, "A single photon avalanche diode implemented in 130-nm CMOS technology," IEEE J. Select. Topics Quantum Electron. (13), 863-869 (2007).

[5.9]. C. Niclass, C. Favi, T. Kluter, M. Gersbach, and E. Charbon, "A 128 128 single-photon image sensor with column-level 10-bit time-to-digital converter array," IEEE J. Solid-State Circuits (43), 2977-2989 (2008).

[5.10]. C. Niclass, M. Soga, H. Matsubara, S. Kato, and M. Kagami, "A 100-m range 10-frame/s 340x96-pixel time-of-flight depth sensor in 0.18µm-CMOS," IEEE J. Solid-State Circuits (48), 559-572 (2013).

[5.11]. C. Veerappan, J. Richardson, R. Walker, D.-U. Li, M. W. Fishburn, Y. Maruyama, D. Stoppa, F. Borghetti, M. Gersbach, and R. K. Henderson, "A 160× 128 single-photon image sensor with on-pixel 55ps 10b time-to-digital converter," *Solid-State Circuits Conference Digest of Technical Papers (ISSCC), 2011 IEEE International*, IEEE, pp. 312-314, (2011).

[5.12]. M. Gersbach, Y. Maruyama, E. Labonne, J. Richardson, R. Walker, L. Grant, R. Henderson, F. Borghetti, D. Stoppa, and E. Charbon, "A parallel 32× 32 time-to-digital converter array fabricated in a 130 nm imaging CMOS technology," *ESSCIRC, 2009.*

ESSCIRC'09. Proceedings of, IEEE, pp. 196-199, (2009).

[5.13]. S. Burri, Y. Maruyama, X. Michalet, F. Regazzoni, C. Bruschini, and E. Charbon, "Architecture and applications of a high resolution gated SPAD image sensor," Opt. Express (22), 17573-17589 (2014).

[5.14]. F. Villa, B. Markovic, S. Bellisai, D. Bronzi, A. Tosi, F. Zappa, S. Tisa, D. Durini, S. Weyers, and U. Paschen, "SPAD smart pixel for time-of-flight and time-correlated single-photon counting measurements," IEEE Photonics J. (4), 795-804 (2012).

[5.15]. F. Villa, R. Lussana, D. Bronzi, S. Tisa, A. Tosi, F. Zappa, A. Dalla Mora, D. Contini, D. Durini, and S. Weyers, "CMOS imager with 1024 SPADs and TDCs for single-photon timing and 3D time-of-flight," IEEE J. Select. Topics Quantum Electron. (2014).

[5.16]. M. Deguchi, T. Maruyama, F. Yamasaki, T. Hamamoto, and A. Izumi, "Microlens design using simulation program for CCD image sensor," IEEE Trans. Consum. Electron. (38), 583-589 (1992).

[5.17]. M. A. Itzler, M. Entwistle, U. Krishnamachari, M. Owens, X. Jiang, K. Slomkowski, and S. Rangwala, "SWIR Geiger-mode APD detectors and cameras for 3D imaging," *SPIE Sensing Technology+ Applications*, International Society for Optics and Photonics, pp. 91140F-91140F-91112, (2014).

[5.18]. W. J. Smith, *Modern optical engineering* (McGraw-Hill, 2000).

[5.19]. P. Nussbaum, R. Voelkel, H. P. Herzig, M. Eisner, and S. Haselbeck, "Design, fabrication and testing of microlens arrays for sensors and microsystems," Pure and Applied Optics: Journal of the European Optical Society Part A (6), 617 (1997).

[5.20]. B. C. Kress, and P. Meyrueis, *Applied digital optics: from micro-optics to nanophotonics* (John Wiley & Sons, 2009).

[5.21]. J. Jahns, and S. J. Walker, "Two-dimensional array of diffractive microlenses fabricated by thin film deposition," Appl. Opt. (29), 931-936 (1990).

[5.22]. J. M. Pavia, M. Wolf, and E. Charbon, "Measurement and modeling of microlenses fabricated on single-photon avalanche diode arrays for fill factor recovery," Opt. Express (22), 4202-4213 (2014).

[5.23]. M. A. Itzler, M. Entwistle, X. Jiang, M. Owens, K. Slomkowski, and S. Rangwala, "Geiger-mode APD single-photon cameras for 3D laser radar imaging,"

Aerospace Conference, 2014 IEEE, IEEE, pp. 1-12, (2014).

[5.24]. Karl Suss, "Suss FC6 Flip-chip Bonder User's Guide " (1998).

[5.25]. Linos Germany, "UV Fiber Light Source LQ UV 1000, with and without Brightness Control. Datasheet. online

(https://www.qioptiq-shop.com/out/pictures/wysiwigpro/12-13%20englisch/21%20Light%20Sources%20and%20Laser.pdf) last accessed 03-09-2015."

[5.26]. Norland Products, "Norland Optical Adhesive 81 Datasheet, online, last accessed 2015-01-30."

[5.27]. S. Donati, G. Martini, and M. Norgia, "Microconcentrators to recover fill-factor in image photodetectors with pixel on-board processing circuits," Opt. Express (15), 18066-18075 (2007).

[5.28]. F. Villa, D. Bronzi, Y. Zou, C. Scarcella, G. Boso, S. Tisa, A. Tosi, F. Zappa, D. Durini, and S. Weyers, "CMOS SPADs with up to 500 μm diameter and 55% detection efficiency at 420 nm," J. Mod. Opt. (61), 102-115 (2014).

[5.29]. P. Blair, H. Lüpken, M. R. Taghizadeh, and F. Wyrowski, "Multilevel phase-only array generators with a trapezoidal phase topology," Appl. Opt. (36), 4713-4721 (1997).

[5.30]. A. Vasara, M. R. Taghizadeh, J. Turunen, J. Westerholm, E. Noponen, H. Ichikawa, J. M. Miller, T. Jaakkola, and S. Kuisma, "Binary surface-relief gratings for array illumination in digital optics," Appl. Opt. (31), 3320-3336 (1992).

[5.31]. M. Taghizadeh, P. Blair, B. Layet, I. Barton, A. Waddie, and N. Ross, "Design and fabrication of diffractive optical elements," Microelectron. Eng. (34), 219-242 (1997).

[5.32]. R. L. Morrison, "Symmetries that simplify the design of spot array phase gratings," J. Opt. Soc. Am. A (9), 464-471 (1992).

[5.33]. D. T. Neilson, S. M. Prince, D. A. Baillie, and F. A. Tooley, "Optical design of a 1024-channel free-space sorting demonstrator," Appl. Opt. (36), 9243-9252 (1997).

[5.34]. R. M. Marino, and J. W. R. Davis, "Jigsaw: A Foliage-Penetrating 3D Imaging Laser Radar System," Lincoln Lab. J. (15), 23-26 (2005).

[5.35]. J. J. Degnan, and D. N. Wells, "Scanner/optical system for three-dimensional lidar imaging and polarimetry," (U.S. Patent 8493445 B2, Jul 23, 2013).

[5.36]. J. J. Degnan, and C. T. Field, "Moderate to high altitude, single photon sensitive, 3D imaging lidars," *SPIE Sensing Technology+ Applications*, International Society for Optics and Photonics, pp. 91140H-91140H-91111, (2014).

[5.37]. F. A. Villa, "Time-of-flight camera for long-distance 3D ranging," PhD Thesis, Politecnico di Milano (2013).

Chapter 6
Multispectral time-of-flight depth profiling using single-photon detection

6.1 Introduction

Over the last two decades, an increase in interest has led to major developments in the field of remote sensing for geosciences applications, e.g. vegetation health monitoring, biomass determination, and investigation of greenhouse gases. Existing optical detection systems for geosciences applications include passive hyperspectral sensors and active monochromatic Light Detection and Ranging (LiDAR) systems. The former systems can only report 2D intensity data with spectral indices relying on the reflected radiation from an external illumination source (e.g. solar radiation) and is dependent on viewing geometry. However, they can resolve almost no depth (or time) resolution directly. Even though some niche examples, such as face reconstruction [6.1], can implement 3D estimation from 2D images, they rely on short ranging distances and carefully pre-defined illumination conditions. In contrast, LiDAR systems are well-established tools for providing vertical canopy structure with moderate depth resolution but lack of sufficient spectral information. The combination of passive hyperspectral data and active LiDAR data can be useful but has limited practicality as it fails to provide full information for biochemical parameters. In practical terms, there remain challenges in accurately synchronising and registering two data sets in space and time. In addition, the measurement of the biochemical (or physiological) parameters of plants reliably is strongly dependent on well-resolved canopy and stand structure [6.2]. In order to retrieve effective biochemical parameters it is necessary to measure reflectance information at multiple wavelengths as a function of canopy height. Therefore, there is clear motivation to construct a full-waveform multispectral LiDAR to determine the structural and physiological variation for the full canopy depth profile directly.

LiDAR systems capable of multispectral detection have been developed and

demonstrated for canopy detection. The Slope Imaging Multi-polarisation Photon Counting LiDAR (SIMPL) [6.3] built by NASA is an active airborne photon counting detection system operating at λ=532 nm and 1064 nm that measures within two orthogonal polarisation channels. Following an earlier attempt by combining a monochromatic LiDAR with passive hyper-spectral imaging [6.4], an eight-wavelength simultaneous detection system was developed by Hakala *et al.* [6.5]. A broadband pulsed supercontinuum laser source and a time-of-flight sensor based on an avalanche photodiode (APD) array operating in linear mode (i.e. "analogue" detection mode) were integrated into the system. They reported laboratory measurements on a Sitka Spruce, deriving simple vegetation indices. Also, a four-wavelength LiDAR system using four separate laser sources was built and applied to a segmentation problem using nine material classes by Wei *et al.* [6.6]. While the conventional canopy LiDAR systems used the analogue signal recording techniques, full-waveform multispectral LiDAR systems based on the Time-Correlated Single Photon Counting (TCSPC) technique feature high-usage of output laser power, shot-noise detection and excellent depth resolution.

The majority of previous work on time-of-flight (TOF) depth profiling at Heriot-Watt University has concentrated on developing monochromatic TCSPC-based LiDAR systems using discrete single photon detectors. Initially, these included imagers using silicon single photon avalanche photodiodes (SPADs) at λ ~ 850 nm [6.7]. This system was adapted for longer wavelengths (operating at λ=1560 nm) by utilising a superconducting nanowire single photon detector (SNSPD) [6.8] (see Chapter 4) and an InGaAs/InP SPAD detector module at λ=1550 nm [6.9] (see Chapter 4). Further adaptation included use of a Si-SPAD 32×32 detector array at an operational wavelength of 817 nm (see Chapter 5). Extending this to multi-spectral sensing, the group developed a non-scanning TCSPC-based full-waveform multispectral LiDAR system 2005 [6.10] using six discrete laser sources. This system was used to demonstrate the capability of depth resolving for closely spaced surfaces in a single point of the scene for different wavelengths and not capable of imaging scenes. In contrast, TCSPC-based multispectral depth imaging will be the subject of this Chapter.

In September 2011, the Single Photon group at Heriot-Watt University received funding from the Centre for Earth Observation Instrumentation (CEOI), UK for a six month proof-of-concept project. The goal was to develop a system that was capable of quantifying spectral variability and recovering physiological parameters of trees (typical

low signature distributed targets in nature) along with their depth profiles. Under the project, the author along with Aongus McCarthy, Gerald S. Buller and Andrew M. Wallace developed a new full-waveform multispectral LiDAR system using a broadband pulsed supercontinuum laser source. A first generation system was constructed and data was successfully acquired from a Nordmann fir tree at a stand-off distance of 45 metres. This system was then characterised more fully in the lab and work was carried out on refining the layout and design in order to improve the system performance. This Chapter describes this work, detailing the results of the LiDAR measurements carried out at Heriot-Watt University with the first generation system and compares them to the ground truth lab measurements on the tree in the lab in Dr. Caroline J. Nichol's group at the University of Edinburgh.

6.2 Physiological parameters of vegetation

The photons that power photosynthesis in arboreal samples (e.g. plants) are absorbed by chlorophyll pigments. The amount of chlorophyll is related to the plants photosynthetic capacity, productivity (or light-use efficiency) and stress level [6.11-6.12]. Chlorophyll a and b are two crucial pigments of terrestrial plants; their characteristics reflect the physiological status of the plants. For example, a reduced total concentration of leaf chlorophyll a and b indicates a plant under stress [6.12-6.13]. Their strong reflectance peak is in the green waveband whereas their strong absorbance peaks are in the blue and red wavebands [6.12, 6.14]. This is derived from the spectrum-dependent chlorophyll levels of the vegetation, in particular for the ones at the spectral "red edge", that is between red and near-infrared wavelengths [6.12, 6.15]. For example, the chlorophyll reflectance of the vegetation changes sharply on the spectral edge from the red wavelengths (e.g. λ=670 nm) to the near-infrared lengths (e.g. λ=780 nm) [6.12]. This suggests that combinations of the chlorophyll reflectance of the vegetation at specific wavelengths can be used to construct effective vegetation indices to evaluate the critical vegetation characteristics [6.12]. There are two typical vegetation indices: (1) normalised differential vegetation index (NDVI) which is related to canopy biomass and light absorption [6.16]; (2) photochemical reflectance index (PRI) which is a measure of vegetation light use efficiency [6.17].

According to the reflectance spectra of photosynthetic green vegetation and two non-photosynthetic materials, dry vegetation and soil, as shown in Figure 6-1, the "red edge" of vegetation reflectance is able to survive the superimposition of photosynthetic

vegetation (PV) and non-photosynthetic vegetation (NPV) signatures [6.18]. The NDVI is formed from the normalised reflectance values either side of the "red edge". Therefore, live greens and other canopy material can be discriminated by using the NDVI value which is defined as:

$$NDVI = \frac{R_{NIR} - R_{RED}}{R_{NIR} + R_{RED}} \qquad \text{Equation (6.1)}$$

where R_{NIR} is the reflectance within the near-infrared wavelength range and R_{RED} is the reflectance within the visible wavelength range. Note that the two wavelengths of interest for NDVI estimations in the measurements described in this Chapter are 670 nm and ~780 nm.

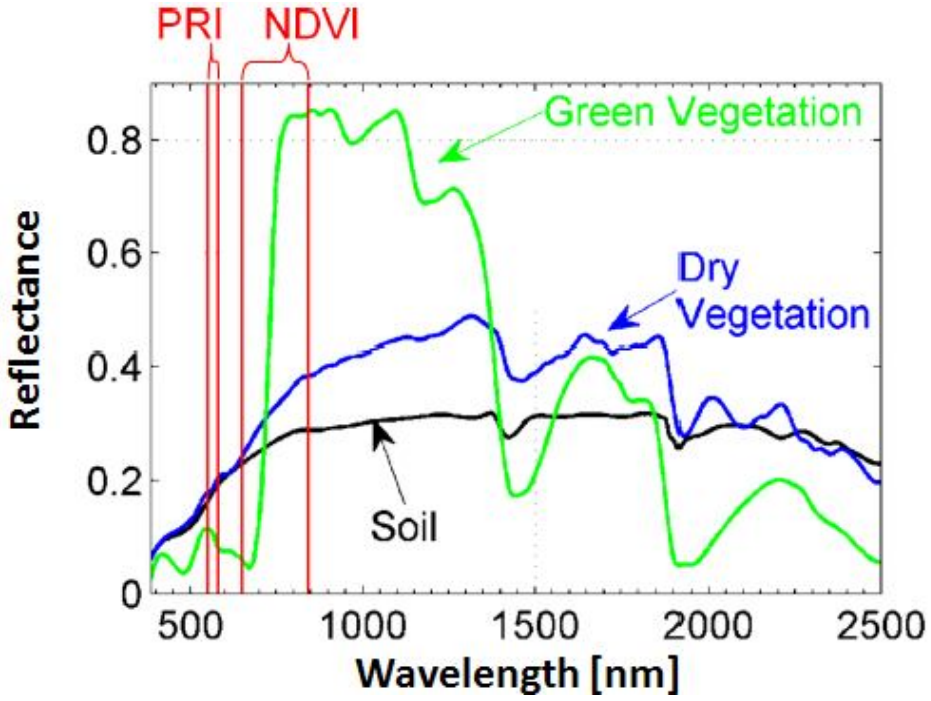

Figure 6-1 Reflectance spectra of photosynthetic green vegetation, dry vegetation and soil (non-photosynthetic material) [6.17].

In addition, the PRI can be obtained by examining the reflectance peak at a wavelength of 531 nm in green wavebands, and comparing that with a nearby reference wavelength (e.g. λ=570 nm is considered in this Chapter) and is defined as:

$$PRI = \frac{R_{\lambda=570nm} - R_{\lambda=531nm}}{R_{\lambda=570nm} + R_{\lambda=531nm}} \qquad \text{Equation (6.2)}$$

where $R_{\lambda=531nm}$ and $R_{\lambda=570nm}$ are the reflectance at λ=531 nm and 570 nm respectively.

6.3 TCSPC-based multispectral canopy LiDAR system

6.3.1 Overview of the system

A schematic of the TCSPC-based multispectral canopy LiDAR system is shown in Figure 6-2. In addition, a photograph of the experimental setup can be seen in Figure 6-3. The key parameters of the system are summarised in Table 6-1. As shown in Figure 6-2, the system was based on three optical modules: (1) multiple wavelength pulsed input module; (2) scanning transceiver unit; and (3) wavelength routing module.

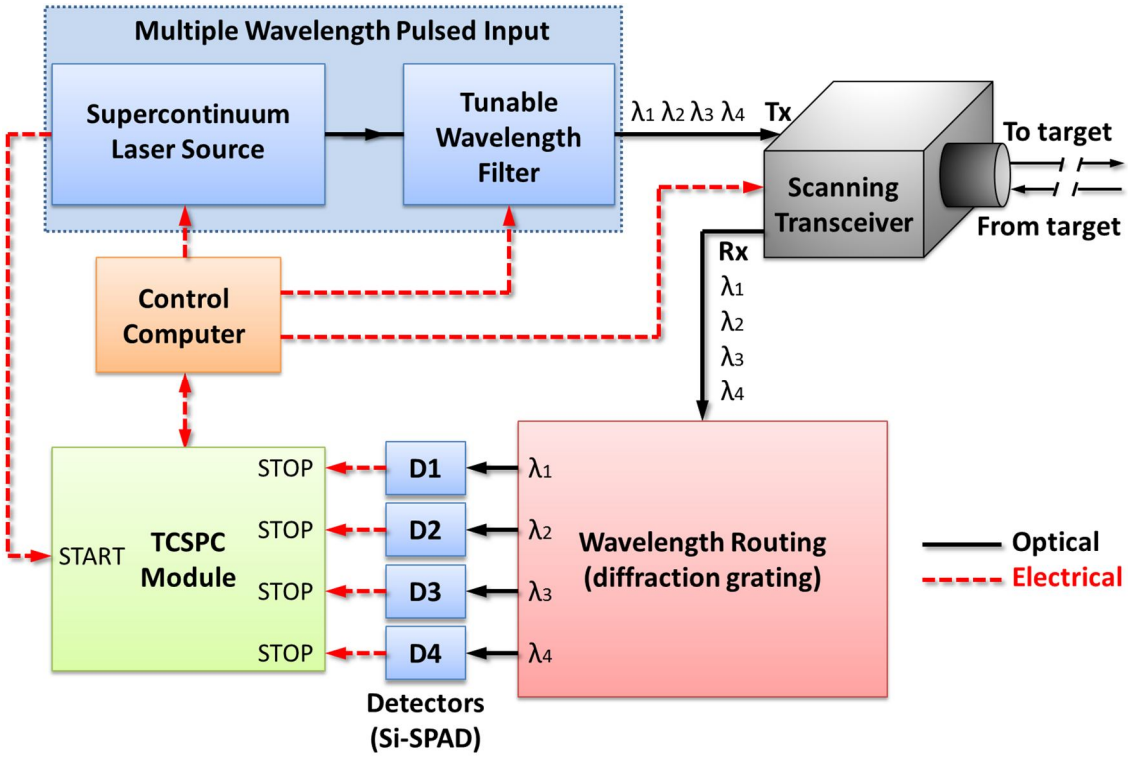

Figure 6-2 Schematic of the TCSPC-based multispectral canopy LiDAR system. The system was based on three optical modules: (1) multiple wavelength pulsed input; (2) scanning transceiver unit; and (3) wavelength routing. The wavelengths for the four different channels are 531 nm, 570, 670 and ~780 nm.

(1) Multiple wavelength pulsed input module. This was based on a pulsed tunable supercontinuum laser source. The laser source (SuperK EXTREME EXW-6, NKT Photonics, Denmark) emits over the wavelength range of 485-2400 nm, and an integrated pulse picker module enables the selection of a preset pulse repetition rate of between approximately 320 kHz and 80 MHz. A tunable wavelength filter (a SuperK SELECT from NKT Photonics, Denmark) was used in conjunction with the supercontinuum source in order to isolate the appropriate wavelengths. This acousto-optic tunable filter (AOTF) configuration was capable of selecting simultaneously up to

eight different wavelengths between 500 and 850 nm. The spectral bandwidth of each of the four wavelengths (531 nm, 570, 670 and ~780 nm) used for this work was measured and found to be less than 8 nm full-width at half-maximum (FWHM), and the system emitted all wavelengths simultaneously. The output of the AOTF was fibre coupled to the transmit channel of our custom-built scanning transceiver [6.19].

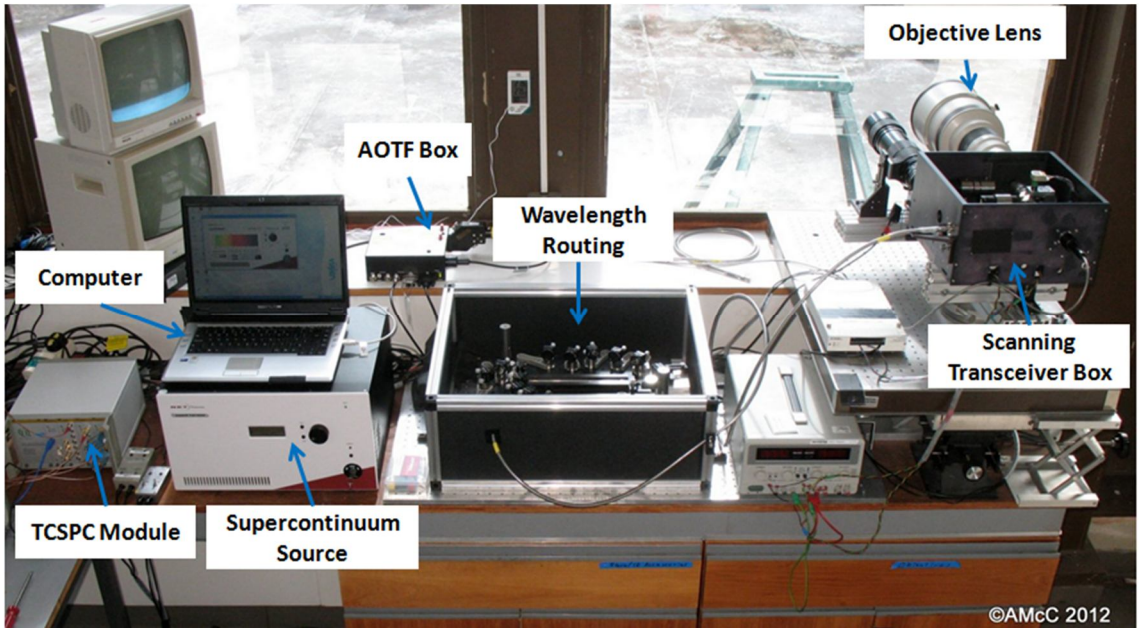

Figure 6-3 Photograph of the experimental setup of the TCSPC-based multispectral canopy LiDAR system. AOTF: acousto-optic tunable filter.

(2) Scanning transceiver unit. The bespoke scanning transceiver unit [6.7] (see Figure 3-2 in Chapter 3 for the system schematic) was reconfigured for use in the wavelength region from 500 -800 nm for the work described in this Chapter. Its optical layout is shown in Figure 6-4. Relay lenses (AC254-030-A-ML and AC254-035-A-ML from Thorlabs, USA) with anti-reflection (AR) coatings for the wavelength range from 400 to 700 nm were used in the transceiver, as well as the polarising beam splitter designed for this spectral region. Note that the refection of the AR coating of the relay lens was 0.22% at λ=531 nm, 0.37% at λ=570 nm, 0.26% at λ=670 nm and 3.72% at λ=780 nm. Therefore, the lenses offer reasonably good transmission for these four wavelengths whereas the slightly higher reflection at λ=780 nm caused increased internal back-reflection, as shown in section 6.3.3. This was required in order to reduce the internal back reflections and achieve a high-quality beam spot for the four coaxial light beams associated with the four selected wavelengths. For each staring point on the scene, the scattered return photons that were collected by the system objective lens were steered by a pair of galvanometer scan mirrors and coupled into a 9 μm diameter core optical

fibre connected to the receive channel of the transceiver. This fibre, used to link the receive channel to the wavelength routing module, had an armoured tubing so as to minimise ambient light ingress into the fibre core along its length and at the connectors – this was a key factor that enabled measurements to be made under bright daylight conditions.

System Parameter	Comment				
Transmit/Receive Alignment	Monostatic: Coaxial transmit and receive channels of all four wavelengths are coaxial				
Laser System	• Pulsed supercontinuum laser source and acousto-optic tunable filter (SuperK EXTREME, EXW6, NKT Photonics, Denmark) • Fibre-coupled to the transceiver unit. Note that the coupling fibre has 9 μm diameter core (FD2, SuperK Fibre Delivery series, NKT Photonics, Denmark)				
Laser Repetition Rate	2 MHz				
Illumination Wavelength	531 nm	570nm	670 nm	780 nm	
Spectral FWHM	~4.1 nm	~4.1 nm	~6.0 nm	~7.4 nm	
	The pulses for all four wavelength are emitted simultaneously				
Laser Pulse Width	<50 ps				
Objective Lens	Canon EF 400 mm f/2.8 IS USM				
Average Output Power	<200 μW total exiting the system				
Output energy per pulse	<100 pJ				
Beam Scanning Mechanism	Galvanometer controlled mirrors (X&Y) common to transmit and receive channels				
Collection Fibre	9 μm diameter core (SMF28), 2 metres long, armoured				
Spectral De-multiplexing	Plane ruled reflection grating from Newport, 1200 grooves per mm, blaze angle:26.7 °, blaze wavelength: 750 nm				
Detectors	Four similar free running, Si-SPAD single photon counting modules (Perkin Elmer), active area diameter 180 μm, thick junction, fibre coupled, dark count rate <500 cps				
	λ (nm)	531	570	670	780
	QE (%)	~50	~58	~62	~58
System Temporal Response (jitter)	λ (nm)	531	570	670	780
	FWHM (ps)	520	496	496	368
System Spatial Resolution (X-Y)	~50 μrad at a stand-off distance of 45 metres, corresponding to a beam spot with the diameter of approximately <3 mm on the target at this distance				
Data Acquisition Module	HydraHarp 400 (PicoQuant, GmbH, Germany)				
Timing Bin	16 ps				

Table 6-1 Summary of key system parameters [6.19]

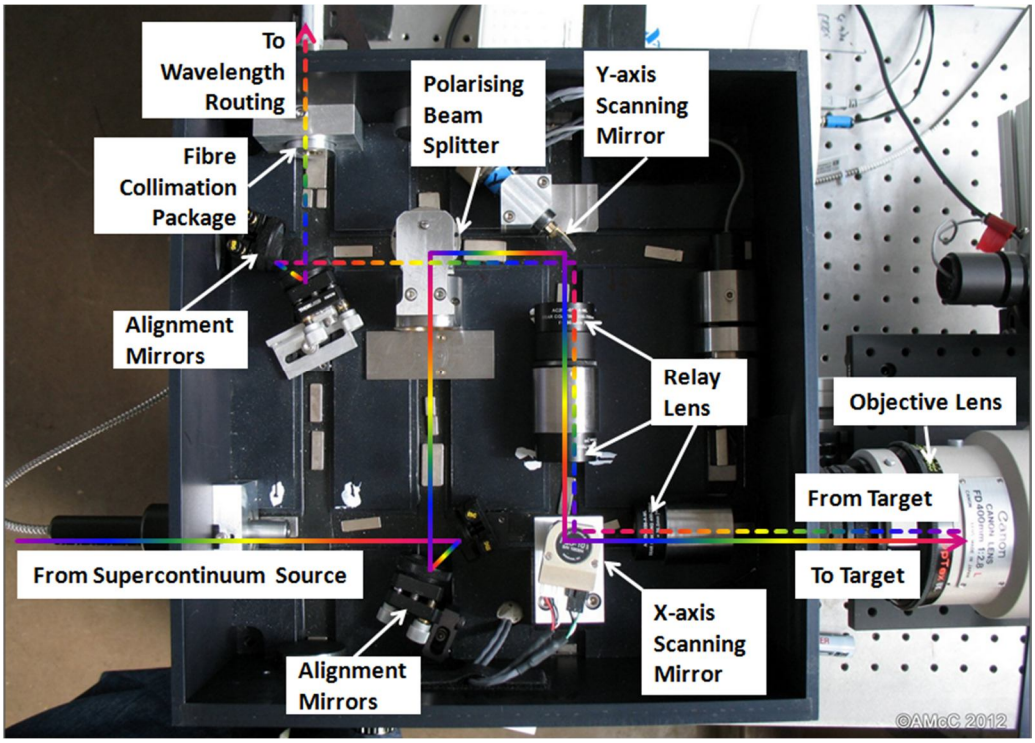

Figure 6-4 Photograph of the scanning transceiver unit employed in the TCSPC-based multispectral canopy LiDAR system shown in Figure 6-3.

(3) Wavelength routing module. The schematic of the wavelength routing module based on a diffraction grating is shown in Figure 6-5 which was similar in layout to the design of a previous multispectral LiDAR [6.10]. The optical fibre from the receive channel of the transceiver unit was connected to the wavelength routing module at **(A)** shown in Figure 6-6. The design of the optical system and associated optomechanics of this module shown in Figure 6-6, allowed flexibility with the choice of wavelengths that could be accommodated and the ease of reconfiguration. Therefore, a grating was used as opposed to an arrangement of spectral filters specific to each wavelength channel. The optomechanics used in the wavelength routing module comprised a mix of custom and off-the-shelf components. The grating spatially separated the multi-wavelength optical return, allowing each wavelength channel to be coupled to its individual detector (D1 to D4 as shown in Figure 6-2) via a short length optical fibre. To achieve the TCSPC measurements, four detectors generated stop triggers for a TCSPC module (i.e. HydraHarp 400 by PicoQuant GmbH) while the start trigger was the synchronisation signal with a Nuclear Instrumentation Module (NIM) pulse train provided by the supercontinuum source.

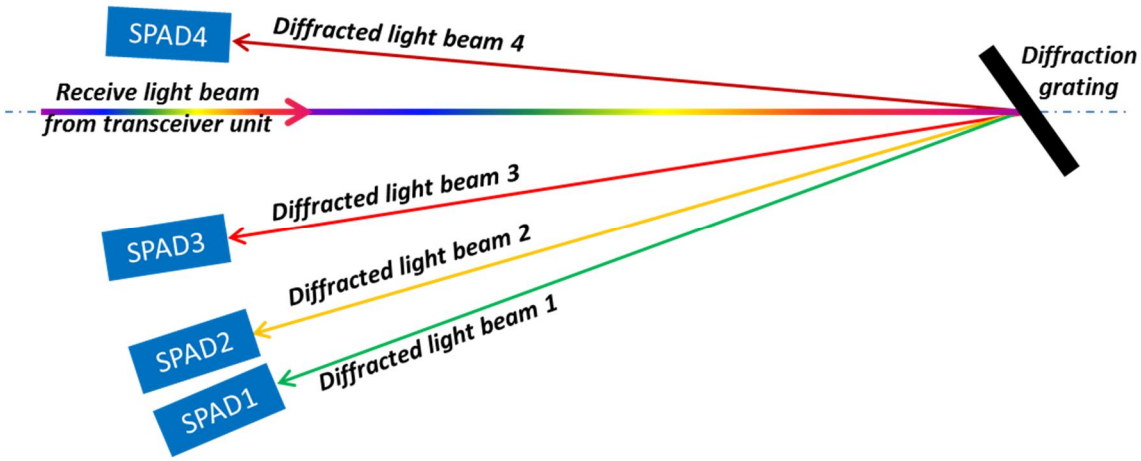

Figure 6-5 Schematic of a wavelength routing module based on a diffraction grating for four single photon detection channels.

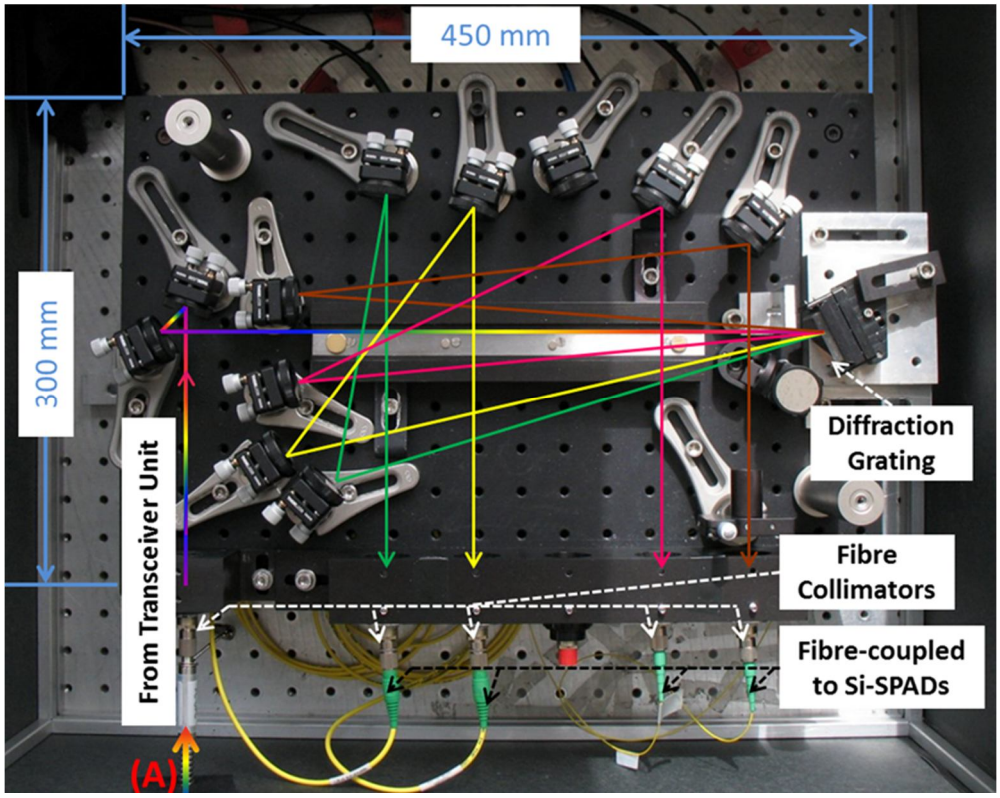

Figure 6-6 Experimental setup photograph of the first generation wavelength routing module used for the measurements reported in section 6.3.3. The receive beam is separated into multiple wavelengths by a diffraction grating. The steering diffracted beam paths associated with four different wavelengths are shown before they are coupled into four different Si-SPAD detectors (green line for the 531 nm channel, yellow line for the 570 nm channel, red line for the 670 nm channel and dark red line for the 780 nm channel).

It should be noted that the configuration of the transceiver for operation at a single wavelength, as in previous depth imaging field trials (see Chapter 4), included

appropriate spectral filters in the receive channel in order to achieve the necessary filtering of the optical return signal. Ambient and solar background photons are a source of noise in a single-photon counting system as they cause "false" detection events at the detector. In previous configurations of this sensor, a narrow band-pass filter (matched to the laser wavelength) was typically used in conjunction with a short-pass and/or long-pass filter to minimise out-of-band radiation being incident on the detector. The filter combination was located immediately in front of the collection lens used to couple the return signal into the fibre connected to the detector. In this multiple-wavelength configuration, no spectral filters were used on the receive channel in the transceiver unit. The degree of spectral filtering achieved with the 1200 lines per millimetre plane ruled reflection grating in this Chapter, and the resulting spatial separation between the wavelength channels due to the layout of the module, meant that the out-of-band optical returns were sufficiently discriminated and not coupled to the detectors [6.19].

6.3.2 Wavelength routing system design

6.3.2.1 Diffraction gratings

According to the Huygens–Fresnel principle, each groove of a diffraction grating can be described as a narrow-slit-shaped source of diffracted light (or wavelet) with an individual wavefront. As an illustration of grating diffraction in Figure 6-7(a), given a beam with an incident angle (α), the geometrical path difference is equal to $d\sin\alpha + d\sin\beta$ between the diffracted light from adjacent grooves along a same unique diffraction angle (β). Only when this difference is equal to $m\lambda$ ($m \neq 0$) will the wavelets related to the diffracted light interfere constructively as their wavefronts are in phase. This leads to the grating equation given as (refer to Page 22 of [6.20]) in Equation (6.3) and it suggests that β is dependent on λ when α is constant.

$$m\lambda = dsin\,\alpha + dsin\,\beta_m \ \ (m = \pm1, \pm2\ ...) \qquad \text{Equation (6.3)}$$

The diffraction grating used in the wavelength routing described in this Chapter is based on the surface structure of a blazed grating. This type of grating is designed to maximise power efficiency in a specific diffraction order by minimising power lost in other orders (particularly the 0^{th} order). There is a rule of thumb that using a reflection grating under the blaze condition can optimise its efficiency (refer to Pages 23-24 of

[6.20]):

$$m\lambda = 2d\ sin\,\theta_B \qquad \text{Equation (6.4)}$$

where θ_B is the blaze angle which is between the face of the groove and the plane of the grating (see Figure 6-7(b)). In addition, it is equal to the angle between the grating normal (GN) and the facet normal (FN) shown in Figure 6-7(b). Note that the blaze arrow indicates the direction from GN to FN. Once the blaze condition is satisfied and by following the law of reflection when viewed from the facet, the relationship of the incident and diffracted rays can be expressed as:

$$\beta - \theta_B = \alpha - \theta_B \qquad \text{Equation (6.5)}$$

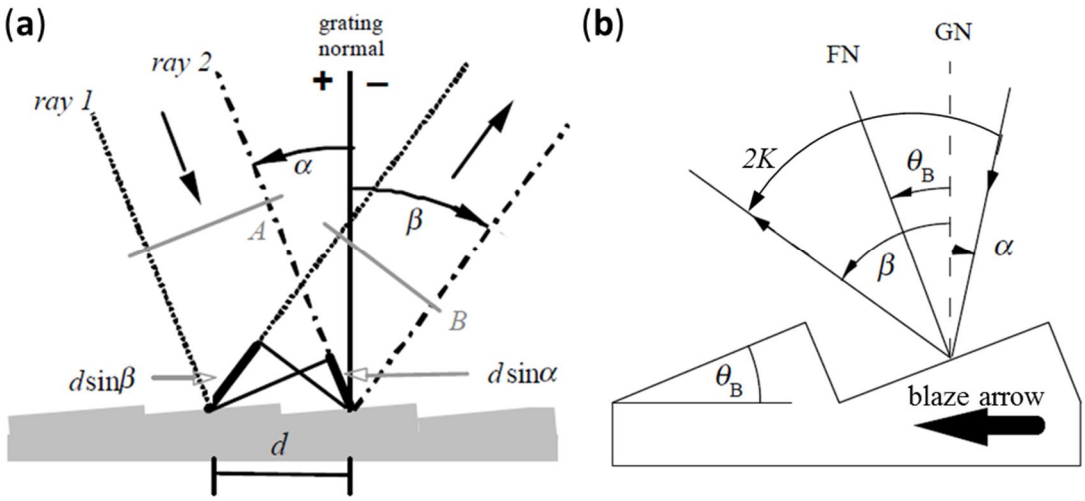

Figure 6-7 Diffraction on plane gratings. (a) Geometry of diffraction, for planar wavefronts. Two parallel rays (i.e. ray1 and ray2) are incident on the grating one groove spacing of d apart. They are in phase with each other measured at wavefront A within a phase plane whose normal is parallel to ray1 and ray2. Upon diffraction and being derived by the principle of constructive interference, these rays are in phase at diffracted wavefront B if a geometrical path difference of $dsin\,\alpha + dsin\,\beta$ is an integral number of wavelengths, in turn leading to the grating equation. (b) Blaze condition. The blaze angle θ_B is the angle between the face of the groove and the plane of the grating and also equals to the angle between the grating normal (GN) and the facet normal (FN). The blaze arrow (shown in the figure) indicates the direction from GN to FN. (Reproduced from Pages 21-22 of [6.20]).

Generally, when *2K* that is the angle between the incident and diffracted rays which bisected by the facet normal is equal to 0, it can lead to the highest efficiency, i.e. it corresponds to:

$$2K = \alpha - \beta = 0 \qquad \text{Equation (6.6)}$$

This results in the Littrow blaze condition by following Equation (6.4) to (6.6) (refer to Page 39 of [6.20]). Hence, the designed blaze angle θ_B along with the blaze wavelength λ_B derived by Equation (6.4) and the groove spacing d are three main characteristics of the blazed grating. In practice, it is preferable that the incident of the light beam is as close as possible to the diffracted angle of the beam at λ_B. This can be used to determine the blaze grating operating in the condition with high efficiency (i.e. as $|2K| \approx 0$). On the contrary, larger values of $|2K|$ cause lower efficiency. The grating efficiency also depends on the polarisation of the incident light optical quality of the grating surface and the uniformity of the groove spacing. In addition, the larger the diameter of the beam spot incident on the grating surface the greater the power that can be resolved. As shown in Figure 6-8, spectral efficiency plots of the diffraction grating, which was used in a wavelength routing system described later, is polarisation-dependent due to the expected polarisation effect to the one-dimensional grating groove pattern. The polarised incident light was aligned parallel to the grooves for the wavelength routing system so that it allows increased power efficiency at each of the four wavelengths.

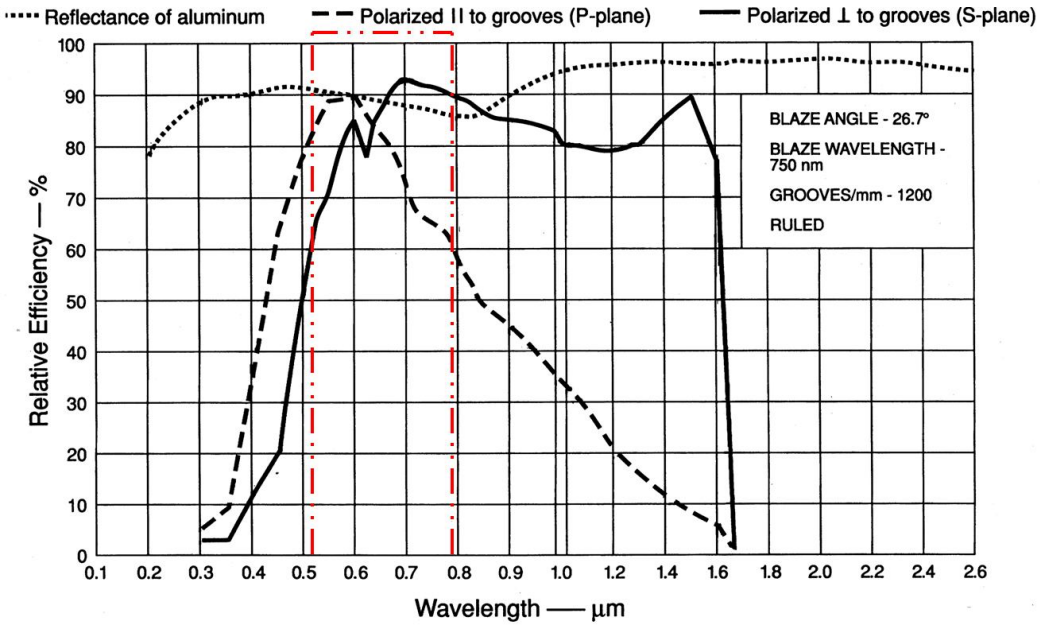

Figure 6-8 Optical property of the employed diffraction grating (1200 grooves/mm plane ruled reflection grating with a nominal blaze angle of 26.7° and a nominal blaze wavelength (1st order Littrow) of 750 nm from Newport, refer to [6.21]). The red box indicates the wavelength range used in our measurements.

6.3.2.2 Simulations of a diffraction-grating-based wavelength routing system

As part of the design refinement, some simulations were carried out on a diffraction-grating-based wavelength routing system using Zemax OpticStudio 14.2 (by Zemax, USA). The parameters used for the simulations are as shown in Table 6-2.

Wavelength channels	λ_{1c}=531 nm		λ_{2c}=570 nm		λ_{3c}=670 nm		λ_{4c}=783 nm	
Diffraction angle (degree)	10.79		13.53		20.73		29.31	
Spectrum of the input light (nm)	From	To	From	To	From	To	From	To
	528.65	532.78	567.54	571.65	667.40	673.33	779.22	786.61
Diffraction angle (degree)	10.63	10.91	13.36	13.65	20.54	20.98	29.02	29.60
Angle difference (degree)	0.28		0.29		0.44		0.58	
Spectral FWHM (nm)	4.13		4.11		5.93		7.39	

Table 6-2 Spectra of the input light for the wavelength routing, and also diffraction angles in four different central wavelength channels after a ruled reflection grating with 1200 lines per mm and a blaze angle of 26.74 degrees and a blaze wavelength of 750 nm.

They include the spectra of the input light for the wavelength routing, and the diffraction angles for the four different wavelength (λ_c) channels after a plane ruled reflection grating with 1200 lines per mm. In addition, the blaze angle of 26.74 degrees corresponds to a blaze wavelength of 750 nm. The optical layout of the wavelength routing in Zemax is shown in Figure 6-9. A collimation lens is used in the input channel to form a collimated optical beam on the diffraction grating. The distance between the collimation lens and the diffraction grating is defined as L_L. The incident beam is spatially separated into different beam channels (i.e. light beams at λ_{1c}=531, λ_{2c}=570, λ_{3c}=670 and λ_{4c}=783 nm channels). A collection lens is used at each wavelength channel to collect light from the diffracted beam into each of the four wavelength channels. Thus, for each wavelength, a diffracted beam is focussed and then coupled into a delivery optical fibre, which is connected to the SPAD assigned to that wavelength channel. As seen in Figure 6-9, only the fibre coupled to the SPAD is shown in the λ_{1c}=531 nm channel for clarity. The distance between the diffraction grating and the collection lens is defined as L_D. This corresponds to the length of the diffracted beam path. The extent (D_{Fan}) of the spread of the beam in the Y-Z plane just in front of each collection lens is measured (see Figure 6-10 for the beam in the

λ_{4c}=783 nm channel). In addition, the extent (D_{Focus}) of the focusing of the beam spot is assessed between the root mean square (RMS) centroids of the upper-edge and lower-edge focusing beams as shown in Figure 6-11. The relation between D_{Fan} and L_D can be seen in Figure 6-12. It can be found that longer L_D corresponds to larger D_{Fan}. This means that a larger clear aperture for the collection lens is required to obtain higher light coupling efficiency.

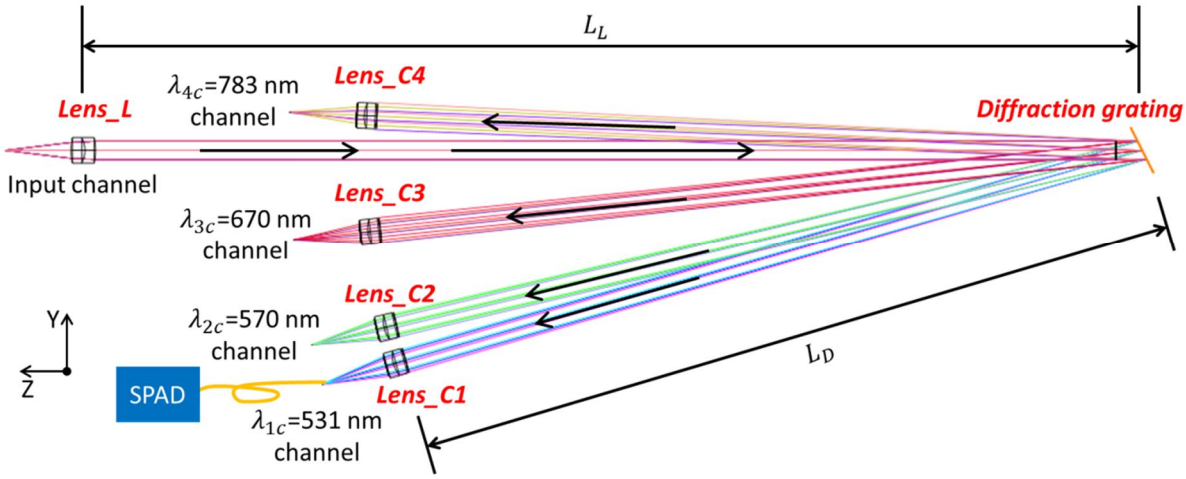

Figure 6-9 The optical layout of a wavelength routing system modelled in Zemax. Lens_L: Collimation lens in the input channel; Lens_C1, Lens_C2, Lens_C3 and Lens_C4: Four collection lenses for four different wavelength channels respectively. L_L is the distance between the collimation lens and the diffraction grating, and L_D is the distance between the diffraction grating and the collection lens.

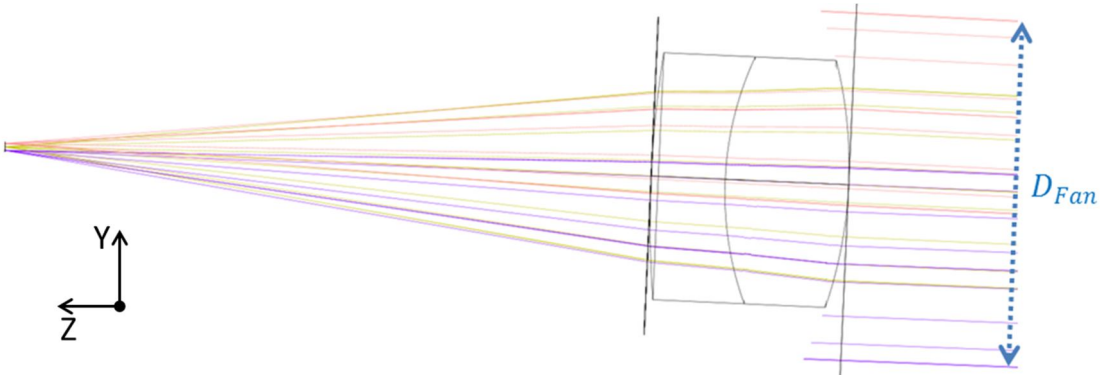

Figure 6-10 Example Y-Z mapping light ray traces through (from right to left) an achromatic collection lens in the λ_{4c}=783 nm diffraction channel. The extent (D_{Fan}) of the λ_{4c}=783 nm channel beam in the Y-Z plane just in front of the collection lens is indicated.

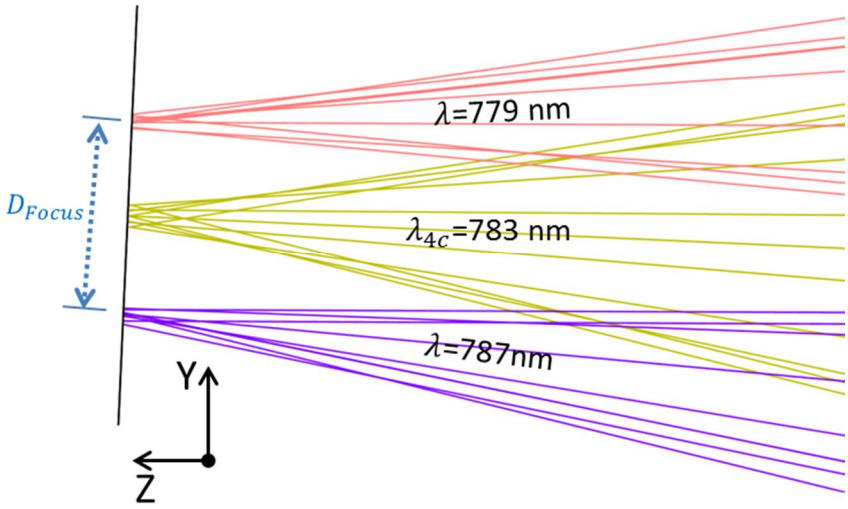

Figure 6-11 Example Y-Z mapping light ray traces around the focal image plane at the λ_{4c}=783 nm channel with the upper-edge beam at λ=779 nm and the lower-edge beam at λ=787 nm. The extent (D_{Focus}) of the focusing of the beam spot is assessed between the root mean square (RMS) centroids of the upper-edge and lower-edge focusing beams.

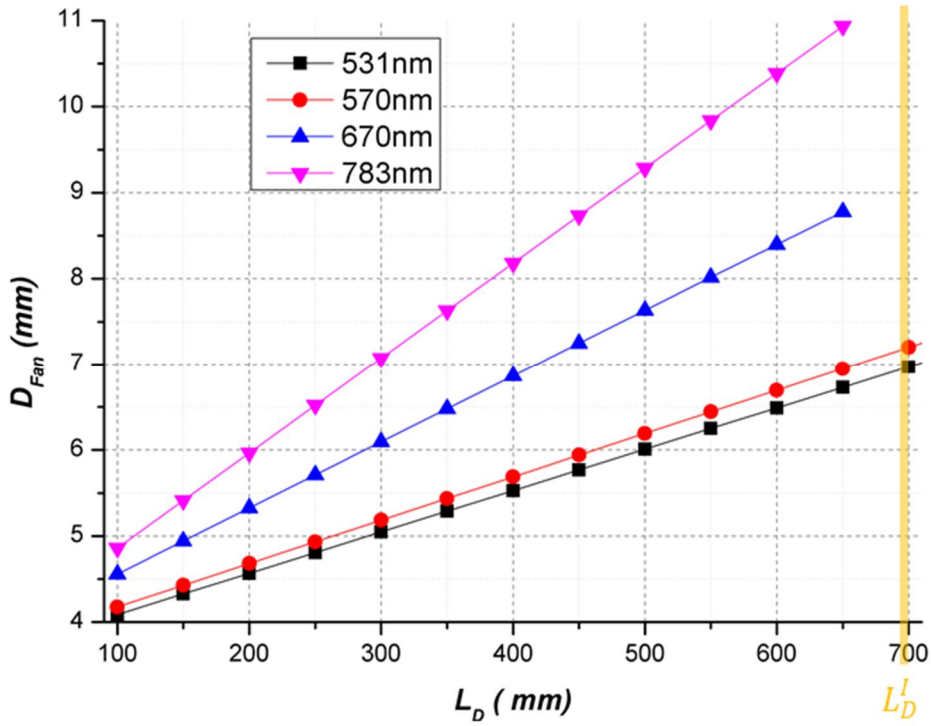

Figure 6-12 Plots of the extent (D_{Fan}) of the diffracted beam in Y-Z plane just in front of the collection lens versus the distance from the diffraction grating to the collection lens (L_D) for four different wavelength channels. The first generation wavelength routing system had an average diffracted beam path length of 700 mm (i.e. L_D^I=700 mm indicated in the figure).

6.3.2.3 Characterisation of the first generation wavelength routing system

As shown in Figure 6-6, the experimental setup of the first generation wavelength routing system is based on the wavelength de-multiplexor design shown in Figure 6-9. An input light beam with an optical power of P_i was fibre-delivered from the transceiver unit. Fibre collimators were employed as the collimation lens in the input channel and the collection lenses in the diffracted wavelength channels. The spectral and polarisation characteristics of the ruled reflection grating employed in our system are shown in Figure 6-8. The grating plays the role of a filter, which is used to separate different wavelengths and has reduced optical crosstalk among four channels. The relative efficiencies at λ_{1c}=531, λ_{2c}=570, λ_{3c}=670 and λ_{4c}=783 nm of the grating in the wavelength routing system are all higher than 60% in the first order diffraction for two orthogonal polarisations. This suggests that the grating offers relatively high-efficient light delivery compared to the free-space-to-fibre light coupling of the fanout diffracted beam to the detectors. If the output optical power of the optical fibre end prior to connecting to the Si-SPAD detector is denoted as P_o, then to evaluate the light delivery performance of the wavelength routing system, a coupling power efficiency (PE) can be used:

$$PE = \frac{P_o}{P_i} \qquad \text{Equation (6.7)}$$

According to the results shown in Table 6-3, the spectral FWHM when using a multi-mode fibre (MMF) with a core diameter of 50 µm for the light coupling into the detector is broader than the one associated with a single-mode fibre (SMF) with a core diameter of 10 µm. This signifies that coupling power efficiency of the wavelength router can be enhanced by approximately one order when increasing the core diameter of the coupling fibre from 10 µm to 50 µm. As shown in Figure 6-12, the diffracted beams (in particular for the beams associated with longer wavelengths) approximately 700 mm away from the grating were spread to a larger extent than the clear aperture diameters of the employed fibre collimators (i.e. collection lenses). Thus, given a certain wavelength channel in the wavelength router, reducing the diffracted path length is another option that can be implemented in order to improve the coupling power efficiency. This will be discussed in section 6.4 for the refined design of the wavelength routing.

Wavelength channels		λ_{1c}=531 nm	λ_{2c}=570 nm	λ_{3c}=670 nm	λ_{4c}=780 nm
Spectral FWHM of input beam (nm)		4.13	4.11	5.93	7.39
Input power (μW)		7.3	14.4	85.5	81.1
L_D (mm)		696	704	750	755
Fibre collimators	CA	5.5 mm diameter			
	f (mm)	15	18.4	12	15
	NA	0.18	0.15	0.22	0.18
Diffracted beams coupled to Si-SPADs using SMFs with 10 μm diameter core					
Spectral FWHM (nm)		2.75	2.29	2.73	2.31
Coupling power efficiency (%)		**7**	**3.2**	**2.8**	**1.8**
Diffracted beams coupled to Si-SPADs using a MMFs with 50 μm diameter core					
Spectral FWHM (nm)		3.21	3.19	3.19	2.77
Coupling power efficiency (%)		**34.4**	**24**	**20**	**12.9**

Table 6-3 Comparison of the light collection performance when the diffracted beams are coupled to Si-SPADs using 1-metre-long SMFs with 10 μm diameter core and 0.5-metre-long MMFs with 50 μm diameter core. CA: clear aperture; NA: numerical aperture.

6.3.3 Preliminary field trial results

To complete the entire detection system of the TCSPC-based multispectral canopy LiDAR system, four PerkinElmer Si-SPAD detector modules (see Table 6-1) coupled with 10 μm diameter core SMFs were mounted underneath the wavelength router as shown in Figure 6-13. They were housed inside a light-proof, black box to minimise the ambient light levels. In order to obtain calibration and comparison of the signals from the four wavelength channels, a diffuse reflectance target (5"×5" Spectralon panel by Labsphere) was used as a reference target for measurements. The Spectralon panel had a typical hemispherical reflectance of > 95% at wavelengths from 250 nm to 2500 nm. The single-pixel calibration measurements on the Spectralon panel were carried out at a stand-off distance of 45 m. The acquired histograms of photon count versus time on the Spectralon panel of four wavelength channels (i.e. λ_{1c} =531, λ_{2c} =570, λ_{3c} =670 and λ_{4c} =783 nm channels corresponding to the highlighted wavelengths in Figure 6-14) are shown in Figure 6-15. From the histograms, we can see the background light level, significant peaks of internal back reflections from surfaces of optical components, and return signal peaks from the Spectralon panel.

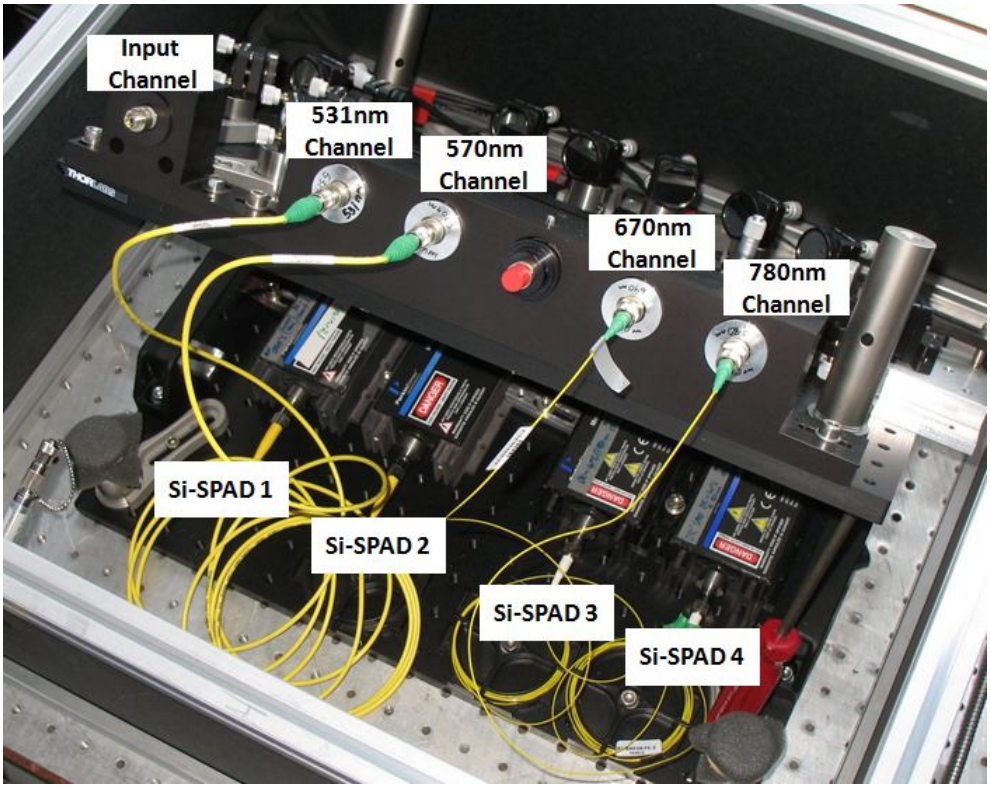

Figure 6-13 Photograph of the first-generation wavelength router (see Figure 6-6) and four Si-SPADs coupled with 10 µm diameter core SMFs in a light-proof, black box. Si-SPAD1, Si-SPAD2, Si-SPAD3 and Si-SPAD4 are for λ_{1c}=531, λ_{2c}=570, λ_{3c}=670 and λ_{4c}=783 nm channels respectively.

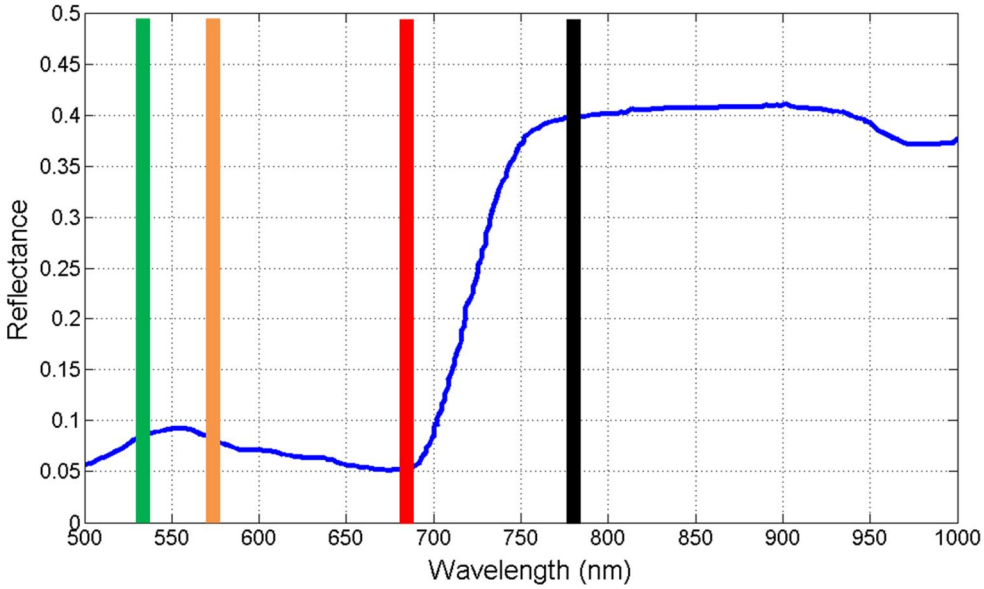

Figure 6-14 Reflectance spectra of the needles of a Nordmann fir tree. A set of four wavelengths are highlighted in colour: The "green peak" (531 nm in green bar and 570 nm in orange bar) and the "red edge" (670 nm in red bar and 780 nm in black bar). (After [6.19]).

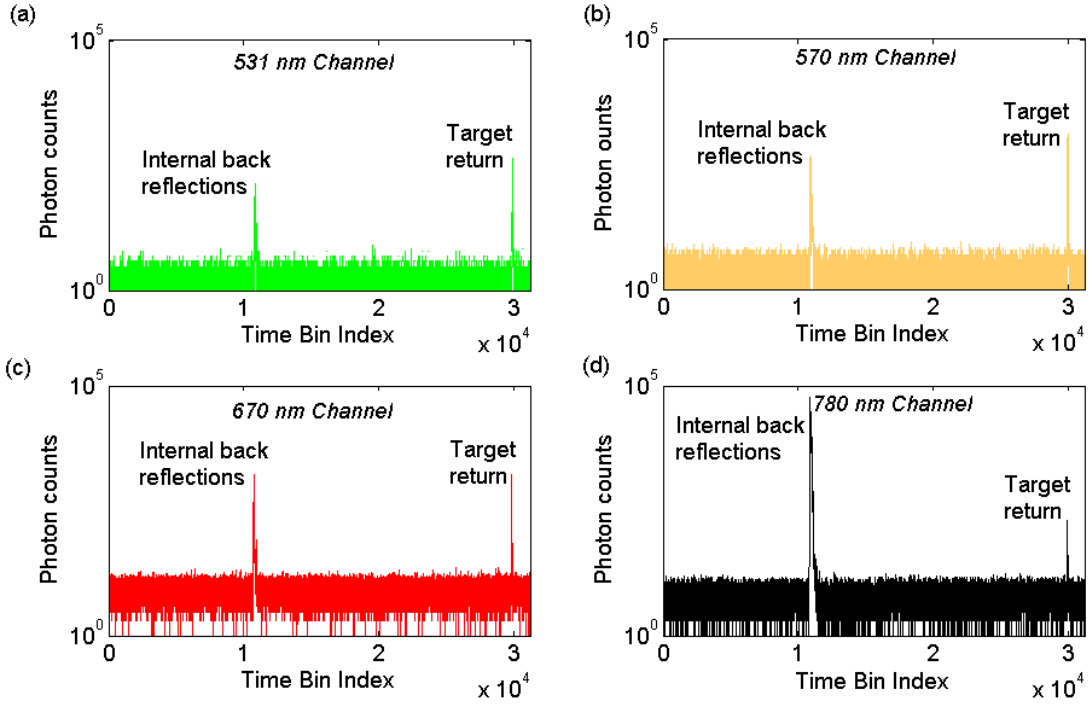

Figure 6-15 Four-wavelength-channel histograms (log vertical scale) of photon counts versus time obtained from a single position on the Spectralon panel at a stand-off distance of 45 m in sunny daylight. Histograms associated with (a) λ_{1c}=531 nm channel, (b) λ_{2c}=570 nm channel, (c) λ_{3c}=670 nm channel and (d) λ_{4c} =780 nm channel with the acquisition time of 20 s. Note that the peaks on the left hand side within each of the histograms derive from internal back reflections while the ones on the right hand side are target returns.

Concentrating on the target returns for the four channels, portion of histograms of photon counts versus distance can be seen in Figure 6-16. The known position (or temporal) offsets, amplitude variation and temporal response on the Spectralon panel can provide prior information for the post-processing of the data acquired by the LiDAR system. Note that the temporal offsets were caused by unequal electrical and optical fibre lengths for the four different channels in the system. The amplitude variation presents the wavelength dependent power characteristics of each wavelength channel while their timing jitter performance can be characterised by the temporal responses. In terms of the target setup, a Nordmann fir tree was mounted horizontally and positioned within the line-of-sight of the transceiver system housed in the rooftop lab. The tree was approximately 45 m away from the system (see Figure 6-17(a)). In sunny daylight conditions, a raster scan measurement with 20×5 pixels covering the area of the tree and back plywood board was carried out. The scan area indicated within the shadowed box is illustrated in Figure 6-17(b). The acquisition time per pixel was 20 s. This corresponds to the total scan time ~34 minutes for 100 pixels.

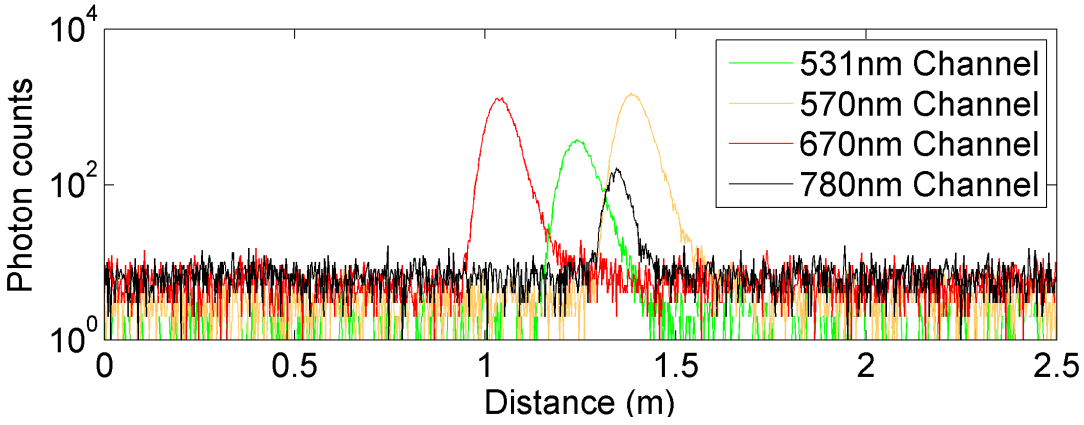

Figure 6-16 Portion of histograms of photon counts versus distance with only target returns from Figure 6-15. The distance (or temporal) offsets as well as amplitude variation along with the temporal responses of LiDAR system (log scale) of the Spectralon reflection can be revealed for the four wavelength channels.

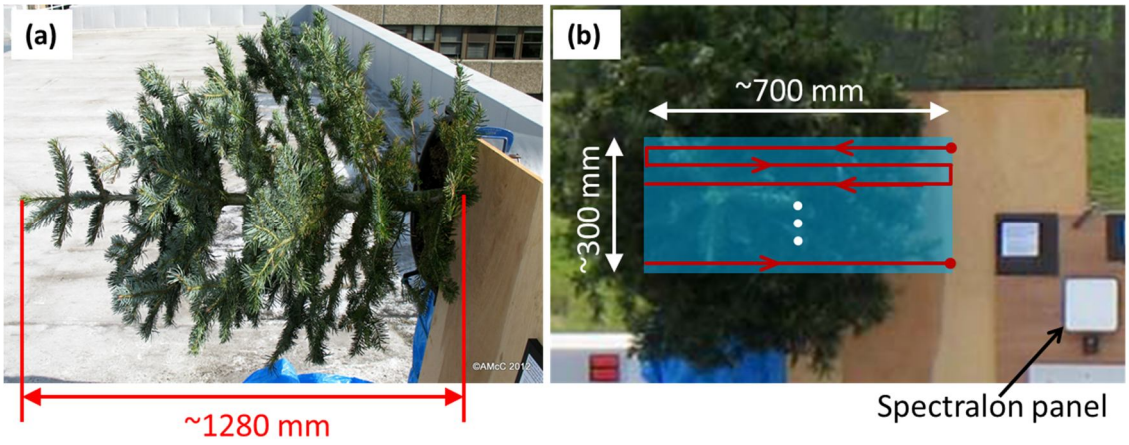

Figure 6-17 A Nordmann fir tree is mounted horizontally and pointing towards the transceiver system housed in roof lab approximately 45m away. (a) Close-up image of side view of the tree. The height of the tree is about 1280 mm from the top to the plywood board. (b) Annotated image of front view of the tree was taken using the alignment camera alongside the sensor while tree scan was performed at a stand-off distance of 45 m. A shadowed box indicates the area of the tree covered with the 20×5 pixel scan with an acquisition time per pixel of 20 s, where ~700 mm in X scan and ~300 mm in Y scan are covered.

It should be noted that the average output illumination power of <200 μW across four wavelength channels was used for the scan measurements on a tree at a stand-off distance of 45 m, which is a low-signature distributed target. In addition, multiple return peaks occur in each photon count histogram of each wavelength channel. Thus, even using 20 s acquisition time per pixel, reasonably low signal-to-noise ratios (<10) were for the obtained photon data for all four wavelength channels, as shown in Table 6-4 by investigating one example pixel on the tree. Increased average output power might

allow measurements with reduce the acquisition time, but this is constrained by the power levels in the retinal hazard region of the spectrum from 400 to 1400 nm and the available power provided by the source used. In addition, it might speed up the measurements by the use of higher detection efficient Si-SPAD detectors, but this is limited to the choice for the off-the-shelf detectors and will be limited to improvements of no more than a factor of two in efficiency. One of the largest areas of potential reduction in data acquisition time will come from improving the power coupling efficiency of the wavelength routing system (see Table 6-3 and more discussion in section 6.4).

λ	Peak counts	Background counts per bin	SNR	SBR
531 nm	5	0.17	2.20	29.41
570 nm	18	0.27	4.21	66.67
670 nm	39	0.40	6.21	97.50
780 nm	54	4.96	7.03	10.89

Table 6-4 Signal-to-noise ratio (SNR) calculated by Equation (2.6) and signal-to-background ratio (SBR) calculated by Equation (2.7) of the photon count histogram of Pixel 50 with 20 s acquisition time of the 20×5 pixel tree scan measurement at a stand-off distance of 45 m.

By integrating all-pixel contributions of the 20×5 pixel tree scan measurement, the resultant full waveform histograms of photon counts versus distance were obtained (see Figure 6-18(a)). They were compensated for the distance offsets and normalised by the ratios of the photon return peaks using the data of the λ_{1c}=531 nm channel as a reference. Significant peaks in the histograms that are related to several different layers of the tree as well as the back plywood board can be seen in the data. By using the compensated and normalised full waveform data at λ_{3c}=670 nm and λ_{4c}=780 nm, NDVI values as a function of depth can be worked out (see Figure 6-18(b)). There is a clear discrimination between the photosynthetic signature (e.g. needles) and non-photosynthetic signature (e.g. plywood) in the NDVI profile as higher NDVI values (i.e. values of > 0.9) are observed for the tree needles in comparison to the values associated with the plywood board (i.e. ≤ 0.8). A visual analysis of the separation between the leftmost (at ~0.7 m) and rightmost (at ~1.9 m) dips in the histograms yields a distance (equivalent to the height of the tree) of ~1.2 m – this approximation tallies reasonably well with the measured height of the tree (i.e. ~1.28 m shown in Figure 6-17).

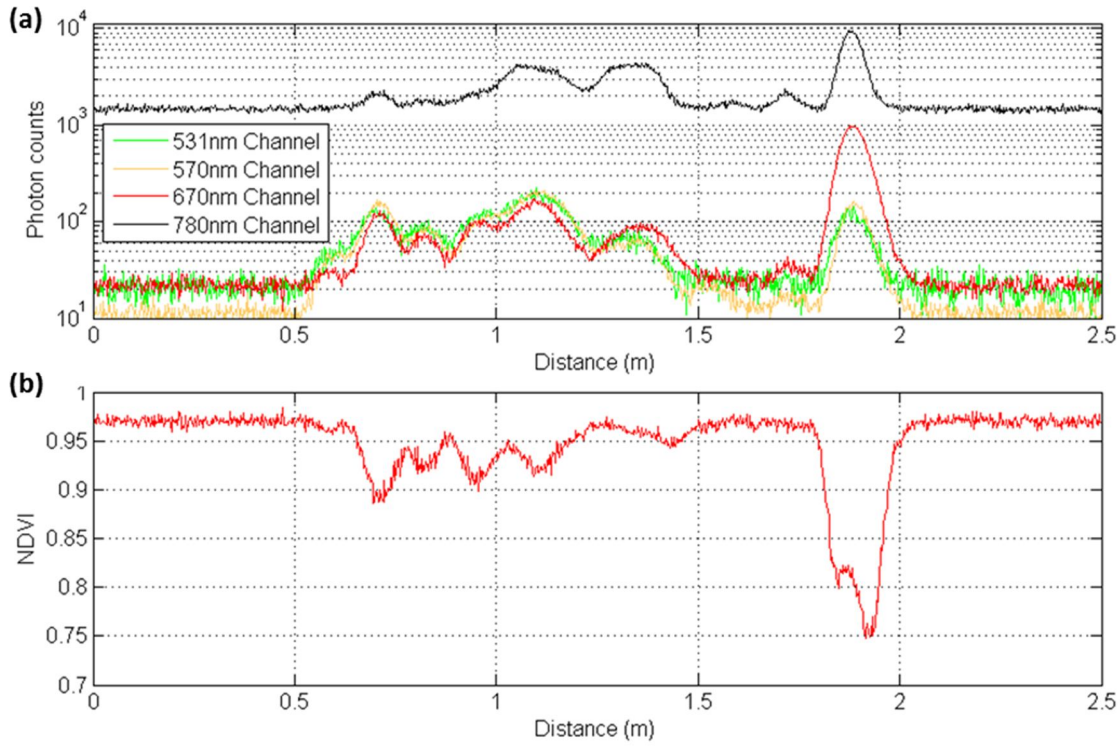

Figure 6-18 (a) Full waveform integrated histograms (log vertical scale) by summing all-pixel contributions of the 20×5 pixel tree scan with 20 s dwell time per pixel at a stand-off distance of 45 m in sunny daylight and the scan area shown in Figure 6-17. The histograms were processed by compensating for temporal offsets and normalising the photon counts for the four wavelength channels. (b) The plot of NDVI versus the distance was obtained using the compensated and normalised full waveform data at λ_{3c}=670 nm and λ_{4c}=780 nm.

Compared to the daylight field-trial measurements, a 10×10 pixel raster scan with an acquisition time per pixel of 20 s over a smaller field of view (FOV) on the tree was carried out. This was done around the tree apex at a stand-off distance of 45 m in the dark in order to minimise the background noise. As seen in Figure 6-19(a), the tree was mounted horizontally in the target setup for measurements. The scan area of interest was indicated with the grid spots as shown in Figure 6-19(b). Single-pixel measurements of four wavelength channels were acquired on two specific positions shown by the two black cross-haired circles in Figure 6-19(b). As shown Figure 6-20(a), the normalised returned photon counts for the λ_{4c}=780 nm channel of the needle on the tree apex are significantly greater than the other three channels. This is consistent with the needle reflectance property of spectra shown in Figure 6-14. It can also be found that only one individual peak appears in each wavelength channel. This is because the light beam with a small laser footprint (i.e. a beam spot with the diameter of approximately <3 mm on the target at a stand-off distance of 45 m) covered only the

tree apex and was blocked by the deeper layer of the tree, e.g. the branches of the tree.

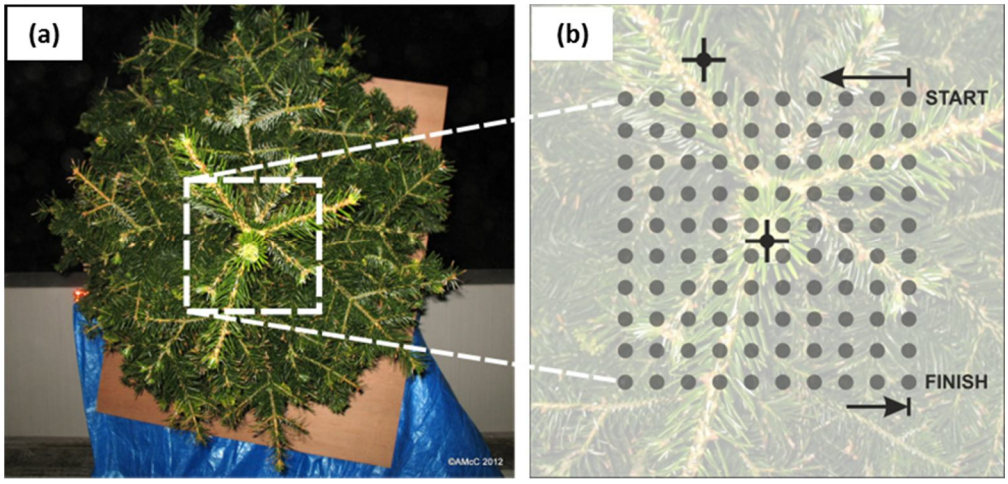

Figure 6-19 (a) Close-up photograph of the top view of a conifer canopy and scan area with sampling grid along the line-of-sight of the LiDAR. (b) Annotated scan area (~120 × 120 mm) with 10×10 pixels with an acquisition time per pixel of 20 s. As for the single point measurements made after the scan, two full waveform LiDAR signals were recorded on the tree apex (with 20 s acquisition time) and on the patch of dense needles (with 90 s acquisition time). Their approximate positions are indicated by the two black cross-haired circles.

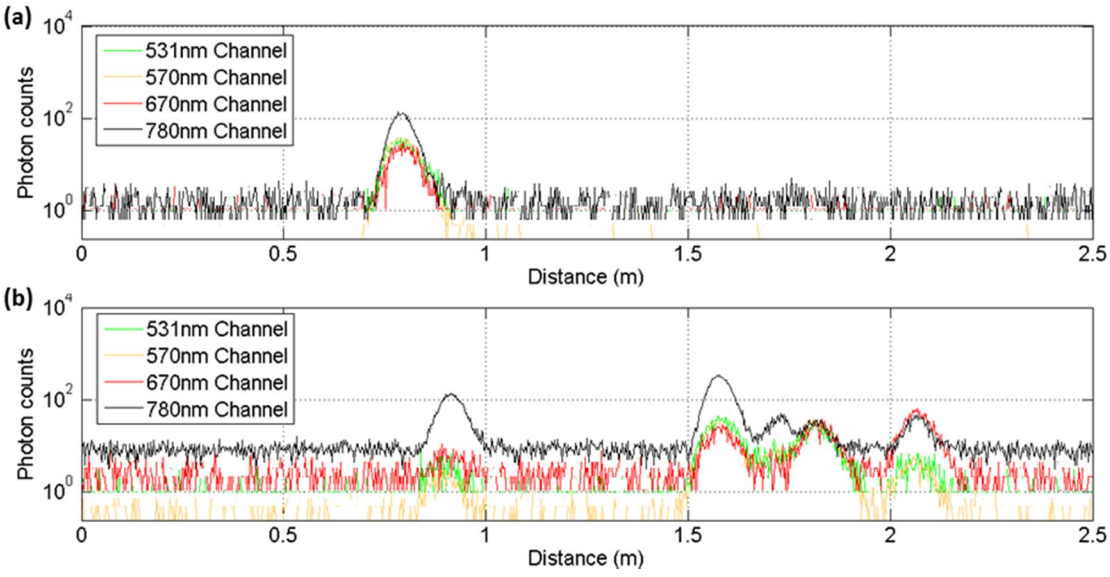

Figure 6-20 (a) Full histogram multispectral LiDAR data with an acquisition time of 20 s for a single pixel recorded on the tree apex shown by the lower black cross-haired circle in Figure 6-19(b). (b) Full histogram multispectral LiDAR data with an acquisition time of 90 s for a single pixel recorded on the patch of dense needle shown by the upper black cross-haired circle in Figure 6-19(b).

In contrast, the laser beam through the tree in the other specific location was observed during the measurement. Several layers related to the tree and back plywood board can

be resolved according to the peaks in the photon counts histogram with longer acquisition times (see Figure 6-20(b)). This suggests that there is high potential to have inconsistencies between return responses from different pixels.

In comparison to the single-pixel measurement results based on the small laser footprint, measurements on the canopy with a larger laser footprint in general the better representation of a mixture of needle and bark response can be obtained when considering the light penetration and absorption in the canopy. This can be approximately obtained by accumulating the full waveform multispectral LiDAR data for all 10×10 pixels covering an area of ~120 × 120 mm. Figure 6-21 shows the accumulated photon count responses, in which the bulk of the canopy returns is between approximately 0.7 and 1.6 m and the ground plane return is at approximately 1.9 m. In addition, different background levels for the four channels occurred during measurements can be found in the same figure. Compared to the single-pixel measurement result shown in Figure 6-20(b), the accumulated responses have more consistent behaviour through the canopy for each of the four channels. From this data, the tree height can be easily measured as ~1.2 m. In addition, accumulated sampling over many pixels and peaks compensates for outlying single point measurements and corresponds more closely to wider area measurement. Therefore, these accumulated sampling results were used for further analysis using the Reversible-jump Markov chain Monte Carlo (RJMCMC) algorithm to recover layer positions and signal amplitudes [6.19]. Subsequently, the RJMCMC-based NDVI profile can be determined.

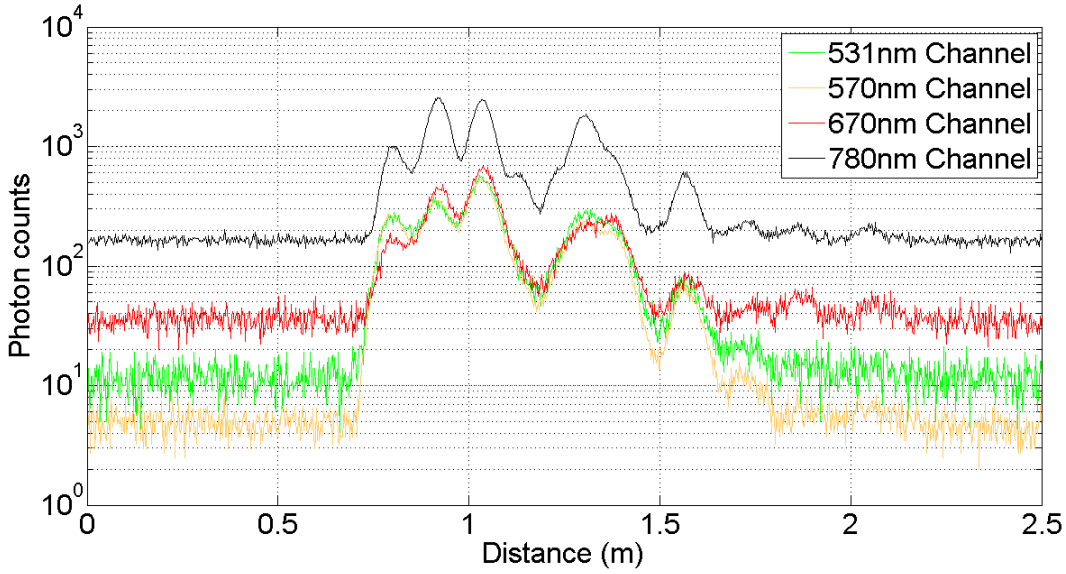

Figure 6-21 Accumulated full waveform multispectral LiDAR data for all 100 pixels. Note that a 10×10 pixel raster scan measurement was carried out at night time.

In order to investigate the Nordmann fir tree in the lab under conditions that were as similar as possible to the physiological status during the field trials, the ground truth measurements of physiological parameters of the tree were carried out shortly after the field trials. Figure 6-22(a) shows nine labelled heights throughout the profile of the tree. They were associated with nine sets of needle and bark samples which were cut from the tree. The NDVI values of these samples were measured manually in the laboratory using a spectrometer. Figure 6-22(b) illustrates a comparison of NDVI values between the LiDAR data and laboratory data. It can be found that the analysed NDVI values ($\mu = 0.713$, $\sigma = 0.226$) from the LiDAR data by the RJMCMC process are comparable to the laboratory data ($\mu = 0.766$, $\sigma = 0.0132$).

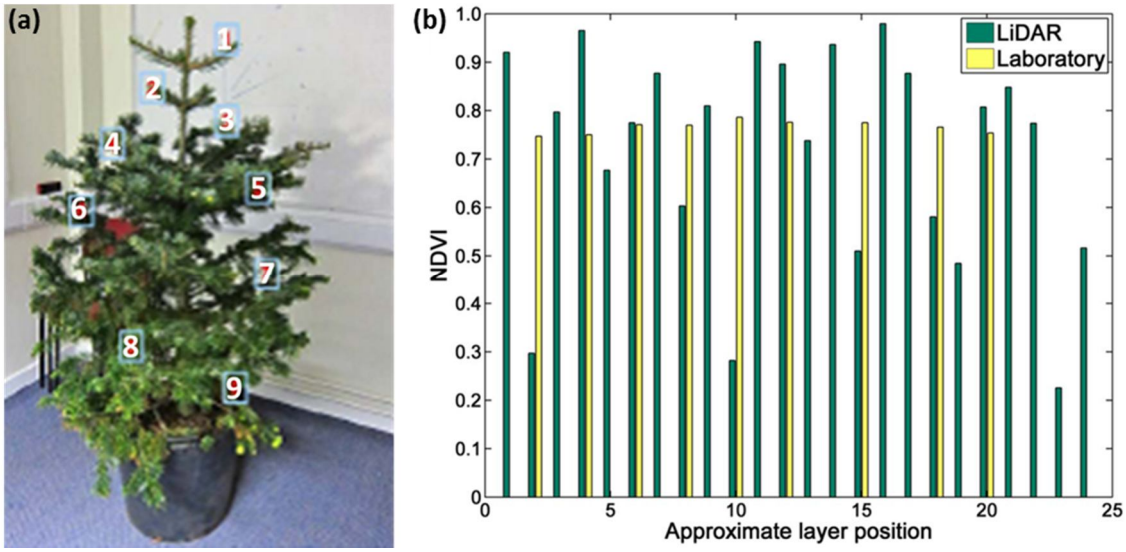

Figure 6-22 (a) Nine labelled heights throughout the profile of the tree. They were associated with nine sets of needle and bark samples which were cut from the tree. The samples were measured manually in the laboratory using a spectrometer. (b) Comparison of NDVI values between the LiDAR data and laboratory data. The NDVI values of LiDAR data of 24 recovered layer positions by the Reversible-jump Markov chain Monte Carlo (RJMCMC) process are shown in green bars, and the yellow bars represent the NDVI values of nine needle samples shown in (a). (Reproduced from [6.19]).

In comparison to the measured NDVI values in the lab, much greater variation for the NDVI values based on the LiDAR data might be expected as the measurements were performed remotely in the presence of a large noise background, and over modest acquisition times when compared to the laboratory comparisons. In addition, the angular distributions of the targets are unlikely to be as uniform as the laboratory comparisons. There is also likely to be the effect of scintillation from

atmospheric turbulence on some of the measurements. The RJMCMC technique was explained in section 2.4.2 of Chapter 2. The details of the RJMCMC process used for the single photon data on the tree can be seen in [6.19]. The RJMCMC process used does not require any previously known information about the target in order to perform signal reconstruction. In addition, using LiDAR to acquire data is a more efficient and non-destructive method in comparison to the time-consuming measurements in the lab using a spectrometer on the samples which were required to cut destructively from the tree.

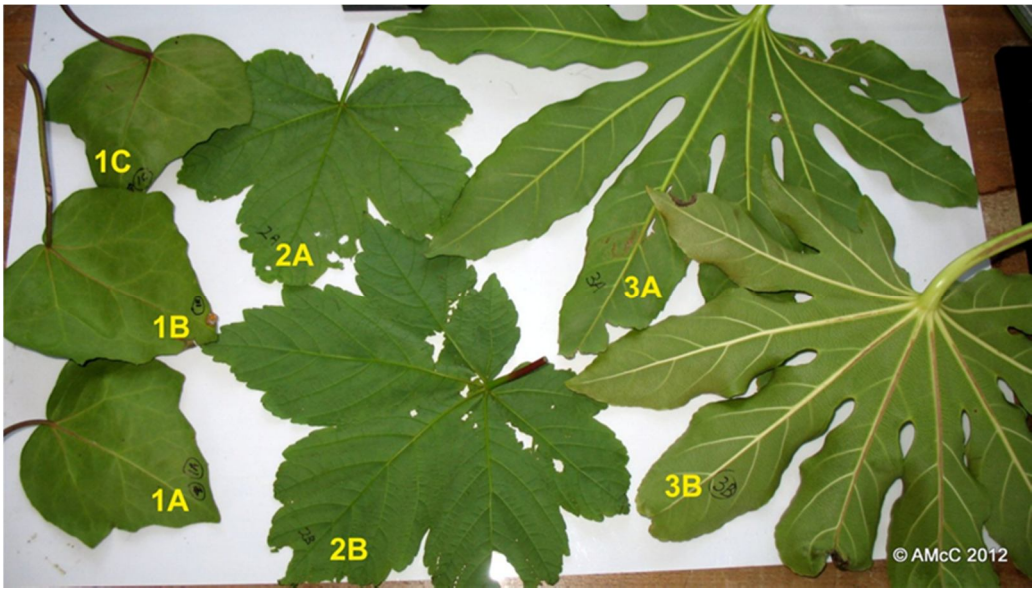

Figure 6-23 Example specimens (leaves) were employed to investigate the capability of the TCSPC-based multispectral canopy LiDAR system to retrieve physiological estimates (e.g. PRI and NDVI). The measurements on several green leaves of the broadleaf trees were carried out at a stand-off distance of 45 metres.

Leaves	**1A**		**2A**		**3A**		**3B**	
	Upper side	Lower side	Upper side	Lower side	Upper side	Lower side	Upper side	Lower side
PRI	0.1011	0.0741	0.1221	0.0175	0.0359	-0.0949	0.1301	-0.0396
NDVI	0.9629	0.7616	0.9647	0.8232	0.9681	0.6285	0.7097	0.7741

Table 6-5 Estimations by a cross-correlation method of PRI and NDVI on four example leaves shown in Figure 6-23 using the TCSPC-based multispectral canopy LiDAR system

The TCSPC-based multispectral canopy LiDAR system has been shown to retrieve physiological estimates (e.g. PRI and NDVI) of the photosynthetic targets (e.g. leaves,

see Figure 6-23) at a stand-off distance of 45 m. The estimated data using a cross-correlation method are summarised in Table 6-5. Since we see higher PRI values for the upper sides of the leaves (see third row of Table 6-5), it suggests higher photosynthesis efficiency for the leaves under test occurs in this location. This agrees with the standard photosynthetic nature of most leaves. In addition, since the results show that the NDVI value of Leaf 3B's upper side is smaller than the one of its lower side, in comparison to the NDVI values of similar leaves, this suggests that Leaf 3B was stressed.

6.4 Discussion and outlook

As shown in Table 6-3, the coupling efficiency of the first generation wavelength router when using SMFs was relatively low (<10%). It was necessary to refine the wavelength routing system to enhance its coupling power efficiency and improve the performance of the LiDAR system. The layout of the refined design of the four-wavelength router can be seen in Figure 6-24. It is also based on the schematic shown in Figure 6-5. Employing a D-shape mirror can help perfectly separate two close beams by reflecting one while passing the other. As the input beam is very close to the diffracted beam associated with λ_{4c}=783 nm channel, one D-shaped mirror is employed to reflect the former beam without blocking the latter beam. By using the same technique, the other D-shaped mirror is employed to separate two close diffracted beams associated with λ_{1c}=531 and λ_{2c}=570 nm channels.

Therefore, the refined design features a more compact arrangement of components and thus significantly shortened diffracted optical paths (average total lengths are ~400 mm) for all four wavelength channels (i.e. λ_{1c}=531, λ_{2c}=570, λ_{3c}=670 and λ_{4c}=783 nm channels) in comparison to the first-generation wavelength router (average total lengths are ~700 mm) shown in Figure 6-6. According to the trends shown in Figure 6-12, shorter diffracted optical paths result in a narrowing of the fanout diffracted beams, which is preferable in order to achieve higher light collection by the collection lenses.

An illumination beam with an NA of 0.12 was used for the input channel in the Zemax model shown in Figure 6-9. Several simulations using the parameters shown in Table 6-6 were performed to evaluate D_{Focus} and spectral-spread spots for each wavelength channel. The spot diagrams can be seen in Figure 6-25 and the D_{Focus} values are 64 µm, 60 µm, 59 µm and 102 µm for λ_{1c}=531, λ_{2c}=570, λ_{3c}=670 and λ_{4c}=783 nm channels respectively. This illustrates how the selection of a large core diameter fibre will help to couple light with higher efficiency. For example, the improvement of using

50 µm diameter core MMFs rather than 10 µm diameter core SMFs for coupling light can be seen from the measured coupling power efficiency results (see Table 6-3) based on the first-generation wavelength router even though the diffraction optical path was long.

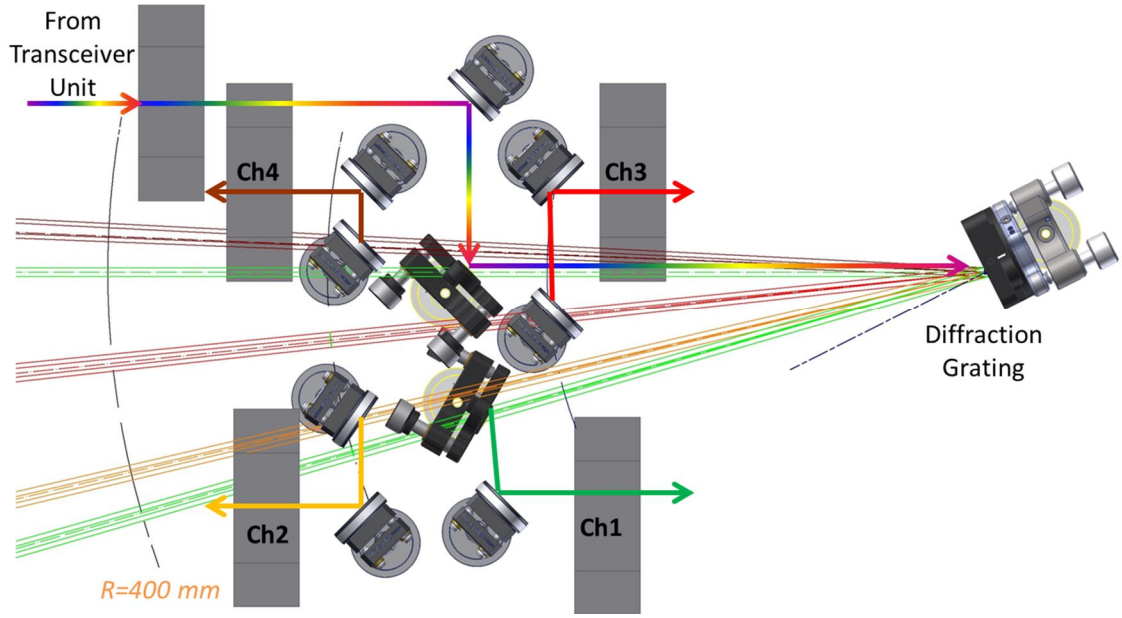

Figure 6-24 Computer-aided design (CAD) model of the refined design of the wavelength-router. The layout features significantly reduced diffraction optical paths (average total lengths are ~400 mm) for four wavelength channels. Although the input beam was very close to the diffracted beam associated with the λ_{4c}=783 nm channel, one D-shaped mirror is employed to reflect the former beam without blocking the latter beam. The other D-shaped mirror is employed to separate two close diffracted beams associated with the λ_{1c}=531 and λ_{2c}=570 nm channels. Note that the λ_{1c}=531 nm channel (Ch1) is in green, the λ_{2c}=570 nm channel (Ch2) is in yellow, the λ_{3c}=670 nm channel (Ch3) is in red and the λ_{4c}=783 nm channel (Ch4) is in dark red.

Wavelength channels		λ_{1c}=531 nm	λ_{2c}=570 nm	λ_{3c}=670 nm	λ_{4c}=783 nm
Spectrum of the input light (nm)		529 - 533	568 - 572	667 - 673	779 - 787
Fibre collimator in the input channel	CA	5.5 mm diameter			
	f (mm)	15			
	NA	0.18			
L_D (mm)		400			
Fibre collimators in the receive channels	CA	5.5 mm diameter			
	f (mm)	15	15	12	12
	NA	0.18	0.18	0.22	0.22

Table 6-6 Main parameters were employed for the simulations of the refined design of the wavelength-router. CA: clear aperture; NA: numerical aperture.

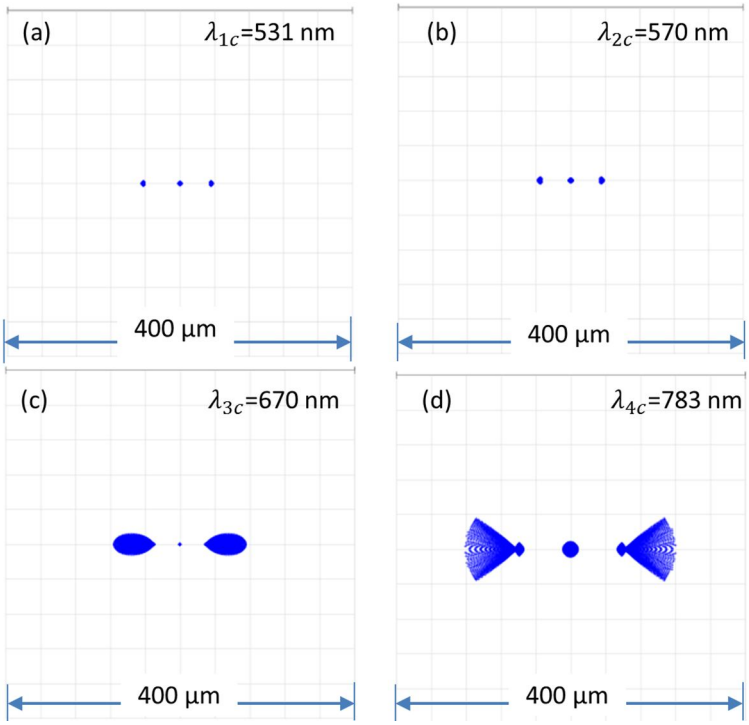

Figure 6-25 Spot diagrams in the image planes of the collection lenses for four wavelength channels. The scale bar size is 400 µm and thus the grid size is 40 µm. The central spot represents to the chief light ray.

As a whole, if the tailored shorter diffracted optical paths can be implemented and the diffracted beams are focussed into 50 µm diameter core MMFs, the refined setup is expected to have even higher coupling power efficiency than the values shown in the twelfth row of Table 6-3. It should be noted that the upper- and lower-edge spectral spots of λ_{3c} =670 and λ_{4c} =783 nm channels are diffused more significantly than the ones of the other two channels (see Figure 6-25). Thus, there is the potential to induce light decoupling with wider bandwidth for the λ_{3c} =670 and λ_{4c} =783 nm channels and hence they have less coupling power efficiency.

6.5 Conclusions

We have constructed a novel multispectral LiDAR system based on a broadband tunable pulsed supercontinuum laser source and time-correlated single photon counting receiver technology in conjunction with a diffraction-grating-based wavelength routing system designed specifically to recover structural and physiological parameters from tree samples. We have scanned a small Nordmann fir tree sample using this system, and extracted full waveform data at four wavelengths corresponding to the NDVI and PRI values. We have compared the NDVI depth profile measured by the system with validating laboratory measurements using a spectrometer to demonstrate a good

agreement. To achieve high-efficient single-photon detection for multispectral time-of-flight depth profiling, it is necessary to improve the performance of the wavelength input and routing modules. This could be achieved by upgrading the system through use of high-performance components in the transceiver unit and particularly the refinement of the wavelength routing system.

The author with assistance from Dr. Aongus McCarthy (AMcC), modelled the wavelength routing system, using Zemax, and made key contributions to the optical component determination, alignment and specification of the wavelength routing system (section 6.3.2 and section 6.4). The author along with AMcC developed the multispectral TOF depth imaging system, and carried out all the field trial measurements. In section 6.3.3, Daniel Martinez-Ramirez and Prof. Andrew M. Wallace processed the measurement data. Simone Morak and Dr. Caroline J. Nichol provided the NDVI comparisons using reflectance spectrophotometry. The majority of results reported this Chapter were performed by the author. All of the work in this Chapter was supervised by Prof Gerald S. Buller.

6.6 References

[6.1]. I. Kemelmacher-Shlizerman, and R. Basri, "3d face reconstruction from a single image using a single reference face shape," IEEE Trans. Pattern Anal. Mach. Intell. (33), 394-405 (2011).

[6.2]. J. Verrelst, M. Schaepman, Z. Malenovsky, and J. Clevers, "Effects of woody elements on simulated canopy reflectance: Implications for forest chlorophyll content retrieval," Remote Sens. Environ. (114), 647-656 (2010).

[6.3]. P. Dabney, D. Harding, J. Abshire, T. Huss, G. Jodor, R. Machan, J. Marzouk, K. Rush, A. Seas, C. Shuman, X. Sun, S. Valett, A. Vasilyev, A. Yu, and Y. Zheng, "The Slope Imaging Multi-polarization Photon-counting Lidar: Development and performance results," 2010 IEEE International Geoscience and Remote Sensing Symposium, 653-656 (2010).

[6.4]. J. Suomalainen, T. Hakala, H. Kaartinen, E. Räikkönen, and S. Kaasalainen, "Demonstration of a virtual active hyperspectral LiDAR in automated point cloud classification," ISPRS J. Photogramm. Remote Sens. (66), 637-641 (2011).

[6.5]. T. Hakala, J. Suomalainen, S. Kaasalainen, and Y. Chen, "Full waveform hyperspectral LiDAR for terrestrial laser scanning," Opt. Express (20), 7119-7127

(2012).

[6.6]. G. Wei, S. Shalei, Z. Bo, S. Shuo, L. Faquan, and C. Xuewu, "Multi-wavelength canopy LiDAR for remote sensing of vegetation: Design and system performance," ISPRS J. Photogramm. Remote Sens. (69), 1-9 (2012).

[6.7]. A. McCarthy, R. J. Collins, N. J. Krichel, V. Fernandez, A. M. Wallace, and G. S. Buller, "Long-range time-of-flight scanning sensor based on high-speed time-correlated single-photon counting," Appl. Opt. (48), 6241-6251 (2009).

[6.8]. A. McCarthy, N. J. Krichel, N. R. Gemmell, X. Ren, M. G. Tanner, S. N. Dorenbos, V. Zwiller, R. H. Hadfield, and G. S. Buller, "Kilometer-range, high resolution depth imaging via 1560 nm wavelength single-photon detection," Opt. Express (21), 8904-8915 (2013).

[6.9]. A. McCarthy, X. Ren, A. Della Frera, N. R. Gemmell, N. J. Krichel, C. Scarcella, A. Ruggeri, A. Tosi, and G. S. Buller, "Kilometer-range depth imaging at 1550 nm wavelength using an InGaAs/InP single-photon avalanche diode detector," Opt. Express (21), 22098-22113 (2013).

[6.10]. G. S. Buller, R. D. Harkins, A. McCarthy, P. A. Hiskett, G. R. MacKinnon, G. R. Smith, R. Sung, A. M. Wallace, R. A. Lamb, and K. D. Ridley, "Multiple wavelength time-of-flight sensor based on time-correlated single-photon counting," Rev. Sci. Instrum. (76), 083112 (2005).

[6.11]. Y. Zhang, J. M. Chen, J. R. Miller, and T. L. Noland, "Leaf chlorophyll content retrieval from airborne hyperspectral remote sensing imagery," Remote Sens. Environ. (112), 3234-3247 (2008).

[6.12]. O. Nevalainen, T. Hakala, J. Suomalainen, R. Mäkipää, M. Peltoniemi, A. Krooks, and S. Kaasalainen, "Fast and nondestructive method for leaf level chlorophyll estimation using hyperspectral LiDAR," Agric. For. Meteorol. (198), 250-258 (2014).

[6.13]. A. A. Gitelson, and M. N. Merzlyak, "Signature analysis of leaf reflectance spectra: algorithm development for remote sensing of chlorophyll," J. Plant Physiol. (148), 494-500 (1996).

[6.14]. S. L. Ustin, A. A. Gitelson, S. Jacquemoud, M. Schaepman, G. P. Asner, J. A. Gamon, and P. Zarco-Tejada, "Retrieval of foliar information about plant pigment systems from high resolution spectroscopy," Remote Sens. Environ. (113), S67-S77 (2009).

[6.15]. R. Main, M. A. Cho, R. Mathieu, M. M. O'Kennedy, A. Ramoelo, and S. Koch, "An investigation into robust spectral indices for leaf chlorophyll estimation," ISPRS J. Photogramm. Remote Sens. (66), 751-761 (2011).

[6.16]. C. J. Tucker, "Red and photographic infrared linear combinations for monitoring vegetation," Remote Sens. Environ. (8), 127-150 (1979).

[6.17]. J. A. Gamon, L. Serrano, and J. S. Surfus, "The photochemical reflectance index: an optical indicator of photosynthetic radiation use efficiency across species, functional types, and nutrient levels," Oecologia (112), 492-501 (1997).

[6.18]. A. M. Wallace, C. Nichol, and I. Woodhouse, "Recovery of Forest Canopy Parameters by Inversion of Multispectral LiDAR Data," Remote Sens. (4), 509-531 (2012).

[6.19]. A. M. Wallace, A. McCarthy, C. J. Nichol, X. Ren, S. Morak, D. Martinez-Ramirez, I. H. Woodhouse, and G. S. Buller, "Design and Evaluation of Multispectral LiDAR for the Recovery of Arboreal Parameters," IEEE Trans. Geosci. Remote Sens. (52), 4942-4954 (2014).

[6.20]. C. A. Palmer, and E. G. Loewen, *Diffraction grating handbook (sixth edition)* (Newport Corporation 2004).

[6.21]. Newport Corporation, "Catalog no.: 53-*-360R. Diffraction grating specification sheet. online (http://www.gratinglab.com/Products/Product_Tables/Efficiency/Efficiency.aspx?catalog=53-*-360R) last accessed 15-04-2015."

Chapter 7
Temporal and spatial characterisation of scanning time-of-flight single-photon depth imagers

7.1 Introduction

A scanning time-of-flight single photon depth imaging system using the Time Correlated Single Photon Counting (TCSPC) technique is capable of measuring remote targets with depth information. In order to perform a N-pixel depth image, N TCSPC-based pixel-wise waveform measurements need to be carried out sequentially by scanning between discrete spatial points. From the quantitative perspective, the spatial origin of the entire scan can be described using a spatial measurement matrix (Φ) [7.1] which is constructed using a collection of $N \times N$ spatial sampling entries. For the point-wise scan [7.1], Φ is a $N \times N$ identity matrix (I) and each entry in the primary diagonal of Φ corresponds to each step of the scan. Correspondingly, the depth profile can be expressed as: $D = \Phi d = Id$, where d represents N depths estimated from the TCSPC-based pixel-wise waveforms. Given a per-pixel acquisition time of t, the total acquisition time for the entire image will be Nt (ignoring the switching time between pixels). Thus, single-photon depth images with pre-determined spatial sampling points (for desirable pixel density) and per pixel acquisition time can be achieved by the TCSPC-based scanning depth imaging systems in comparison to the non-scanning imaging systems by the use of arrayed detectors with a fixed pixel number.

The original custom scanning transceiver system [7.2], in use in 2009 by the Single Photon group, operated using an illumination of λ=842 nm from a gain-switched picosecond diode laser, a 200 mm focal length objective lens, and a free-running Perkin Elmer thick junction SPAD module [7.3] connected with ~5 μm diameter core receive fibre. The instrumental response had a timing jitter of ~400 ps Full Width at Half Maximum (FWHM). A number of significant changes were made to the system in 2014 to enhance operation at λ=842 nm. These changes included the incorporation of a

pulsed tunable supercontinuum laser source, a longer focal length objective lens (500 mm), and a thin-junction Si-SPAD operating in gated mode. This improved depth imager was developed by Dr. Aongus McCarthy and the author. The operating wavelength allowed measurements with a higher level of eye-safety in comparison to visible wavelengths. Better performance of ambient light reduction was achieved using the tunable supercontinuum laser source for matching to the narrow band-pass filters at the receiver. By using a longer focal length objective lens, improved spatial resolution was achieved. The off-the-shelf thin junction Si-SPAD (PDM series, MPD Si-SPAD [7.4]) offered reduced timing jitter. In addition, new custom scan control and data acquisition software was upgraded by Dr. Nathan R. Gemmell, Dr. Robert J. Collins and the author based on the original which was developed by Dr. Nils J. Krichel. This original software used for the depth imagers described in Chapter 4 and 6. It generated a pixel-wise photon count histogram in ASCII format that was then transferred to computer storage. In this case, the time taken for dumping data pixel by pixel increases dramatically when a higher number of scan pixels were measured. For the upgraded software, the data stream in binary format from the data acquisition module was written directly to the computer storage continuously to maximise throughput. In other words, this software was capable of high-speed recording TCSPC-based time-tagged data in binary format. Thus, it allowed the depth imagers to implement scans with high-density pixels (e.g. 1000×1000 pixels or higher) as well as fast data transfer using reduced memory space. The recorded time-tagged raw data offered greater flexibility in analysis of photon event data using individual photon arrival times. This allows greater scope for post-processing of the data such as routine comparisons of different acquisition times in each depth image.

In order to investigate the performance of the depth imaging system during field trials, a number of characterisation measurements and analysis are reported in this Chapter. These include depth imaging using sparse single photon [7.5] (The data processing of this work was done by Dr. Yoann Altmann). Also included is the characterisation of refractive-turbulence-induced scintillation for the active imager in which the laser beam goes through the atmosphere twice (The data analysis of this work was done by Dr. Yoann Altmann and the author). This Chapter also discusses more detailed assessment of depth and spatial resolution. These characterisation results can provide knowledge for further data analysis and system optimisation.

7.2 Overview of the investigated time-of-flight scanning depth imaging systems

The schematic diagrams of the two time-of-flight scanning depth imaging systems used in this Chapter are shown in Figure 7-1. They featured data acquisition using two different time-tagged modes (i.e. T2 and T3 modes [7.6-7.7]) of the TCSPC modules in conjunction with the single photon detector operating in gated mode. Note that as described in section 2.2.4 of Chapter 2, T2 mode of the TCSPC module operates with two functionally identical input channels and records the macro-time independently for both channels. The T3 mode of the TCSPC module is specifically designed to use periodic synchronisation signals and allows operations at high synchronisation rates (up to 150 MHz). For the imager with data acquisition in T2 mode (see Figure 7-1(a)), an electrical pulse train with a repetition rate of 19.5 MHz synchronised to the pulsed supercontinuum laser source was clocked in a pulse pattern generator (PPG). Two signal pulse trains with a synchronisation frequency of 19.5 MHz output from two separated channels of the PPG simultaneously. One was down-divided to ~1.95 MHz (by a factor of 10) using a constant function discriminator (CFD) hardware module and connected to the start-input of the PicoHarp 300 (from PicoQuant GmbH) in order to avoid any issues due to the long dead time (typically 90ns in this case). The other pulse train was used to gate the Si-SPAD. When the timing bin size of 16 ps in the PicoHarp 300 was used, the photon timing (i.e. start-stop timing) histogram acquired by the system can be seen in Figure 7-2(a) and its FWHM timing jitter was characterised with ~96 ps (see inset of 7-3(b)).

By contrast, when the imager operates with data acquisition in T3 mode, the electrical pulse train from the pulsed laser source was split by a power splitter into two signal pulse trains, as shown in Figure 7-1(b). Particularly, one of the pulse trains was delivered into the start-input (i.e. “Sync in” channel) of the HydraHarp 400 (from PicoQuant GmbH) as a synchronisation rate. A signal with a synchronisation frequency of 19.5 MHz was divided using an internal synchronisation divider of 8 of the HydraHarp 400 to avoid the dead time issue. When a timing bin size of 2 ps was used, the photon timing histogram acquired by the system can be seen in Figure 7-3(a) and the FWHM timing jitter of the system was characterised with ~60 ps (see Figure 7-3(b)).

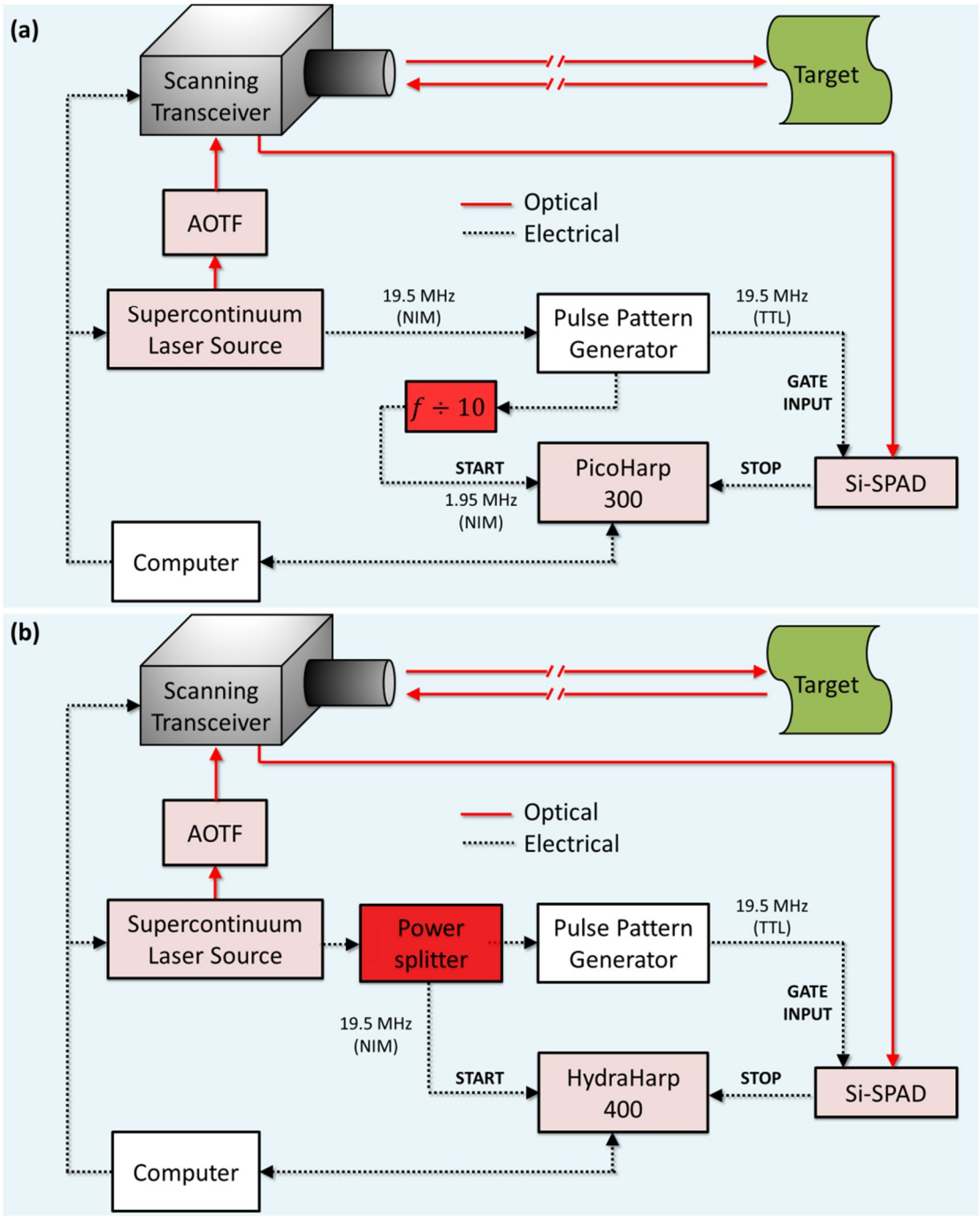

Figure 7-1 Schematic diagrams of scanning depth imagers operating in two different time-tagged data acquisition modes (i.e. T2 and T3 modes [7.6-7.7]) of the TCSPC modules. (a) The TCSPC module is PicoHarp 300 [7.8] (from PicoQuant GmbH) in T2 mode. The setup in (b) uses the HydraHarp 400 TCSPC module [7.9] (from PicoQuant GmbH) in T3 mode. AOTF: acousto-optic tunable filter.

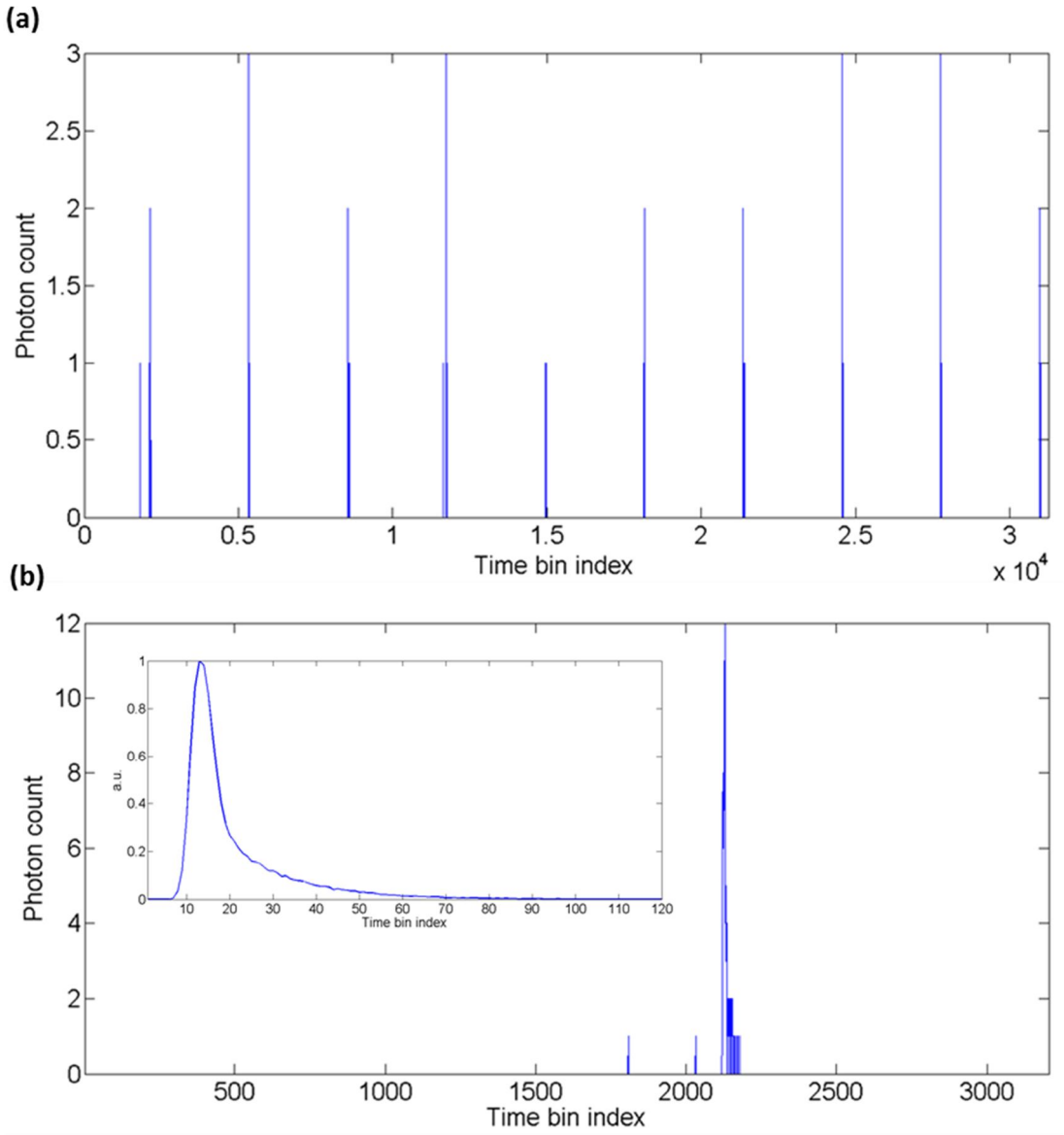

Figure 7-2 (a) An example of a photon timing (i.e. start-stop timing) histogram for a single pixel with an acquisition time of 50 ms acquired by the depth imager shown in Figure 7-1(a) operating in T2 mode. As a repetition rate of 19.5 MHz from the pulsed laser source was used while the synchronisation frequency of the PicoHarp 300 was 1.95 MHz, 10 peaks appear in each pixel-wise histogram. (b) By gathering 10 time-bin-cycles photon histograms (a time bin cycle corresponds to a period of output laser pulses) into one, an accumulated photon timing histogram can be generated. The inset shows the normalised system temporal response with a timing bin size of 16 ps of the system on a standard Spectralon panel. The FWHM timing jitter was 96 ps.

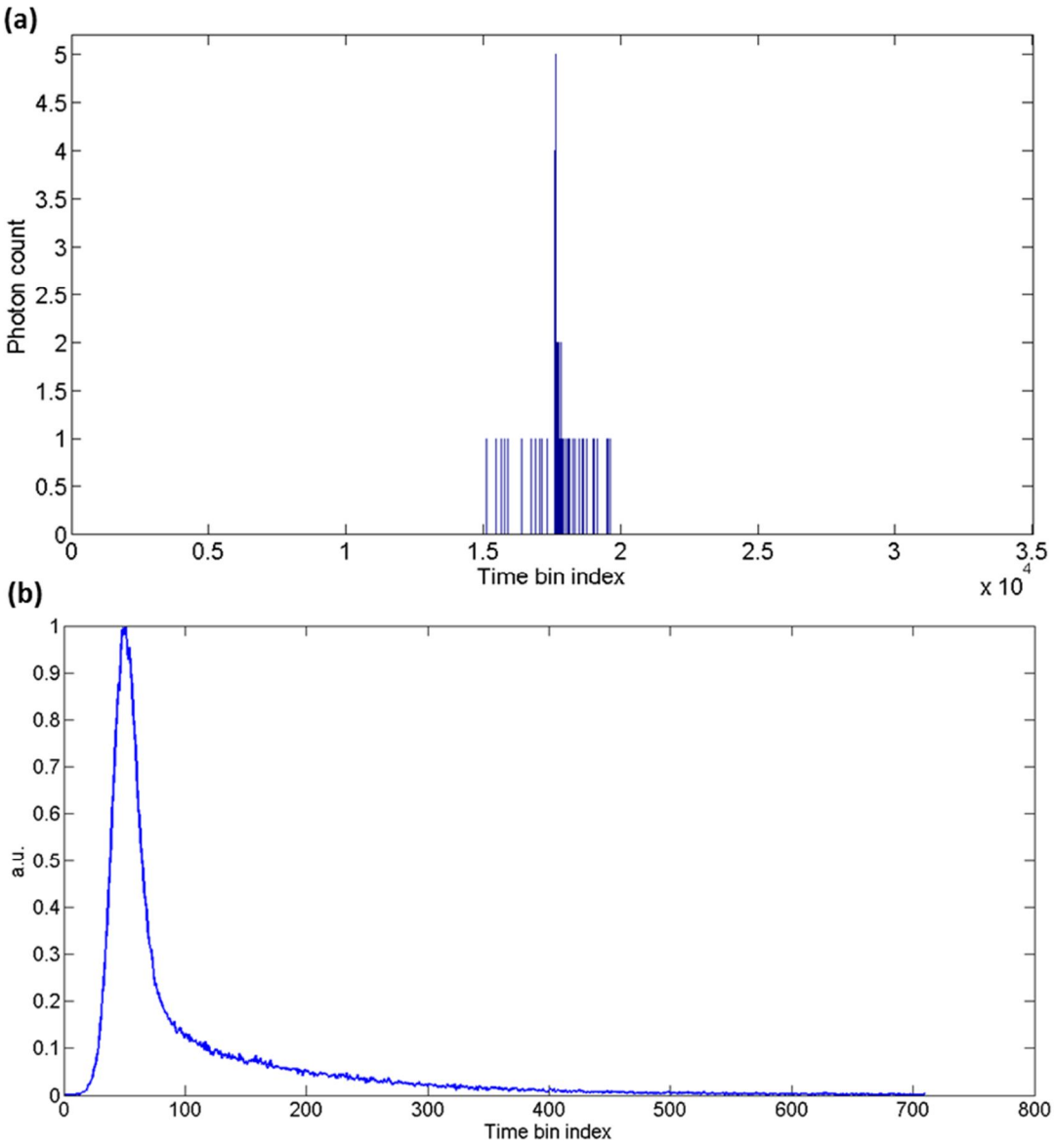

Figure 7-3 (a) An example photon timing (i.e. start-stop timing) histogram for a single pixel with an acquisition time of 200 ms acquired by the depth imager shown in Figure 7-1(b) operating in T3 mode. (b) Normalised system temporal response with the timing bin size of 2 ps on a standard Spectralon panel. The FWHM timing jitter was ~60 ps.

When operating in T2 mode, the two input channels are identical and neither requires a synchronisation signal with precise period while time tags of both channels are recorded. The main advantage of T2 mode operation is its independence to a synchronisation signal. However, this results in large format recorded time tags not only for photon events but also for the large proportion of non-photon start signals. This means that a significant amount of useless data is recorded along with the photon measurements. By contrast, T3 mode does not record the unused start signals and more efficiently records data. However, it can increase the overall timing jitter due to a

contribution from the synchronisation signal. In our measurements, the synchronisation signal had negligible jitter contribution. The overall jitter performance in T3 mode was excellent – with ~60 ps FWHM overall. Therefore, T3 mode offers the possibility to obtain large format raster scans with only moderate photon counts per pixel.

The key parameters of the investigated time-of-flight scanning depth imaging systems are summarised in Table 7-1.

System Parameter	**Comment**
Transmit/Receive Alignment	Monostatic: Coaxial transmit and receive channels
Laser	• Pulsed supercontinuum laser (SuperK EXTREME, EXW12, NKT Photonics, Denmark) • Fibre-coupled to the transceiver unit. Note that the coupling fibre is a large mode area and polarisation-maintaining photonic crystal fibre (FD7, SuperK Fibre Delivery series, NKT Photonics, Denmark)
Laser Repetition Rate	19.5 MHz
Illumination Wavelength	~840 nm
Laser Pulse Width	<50 ps
Average Output Power	maximum <240 μW exiting the system
Objective Lens Options	(a) Canon EF 200 mm f/2.8L II USM (b) Canon EF 500 mm f/4 IS USM
Range	Scans performed at 40 and 325 metres
Beam Scanning Mechanism	Galvanometer controlled mirrors (X&Y) common to transmit and receive channels
Spectral Filters in Detection Channel	Two band-pass filters with a central wavelength of 842.5 nm and a bandwidth of 2 nm (FWHM) by Omega Optical
Fibre Options in Receive-channel (Rx)	(a) 10 μm core diameter fibre with 9 mm diameter stainless steel armouring (Alker) (b) 25 μm core diameter fibre with standard 3 mm diameter furcation jacket, FC/APC connector on both ends (c) 50 μm core diameter fibre with 6.1 mm diameter stainless steel tubing and black plastic sheath (Thorlabs) (d) 50 μm core diameter fibre with 9 mm diameter stainless steel armouring (Alker) Fibres (b) and (c) were jacketed with black heat-shrink material for the measurements.
Detector	PDM series silicon Single Photon Avalanche Diodes (SPAD) by Micro Photon Devices: • ~10% SPDE at λ ~ 840 nm with 50 μm diameter active area • A fast gating operation gates the detector by simply applying an external TTL signal with a frequency of 19.5 MHz and gate on width of 20 ns from a Pulse Pattern Generator (PPG)

Data Acquisition Module Option	(a) PicoHarp 300 by PicoQuant • 16 ps timing bin width • Synchronisation rate of 1.95 MHz for Channel0 in PicoHarp 300: To avoid any problem due to the long dead time of the electronics (typically 90 ns), a signal with a synchronisation frequency of 19.5 MHz is down divided to 1.95 MHz with a factor of 10 by using a constant fraction discriminator (CFD) hardware module. • Data acquisition in T2 mode • System Temporal Response (jitter): ~96 ps FWHM (b) HydraHarp 400 by PicoQuant. • 2 ps timing bin width • Synchronisation rate of ~19.5 MHz for "Sync in" channel on HydraHarp 400: To avoid any problem due to the long dead time of the electronics (Typically 80 ns), a signal with a synchronisation frequency of 19.5 MHz is reduced using an internal sync divider of 8 of the HydraHarp 400. • Data acquisition in T3 mode • System Temporal Response (jitter): ~60 ps FWHM

Table 7-1 Summary of key system parameters

7.3 LiDAR-waveform-based low photon count depth imaging

7.3.1 Photon count extraction from time-tagged raw data

A scan centred on a life-size polystyrene head with 142×142 pixels (covering an area of 285×285 mm at the scene seen in Figure 7-4) was carried out using the depth imager operating in T2 mode with per-pixel acquisition time of 30 ms at λ=842 nm. Note that an objective lens with a focal length of 500 mm in the transceiver system and 10 μm core diameter fibre in its receive channel were used in the depth imager.

The acquisition time per pixel of 30 ms was implemented between two scan markers. A marker is inserted in the time-tagging data recording whenever the scanning galvo mirrors are advanced to a new pixel position. For example, as shown in Figure 7-5, Marker 1 and Marker 2 correspond to two positions of the scan mirror for Pixel no.1 and no.2. The time difference (i.e. marker period) between Marker 1 and Marker 2 was 30 ms. This means that the depth imager stared at the target associated with Pixel no.1 for 30 ms in order to record photon count events. The pink bullets denote example photon count events. As the time tags were recorded in T2 mode of PicoHarp 300, pixel-wise photon counts can be extracted in terms of different acquisition times within a marker period. For example, a new algorithm [7.5] was evaluated for acquisition times of 0.06, 0.3, 0.6, 3, 6 and 30 ms, which were measured from the start of the marker (see Figure 7-5).

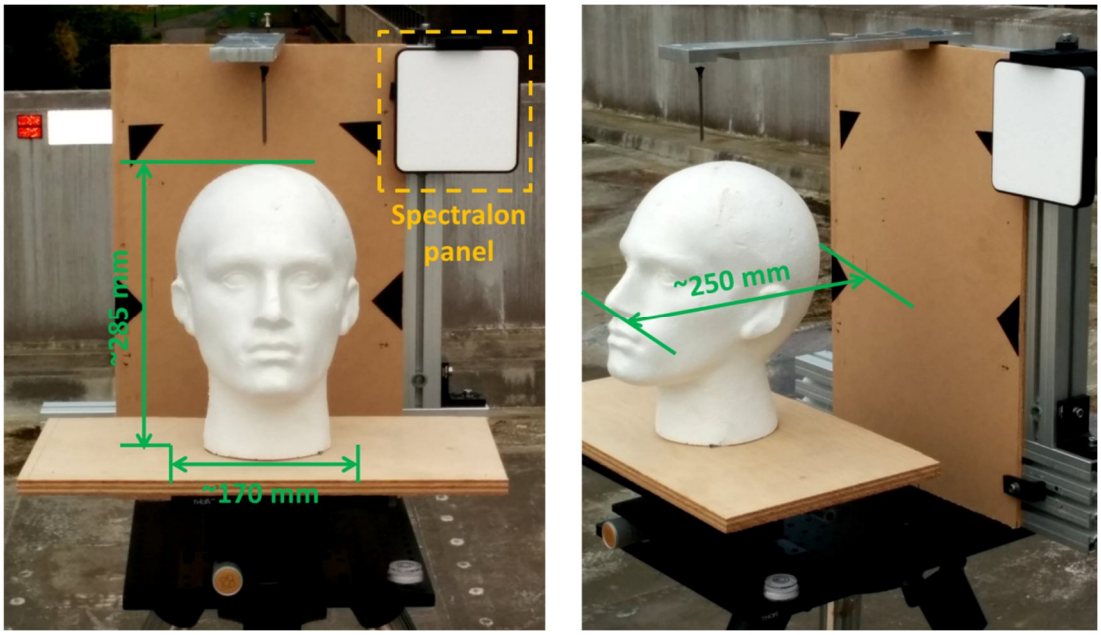

Figure 7-4 Photographs in two views show the setup used for the measurements on a life-size polystyrene head (170 mm × 285 mm × 250 mm in W×H×D when viewed from the front) at a stand-off distance of 40 metres. The face of the polystyrene head was pointing towards the scanning transceiver system housed in the roof lab and a flat Medium Density Fibreboard (MDF) sheet mounted behind the head target acted as a backplane. In addition, a Spectralon panel, used as the calibration target, was mounted on the top right corner of the backplane.

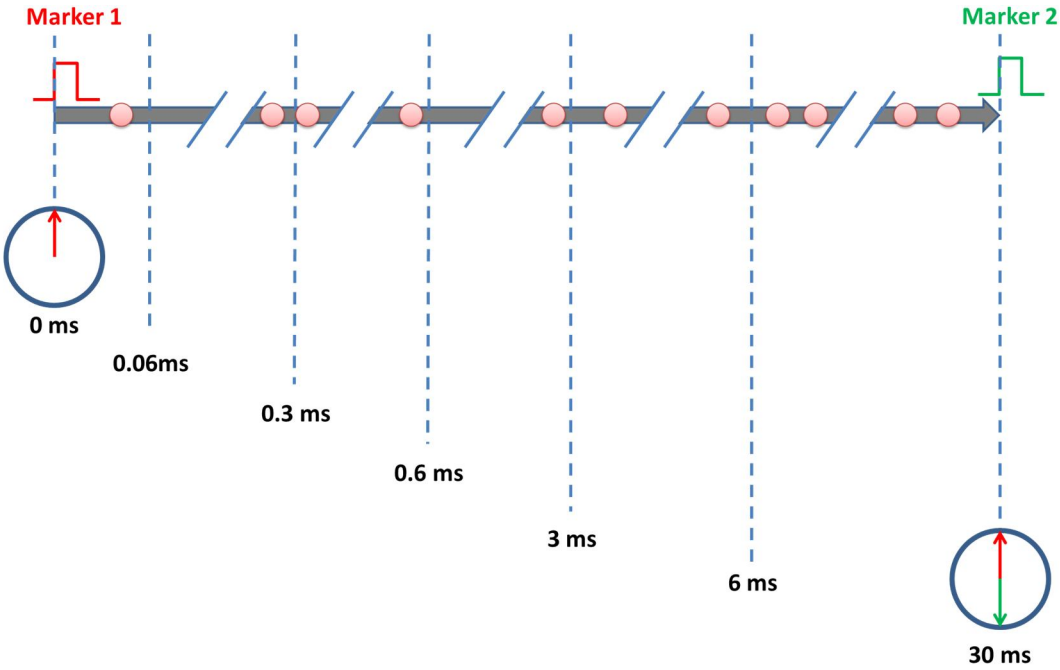

Figure 7-5 Illustration of photon count extraction with different acquisition times from pixel-wise time-tagged raw data. As Marker 1 was inserted in the time-tagging data recording when the scanning galvo mirrors were advanced to Pixel no.1, the time-tagged raw data for photon count extraction is for this specified pixel.

Table 7-2 provides details of the amount of recorded photons when the acquisition time was varied. The average number of recorded photons per pixel drops from ~420 for the acquisition time of 30 ms to as low as ~0.8 photons for an acquisition time of 0.06 ms, as the number of recorded photons decreases linearly with exposure time of the depth imager. As seen in Table 7-2, a large proportion of pixels (48.7%) do not contain any photon counts (i.e. empty pixels) for a per-pixel acquisition time of 0.06 ms.

Acquisition time (ms)	30	6	3	0.6	0.3	0.06
Average photon counts per pixel	418.6	83.7	42.0	8.4	4.2	0.8
Empty pixels (%)	0	0	≥ 0.1	1.7	7.5	48.7

Table 7-2 Average number of recorded photons per pixel and proportion of empty pixels as a function of the acquisition time. (Reproduced from [7.5]).

7.3.2 Reconstruction results

A new Bayesian model was proposed for LiDAR-waveform-based, low photon count imaging of single-layered targets (or non-distributed targets) [7.5]. In the Bayesian framework, prior distributions were assigned to the unknown target depths and intensity to account for the intrinsic correlations between neighbouring pixels (i.e. spatial correlations). There is an assumption of the laser beam associated with a given pixel, which hits a single surface. An adaptive Markov chain Monte Carlo (MCMC) method was then developed to estimate unknown parameters of the model, thus relieving users from setting these parameters by cross-validation. According to the depth and intensity reconstructions of the life-size polystyrene head at a stand-off distance of 40 m (see Figure 7-6 and Figure 7-7), the proposed model and method were validated using real LiDAR data. The proposed method has advantages over the pixel-wise cross-correlation method used when the number of recorded photons was low (see Figure 7-8). Note that the pixel-wise cross-correlation method is a standard pointwise maximum likelihood method. It considers the cross-correlation between the pixel-wise accumulated photon timing histogram (e.g. the one shown in Figure 7-2(b)) and the normalised temporal response of the system (e.g. the one shown in inset of Figure 7-2(b)).

(1) Figure 7-6(a) compares the estimated depth maps obtained by the proposed algorithm and pixel-wise cross-correlation method. These results show that for a long acquisition time per pixel (e.g. 30 ms acquisition time per pixel), both methods provide similar results. However, when the acquisition time per pixel decreases, the pixel-wise

cross-correlation method starts to fail in identifying the target positions, especially in pixels where no photon is detected. The results with 0.6, 0.3 and 0.06 ms acquisition times per pixel with fewer than 10 average photons per pixel indicate that the proposed method is more robust in the absence of signal in some pixels. In particular, the depth estimations associated with 0.6 and 0.3 ms acquisition times per pixel present superior reconstructions of the polystyrene head.

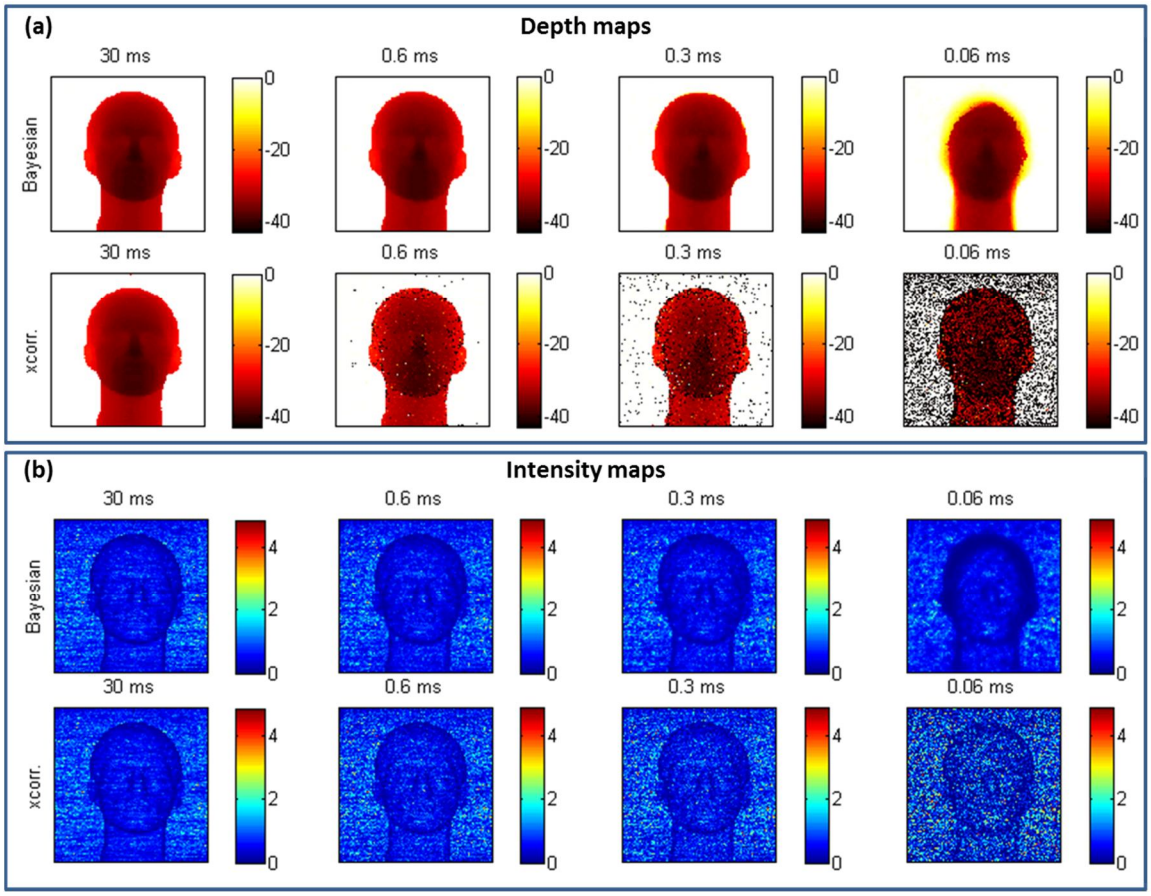

Figure 7-6 (a) Depth maps with 142×142 pixels for the life-size polystyrene head at a stand-off distance of 40 m and for different per-pixel acquisition times, estimated by the proposed Bayesian algorithm (top) and the pixel-wise cross-correlation method (bottom). Distances shown are in centimetres and the reference distance is the distance of the backplane. Black pixels correspond to pixels where no photons are recorded and for which the pixel-wise cross-correlation method cannot identify the target distance. (b) Intensity maps for the life-size polystyrene head at a stand-off distance of 40 m and for different per-pixel acquisition times, estimated by the proposed Bayesian algorithm (top) and the pixel-wise cross-correlation method (bottom).

As for the result with a 0.06 ms acquisition time per pixel, anomalies of the depth reconstruction occur around the head, thus blurring its shape. This is because far fewer

or even no scattered photons return from the sharp edges due to the illuminating beam striking the material at glancing angles in comparison to the portion of the head that features smoothly varying surfaces and the flat backplane. Thus, due to the significant contrast in photon counts between the backplane and the head edges, the depth estimation around the head cannot have high confidence, even when using the proposed method.

(2) Figure 7-6(b) compares the estimated intensity maps obtained through both methods. These results show that both methods provide similar results for the long acquisition times per pixel and that the proposed method is more robust in the lack/absence of detected photons. In particular, for an acquisition time per pixel of 0.06 ms, few photons are detected in the pixels around the head, resulting in an average of fewer than one detected photon per pixel. Here, the proposed algorithm provides a smoother intensity image due to consideration of spatial correlations, in comparison with the pixel-wise cross-correlation method, which process the pixels independently.

(3) Figure 7-7 compares the depth/intensity estimation results obtained by both methods for an acquisition time per pixel of 0.3 ms. It has an average photon count per pixel of 4.2. As shown in Figure 7-7(a), a huge amount of pixels on the target cannot be locked on using the pixel-wise cross-correlation method. By contrast, Figure 7-7(b) illustrates the ability of the proposed model to handle low photon returns using the spatial correlation of the depths and intensities.

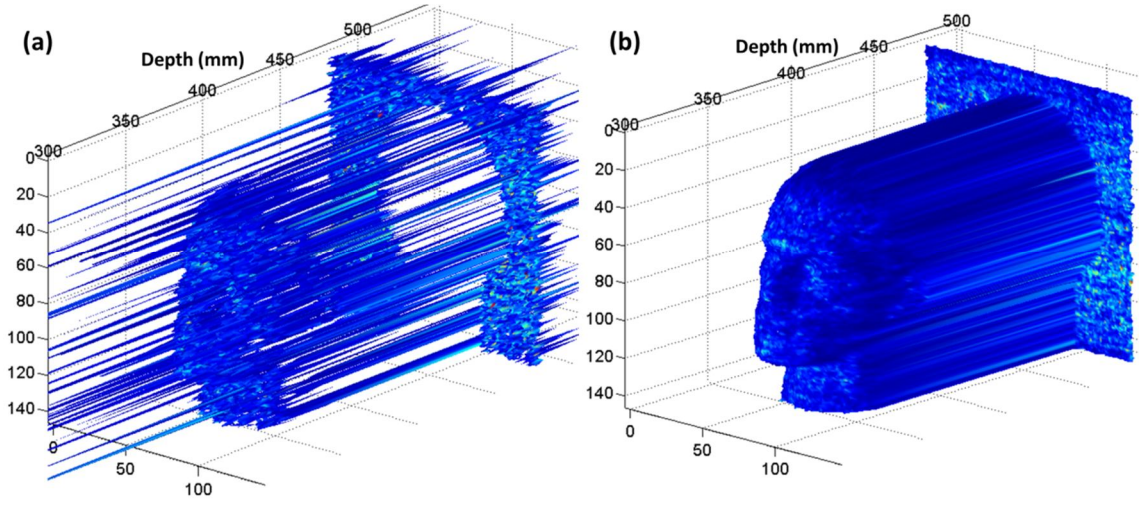

Figure 7-7 Depth/intensity reconstruction with 142×142 pixels of the target, estimated by the pixel-wise cross-correlation method (a) and the proposed Bayesian algorithm (b) for the per-pixel acquisition time of 0.3 ms. The colours represent the target intensity (dark blue for low intensity coefficients).

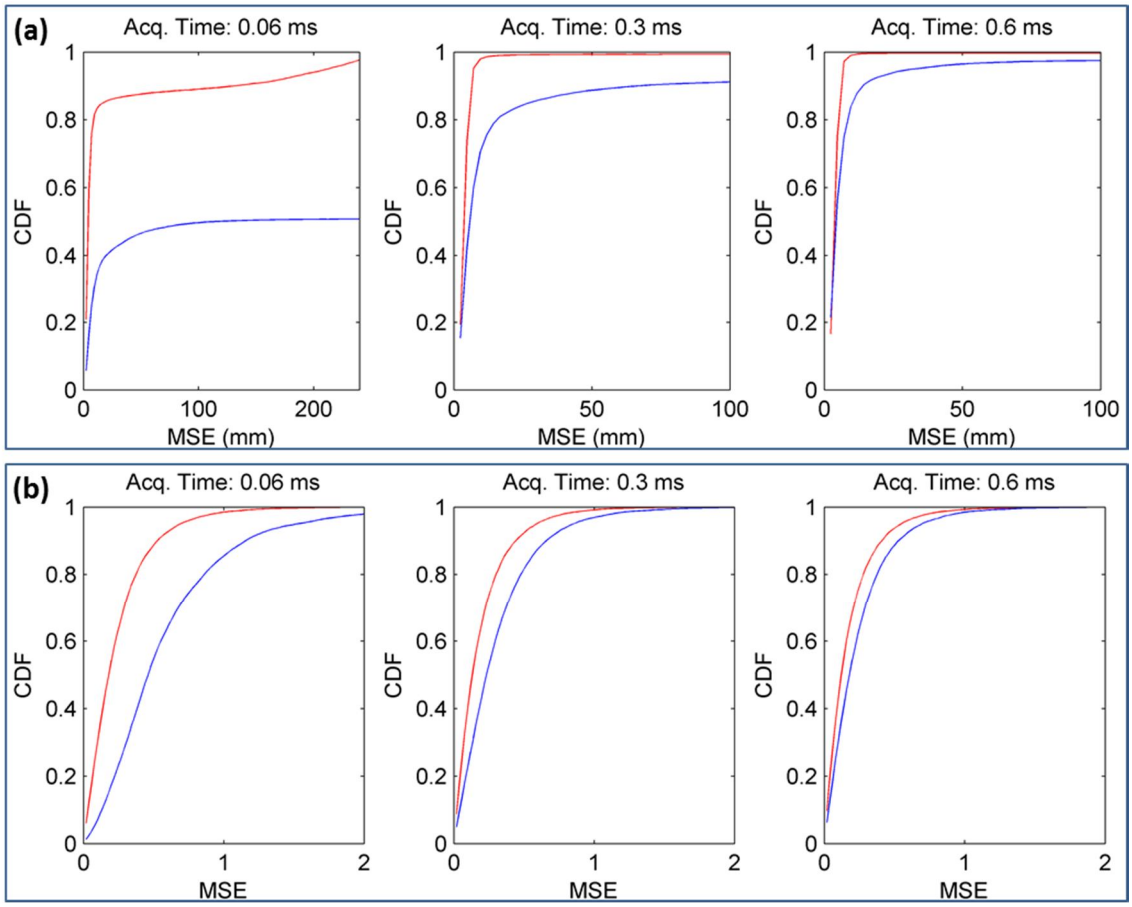

Figure 7-8 Depth (a) and intensity (b) cumulative density functions (CDFs) of mean squared errors (MSEs) provided by the proposed Bayesian algorithm (red) and the pixel-wise cross-correlation method (blue) for the life-size polystyrene head at a stand-off distance of 40 m. Note that the MSEs were calculated by comparing the depth and intensity estimations associated with different per-pixel acquisition times (e.g. 0.06, 0.3 and 0.6 ms) to the depth and intensity ground truths. The ground truths correspond to the values, which were estimated by the pixel-wise cross-correlation method for the longest acquisition time (30 ms).

(4) The performance of the proposed Bayesian algorithm and the pixel-wise cross-correlation method can be quantitatively evaluated using the cumulative density functions (CDFs) of the depth and intensity mean squared errors (MSEs), as shown in Figure 7-8. Note that the MSEs were calculated by comparing the depth and intensity estimations associated with different acquisition times (e.g. 0.06, 0.3 and 0.6 ms) to the depth and intensity ground truths. The ground truths correspond to the values, which were estimated by the pixel-wise cross-correlation method for the longest acquisition time (30 ms). Figure 7-8 shows that the proposed method is more robust than the standard method (i.e. pixel-wise cross-correlation method) when the acquisition time is reduced and provides more consistent estimated results. More specifically, by taking

into account a fixed MSE value (e.g. 50 mm in Figure 7-8(a) or 0.5 in Figure 7-8(b)) the CDF values (for different acquisition times) for the proposed method are higher than the values for the pixel-wise cross-correlation method. This means that higher proportion of pixels having estimation errors that are less than or equal to the given value can be locked on the target for the results estimated using the proposed method. This also highlights the ability of the proposed method to process pixels for which no photons are detected as the CDFs are upper constrained by the proportion of pixels, which can be processed by each method.

7.4 Characterisation of refractive-turbulence-induced scintillation

7.4.1 Laser beam scintillation

Laser beam scintillation can be represented by the intensity (or photon counts) fluctuation of the laser beam primarily due to refractive turbulence induced by thermal and air flow variations in the atmosphere. When a laser beam propagates through the atmosphere, laser beam scintillation will occur, even over a short propagation path (e.g. 10's metres). Laser beam scintillation is particularly evident for horizontal propagation path above the ground, when effects can occur at heights of less than 10 metres (refer to Page 5-10 of [7.10]). The scintillation index (SI) can be applied to characterise the intensity fluctuation (refer to Page 67 of [7.10]):

$$\sigma_I^2 = \frac{< I(t)^2 > - < I(t) >^2}{< I(t) >^2} \qquad \text{Equation (7.1)}$$

where $I(t)$ and $< I(t) >$ denote the instantaneous laser intensity and the relevant temporal average.

As for the weak intensity fluctuation, the scintillation index can be described by Rytov approximation for a plane wave (refer to Page 67 of [7.10]):

$$\sigma_I^2 = 1.23 C_n^2 k^{7/6} L^{11/6} \qquad \text{Equation (7.2)}$$

where C_n^2 is the refractive-index structure parameter, $k = 2\pi/\lambda$ and λ is the wavelength of interest, and L is the distance of the laser beam propagation path. Therefore, a longer propagation path corresponds to a higher degree of laser beam scintillation. As C_n^2 represents the atmospheric refractive turbulence, it is dependent on the temporal atmospheric conditions (see Figure 7-9(a)), the altitude of the laser beam propagation

path as well as wind speed (see Figure 7-9(b)). Hence, these factors all affect the scintillation index.

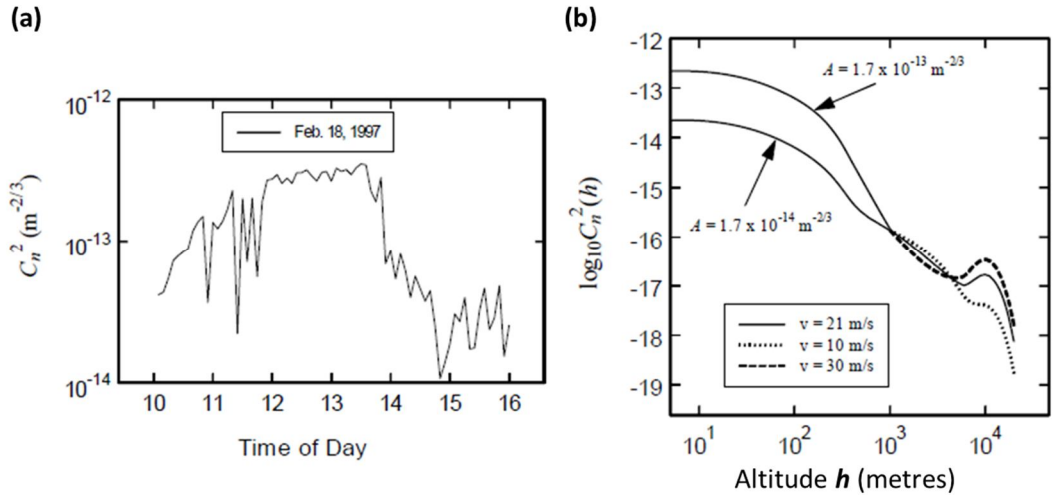

Figure 7-9 (a) Typical C_n^2 for the horizontal propagation laser beam above ground with 1.5 m over six hours of the day on the 18th February 1997 in central Florida, USA during the winter season. (Reproduced from Page 9 of [7.10]). (b) Plots of typical average C_n^2 for the horizontal propagation laser beam versus altitude. Note that h is the altitude, v is the root mean square wind speed, and A is the nominal $C_n^2(0)$ on the ground. (Reproduced from Page 10 of [7.10]).

The laser beam from the active imaging systems (e.g. the scanning depth imagers schematically shown in Figure 7-1) is affected by the refractive turbulence during field trials. Therefore, the centroid trace of the instantaneous beam spots is randomly wandering on the plane of a receiver aperture, as illustrated in Figure 7-10. The variation of beam wander ($< r^2 >$) can be described as (refer to Page 30 of [7.10]):

$$\sqrt{< r^2 >} = \sqrt{r_e^2 - r_0^2} \qquad \text{Equation (7.3)}$$

where r_0 denotes the radius of the instantaneous beam spot and r_e denotes the effective radius of the long-term average beam spot.

For example, the beam wander inspection at a stand-off distance of 325 m is shown in Figure 7-11. Although the illuminating beam was at λ=632 nm, not the illumination wavelength (~840 nm), for the scanning depth imagers shown in Figure 7-1, this still provides a good indication on how was the beam wandering over long distance propagation. The spatial variation of the beam wander on the target can be approximated as (refer to Page 31 of [7.10]):

$$< r^2 > = 2.87 C_n^2 L^3 r_0^{-1/3}$$ Equation (7.4)

It should be noted that the temporal variation of the beam wander is approximately inversely proportional to its time constant (τ_w) which is on the order of the ratio of the beam spot size (with a diameter of $2r_e$) to the wind speed (v_w) of the day (refer to Page 29 of [7.10]):

$$\tau_w \propto 2r_e / v_w$$ Equation (7.5)

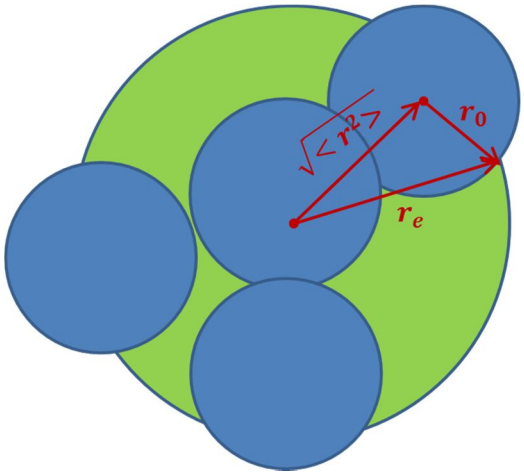

Figure 7-10 Illustration of beam wander described by $< r^2 >$. Note that blue solid circle represents the instantaneous beam spot with a radius of r_0 and green solid circle is for the long-term average beam spot with an effective radius of r_e. (After Page 30 of [7.10]).

Figure 7-11 Four time-elapsed frames recorded four instantaneous beam spots (left to right). Note that approximately 1 s was elapsed between these four frames. They are extracted from the video recorded with 29 frames per second (i.e. the frame exposure time was 34.5 ms) of beam wander investigation at a stand-off distance of 325 m for an illuminating laser beam at λ=632 nm.

The effective beam diameter (i.e. $D_e = 2r_e$) of the long-term average beam spot associated with the beam wander was characterised. This was carried out using the

depth imager described in Figure 7-1(b). The target setup, with two separated plates along the line-of-sight of the imager (see Figure 7-12), was scanned at a stand-off distance of 325 m. The intensity maps are shown in Figure 7-13 and the resultant intensity profile shown in Figure 7-14(a) or (b) clearly reveal the region where two return peaks occur as the scanning beam spot covers two plates simultaneously. In a qualitative sense, as it can be seen from the highlighted boxes in Figure 7-14(a) and (b), D_e associated with the f=500 mm objective is larger than the one associated with the f=200 mm objective.

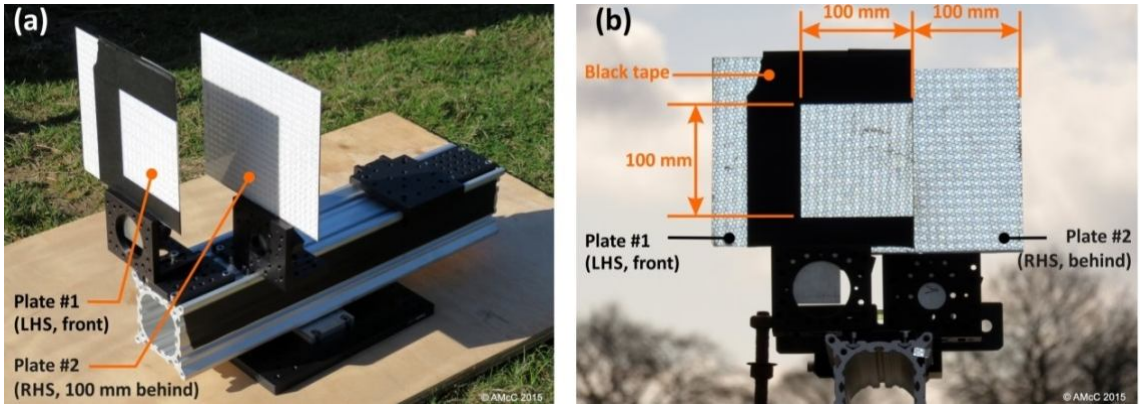

Figure 7-12 Target setup at a stand-off distance of 325 m used to characterise the effective beam diameter of the long-term average beam spot. The image in (a) is annotated to highlight two separated plates in the setup. Plate #1 (closer to the system) was at the left hand side of the transceiver system in the rooftop lab and in front of Plate #2. Plate #2 was 100 mm behind Plate #1 and at the right hand side of the system. The image in (b), annotated with dimensions, shows the setup as viewed from the approximate line-of-sight of the transceiver system. Within a scan area of ~240 mm×~120 mm, a central area of 200 mm×100 mm was covered with white retro-reflective material (high intensity prismatic grade, Avery Dennison T6500 HIP).

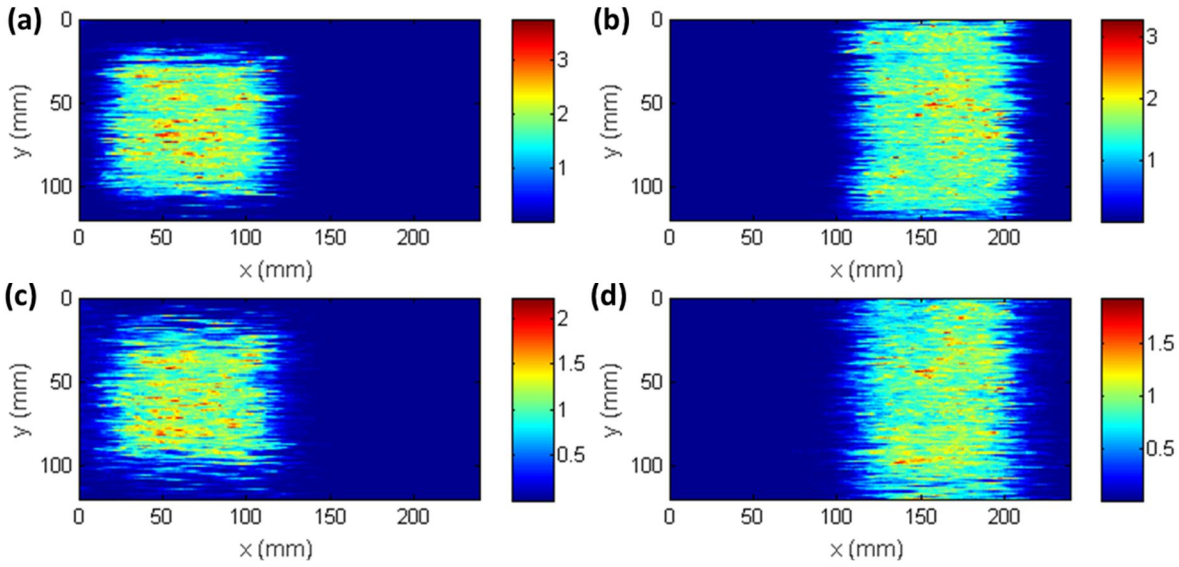

Figure 7-13 Intensity maps obtained by the raster scans of 240×120 pixels that covers an area of 240 mm×120 mm and with a per pixel acquisition time of 1 ms. (a) and (b) show the maps associated with Plate #1 and #2 (shown in Figure 7-12) respectively using a f=500 mm objective lens in the depth imager and when the focal beam spot was on Plate #2 for implementation the raster scans. (c) and (d) show the maps associated with Plate #1 and #2 respectively using a f=200 mm objective lens in the depth imager and when the beam spot was focussed appropriately on Plate #2 for the raster scans.

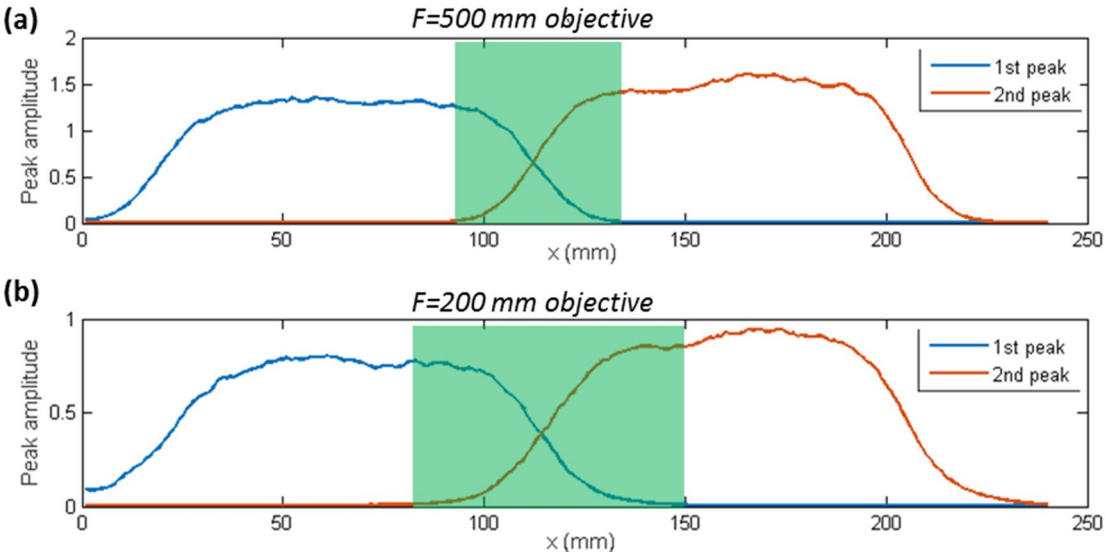

Figure 7-14 The profiles of peak amplitude versus length in X. They were obtained by averaging the rows of the images shown in Figure 7-13. In terms of the plots in (a) for the f=500 mm objective lens that was employed in the imager, the blue curve for 1st peak and the red curve for 2nd peak correspond to Plate #1 in Figure 7-13(a) and Plate #2 in Figure 7-13(b) respectively. In terms of the plots in (b), for the f=200 mm objective lens that was employed in the imager, the blue curve for 1st peak and the red curve for 2nd peak correspond to Plate #1 in Figure 7-13(c) and Plate #2 in Figure 7-13(d) respectively. The boxes in green highlight a region where two return peaks occur as the scanning beam spot covers two plates simultaneously.

In a quantitative sense, as the core diameter of the input fibre (FD7, NKT Photonics, Demark) was slightly larger than 5 μm, it was magnified by ~1.7 via the optics in the transmit channel of the transceiver onto the object plane of the objective lens. When the system was aligned and focused on the target at a stand-off distance of 325 m using the f=500 mm or f=200 mm objective lens, the relevant focused beam spot had a diameter of ~12 mm or ~30 mm respectively. Thus, for the target distance of 325 m, this corresponds to the beam spot with r_0 =~6 mm for the f =500 mm objective and r_0=~15 mm for the f=200 mm objective. Given $C_n^2 = 1.7 \times 10^{-13} m^{-2/3}$, r_e can be

predicted using Equation (7.3) and Equation (7.4). The values were calculated to be ~11 mm for the f=500 mm objective lens and ~17 mm for the f=200 mm objective lens. The measured beam diameters were ~23 mm and ~28 mm associated with the f=500 mm and f=200 mm objective lenses respectively. Note that the measured beam diameters were estimated by considering the averaged differences in X between 10% and 90% of the maximum amplitudes on the falling edge for the 1st return peak (or the rising edge for the 2nd return peak) shown in Figure 7-14. Therefore, it has a reasonably good agreement between the predicted and measured values in terms of the effective beam diameter of the long-term average beam spot associated with the beam wander. In addition, according to Equation (7.5), the estimated time constants of the beam wander for the f=500 mm and f=200 mm objective lenses were in the range of 1 ms to 10 ms depending on the wind speed at a stand-off distance of 325 m. It is worth pointing out that the minimum acquisition time per pixel for the raster scan is constrained by the time constant of the significant beam wander. This is because if the beam wander is significant and the acquisition time is too short (shorter than the time constant of the beam wander), it is impossible to determine where the sensor is staring or sampling. Only the average area associated with multiple scan pixels is known. Thus, it is more of challenge to obtain the optimum spatial resolution.

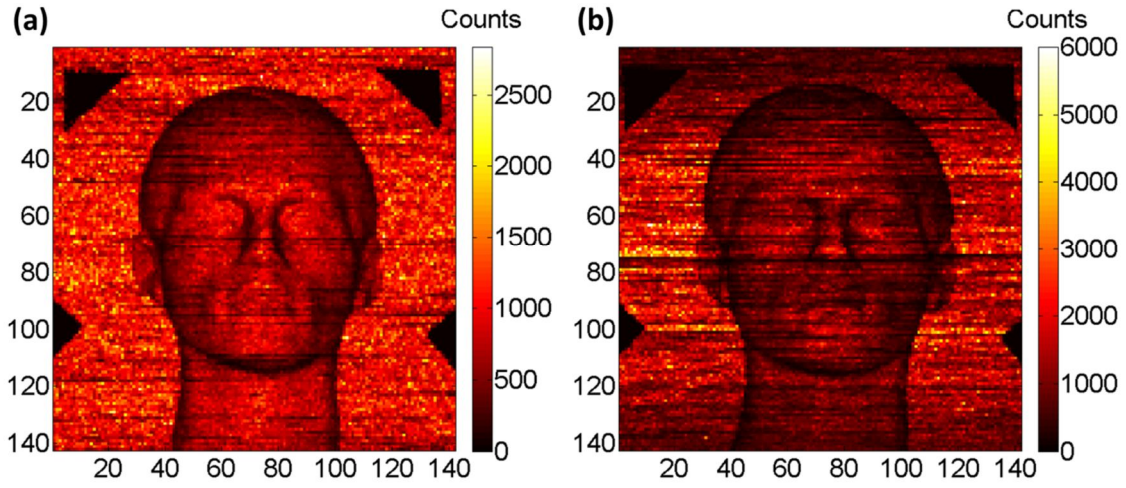

Figure 7-15 Photon count maps with 142×142 pixel of a life-size polystyrene head at a stand-off distance of 40 metres. They were estimated (using pixel-wise cross-correlation method) from the data, with a per pixel acquisition time of 20 ms, by the depth imaging systems using objective lenses. This included a focal length of 200 mm (a) and 500 mm (b) combined with a 10 μm core diameter fibre in the receive channel. Note that the face of the polystyrene head was pointing towards the scanning transceiver system housed in the roof lab with a flat MDF sheet mounted behind the head target acting as a backplane.

There is another important aspect of the scintillation effect for TCSPC measurements in terms of the double-pass laser beam of the transceiver. As shown in Figure 7-15, two photon count maps at a stand-off distance of 40 m were acquired using the data of the raster-scan measurements on a life-size polystyrene head. A 10 µm core diameter fibre was used in the receive channel. Objective lenses with a focal length of 200 mm and 500 mm were used for the scans. The focussed beam spots incident on the target had diameters of ~2.5 mm and ~1 mm respectively. Although the latter had a smaller focussed spot for the scans, its temporal variation of beam wander was greater and the scintillation of photon counts was more significant. Thus, this resulted in the presence of more distorted dark rows in the photon count map. This can be verified by investigating the pixel-wise photon counts on the flat backplane. The surface normal of the backplane was approximately parallel to the line-of-sight of the transceiver. The backplane is relatively flat and thus should provide returns that are more consistent in comparison to the head, which presents a much greater variation in the surface normal and thus high reflectivity variations. It should also provide a quantifiable and repeatable basis for characterisation of the laser beam scintillation. As shown in Figure 7-16, the scintillation index associated with the objective lens with a focal length of 500 mm is 22.46% but only 8.59% for the objective lens with a focal length of 200 mm. Again, using a f=500 mm objective lens indicates higher photon counts scintillation.

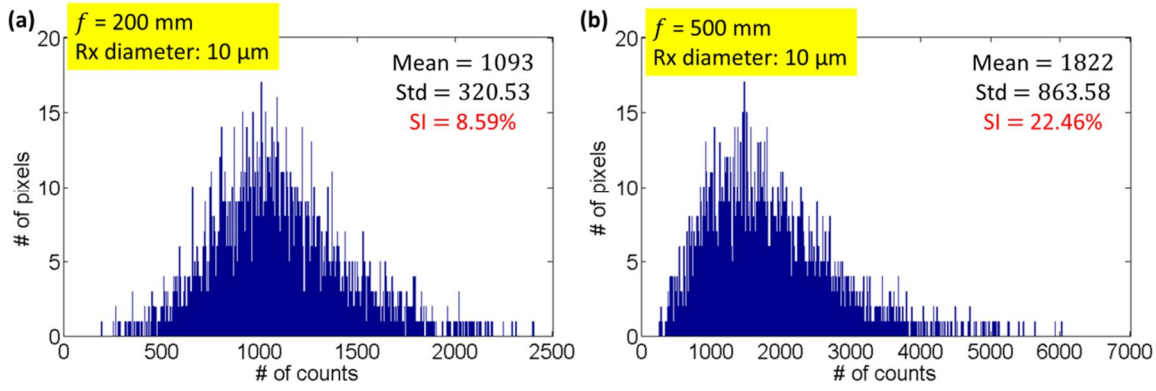

Figure 7-16 Photon counts of 2800 pixels on the backplane (i.e. a flat MDF sheet) were investigated. The photon counts were extracted from the photon counts maps shown in Figure 7-15. (a) and (b) show the histograms of number of pixels versus number of counts for two different objective lenses with focal lengths of 200 mm and 500 mm, respectively. Note that Rx: receiver; Mean: mean of counts; Std: standard derivation of counts; SI: scintillation index (estimated using Equation (7.1)).

Higher photon counts scintillation could incur detection that is more anomalous.

Hence, it is necessary to properly design the system and select the appropriate components in order to minimise the scintillation effects. Doing so will enable high quality depth imaging using e.g. spatial-correlation-based algorithms [7.5, 7.11].

7.4.2 Photon count scintillation at the receiver

As studied in [7.12-7.14], atmospheric turbulence can have a significant impact on the distribution of the recorded photons, in particular for long-range depth imaging on targets. Single-pixel scintillation measurements were carried out using the TCSPC-based depth imager shown in Figure 7-1(b). The central field of view of the transceiver was aligned to a flat panel covered with white retro-reflective material (high intensity prismatic grade, Avery Dennison T6500 HIP) at a stand-off distance of 325 m in daylight. The imager in conjunction with different combinations of objective lens (200 & 500 mm focal lengths) and receive-channel optical fibre (core diameters of 10, 25, & 50 µm) was investigated. The boxes highlighted in red in Figure 7-17 indicate the objective lens and the receive-channel optical fibre in the setup.

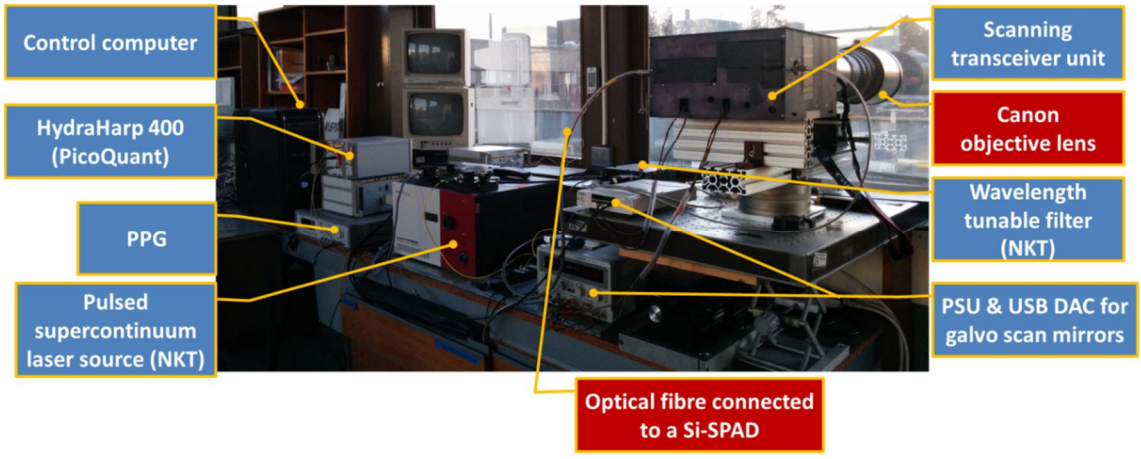

Figure 7-17 Photograph shows the key hardware components of the time-of-flight system at λ=843 nm in the roof laboratory during field trials.

The receive fibre was used to deliver light from the receive channel of the transceiver to the single-photon detector. The single-pixel scintillation measurement using individual lens-fibre combination was fast tracking by means of 100,000 sampling frames with per-frame sampling time of 1 ms. Figure 7-18 shows the variation of the scattered return photon counts, primarily due to atmosphere turbulence, as a function of time. The probability density functions (PDFs) of temporal photon counts for various lens-fibre combinations are shown in Figure 7-19 and Figure 7-20. The standard derivation and mean of the time-variable counts for each combination of objective lens and

receive-channel optical fibre are summarised in Table 7-3. Note that by using Equation (7.1) the scintillation index values can be worked out and can be used to characterise the scintillation effect on the photon counts. Signal-to-background ratio of each measurement is also shown in Table 7-3. Assuming that the atmospheric conditions (e.g. temperature, humidity, and wind speed) were relatively constant during the measurements, the different lens-fibre configurations can be compared in terms of the results in Table 7-3.

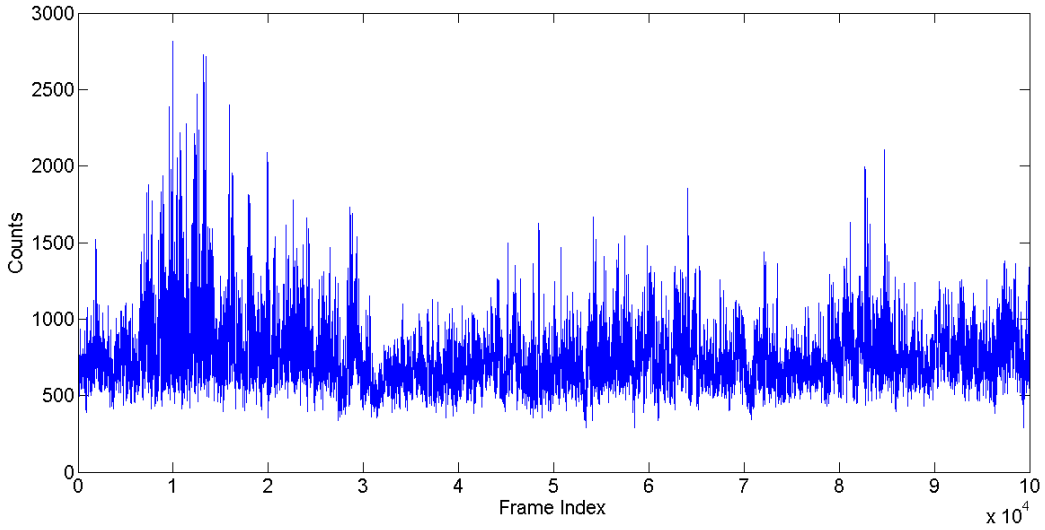

Figure 7-18 An example of a single-pixel scintillation measurement was carried out with the transceiver "staring" at the same point on the retro-reflective target board at a stand-off distance of 325 m for 100 s. The example plot above shows the counts versus frame number for the raw data from 100,000 frames recorded at 1 ms per frame. Note that frame-wise counts are obtained by accumulating 1-ms-acquisition-time counts of all timing bins.

As aperture averaging can lower the receive signal fluctuation [7.15], the effective receive aperture with larger diameter (i.e. larger core diameter for the receive fibre) is preferable to reduce the scintillation index of recorded photon counts as shown in the fourth column of Table 7-3, Figure 7-19 and Figure 7-20 for both lenses. As shown in Table 7-3, the target return peak (see the fifth column) and background counts (see the sixth column) are higher for the receive fibre with larger core diameter, but resulted in lower SBRs in bright daylight conditions (see the seventh column). In terms of each objective lens combined with different core diameter fibres in the receive channel, the configurations with a 50 µm core diameter fibre offer better photon count detection performance. This is inferred by comparing the decline rate of photon count scintillations to the decline rate of the SBRs with increasing fibre core diameter. In

terms of the spatial resolution between these different configurations, the f=500 mm objective lens can provide a smaller effective focussed beam spot for the raster scan even when taking the beam wander in to consideration. Hence, they are preferable to the f=200 mm objective lens when a higher spatial resolution is sought after.

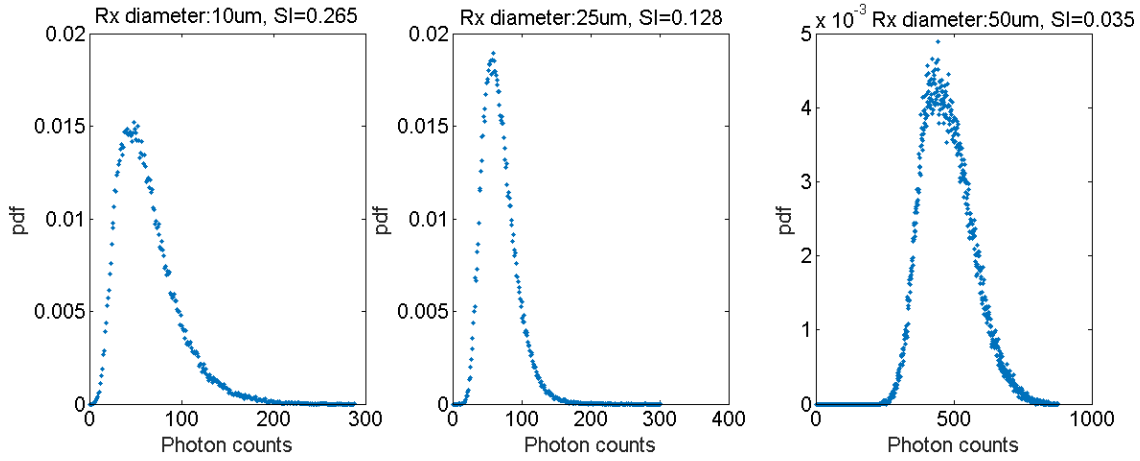

Figure 7-19 Probability density functions (PDFs) of temporal photon counts (in blue circle) observed using the 200 mm focal length Canon objective lens as the transceiver objective lens, and three different receive-channel optical fibres with core diameters of 10 (left), 25(middle), & 50 μm(right). The estimated scintillation indexes (SIs) (see Table 7-3) by Equation (7.1).

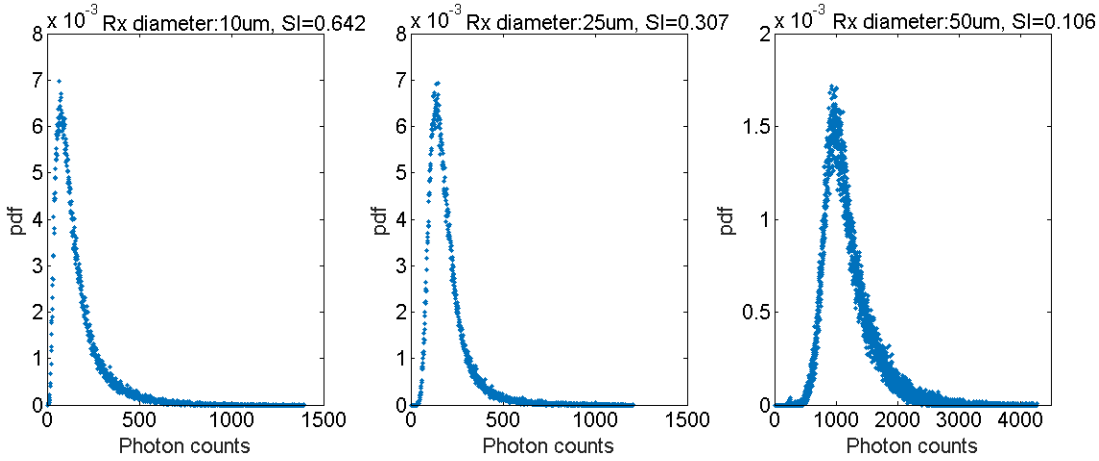

Figure 7-20 Probability density functions (PDFs) of temporal photon counts (in blue circle) observed using the 500 mm focal length Canon objective lens as the transceiver objective lens, and three different receive-channel optical fibres with core diameters of 10 (left), 25(middle), & 50 μm(right). The estimated scintillation indexes (SIs) (see Table 7-3) by Equation (7.1).

200 mm focal length Canon objective lens							
Rx fibre core diameter	**Std**	**Mean**	**SI**	**Peak counts**	**Background counts/bin**	**SBR**	**Record time**
10 µm	32.5	63.2	0.265	130834	22	5966.3	15:36hrs
25 µm	24.3	67.7	0.128	135900	36	3743.6	15:51hrs
50 µm	91.5	477.4	0.035	897630	233	3860.4	16:10hrs
500 mm focal length Canon objective lens							
Rx fibre core diameter	**Std**	**Mean**	**SI**	**Peak counts**	**Background counts/bin**	**SBR**	**Record time**
10 µm	124.0	154.8	0.642	326545	41	7886.0	15:24hrs
25 µm	107.0	193.2	0.307	406211	69	5870.0	14:54hrs
50 µm	382.4	1175.9	0.106	2247539	555	4050.3	14:15hrs

Table 7-3 Results of scintillation measurements made on a target board at a stand-off distance of 325 m in daylight on 27th February 2015. Std: standard derivation; SI: scintillation index (estimated by Equation (7.1)); SBR: signal to background ratio; Rx: receive channel.

To further assess the spatial resolution of the various configurations of the f=500 mm objective lens combined with different fibres, a black and white circular sector star printed on paper was used as the spatial resolution target. Spatial resolution values of ~10 mm, ~12 mm and ~14 mm for the receive fibres with 10 µm, 25 µm and 50 µm core diameters respectively can be obtained with high confidence from the estimated photon count maps of the target at a stand-off distance of 325 m (see Figure 7-21). This verifies that a combination of the f=500 mm objective lens and the receive fibre with 50 µm core diameter is among the best of the configurations investigated. This lens-fibre combination can provide moderate scintillation index, signal-to-background ratio and spatial resolution.

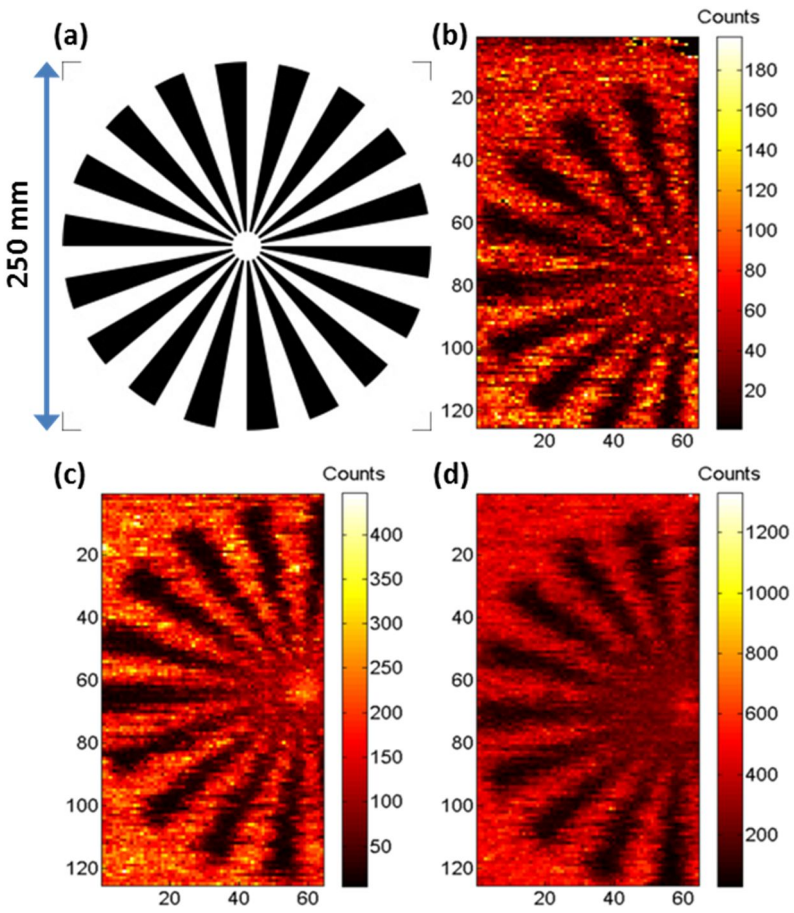

Figure 7-21 (a) A black and white circular sector star target printed on paper used as a spatial resolution target. It has 18 equal bar and space pairs, 20° per cycle, 10° per spoke. Its outer diameter is 250 mm and its centre circle diameter is 20 mm. Photon count maps were estimated using the pixel-wise cross-correlation method from the scans with 64×125 pixels on the spatial resolution target (see (a)) mounted on a plywood board at a stand-off distance of 325 m. The scans covered an area of approximately 125 mm × 250 mm in XY and a per-pixel acquisition time of 100 ms was used. Combinations of a Canon objective lens with a focal length of 500 mm and a receive channel optical fibre having a core diameter of 10 µm (b), 25 µm (c), and 50 µm (d) were investigated and their background level were 160, 417 and 8970 cps respectively.

7.4.3 Depth profiling using a scintillation-reduced configuration

Field trial measurements made using the LiDAR system with an objective lens with a focal length of 500 mm and an 50 µm core diameter receive fibre were carried out at a stand-off distance of 325 m. Note that the target setup was similar to the one shown in Figure 7-4. The target was raster scanned with 200×200 pixels and an acquisition time per pixel of 30 ms covering an area of 300 mm×300 mm. The resultant depth/photon count maps as well as a depth plot are shown in Figure 7-22 with an estimated

scintillation index of ~0.009. The ears, eyes and nose of the polystyrene head are apparent even at such a long working distance. Even though the photon count map shown in in Figure 7-22(b) was acquired at longer working distance, it has significantly fewer distorted rows, in comparison to the results shown in Figure 7-15(b), and thus represents less photon counts scintillation. It means that the combination of the f=500 mm objective lens and the 50 μm core diameter receive fibre can significantly reduce the refractive-turbulence-induced scintillation for photon counting, thus being preferable when looking to achieve high-quality long range depth imaging.

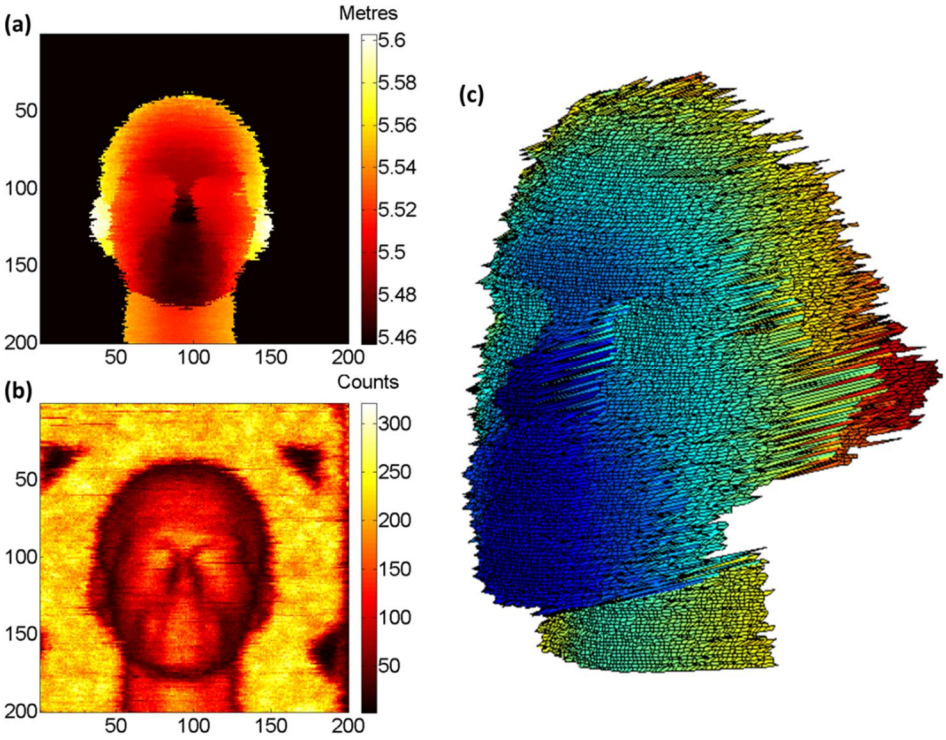

Figure 7-22 The 200×200 pixel with acquisition time per pixel of 30 ms depth map (a) and photon-count map (b) as well as depth plot (c) of the polystyrene head at a stand-off distance of 325 m. The depth map is estimated by the pixel-wise cross-correlation method. The photon-count map is formed by summing up photon counts within 31 timing bins of the histogram peak for each pixel.

7.5 Assessment of depth and spatial resolutions

The instrumental response and timing bin width of the TCSPC-based time-of-flight depth imaging system will represent a temporal characterisation of the system, but the time resolution, and depth resolution will not be wholly dependent on these factors. This will also depend on the number of photons in the return, and the background noise. In addition, there is potential to have increased precision (better than the electrical timing jitter or bin width) of the peak position determination using advanced peak-finder algorithms to process photon data with moderate SNR. The spatial resolution of the system will be affected by a number of factors. These include the focal lengths of the lenses and the core diameter of the received fibre [7.2]. However, effects such as optical aberrations, and scintillation effects due to atmospheric turbulence are likely to have a large influence on the measured spatial resolution. Even assuming that the beam intensity distribution is Gaussian, it is still challenging to directly assess the system spatial resolution without any direct characterisation measurements.

To the best of my knowledge, there is not a standardised target for assessing both depth and spatial resolutions of depth imaging systems to date. Hence, a custom-designed target was 3D-printed and employed to evaluate depth and spatial resolving capabilities of our raster-scan-based time-of-flight single-photon depth imagers. The design of the custom resolution target is based on the formation of arrays of pillars and holes. In terms of the array of pillars or holes: (1) Each radial line contains a set of nine pillars all with the same height but with varying diameter. As shown in Figure 7-23, the diameters start at 2 mm and increase by a factor of $\sqrt{2}$, up to 32 mm. Six radial lines have been included for pillar heights of 1, 2, 4, 8, 16, & 32 mm; (2) A set of six holes have the same arrangement as in (1). As shown in Figure 7-23, the diameters also start at 2 mm and increase by a factor of $\sqrt{2}$, up to 11.31 mm. Six radial lines have been included for hole depths of 0.25, 0.5, 1, 2, 4, & 8 mm. This custom resolution target, as a non-cooperative target, is compatible with on-demand assessments of depth and spatial resolution for the scanning depth imagers with moderate working distances and without prior knowledge of the focal beam spot size.

In order to investigate the capability of the imager to resolve the depth and spatial resolutions, the field trial measurements on the custom resolution target were carried out using the depth imager system shown schematically in Figure 7-1(b). An objective lens with a focal length of 500 mm and a receive fibre with a core diameter of 50 μm were

used in the imager. For the measurements, the custom-designed resolution target was placed at stand-off distances of 40 metres (see Figure 7-24(a)) and 325 metres (Figure 7-24(a) and (b)). The resolution target pointed towards the scanning transceiver system housed in the roof lab.

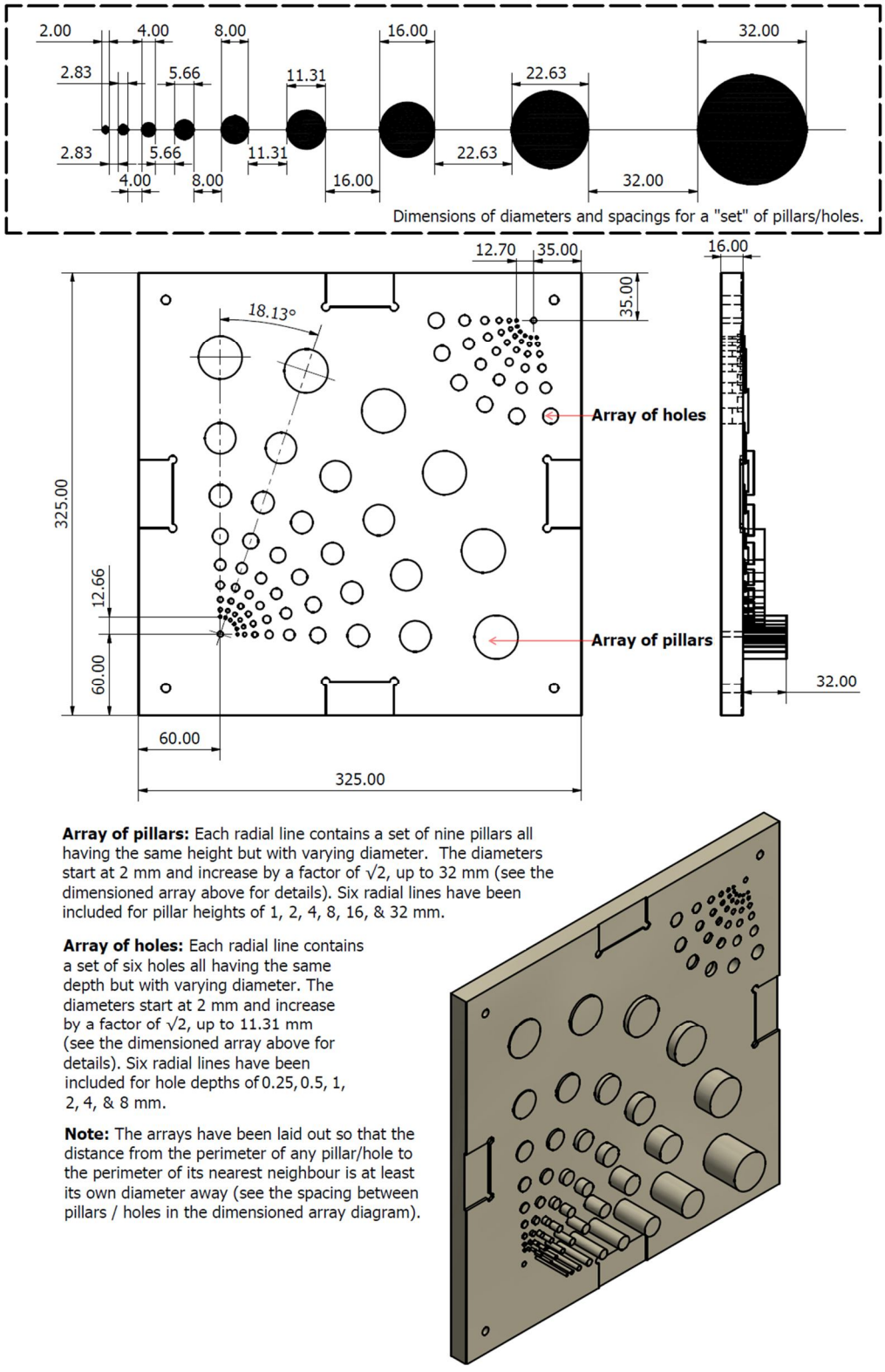

Figure 7-23 Dimensions in mm of a custom-designed resolution target. It consists of arrays of pillars and holes.

For the results estimated using the pixel-wise cross-correlation method at a stand-off distance of 40 m, it is evident that the following features of the target can be resolved:

(1) hole depths as shallow as 0.25 mm, see top right of Figure 7-24(b) and (c);

(2) hole and pillar diameter of 2 mm (the minimum diameter included on the target), see Figure 7-24(b).

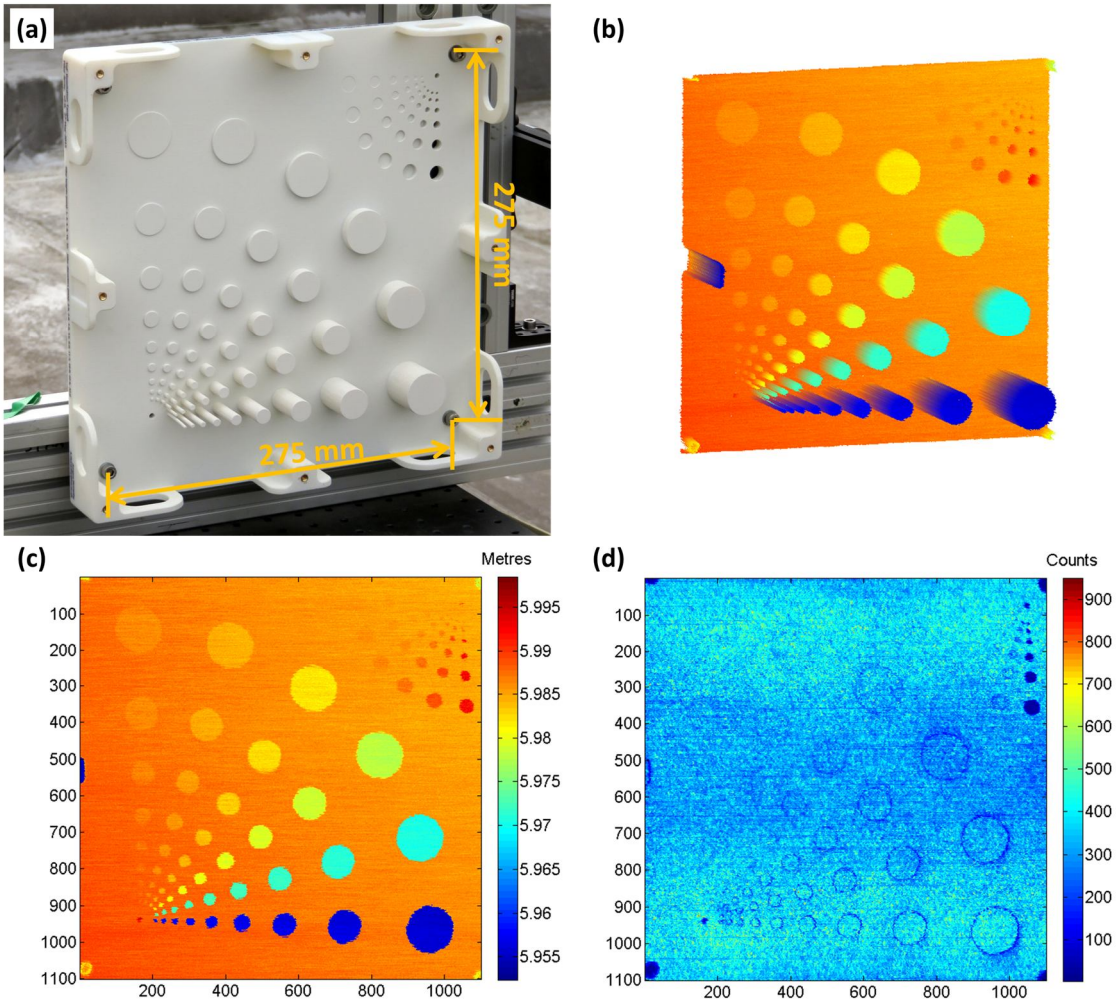

Figure 7-24 (a) shows the close-up photograph of the custom resolution target at a stand-off distance of 40 metres. The scan area was 275 mm × 275 mm. (b) shows the estimated depth plot of the target with the same pixel number and acquisition time per pixel as (c) and (d) showing the 1100×1100 pixel estimated depth and photon counts maps respectively with 1 ms per pixel acquisition time. All the maps and plots were estimated by the pixel-wise cross-correlation method.

At a stand-off distance of 325 m, some of the 16 mm diameter pillars can be clearly outlined as shown in Figure 7-25(c) using the pixel-wise cross-correlation method. Some of the pillars with a height of 1 mm can also be resolved (see Figure 7-25(c) and (e)). Therefore, it is evident that the system is easily capable of millimetre-scale depth

resolution measurements at stand-off distances of up to 300 metres. In addition, the resolved spatial resolutions have good agreement to the nominal focussed beam diameters of ~1 mm and ~12 mm at stand-off distances of 40 and 325 m respectively using an objective lens with a focal length of 500 mm.

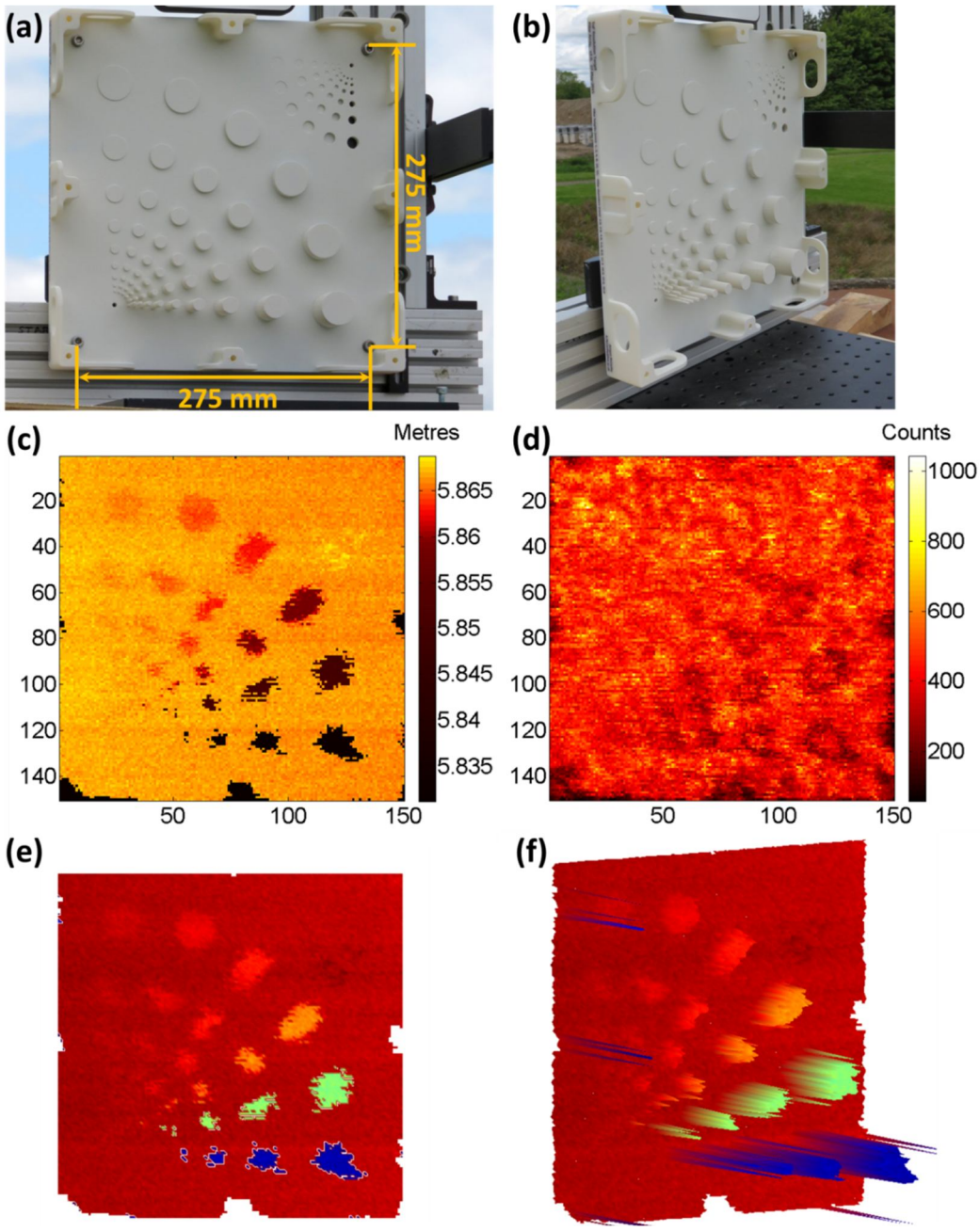

Figure 7-25 (a) and (b) show the close-up photographs with two different views of the custom resolution target at a stand-off distance of 325 metres. The scan area was 275 mm × 275 mm. (c) and (d) show the 150×150 pixel estimated depth and photon counts maps respectively with 100 ms per pixel acquisition time. (e) and (f) show two different views of the depth plots of the target. All of the maps and plots were estimated using the pixel-wise cross-correlation method.

7.6 Conclusions

A number of characterisation measurements using an improved design of the raster-scan single-photon depth imagers have been carried out to investigate the systems' temporal and spatial characterisation. By using the time-tagged LiDAR waveform data, photon events exacted with pre-determined acquisition time can be employed to estimate depth images of the remote targets. The proposed Bayesian-model-based algorithm using spatial correlations offers improved estimations of depth and intensity in comparison to the pixel-wise cross-correlation method. This is especially true in the case of sparse photon data.

The refractive-turbulence-induced photon count scintillation can be estimated using high-speed TCSPC-based tracking measurements. Scintillation estimates were made using different optical configurations to reduce the effect of turbulence on measurements. A depth and spatial resolution 3D target was custom-designed. It was used to assess system performance at stand-off distances of 40 and 325 metres. Depth profiles of the custom-designed resolution target with millimetre-scale depth and spatial resolutions were estimated at a high confidence level, even when using the pixel-wise cross-correlation method. Also, the targets will be used for the performance estimation of a range of new data processing algorithms using spatial correlations [7.11].

The author along with Dr. Aongus McCarthy (AMcC) developed the imaging systems and carried out all the field trials. Dr. Robert J. Collins gave advice on the upgrade of the custom scan control and data acquisition software for the system. The author, with assistance from Dr. Nathan R. Gemmell, updated the custom software. The author solely programed Matlab scripts to process the measurement data and obtain majority of the results presented in this Chapter. In section 7.3, with the help of the explanation information provided by the author, Dr. Yoann Altmann (YA) in Prof. Steve McLaughlin's group processed the data using his proposed algorithm with prior distributions. The information of the relevant prior distributions was from the discussions with AMcC and the author. In section 7.4, the author, with assistance from AMcC and YA, devised the scintillation monitoring technique and processed the data. In section 7.5, AMcC with Dr. Kirmani Ahmed (MIT, USA) and the author designed the resolution target. Prof. Gerald S. Buller supervised all of the work in this Chapter.

7.7 References

[7.1]. M. F. Duarte, M. A. Davenport, D. Takhar, J. N. Laska, T. Sun, K. E. Kelly, and R. G. Baraniuk, "Single-pixel imaging via compressive sampling," IEEE Signal Process Mag. (25), 83 (2008).

[7.2]. A. McCarthy, R. J. Collins, N. J. Krichel, V. Fernandez, A. M. Wallace, and G. S. Buller, "Long-range time-of-flight scanning sensor based on high-speed time-correlated single-photon counting," Appl. Opt. (48), 6241-6251 (2009).

[7.3]. PerkinElmer (now Excelitas Technologies Corp.), "SPCM-AQR(Single Photon Counting Module).Datasheet. online (http://www.excelitas.com/Downloads/DTS_SPCM-AQRH.pdf) last accessed 16-04-2015," (Canada, 2014).

[7.4]. Micro Photon Devices Italy, "MPD PDM series. Datasheet. online (http://www.micro-photon-devices.com/Docs/Datasheet/PDM.pdf) last accessed 20-02-2015."

[7.5]. Y. Altmann, X. Ren, A. McCarthy, G. S. Buller, and S. McLaughlin, "Lidar waveform based analysis of depth images constructed using sparse single-photon data," arXiv preprint arXiv:1507.02511 (2015).

[7.6]. M. Wahl, H.-J. Rahn, I. Gregor, R. Erdmann, and J. Enderlein, "Dead-time optimized time-correlated photon counting instrument with synchronized, independent timing channels," Rev. Sci. Instrum. (78), 033106 (2007).

[7.7]. M. Wahl, "Modern TCSPC electronics: principles and acquisition modes," Springer Series on Fluorescence (2014).

[7.8]. "PicoHarp 300 User's Manual and Technical Data," PicoQuant GmbH, Ver (2.3).

[7.9]. "HydraHarp 400 User's Manual and Technical Data," PicoQuant GmbH, Ver (3.0).

[7.10]. L. C. Andrews, R. L. Phillips, and C. Y. Hopen, *Laser beam scintillation with applications* (SPIE press, 2001).

[7.11]. A. Kirmani, D. Venkatraman, D. Shin, A. Colaço, F. N. Wong, J. H. Shapiro, and V. K. Goyal, "First-Photon Imaging," Science (343), 58-61 (2014).

[7.12]. P. W. Milonni, J. H. Carter, C. G. Peterson, and R. J. Hughes, "Effects of propagation through atmospheric turbulence on photon statistics," Journal of Optics B:

Quantum and Semiclassical Optics (6), S742 (2004).

[7.13]. I. Capraro, A. Tomaello, A. Dall'Arche, F. Gerlin, R. Ursin, G. Vallone, and P. Villoresi, "Impact of turbulence in long range quantum and classical communications," Phys. Rev. Lett. (109), 200502 (2012).

[7.14]. M. Henriksson, and L. Sjöqvist, "Scintillation index measurement using time-correlated single-photon counting laser radar," Opt. Eng. (53), 081902-081902 (2014).

[7.15]. J. H. Churnside, "Aperture averaging of optical scintillations in the turbulent atmosphere," Appl. Opt. (30), 1982-1994 (1991).

Chapter 8
Conclusions and outlook

8.1 Conclusions

Light Detection and Ranging (LiDAR) systems are powerful tools in remote sensing applications to profile the illuminated remote objects. These systems can also resolve physical properties of reflections along the light beam propagation path at variable working distances. When sensitive optical detection schemes are employed in LiDAR systems, for example when using single-photon detectors, lower power laser sources and smaller receiver apertures can be used. In turn, this can reduce the size of the illumination source and system objective, making the whole instrument more compact. Alternatively, increased range with potentially lower average optical power levels can also be achieved. With appropriate single-photon detection, the added advantage of improved surface-to-surface resolution can be realised.

In this Thesis, several time-of-flight (TOF) scanning depth imagers with a monostatic transceiver configuration were demonstrated. They were based on the Time-Correlated Single-Photon Counting (TCSPC) technique using modern pulsed laser sources and recently developed single photon detectors. These imagers were all LiDAR-based imaging systems using a custom transceiver unit with a pair of galvanometric mirrors for scanning. The output pulsed laser light was raster scanned over the remote object of interest and the single-photon detector were used to detect the back-scattered photons. These systems were capable of operating in bright daylight as excellent filtering approaches were adopted to significantly reduce the background light at their receivers.

In Chapter 4, two kilometre-range TOF scanning depth imaging systems were demonstrated. One used a Superconducting Nanowire Single Photon Detector (SNSPD) with low noise and excellent timing jitter performance at λ=1560 nm. The other used an InGaAs/InP Single Photon Avalanche Diode (SPAD) detection module at λ=1550 nm.

Both scanning depth imagers used an average output laser power of less than 1 mW. This facilitated the acquisition of depth profile images on non-cooperative targets in bright daylight with millimetre-scale depth resolution up to kilometre ranges, far beyond the capabilities of other current single-photon approaches at such ranges. These results demonstrated the flexibility of the TCSPC technique in negotiating the trade-offs between depth resolution, data acquisition times and optical power. High-performance SNSPDs typically operate at ultra-low temperatures (e.g. the NbTiN SNSPD employed in the former system at a temperature of less than 4 K). Nevertheless, if the detection sub-system plays a crucial role in the whole system for on-demand applications (e.g. ground-based LiDAR imaging system), its relatively large dimensions and high power consumption are not prohibitive factors. The field trial results based on the latter system pointed the way towards the practical implementation of an eye-safe, 1550 nm wavelength depth imaging system with realistic potential of compact construction and low-power operation (optical and electrical). This is therefore compatible with a number of remote 3D imaging applications, including those using mobile platforms.

In Chapter 5, a TOF depth imager was developed using a Diffractive Optical Element (DOE) to generate structured illumination to match an arrayed 32×32 CMOS Si-SPAD detector array. The detector was a High-Voltage Complementary Metal Oxide Semiconductor (HV-CMOS) SPAD array fabricated using 0.350 μm CMOS technology. The system was galvo-scanned and evaluated for long-range depth profiling using an average output laser power of less than 100 μW at λ=817 nm. It facilitated the acquisition of depth images with up to 128×64 pixels using short exposure times (<300 ms per entire 32×32 array) at stand-off distances of 45 and 325 metres.

By using the flip-chip bonding technique with micron-scale lens-to-chip placement error (typically ~1 to 5 μm), both refractive and diffractive microlens arrays were successfully integrated with front-illuminated HV-CMOS Si-SPAD arrays. These SPAD detector arrays were constructed with a fill factor of only 3.14%. The bonded assemblies of SPAD and diffractive microlens arrays were fully characterised using a telecentric imaging system with uniform field illumination. The improvement factors (up to 15) for fill-factor recovery were reported. To the best of my knowledge, they were the highest values of fill factor across an entire working SPAD array reported.

In Chapter 6, we developed a novel multispectral LiDAR system based on a broadband pulsed supercontinuum laser source and the TCSPC receiver technology designed

specifically to recover structural and physiological parameters from tree samples. This provided illumination containing output light at four wavelengths simultaneously (i.e. at λ=531, 570, 670 and ~780 nm) on the target. A wavelength routing system with four channel de-multiplexing capability was designed and used for the high-speed TCSPC measurements. A Nordmann fir tree sample was raster scanned using the system at stand-off distances of 40 and 325 metres. Full waveform data at four wavelengths was extracted to resolve the Normalised Differential Vegetation Index (NDVI) and Photochemical Reflectance Index (PRI) values of the remotely characterised tree sample. The NDVI depth profile measured by the system was consistent with laboratory reflectance measurements taken using a spectrometer of samples selected from the same Nordmann fir tree. These results indicate that multispectral LiDAR system is a promising means to achieve the remote recovery of structural and physiological parameters along tree profile non-destructively with high efficiency.

In Chapter 7, two TCSPC-based TOF scanning depth imaging systems at λ ~ 840 nm were developed using data acquisition modules in two different Time-Tagged-Time-Resolved modes (T2 and T3 modes) – i.e. PicoHarp 300 in T2 mode with a 16 ps timing bin and HydraHarp 400 in T3 mode with a 2 ps timing bin. By the use of time-tagged LiDAR waveform data recorded by the system in T2 mode, photon events acquired with a pre-determined acquisition time can be employed for depth image measurements. In comparison to the pixel-wise cross-correlation method, much improved estimations on depth and intensity were achieved by the use of a Bayesian-model-based algorithm using spatial correlations. This was particularly true for sparse photon data, where the average photon count per pixel was less the one. The refractive-turbulence-induced photon count scintillation was estimated using high-speed TCSPC-based tracking measurements by the system in T3 mode. As this system had excellent timing jitter performance (i.e. ~60 ps), sub-centimetre depth and spatial resolution for depth imaging at working distances of 40 and 325 metres were resolved on the custom-designed resolution target using the routine pixel-wise cross-correlation method. As a whole, the temporal and spatial characterisation of the scanning TOF single-photon depth imaging systems using illumination at λ ~ 840 nm was investigated. The relevant characterised results can have a better understanding of the system performance and aid selection of optimum system configuration. In addition, they can be used for further data analysis algorithms and to refine the system.

8.2 Outlook

The future research directions of the TCSPC-based long-range TOF depth imaging techniques will focus particularly on improving the data measurement time. This includes hardware advances to reduce jitter, increase single-photon detection efficiency and the design of optical systems with improved filtering of background light levels. One approach that has shown potential for significant reductions in measurement times is the emergence of novel algorithms using spatial correlations to reconstruct images from sparse photon data.

In fact, the systems with different configurations and functions developed in this Thesis are all excellent prototypes for the future implementation of hardware approaches with higher performance. In this scenario, the hardware improvement and the refinement of these systems might be an area of immediate attention. For example, there is potential to improve the systems described in Chapter 4 at λ~1550 nm by the employment of faster single photon detectors with lower noise and higher system detection efficiency, which have been recently developed. They include the new generation SNSPD [8.1] and the high-performance InGaAs/InP SPAD devices [8.2]. As for the high-speed depth imager incorporated a free space coupled detector array device (i.e. HV-CMOS 32×32 Si-SPAD array) in Chapter 5, appropriate filtering approaches are necessarily required for shielding the receiver from background noise in order to increase the detection SNR. The arrayed detection system described in Chapter 5 can also allow the detection with increased SNR based on the structured illumination with higher power by the use of DOEs with increased transmission efficiency, in conjunction with more powerful and narrower linewidth laser sources. In order to establish the multispectral depth imaging system with highly efficient multiple single-photon detection channels simultaneously, the transceiver can be re-designed with higher transmission optics and refine the wavelength routing system. This latter refinement can be achieved by shortening diffraction optical paths and using fibres with larger core diameters in the detection channel.

The fields of single-photon imaging and computational imaging techniques start to work together [8.3-8.6] to investigate sparse-photon-based depth imaging. Ongoing work in this area will be to optimise signal and image processing algorithms for the reconstruction of higher-quality depth images with, on average, fewer than one detected photon per pixel from the time-tagged time-resolved raw photon data. This is particularly important for the free space depth profiling on targets at very long distances

(i.e. >1 km) and might be extended to sparse single photon depth imaging in turbid media, e.g. underwater depth imaging.

Overall, the integration of improved optical and electronic hardware with advanced bespoke image processing approaches can facilitate significant improvements in the overall performance of TCSPC-based long-range TOF depth imaging techniques and widen the scope of the emerging imaging application areas.

8.3 References

[8.1]. F. Marsili, V. Verma, J. Stern, S. Harrington, A. Lita, T. Gerrits, I. Vayshenker, B. Baek, M. Shaw, and R. Mirin, "Detecting single infrared photons with 93% system efficiency," Nat. Photonics (7), 210-214 (2013).

[8.2]. X. Jiang, M. A. Itzler, K. O'Donnell, M. Entwistle, M. Owens, K. Slomkowski, and S. Rangwala, "InP-based Single Photon Detectors and Geiger mode APD Arrays for Quantum Communications Applications," IEEE J. Select. Topics Quantum Electron. (2015).

[8.3]. A. Kirmani, D. Venkatraman, D. Shin, A. Colaço, F. N. Wong, J. H. Shapiro, and V. K. Goyal, "First-Photon Imaging," Science (343), 58-61 (2014).

[8.4]. Y. Altmann, X. Ren, A. McCarthy, G. S. Buller, and S. McLaughlin, "Lidar waveform based analysis of depth images constructed using sparse single-photon data," arXiv preprint arXiv:1507.02511 (2015).

[8.5]. D. Shin, J. H. Shapiro, and V. K. Goyal, "Single-Photon Depth Imaging Using a Union-of-Subspaces Model," arXiv preprint arXiv:1507.06985 (2015).

[8.6]. D. Shin, A. Kirmani, V. K. Goyal, and J. H. Shapiro, "Photon-Efficient Computational 3D and Reflectivity Imaging with Single-Photon Detectors," arXiv preprint arXiv:1406.1761 (2014).